Kuo-Tsong Yu
Xigang Yuan

Introduction to Computational Mass Transfer

With Applications to Chemical Engineering

Springer

Heat and Mass Transfer

Series editors

Dieter Mewes, Hannover, Germany
Franz Mayinger, Mayinger, Germany

Kuo-Tsong Yu · Xigang Yuan

Introduction to Computational Mass Transfer

With Applications to Chemical Engineering

Springer

Kuo-Tsong Yu
Xigang Yuan
School of Chemical Engineering
and Technology
Tianjin University
Tianjin
People's Republic of China

Preface

With the rapid development and continuing advances of computer technologies and numerical computation, many new multidisciplinary research areas have emerged, including computational chemistry, computational physics, computational biology, and others. It is recognized that computational methodology has now became one of the three basic methodologies of conducting scientific and engineering research, along with theoretical investigation and experimental studies.

In the 1970s, the cross-disciplinary studies of fluid dynamics and numerical computation had led to the new research area of computational fluid-dynamics (CFD). This multidisciplinary development later on extended to heat transfer; and consequently the field of computational heat transfer (CHT), or numerical heat transfer (NHT) was introduced. The establishment of these two new research areas has helped scientists and engineers solve many difficult problems, such as the prediction of flow and heat transfer behaviors in engineering design and applications.

Nevertheless, what chemical engineers deal with includes not only fluid flows and heat transfer, but also mass transfer and chemical reactions. The detailed information of mass transfer, especially the concentration distribution, is essential to the design and the assessment of chemical equipment as it serves as the basis in evaluating the process effectiveness or efficiency. The conventional approach to predict the concentration field is by the empirical method which is not only unreliable but also lacking of theoretical foundation. Thus a rigorous method for accurate predictions needs to be investigated.

Mass transfer processes are complicated, usually involving turbulent flow, heat transfer, multiple phases, chemical reactions, unsteady operation, as well as the influences from internal construction of the equipment and many other factors. To study such complicated system, we propose a novel scientific computing framework in which all the relevant equations on mass transfer, fluid-dynamics, heat transfer, chemical reactions, and all other influencing factors are involved and solved numerically. This is the main task and research methodology of computational mass transfer (CMT).

Moreover, all mass transfer processes involve the diffusion through the interface between adjacent phases. Interfacial effects, such as the Marangoni convection and the Rayleigh convection, cannot be ignored. Therefore, the study of interfacial effects is another important aspect of CMT.

In recent years, we explored in this new area on the closure of the differential turbulent mass transfer equation by proposing the two-equation $\overline{c'^2} - \varepsilon_{c'}$ model and the Reynolds mass flux (fluctuating mass flux) $\overline{u_i'c}$ model. Our approach has been successfully applied to various chemical processes and equipments, including distillation, absorption, adsorption and catalytic reaction. The interfacial behaviors of mass transfer were also studied extensively by both simulations and experiments.

This book is chiefly based on our published research work and graduate dissertations in the area of CMT. The purpose of writing this book is firstly to serve as a text book for the graduate course titled "Introduction to the Computational Mass Transfer", offered in the School of Chemical Engineering and Technology of Tianjin University; and secondly as a reference book for those who are interested in this area.

The contents of this book can be divided into two parts. The first part, *Process Computation*, involves the prediction of concentration, velocity and temperature distributions in chemical engineering equipment. The second part, *Interface Computation*, concerns the prediction of interfacial effect on mass transfer behaviors.

The first two chapters of this book, which serve as the preparatory materials on computational methodology, cover the fundamentals of CFD and CHT. Chapters 3–7 discuss the process computation of various gas–liquid contacting and catalytic reaction processes and equipments in chemical engineering. Chapters 8 and 9 introduce the computation of Marangoni and Rayleigh convections and their influence on mass transfer by using differential equations and the lattice-Boltzmann method.

We warmly welcome any suggestions, discussions, and criticism on this book.

September 2013   Kuo-Tsong Yu
                                                                                          Xigang Yuan

Contents

Chapter 1
Related Field (I): Fundamentals of Computational Fluid Dynamics

Abstract Computational fluid dynamics (CFD) is the basic methodology used extensively in engineering works and also accompanied with the computational mass transfer (CMT) method as presented in this book. In this chapter, the Reynolds averaging method in CFD for turbulent flow is summarized as a preparatory material on computational methodology in this book. Emphasis is made on developing approaches to the closure of the time-averaged Navier–Stokes equations by modeling the second-order covariant term in the equations. Two modeling methods are described in detail: the k-ε method, which is a widely adopted two-equation model for engineering applications, and the Reynolds stress modeling method, in which the covariant term is modeled and computed directly. The k-ε method is easy to apply but its weakness is that an isotropic eddy viscosity must be adopted and may result in discrepancy when applying to the case of anisotropic flow. The Reynolds stress method needs more computational work, but it is anisotropic and rigorous. For reducing the computing load, an Algebraic Reynolds stress model is also introduced.

Keywords Computational fluid dynamics (CFD) · Reynolds averaging · Closure of Reynolds-averaged Navier–Stokes equations · Two-equation model · Reynolds stress model

Nomenclature

k	Turbulent kinetic energy, $m^2\ s^{-2}$
P	Time-averaged pressure, $kg\ m^{-1}\ s^{-2}$
p	Instantaneous pressure, $kg\ m^{-1}\ s^{-2}$
p'	Fluctuating pressure, $kg\ m^{-1}\ s^{-2}$
Re	Reynolds number
S	Source term, $kg\ m\ s^{-2}$
t	Time, s
u	Instantaneous velocity, $m\ s^{-1}$
$u'v'w'$	Fluctuating velocity, $m\ s^{-1}$
u_τ	Frictional velocity, $m\ s^{-1}$

u^+	Dimensionless velocity
U	Time-averaged velocity, m s^{-1}
$\hat{U}$	Velocity of large-scale eddy in turbulent flow, m s^{-1}
x, y	Coordinate
y^+	Dimensionless distance
δ	Kronecker symbol; thickness of shearing layer, m
ε	Dissipation rate of turbulent kinetic energy, m^2 s^{-3}
κ	Karman constant
μ	Viscosity, kg m^{-1} s^{-1}
μ_t	Turbulent viscosity, kg m^{-1} s^{-1}
ρ	Density, kg m^{-3}
$\sigma_k, \sigma_\varepsilon$	Correction factor
τ	Shearing force, kg m^{-1} s^{-2}

Computational fluid dynamics (CFD) has been developed since the seventies of last century by the cross-discipline between fluid dynamics and numerical computation. It feathers the use of numerical method to solve the differential equation of fluid motion so as to obtain the velocity distribution (velocity field) and related flow parameters.

1.1 Equation of Momentum Conservation and its Closure

In CFD, the governing equations for simulating Newtonian fluid are the continuity and the momentum conservation equations (Navier–Stokes equation). Their basic forms for incompressible three-dimensional flow are as follows:

Continuity equation

$$\frac{\partial \rho}{\partial t} + \frac{\partial \rho u_i}{\partial x_i} = 0, \qquad i = i, j, k \tag{1.1}$$

Momentum conservation equation

$$\frac{\partial \rho u_i}{\partial t} + \frac{\partial \rho u_i u_j}{\partial x_j} = -\frac{\partial p}{\partial x_i} + \mu \frac{\partial^2 u_i}{\partial x_j \partial x_j} + \rho S_i \tag{1.2}$$

where fluid velocity u_i and pressure p are instantaneous values; ρ, μ are, respectively, the fluid density and viscosity, and S_i is the source term. Although the foregoing equations can be solved by direct numerical simulation, the limitation of computer facility restricts such method so far only applicable to low-Reynolds-number simple flow. Instead, there are indirect numerical methods for solving Eq. (1.2), such as Reynolds-averaged numerical simulation (RANS) and large

eddy simulation (LES), among which the RANS is most commonly used nowadays, and therefore, it is briefly reviewed in this chapter.

1.1.1 Reynolds-Averaged Navier–Stokes Equation

For the turbulent flow, according to the basic concept of Reynolds-Averaged Navier–Stokes Equation (RANS), any instantaneous quantity can be resolved into two parts: the time-averaged quantity and the fluctuating quantity, the latter is oscillating positively and negatively around the former. Thus, u_i and p can be expressed as follows:

$$u_i = U_i + u_i'$$
$$p = P + p'$$

where U_i is the time-averaged velocity, u_i' and p' are, respectively, the fluctuating velocity and fluctuating pressure. Substituting the foregoing relationship to Eq. (1.1) and (1.2), the following time-averaged equations of continuity and momentum are obtained:

$$\frac{\partial \rho}{\partial t} + \frac{\partial \rho U_i}{\partial x_i} = 0 \tag{1.3}$$

$$\frac{\partial \rho U_i}{\partial t} + \frac{\partial \rho U_i U_j}{\partial x_j} = -\frac{\partial P}{\partial x_i} + \mu \frac{\partial^2 U_i}{\partial x_j \partial x_j} + \frac{\partial \left(-\rho \overline{u_i' u_j'} \right)}{\partial x_j} + \rho S_i \tag{1.4}$$

If the fluid density ρ is a constant, we have $\frac{\partial U_i}{\partial x_i} = 0$ from Eq. (1.3), then Eq. (1.4) becomes

$$\frac{\partial \rho U_i}{\partial t} + U_j \frac{\partial \rho U_i}{\partial x_j} = -\frac{\partial P}{\partial x_i} + \mu \frac{\partial^2 U_i}{\partial x_j \partial x_j} + \frac{\partial \left(-\rho \overline{u_i' u_j'} \right)}{\partial x_j} + \rho S_i \tag{1.5}$$

In view of that the dimension of the term $-\rho \overline{u_i' u_j'}$ [kg m^{-1} s^{-2}] in the foregoing average Navier-Stokes equation, which was introduced by O. Reynolds (1894), is identical with stress, such term is terminologically called Reynolds stress. Equation (1.4) or (1.5) is thus commonly regarded as Reynolds stress equation. If the fluctuating velocity component u_i', u_j', u_k' are denoted, respectively, by u', v', w', the term $-\rho \overline{u_i' u_j'}$ involves implicitly six unknown variables: $-\rho \overline{u'^2}$, $-\rho \overline{v'^2}$, $-\rho \overline{w'^2}$, $-\rho \overline{u'v'}$, $-\rho \overline{u'w'}$, and $-\rho \overline{v'w'}$.

In Eqs. (1.4) and (1.1), there are ten unknown quantities, they are $U_i (i = U, V, W)$, P, and $-\rho \overline{u_i' u_j'}$ (six unknowns), but the number of equations available for solution are as follows: six equations from Eq. (1.4) and three equations from Eq. (1.1), totally nine equations. The number of equation in hand is

insufficient to achieve solution unless the Reynolds stress $-\rho\overline{u_i'u_j'}$ can be evaluated to reduce the number of unknown quantity.

1.1.2 Reynolds Stress Equation

The equation expressing $-\rho\overline{u_i'u_j'}$ or $\overline{u_i'u_j'}$ can be further derived as follows. Subtracting Eq. (1.5) from Eq. (1.2) to obtain the u_i' equation:

$$\frac{\partial \rho u_i'}{\partial t} + U_j\frac{\partial \rho u_i'}{\partial x_j} + u_j'\frac{\partial \rho U_i}{\partial x_j} = \frac{\partial p'}{\partial x_i} + \mu\frac{\partial^2 u_i'}{\partial x_j \partial x_j} - \frac{\partial}{\partial x_j}\rho\left(u_i'u_j' - \overline{u_i'u_j'}\right)$$

Similarly, we have the u_j' equation. Let u_i' equation be multiplied by u_j' and u_j' equation be multiplied by u_i'; then, the two resulting equations are added and averaged to yield the following Reynolds stress transport equation:

$$\begin{aligned}
\frac{\partial \rho\overline{u_i'u_j'}}{\partial t} + U_k\frac{\partial \rho\overline{u_i'u_j'}}{\partial x_k} =& \frac{\partial}{\partial x_k}\left(\mu\frac{\partial\overline{u_i'u_j'}}{\partial x_k}\right) - \frac{\partial}{\partial x_k}\left(\rho\overline{u_i'u_j'u_k'} + \delta_{jk}\overline{u_i'p'} + \delta_{ik}\overline{u_j'p'}\right) \\
&- \rho\overline{u_i'u_k'}\frac{\partial U_j}{\partial x_k} - \rho\overline{u_j'u_k'}\frac{\partial U_i}{\partial x_k} + \overline{p'\left(\frac{\partial u_i'}{\partial x_j} + \frac{\partial u_j'}{\partial x_i}\right)} - 2\mu\overline{\frac{\partial u_i'}{\partial x_k}\frac{\partial u_i'}{\partial x_k}}
\end{aligned} \tag{1.6}$$

where δ is Kronecker symbol:

$$\delta_{ik} = \left\{\begin{array}{l} 1(i = k) \\ 0(i \neq k) \end{array}\right. \quad \delta_{jk} = \left\{\begin{array}{l} 1(j = k) \\ 0(j \neq k) \end{array}\right\}$$

In Eq. (1.6), the two terms on the left side represent, respectively, the increase in Reynolds stress with respect to time and coordinate (three-dimensional); the terms on the right side denote, respectively, the molecular diffusion, the turbulent diffusion, the stress production, the pressure-stain of the flow, and the dissipation of turbulent kinetic energy.

Although six equations can be written from Eq. (1.6), yet another three unknown terms $\overline{u_i'u_j'u_k'}$, $\overline{u_i'p'}$, and $\mu\overline{\frac{\partial u_i'}{\partial x_k}\frac{\partial u_i'}{\partial x_k}}$ are appeared to make it unsolvable; thus Eq. (1.5) is still not closed.

1.1.3 Basic Models for the Simulation of Turbulent Flow

Several models have been proposed for solving Navier–Stokes equations in turbulent flow besides the direct numerical simulation (DNS), among which are chiefly:

- Turbulent viscosity model in which a postulate is applied to simply the Reynolds stress Eq. (1.5);
- Reynolds stress model (RANS) in which the Reynolds stress transport equation is computed directly by modeling Eq. (1.6) to the form suitable for numerical computation;
- Large Eddy Simulation (LES) model in which large-scale eddies caused by turbulence is simulated using Navier–Stokes equation, and the small eddies are simulated by a sub-grid scale model. This model can be regarded as the combination of DNS and Reynolds-averaged method.

At present, the eddy viscosity model and Reynolds stress model are commonly used in engineering field. These two kinds of model are described briefly in the subsequent sections. The LES model requires large computing capacity as well as heavy computation work so as the application of this model is limited and still under further development; thus only basic idea of this method is given in subsequent section.

1.2 Turbulent Viscosity Model

1.2.1 Boussinesq Postulation

In 1877, Boussinesq [1] postulated that the Reynolds stress in turbulent flow was proportional to the time-averaged velocity gradient. Mathematically, it can be expressed as:

$$-\rho \overline{u_i' u_j'} = \mu_t \left(\frac{\partial U_i}{\partial x_j} + \frac{\partial U_j}{\partial x_i} \right) - \frac{1}{3} \rho \delta_{ij} \overline{u_i' u_i'}$$

$$\delta_{ij} = \begin{cases} 0, & i \neq j \\ 1, & i = j \end{cases} \tag{1.7}$$

where μ_t is called the turbulent viscosity (or turbulent diffusivity, eddy diffusivity, eddy viscosity, and kinematic viscosity) of the fluid which is a variable dependent on the condition of turbulent flow. The last term on the right side of Eq. (1.7), $-\frac{1}{3} \rho \delta_{ij} \overline{u_i' u_i'}$, is necessary; otherwise when $i = j$, the terms $\frac{\partial U_i}{\partial x_j}$ and $\frac{\partial U_j}{\partial x_i}$ in Eq. (1.7) become zero according to continuity equation so as to make the Reynolds stress equal to zero, which is obviously unreasonable.

Let k represent the average of turbulent fluctuating kinetic energy of the fluid, i.e.,

$$k = \frac{1}{2} \left(\overline{u_i' u_i'} \right) = \frac{1}{2} \left(\overline{u'^2} + \overline{v'^2} + \overline{w'^2} \right)$$

Then, Eq. (1.7) can be written as:

$$-\rho\overline{u_i'u_j'} = \mu_t\left(\frac{\partial U_i}{\partial x_j} + \frac{\partial U_j}{\partial x_i}\right) - \frac{2}{3}\rho\delta_{ij}k \tag{1.8}$$

As seen in this model, the Reynolds stress that involves six unknown variables has been reduced to only μ_t and k. Since the value of μ_t is a unique value in x, y, z directions, it is isotropic; thus the anisotropic quantity $\overline{u_i'u_j'}$ is being treated as isotropic if Eq. (1.8) is applied.

1.2.2 The k Equation

The equation for k can be obtained from Eq. (1.6) by setting $i = j$ and multiplying both sides by 2 to yield the following form:

$$\frac{\partial\rho k}{\partial t} + U_k\frac{\partial\rho k}{\partial x_k} = \frac{\partial}{\partial x_k}\left(\mu\frac{\partial k}{\partial x_k}\right) - \frac{\partial}{\partial x_k}(\rho\overline{k\,u_k'} + \overline{p'u_k'}) - \rho\overline{u_i'u_k'}\frac{\partial U_i}{\partial x_k} - \mu\overline{\frac{\partial u_i'}{\partial x_k}\frac{\partial u_i'}{\partial x_k}}$$
$$\tag{1.9}$$

where the first and second terms on the right side represent, respectively, the molecular diffusion and the turbulent diffusion, the third and fourth terms represent the production of Reynolds stress and dissipation of turbulent energy. For convenience, define ε to be the rate of dissipation,

$$\varepsilon = \frac{\mu}{\rho}\overline{\frac{\partial u_i'}{\partial x_k}\frac{\partial u_i'}{\partial x_k}} \tag{1.10}$$

In practice, Eq. (1.9) should be modeled to make it suitable for numerical computation.

The use of modeling method for calculating the complicated differential equation is commonly employed in CFD. There are several rules for the modeling, among which the following two are the most important:

1. The diffusion of all turbulent transport quantities by fluid motion, such as $\overline{u_iu_j}$, k, and ε, is proportional to its own gradient.
2. The term in the mathematical model after modeling must be retained by the same dimension using the combination of k, ε. For instance, time (t) can be represented by k/ε and length (l) by $k^{3/2}/\varepsilon$.

Applying the modeling rule, Eq. (1.9) can be modeled as follows.
The first term need not be modeled.
The second term on the right side of Eq. (1.9) is considered proportional to the gradient of k and $\overline{u_i'u_j'}$. According to the modeling rule of dimensional equality, the proportional coefficient should have the dimension of (length)^2/time, i.e., m^2 s^{-1}. We may employ the product of $\frac{k}{\varepsilon}$ (dimension s) and $\overline{u_i'u_j'}$ (dimension m^2 s^{-2}) to keep the dimension before and after modeling consistent as follows:

$$\left(\rho\overline{ku'_k + p'u'_k}\right) = C_k\rho\left(\frac{k}{\varepsilon}\right)\overline{u'_i u'_j}\frac{\partial k}{\partial x_k}$$

where C_k is dimensionless constant.

The third term remains unchanged.

For the dissipation term, it can be written as $\rho\varepsilon$ by Eq. (1.10).

Then, Eq. (1.9) takes the following form after modeling:

$$\frac{\partial \rho k}{\partial t} + U_k\frac{\partial \rho k}{\partial x_k} = \frac{\partial}{\partial x_k}\left[\left(\mu + C_k\rho\frac{k}{\varepsilon}\overline{u'_i u'_j}\right)\frac{\partial k}{\partial x_k}\right] + \rho\overline{u'_i u'_j}\frac{\partial U_i}{\partial x_k} - \rho\varepsilon \qquad (1.11)$$

For the isotropic flow, $\overline{u'_i u'_j}$ can be further simplified using Eq. (1.8) under $i = j$ and applied $\mu_t = C_k\rho\frac{k^2}{\varepsilon}$ as given by Eq. (1.14) in Sect. 1.2.4, Eq. (1.11) becomes:

$$\frac{\partial \rho k}{\partial t} + U_k\frac{\partial \rho k}{\partial x_k} = \frac{\partial}{\partial x_k}\left[\left(\mu + \frac{\mu_t}{\sigma_k}\right)\frac{\partial k}{\partial x_k}\right] + G_k - \rho\varepsilon$$

$$G_k = \mu_t\left(\frac{\partial U_j}{\partial x_i} + \frac{\partial U_i}{\partial x_j}\right)\frac{\partial U_i}{\partial x_k} \qquad (1.11a)$$

where σ_k is a correction factor, usually taken as $\sigma_k = 1$.

It should be noted that Eq. (1.11a) is applicable to isotropic flow, while Eq. (1.11) can be used in the anisotropic case.

The foregoing k equation involves μ_t and ε two unknown variables and can not be solved independently unless μ_t and ε can be evaluated as given in the following section.

1.2.3 The ε Equation

The ε equation can be derived as follows. Differentiate Eq. (1.5) with respect to x_k and exchange the order of $\frac{\partial}{\partial x_k}$ and $\frac{\partial}{\partial t}$, multiply by $2\frac{\mu}{\rho}\frac{\partial u'_i}{\partial x_k}$ on both sides, and take the average; then the following ε equation is obtained:

$$\frac{\partial \rho\varepsilon}{\partial t} + U_k\frac{\partial \rho\varepsilon}{\partial x_k} = \frac{\partial}{\partial x_k}\left[\mu\frac{\partial \varepsilon}{\partial x_k} - \mu\overline{u'_j\frac{\partial u'_i}{\partial x_k}\frac{\partial u'_i}{\partial x_k}} - 2\frac{\mu}{\rho}\overline{\frac{\partial u'_k}{\partial x_j}\frac{\partial p'}{\partial x_j}}\right] - 2\mu\,\overline{u'_k\frac{\partial u'_i}{\partial x_k}}\frac{\partial^2 U_i}{\partial x_k\partial x_j}$$
$$- 2\mu\frac{\partial U_i}{\partial x_j}\left(\overline{\frac{\partial u'_i}{\partial x_k}\frac{\partial u'_k}{\partial x_k}} + \overline{\frac{\partial u'_j}{\partial u'_k}\frac{\partial u'_j}{\partial u'_k}}\right) - 2\mu\overline{\frac{\partial u'_i}{\partial x_j}\frac{\partial u'_i}{\partial x_j}\frac{\partial u'_i}{\partial x_k}} - 2\left(\mu\overline{\frac{\partial^2 u'_i}{\partial x_j x_k}}\right)^2 \qquad (1.12)$$

The various terms in the foregoing equation should be modeled as follows [2].

The first term on the right side, represented the molecular and turbulent diffusion, can be considered proportional to the ε gradient and $\overline{u_i' u_j'}$, which can be expressed in the following form:

$$\left[\mu \frac{\partial \varepsilon}{\partial x_k} - \overline{\mu u_j' \frac{\partial u_i'}{\partial x_k} \frac{\partial u_i'}{\partial x_k}} - 2 \frac{\mu}{\rho} \overline{\frac{\partial u_k'}{\partial x_j} \frac{\partial p'}{\partial x_j}} \right] = \left(\mu + C_k \rho \frac{k}{\varepsilon} \overline{u_i' u_j'} \right) \frac{\partial \varepsilon}{\partial x_k}$$

where the coefficient $\frac{k}{\varepsilon}$ representing the dimension "t" added to the $\overline{u_i' u_j'}$ term is necessary in order to keep the dimension of both sides consistent.

The second and third terms, represented the production of turbulent kinetic energy, can be considered proportional to the gradient of U_i and $\overline{u_i' u_k'}$ as follows:

$$2\mu \overline{u_k' \frac{\partial u_i'}{\partial x_k} \frac{\partial^2 U_i}{\partial x_k \partial x_j}} + 2\mu \frac{\partial U_i}{\partial x_j} \left(\overline{\frac{\partial u_i'}{\partial x_k} \frac{\partial u_k'}{\partial x_k}} + \overline{\frac{\partial u_j'}{\partial x_k} \frac{\partial u_i'}{\partial u_k'}} \right) = C_{1\varepsilon} \rho \frac{\varepsilon}{k} \overline{u_i' u_k'} \frac{\partial U_i}{\partial x_k}$$

The fourth and fifth terms, represented the dissipation of turbulent kinetic energy, can be modeled as the product of "time" ($\frac{\varepsilon}{k}$) and the dissipation rate ε:

$$2\mu \overline{\frac{\partial u_i'}{\partial x_j} \frac{\partial u_i'}{\partial x_j} \frac{\partial u_i'}{\partial x_k}} + 2 \left(\overline{\mu \frac{\partial^2 u_i'}{\partial x_j x_k}} \right)^2 = C_{2\varepsilon} \rho \frac{\varepsilon}{k} \varepsilon$$

The ε equation after modeling gives the following forms:

$$\frac{\partial (\rho \varepsilon)}{\partial t} + U_k \frac{\partial (\rho \varepsilon)}{\partial x_k} = \frac{\partial}{\partial x_k} \left[\left(\mu + C_k \rho \frac{k}{\varepsilon} \overline{u_i' u_j'} \right) \frac{\partial \varepsilon}{\partial x_k} \right] + C_{1\varepsilon} \rho \frac{\varepsilon}{k} \overline{u_i' u_j'} \frac{\partial U_i}{\partial x_k} - C_{2\varepsilon} \rho \frac{\varepsilon^2}{k} \quad (1.13)$$

where $C_{1\varepsilon}$ and $C_{2\varepsilon}$ are constants.

For isotropic flow, the $\overline{u_i' u_j'}$ can be simplified at $i = j$ using Eq. (1.8) to yield the following equation:

$$\frac{\partial (\rho \varepsilon)}{\partial t} + U_k \frac{\partial (\rho \varepsilon)}{\partial x_k} = \frac{\partial}{\partial x_k} \left[\left(\mu + C_k \rho \frac{k^2}{\varepsilon} \right) \frac{\partial \varepsilon}{\partial x_k} \right] + C_{1\varepsilon} \frac{\varepsilon}{k} G_k - C_{2\varepsilon} \rho \frac{\varepsilon^2}{k}$$

$$G_k = \mu_t \left(\frac{\partial U_j}{\partial x_i} + \frac{\partial U_i}{\partial x_j} \right) \frac{\partial U_i}{\partial x_k}$$

or expressing in terms of μ_t as follows:

$$\frac{\partial (\rho \varepsilon)}{\partial t} + U_k \frac{\partial (\rho \varepsilon)}{\partial x_k} = \frac{\partial}{\partial x_k} \left[\left(\mu + \frac{\mu_t}{\sigma_\varepsilon} \right) \frac{\partial \varepsilon}{\partial x_k} \right] + C_{1\varepsilon} \frac{\varepsilon}{k} G_k - C_{2\varepsilon} \rho \frac{\varepsilon^2}{k} \quad (1.13a)$$

where the model constants should be determined by experiment. The experimental determination is based on the principle that the complicated flow equation is also applicable to the simple flow, such as one-dimensional uniform flow, which can conveniently perform and obtain the corresponding constants. The conventionally

adopted constants in Eq. (1.13a) are [3]: $C_{1\varepsilon} = 1.44$, $C_{2\varepsilon} = 1.92$, and $\sigma_\varepsilon = 1.3$. Note that these model constants may be adjusted by different authors to suit different kinds of flow.

In some literature, the subscript in k and ε equations are expressed by i, j instead of i, k, then Eq. (1.11a) and (1.13a) can also be written in the following equivalent forms:

$$\frac{\partial \rho k}{\partial t} + U_i \frac{\partial \rho k}{\partial x_i} = \frac{\partial}{\partial x_i}\left[\left(\mu + \frac{\mu_t}{\sigma_k}\right)\frac{\partial k}{\partial x_i}\right] + G_k - \rho\varepsilon \tag{1.11a}$$

$$\frac{\partial(\rho\varepsilon)}{\partial t} + U_i \frac{\partial(\rho\varepsilon)}{\partial x_i} = \frac{\partial}{\partial x_i}\left[\left(\mu + \frac{\mu_t}{\sigma_\varepsilon}\right)\frac{\partial\varepsilon}{\partial x_i}\right] + C_{1\varepsilon}\frac{\varepsilon}{k}G_k - C_{2\varepsilon}\rho\frac{\varepsilon^2}{k} \tag{1.13a}$$

1.2.4 The μ_t Equation

The turbulent viscosity μ_t is considered proportional to the density ρ, the mean fluctuating velocity (expressed by $k^{0.5}$), and the fluctuating characteristic length; the latter being proportional to both the mean fluctuating velocity $k^{0.5}$ and the time (expressed by $\frac{k}{\varepsilon}$). Combining these relationships, $\mu_t \propto k^{0.5} \cdot k^{0.5} \cdot \frac{k}{\varepsilon}$, we have

$$\mu_t = C_\mu \rho \frac{k^2}{\varepsilon} \tag{1.14}$$

where the constant C_μ is equal to 0.09 [2].

1.2.5 Standard $k - \varepsilon$ Model (Two-Equation Model)

The model equations for turbulent viscosity model are as follows:

Continuity equation Eq. (1.3)
Momentum conservation equation Eq. (1.4)
$\overline{u_i' u_j'}$ *equation* Eq. (1.8) (Boussinesq postulate)
k equation Eq. (1.11a)
ε equation Eq. (1.13a)
μ_t equation Eq. (1.14)

In foregoing model equation set, there are seven unknown variables in foregoing model equations: $U_i, U_j, U_k, P, k, \varepsilon, \mu_t$, while the number of equations available is also seven: one from continuity equation, three from momentum equation, and the k, ε, and μ_t equations. The solution of this model equations is able to give the three-dimensional velocity profiles and related flow parameters.

1.2.6 Renormalization Group Model (RNG Model) [4, 5]

Since the $k - \varepsilon$ model is isotropic due to applying the Boussinesq postulate Eq. (1.7), the RNG model modifies it to approximate the anisotropic character of some flow process and gives better result. The governing equations are similar to $k - \varepsilon$ model as shown below:

$$\frac{\partial(\rho k)}{\partial t} + \frac{\partial(\rho k U_i)}{\partial x_i} = \frac{\partial}{\partial x_i}\left(\alpha_k \mu_{\text{eff}} \frac{\partial k}{\partial x_i}\right) + G_k - \rho \varepsilon \qquad (1.15)$$

$$\frac{\partial(\rho \varepsilon)}{\partial t} + \frac{\partial(\rho \varepsilon U_i)}{\partial x_i} = \frac{\partial}{\partial x_i}\left(\alpha_\varepsilon \mu_{\text{eff}} \frac{\partial \varepsilon}{\partial x_i}\right) + C_{1\varepsilon}^* \frac{\varepsilon}{k} G_k - C_{2\varepsilon}\rho \frac{\varepsilon^2}{k} \qquad (1.16)$$

where

$$\mu_{\text{eff}} = \mu + \mu_t = \mu + \rho C_\mu \frac{k^2}{\varepsilon}$$

$$C_{1\varepsilon}^* = C_{1\varepsilon} - \frac{\eta(1 - \eta/\eta_0)}{1 + \beta\eta^3}$$

$$\eta = \left(2E_{\text{ij}} \cdot E_{\text{ij}}\right)^{1/2}\frac{k}{\varepsilon}$$

$$E_{\text{ij}} = \frac{1}{2}\left(\frac{\partial u_i}{\partial x_j} + \frac{\partial u_j}{\partial x_i}\right)$$

Model constants are: $C_\mu = 0.0845$, $\alpha_k = \alpha_\varepsilon = 1.39$, $C_{1\varepsilon} = 1.42$, $C_{2\varepsilon} = 1.68$, $\eta_0 = 4.377$, and $\beta = 0.012$.

1.2.7 Low Reynolds Number $k - \varepsilon$ Model [6]

The foregoing two models are suitable to the high Reynolds number flow. For low Reynolds number, the $k - \varepsilon$ model could be modified as follows: the model constants are related to turbulent Reynolds number Re_t and an extra term is added to the k, and ε equations as shown below:

$$\frac{\partial(\rho k)}{\partial t} + \frac{\partial(\rho k U_i)}{\partial x_i} = \frac{\partial}{\partial x_i}\left[\left(\mu + \frac{\mu_t}{\sigma_k}\right)\frac{\partial k}{\partial x_i}\right] + G_k - \rho\varepsilon - 2\mu\left(\frac{\partial k^{1/2}}{\partial n}\right)^2 \qquad (1.17)$$

$$\frac{\partial(\rho\varepsilon)}{\partial t} + \frac{\partial(\rho\varepsilon U_i)}{\partial x_i} = \frac{\partial}{\partial x_i}\left[\left(\mu + \frac{\mu_t}{\sigma_\varepsilon}\right)\frac{\partial\varepsilon}{\partial x_i}\right] + f_1 C_{1\varepsilon}\frac{\varepsilon}{k}G_k - f_2 C_{2\varepsilon}\frac{\varepsilon^2}{k} + 2\frac{\mu\mu_t}{\rho}\left(\frac{\partial^2 u}{\partial n^2}\right)^2$$

$$\mu_t = f_\mu C_\mu \rho \frac{k^2}{\varepsilon} \qquad\qquad\qquad\qquad\qquad\qquad\qquad\qquad\qquad\qquad\qquad (1.18)$$

where n is the normal coordinate of the wall, $f_1 = 1.0$, $f_2 = 1.0 - 0.3\exp(-\mathrm{Re}_t^2)$, $f_\mu = \exp\left[-\dfrac{2.5}{(1 + \mathrm{Re}_t/50)}\right]$, and $\mathrm{Re}_t = \frac{\rho k^2}{\eta \varepsilon}$.

This model is suitable for $\mathrm{Re}_t \leq 150$.

1.2.8 Near Wall Condition

The low Reynolds number $k - \varepsilon$ model can be used to describe the near wall flow. In considering no slip condition (velocity equal to zero) on the wall surface, the velocity gradient near the wall is very steep to form a "boundary layer" in which very high velocity gradient is established from zero velocity to the velocity of the bulk flow. Thus, the network grid size should be set to very small to suit such high gradient so that the computer load is increased greatly. Alternatively, a more convenient way, the surface function method, is frequently used.

Many investigations reveal that the boundary involves three subordinate layers from the wall surface to the border of main flow, namely the laminar sub-layer, transition layer, and turbulent layer. Outside of the boundary layer (three subordinate layers) is the bulk turbulent flow, which is characterized by the individually specified condition, such as the flow through packing in the packed column.

In the laminar sub-layer, the viscous force and molecular diffusion are dominant; while in the turbulent layer the Reynolds stress and turbulent diffusion are dominant. In the transition layer, both viscous force and Reynolds stress as well as molecular and turbulent diffusions are equally important. In practice, the transition layer is usually neglected or combined with the laminar sub-layer, and thus only two layers are concerned.

Let τ_s and τ_t be the viscous shearing stress and Reynolds stress, respectively, the total stress in the layers can be expressed as:

$$\tau = \tau_s + \tau_t = \rho u_\tau^2$$

where u_τ is the friction velocity.

1. *Laminar sub-layer*: Since $\tau_t = 0$, we have

$$\tau = \tau_s = \mu \frac{\partial U}{\partial y} = \rho u_\tau^2$$

where y is the coordinate normal to the wall surface. After integrating at constant u_τ, we obtain:

$$\frac{U}{u_\tau} = \frac{y u_\tau}{\mu / \rho} \tag{1.19}$$

If the left side of foregoing equation is denoted by $u^+ (u^+ = \frac{U}{u_\tau})$, called dimensionless velocity, and the right side is denoted by $y^+ (y^+ = \frac{yu_\tau}{\mu/\rho})$, called dimensionless distance, we have in the laminar sub-layer

$$u^+ = y^+$$

2. *Turbulent layer*: Since $\tau_s = 0$, and shearing velocity u_τ can be considered proportional to the gradient $\frac{\partial U}{\partial y}$ and the distance from the wall y, i.e., $u_\tau = \kappa y \frac{\partial U}{\partial y}$, where κ is a constant (Karman constant), we have at constant u_τ

$$\partial u^+ = \partial \left(\frac{U}{u_\tau} \right) = \frac{1}{\kappa} \frac{\partial y}{y} \tag{1.19b}$$

After integrating, we obtain

$$u^+ = \frac{1}{\kappa} \ln y^+ + B = \frac{1}{\kappa} \ln(Ey^+) \tag{1.20}$$

where the constants $B = 5.5$, $E = 9.8$, $\kappa = 0.418$ for smooth wall surface. Equation (1.20) is called "logarithmic rule," and the turbulent sub-layer is also regarded as logarithmic layer. Note that such logarithmic relationship is based o n the constant shearing velocity u_τ, and the constant B and E should be adjusted if necessary.

3. *The borderline between two layers*: Different authors give different values based on their study. For instance, Versteeg [7] recommend the borderline at $y^+ = 11.63$, below such value is the laminas sub-layer and above that is the turbulent layer; while the software FLUENT™ [8] designate the border at $y^+ = 11.225$.
4. *The calculation of u^+ and y^+*: The value of u^+ and y^+ need to known for near wall flow calculation. Since the laminar friction velocity u_τ can be derived for two-dimensional flow in laminar sub-layer to obtain $u_\tau = C_\mu^{1/4} k^{1/2}$, we have from the definition

$$u^+ = \frac{U}{u_\tau} = \frac{U}{C_\mu^{1/4} k^{1/2}} \tag{1.21}$$

$$y^+ = \frac{yu_\tau}{v} = \frac{yC_\mu^{1/4} k^{1/2}}{v} \tag{1.22}$$

In practice, the initial value of y is usually selected outside of the laminar sub-layer so as to neglect such layer in the computation.

1.3 Reynolds Stress Model

The feature of this model is to solve the Reynolds stress Eq. (1.6) directly instead of using the Boussinesq postulate.

1.3.1 Standard Reynolds Stress Model

The Reynolds stress Eq. (1.6) should be modeled to make the numerical computation possible as shown below.

The first term (turbulent diffusion) on the right side of the equation is considered to be proportional to $\overline{u_i'u_j'}$ and its gradient. Since the dimension of proportional coefficient should be $m^2\,s^{-1}$ in order to keep the dimension consistent in both sides, we should add $\frac{k}{\varepsilon}$ as dimension "time" to the coefficient as follows:

$$-\left(\rho\overline{u_i'u_j'u_k'} + \delta_{jk}\overline{u_i'p'} + \delta_{ik}\overline{u_j'p'}\right) = -\rho C_0 \frac{k}{\varepsilon}\overline{u_i'u_j'}\left(\frac{\partial\overline{u_i'u_j'}}{\partial x_k}\right)$$

The second term (molecular diffusion) and the third term (production of Reynolds stress) are remained unchanged.

The fourth term (pressure-strain) can be modeled as [8]:

$$\overline{p'\frac{\partial u_i'}{\partial x_j}\frac{\partial u_j'}{\partial x_i}} = -C_1\rho\frac{\varepsilon}{k}\left(\overline{u_iu_j} - \frac{2}{3}k\delta_{ij}\right) - C_2\rho\left(\overline{u_i'u_k'}\frac{\partial U_j}{\partial x_k} + \overline{u_j'u_k'}\frac{\partial U_i}{\partial x_k} - \frac{2}{3}\delta_{ij}\overrightarrow{u_i'u_j'}\frac{\partial U_i}{\partial x_k}\right)$$

The fifth term (dissipation) can be expressed by ε provided the dissipation is through small isotropic eddies:

$$-2\mu\overline{\frac{\partial u_i'}{\partial x_k}\frac{\partial u_i'}{\partial x_k}} = -\frac{2}{3}\rho\varepsilon\delta_{ij}$$

After modeling, the Reynolds stress Eq. (1.6) takes the following form:

$$\begin{aligned}
\frac{\partial\rho\overline{u_i'u_j'}}{\partial t} + U_k\frac{\partial\rho\overline{u_i'u_j'}}{\partial x_k} &= \frac{\partial}{\partial x_k}\left(\rho C_0\frac{k}{\varepsilon}\overline{u_i'u_j'}\frac{\partial\overline{u_i'u_j'}}{\partial x_k} + \mu\frac{\partial\overline{u_i'u_j'}}{\partial x_k}\right) \\
&- \rho\left(\overline{u_i'u_k'}\frac{\partial U_j}{\partial x_k} + \overline{u_j'u_k'}\frac{\partial U_i}{\partial x_k}\right) - C_1\rho\frac{\varepsilon}{k}\left(\overline{u_i'u_j'} - \frac{2}{3}k\delta_{ij}\right) \quad (1.23) \\
&- C_2\rho\left(\overline{u_i'u_k'}\frac{\partial U_j}{\partial x_k} + \overline{u_j'u_k'}\frac{\partial U_i}{\partial x_k} - \frac{2}{3}\delta_{ij}\overrightarrow{u_i'u_j'}\frac{\partial U_i}{\partial x_j}\right) - \frac{2}{3}\rho\varepsilon\delta_{ij}
\end{aligned}$$

where the constants are: $C_0 = 0.09$, $C_1 = 2.3$, $C_2 = 0.4$ [8, 9].

Equation (1.23) can be written by combining the $\left(\overline{u'_i u'_k} \frac{\partial U_i}{\partial x_k} + \overline{u'_j u'_k} \frac{\partial U_i}{\partial x_k} \right)$ term under constant ρ to give:

$$
\begin{aligned}
\frac{\partial \overline{u'_i u'_j}}{\partial t} + U_k \frac{\partial \overline{u'_i u'_j}}{\partial x_k} = {} & \frac{\partial}{\partial x_k} \left(C_0 \frac{k}{\varepsilon} \overline{u'_i u'_j} + \frac{\mu}{\rho} \right) \frac{\partial u'_i u'_j}{\partial x_k} \\
& - C_1 \frac{\varepsilon}{k} \left(\overline{u'_i u'_j} - \frac{2}{3} k \delta_{ij} \right) - C_2 \left(\overline{u'_i u'_k} \frac{\partial U_j}{\partial x_k} + \overline{u'_j u'_k} \frac{\partial U_i}{\partial x_k} - \frac{2}{3} \delta_{ij} \overrightarrow{u'_i u'_j} \frac{\partial U_i}{\partial x_j} \right) \\
& - \frac{2}{3} \varepsilon \delta_{ij}
\end{aligned}
$$

$$(1.23a)$$

In the foregoing form, the constants remain $C_0 = 0.09$, $C_1 = 2.3$, $C_2 = 0.4$.

It is noted that when applying the standard Reynolds model, the k and ε expression by Eqs. (1.11) and (1.13) should be accompanied with Eq. (1.23a) as auxiliary equations. However, the use of k and ε equations does not imply the implementation of $k - \varepsilon$ model.

The model equations of standard Reynolds stress model are:

Continuity equation Eq. (1.3)
Momentum conservation equation Eq. (1.4),
$\overline{u'_i u'_j}$ *equation* Eq. (1.23a)
k *equation* Eq. (1.11)
ε *equation* Eq. (1.13)

The number of unknown variables involved is twelve, i.e., U_i, U_j, U_k, P, six unknown from $\overline{u'_i u'_j}$, k and ε. Whereas the number of equations available is also twelve: one continuity equation, three momentum equations, six Reynolds stress equations, k and ε equations. Thus the model is closed and solvable.

The standard Reynolds stress model has anisotropic character and thus can give better result than the $k - \varepsilon$ model in predicting anisotropic flow, although more equations need be solved. Note that the model constants may be adjusted for different flow problems.

1.3.2 Algebraic Reynolds Stress Model

The complicated Reynolds stress differential equation can be approximated by transforming to algebraic form.

Under steady condition, assuming the turbulent and molecular diffusions are compensated by the convection term in the left side, Eq. (1.23) becomes

$$\rho\left(\overline{u_j'u_k'}\frac{\partial U_j}{\partial x_k} + \overline{u_j'u_k'}\frac{\partial U_i}{\partial x_k}\right) - C_1\rho\frac{\varepsilon}{k}\left(\overline{u_i'u_j'} - \frac{2}{3}k\delta_{ij}\right)$$

$$- C_2\rho\left(\overline{u_i'u_k'}\frac{\partial U_i}{\partial x_k} + \overline{u_j'u_k'}\frac{\partial U_i}{\partial x_k} - \frac{2}{3}\delta_{ij}\overrightarrow{u_i'u_k'}\frac{\partial U_i}{\partial x_k}\right) - \frac{2}{3}\rho\varepsilon\delta_{ij} = 0$$

After rearranging, we obtain the following algebraic $\overline{u_i u_j}$ equation:

$$\overline{u_i'u_j'} = -\frac{k}{C_1\varepsilon}\left(\overline{u_j'u_k'}\frac{\partial U_j}{\partial x_k} + \overline{u_j'u_k'}\frac{\partial U_i}{\partial x_k}\right) - \frac{kC_2}{C_1\varepsilon}\left(\overline{u_i'u_k'}\frac{\partial U_j}{\partial x_k} + \overline{u_j'u_k'}\frac{\partial U_i}{\partial x_k} - \frac{2}{3}\overline{u_i'u_k'}\frac{\partial U_i}{\partial x_k}\delta_{ij}\right)$$

$$+ \frac{2}{3}\frac{1}{C_1}k\delta_{ij}$$

$$\text{(1.24)}$$

where $C_1 = 2.3$ and $C_2 = 0.4$ [8, 9].

Similar to the standard Reynolds stress model, the algebraic model involves twelve variables and twelve model equations. The model is closed and solvable.

1.4   Large Eddy Simulation Model

It is commonly recognized that the turbulent flow is composed of eddies (swirling fluid) in different size, among which the large-scale eddies are responsible to the creation and transport of Reynolds stress, which is closely related with the type of flow and boundary conditions, while the small-scale eddies play the role of dissipation in the action with viscous force.

The basic idea of LES model is to use Navier–Stokes equation for simulating the motion of large eddies after filtering the small-scale eddies, and the small-scale eddies are simulated by sub-grid scale model. Thus, the first step of LES is to filter out the small eddies from Navier–Stokes equation to establish an equation describing the motion of large eddies, in which the instantaneous velocity u is resolved into large eddies velocity $\hat{U}$ and corresponding fluctuation $\hat{u}$:

$$u_i = \hat{U} + \hat{u}_i$$

The instantaneous governing equations for the motion of large eddy are:

$$\frac{\partial\rho\hat{U}_i}{\partial t} + \frac{\partial\rho\hat{U}_i\hat{U}_j}{\partial x_i} = \frac{\partial\hat{P}}{\partial x_i} + \mu\frac{\partial^2\hat{U}_i}{\partial x_i\partial x_j} + \frac{\partial\rho\left(\overline{\hat{u}_i\hat{u}_j} - \hat{U}_i\hat{U}_j\right)}{\partial x_i}$$

where the term $\rho\left(\overline{\hat{u}_i\hat{u}_j} - \hat{U}_i\hat{U}_j\right)$ is similar to the Reynolds stress, called sub-grid scale stress, representing the transport and the influence of small-scale eddies in

the large-scale flow. Such term is unknown and needs to be closed. Different closing models for this purpose have been reported in literature.

The solution of LES model is similar to the direct numerical simulation (DNS), requiring very fine grid network and supercomputer to carry out the numerical computation. Thus, the application of LES model to the ordinary engineering work is limited. However, LES model is still under investigation and expects to be an advanced prospective model in CFD.

1.5 Summary

Most of the fluid processes are under the condition of turbulent flow. The basic Reynolds-averaged modeling equations describing the flow are:

- Continuity equation, Eq. (1.3)
- Momentum conservation equation, Eq. (1.4).

The question raised from Eq. (1.4) is that the Reynolds stress term $-\rho \overline{u_i' u_j'}$ is unknown so that Eq. (1.4) is unsolvable. There are two main models in computational field to solve this problem.

1. Turbulent (Eddy) diffusivity model in which a turbulent (eddy) diffusivity μ_t is introduced according to Eq. (1.7) to replace unknown $-\rho \overline{u_i' u_j'}$, called Boussinesq postulate. The μ_t is obtained by Eq. (1.14) where two unknowns k and ε are involved. They are represented, respectively, by Eqs. (1.11a) and (1.13a). These equations should be further modeled to suit numerical computation. This model is commonly called $k - \varepsilon$ model. Several modifications have been made to extent its application. The weakness of this model is that the μ_t is isotropic and results in discrepancy when applying to the case of anisotropic flow.
2. Reynolds stress model, in which the unknown $-\rho \overline{u_i' u_j'}$, is calculated directly by the modeled Eq. (1.23a). The advantage of this model is anisotropy and more rigorous, while its weakness is the need of much computer work. It is called standard Reynolds stress model. For reducing the computer load, a simplified model, called Algebraic Reynolds stress model, Eq. (1.24) is used instead of Eq. (1.23a). The accuracy of simplified model is comparable to the standard Reynolds stress model.

References

1. Boussinesq J (1877) Essai sur la théorie des eaux courantes. Mémoires présentés par divers savants à l'Académie des Sciences 23(1):1–680

2. Launder BE, Spalding DB (1972) Mathematical methods of turbulence. Academic Press, London
3. Launder BE, Spalding DB (1974) The numerical computation of turbulent flows. Compt Methods Appl Mech Eng 3:269–289
4. Yakhot V, Orszag SA (1986) Renormalization group analysis of turbulence. I. Basic theory. J Sci Comput 1(1):3–51
5. Speziale CG, Gatski TB, Fitzmaurice N (1991) An analysis of RNG-based turbulence models for homogeneous shear flow. Phys Fluids A (Fluid Dynamics) 3(9):2278–2281
6. Jones WP, Launder BE (1970) The calculation of Low-Raynolds-number phenomena with a two-equation model of turbulence. Int J Heat Mass Transfer 16:1119–1130
7. Versteeg HK, Malalasekera W (2005) An introduction to computational fluid dynamic. Wiley, New York
8. Fluent 6.2 Documentation, 2006
9. Chen CJ, Jaw SY (1998) Fundamentals of turbulence modeling. Taylor and Francis, UK

Chapter 2
Related Field (II): Fundamentals of Computational Heat Transfer

Abstract Computational heat transfer (CHT) should be included in the computational mass transfer (CMT) model system if thermal effect is involved in the simulated process. In this chapter, as a preparatory material parallel to Chap. 1, the CHT method for turbulent flow is summarized. This chapter focuses on the closure of the time-averaged energy equation. The unknown term to be solved is the covariant composed of the velocity and temperature fluctuations. Two modeling methods for this term are introduced, namely: the two-equation $\overline{T'^2} - \varepsilon_{T'}$ method and the Reynolds heat flux method. The former is easy to apply but must introduce the isotropic eddy heat diffusivity; and thus, it is not suitable for the case of anisotropic flow. The Reynolds heat flux method needs more computational work, but it is anisotropic and rigorous.

Keywords Computational heat transfer (CHT) · Numerical heat transfer · Reynolds averaging · Closure of time-averaged energy equation · Two-equation model · Reynolds heat flux model

Nomenclature

C_p Specific heat, kJ kg^{-1} K^{-1}
k Turbulent kinetic energy, m^2 s^{-2}
p' Fluctuating pressure, kg m^{-1} s^{-2}
P Time-averaged pressure, kg m^{-1} s^{-2}
Pr Molecular Prandtl number
Pr_t Turbulent Prandtl number
q_w Density of surface heat flux, kJ m^{-3}
S_T Source term
T Time-averaged temperature, K
T' Fluctuating temperature, K
$\overline{T'^2}$ Variance in fluctuating temperature, K^2
$\tilde{T}$ Instantaneous temperature, K
T^+ Dimensionless temperature
u Instantaneous velocity, m s^{-1}

u'	Fluctuating velocity, m s^{-1}
U	Time-averaged velocity, m s^{-1}
x, y	Coordinate
y^+	Dimensionless distance, m
α	Thermal diffusivity, m^2 s^{-1}
α_t	Turbulent thermal diffusivity, m^2 s^{-1}
δ	Kronecker symbol
ε	Dissipation rate of turbulent kinetic energy, m^2 s^{-3}
$\varepsilon_{T'}$	Dissipation rate of temperature variance, K^2 s^{-1}
λ	Thermal conductivity, kJ s^{-1} K^{-1} m^{-1}
μ	Viscosity, kg m^{-1} s^{-1}
v	Kinematic viscosity, m^2 s^{-1}
μ_t	Turbulent viscosity, kg m^{-1} s^{-1}
ρ	Density, kg m^{-3}
σ	Correction factor

Computational heat transfer (CHT) or numerical heat transfer (NHT) was established after CFD for solving the heat transfer problems by numerical method. The CHT methodology has been applied successfully to the engineering and scientific areas for predicting the temperature profile and related parameters.

The mathematical model of computational heat transfer in the flow process consists of a set of basic differential equations involving momentum conservation and energy conservation. Similar to CFD, the basic equation set of computational heat transfer is not closed; and thus, the closure problem is the most important point to be studied.

2.1 Equation of Energy Conservation and its Closure

In this chapter, the energy equation is focused to the heat transfer resulting from all sources of heat effects; the conservation equation of energy can be obtained by the following heat balance:

$$\frac{\partial \rho C_{\mathrm{p}} \tilde{T}}{\partial t} + \frac{\partial u_i \rho C_{\mathrm{p}} \tilde{T}}{\partial x_i} = \lambda \frac{\partial^2 \rho \tilde{T}}{\partial x_i \partial x_i} + S_{\mathrm{T}}^0 \tag{2.1}$$

where $\tilde{T}$ is the instantaneous temperature, u_i is the instantaneous velocity ($i = i, j, k$), t is the time, λ is the thermal conductivity, C_{p} is the specific heat, ρ is the density, and S_{T}^0 is the source term. The first and second terms on the right side represent, respectively, the thermal (temperature) diffusion and the heat source. The heat source includes the heat transfer from outside, heat lost to the environment, heat generated or absorbed from chemical reaction, frictional heat and so forth. In Eq. (2.1), both $\tilde{T}$ and u_i are variables and the equation is not closed.

If ρ and C_p are considered as constants, Eq. (2.1) becomes:

$$\frac{\partial \tilde{T}}{\partial t} + \frac{\partial u_i \tilde{T}}{\partial x_i} = \alpha \frac{\partial^2 \tilde{T}}{\partial x_i \partial x_i} + S_T \tag{2.1a}$$

where $\alpha = \frac{\lambda}{C_p \rho}$ is called thermal diffusivity.

In turbulent heat transfer, the temperature is fluctuating. Similar to the instantaneous velocity, the instantaneous $\tilde{T}$ can be resolved into time-averaged temperature T and fluctuating temperature T' as follows

$$\tilde{T} = T + T' \tag{2.2}$$

Substituting this in Eq. (2.1) and also with $u_i = U_i + u_i'$, we obtain:

$$\frac{\partial \rho T}{\partial t} + \frac{\partial \rho U_i T}{\partial x_i} = \frac{\lambda}{C_p} \frac{\partial^2 T}{\partial x_i \partial x_i} + \frac{\partial \left(-\rho \overline{u_i' T'} \right)}{\partial x_i} + S_T^0 \tag{2.3}$$

The first term on the right side of foregoing equation represents the thermal diffusion; the second term represents the gradient of $-\rho \overline{u_i' T'}$. Since the term $-\rho \overline{u_i' T'}$ is similar to the Reynolds stress $\tau_t = -\rho \overline{u_i' u_j'}$, it is customary called it as Reynolds heat flux.

In Eq. (2.3), if U_i can be obtained by employing CFD, there are four unknowns $(T, \rho \overline{u_i' T'}, \rho \overline{u_j' T'}, \rho \overline{u_k' T'})$ in the equation; while the number of equation available is only three by letting $\rho \overline{u_i' T'}$ be $\rho \overline{u_i' T'}, \rho \overline{u_j' T'}, \rho \overline{u_k' T'}$ separately in Eq. (2.3). Thus, energy equation is not closed.

Under the condition that ρ is constant, $\frac{\partial U_i}{\partial x_i} = 0$ from Eq. (1.3), then Eq. (2.3) is simplified to:

$$\frac{\partial T}{\partial t} + U_i \frac{\partial T}{\partial x_i} = \alpha \frac{\partial^2 T}{\partial x_i \partial x_i} + \frac{\partial \left(-\overline{u_i' T'} \right)}{\partial x_i} + S_T \tag{2.3a}$$

One way to close foregoing equation is to postulate that, similar to Bossinesq postulate or Fourier's law, the Reynolds heat flux $-\overline{u_i' T'}$ is proportional to the time-averaged temperature gradient,

$$-\overline{u_i' T'} = \alpha_t \frac{\partial T}{\partial x_i} \tag{2.4}$$

where the turbulent thermal diffusivity (or eddy thermal diffusivity) α_t is depending on the heat transfer and flow conditions. Substituting Eq. (2.4) to Eq. (2.3a) yields:

$$\frac{\partial T}{\partial t} + U_i \frac{\partial T}{\partial x_i} = (\alpha + \alpha_t) \frac{\partial^2 T}{\partial x_i \partial x_i} + S_T \tag{2.5}$$

Then, Eq. (2.3a) is simplified to Eq. (2.5), which is reduced to only two unknowns, T and α_t besides U_i can be found using CFD.

2.2 Turbulent Thermal Diffusivity Model

2.2.1 Turbulent Prandtl Number Model

From the viewpoint of similarity between heat and momentum transfer, it has been suggested that the ratio of $\frac{\mu_t}{\rho}$ and α_t could be a constant, called turbulent Prandtl number, Pr_t,

$$Pr_t = \frac{\mu_t}{\rho \alpha_t}$$

If the turbulent viscosity μ_t is obtained from CFD, the α_t can be found by assuming a Pr_t number. Many investigations reveal that the value of Pr_t is varied from 0.5 to 1.0 under different conditions of heat transfer. Although this method is easy to use, but it is difficult to make the right choice of Pr_t and the incorrect guess may result serious error.

2.2.2 $\overline{T'^2} - \varepsilon_{T'}$ Model (Two-Equation Model)

Similar to the $k - \varepsilon$ model in CFD, Nagano proposed $\overline{T'^2} - \varepsilon_{T'}$ model for heat transfer [1] in which the turbulent thermal diffusivity α_t can be calculated by:

$$\alpha_t = C_{T0} f_h \, k \left(\frac{k}{\varepsilon} \frac{\overline{T'^2}}{\varepsilon_{T'}} \right)^{\frac{1}{2}} \tag{2.6}$$

where $\overline{T'^2}$ and $\varepsilon_{T'}$ are, respectively, the variance in fluctuating temperature and its dissipation rate; f_h is model function, equal to 1 at high Reynolds number flow; C_{T0} is a model constant. There are sill two unknown quantities, $\overline{T'^2}$ and ε_t, should be found in order to obtain α_t.

Similar to the derivation of k equation in CFD, the $\overline{T'^2}$ equation can be derived to be:

$$\frac{\partial \rho \overline{T'^2}}{\partial t} + U_i \frac{\partial \rho \overline{T'^2}}{\partial x_i} = -\frac{\partial}{\partial x_i} \left(\rho \overline{u'_i T'} - \rho \alpha_t \frac{\partial \overline{T'^2}}{\partial x_i} \right) - 2\rho \overline{u'_i T'} \frac{\partial T}{\partial x_i} - 2\rho \alpha \frac{\overline{\partial T'}}{\partial x_i} \frac{\partial T'}{\partial x_i} \tag{2.7}$$

which can be simplified by letting:

Table 2.1 Model constants of Eq. (2.10) by different authors

Model	C_{T1}	C_{T2}	C_{T3}	C_{T4}
Nagano and Kim [1]	0	1.4	2.0	0.52
Elghobashi and Launder [2]	1.8	0	2.2	0.8
Yoshizawa [3]	1.2	0.52	1.2	0.52
Elghobashi and LaRue [4]	1.8	0.8	2.2	0.8
Sommer and So [5]	1.8	0.72	2.2	0.8

$$-\overline{u_i' T'^2} = \frac{\alpha_t}{\sigma_{T'}} \frac{\partial \overline{T'^2}}{\partial x_i}$$

$$\alpha \overline{\frac{\partial T'}{\partial x_i} \frac{\partial T'}{\partial x_i}} = \varepsilon_{T'}$$

where $\sigma_{T'}$ is a correction factor. Eq. (2.7) becomes

$$\frac{\partial \rho \overline{T'^2}}{\partial t} + \frac{\partial \rho U_i \overline{T'^2}}{\partial x_i} = \frac{\partial}{\partial x_i} \rho \frac{\partial \overline{T'^2}}{\partial x_i} \left(\frac{\alpha_t}{\sigma_{T'}} + \alpha \right) - 2\rho \alpha_t \frac{\partial T}{\partial x_i} \frac{\partial T}{\partial x_i} - 2\rho \varepsilon_{T'} \qquad (2.7a)$$

At constant ρ, Eq. (2.7a) is simplified to:

$$\frac{\partial \overline{T'^2}}{\partial t} + U_i \frac{\partial \overline{T'^2}}{\partial x_i} = \frac{\partial}{\partial x_i} \frac{\partial \overline{T'^2}}{\partial x_i} \left(\frac{\alpha_t}{\sigma_{T'}} + \alpha \right) - 2\alpha_t \left(\frac{\partial T}{\partial x_i} \right)^2 - 2\varepsilon_{T'} \qquad (2.8)$$

Similar to the derivation of ε in CFD, the $\varepsilon_{T'}$ equation can be obtained as follows:

$$\frac{\partial \rho \varepsilon_{T'}}{\partial t} + U_i \frac{\partial \rho \varepsilon_{T'}}{\partial x_i} = \frac{\partial}{\partial x_i} \rho \left(\alpha \frac{\partial \varepsilon_{T'}}{\partial x_i} - \overline{u_i' \varepsilon_{T'}} \right) - 2\rho \alpha \overline{\frac{\partial u_i'}{\partial x_k} \frac{\partial T'}{\partial x_k} \frac{\partial T'}{\partial x_i}} - 2\rho \alpha^2 \overline{\left(\frac{\partial^2 T'}{\partial x_i \partial x_k} \right)^2}$$
$$- 2\rho \alpha \left(\overline{\frac{\partial u_i'}{\partial x_k} \frac{\partial T'}{\partial x_k}} \frac{\partial T}{\partial x_i} + \overline{\frac{\partial T'}{\partial x_k} \frac{\partial T'}{\partial x_i}} \frac{\partial U_i}{\partial x_k} + \overline{u_i' \frac{\partial T'}{\partial x_k}} \frac{\partial^2 T}{\partial x_i \partial x_k} \right) \qquad (2.9)$$

Different modeling forms of $\varepsilon_{T'}$ equation were reported in literature, which can be summarized in the following form and the constants involved are given in Table 2.1:

$$\frac{\partial \varepsilon_{T'}}{\partial t} + U_i \frac{\partial \varepsilon_{T'}}{\partial x_i} = \frac{\partial}{\partial x_i} \left[\left(\alpha + \frac{\alpha_t}{\sigma_{T'}} \right) \frac{\partial \varepsilon_{T'}}{\partial x_i} \right] - C_{T1} \frac{\varepsilon_{T'}}{\overline{T'^2}} \overline{u_i' T'} \frac{\partial T}{\partial x_i}$$
$$- C_{T2} \frac{\varepsilon_{T'}}{k} \overline{u_i' u_j'} \frac{\partial U_i}{\partial x_i} - C_{T3} \frac{\varepsilon_{T'}^2}{\overline{T'^2}} - C_{T4} \frac{\varepsilon}{k} \varepsilon_{T'} \qquad (2.10)$$

The model equations of $\overline{T'^2} - \varepsilon_{T'}$ two-equation model are as follows:

Energy conservation equation Eqs. (2.3) or (2.3a)

$\overline{u_i'T'}$ *equation* Eq. (2.4)

$\overline{T'^2}$ *equation* Eq. (2.7a)

$\varepsilon_{T'}$ *equation* Eq. (2.10)

α_t *equation* Eq. (2.6)

And CFD equation set to find U_i.

The unknown quantities in the $\overline{T'^2} - \varepsilon_{T'}$ model are U_i (involves $U_i, U_j, U_k, p, \mu_t, k, \varepsilon$ unknowns), $\alpha_t, \overline{T'^2}, \varepsilon_{T'}$ and T, totally eleven. The model equations available are also eleven: one from continuity, three from momentum, the k, ε, μ_t equations and Eqs. (2.5), (2.6), (2.8), and (2.10). The model is closed and solvable.

2.2.3 Other $\overline{T'^2} - \varepsilon_{T'}$ Models

Many other $\overline{T'^2} - \varepsilon_{T'}$ models are reported in literature based on modifying α_t, $\overline{T'^2}$ and $\varepsilon_{T'}$ equations in order to give better result for different heat processes. A modified model is given below as an example.

Rhee modified the model applicable to the heat transfer in the low Reynolds number flow in the following form [6]:

$$U_i \frac{\partial \overline{T'^2}}{\partial x_i} = \frac{\partial}{\partial x_i}\left[\left(f_h \frac{\alpha_t}{\sigma_{T'}} + \alpha\right)\frac{\partial \overline{T'^2}}{\partial x_i}\right] - 2\overline{u_i'T'}\frac{\partial T}{\partial x_i} - \varepsilon_{T'}$$

$$U_i \frac{\partial \varepsilon_{T'}}{\partial x_i} = \frac{\partial}{\partial x_i}\left[\left(f_h \frac{\alpha_t}{\sigma_{\varepsilon_{T'}}} + \alpha\right)\frac{\partial \varepsilon_{T'}}{\partial x_i}\right] - C_{T1} \frac{\varepsilon_{T'}}{\overline{T'^2}}\overline{u_i'T'}\frac{\partial T}{\partial x_i} \qquad (2.11)$$

$$- C_{T2} \frac{\varepsilon_{T'}}{k}\overline{u_i'u_j'}\frac{\partial U_i}{\partial x_i} - C_{T3}f_3 \frac{\varepsilon_{T'}^2}{\overline{T'^2}} - C_{T4}f_4 \frac{\varepsilon \varepsilon_{T'}}{k}$$

where:

$$\begin{cases} -\overline{u_i'T'} = \alpha_t \frac{\partial T}{\partial x_i} \\ \alpha_t = c_{T0}f_t \frac{k^2}{\varepsilon} \end{cases}$$

$$\begin{cases} f_h = 1 + 50\exp\left[-\frac{R_t}{150}\frac{R_t}{25/\sqrt{r_t Pr}}\right] \\ f_t = \frac{6(1-T_{W_1})(1+10T_{W_1}/R_t^{1.25})}{6-(2\overline{u_iT'}/\varepsilon_{T'}\partial T/\partial x_i+1)r_t} \\ T_{W_1} = \exp\left[-\left(\frac{R_y}{80/\sqrt{Pr}}\right)^2\right] \\ R_y \equiv k^{1/2}y/v \end{cases}$$

The model constants are: $C_{T1} = 0.9$, $C_{T2} = 0.72$, $C_{T3} = 1.0$, and $C_{T4} = 0.9$.

2.2.4 Near Wall Computation

Usually, the location of the grid network near the wall surface is outside of the laminar sub-layer, i.e., it is in the region of turbulent layer, so that the computation in the laminar sub-layer is usually being neglected.

Versteeg [7] recommended the following logarithmic equation for temperature distribution in the turbulent layer:

$$T^+ = Pr_t \left[\frac{1}{\kappa} \ln Ey^+ + P \right]$$

$$P = 9.24 \left[\left(\frac{Pr}{Pr_t} \right)^{3/4} - 1 \right] \left(1 + 0.28\, e^{-0.007 Pr/Pr_t} \right)$$

where Pr is molecular Prandtl number; Pr_t is set equal to 0.9; y^+ is dimensionless distance, $y^+ = \frac{yu_\tau}{\mu/\rho}$, in which u_τ is the friction velocity; T^+ is dimensionless temperature equal to

$$T^+ \equiv \frac{(T_w - T_p)\rho C_p C_\mu^{1/4} k_p^{1/2}}{q_w}$$

where q_w is the density of heat flux at the wall; T_p is the average temperature at point P under consideration; T_w is the wall temperature; k_p is the value of k at point P.

In software FLUENT 6.2, the T^+ is designated to be

$$T^+ = \begin{cases} Pr\, y^+ + \frac{1}{2}\rho\, Pr \frac{C_\mu^{1/4} k_p^{1/2} U_p^2}{q_w} & (y^+ < y_T^+) \\ Pr_t \left[\frac{1}{\kappa} \ln(Ey^+) + P \right] + \frac{1}{2}\rho\, Pr \frac{C_\mu^{1/4} k_p^{1/2}}{q_w} \left[Pr_t\, U_p^2 + (Pr - Pr_t) U_c^2 \right] \\ \hfill (y^+ > y_T^+) \end{cases}$$

where Pr_t is equal to 0.8, y_T^+ is thickness of laminar sub-layer, and U_p is the fluid velocity at point P.

2.3 Reynolds Heat Flux Model

2.3.1 Standard Reynolds Heat Flux Model

The feature of Reynolds heat flux model is to close Eq. (2.3a) by solving $-\overline{u_i' T'}$ directly. Similar to the derivation of Reynolds stress equation, the $-\overline{u_i' T'}$ equation can be obtained as follows:

$$\frac{\partial \overline{u_i'T'}}{\partial t} + U_i \frac{\partial \overline{u_i'T'}}{\partial x_k} = \frac{\partial}{\partial x_k}\left[-\overline{u_i'u_k'T'} - \delta_{ij}\frac{\overline{p'T'}}{\rho} + \alpha_t \overline{u_i'\frac{\partial T'}{\partial x_k}} + \frac{\mu}{\rho}\overline{T'\frac{\partial u_i'}{\partial x_k}} \right]$$
$$- \left(\overline{u_i'u_k'}\frac{\partial T}{\partial x_k} + \overline{u_k'T'}\frac{\partial U_i}{\partial x_k} \right) - (\alpha_t + \frac{\mu}{\rho})\overline{\frac{\partial T}{\partial x_k}\frac{\partial u_i'}{\partial x_k}} + \overline{\frac{p'}{\rho}\frac{\partial T'}{\partial x_k}} \qquad (2.12)$$

The first term on the right side of foregoing equation represents turbulent diffusion and molecular diffusion of Reynolds heat flux; the second and third terms represent, respectively, the production and dissipation of Reynolds heat flux; the fourth term represents the fluctuating pressure and temperature relationship.

The modeling of Eq. (2.12) by different authors gave different forms; one form is shown below [8] as an example:

$$\frac{\partial \overline{u_i'T'}}{\partial t} + U_i \frac{\partial \overline{u_i'T'}}{\partial x_k} = \frac{\partial}{\partial x_k}\left[\left(C_{T1}\frac{k}{\varepsilon}\overline{u_i'u_j'} + \alpha \right)\frac{\partial \overline{u_i'T'}}{\partial x_k} \right]$$
$$- \left(\overline{u_i'u_k'}\frac{\partial T}{\partial x_k} + \overline{u_k'T'}\frac{\partial U_j}{\partial x_k} \right) - C_{T2}\frac{\varepsilon}{k}\overline{u_i'T'} + C_{T3}\overline{u_k'T'}\frac{\partial U_i}{\partial x_k} \qquad (2.13)$$

where $C_{T1} = 0.07$, $C_{T2} = 3.2$, and $C_{T3} = 0.5$.

The standard Rayleigh heat flux model equations are as follows:

Energy conservation equation Eqs. (2.3) or (2.3a)
$\overline{u_i'T'}$ *equation* Eq. (2.13)
$\overline{T'^2}$ *equation* Eq. (2.7a)
$\varepsilon_{T'}$ *equation* Eq. (2.10)
α_t *equation* Eq. (2.6)

And CFD equation set to find U_i.

Under steady condition, the number of unknown in foregoing model equations is sixteen: U_i (three unknowns), P, k, ε, $\overline{u_i'u_j'}$ (six unknowns), $\overline{u_i'T'}$ (three unknowns) and T; while the model equations are also sixteen: one from continuity, three from momentum, the k, ε equations, six from $\overline{u_i'u_j'}$ equation Eq. (1.23), three from Eq. (2.13) and Eq. (2.3a). The model is closed.

2.3.2 Algebraic Reynolds Heat Flux Model

In Eq. (2.13) under steady condition, if the left side (convection) is considered equal to the first term (diffusion) of the right side, the following algebraic form is obtained:

$$- \left(\overline{u_i'u_k'}\frac{\partial T}{\partial x_k} + \overline{u_k'T'}\frac{\partial U_j}{\partial x_k} \right) - C_{T2}\frac{\varepsilon}{k}\overline{u_i'T'} + C_{T3}\overline{u_k'T'}\frac{\partial U_i}{\partial x_k} = 0 \qquad (2.14)$$

The algebraic model equations are similar to the standard Reynolds heat flux model except using Eq. (2.14) to replace Eq. (2.13) for reducing the computer load.

2.4 Summary

The energy conservation equation Eq. (2.3a) involves two unknowns: the time-averaged velocity U and the Reynolds heat flux $-\rho\overline{u_i'T'}$, the former can be found using CFD, and the latter can be solved by employing one of the following models:

(1) Turbulent thermal diffusivity model, in which the thermal diffusivity α_t, calculated by Eq. (2.6), is introduced to eliminate $-\rho\overline{u_i'T'}$ by Eq. (2.4) for the closure of Eq. (2.3). In calculating α_t, the $\overline{T'^2}$ and $\overline{T'^2} - \varepsilon_{T'}$ equations are necessary, which are given, respectively, by Eqs. (2.8) and (2.10). This model is commonly called $\overline{T'^2}$ model, which is isotropic.

(2) Reynolds heat flux model, in which the unknown $-\rho\overline{u_i'T'}$ is calculated directly using its modeled Eq. (2.13). Although the computer load is increased, it is rigorous and anisotropic. The Algebraic Reynolds heat flux model as given by Eq. (2.14) is the simplified form.

References

1. Nagano Y, Kim C (1988) A two-equation model for heat-transport in wall turbulent shear flows. J Heat Trans-T Asme 110(3):583–589
2. Elghobashi SE, Launder BE (1983) Turbulent time scales and the dissipation rate of temperature variance in the thermal mixing layer. Phys Fluids 26(9):2415–2419
3. Yoshizawa A (1988) Statistical modeling of passive-scalar diffusion in turbulent shear flows. J Fluid Mech 195:541–555
4. Elghobashi SE, LaRue JG (1983) The effect of mechanical stream on the dissipation rate of a scalar variance. In: 4th symposium on turbulent shear flows, Karlsruhe
5. Sommer TP, So MRC (1995) On the modeling of homogeneous turbulence in a stably stratified flow. Phys Fluids 7:2766–2777
6. Rhee GH, Sung HJ (1996) A nonlinear Low-Reynolds-number $k-\varepsilon$ model for turbulent separated and reattaching flow II, thermal field computation. Int J Heat and Mass Transfer 39(16):3465–3474
7. Versteeg HK, Malalasekera W (2005) An introduction to computational fluid dynamic. Wiley, New York
8. Chen CJ, Jaw SY (1998) Fundamentals of turbulence modeling. Taylor and Francis, London

Chapter 3
Basic Models of Computational Mass Transfer

Abstract The computational mass transfer (CMT) aims to find the concentration profile in process equipment, which is the most important basis for evaluating the process efficiency as well as the effectiveness of an existing mass transfer equipment. This chapter is dedicated to the description of the fundamentals and the recently published models of CMT for obtaining simultaneously the concentration, velocity and temperature distributions. The challenge is the closure of the differential species conservation equation for the mass transfer in a turbulent flow. Two models are presented. The first is a two-equation model termed as $\overline{c'^2} - \varepsilon_{c'}$ model, which is based on the Boussinesq postulate by introducing an isotropic turbulent mass transfer diffusivity. The other is the Reynolds mass flux model, in which the variable covariant term in the equation is modeled and computed directly, and so it is anisotropic and rigorous. Both methods are validated by comparing with experimental data.

Keywords Computational mass transfer · Reynolds averaging · Closure of time-averaged mass transfer equation · Two-equation model · Turbulent mass transfer diffusivity · Reynolds mass flux model

Nomenclature

[B]	Matrix of inverted Maxwell–Stefan Diffusivities, m^{-2} s
c	Instantaneous mass concentration of species i, kg m^{-3}; Molar concentration of species i in Sect. 3.4.2, mol s^{-3}
c_t	Total molar concentration of component i per m^3, mol m^{-3}
C	Time-average concentration, bulk concentration, kg m^{-3} in Table 3.1 mass fraction
C^+	Dimensionless concentration
c'	Fluctuating concentration, kg m^{-3}
$\overline{c'^2}$	Variance of fluctuating concentration, kg^2 m^{-6}
D	Molecular diffusivity, m^2 s^{-1}
D_e	Effective mass diffusivity, m^2 s^{-1}
D_t	Isotropic turbulent mass diffusivity, m^2 s^{-1}

D   Maxwell-Stefan diffusivity, $m^2 s^{-1}$
$\mathbf{D}_t$ Anisotropic turbulent mass diffusivity, $m^2 s^{-1}$
g Gravity acceleration, $m s^{-2}$
$[I]$ Identity matrix, dimensionless
J_w Mass flux at wall surface, $kg m^{-2} s^{-1}$
k Fluctuating kinetic energy, $m^2 s^{-2}$; mass transfer coefficient, $m s^{-1}$
$[k]$ Matrix of mass transfer coefficients, $m s^{-1}$
l Characteristic length, m
$[N_i]$ Molar mass flux of diffusing species i, $mol^{-2} s^{-1}$
$[N_t]$ Molar mass flux of multicomponent solution, $mol^{-2} s^{-1}$
p' Fluctuating pressure, $kg m^{-1} s^{-2}$
P Time-average pressure, $kg m^{-1} s^{-2}$
Pe Peclet number
$[R]$ Matrix of inverted mass transfer coefficients, $m^{-1} s$
r_c Ratio of fluctuating velocity dissipation time and fluctuating concentration dissipation time
S Source term
Sc Schmidt number
Sc_t Turbulent Schmidt number
t Time, s
$T^{'}$ Fluctuating temperature, K
$\overline{T'^2}$ Variance of fluctuating temperature, K^2
T Time-average temperature, K
u Instantaneous velocity of species i, $m s^{-1}$
u' Fluctuating velocity, $m s^{-1}$
u_τ Frictional velocity, $m s^{-1}$
u^+ Dimensionless velocity, $m s^{-1}$
U, V, W Time-average velocity in three directions, $m s^{-1}$
$[X]$ Matrix of correction factor
y^+ Dimensionless distance, m
α_t Turbulent thermal diffusivity, $m^{-1} s^{-1}$
$[\beta]$ Matrix of molar exchange of mass transfer in counter-diffusion due to the difference of latent hear of vaporization between component i and j, dimensionless
δ Kronecker sign; thickness of fluid film, m
ε Dissipation rate of turbulent kinetic energy, $m^2 s^{-3}$
$\varepsilon_{c'}$ Dissipation rate of concentration variance, $kg^2 m^{-6} s^{-1}$
ε_t Dissipation rate of temperature variance, $K^2 s^{-1}$
μ Viscosity, $kg m^{-1} s^{-1}$
μ_t Turbulent viscosity, $kg m^{-1} s^{-1}$
v_e Effective turbulent diffusivity, $m^2 s^{-1}$
ρ Density, $kg m^{-3}$
$[\Gamma]$ Matrix of non-ideality factor (in terms of activity coefficient γ), dimensionless

τ_μ, τ_c, τ_m Characteristic time scale, s

τ_w Near-wall stress, kg m^{-1} s^{-2}

The preceding two chapters review briefly the fundamentals of computational fluid dynamics (CFD) and computational heat transfer (CHT) for predicting the fluid velocity and temperature profiles as well as the relevant parameters for a specified process; such methodologies have been applied to the engineering and scientific areas with success.

Nevertheless, the computational methodology for mass transfer so far receives less attention. In many chemical engineering processes, the concentration profile is chiefly concerned as it is the basis for calculating the mass transfer efficiency. The conventional way to predict the concentration profile is using some simple but unreliable methods. The recent development of computation mass transfer (CMT) as described in this book provides a rigorous basis for dependable predictions of both concentration profile and the effectiveness of the mass transfer process as well as the interfacial effects on mass transfer efficiency.

The chemical process equipment involving mass transfer is always accompanied with fluid flow and heat transfer to form a complicated transport system. The model equations of mass transfer inevitably include fluid flow and heat transfer. Yet such large differential equation system is unclosed, and the method of closure is also a task to be tackled.

The process of mass transfer is realized by the mass transport from interfacial surface to the bulk fluid. Thus, the CMT covers the following two parts:

- **Process computation**: It aims at finding the local and the overall (whole equipment) concentration as well as velocity and temperature distributions and also their relevant parameters, which are essential in scale-up, better design and assessment of the efficiency of mass transfer equipment. The basic models of which are introduced in this chapter.
- **Interface computation**: It aims at predicting the influence of interfacial effect on the mass transfer, such as Marangoni convection and Rayleigh convection. Such effects may lead to the increase in the separation efficiency. Besides, the investigation of interfacial behaviors is also the basic step to understand the details of mass transferred from one phase to the other. This part of computation is described in the last two chapters of this book.

3.1 Equation of Mass Conservation and its Closure

For the mass transfer at low Reynolds number flow (no turbulence), the conversation equation of a mass species (component substance) is known to be

$$\frac{\partial c}{\partial t} + \frac{\partial}{\partial x_i}(u_i c) = \frac{\partial}{\partial x_i}\left(D \frac{\partial c}{\partial x_i}\right) + S_n \tag{3.1}$$

where c is the mass concentration of component species n (hereafter, the subscript n is omitted for simplifying the notation); u_i is the velocity of fluid ($i = i, j, k$); $u_i c$ is the mass flux of component species n; D is the molecular diffusivity of species n; S_n is the source term of species mass transferred from adjacent phase to the phase concerned or the species mass generated from chemical reaction. Note that, the unit of mass concentration c in this chapter is kg m^{-3} except in Sect. 3.4.2. In some literatures, the concentration is also expressed as mass fraction c_{mf}; the conversion is $c = \rho c_{mf}$ where ρ is the density of the mixture.

In chemical engineering practice, the mass transfer equipments, like distillation, absorption, and many others, are operated under turbulent flow condition. The u_i and c in Eq. (3.1) becomes instantaneous value, and their fluctuating character should be considered.

Similar to the average concept in CFD, the instantaneous concentration c in turbulent mass transfer can be resolved into time-averaged concentration C and fluctuating concentration c':

$$c = C + c'$$

Also as given in Chap. 1,

$$u_i = U_i + u_i'$$

Substitute foregoing relationship to Eq. (3.1) and take time average of each term, and note that

$$u_i c = U_i C + \overline{u_i' c'} \tag{3.2}$$

Substitute to Eq. (3.1) and after time-averaging yields the following form under turbulent condition:

$$\frac{\partial C}{\partial t} + \frac{\partial \left(U_i C + \overline{u_i' c'} \right)}{\partial x_i} = \frac{\partial}{\partial x_i} \left(D \frac{\partial C}{\partial x_i} \right) + S_n$$

which can be written as:

$$\frac{\partial C}{\partial t} + \frac{\partial U_i C}{\partial x_i} = \frac{\partial}{\partial x_i} \left(D \frac{\partial C}{\partial x_i} - \overline{u_i' c'} \right) + S_n \tag{3.3}$$

or

$$\frac{\partial C}{\partial t} + \frac{\partial U_i C}{\partial x_i} = \frac{\partial}{\partial x_i} D \frac{\partial C}{\partial x_i} - \frac{\partial \overline{u_i' c'}}{\partial x} + S_n \tag{3.3a}$$

The left sides of the foregoing equations represent, respectively, the increasing rate of time-average C and mass flux $U_i C$ with respect to time t and x_i. The first

term on the right side represents the molecular diffusion; the second term represents the turbulent diffusion in terms of $-\overline{u_i'c'}$ gradient which is unknown.

The term $-\overline{u_i'c'}$ (or its equivalent $-\rho\overline{u_i'c_{\mathrm{mf}}'}$) resembles the Reynolds stress $-\rho\overline{u_i'u_j'}$ and Reynolds heat flux $-\rho\overline{u_i'T'}$, and thus, we may call it as Reynolds mass flux for the convenience of terminology. The negative Reynolds mass flux, $-\left(-\overline{u_i'c'}\right) = \overline{u_i'c'}$, is called fluctuating mass flux hereafter as it is frequently appeared in the model calculation.

Since concentration is scalar quantity, $-\overline{u_i'c'}$ implies only three unknown quantities $\left(-\overline{u_i'c'}, -\overline{u_j'c'}, -\overline{u_k'c'}\right)$. If U_i can be found by CFD, Eq. (3.3) involves four unknowns $\left(C, -\overline{u_i'c'}, -\overline{u_j'c'}, -\overline{u_k'c'}\right)$; yet only three equation can be written from Eq. (3.3), it is unclosed and insufficient to obtain solution.

There are two categories of mathematical models for closing Eq. (3.3).

1. **Turbulent mass diffusivity models**: This category of models is conventional, which features to evaluate the unknown $-\overline{u_i'c'}$ in terms of a new variable: the turbulent mass diffusivity D_{t}. The following models belong to this category:

   - Turbulent Schmidt number model
   - Inert tracer model
   - Two-equation $\left(\overline{c'^2} - \varepsilon_{c'}\right)$ model.

2. **Reynolds mass flux models**: This category of models features to solve the unknown $-\overline{u_i'c'}$ directly instead of in terms of D_{t}. This category of models includes

   - Standard Reynolds mass flux model
   - Hybrid Reynolds mass flux model
   - Algebraic Reynolds mass flux model.

3.2 Turbulent Mass Diffusivity Model

Similar to the Boussinesq's postulate in CFD, the unknown $-\overline{u_i'c'}$ can be set to be proportional to the gradient of C:

$$-\overline{u_i'c'} = D_{\mathrm{t}}\frac{\partial C}{\partial x_i} \tag{3.4}$$

where D_{t} is the proportional coefficient and conventionally called it as turbulent mass diffusivity of species n (subscript n is omitted hereafter for simplifying the notation), which is still an unknown pending to find out. It should be pointed out that the D_{t} in Eq. (3.4) is isotropic in spite of $\frac{\partial C}{\partial x_i}$ is directional.

From Eq. (3.4), the fluctuating mass flux $\overline{u_i'c'}$ can be also expressed as proportional to the negative gradient of C as follows:

$$\overline{u_i'c'} = D_t\left(-\frac{\partial C}{\partial x_i}\right) \tag{3.4a}$$

In chemical engineering literature, Eq. (3.4a) is substantially the well-known Fick's law, which states that the mass flux flow is proportional to the negative concentration gradient due to the fact that the flow of mass flux is from high to the low concentration, or the flow any mass flux should be under negative concentration gradient.

Substituting Eqs. (3.4) to (3.3), we have

$$\frac{\partial C}{\partial t} + \frac{\partial U_i C}{\partial x_i} = \frac{\partial}{\partial x_i}(D + D_t)\frac{\partial C}{\partial x_i} + S_n \tag{3.5}$$

If U_i can be found from CFD, there are only two unknown variables in foregoing equation: C and D_t. The closure of Eq. (3.5) relies on the evaluation of D_t.

3.3 Conventional Turbulent Mass Diffusivity Model

3.3.1 Turbulent Schmidt Number Model

By considering the analogy between mass transfer and fluid flow, the turbulent mass diffusivity D_t may be analogous to the turbulent diffusivity (eddy diffusivity) $v_t\left(v_t = \frac{\mu_t}{\rho}\right)$ and independent of concentration. In other words, D_t is solely proportional to the turbulent diffusivity v_t, and can be represented by a dimensionless ratio, called turbulent Schmidt number, which is defined as $Sc_t = \frac{v_t}{D_t} = \frac{\mu_t}{\rho D_t}$, i.e., $D_t = \frac{1}{Sc_t}\frac{\mu_t}{\rho}$.

In the literature, Sc_t is usually assumed to be a constant ranging from 0.5 to 1.2 for different processes and operating conditions. Although this is the simplest way to obtain D_t, yet the correct value of Sc_t is hard to guess. Moreover, the relationship between D_t and μ_t is complicated as seen from Eq. (3.4) for D_t and Eq. (1.7) for μ_t; the assumption of constant Sc_t throughout the process and equipment cannot be proved and remains questionable.

3.3.2 Inert Tracer Model

Instead of assuming Sc_t, many authors employed the inert tracer technique to measure the time-average concentration C of an inert tracer in a simulator to find

the D_t experimentally. They customarily used the turbulent Peclet number Pe_t to express their experimental result. Pe_t is defined as $Pe_t = \frac{UL}{D_t}$, where U is the superficial or time-average fluid velocity and L is the characteristic length. The experimental Pe_t is usually reported as either a constant or as an empirical equation involving some constructional or operational variables, such as characteristic dimensions, Reynolds number, and others. Nevertheless, the D_t determined by inert tracer technique without mass transfer (denoted by $D_{t,tracer}$) is entirely different from that with mass transfer as seen by comparing the following two-species mass conservation equations from Eq. (3.5):

For the inert tracer process without mass transfer:

$$\frac{\partial C}{\partial t} + \frac{\partial U_i C}{\partial x_i} = \frac{\partial}{\partial x_i}\left(D + D_{t,tracer}\right)\frac{\partial C}{\partial x_i}$$

For the process with mass transfer:

$$\frac{\partial C}{\partial t} + \frac{\partial U_i C}{\partial x_i} = \frac{\partial}{\partial x_i}\left(D + D_t\right)\frac{\partial C}{\partial x_i} + S_n$$

Obviously, by comparing the foregoing two equations, D_t and $D_{t,tracer}$ is not equal; the difference between them is depending on the value of the source term S_n, which represents the rate of species mass to be transferred in the process.

In view of the drawbacks of foregoing models in applying Sc_t or using experimental correlation obtained by the inert tracer technique, some dependable models have been recently developed to overcome such insufficiency as shown in subsequent sections.

3.4 $\overline{c'^2} - \varepsilon_c$ Model (Two-Equation Model)

The investigation on using $\overline{c'^2} - \varepsilon_c$ two-equation model to calculate D_t was undertaken in recent years and had been applied with success to distillation, chemical absorption, adsorption, and catalytic reactor [1–11].

From the general concept of diffusion, the diffusivity is proportional to the diffusion velocity times the diffusion length. The former, represented by characteristic fluctuating velocity, can be proportional to $k^{0.5}$; here, k is the average fluctuating kinetic energy ($k = \frac{1}{2}\overline{u_i' u_i'}$, see Chap. 1). The latter, fluctuating diffusion length, can be considered to be the product of characteristic fluctuating velocity $k^{0.5}$ and fluctuating dissipation time τ_m. Then, we have $D_t \propto k^{0.5}\left(k^{0.5}\tau_m\right)$. The τ_m is referred to both the dissipation time of the characteristic velocity τ_μ and the fluctuating concentration τ_c. Since τ_μ and τ_c are not equal, we may take their geometric average τ_m, i.e., $\tau_m = \sqrt{\tau_\mu \tau_c}$.

As we know, $\tau_\mu = k/\varepsilon$, and similarly we may let $\tau_c = \overline{c'^2}\big/\varepsilon_{c'}$, where $\overline{c'^2} = \overline{c'c'}$ is the variance of average fluctuating concentration (dimension $kg^2\ m^{-6}$), and $\varepsilon_{c'}$ is its dissipation rate (dimension $kg^2\ m^{-6}\ s^{-1}$) so as both k/ε and $\overline{c'^2}\big/\varepsilon_{c'}$ have the dimension of "time" (t).

From the foregoing relationship, we obtain the following equation for calculating D_t:

$$D_t = C_{c0}k\left(\frac{k\overline{c'^2}}{\varepsilon\varepsilon_{c'}}\right)^{\frac{1}{2}} \tag{3.6}$$

where C_{c0} is a proportional constant. Since k and ε can be calculated by Eqs. (1.11a) and (1.13a) from CFD of Chap. 1, while $\overline{c'^2}$ and $\varepsilon_{c'}$ can be evaluated by the equations given in subsequent sections, the D_t can be obtained.

It is important to note that the ratio of $\frac{k}{\varepsilon}\big/\frac{\overline{c'^2}}{\varepsilon_{c'}}$ had been studied experimentally and found to be varying under different conditions [12–14]. Thus, D_t as given by Eq. (3.6) is a variable coefficient.

3.4.1 The $\overline{c'^2}$ and $\varepsilon_{c'}$ Equations

1. Exact $\overline{c'^2}$ equation

Substituting Eqs. (3.2) to (3.1) and subtracting Eq. (3.3), we have the transport equation for the fluctuating concentration c' as follows:

$$\frac{\partial c'}{\partial t} + \frac{\partial U_i c'}{\partial x_i} = \frac{\partial}{\partial x_i}\left(D\frac{\partial c'}{\partial x_i}\right) - \frac{\partial}{\partial x_i}\left(u_i'C + u_i'c' - \overline{u_i'c'}\right) \tag{3.7}$$

Multiply both sides by $2c'$ and take the average, i.e.,

$$\overline{2c'\left[\frac{\partial c'}{\partial t} + \frac{\partial}{\partial x_i}\left(U_i c'\right)\right]} = \overline{2c'\left[\frac{\partial}{\partial x_i}\left(D\frac{\partial c'}{\partial x_i}\right) - \frac{\partial}{\partial x_i}\left(u_i'C + u_i'c' - \overline{u_i'c'}\right)\right]} \tag{3.8}$$

The left side of the foregoing equation can be written as

$$\overline{2c'\left[\frac{\partial c'}{\partial t} + \frac{\partial}{\partial x_i}\left(U_i c'\right)\right]} = \frac{\partial\left(\overline{c'^2}\right)}{\partial t} + \frac{\partial}{\partial x_i}\left(U_j\overline{c'^2}\right)$$

For the simplification of the right side, let us note that according to the following derivation,

$$\frac{\partial^2\left(c'^2\right)}{\partial x_i\partial x_i} = \frac{\partial}{\partial x_i}\left[\frac{\partial(c'^2)}{\partial x_i}\right] = \frac{\partial}{\partial x_i}\left[2c'\frac{\partial c'}{\partial x_i}\right] = 2\left[\frac{\partial c'}{\partial x_i}\frac{\partial c'}{\partial x_i} + c'\frac{\partial^2 c'}{\partial x_i}\right]$$

and after rearranging to yield the following relationship:

$$2c' \frac{\partial^2 c'}{\partial x_i \partial x_i} = \frac{\partial^2 (c'^2)}{\partial x_i \partial x_i} - 2 \frac{\partial c' \partial c'}{\partial x_i \partial x_i}$$

Take the average of the foregoing equation and multiply by D, also define the dissipation rate of fluctuating concentration variance $\varepsilon_{c'}$ to be

$$\varepsilon_{c'} = D \overline{\frac{\partial c'}{\partial x_i} \frac{\partial c'}{\partial x_i}} \tag{3.9}$$

Then, the first term on the right side of Eq. (3.8) takes the following form:

$$\overline{2c' \left[\frac{\partial}{\partial x_i} \left(D \frac{\partial c'}{\partial x_i} \right) \right]} = D \left[\frac{\partial^2 \overline{c'^2}}{\partial x_i \partial x_i} - 2 \overline{\frac{\partial c'}{\partial x_i} \frac{\partial c'}{\partial x_i}} \right] = D \frac{\partial^2 \overline{c'^2}}{\partial x_i \partial x_i} - 2\varepsilon_{c'}$$

For the second term, since $\frac{\partial u_i'}{\partial x_i} = 0$, it becomes

$$\overline{-2c' \frac{\partial}{\partial x_i} (u_i' C)} = -2\overline{c' \left[C \frac{\partial u_i'}{\partial x_i} + u_i' \frac{\partial C}{\partial x_i} \right]} = -2\overline{c' C \frac{\partial u_i'}{\partial x_i}} - 2\overline{c' u_i'} \frac{\partial C}{\partial x_i} = -2\overline{c' u_i'} \frac{\partial C}{\partial x_i}$$

For the third term, due to

$$\frac{\partial}{\partial x_i} (-u_i' c'^2) = - \left[2u_i' c' \frac{\partial c'}{\partial x_i} + c'^2 \frac{\partial u_i'}{\partial x_i} \right] = -2c' \frac{\partial u_i' c'}{\partial x_i}$$

we obtain

$$-2\overline{c' \frac{\partial}{\partial x_i} (u_i' c')} = - \frac{\partial}{\partial x_i} \left[\overline{u_i' c'^2} \right]$$

The fourth term can be neglected, i.e.,

$$2\overline{c' \frac{\partial}{\partial x_i} (\overline{u_i' c'})} = 0$$

After the foregoing arrangement, the exact equation of $\overline{c'^2}$ takes the following form:

$$\frac{\partial \left(\overline{c'^2} \right)}{\partial t} + \frac{\partial}{\partial x_i} \left(U_i \overline{c'^2} \right) = \frac{\partial}{\partial x_i} \left[D \frac{\partial \overline{c'^2}}{\partial x_i} - \overline{u_i' c'^2} \right] - 2\overline{u_i' c'} \frac{\partial C}{\partial x_i} - 2\varepsilon_{c'} \tag{3.10}$$

The first term on the right side of the foregoing equation represents the transport of $\overline{c'^2}$ due to molecular motion and turbulent fluctuation; the second term represents the production of fluctuating mass flux due to average concentration gradient; the third term represents the dissipation. Equation (3.10) should be further modeled to suit computation as shown in subsequent section.

2. Modeling of $\overline{c'^2}$ equation

Similar to the Boussinesq postulate or Fick's law, the $\overline{u_i'c'^2}$ and $\overline{u_i'c'}$ on the right side of Eq. (3.10) can be considered proportional to the corresponding negative gradients as shown below

$$\overline{u_i'c'^2} = \frac{D_t}{\sigma_{c'^2}}\left(-\frac{\partial \overline{c'^2}}{\partial x_i}\right)$$

$$\overline{u_i'c'} = D_t\left(-\frac{\partial C}{\partial x_i}\right)$$

where $\sigma_{c'^2}$ is correction factor, usually taken as 1. Then, the modeled $\overline{c'^2}$ equation becomes

$$\frac{\partial \overline{c'^2}}{\partial t} + \frac{\partial U_i \overline{c'^2}}{\partial x_i} = \frac{\partial}{\partial x_i}\left[\left(D + \frac{D_t}{\sigma_{c'^2}}\right)\frac{\partial \overline{c'^2}}{\partial x_i}\right] - 2D_t\left(\frac{\partial C}{\partial x_i}\right)^2 - 2\varepsilon_{c'} \quad (3.11)$$

The foregoing equation still involves two unknown quantities: D_t and $\varepsilon_{c'}$; the evaluation of $\varepsilon_{c'}$ is given in subsequent section.

3. Exact $\varepsilon_{c'}$ equation

Differentiate Eq. (3.1) with respect to x_k to get

$$\frac{\partial}{\partial t}\left(\frac{\partial c}{\partial x_k}\right) + \frac{\partial}{\partial x_k}\left[\frac{\partial}{\partial x_i}(u_i c)\right] = D\frac{\partial^2}{\partial x_i \partial x_i}\left(\frac{\partial c}{\partial x_k}\right)$$

Multiply by $2D\partial C/\partial x_k$ to obtain

$$\frac{\partial}{\partial t}\left(D\frac{\partial c}{\partial x_k}\frac{\partial c}{\partial x_k}\right) + u_i\frac{\partial}{\partial x_i}\left(D\frac{\partial c}{\partial x_k}\frac{\partial c}{\partial x_k}\right) + 2D\frac{\partial u_i}{\partial x_k}\frac{\partial c}{\partial x_k}\frac{\partial c}{\partial x_i}$$
$$= D\frac{\partial^2}{\partial x_i x_i}\left(D\frac{\partial c}{\partial x_k}\frac{\partial c}{\partial x_k}\right) - 2D^2\frac{\partial^2 c}{\partial x_k \partial x_i}\frac{\partial^2 c}{\partial x_i x_k} \quad (3.12)$$

Substituting $u_i = U_i + u_i'$ and $c = C + c'$ to the foregoing equation and taking the time-average, we have

$$\frac{\partial}{\partial t}\left(D\frac{\partial C}{\partial x_k}\frac{\partial C}{\partial x_k}\right) + \frac{\partial}{\partial t}\left(D\overline{\frac{\partial c'}{\partial x_k}\frac{\partial c'}{\partial x_k}}\right) + U_i\frac{\partial}{\partial x_i}\left(D\frac{\partial C}{\partial x_k}\frac{\partial C}{\partial x_k}\right) + U_i\frac{\partial}{\partial x_i}\left(D\overline{\frac{\partial c'}{\partial x_k}\frac{\partial c'}{\partial x_k}}\right)$$
$$+ 2D\frac{\partial}{\partial x_i}\left[\overline{u_i'\frac{\partial c'}{\partial x_k}}\frac{\partial C}{\partial x_k}\right] + D\frac{\partial}{\partial x_i}\left(\overline{u_i'\frac{\partial c'}{\partial x_k}\frac{\partial c'}{\partial x_k}}\right) + 2D\frac{\partial U_i}{\partial x_k}\frac{\partial C}{\partial x_i}\frac{\partial C}{\partial x_k} + 2D\overline{\frac{\partial u_i'}{\partial x_k}\frac{\partial c'}{\partial x_k}}\frac{\partial C}{\partial x_i}$$
$$+ 2D\overline{\frac{\partial u_i'}{\partial x_k}\frac{\partial c'}{\partial x_i}}\frac{\partial C}{\partial x_k} + 2\rho D\overline{\frac{\partial c'}{\partial x_i}\frac{\partial c'}{\partial x_k}}\frac{\partial U_i}{\partial x_k} + 2D\overline{\frac{\partial u_i'}{\partial x_k}\frac{\partial c'}{\partial x_i}\frac{\partial c'}{\partial x_k}} = D\frac{\partial^2}{\partial x_i \partial x_i}\left(D\frac{\partial C}{\partial x_k}\frac{\partial C}{\partial x_k}\right)$$
$$+ D\frac{\partial^2}{\partial x_i \partial x_i}\left(D\overline{\frac{\partial c'}{\partial x_k}\frac{\partial c'}{\partial x_k}}\right) - 2D^2\frac{\partial^2 C}{\partial x_k \partial x_i}\frac{\partial^2 C}{\partial x_i \partial x_k} - 2D^2\overline{\frac{\partial^2 c'}{\partial x_k \partial x_i}\frac{\partial^2 c'}{\partial x_i \partial x_k}}$$

$$(3.13)$$

Differentiate Eq. (3.3) with respect to x_k, then multiply by $2D\frac{\partial C}{\partial x_k}$ and take the time-average, we get

$$
\frac{\partial}{\partial t}\left(D\frac{\partial C}{\partial x_k}\frac{\partial C}{\partial x_k}\right) + U_i\frac{\partial}{\partial x_i}\left(D\frac{\partial C}{\partial x_k}\frac{\partial C}{\partial x_k}\right) + 2D\frac{\partial U_i}{\partial x_k}\frac{\partial C}{\partial x_i}\frac{\partial C}{\partial x_k}
$$
$$
= D\frac{\partial^2}{\partial x_i \partial x_i}\left(D\frac{\partial C}{\partial x_k}\frac{\partial C}{\partial x_k}\right) - 2D^2\frac{\partial^2 C}{\partial x_k \partial x_i}\frac{\partial^2 C}{\partial x_i \partial x_k} - 2D\frac{\partial}{\partial x_i}\left[\overline{u'_i\frac{\partial c'}{\partial x_k}}\frac{\partial C}{\partial x_k}\right] \quad (3.14)
$$
$$
- 2D\overline{\frac{\partial u'_i}{\partial x_k}\frac{\partial c'}{\partial x_i}}\frac{\partial C}{\partial x_k}
$$

Subtracting Eqs. (3.14) from (2.13) and noting that $\varepsilon_{c'} = D\overline{\frac{\partial c'}{\partial x_i}\frac{\partial c'}{\partial x_i}}$, we have the following exact transport equation of $\varepsilon_{c'}$:

$$
\frac{\partial \varepsilon_{c'}}{\partial t} + \frac{\partial U_i \varepsilon_{c'}}{\partial x_i} = \frac{\partial}{\partial x_i}\left(D\frac{\partial \varepsilon_{c'}}{\partial x_i} - \overline{\varepsilon_{c'}u'_i}\right) - 2D\overline{\frac{\partial u'_i}{\partial x_k}\frac{\partial c'}{\partial x_k}}\frac{\partial C}{\partial x_i}
$$
$$
- 2D\overline{\frac{\partial c'}{\partial x_i}\frac{\partial c'}{\partial x_k}}\frac{\partial U_i}{\partial x_k} - 2\rho D\overline{u'_i\frac{\partial c'}{\partial x_k}}\frac{\partial^2 C}{\partial x_i \partial x_k} - 2D^2\overline{\frac{\partial^2 c'}{\partial x_k \partial x_i}\frac{\partial^2 c'}{\partial x_i \partial x_k}} - 2D\overline{\frac{\partial u'_i}{\partial x_k}\frac{\partial c'}{\partial x_i}\frac{\partial c'}{\partial x_k}}
$$
$$
\quad (3.15)
$$

The first term on the right side of the foregoing equation represents the molecular and turbulent diffusion of $\varepsilon_{c'}$; the second, third, and fourth terms, represent, respectively the production of $\varepsilon_{c'}$ by average concentration gradient, average velocity gradient, and velocity fluctuation; the fifth and sixth terms represent the dissipation. Equation (3.15) should be further modeled to the form suitable for numerical computation as shown below.

4. Modeling of $\varepsilon_{c'}$ equation

Let $\overline{u'_i\varepsilon_{c'}}$ be proportional to the negative gradient of $\varepsilon_{c'}$

$$
\overline{u'_i\varepsilon_{c'}} = -\frac{D_t}{\sigma_{\varepsilon_{c'}}}\frac{\partial \varepsilon_{c'}}{\partial x_i}
$$

where $\varepsilon_{c'}$ is a correction factor, usually letting $\sigma_{c'} = 1$ except for some special cases. Thus, the first term on the right side of Eq. (3.15) can be modeled as follows:

$$
\frac{\partial}{\partial x_i}\left(D\frac{\partial \varepsilon_{c'}}{\partial x_i} - \overline{\varepsilon_{c'}u'_i}\right) = \frac{\partial}{\partial x_i}\left(D + \frac{D_t}{\sigma_{\varepsilon_{c'}}}\right)\frac{\partial \varepsilon_{c'}}{\partial x_i}
$$

The second term can be considered proportional to the product of $\overline{c'u'_i}$ and the concentration gradient $\frac{\partial C}{\partial x_i}$. According to the modeling rule, the dimension of a term before and after modeling should be equal, the proportional coefficient is set to be $C_{c1}\frac{\varepsilon_{c'}}{\overline{c'^2}}$ where C_{c1} is constant and $\frac{\varepsilon_{c'}}{\overline{c'^2}}$ represents the dimension ($1/t$). Then, we have

$$-2D\overline{\frac{\partial u_i'}{\partial x_k}\frac{\partial c'}{\partial x_k}}\frac{\partial C}{\partial x_i} = -C_{c1}\frac{\varepsilon_{c'}}{c'^2}\overline{c'u_i'}\frac{\partial C}{\partial x_i}$$

The third term can be considered proportional to the product of $\overline{u_i'u_j'}$ and the velocity gradient $\frac{\partial U}{\partial x_i}$; the proportion coefficient is equal to $C_{c2}\frac{\varepsilon_{c'}}{k}$ from the modeling rule of dimensional equality. We have

$$-2D\overline{\frac{\partial c'}{\partial x_i}\frac{\partial c'}{\partial x_k}}\frac{\partial U_i}{\partial x_k} = -C_{c2}\frac{\varepsilon_{c'}}{k}\overline{u_i'u_j'}\frac{\partial U_i}{\partial x_i}$$

The fourth term can be modeled as

$$-2D\overline{u_i'\frac{\partial c'}{\partial x_k}}\frac{\partial^2 C}{\partial x_i\partial x_k} = -DD_t\left(\frac{\partial^2 C}{\partial x_i\partial x_i}\right)^2$$

The fifth term can be considered proportional to $\varepsilon_{c'}^2$; the proportional coefficient is $C_{c3}\frac{1}{c'^2}$ by considering the dimension equality, so that

$$-2D^2\overline{\frac{\partial^2 c'}{\partial x_k\partial x_i}\frac{\partial^2 c'}{\partial x_i\partial x_k}} = -C_{c3}\frac{\varepsilon_{c'}^2}{c'^2}$$

The sixth term can be considered proportional to $\varepsilon_{c'}$ as follows and the proportional coefficient is $C_{c4}\frac{\varepsilon}{k}$ accordingly.

$$-2D\overline{\frac{\partial u_j'}{\partial x_k}\frac{\partial c'}{\partial x_i}\frac{\partial c'}{\partial x_k}} = -C_{c4}\frac{\varepsilon\varepsilon_{c'}}{k}$$

With all modeling terms, Eq. (3.15) becomes

$$\frac{\partial\varepsilon_{c'}}{\partial t} + \frac{\partial U_i\varepsilon_{c'}}{\partial x_i} = \frac{\partial}{\partial x_i}\left[\left(D + \frac{D_t}{\sigma_{\varepsilon_{c'}}}\right)\frac{\partial\varepsilon_{c'}}{\partial x_i}\right] - C_{c1}\frac{\varepsilon_{c'}}{c'^2}\overline{u_j'c'}\frac{\partial C}{\partial x_i}$$
$$- C_{c2}\overline{u_i'u_j'}\frac{\partial U_i}{\partial x_i}\frac{\varepsilon_c}{k} - C_{c3}\frac{\varepsilon_{c'}^2}{c'^2} - C_{c4}\frac{\varepsilon\varepsilon_{c'}}{k} - DD_t\left(\frac{\partial^2 C}{\partial x_i\partial x_i}\right)^2$$

Since the value DD_t is very small, the term $DD_t\left(\frac{\partial^2 C}{\partial x_i\partial x_i}\right)^2$ can be neglected. The final modeling form of $\varepsilon_{c'}$ equation is as follows (*modeling form 1*):

$$\frac{\partial\varepsilon_{c'}}{\partial t} + \frac{\partial U_i\varepsilon_{c'}}{\partial x_i} = \frac{\partial}{\partial x_i}\left[\left(D + \frac{D_t}{\sigma_{\varepsilon_c}}\right)\frac{\partial\varepsilon_{c'}}{\partial x_i}\right] - C_{c1}\frac{\varepsilon_{c'}}{c'^2}\overline{u_j'c'}\frac{\partial C}{\partial x_i}$$
$$- C_{c2}\overline{u_i'u_j'}\frac{\partial U_i}{\partial x_i}\frac{\varepsilon_c}{k} - C_{c3}\frac{\varepsilon_{c'}^2}{c'^2} - C_{c4}\frac{\varepsilon\varepsilon_{c'}}{k} \qquad (3.16)$$

Sun et al. [4] further simplified the second and third terms of Eq. (3.16) to be

$$C_{c1}\frac{\varepsilon_{c'}}{\overline{c'^2}}\overline{u'_j c'}\frac{\partial C}{\partial x_i} + C_{c2}\overline{u'_i u'_j}\frac{\partial U_i}{\partial x_i} = C_{c1}\frac{\varepsilon_{c'}^2}{\overline{c'^2}}\left(\frac{\partial C}{\partial x_i}\right)^2$$

Then, $\varepsilon_{c'}$ equation becomes (*modeling form 2*)

$$\frac{\partial \varepsilon_{c'}}{\partial t} + \frac{\partial U_i \varepsilon_{c'}}{\partial x_i} = \frac{\partial}{\partial x_i}\left[\left(D + \frac{D_t}{\sigma_{\varepsilon_{c'}}}\right)\frac{\partial \varepsilon_{c'}}{\partial x_i}\right] - C_{c1}D_t\frac{\varepsilon_{c'}}{\overline{c'^2}}\left(\frac{\partial C}{\partial x_i}\right)^2 - C_{c4}\frac{\varepsilon\varepsilon_{c'}}{k} \qquad (3.17)$$

After a numbers of calculations, it was found [4] that the $C_{c4}\frac{\varepsilon\varepsilon_{c'}}{k}$ term is much greater than the $C_{c3}\frac{\varepsilon_{c'}^2}{\overline{c'^2}}$ term, and the neglect of the latter do not affect substantially the simulated result. Thus, $\varepsilon_{c'}$ equation can be further simplified to (*modeling form 3*):

$$\frac{\partial \varepsilon_{c'}}{\partial t} + \frac{\partial U_i \varepsilon_{c'}}{\partial x_i} = \frac{\partial}{\partial x_i}\left[\left(D + \frac{D_t}{\sigma_{\varepsilon_{c'}}}\right)\frac{\partial \varepsilon_{c'}}{\partial x_i}\right] - C_{c1}D_t\frac{\varepsilon_{c'}}{\overline{c'^2}}\left(\frac{\partial C}{\partial x_i}\right)^2 - C_{c4}\frac{\varepsilon}{k}\varepsilon_{c'} \qquad (3.18)$$

5. Determination of model constants
(a) *Model constants in Eq*. (3.16)

Principally, since both concentration and temperature are scalar quantity, Eqs. (3.16) and (2.10) belong to the same kind of scalar equation. By comparison, the $\varepsilon_{c'}$ Eq. (3.16) is identical with Eq. (2.10) if concentration C is replaced by temperature T and D_t is changed to α_t. Thus, their model constants can be considered approximately to be interchangeable. Referring to Table 2.1 in Chap. 2, the model constant given in the table can be used for $\varepsilon_{c'}$ equation. For instance, according to Sommer model, the model constants are [15]: $C_{c1} = 1.8$, $C_{c2} = 0.72$, $C_{c3} = 2.2$, $C_{c4} = 0.8$, $\sigma_{\varepsilon_{c'}} = 1.0$ and $C_{c0} = 0.11$.

The model constants can be modified to achieve more accurate simulation for an individual process.

(b) **Model constants in Eqs**. (3.17) **and** (3.18)
1. **Model constant C_{c1}**

In view of insufficient research on the determining the model constant C_{c1}, we may take the result by Sun [2] that the value of C_{c1} for the best fitting of experimental data is $C_{c1} = 1.8$ in using Eq. (3.17) and $C_{c1} = 2.0$ in using Eq. (3.18).

2. **Model constant C_{c2} and C_{c3}**

By the principle that all anisotropic complicated transport equation should be also valid for isotropic simple case; the model constants can be obtained by reducing the corresponding equation to the simple flow and transport conditions.

For the uniform one-dimensional isotropic steady turbulent flow and mass transfer, the equations of k, ε, $\overline{c'^2}$ and $\varepsilon_{c'}$ are reduced to the following forms:

$$U\frac{\mathrm{d}k}{\mathrm{d}x} = -\varepsilon$$

$$U\frac{\mathrm{d}\varepsilon}{\mathrm{d}x} = -C_{\varepsilon2}\frac{\varepsilon^2}{k}$$

$$U\frac{\mathrm{d}\overline{c'^2}}{\mathrm{d}x} = -2\varepsilon_{c'} \tag{3.19}$$

$$U\frac{\mathrm{d}\varepsilon_{c'}}{\mathrm{d}x} = -C_{c3}\frac{\varepsilon_{c'}^2}{\overline{c'^2}} - C_{c4}\frac{\varepsilon\varepsilon_{c'}}{k}$$

Let $r_c = \left(\frac{\overline{c'^2}}{\varepsilon_{c'}}\right)\Big/\left(\frac{k}{\varepsilon}\right)$, the $\varepsilon_{c'}$ can be expressed as follows

$$\varepsilon_{c'} = \frac{\varepsilon\overline{c'^2}}{r_c k} \tag{3.20}$$

Substituting to Eq. (3.19) and rearranging, we have

$$
\begin{aligned}
U\frac{\mathrm{d}\varepsilon_{c'}}{\mathrm{d}x} &= \frac{U}{r_c}\frac{\mathrm{d}\left(\overline{\varepsilon c'^2}\Big/k\right)}{\mathrm{d}x} \\
&= \frac{U}{r_c}\left[-\frac{\varepsilon\overline{c'^2}}{k^2}\frac{\mathrm{d}k}{\mathrm{d}x} + \frac{\overline{c'^2}}{k}\frac{\mathrm{d}\varepsilon}{\mathrm{d}x} + \frac{\varepsilon}{k}\frac{\mathrm{d}\overline{c'^2}}{\mathrm{d}x}\right] \\
&= \frac{1}{r_c}\left(\frac{\varepsilon^2\overline{c'^2}}{k^2} - C_{\varepsilon2}\frac{\varepsilon^2\overline{c'^2}}{k^2} - 2\frac{\varepsilon\varepsilon_{c'}}{k}\right) \\
&= -\frac{2}{r_c}\frac{\varepsilon\varepsilon_{c'}}{k} - r_c(C_{\varepsilon2}-1)\frac{\varepsilon_{c'}^2}{\overline{c'^2}}
\end{aligned}
\tag{3.21}
$$

Comparing Eqs. (3.19) and (3.21), the following relationships are obtained:

$$C_{c3} = r_c(C_{\varepsilon2}-1)$$

$$C_{c4} = \frac{2}{r_c}$$

If r_c is considered approximately constant and set to be 0.9 [1] and $C_{\varepsilon2} = 1.92$ is taken from standard k–ε model, we have $C_{c3} = 0.83$, $C_{c4} = 2.22$. Note that, C_{c2} and C_{c3} may be changed depending on the value of r_c chosen under different conditions.

3. **Model constant C_{c0}**

Combining the following equations,

$$\mu_t = C_\mu\rho\frac{k^2}{\varepsilon}, \quad Sc_t = \frac{\mu_t}{\rho D_t}, \quad r_c = \left(\frac{\overline{c'^2}}{\varepsilon_c}\right)\Big/\left(\frac{k}{\varepsilon}\right), \quad D_t = C_{c0}k\left(\frac{k\overline{c'^2}}{\varepsilon\varepsilon_{c'}}\right)^{\frac{1}{2}},$$

we get the following relationship to calculate C_{c0}

$$C_{c0} = \frac{C_\mu}{Sc_t\sqrt{r_c}}$$

Since Sc_t and r_c are indeterminate, the C_{c0} cannot be obtained. However, if we take the approximate value of $Sc_t = 0.7$ and $r_c = 0.9$ as given by Scherwood [16], and $C_\mu = 0.09$ from standard k–ε model, we obtain approximately $C_{c0} = 0.14$. On the other hand, if taking $Sc_t = 0.85$, we get $C_{c0} = 0.11$. Thus, C_{c0} may be set within the range of 0.11 to 0.14 to suit different processes.

(c) **Summary**

Model constants in Eq. (3.16) (*modeling form 1*), $C_{c1} = 1.8$, $C_{c2} = 0.72$, $C_{c3} = 2.2$, $C_{c4} = 0.8$, and $C_{c0} = 0.11$.

Model constants in Eq. (3.17), (*modeling form 2*), $C_{c1} = 1.8$, $C_{c3} = 0.83$, $C_{c4} = 2.22$, and $C_{c0} = 0.14$.

Model constants in Eq. (3.18), (*modeling form 3*), $C_{c1} = 2.0$, $C_{c4} = 2.22$, and $C_{c0} = 0.14$.

6. **Comparison of simulated results using different modeling form of $\varepsilon_{c'}$ equation**

The use of two-equation model to close mass conservation equation Eq. (3.5) involves four unknowns (C, D_t, $\overline{c'^2}$, $\varepsilon_{c'}$) as the U_i can be calculated by CFD. While the model equations are also four, i.e., Eqs. (3.5) and (3.6), $\overline{c'^2}$ and $\overline{c'^2}$ equations, so that Eq. (3.5) can be closed and solved.

Sun simulated the concentration profile of an industrial scale distillation tray [17] with different modeling form of $\varepsilon_{c'}$ equation [2]. The simulated results are shown in Figs. 3.1 and 3.2.

As seen from Fig. 3.1, the simulated contours of concentration are almost the same in spite of using different form of $\varepsilon_{c'}$ modeling equation. Similar situation is also seen in Fig. 3.2; all the volume averages D_t are close to the experimental measurement by Cai [17]. Therefore, it is not surprised that the use of different modeling equation and different model constants may give very close result.

Among three $\varepsilon_{c'}$ modeling equations, Eq. (3.17) looks appropriate as it involves only three constants rather than four. However, these constants may be adjusted to suit different processes if necessary.

3.4.2 The $\overline{c'^2} - \varepsilon_{c'}$ Model Equation Sets

If no heat effect is involved in the mass transfer process, the two-equation model consists of two sets of equations, i.e., the CFD equation set for computing velocity U_i distribution and the mass transfer equation set for computing the concentration
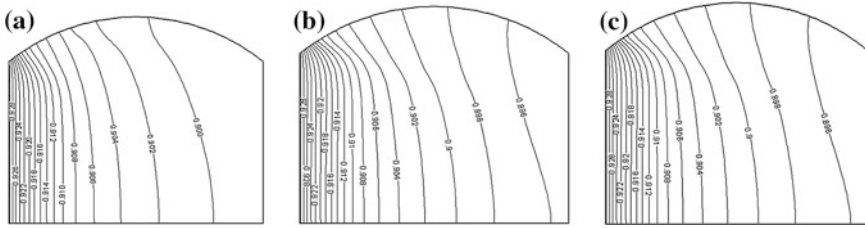
Fig. 3.1 The simulated concentration contours on a column tray using different $\varepsilon_{c'}$ modeling equations and model constants (I) Operating condition: pressure 165 kPa, liquid rate 30.66 m^3 h^{-1}, vapor rate 5.75 kg s^{-1}, tray No. 2, 20 mm above tray floor, separating system: methylcyclohexane and *n*-heptane **a** using Eq. (3.16) and $C_{c0} = 0.11$, $C_{c1} = 1.8$, $C_{c2} = 0.72$, $C_{c3} = 2.2$, $C_{c4} = 0.8$, $\sigma_{c'^2} = 1.0$, $\sigma_{\varepsilon_{c'}} = 1.0$, **b** using Eq. (3.17) and $C_{c0} = 0.14$, $C_{c1} = 1.8$, $C_{c3} = 0.83$, $C_{c4} = 2.22$, $\sigma_{c'^2} = 1.0$, $\sigma_{\varepsilon_{c'}} = 1.0$, **c** using Eq. (3.18) and $C_{c0} = 0.14$, $C_{c1} = 2.0$, $C_{c4} = 2.22$, $\sigma_{c'^2} = 1.0$, $\sigma_{\varepsilon_{c'}} = 1.0$ (Reprinted from Ref. [4], Copyright 2007, with permission from Elsevier)
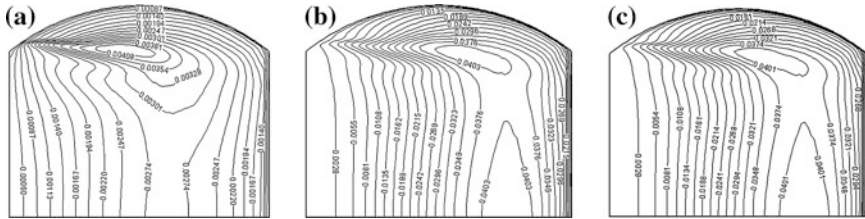
Fig. 3.2 The simulated mass diffusivity D_t contours on a column tray using different $\varepsilon_{c'}$ modeling equations and model constants (II) The conditions of **a**, **b**, and **c** are given in Fig. 3.1 (Reprinted from Ref. [4], Copyright 2007, with permission from Elsevier)

distribution. In some mass transfer equipments, if heat transfer is involved, the heat transfer equation set should be added to the model equation system.

Several points should be mentioned for applying model equations:

- Since the mass transfer process usually involves two phases, the governing equations should be written for a designated phase, such as liquid phase or gas phase.
- In the mass transfer processes, the volume and density of each phase are changing due to the mass transferred from one phase to the other.
- In considering the total mass of a fluid phase is not remained constant due to undertaking mass transfer, the continuity equation in CFD is not equal to zero and also lost its meaning. A source term S_m is added to the continuity equation representing the rate of mass change or generated by chemical reaction in the fluid phase concerned; the new equation $\frac{\partial \rho}{\partial t} + \frac{\partial \rho U_i}{\partial x_i} = S_n$ is designated as overall mass conservation equation. Note that, in this case, $\frac{\partial U_i}{\partial x_i} \neq 0$ even at constant ρ;

thus, Eq. (1.5), in which the assumption of $\frac{\partial U_i}{\partial x_i} = 0$ is not valid for the fluid flow involving mass transfer.

- Since the mass transfer process involves two or more phases (see Sect. 3.6), the interacted liquid-phase model is convenient for the process simulation by CMT. In applying this model, all parameters involved, such as U, u, ρ, k, ε, μ, μ_t, α, α_t, T, T', $k_{T'}\varepsilon_{T'}c$, C, D, D_t, $k_{c'}$, $\varepsilon_{c'}$ in the model equation are denoted to liquid phase.

The $\overline{c'^2} - \varepsilon_{c'}$ model equation sets are given below.

(I) Fluid dynamic equation set (*k*–*ε* model):

Overall Mass conservation equation

$$\frac{\partial \rho}{\partial t} + \frac{\partial \rho U_i}{\partial x_i} = S_m \tag{3.22}$$

Momentum conservation equation

$$\frac{\partial \rho U_i}{\partial t} + \frac{\partial \rho U_i U_j}{\partial x_i} = -\frac{\partial P}{\partial x_j} + \mu \frac{\partial^2 U_i}{\partial x_i \partial x_i} + \frac{\partial \left(-\rho \overline{u_i' u_j'}\right)}{\partial x_i} + \rho S_i$$
$$- \rho \overline{u_i' u'}_j = \mu_t \left(\frac{\partial U_i}{\partial x_j} + \frac{\partial U_j}{\partial x_i}\right) - \frac{1}{3} \rho \delta_{ij} \overline{u_i' u_i'} \tag{1.4}$$

k equation

$$\frac{\partial (\rho k)}{\partial t} + \frac{\partial (\rho U_i k)}{\partial x_i} = \frac{\partial}{\partial x_i} \left[\left(\mu + \frac{\mu_t}{\sigma_k}\right) \frac{\partial k}{\partial x_i}\right] + G_k - \rho \varepsilon$$
$$G_k = \mu_t \left(\frac{\partial U_j}{\partial x_i} + \frac{\partial U_i}{\partial x_j}\right) \frac{\partial U_j}{\partial x_i} \tag{1.11a}$$

ε equation

$$\frac{\partial (\rho \varepsilon)}{\partial t} + \frac{\partial (\rho U_i \varepsilon)}{\partial x_i} = \frac{\partial}{\partial x_i} \left[\left(\mu + \frac{\mu_t}{\sigma_\varepsilon}\right) \frac{\partial \varepsilon}{\partial x_i}\right] + C_{1\varepsilon} \frac{\varepsilon}{k} G_k - C_{2\varepsilon} \rho \frac{\varepsilon^2}{k} \tag{1.13a}$$

μ_t *equation*

$$\mu_t = C_\mu \rho \frac{k^2}{\varepsilon} \tag{1.14}$$

Model constant: $C_\mu = 0.09$, $C_{1\varepsilon} = 1.44$, $C_{2\varepsilon} = 1.92$, $\sigma_k = 1.0$, $\sigma_\varepsilon = 1.3$.

(II) Heat transfer equation set ($\overline{T'^2} - \varepsilon_{T'}$ model):

Energy conservation equation

$$\frac{\partial \rho T}{\partial t} + U_i \frac{\partial \rho T}{\partial x_i} = \frac{\lambda}{C_p} \frac{\partial^2 T}{\partial x_i \partial x_i} + \frac{\partial \left(-\rho \overline{u_i' T'} \right)}{\partial x_i} + \rho S_T \tag{2.3}$$

or written as:

$$\frac{\partial T}{\partial t} + U_i \frac{\partial T}{\partial x_i} = \frac{\lambda}{\rho C_p} \frac{\partial^2 T}{\partial x_i \partial x_i} + \frac{\partial \left(-\overline{u_i' T'} \right)}{\partial x_i} + S_T$$

$$= \alpha \frac{\partial^2 T}{\partial x_i \partial x_i} + \frac{\partial \left(-\overline{u_j' T'} \right)}{\partial x_i} + S_T \tag{2.3a}$$

$$-\overline{u_i' T'} = \alpha_t \frac{\partial T}{\partial x_i} \tag{2.4}$$

$\overline{T'^2}$ *equation*

$$\frac{\partial \rho \overline{T'^2}}{\partial t} + \frac{\partial \rho U_i \overline{T'^2}}{\partial x_i} = \frac{\partial}{\partial x_i} \rho \frac{\partial \overline{T'^2}}{\partial x_i} \left(\frac{\alpha_t}{\sigma_{T'}} + \alpha \right) - 2\rho \alpha_t \frac{\partial T}{\partial x_i} \frac{\partial T}{\partial x_i} - 2\rho \varepsilon_{T'} \tag{2.7a}$$

$\varepsilon_{T'}$ *equation*

$$\frac{\partial \rho \varepsilon_{T'}}{\partial t} + \frac{\partial \rho U_i \varepsilon_{T'}}{\partial x_i} = \frac{\partial}{\partial x_i} \left[\rho \left(\frac{\alpha_t}{\sigma_{\varepsilon_{T'}}} + \alpha \right) \frac{\partial \varepsilon_{T'}}{\partial x_i} \right] - C_{T1} \rho \frac{\varepsilon_{T'}}{\overline{T'^2}} \overline{u_i' T'} \frac{\partial T}{\partial x_i} - C_{T2} \rho \frac{\varepsilon_{T'}^2}{\overline{T'^2}}$$

$$- C_{T3} \rho \frac{\varepsilon \varepsilon_{T'}}{k} \tag{2.10}$$

α_t *equation*

$$\alpha_t = C_{T0} k \left(\frac{k}{\varepsilon} \frac{\overline{T'^2}}{\varepsilon_{T'}} \right)^{\frac{1}{2}} \tag{2.6}$$

Model constant are: $C_{T0} = 0.11$, $C_{T1} = 1.8$, $C_{T3} = 2.2$, $C_{T2} = 0.8$, $\sigma_{T'} = 1.0$, $\sigma_{\varepsilon_{T'}} = 1.0$.

(III) **Mass transfer equation set ($\overline{c'^2} - \varepsilon_{c'}$ model):**

Species mass conservation equation

$$\frac{\partial C}{\partial t} + \frac{\partial U_i C}{\partial x_i} = \frac{\partial}{\partial x_i} \left(D \frac{\partial C}{\partial x_i} - \overline{u_i' c'} \right) + S_n V \tag{3.3}$$

$$-\overline{u_i' c'} = D_t \frac{\partial C}{\partial x_i} \tag{3.4}$$

$\overline{c'^2}$ *equation*

$$\frac{\partial \overline{c'^2}}{\partial t} + \frac{\partial U_i \overline{c'^2}}{\partial x_i} = \frac{\partial}{\partial x_i}\left[\left(\frac{D_t}{\sigma_{c'^2}} + D\right)\frac{\partial \overline{c'^2}}{\partial x_i}\right] - 2D_t\left(\frac{\partial C}{\partial x_i}\right)^2 - 2\varepsilon_{c'} \qquad (3.10)$$

$\varepsilon_{c'}$ equation

$$\frac{\partial \varepsilon_{c'}}{\partial t} + \frac{\partial U_i \varepsilon_{c'}}{\partial x_i} = \frac{\partial}{\partial x_i}\left[\left(\frac{D_t}{\sigma_{\varepsilon_{c'}}} + D\right)\frac{\partial \varepsilon_{c'}}{\partial x_i}\right] - C_{c1}\frac{\varepsilon_{c'}}{\overline{c'^2}}\overline{c'u_i'}\frac{\partial C}{\partial x_i} - C_{c2}\frac{\varepsilon}{k}\varepsilon_{c'} - C_{c3}\frac{\varepsilon_{c'}}{\overline{c'^2}}\varepsilon_{c'} \qquad (3.17)$$

D_t equation

$$D_t = C_{c0}k\left(\frac{k\overline{c'^2}}{\varepsilon\varepsilon_{c'}}\right)^{\frac{1}{2}} \qquad (3.6)$$

Model constant are: $C_{c0} = 0.11$ $C_{c1} = 1.8$, $C_{c2} = 2.2$, $C_{c3} = 0.8$, $\sigma_{c'^2} = 1.0$, $\sigma_{\varepsilon_{c'}} = 1.0$.

Applying the foregoing equation sets to solve the problem involving flow, heat and mass transfer, there are fifteen unknown quantities, i.e.:

$$U_i, U_j, U_k, p, \mu_t, k, \varepsilon, T, \alpha_t, \overline{T'^2}, \varepsilon_{T'}, C, D_t, \overline{c'^2}, \varepsilon_{c'}.$$

The model equations available is also fifteen, namely seven equations from CFD, four equations from heat transfer and four equations from mass transfer.

The solution of the foregoing equation set is tedious and required heavy computer work. Thus, the use of commercial software, like FLUENT, STAR CD, CFX, and many others, is very helpful.

In some special cases, if the temperature change in the simulated object is small, such as in a distillation tray, the heat transfer equation set can be omitted to simplify the computation.

3.4.3 Determination of Boundary Conditions

The simulation of a process involving momentum, heat, and mass transfer by numerical method requires not only appropriate mathematic model but also its boundary conditions. The boundary condition of velocity, temperature, concentration, and pressure is depending on the simulated object, while that of k, ε, $\overline{T'^2}$, $\varepsilon_{T'}$, $\overline{c'^2}$, $\varepsilon_{c'}$ should be found by experimental or empirical method.

(a) **Inlet boundary condition**

The boundary condition of k–ε model has long been investigated and found that the inlet condition of k is proportional to the average kinetic energy (represented by U^2), that is [18]:

$$k_{\text{in}} = (0.003 - 0.005)U^2$$

The inlet condition of ε is set to be related to k as follows

$$\varepsilon_{\text{in}} = C_{\text{D}} \frac{k_{\text{in}}^{3/2}}{l}$$

where $0.09 \leq C_{\text{D}} \leq 0.164$ depending on the process to be simulated, l is the characteristic length, it can be the inlet diameter or others to be defined by different authors to suit their simulation. Nevertheless, Patankar et al. [19] pointed out that for the condition of fully developed flow, the choice of different inlet condition did not affect appreciably the simulated result.

For the inlet $\overline{T'^2}$, the investigation by Tavoularisand [20] showed that

$$\overline{T_{\text{in}}'^2} = (0.083\Delta T_{\text{in}})^2$$

Recently Ferchichi and Tavoularis [21] reported that

$$\overline{T_{\text{in}}'^2} = (0.08\Delta T_{\text{in}})^2$$

Taking the average, it is

$$\overline{T_{\text{in}}'^2} = (0.082\Delta T_{\text{in}})^2 = 0.0067\left(\Delta T_{\text{in}}^2\right)$$

The report on inlet $\varepsilon_{T'\,\text{in}}$ is scarce. Liu suggested that [6, 7]

$$\varepsilon_{T'\,\text{in}} = 0.4\left(\frac{\varepsilon}{k}\right)\overline{T'^2}$$

For the inlet $\overline{c_{\text{in}}'^2}$, Sun considered that it was proportional to C_{in}^2 and proposed [3, 4]

$$\overline{c_{\text{in}}'^2} = (0.082C_{\text{in}})^2 = 0.0067C_{\text{in}}^2$$

Sun also set $\varepsilon_{c'\text{in}}$ for tray column to be [3, 4]

$$\varepsilon_{c'\,\text{in}} = 0.9\left(\frac{\varepsilon}{k}\right)\overline{c_{\text{in}}'^2}$$

Liu found that better simulated results were obtained in packed column if [6–9]

$$\varepsilon_{c'\,\text{in}} = 0.4\left(\frac{\varepsilon}{k}\right)\overline{c_{\text{in}}'^2}$$

(b) *Outlet boundary condition*

The outlet boundary is usually set to the condition where the flow is fully developed to turbulence, so that in the main flow direction x, all physical quantities Φ except pressure are set to be:

$$\frac{\partial \Phi}{\partial x} = 0$$

(c) **Wall surface boundary condition**

At the wall surface, no-slip condition is applied so that U, k, ε are equal to zero.

3.4.4 Experimental Verification of Model Prediction

The simulation using CMT $\overline{c'^2} - \varepsilon_{c'}$ model as described in the foregoing sections has been applied and verified by comparing with the experimental data (such as separation efficiency) of different kinds of chemical equipment reported in the literature as given in subsequent chapters.

Nevertheless, no published data are available regarding the important aspect, i.e., the inside concentration distribution of an equipment. Thus, experimental work was conducted for the purpose of obtaining the concentration distribution in the equipment for the comparison with model prediction.

(a) **Experimental installation**

The experimental installation [22] is shown schematically in Fig. 3.3 for the desorption of dissolved oxygen in water by blowing air.

The simulator is a single-pass sieve tray of 1.2 m in diameter with 4.6 mm holes and having 4.6 % opening of the tray area. The length of the outlet weirs is 0.79 m. The clearance under the inlet downcomer is 60 mm. The height of the outlet weir is set separately to be 60, 80, and 100 mm. The air rate, ranging from 2,600 to 4,000 m³/h, was fed to the column by a blower and flow through a distributor to ensure uniform inlet condition. The water at the rate of 10 to 20 m³ h⁻¹ was pumped from the storage tank to the downcomer after saturated with oxygen in the static mixer. The water was circulated back to the storage tank after flowing through the tray. The oxygen was supplied by an oxygen cylinder.

The local concentration of dissolved oxygen in the water was measured by a measuring probe. The measuring range of the probe is from 0 to 100 mg/l dissolved oxygen with accuracy of 0.1 mg/l. The temperature compensation was automatic. The probe was fixed to a slider, which was attached to a truss with cross-guide ways on the top of the tray. The probe, submerged in the liquid, could be moved in three directions. The positioning of the measuring points is shown in Fig. 3.4. The depth of submergence for the measurement was at 10 and 20 mm above the tray deck. To ensure reliable experimental results, the operation was run until reaching the steady state where the variation in measured concentration was reduced to very small, and the average value was taken as the measuring data. The measurement was point by point with one probe in order to minimize the disturbance to the flow field. Although the concentration distribution over the whole tray
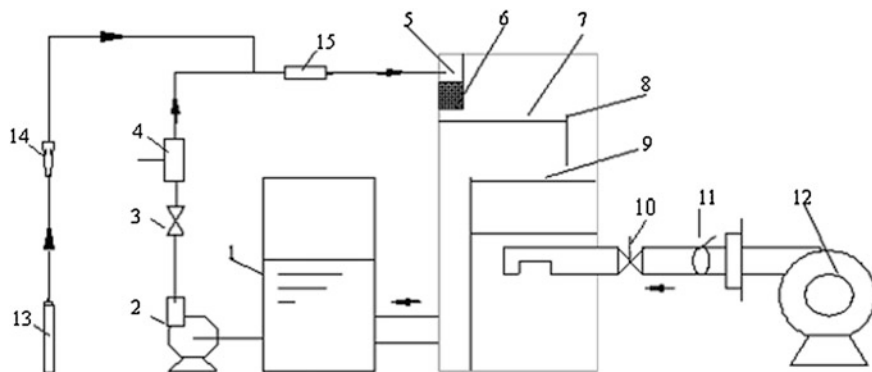
Fig. 3.3 Schematic setup of the experiment for concentration measurement *1* storage tank, *2* water pump, *3* control valve, *4* flow meter, *5* downcomer, *6* packing, *7* sieve tray, *8* outlet weir, *9* gas distributor, *10* control valve, *11* primary control valve, *12* blower, *13* oxygen cylinder, *14* flow meter, *15* static mixer (reprinted from Ref. [22], Copyright 2011, with permission from CIESC)

Fig. 3.4 Arrangement of measuring points on the experimental tray (reprinted from Ref. [11], Copyright 2011, with permission from Elsevier)
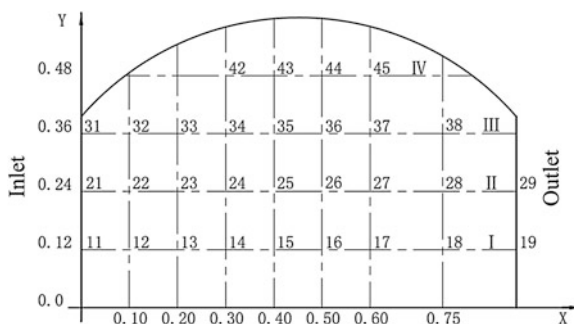
was not taken simultaneously, it is the convenient way to provide an experimental basis to verify the predicted concentration at a point on the sieve tray. As the model prediction is three-dimensional, the planar concentration measurement was conducted at the depth of 10 and 20 mm above the tray deck in order to allow the comparison in three dimensions.

(b) *Comparison between model simulation and experimental data*

The liquid-phase–gas-phase-interaction model (interacted liquid-phase model) accompanied with $\overline{c'^2} - \varepsilon_{c'}$ model as described in preceding sections were used to predict the concentration distribution and compared with the experimental data as shown in Fig. 3.5.

As seen from Fig. 3.5, the model predictions are reasonably agreed with the experimental measurement in consideration of some inaccuracies involved in both simulation and experiment. The obvious discrepancy between the experimental
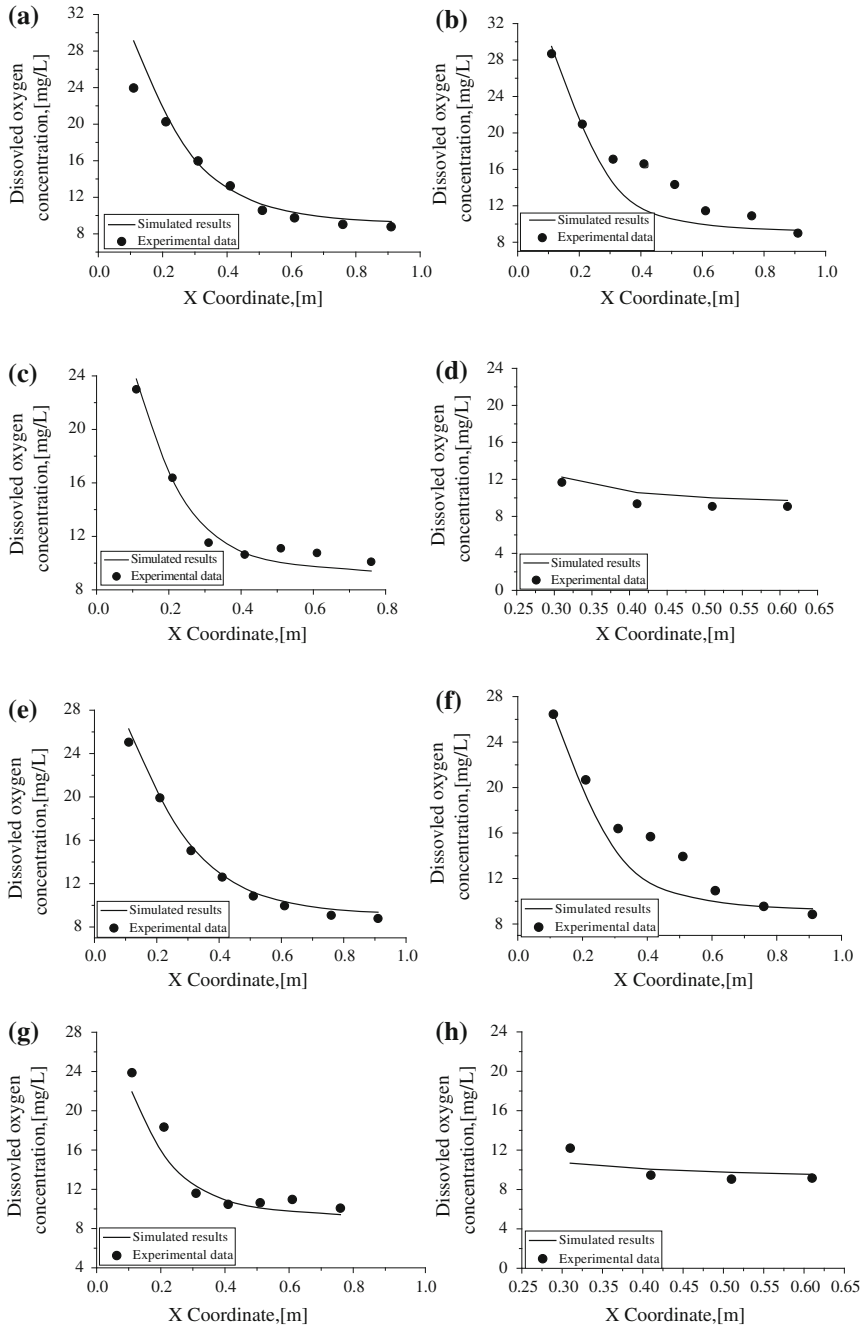
Fig. 3.5 Simulated concentration and experimental measurement, $Q_L = 17.2$ m^{-3} h^{-1}, $G = 4,000$ m^{-3} h^{-1}, $h_W = 100$ mm **a** line I for $z = 10$ mm, **b** line II for $z = 10$ mm, **c** line III for $z = 10$ mm, **d** line IV for $z = 10$ mm, **e** line I for $z = 20$ mm, **f** line II for $z = 20$ mm, **g** line III for $z = 20$ mm, **h** line IV for $z = 20$ mm (reprinted from Ref. [11], Copyright 2011, with permission from Elsevier)

and simulated results is seen in the middle region of Line II; it may be attributed to the fact that this area is around the border between forward and reversed or vortex flow created in the segmental region, in which the flowing condition is in transition to the violent turbulence and appears high fluctuation as observed in our experiment.

3.4.5 Analogy Between Transport Diffusivities

As shown in preceding chapters, on the basis of Boussinesq postulate, the Reynolds stress $-\rho \overline{u_i' u_j'}$, Reynolds heat flux $-\rho \overline{u_i' T'}$, and Reynolds mass flux $-\overline{u_i' c'}$ (or $-\rho \overline{u_i' c_{mf}'}$) can be expressed respectively as proportional to their gradients of average velocity, temperature, and concentration:

$$-\overline{u_i' u_j'} = \frac{\mu_t}{\rho} \left(\frac{\partial U_i}{\partial x_j} + \frac{\partial U_j}{\partial x_i} \right) - \frac{2}{3} \delta_{i,j} \overline{u_i' u_i'} \tag{1.8}$$

$$-\overline{u_i' T'} = \alpha_t \frac{\partial T}{\partial x_i} \tag{2.4}$$

$$-\overline{u_i' c'} = D_t \frac{\partial C}{\partial x_i} \tag{3.4}$$

The correspondent coefficients are designated, respectively, as turbulent diffusivity $v_t = \mu_t / \rho$, turbulent thermal diffusivity α_t, and turbulent mass diffusivity $D_{t,i}$. The equations for calculating the following diffusivities are also seen in similarity:

$$v_t = \frac{\mu_t}{\rho} = C_\mu \frac{k^2}{\varepsilon} = C_\mu k \left(\frac{k}{\varepsilon} \frac{k}{\varepsilon} \right)^{1/2} = C_\mu k \left(\tau_\mu \tau_\mu \right)^{1/2} \tag{1.14}$$

$$\alpha_t = C_{T0} k \left(\frac{k}{\varepsilon} \frac{\overline{T'^2}}{\varepsilon_{T'}} \right)^{1/2} = C_{T0} k \left(\tau_\mu \tau_T \right)^{1/2} \tag{2.6}$$

$$D_t = C_{c0} k \left(\frac{k}{\varepsilon} \frac{\overline{c'^2}}{\varepsilon_{c'}} \right)^{1/2} = C_{c0} k \left(\tau_\mu \tau_c \right)^{1/2} \tag{3.6}$$

The following points should be noted:

1. The analogy between the fluctuating flux and diffusivities is obvious. The similarity of $k-\varepsilon$, $T'^2 - \varepsilon_{T'}$ and $c'^2 - \varepsilon_{c'}$ models demonstrates that the "fluctuation variance-dissipation" pattern is the common methodology for closing the transport equation. Starting from this viewpoint, a unified model of computational transport has been suggested by Liu [5] as shown in subsequent section. Notice should be made that in spite of some newer CFD model is

emerging, the use of k–ε model in cooperation of present $T'^2 - \varepsilon_{T'}$ model and $c'^2 - \varepsilon_{c'}$ model is necessary for the methodological consistence.

2. The coefficients C_μ, C_{T0}, and C_{c0} are given differently by different authors; the commonly accepted values are $C_\mu = 0.09$, $C_{T0} = 0.11$, $C_{c0} = 0.11$ or 0.14, although slight change on these values does not give substantial difference in final simulated result.

3. The turbulent diffusivities v_t, α_t, and D_t as well as their ratio, $\frac{v_t}{D_{t,i}}(=Sc_t) \frac{v_t}{\alpha_t}(=Pr_t)$ and $\frac{UL}{D_{t,i}}(=Pe_t)$ are varying and not a constant in the process concerned because k, ε, $\overline{T'^2}, \varepsilon_{T'}, \overline{c'^2}, \varepsilon_{c'}$ are function of position.

4. Moreover, the turbulent diffusivities, v_t, α_t, and D_t obtained by the two-equation model as given above are applicable to all directions, and therefore, they are isotropic.

3.4.6 Generalized Equations of Two-Equation Model

As seen from the foregoing sections, the transports of momentum, heat, and mass obey the law of conservation and the model equations are similar in form. The generalization of the "fluctuation variance-dissipation" two-equation model as given in Appendix 1 may help to broaden the understanding of relevant equations and facilitate the making of computer programming.

3.5 Reynolds Mass Flux Model

Besides applying the postulation similar to the Boussinesq's (or Fick's law) to solve the Reynolds mass flux $-\overline{u_i'c'}$ in terms of isotropic turbulent mass diffusivity D_t as described in preceding Sect. 3.2 by $\overline{c'^2} - \varepsilon_{c'}$ two-equation model, another model has been recently developed to solve the anisotropic Reynolds mass flux $-\overline{u_i'c'}$ directly instead of using D_t to close the turbulent species mass conservation equation. The Reynolds mass flux model discussed in this section could be known as a result following the turbulence closure postulations for the second-order closure turbulence model in the book of Chen and Jaw [23].

3.5.1 Standard Reynolds Mass Flux Model

For the convenience of derivation, the negative Reynolds mass flux $\overline{u_i'c'}$ is concerned instead of $-\overline{u_i'c'}$. The exact $\overline{u_i'c'}$ transport equation can be derived as follows. Subtracting Eqs. (3.1) from (3.3), we have

$$\frac{\partial c'}{\partial t} + \frac{\partial U_i c'}{\partial x_i} + u_i' \frac{\partial c'}{\partial x_i} = D \frac{\partial^2 c'}{\partial x_i \partial x_i} + \frac{\overline{u_i' c'}}{\partial x_i} \tag{3.23}$$

Multiply Eq. (3.23) by u_j' and multiply Eq. (1.5) by c'; the sum of the two equations is averaged and rearranged to yield the following Reynolds mass flux equation (in the form of fluctuating mass flux $\overline{u_i' c'}$):

$$\begin{aligned}
\frac{\partial \overline{u_i' c'}}{\partial t} + \frac{\partial U_j \overline{u_i' c'}}{\partial x_j} = &\frac{\partial}{\partial x_j} \left[-\overline{u_i' u_j' c'} - \delta_{ij} \frac{\overline{p' c'}}{\rho} + D \overline{u_i' \frac{\partial c'}{\partial x_j}} + \frac{\mu}{\rho} \overline{c' \frac{\partial u_i'}{\partial x_j}} \right] + \frac{\overline{p'}}{\rho} \frac{\partial c'}{\partial x_j} \\
&- \left(\overline{u_i' u_j'} \frac{\partial C}{\partial x_j} + \overline{u_j' c'} \frac{\partial U_i}{\partial x_j} \right) - \left(D + \frac{\mu}{\rho} \right) \overline{\frac{\partial c'}{\partial x_j} \frac{\partial u_i'}{\partial x_j}}
\end{aligned} \tag{3.24}$$

where $\delta_{ij} = \begin{cases} 1(i=j) \\ 0(i \neq j) \end{cases}$

The bracketed first term on the right side represents the turbulent and molecular diffusions; the second term represents the influence of fluctuating pressure and concentration on the distribution of Reynolds mass flux; the third term represents the production of $\overline{u_i' c'}$; the fourth term represents the dissipation.

Equation (3.24) should be modeled to suit computation. Applying the modeling rule, the bracketed first term on the right side of Eq. (3.24) can be considered proportional to the gradient of $\overline{u_i' c'}$ and the $\overline{u_i' u_j'}$ for turbulent diffusion and molecular diffusion. The modeling form is as follows:

$$- \left[-\overline{u_i' u_j' c'} - \delta_{ij} \frac{\overline{p' c'}}{\rho} + D \overline{u_i' \frac{\partial c'}{\partial x_j}} + \frac{\mu}{\rho} \overline{c' \frac{\partial u_i'}{\partial x_j}} \right] = - \left(C_{c1} \frac{k}{\varepsilon} \overline{u_i' u_j'} + D \right) \frac{\partial \overline{u_i' c'}}{\partial x_k}$$

The addition of $\frac{k}{\varepsilon}$ as coefficient is necessary in order to keep the dimension kg m^{-1} s^{-1} consistent on both sides. It should be stressed that the use of quantity $\frac{k}{\varepsilon}$ is only in accordance with the modeling rule for representing the dimension "time." The use of k and ε equations here as auxiliary parameters in modeling is by no means in connection with the isotropic k–ε model, and the foregoing modeling term is retained anisotropic.

The modeling of second term is complicated, it can be considered to be related to the fluctuating velocity and the average velocity gradient as follows:

$$\frac{\overline{p'}}{\rho} \frac{\partial c'}{\partial x_j} = -C_{c1} \frac{\varepsilon}{k} \overline{u_i' c'} - C_{c2}' \overline{u_i' c'} \frac{\partial U_i}{\partial x_j}$$

The third term remains unchanged.

For the fourth term, since the dissipation rate through molecular diffusion is very small, we let

$$-\left(D+\frac{\mu}{\rho}\right)\overline{\frac{\partial c'}{\partial x_j}\frac{\partial u'_i}{\partial x_j}}=0$$

After modeling, Eq. (3.24) becomes

$$\frac{\partial \overline{u'_i c'}}{\partial t}+\frac{\partial U_j \overline{u'_i c'}}{\partial x_j}=\frac{\partial}{\partial x_j}\left[\left(C_{c1}\frac{k}{\varepsilon}\overline{u'_i u'_j}+D\right)\frac{\partial \overline{u'_i c'}}{\partial x_j}\right]-\left(\overline{u'_i u'_j}\frac{\partial C}{\partial x_j}+\overline{u'_j c'}\frac{\partial U_i}{\partial x_j}\right)$$
$$-C_{c2}\frac{\varepsilon}{k}\overline{u'_i c'}+C'_{c3}\overline{u'_j c'}\frac{\partial U_i}{\partial x_j}\tag{3.25}$$

By combining $\overline{u'_j c'}\frac{\partial U_i}{\partial x_j}$ term, the following form is obtained:

$$\frac{\partial \overline{u'_i c'}}{\partial t}+\frac{\partial U_j \overline{u'_i c'}}{\partial x_j}=\frac{\partial}{\partial x_j}\left[\left(C_{c1}\frac{k}{\varepsilon}\overline{u'_i u'_j}+D\right)\frac{\partial \overline{u'_i c'}}{\partial x_j}\right]-\left(\overline{u'_i u'_j}\frac{\partial C}{\partial x_j}\right)$$
$$-C_{c2}\frac{\varepsilon}{k}\overline{u'_i c'}+C_{c3}\overline{u'_j c'}\frac{\partial U_i}{\partial x_j}\tag{3.25a}$$

It was found that the model constants to be $C_{c1}=0.18$, $C_{c2}=3.2$, $C_{c3}=0.55$.

After several examples of computation for the mass transfer process, the computed results show that the $C_{c3}\overline{u'_j c'}\frac{\partial U_i}{\partial x_j}$ term is much less than the $C_{c2}\frac{\varepsilon}{k}\overline{u'_i c'}$ term and can be neglected. Hence, another form of modeled $\overline{u_i c'}$ equation is

$$\frac{\partial \overline{u'_i c'}}{\partial t}+\frac{\partial U_j \overline{u'_i c'}}{\partial x_j}=\frac{\partial}{\partial x_j}\left[\left(C_{c1}\frac{k}{\varepsilon}\overline{u'_i u'_j}+D\right)\frac{\partial \overline{u'_i c'}}{\partial x_j}\right]-\left(\overline{u'_i u'_j}\frac{\partial C}{\partial x_j}\right)-C_{c2}\frac{\varepsilon}{k}\overline{u'_i c'}$$
$$\tag{3.25b}$$

where the constants are: $C_{c1}=0.18$, $C_{c2}=3.2$.

3.5.1.1 Model Equation Set

The modeling equation set of Reynolds stress model under the condition of having heat effect are given below.

(I) **Fluid dynamic equation set (Reynolds stress model):**

   Overall Mass conservation equation

$$\frac{\partial \rho}{\partial t}+\frac{\partial \rho U_i}{\partial x_i}=S_{\mathrm{m}}\tag{3.26}$$

   Momentum conservation equation

$$\frac{\partial \rho U_i}{\partial t}+\frac{\partial \rho U_i U_j}{\partial x_i}=-\frac{\partial P}{\partial x_j}+\mu\frac{\partial^2 U_i}{\partial x_i \partial x_i}+\frac{\partial\left(-\rho\overline{u'_i u'_j}\right)}{\partial x_i}+\rho S_i\tag{3.27}$$

where $\overline{u_i'u_j'}$ is calculated by:

$$
\begin{aligned}
\frac{\partial \rho \overline{u_i'u_j'}}{\partial t} + U_k \frac{\partial \rho \overline{u_i'u_j'}}{\partial x_k} &= \frac{\partial}{\partial x_k}\left(\rho C_k \frac{k}{\varepsilon}\overline{u_i'u_j'}\frac{\partial \overline{u_i'u_j'}}{\partial x_k} + \mu \frac{\partial \overline{u_i'u_j'}}{\partial x_k}\right) \\
&\quad - C_1 \rho \frac{\varepsilon}{k}\left(\overline{u_i'u_j'} - \frac{2}{3}k\delta_{ij}\right) \\
&\quad - C_2\rho\left(\overline{u_i'u_k'}\frac{\partial U_j}{\partial x_k} + \overline{u_j'u_k'}\frac{\partial U_i}{\partial x_k} - \frac{2}{3}\delta_{ij}\overrightarrow{u_i'u_j'}\frac{\partial U_i}{\partial x_j}\right) - \frac{2}{3}\rho\varepsilon\delta_{ij}
\end{aligned}
\tag{1.23a}
$$

where $C_k^* = 0.18, C_1 = 2.3, C = 0.55$.

(II) **Heat transfer equation set (Reynolds heat flux model):**

Energy conservation equation

$$
\frac{\partial \rho T}{\partial t} + U_i \frac{\partial \rho T}{\partial x_i} = \frac{\lambda}{C_p}\frac{\partial^2 T}{\partial x_i \partial x_i} + \frac{\partial\left(-\rho\overline{u_i'T'}\right)}{\partial x_i} + S_T
\tag{2.3a}
$$

where $\overline{u_i'T'}$ is calculated by [23]

$$
\begin{aligned}
\frac{\partial \overline{u_j'T'}}{\partial t} + U_i \frac{\partial \overline{u_j'T'}}{\partial x_k} &= \frac{\partial}{\partial x_k}\left[\left(C_{T1}\frac{k}{\varepsilon}\overline{u_i'u_j'} + \alpha\right)\frac{\partial \overline{u_j'T'}}{\partial x_k}\right] \\
&\quad - \left(\overline{u_i'u_k'}\frac{\partial T}{\partial x_k} + \overline{u_k'T'}\frac{\partial U_j}{\partial x_k}\right) - C_{T2}\frac{\varepsilon}{k}\overline{u_j'T'} + C_{T3}\overline{u_k'T'}\frac{\partial U_j}{\partial x_k}
\end{aligned}
\tag{2.13}
$$

where $C_{T1} = 0.07$, $C_{T2} = 3.2$, $C_{T3} = 0.5$.

(III) **Mass transfer equation set (Reynolds mass flux model):**

Species mass conservation equation

$$
\frac{\partial C}{\partial t} + \frac{\partial U_i C}{\partial x_i} = \frac{\partial}{\partial x_i}\left(D\frac{\partial C}{\partial x_i} - \overline{u_i'c'}\right) + S_n
\tag{3.3}
$$

where $\overline{u_i'c'}$ is calculated by

$$
\begin{aligned}
\frac{\partial \overline{u_i'c'}}{\partial t} + \frac{\partial U_j\overline{u_i'c'}}{\partial x_j} &= \frac{\partial}{\partial x_j}\left[\left(C_{c1}\frac{k}{\varepsilon}\overline{u_i'u_j'} + D\right)\frac{\partial \overline{u_i'c'}}{\partial x_j}\right] - \left(\overline{u_i'u_j'}\frac{\partial C}{\partial x_j}\right) - C_{c2}\frac{\varepsilon}{k}\overline{u_i'c'} \\
&\quad + C_{c3}\overline{u_j'c'}\frac{\partial U_i}{\partial x_j}
\end{aligned}
\tag{3.25a}
$$

where $C_{c1} = 0.09$, $C_{c2} = 3.2$, $C_{c3} = 0.55$.

The auxiliary equations k and ε are calculated by:

k equation: Eq. (1.11)
ε equation; Eq. (1.13)

Thus, Reynolds mass flux model involves Reynolds stress, Reynolds heat flux and Reynolds (fluctuating) mass flux equations, the unknown quantity is increased to twelve to make the total unknown quantities become twenty; they are:

$$U_i, U_j, U_k, p, \overline{u_i'u_j'} \text{ (six unknowns) }, T, \overline{u_i'T'} \text{ (three unknowns),}$$
$$C, \overline{u_i'c'} \text{ (three unknowns)}, k, \varepsilon$$

The model equations available is also twenty, namely ten equations from CFD, four equations from heat transfer, and six equations from mass transfer.

The feature of this model is rigorous and anisotropic, yet more equations are needed to solve which requires not only more computer load but also harder to converge.

3.5.1.2 Determination of Boundary Conditions

(A) *Inlet boundary condition*

At the top of the column, the boundary condition for the liquid phase is set to be [24]

$$\overline{U} = \overline{U_{\text{in}}}, \ \overline{C} = \overline{C_{\text{in}}}, \ k = 0.003\overline{U_{\text{in}}}^{2}, \ \varepsilon_{in} = 0.09\frac{k_{\text{in}}^{1.5}}{d_{\text{H}}}$$

where d_{H}. is the hydraulic diameter of random packing, which can be calculated by [25]:

$$d_{\text{H}} = \frac{4\gamma_{\infty}}{a(1 - \gamma_{\infty})}.$$

There are no experimental measurements reported or empirical correlations available from the literature for determining the inlet condition of the fluctuating mass flux $\overline{u_i'c'}_{\text{in}}$ and the fluctuating heat flux $\overline{u_i'T'}_{\text{in}}$. In some cases, the following conditions for $\overline{u_i'c'}$ and $\overline{u_i'T'}$ were found to be suitable at the inlet [26]:

$$\left(\overline{u_i'c'}\right)_{\text{in}} = -0.7(\partial C/\partial x_i)|_{\text{in}} \ \left(\overline{u_i'T'}\right)_{\text{in}} = -0.9\frac{\mu_{t,\text{in}}}{\rho}(\partial T/\partial x_i)|_{\text{in}}$$

where $\mu_{t,\text{in}} = C_\mu \frac{k_{\text{in}}^2}{\rho\varepsilon_{\text{in}}}$. We found that the foregoing inlet condition is more convenient to use; however, another expression for the inlet condition may be suggested to suit different simulation.

(B) *Outlet boundary condition*

The flow in the packed column at the outlet is considered as fully developed in turbulent state; the zero normal gradients are applied to all variables except pressure.

(C) *Wall boundary condition*

The no-slip condition of flow is applied to the wall, and the zero flux condition at the wall is adopted.

3.5.1.3 Influence of Reynolds Mass Flux on Mass Transfer

For the convenience of expression, the negative Reynolds mass flux (also known as fluctuating mass flux) $\overline{u_i'c'}$ [kg m^{-2} s^{-1}], which denotes the rate of fluctuating mass to be transported per unit time (second) per unit cross-sectional area (m^2), is mentioned in this section instead of $-\overline{u_i'c'}$.

The directional $\overline{u_i'c'}(i = x, y, z)$ complies $\overline{u_x'c'}$, $\overline{u_y'c'}$ and $\overline{u_z'c'}$, the following analysis of $\overline{u_i'c'}$ refers to one of direction, for instance in x direction, $\overline{u_i'c'}$ becomes $\overline{u_x'c'}$.

In the turbulent mass transfer process, the velocity gradient and concentration gradient are established as well as the $\overline{u_i'c'}$ gradient. The transport of $\overline{u_i'c'}$ is implemented by the turbulent fluid flow and the fluctuated mass flux diffusion. As the velocity eddy, which is the elements of turbulent flow, is the carrier of $\overline{u_i'c'}$, the transport of $\overline{u_i'c'}$ also follows the pattern of the velocity eddy flow and the fluctuated diffusion.

The influence of fluctuating mass flux $\overline{u_i'c'}$ on mass transfer is in several aspects as described below:

Turbulence and species concentration gradient

The term $\overline{u_i'c'}$ is the average of the fluctuated mass flux $u'c'$. As the fluctuations originate from fluid turbulence, $\overline{u_i'c'}$ may be regarded as "turbulent mass flux."

The value of $\overline{u_i'c'}$ reflects the extent of flow turbulence (or the magnitude of u') as well as the gradient of species concentration C from which the fluctuation c' is created. Thus, a certain value of $\overline{u_i'c'}$ may come from either high turbulence with low species concentration or low turbulence with high species concentration gradient. Nevertheless, for most mass transfer process, the instantaneous velocity u of the bulk fluid is substantially constant, so that the variation in u' is small; thus, the value of $\overline{u_i'c'}$ depends mostly on the value of c' or implicitly the gradient of concentration C.

As seen from Eq. (3.2) where $\overline{u_i c} = U_i C + \overline{u_i'c'}$, the term $\overline{u_i'c'}$ generally is positive but its components $\overline{u_x'c'}$, $\overline{u_y'c'}$ and $\overline{u_z'c'}$ may be positive or negative. According to the potential concept (Fick's law), the flow of mass flux along a path should be under its negative gradient, thus the diffusion of positive $\overline{u_i'c'}$ should follow this rule. If the bulk concentration of the process is decreasing, such as the absorption of CO_2 by water, the diffusion direction of $\overline{u_i'c'}$ is consistent with the C decreasing gradient, the bulk mass flux $\overline{u_i c}$ is $U_i C$ but promoted (enhanced) by the $\overline{u_i'c'}$ diffusion (regarded as promoted or forward diffusion). Inversely, if $\overline{u_i'c'}$ is

negative, its diffusion should be under positive C gradient, i.e., along C increasing direction. The diffusion under positive gradient seems contradiction to the concept of potential flow, but it can be explained as follows.

Rearranging Eq. (3.2), we have $\overline{u_i'c'} = \overline{u_i c} - U_i C$, thus negative $\overline{u_i'c'}$ implies $\overline{u_i c} < U_i C$, and the instantaneous mass flux becomes less than the average mass flux $U_i C$. In other words, the process mass flux $u_i c$ is lost by the amount $\overline{u_i'c'}$, which may be considered that such loss is as a result of the counteraction by $\overline{u_i'c'}$ diffusion, i.e., the mixing between $u_i c$ flow and $\overline{u_i'c'}$ diffusion. Thus, for the absorption process where bulk concentration C is increasing, the diffusion of negative $\overline{u_i'c'}$ counteracts the $\overline{u_i c}$ (or $U_i C$) flow and results the disappearance of $\overline{u_i'c'}$ at the expense of diminishing some amount of $\overline{u_i c}$ (or $U_i C$). It is regarded as backward or suppressed diffusion of $\overline{u_i'c'}$.

Local mixing

In the course of turbulent mass transfer process, the fluctuation u_i' from the velocity eddies as well as the fluctuation c' from concentration eddies are dissipated sooner or later through the mutual mixing of eddies so as to produce local mixing with neighboring velocity and concentration. The dissipation and generation of eddies are going on unceasingly during the progress of the mass transfer process; therefore, the diffusion of $\overline{u_i'c'}$ is accompanied with unstoppable local (eddies) mixing.

Process concentration profile

Under turbulent flow condition, the transfer of species (mass) from adjacent phase to the phase concerned, such as physical absorption like the absorption of CO_2 by water, the following steps are undertaken in sequence:

(a) The CO_2 diffuse from gas phase to the gas–liquid interface;
(b) The diffusion of CO_2 from gas–liquid interface to the bulk fluid (water);
(c) The bulk fluid carrying the diffused species CO_2 at average fluid concentration C and its fluctuating concentration c' is flowing along the flow path, forming positive CO_2 gradient (c or C increasing profile);
(d) The turbulent product $\overline{u_i'c'}$ is in action (diffusion) at the same time. Generally, $\overline{u_i'c'}$ is positive, which intends to diffuse under negative $\overline{u_i'c'}$ gradient along the flow path, i.e., aims to diffuse from high $\overline{u_i'c'}$ to the low $\overline{u_i'c'}$ (negative $\overline{u_i'c'}$ gradient), which corresponds to negative c or C gradient (c or C decreasing profile).

It is obvious that steps (c) counteracts step (d), i.e., the conflict between the flow of bulk mass flux $U_i C$ from high C to low C by absorption and the diffusion of $\overline{u_i'c'}$ from low C to high C. As the amount of $\overline{u_i'c'}$ backward diffusion in step (d) is much less than the amount of bulk $U_i C$ forward flow in step (c), the final result of counteraction is that the backward diffusion $\overline{u_i'c'}$ cause reduction in $U_i C$ to some extent, which means the absorption process is interfered or suppressed.

Table 3.1 Influence of $\overline{u_i'c'}$ on mass transfer process ($i = x, y, z$)

Process[a]	Process C gradient along x_i direction (A)	Sign of $\overline{u_i'c'}$	$\overline{u_i'c'}$ diffusion gradient along x_i direction (B)	Interaction between gradients (A) and (B)	Influence on the process
Bulk C increasing	+	+	−Backward diffusion	Counteraction	Unfavorable (suppressed transfer)
Bulk C increasing	+	−	+Forward diffusion	Co-action	Favorable (promoted transfer)
Bulk C decreasing	−	+	–Backward diffusion	Co-action	Favorable (promoted transfer)
Bulk C decreasing	−	−	+Forward diffusion	Counteraction	Unfavorable (suppressed transfer)

[a] C increasing process denotes the concentration increases along direction $i(i = x, y, z)$. For instance, absorption is C increasing process along x (axial) direction in a packed column
C decreasing process denotes the concentration decreases along direction $i(i = x, y, z)$. For instance, desorption is C decreasing process along x (axial) direction in a packed column

For the other mass transfer process, such as desorption like CO_2, saturated water is desorbed by air, the CO_2 concentration of the fluid (water) along x_i (axial) direction is decreasing (negative gradient) instead of increasing (positive gradient), the steps (c) and (d) are not in conflict but in cooperation (coordination) each other, thus the bulk U_iC flow and $\overline{u_i'c'}$ diffusion are consistent in the same direction which means the desorption process is promoted (enhanced) by $\overline{u_i'c'}$ diffusion without interference by counteraction.

The foregoing analysis is based on positive $\overline{u_i'c'}$. On the other hand, if $\overline{u_i'c'}$ is negative, the situation becomes reversed; Table 3.1 is the summary.

Diffusion rate

The rate of $\overline{u_i'c'}$ diffusion, $\frac{\partial \overline{u_i'c'}}{\partial x_i}$, is indicated by the slope of $\overline{u_i'c'}$ versus x_i plot. Positive slope means the diffusion rate is increasing, while negative slope implies decreasing rate.

Remarks

In brief, the diffusion of turbulent mass flux $\overline{u_i'c'}$ is influential to the process concentration profile; the latter is important as it indicates the effectiveness of a mass transfer process. The effect of turbulent diffusion on process gradient may be promoted (enhanced) or suppressed dependents on the character of the process and the sign of $\overline{u_i'c'}$. However, the analysis of $\overline{u_i'c'}$ is complicated, yet more information of mass transfer can be obtained as seen in the subsequent chapters.

3.5.1.4 Anisotropic Turbulent Mass Diffusivity

Using the Reynolds mass flux model, the directional $-\overline{u_i'c'}$ can be calculated separately as $-\overline{u_x'c'}$, $-\overline{u_y'c'}$ and $-\overline{u_z'c'}$, so that the anisotropic turbulent mass diffusivity can be obtained.

As stated in preceding section, the diffusion of $\overline{u_i'c'}$ should under the negative C gradient. Let J_i in the Fick's law equation be the fluctuating mass flux $\overline{u_i'c}$ and the driving gradient is $(\partial C/\partial x)$, the following relationship can be established:

$$\overline{u_i'c'} = \mathbf{D}_{t,i}\left(-\frac{\partial C}{\partial x_i}\right), \ i = x, \ y, \ z \tag{3.28}$$

$$\mathbf{D}_{t,x} = \frac{\overline{u_x'c'}}{\left(-\frac{\partial C}{\partial x}\right)}, \quad \mathbf{D}_{t,y} = \frac{\overline{u_y'c'}}{\left(-\frac{\partial C}{\partial y}\right)}, \quad \mathbf{D}_{t,z} = \frac{\overline{u_z'c'}}{\left(-\frac{\partial C}{\partial z}\right)} \tag{3.29}$$

where the coefficients $\mathbf{D}_{t,x}$, $\mathbf{D}_{t,y}$, $\mathbf{D}_{t,z}$ are the anisotropic turbulent mass diffusivities in x, y, z directions, respectively.

The Fick's law coefficient $\mathbf{D}_{t,i}$, which is defined as the mass of species transferred per unit area per unit time under unit concentration gradient, represents the ability of a species to undergo diffusion. Thus, $\mathbf{D}_{t,i}$ reflects the capability of turbulent fluctuating mass flux $\overline{u_i'c'}$ diffusion along direction i.

It should be noted that the $\mathbf{D}_{t,i}$ obtained from Reynolds mass flux model and the D_t obtained from two-equation model is entirely different, as $\mathbf{D}_{t,i}$ is calculated from $\overline{u_ic'}$ while D_t is given by the equation $D_t = C_{c0}k\left(\frac{k}{\varepsilon}\frac{\overline{c'^2}}{\varepsilon_{c'}}\right)^{1/2}$. From theoretical viewpoint, the anisotropic $\mathbf{D}_{t,i}$ is more rigorous than the isotropic D_t. The present derivation and discussion of $\mathbf{D}_{t,i}$ are only to demonstrate the anisotropic nature of mass transfer diffusivity and its influence. In the process simulation by Reynolds mass flux model, the $\mathbf{D}_{t,i}$ need not be evaluated.

Strictly speaking, all mass transfer processes are anisotropic. Nevertheless, the flow, heat, and mass transfer in most processes are dominant in one direction, such as the axial direction is governing in most packed column, the use of isotropic model may give satisfactory result of simulation. Yet in large diameter packed column the anisotropic nature is magnified and should be concerned its anisotropy as the radial effect cannot be ignored. Thus, for the simulation of large scale or anisotropic mass transfer equipment, the Reynolds mass flux model should be the choice for accounting the anisotropy.

For illustrating the advantage of using anisotropic Reynolds mass flux model, the simulation of absorption of CO_2 by MEA solution (see Chap. 5) using isotropic $\overline{c'^2} - \varepsilon_c$ two-equation model and one-dimensional model by Tontiwachwuthikul [18] versus anisotropic Reynolds mass flux model is given in Fig. 3.6a for a packed column of 0.1 m in diameter and Fig. 3.6b for a packed column of 1.9 m in
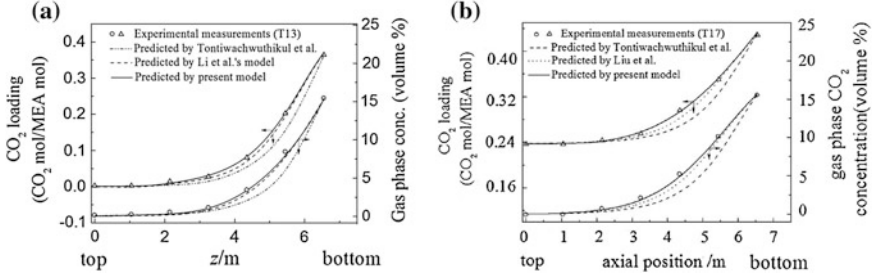
Fig. 3.6 Comparison between isotropic and anisotropic models [27] (*Traingle* Experimental measurement, *Dashed line* Two-equation model, *Hypenated line* One-dimensional model (isotropic), *Solid line* Rayleigh mass flux model) **a** 0.1-m-diameter column, **b** 1.9-m-diameter column

diameter. It is clearly seen from the figures that the present anisotropic model gives good simulated result than the isotropic models.

3.5.2 Hybrid Reynolds Mass Flux Model

In order to reduce the computer load of standard Reynolds mass flux model, the complicated Eq. (1.23a) for expressing $\overline{u_i'u_j'}$ can be replaced by the simpler Eq. (1.8). Then, the model becomes the combination of Reynolds mass flux and the Boussinesq postulate (two-equation model). It is called hereafter as hybrid Reynolds mass flux model. The model equations are given below.

(I) **CFD equation set**:

Overall Mass conservation equation: Eq. (3.26)
Momentum conservation equation: Eq. (1.4)
$\overline{u_i'u_j'}$ equation (*Boussinesq postulate*):

$$-\rho\overline{u_i'u_j'} = \mu_t\left(\frac{\partial U_i}{\partial x_j} + \frac{\partial U_j}{\partial x_i}\right) - \frac{2}{3}\rho\delta_{ij}k \tag{1.8}$$

$$\mu_t = C_\mu\rho\frac{k^2}{\varepsilon} \tag{1.14}$$

where the *k equation* is calculated from Eq. (1.11a) and the involved ε *equation* from Eq. (1.13a).

(II) **Heat transfer equation set (Reynolds heat flux model)**:

Energy conservation equation: Eq. (2.3a)
Fluctuating heat flux equation: Eq. (2.13)

(III) Mass transfer equation set:

Species mass conservation equation: Eq. (3.3)

Fluctuating mass flux equation: Eq. (3.25a)

The unknown quantities in this model are: U_i, U_j, U_k, P, k, ε, μ_t, C, $\overline{u_i'c'}$, $\overline{u_j'c'}$, $\overline{u_k'c'}$, totally eleven versus eleven model equations available. Since this model employ Boussinesq postulate, it is isotropic.

3.5.3 Algebraic Reynolds Mass Flux Model

The Reynolds mass flux model can also be further simplified by letting the convection terms of $\overline{u_i'c'}$ on the left side of Eq. (3.24) equal to the molecular diffusion and turbulent diffusion in terms of $\overline{u_i'c'}$ on the right side, then under steady condition, Eq. (3.25a) becomes

$$-\left(\overline{u_i'u_j'}\frac{\partial C}{\partial x_j} + \overline{u_i'c'}\frac{\partial U_i}{\partial x_j}\right) - C_{c2}\frac{\varepsilon}{k}\overline{u_i'c'} + C_{c3}\overline{u_i'c'}\frac{\partial U_i}{\partial x_j} = 0 \tag{3.30}$$

After arranging, the simplified $\overline{u_i'c'}$ expression is as follows:

$$\overline{u_i'c'} = -\frac{k}{C_{c2}\varepsilon}\left(\overline{u_i'u_j'}\frac{\partial C}{\partial x_j} + \overline{u_i'c'}\frac{\partial U_i}{\partial x_j}\right) + \frac{C_{c3}k}{C_{c2}\varepsilon}\overline{u_i'c'}\frac{\partial U_i}{\partial x_j} \tag{3.31}$$

The number of unknown quantities and equations of this model is the same as the Reynolds mass flux model except using Eq. (3.31) to replace Eq. (3.25a) for calculating $\overline{u_i'c'}$ in order to reduce the load of computation.

3.6 Simulation of Gas (Vapor)–Liquid Two-Phase Flow

Most mass transfer equipments consist of gas (vapor) and liquid two-phase flow, for instance, vapor–liquid two-phase cross-current flow is undertaken in tray distillation column; gas–liquid two-phase countercurrent flow is taken place in packed absorption column. Some processes may also include solid phase, such as adsorption or catalytic reaction. Thus, the fluid system may contain gas and liquid two phases, or gas, liquid single phase besides solid phase.

For the two-phase flow, the modeling equations should be written for the designated phase while such phase occupies only a fraction of the total volume; therefore, the volume fraction of the designated phase should be involved in the equation for the reason that the fluid velocity of the designated phase is determined by the fractional flow area. Note that, the volume fraction is generally varying with position.

Let β_θ be the volume fraction of the designated phase θ (for instance, $\theta = L$ refers to liquid phase $\theta = G$ refers to gas phase), ρ_θ be the density of the designated phase θ. Both β_θ and ρ_θ need to insert into the CFD equation sets.

The simulated two-phase flow model can be in one of the following three forms:

(1) **Two-fluid modeling form**.

There are two kinds of two-fluid models based on different viewpoints:

- *Eularian–Eularian two-fluid model*. In this model, both gas (vapor) and liquid phases are considered as a system to be concerned aiming to obtain the transport information of each phase. Model assumptions are made that both phases (the continuous liquid phase and the dispersed gas phase) are considered as two interpenetrating continua, so that the Eularian method (expressed by volume average Navier–Stokes equation) can be applied to both phases. The model equations for phase θ are as follows:

Mass conservation equation of phase θ

$$\frac{\partial \rho_\theta}{\partial t} + \frac{\partial \rho U_{\theta i}}{\partial x_i} = S_{\theta m}, \ \theta = L, G$$

Momentum conservation equation of phase θ

$$\frac{\partial \rho U_{\theta i}}{\partial t} + \frac{\partial \rho_\theta U_{\theta i} U_{\theta j}}{\partial x_i} = -\frac{\partial P}{\partial x_j} + \mu_\theta \frac{\partial^2 U_{\theta i}}{\partial x_i \partial x_i} + \frac{\partial \left(-\rho \overline{u_{\theta i} u_{\theta j}}\right)}{\partial x_i} + \rho_\theta S_{\theta i}$$

where θ refers either liquid or gas; $S_{\theta n}$ represents the mass exchange between liquid and gas phases; $S_{\theta i}$ represents the gravitational force, interphase momentum exchange and all interacting forces between two phases. In the closure of momentum equation, the k–ε model may be used with consideration of the mutual influence between the Reynolds stresses of liquid and gas phases.

The number of equations needed for two-fluid model is more than that of the following interacted liquid-phase model and requires more computer capacity with the risk of harder convergence. In practice, for instance, the distillation simulation by some authors [28, 29] neglected the turbulent equations of vapor phase to simplify the simulation.

- *Eularian–Lagrangian two-fluid model*. In most gas (vapor)–liquid equipments, the liquid exhibit as continuous phase and the gas (vapor) is dispersed phase. Thus, Eularian method (expressed by volume average Navier–Stokes equation) can be applied to the continuous liquid phase for simulating the flow field; the motion as well as behaviors of dispersed phase is described by Lagrange method, in which the individual dispersed element (bubble) is tracking by an equation of motion, such as Newton's second law, and subjected to the action of all interface forces. However, the bubble motion and

interface forces acting to the bubbles are complicated so as the modeling should concern bubble dynamics with all relevant acting forces (gravity, drag, lift, pressure gradient, virtual mass, etc.) as well as the collision between bubbles and between bubble and the column wall. The coupling between bubble and liquid phases is realized by considering all the interphase forces as source terms in the momentum conservation equation of liquid phase.

The feature of this model is the dispersed phase (bubble) can be described in details but at the expense of more computer load.

(2) **Liquid phase under interaction of gas phase (interacted liquid phase) modeling form**

In this modeling form, abbreviated as *interacted liquid phase model*, the liquid phase is considered as the system to be concerned aiming to obtain the transport information of the *liquid phase*. The dispersed phase is considered as the surroundings. The action of the dispersed phase (bubbles) on the liquid phase is treated as the external forces acting on the system (liquid phase). Thus, the evaluation of source term S_{Li} in Navier–Stokes equation of liquid phase should cover all the acting forces by the dispersed gas phase to the liquid phase. Such model can reduce the number of model equations and computer load. Computation shows that whether the interaction source term S_{Li} is properly considered, the final simulated result is substantially equal to that using two-fluid model (Fig. 3.7).

As an example, the CFD simulations of velocity distribution on a sieve tray of 1.22 m in diameter (Fig. 3.7) reported by Sorari [30] using two-fluid model [28] and interacted liquid-phase k–ε model [31] are shown in Fig. 3.8, in which both simulation are comparable and close to the experimental data.

The CFD model in interacted liquid phase form by Wang [31] is given below:
Overall mass conversation

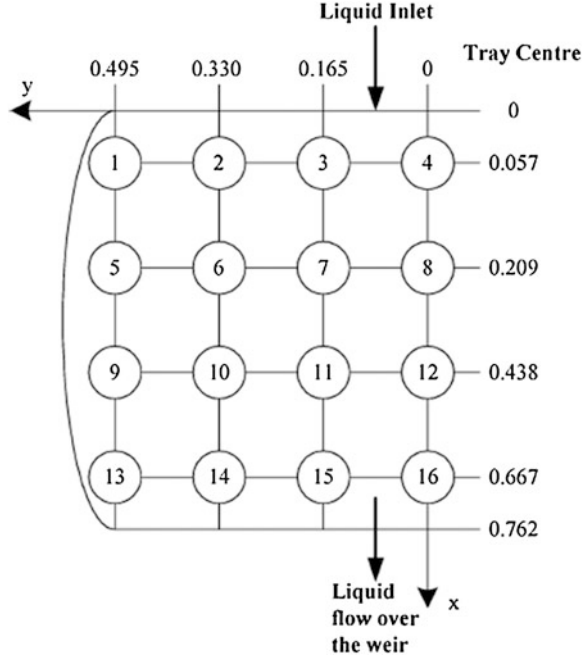$$\frac{\partial(\rho_L \beta_L U_{Li})}{\partial x_i} = S_m$$

Momentum conversation

$$\frac{\partial(\rho_L \beta_L U_{Li} U_{Lj})}{\partial x_i} = -\beta_L \frac{\partial P}{\partial x_j} + \frac{\partial}{\partial x_i}\left[\beta_L v_e\left(\frac{\partial U_{Lj}}{\partial x_i}\right) - \beta_L \rho_L v_e\left(\frac{\partial U_i}{\partial x_j} + \frac{\partial U_j}{\partial x_i}\right)\right]$$
$$+ \beta_L \rho_L S_L$$

For the closure of momentum equation, the effective turbulent diffusivity v_e is calculated using k–ε model as follows:

$$v_e = c_\mu \frac{k^2}{\varepsilon} + \frac{\mu_L}{\rho_L}$$

Fig. 3.7 Positions of experimental probes

where k_{L} equation

$$\frac{\partial \rho_{\mathbf{L}} \beta_{\mathbf{L}} U_i k}{\partial x_i} = \frac{\partial}{\partial x_i}\left[\beta_{\mathrm{L}}\left(\mu + \frac{\mu_t}{\sigma_k}\right)\frac{\partial k}{\partial x_i}\right] - \mu_t \beta_{\mathrm{L}}\left(\frac{\partial U_i}{\partial x_j} + \frac{\partial U_j}{\partial x_i}\right)\frac{\partial U_j}{\partial x_i} + \varepsilon + G_V$$

where G_V is the turbulent energy created by the bubble agitation of the fluid on a tray, $G_V = c_e \frac{\Delta p U_G}{\rho_L h_L}$,

ε_{L} *equation*

$$\frac{\partial \rho_{\mathbf{L}} \beta_{\mathbf{L}} U_i \varepsilon_{\mathbf{L}}}{\partial x_i} = \frac{\partial}{\partial x_i}\left[\beta_{\mathrm{L}}\left(\mu + \frac{\mu_t}{\sigma_\varepsilon}\right)\frac{\partial \varepsilon}{\partial x_i}\right] - C_{\varepsilon 1}\beta_{\mathrm{L}}\frac{\varepsilon}{k}\mu_t\left(\frac{\partial U_j}{\partial x_i} + \frac{\partial U_i}{\partial x_j}\right)\frac{\partial U_j}{\partial x_i}$$
$$+ [c_1 G_V - c_2 \varepsilon]\frac{\varepsilon}{k}$$

For the detailed expression of the gas–liquid interacting forces in the interacted liquid-phase model, the source term $S_{\mathrm{L}i}$, involving gravitational force and interacting forces as given by Wang, is shown below:

$$S_{\mathrm{L}i} = F_{\mathrm{g}} + \begin{bmatrix} F_{\mathrm{L}x} + f_{\mathrm{vmx}} + M_{\mathrm{GL}x} + f_x \\ F_{\mathrm{L}y} + f_{\mathrm{vmy}} + M_{\mathrm{GL}y} + f_y \\ F_{\mathrm{L}z} + f_{\mathrm{vmz}} + M_{\mathrm{GL}z} + f_z \end{bmatrix}$$

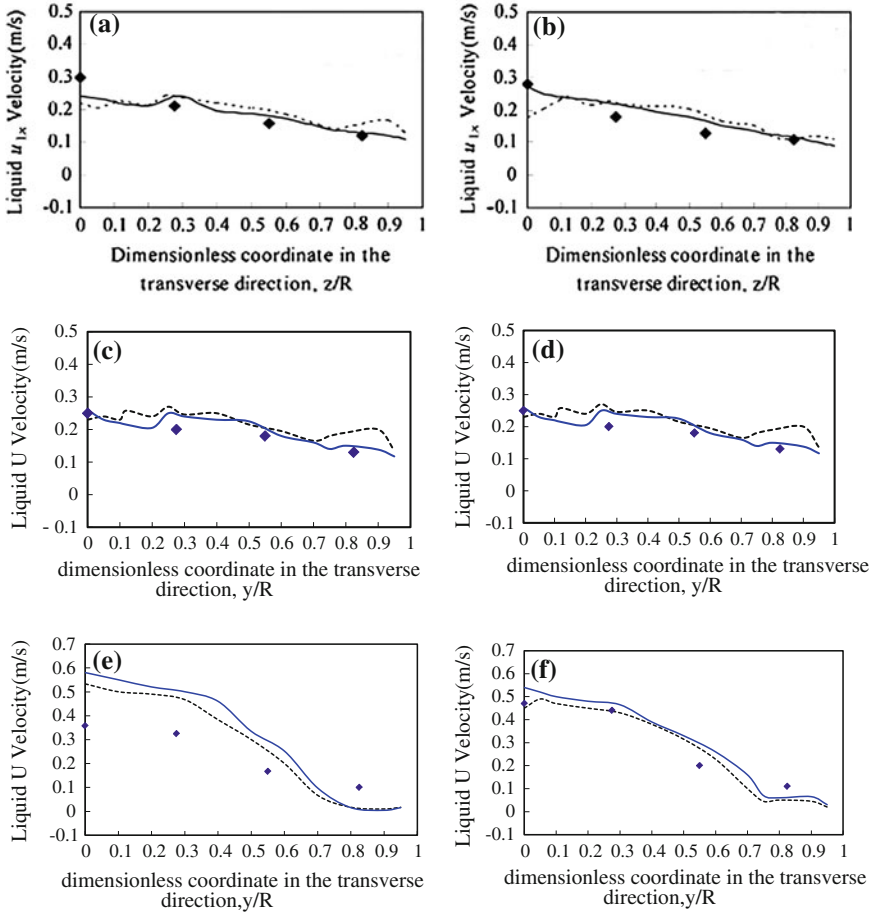*The gravity force*: $F_{\mathrm{g}} = \beta_{\mathrm{L}}\rho_{\mathrm{L}}g$

Fig. 3.8 Comparison between simulations using two-fluid model and interacted liquid-phase model for a sieve tray (*Black diamond* Experimental data [30], *Dashed line* Two-phase model simulation by Gesit [28], *Solid line* Interacted liquid-phase model simulation by Wang) [31]. **a** upstream profile for $Q_L = 6.94 \times 10^{-3}$ m^3/s and $Fs = 1.015$, **b** downstream profile for $Q_L = 6.94 \times 10^{-3}$ m^3/s and $Fs = 1.015$, **c** upstream profile for $Q_L = 6.94 \times 10^{-3}$ m^3/s and $Fs = 1.464$, **d** $Q_L = 6.94 \times 10^{-3}$ m^3/s and $Fs = 1.464$, **e** upstream profile for $Q_L = 17.8 \times 10^{-3}$ m^3/s and $Fs = 0.801$, **f** downstream profile for $Q_L = 17.8 \times 10^{-3}$ m^3/s and $Fs = 0.801$ (reprinted from Ref. [31], Copyright 2004, with permission from American Chemical Society)

The lift forces (Magnus forces): F_{Lx}, F_{Ly}, and F_{Lz}, which represent the forces of generating a sidewise force on the spinning bubble in the liquid phase by the liquid velocity gradient, are given by Auton et al. [32] as

$$F_{Lx} = 0.25\beta_G\rho_L(U_{Lx} - U_G) \times (\nabla U_{Lx})$$
$$F_{Ly} = 0.25\beta_G\rho_L(U_{Ly} - U_G) \times (\nabla U_{Ly})$$
$$F_{Lz} = 0.25\beta_G\rho_L(U_{Lz} - U_G) \times (\nabla U_{Lz})$$

The virtual mass forces: f_{vmx}, f_{vmy}, f_{vmz}, which account for the additional resistance acting by a bubble undergoing acceleration, are given below by Auton et al. [32]

$$-f_{vmx} = 0.5 \times \beta_G\rho_L(u_{Lx} \cdot \nabla u_{Lx})$$
$$-f_{vmy} = 0.5 \times \beta_G\rho_L(u_{Ly} \cdot \nabla u_{Ly})$$
$$-f_{vmz} = 0.5 \times \beta_G\rho_L(u_{Lz} \cdot \nabla u_{Lz})$$

The interphase drag force: M_{GLx}, M_{GLy}, M_{GLz} are given by Krishna et al. [33]

$$-M_{GLx} = \beta_G\alpha_L(\rho_L - \rho_G)g\frac{1}{(u_s/\beta_G)^2}\frac{1}{\beta_L} \times (u_s - u_{Lx})|u_s - u_{Lx}|$$

$$-M_{GLy} = \beta_G\alpha_L(\rho_L - \rho_G)g\frac{1}{(u_s/\beta_G)^2}\frac{1}{\beta_L} \times (u_s - u_{Ly})|u_s - u_{Ly}|$$

$$-M_{GLz} = \beta_G\alpha_L(\rho_L - \rho_G)g\frac{1}{(u_s/\beta_G)^2}\frac{1}{\beta_L} \times (u_s - u_{Lz})|u_s - u_{Lz}|$$

The resistance to the fluid flow: f_x, f_y, f_z, the resistances created by uprising vapor to the fluid flow, is considered to be equivalent to a body force acting vertically and uniformly on the horizontally flowing fluid. This body force, resolved into f_x, f_y, f_z by Yu et al. [34] in the froth regime of fluid flow, can be calculated by means of the froth height h_f as follows:

$$f_x = -\frac{\rho_G u_s}{\rho_L h_f}u_{Lx} \quad f_y = -\frac{\rho_G u_s}{\rho_L h_f}u_{Ly} \quad f_z = -\frac{\rho_G u_s}{\rho_L h_f}u_{Lz}$$

The froth height h_f is evaluated by the Colwell correlation [35],

$$h_L = \beta_{L,avg}\left[h_w + 0.527\left(\frac{Q_L}{C_d\beta_{L,avg}}\right)^{0.67}\right]$$

$$C_d = \begin{cases} 0.61 + 0.08\frac{h_{fow}}{h_w}, & \frac{h_{fow}}{h_w} < 8.315 \\ 1.06\left(1 + \frac{h_w}{h_{fow}}\right)^{1.5}, & \frac{h_{fow}}{h_w} \geq 8.315 \end{cases}$$

$$h_{fow} = h_f - h_w$$

where $\beta_{L,avg}$ represents the liquid average froth volume fraction,

$$\beta_{L,avg} = \frac{1}{12.6F_r'^{0.4}(A_B/A_h)^{0.25} + 1}$$

$$F_r' = F_r\left(\frac{\rho_G}{\rho_L - \rho_G}\right)$$

$$F_r = \frac{u_s}{gh_L}$$

It is assumed that the gas and liquid volume fraction β_G, β_L are not varying with position. The β_G can be estimated by:

$$\beta_G = 1 - \beta_L$$

where volume fraction of liquid phase β_L is given by [36]

$$\beta_L = \exp\left[-12.55\left(u_s\sqrt{\frac{\rho_G}{\rho_L - \rho_G}}\right)^{0.91}\right]$$

(3) **Mixed phase modeling form**:

In this model, the liquid and vapor are considered to be mixed together as a single mixed continuous phase. The difficulty comes from the evaluation of the liquid–vapor interaction within a phase. This model is not yet well established and still under investigation.

Remarks

In our practice, the application of interacted liquid-phase model is successful in simulating liquid–gas (vapor) two-phase processes, such as distillation, absorption, and adsorption, as given in subsequent chapters.

3.7   Calculation of Mass Transfer Rate

In solving the mass transfer Eq. (3.1), the evaluation of the source term S_n, which is the mass rate (mass flux) transferred from adjacent phase (outside of the system concerned) or generated by chemical reaction (inside of the system), is very important as it is highly affect the final result. For the gas–liquid two-phase mass transfer process under steady condition and assuming the driving force of mass transfer is the linear concentration difference, we can write the conventional formula for calculating the mass transfer rate of species i [dimension kg m^{-2} s^{-1}], denoted by S_n or N_i, as follows:

$$S_n = N_i = k_L\left(C_{iL}^* - C_{iL}\right) = k_G\left(C_{iG} - C_{iG}^*\right)$$

Note that, in this section, the subscript i and j denotes species i and j, not the directions i, j; k_L and k_G are, respectively, the film mass transfer coefficient of liquid and gas [m s^{-1}]; C_{iL} and C_{iG} are, respectively, the bulk concentration of component i [kg m^{-3}] in liquid phase and gas phase; C_{iL}^* and C_{iG}^* are, respectively, the concentration of component i at the interface in thermodynamic equilibrium with the C_{iL} and C_{iG} (kg m^{-3}). The importance of evaluation of mass transfer coefficient k_L or k_G is clearly seen from the foregoing equation. Nevertheless, the prediction of the coefficient is difficult, and so far only relies on experimental measurement. There are two different cases:

- For the two-component mass transfer, some empirical correlations based on experimental data are available in literature.
- For the multicomponent mass transfer, the mass transfer rate is closely related to the composition due to the complicated molecular interaction between components and exhibit different characters with two-component system. For instance, for the two-component system, the mass flux is transferred from high to low concentration, yet in multicomponent system, some components can be transferred from low to high concentration. This is what we called "bizarre phenomena" (see Sect. 4.1.3.7). Thus, the mass transfer coefficient in multicomponent system is complicated and can be calculated only under the individual condition based on the coefficients of relevant two-component pairs (see Sect. 3.7.2). For this reason, no general correlation for multicomponent mass transfer coefficient is available.

3.7.1 Mass Transfer in Two-Component (Binary) System

The mass transfer coefficient of two-component system is the basic information necessary for the prediction of mass transfer rate in the process. The calculation of mass transfer for multicomponent system is also based on the mass transfer coefficients of the correspondent binary pairs (see Sect. 4.1.3).

One of the traditional models for predicting the binary mass transfer coefficient is based on the penetration theory by Higbie [37]. It is used as our starting point.

Let us consider the case of a wetted wall (falling film) column undergoing gas absorption with the following assumptions:

1. The component i in gas phase is absorbed by binary liquid absorbent containing components i and j.
2. The velocity of falling absorbent is very low, and mass is transferred by molecular diffusion. The absorption rate is low so as to keep the density of absorbent remains unchanged.
3. Penetration theory is applied, thus a fluid element (cluster of fluid particle) may stochastically move to the interface and stay there from $t = 0$ to $t = t_H$, during

that time interval component i is diffused from gas to liquid phase under unsteady condition.

With the foregoing assumptions, Eq. (3.1) is simplified to the following form:

$$\frac{\partial C_i}{\partial t} = D \frac{\partial^2 C_i}{\partial z^2} \qquad (3.32)$$

where D is the molecular diffusivity of component i in the fluid; z is the direction perpendicular to the interface; C_i is the concentration of component i in the fluid element; C_{iz} is the concentration of i at distance z from interface; C_i^* is the concentration of i at interface in equilibrium with C_i.

The boundary conditions are:

At $t = 0$, $z = 0$, $C_i = C_i$ (fluid element just arrive interface and still remains at the bulk concentration C_i)

At $t > 0$, $z = 0$, $C_i = C_i^*$ (interfacial gas–liquid equilibrium of component i has been established).

At $t > 0$, $z = z$, $C_i = C_{iz}$ (bulk concentration of component i).

The solution of Eq. (3.32) at constant D is found to be

$$\frac{C_i^* - C_i}{C_i^* - C_{iz}} = \operatorname{erf} \frac{z}{2\sqrt{Dt}} \qquad (3.33)$$

Thus, the relationship of C_i along z at different t can be obtained. Let the mass flux of component i diffused from interface to the bulk be J_i, then from the potential concept (or Fick's law), we have $J_i = D\left(-\frac{\partial C_i}{\partial z}\right)_{z=0}$. Combining with foregoing equations and after mathematical treatment, the relationship between J_i and t can be obtained as follows:

$$J_i = \left(C_i^* - C_{iz}\right)\sqrt{\frac{D}{\pi t}}$$

Integrate foregoing equation from $t = 0$ to $t = t_H$, the average rate of mass flux being transferred N_i is obtained:

$$N_i = \frac{\int_0^{t_H} J_i \, dt}{t_H} = 2\left(C_i^* - C_{iz}\right)\sqrt{\frac{D}{\pi t_H}}$$

By the definition of mass transfer coefficient k_L, i.e., $N_i = k_L\left(C_{iL}^* - C_{iL}\right)$, we obtain k_L by employing penetration theory as follows:

$$k_L = 2\sqrt{\frac{D}{\pi t_H}} \qquad (3.34)$$

According to the penetration theory, the t_H is the residence time of a fluid element at the interface undergoing the gas–liquid contact. Thus, $t_H = \frac{l}{u}$ where u is the velocity of the fluid element at the interface (equal to the velocity of falling

absorbent), l is the length of the fluid element travelled with velocity u at the time interface. The k_L equation becomes

$$k_L = 2\sqrt{\frac{Du}{\pi l}}$$

The l here may be regarded as characteristic length. Expressing the k_L in the form of dimensionless Sherwood number Sh_L, we have

$$Sh_L = \frac{k_L l}{D} = 2\frac{l}{D}\sqrt{\frac{D_t u}{\pi l}} = \sqrt{\frac{4lu}{\pi D}} = \sqrt{\frac{4}{\pi}\left(\frac{lu\rho}{\mu}\right)\left(\frac{\mu}{\rho D}\right)} = 1.128(Re)^{0.5}(Sc)^{0.5}$$

In using the foregoing Sh–Re–Sc form for the regression of the experimental data, the exponent 0.5 should be corrected and adjusted. The Sh–Re–Sc form of empirical equation is employed by some authors to fit the experimental data covering both lamina and turbulent flow as shown in Table 3.2:

$$Sh_L = C_0\,Re^a\,Sc^b \tag{3.35}$$

where C_0, a, b are constants to be determined based on experimental data.

As seen from Table 3.2, the exponent in empirical Eq. (3.35) may change greatly by fitting the experimental data.

Equation (3.35), i.e., the Sh–Re–Sc form, is usually modified to suit different equipment and condition of mass transfer by adding extra-geometric term or dimensionless group. Table 3.3 is given some examples.

As indicated in Table 3.3, the mass transfer coefficient k_L in the Sherwood group Sh is not only affected by the geometry of equipment and internal construction, such as the d/l ratio or the ratio of column diameter to packing size, but also the fluid properties such as ρ, μ, σ in the dimensionless group.

Besides Sh–Re–Sc form, the k_L or k_G correlations are usually expressed according to the authors' data analysis. Some empirical correlations are given in Table 3.4 as examples.

In case that the interfacial effects, such as Marangoni interfacial convection, are occurred in the mass transfer process, the influence by the surface tension gradient $\Delta\sigma$ on k_L should also be concerned in the empirical expression (see Chap. 8) so that k_L is generally affected by the following variables:

$$k_L = f(D_t, u, \rho, \mu_t, l, \Delta\sigma)$$

or expressed as an exponential equation

$$k_L = (\text{constant})D_t^a u^b \rho^c \mu_t^d l^e \Delta\sigma^f$$

By dimensional analysis, the following dimensionless equation is obtained:

$$\frac{k_L l}{D_t} = (\text{constant})\left(\frac{l\rho u}{\mu_t}\right)^{\alpha}\left(\frac{\mu_t}{\rho D_t}\right)^{\beta}\left(\frac{\Delta\sigma l}{\mu_t D_t}\right)^{\gamma}$$

Table 3.2 Some published empirical correlations for binary system with Sh–Re–Sc form

Equation	Application	References
$Sh = 0.015\,Re^{0.89}Sc^{0.5}$	Packed column absorption Packing: ceramic saddle	[38]
$Sh = 4.1\,Re^{0.39}Sc^{0.33}$	Packed column absorption Packing: stainless Pall ring	[39]
$Sh = 0.01099\,Re^{0.3955}Sc^{0.5}$	Wetted wall column absorption $Re < 75$	[40]
$Sh = 2.995 \times 10^{-2}Re^{0.2134}Sc^{0.5}$	Falling film column Gas absorption	[40]
$Sh = 2.3\,Re^{0.43}Sc^{0.33}$	Packed column Packing: copper Raschig ring	[41]
$Sh = 3.725 \times 10^{-2}Re^{0.2715}Sc^{0.5}$	Gas absorption Absorbent: $CaCl_2$ solution $100 < Re < 700$	[42]
$Sh = 2.326 \times 10^{-3}Re^{0.6938}Sc^{0.5}$	Gas absorption $700 < Re < 1{,}600$	[42]
$Sh_g = 0.0279\,Re^{0.791}Sc^{0.44}$	Wetted wall tower System: isopropanol–water–air isopropanol–water–N_2	[43]
$Sh = 4.22\,Re^{1/3}Sc^{1/2}$	Gas absorption System: Glucose solution-CO_2	[44]
$Sh = (0.012 \pm 0.001)Re^{0.89\pm0.05}Sc^{0.33}$	Gas absorption System: Sediment water-O_2	[45]
$Sh = 1.15Sc^{1/3}Re^{1/2}$	Fluid-particle ion exchange, $Re < 1{,}000$	[46]
$Sh_G = 0.00031\,Re_G^{1.05}\,Re_L^{0.207}Sc_G^{0.5}$	Concurrent wetted wall column	[47]
$Sh = 1.38\,Re^{0.34}Sc^{0.33}$	Hollow-fiber contactor	[48]
$Sh = 0.648\,Re^{0.379}Sc^{0.33}$	Spiral wound pervaporation	[49]
$Sh = 0.048\,Re^{0.6}Sc^{1/3}$	Hollow-fiber reverse osmosis	[50]

Table 3.3 Some published empirical correlations with modification of Sh–Re–Sc form

Equation	Application	References
$Sh_g = 0.0044\,Re_g Sc_g^{0.5}We_l^{0.111}$	Falling film tower. CO_2 absorption	[51]
$Sh = 1.62\,Re^{0.33}Sc^{0.33}\left(\frac{d}{l}\right)^{0.33}$	Falling film tower. CO_2 absorption by ethanol, water	[52]
$Sh = 2\,Re^{1/2}Sc^{1/2}(d/l)^{1/2}$	Tube reactor, lamina flow	[53]
$Sh = 0.85\,Re^{0.54}Sc^{0.33}\left(\frac{d_p}{d}\right)^{-0.75}\left(\frac{d_p}{L}\right)^{0.43}$	Fluidized bed	[54]
$Sh = 8.748 \times 10^2\,Re^{0.024}Sc^{-0.133}Eu^{-0.012}$	Bubble column reactor, CO/kerosene system	[55]
$Sh = 2.136 \times 10^{-4}\,Re_f^{0.4}Sc^{0.65}Ga_f^{0.52}$	Falling film tower. CO_2 absorption by ethanol, water	[56]

Where $We = \rho\alpha u^2/\sigma$, $Ga = l^3\rho^2 g/\mu^2$, $Bo = q/\gamma\rho_v u_v$, $Fr = u/gl$, $Eu = p/\rho u^2$
α is the diameter of liquid drop, d is the column diameter, l is the characteristic length

Table 3.4 Some empirical mass transfer coefficient equations from experimental data

Equation	Application	References
$k_G = 1.195 u_G \left[\dfrac{d_p \rho_G u_G}{\mu_G (1-\varepsilon)} \right]^{-0.36} Sc_G^{-2/3}$	Random packing	[57]
$k_L = 25.1 \dfrac{D_L}{d_p} \left(\dfrac{d_p \rho_L u_L}{\mu_L} \right)^{0.45} Sc_L^{0.5}$		
$k_L = \dfrac{0.0051}{(a_p d_p)^{-0.4}} \left(\dfrac{\mu_L g}{\rho_L} \right)^{1/3} \left(\dfrac{\rho_L u_L}{a_e \mu_L} \right)^{2/3} Sc_L^{-0.5}$	Random packing	[58]
$k_G = c \left(\dfrac{D_G}{a_p d_p^2} \right) \left(\dfrac{\rho_G u_G}{a_p \mu_G} \right)^{0.7} Sc_G^{1/3}$		
$k_L = C_L \left(\dfrac{\rho_L g}{\mu_L} \right)^{1/6} \left(\dfrac{D_L}{d_h} \right)^{0.5} \left(\dfrac{u_L}{a_p} \right)^{1/3}$	Random packing	[59]
$k_G = C_G \dfrac{a_p^{0.5} D_G}{\sqrt{d_h (\varepsilon - h_L)}} \left(\dfrac{\rho_G u_G}{a_p \mu_G} \right)^{3/4} Sc_G^{1/3}$		
$k_G = 0.0338 \dfrac{D_G}{d_{eq}} \left[\dfrac{\rho_G d_{eq} (u_{L\alpha} + u_{G\alpha})}{\mu_G} \right]^{0.8} Sc_G^{0.33}$	Structured packing	[60]
$k_L = 2 \sqrt{\dfrac{D_L}{\pi_\delta} \left(\dfrac{9 \Gamma^2 g}{8 \rho_L \mu_L} \right)^{1/3}}$		
where $u_{G\alpha} = \dfrac{u_G}{\varepsilon \sin \alpha}$, $u_{L\alpha} = \dfrac{9 \Gamma^2 g}{8 \rho_L \mu_L}$		
$k_G = \sqrt{\left(\dfrac{Sh_{G,lam} D_G}{d_{hG}} \right)^2 + \left(\dfrac{Sh_{G,turb} D_G}{d_{hG}} \right)^2}$	Structured packing	[61]
where $Sh_{G,lam} = 0.664 Sc_G^{1/3} \sqrt{Re_{Grv} \dfrac{d_{hG}}{l_{G,p\alpha}}}$		
$Sh_{G,turb} = \dfrac{(Re_{Grv} Sc_G \xi_{GL} \varphi/8)[1 + (d_{hG}/l_{G,p\alpha})^{2/3}]}{1 + 12.7 \sqrt{\xi_{GL} \varphi/8} (Sc_G^{2/3} - 1)}$		
$k_L = 2 \sqrt{\dfrac{D_L u_{L\alpha}}{0.9 \pi d_{hG}}}$		
$k_L = 2.6 \times 10^{-5} \mu_L^{0.25}$, $k_G = \dfrac{0.13}{\rho_v} - \dfrac{0.065}{\rho_v^2}$	Sieve tray column	[62]

or

$$Sh_L = (\text{constant}) Re^\alpha Sc_t^\beta Ma^\gamma \tag{3.35a}$$

where Ma is Marangoni number (see Chap. 8); α, β, γ are constants.

The importance of considering the interfacial effect on mass transfer coefficient can be seen by the following example. The Sh_L equation for binary system containing phosphoric acid and ethyl hexanol was reported below by Akita and Yoshida [63] with average error of 14.49 %.

$$Sh = 1.263 \, Re^{0.662} Sc^{0.0761}$$

Zhou [64] employed Eq. (3.35a) for the regression of the published data of the same system and obtained the following equation with average error 9.62 %.

$$Sh = 0.0245 Re^{0.5229} Sc^{0.0761} Ma^{0.3427}$$

Thus, the consideration of interfacial effect, such as Marangoni convection, if occurred, is necessary to achieve better regressive empirical k_L equation.

Similar situation can be extended to the interfacial effect by Rayleigh convection (see Chap. 8), which is represented by the Rayleigh number Ra ($Ra = \frac{g\Delta\rho l^3}{D\mu}$ where $\Delta\rho$ is the density difference between interface and the bulk liquid), and Eq. (3.33a) is extended to the following form if necessary.

$$Sh = (\text{constant}) Re^a Sc^b Ma^c Ra^d$$

The constructional characteristics of the equipment cannot be ignored, thus a constructional dimensionless group, denoted as Ψ, is usually added to the k_L equation:

$$Sh = C_0 Re^a Sc^b Ma^d Re^e \Psi^f$$

where exponents a to f are constants.

Similar expressions can also be obtained for the gas-phase mass transfer coefficient k_G.

In short, the determination of mass transfer coefficient of two-component system is still relied on experimental measurement although the use of dimensionless group in the data regression can be helpful and reasonable. The collection of published correlations of mass transfer coefficient by Wang et al. [65] and Zhou [64] can be used as reference.

The calculation of mass transfer rate of multicomponent system will be briefly described in the section below and Sect. 4.1.3 of Chap. 4.

3.7.2 Mass Transfer in Multicomponent System

In practice, most of the mass transfer processes involve multicomponent, and the mass transfer rate should be calculated individually by each component. In some cases for simplifying the calculation, two influential components, called key components, are taken as if a two-component system. However, such simplification may lead to serious error, and the rigorous method is preferable. The calculation of multicomponent mass transfer is by the aid of Maxwell–Stefan equation which is introduced briefly in the section below.

3.7.2.1 The Maxwell–Stefan Equation

Most of the multicomponent systems are non-ideal. From thermodynamic viewpoint, the transfer of mass species i at constant temperature and pressure from one phase to the other in a two-phase system is due to existing the difference of chemical potential $\mu_{i,\,T,\,P}$ between phases, in which $\mu_{i,T,P} = \mu_{i,T,P}^0 + RT \ln \gamma_i x_i$, where γ_i is the activity coefficient of component i; $\mu_{i,T,P}^0$ is $\mu_{i,\,T,\,P}$ at standard state. In other words, for a gas (vapor)–liquid system, the driving force of component i transferred from gas phase to the adjacent liquid phase along direction z is the negative gradient of chemical potential, $-\frac{\partial \mu_{i,T,P}}{\partial z}$.

The transfer (diffusion) of component i from gas phase to the liquid-phase should overcome the resisting force from the adjacent component x_j in the gas phase, such resistance is represented by the frictional force between two fluid molecules, which is proportional to the velocity difference $(u_i - u_j)$ and the activity of component j (denoted by a_j, $a_j = \gamma_j x_j$). If the system under consideration contains n_i moles of species i per m^3, then the balance between driving force and resisting force on m^3 (one cubic meter) basis is as follows [37]:

$$-n_i \frac{d\Delta_{T,P}\mu_i}{dz} = \varphi\left[\gamma_j x_j (u_i - u_j)\right] \tag{3.36}$$

where φ is proportional constant depending on the system concerned;. n_i is the number of moles per m^3.

Assuming the gas phase is an ideal gas, we have $n_i = \frac{p_i}{RT}$, and Eq. (3.36) becomes:

$$\begin{aligned} -\frac{1}{RT}\frac{d\Delta_{T,P}\mu_i}{dz} &= \frac{1}{p_i/\varphi}\left[\gamma_j x_j (u_i - u_j)\right] \\ &= \frac{1}{D_{ij}}\left[\gamma_j x_j (u_i - u_j)\right] \end{aligned}, \quad i = 1, 2, \ldots, n-1,$$

where D_{ij} is called Maxwell–Stefan diffusivity $\left(D_{ij} = \frac{p_i}{\varphi}\right)$, which reflexes the contribution of i–j binary pair diffusion on the multicomponent system. Considering the mass transfer between components is additive, the following generalized Maxwell–Stefan diffusion equation [65, 66] is obtained:

$$\frac{1}{RT}\nabla_{T,P}\mu_i = \sum_{\substack{j=1 \\ j \neq i}}^{n} \frac{\gamma_j x_j (u_j - u_i)}{D_{ij}}, \quad i = 1, 2\ldots, n-1 \tag{3.37}$$

For ideal solution, $\gamma_j = 1$, we have:

$$\frac{1}{RT}\nabla_{T,P}\mu_i = \sum_{\substack{j=1 \\ j \neq i}}^{n} \frac{x_j (u_j - u_i)}{D_{ij}}, \quad i = 1, 2, \cdots, n-1$$

Multiplying foregoing equation by x_i and noting that molar mass flux of component i is equal to $N_i = c_t x_i u_i = J_i + x_i N_t$, we obtain:

$$\frac{x_i}{RT} \nabla_{T,P} \mu_i = \sum_{\substack{j=1 \\ j \neq 1}}^{n} \frac{x_i N_j - x_j N_i}{c_t D_{ij}} = \sum_{\substack{j=1 \\ j \neq 1}}^{n} \frac{x_i J_j - x_j J_i}{c_t D_{ij}}, \quad i = 1, 2, \cdots, n \qquad (3.38)$$

where c_t is the total molar concentration; J_i is the diffusion flux of component i.

The Maxwell–Stefan diffusivity D_{ij} obeys the Onsager reciprocal relation of irreversible thermodynamics, i.e.,

$$D_{ij} = D_{ji}, \quad i, j = 1, 2, \ldots, n$$

3.7.2.2 Calculation of Mass Flux

The boundary conditions of the generalized Maxwell–Stefan equation (3.37) are

$$t > 0, \quad z = 0, \quad (x) = (x_0)$$
$$t > 0, \quad z = \Delta h, \quad (x) = (x_b)$$

where x_b is the concentration of the bulk liquid; x_0 is the liquid concentration at the gas–liquid interface. The solution of Eq. (3.37) should be based on certain simplifications.

3.7.2.3 Based on Two-Film Theory of Mass Transfer

The following assumptions are made:

(a) The diffusivity D_{ij} as well as other parameters is constant throughout the mass transfer process;

(b) The concentration gradient across the fluid film $\frac{d(x)}{dz}$ is linear, equal to $\frac{x_0 - x_b}{\delta}$ where δ is the thickness of the liquid film.

With the foregoing assumptions, Eq. (3.38) can be transformed approximately to the following form as given by Krishna [67] and Song et al. [68]

$$N_i = -c_t [\beta][R]^{-1}[\Gamma] \frac{d(x)}{dz} \qquad (3.39)$$

where $[\beta]$ represents the matrix of molar exchange in counter-diffusion mass transfer, such as distillation, due to the difference of latent heat of vaporization between components. The element of this matrix is given below

$$\beta_{ij} = \delta_{ij} - x_i \left(\frac{\lambda_j - \lambda_n}{\sum_{k=1}^{n} x_k \lambda_k} \right), \quad i,j = 1, 2, \ldots, n-1$$

where δ_{ij} is Kronecker delta, $\delta_{ij} = 1$ for $i = j$, $\delta_{ij} = 0$ for $i \neq j$.

The $[R]$ is the matrix of mass transfer coefficients with the following elements:

$$R_{ii} = \frac{x_i}{\mathbf{D}_{in}/\delta} + \sum_{\substack{k=1 \\ k \neq i}}^{n} \frac{x_k}{\mathbf{D}_{ik}/\delta}, \quad i = 1, 2, \ldots, n-1$$

$$R_{ij} = -x_i \left(\frac{1}{\mathbf{D}_{ij}/\delta} - \frac{1}{\mathbf{D}_{in}/\delta} \right), \quad i = 1, 2, \ldots, n-1$$

According to the two-film theory of mass transfer, k_{ij} is equal to:

$$k_{ij} = \frac{\mathbf{D}_{ij}}{\delta}$$

Then, the elements of $[R_{ij}]$ can be changed to the following form:

$$R_{ii} = \frac{x_i}{k_{in}} + \sum_{\substack{k=1 \\ k \neq i}}^{n} \frac{x_k}{k_{ik}}, \quad i = 1, 2, \ldots, n-1$$

$$R_{ij} = -x_i \left(\frac{1}{k_{ij}} - \frac{1}{k_{in}} \right), \quad i = 1, 2, \ldots, n-1$$

In the foregoing $[R_{ij}]$ expression, the binary mass transfer coefficient k_{ij} cannot be calculated using $\frac{\mathbf{D}_{ij}}{\delta}$ because the film thickness δ is hard to estimate. Instead, it is suggested that k_{ij} may be calculated using (3.34) from penetration theory as a substitute [67], i.e., $k_{ij} = 2\sqrt{\frac{\mathbf{D}_{ij}}{\pi t_{\mathrm{H}}}}$, where t_{H} is the time of contact between two phases.

The matrix $[\Gamma]$ represents thermodynamic correction factor (activity coefficient γ) with following elements

$$\Gamma_{ij} = \delta_{ij} + \frac{x_i}{x_j} \frac{\partial \ln \gamma_i}{\partial \ln \gamma_j}, \quad i,j = 1, 2, \ldots, n-1$$

Equation (3.38) can be written as follows for liquid-phase mass transfer flux with preceding assumptions:

$$N_i = -c_t [\beta][R]^{-1}[\Gamma](x_0 - x_b) \tag{3.40}$$

also can be written for the liquid phase as

$$N_i^L = -c_t [\beta^L][R^L]^{-1}[\Gamma^L](x_0 - x_b) \tag{3.41}$$

Similarly, we have

$$N_i^V = -c_t \left[\beta^V\right]\left[R^V\right]^{-1}\left[\Gamma^V\right](y_0 - y_b) \tag{3.42}$$

As the overall mass transfer flux N_T is equal to N_i^L or N_i^V under steady condition, Eq. (3.41) or Eq. (3.42) is more convenient for the calculation. Nevertheless, all the parameter in the equation is based on the average composition, i.e.,$(x_0 - x_b)/2$, therefore stepwise iteration should be used.

3.7.2.4 Based on Penetration Theory of Mass Transfer

Wang [69] employed the penetration theory of mass transfer instead of two-film theory to solve Eq. (3.38) mathematically to yield the following results:

$$(N_i) = c_t[\beta][k][X](x_0 - x_b) \tag{3.43}$$

where $[k]$ is the mass transfer coefficient matrix with the following elements:

$$[k] = \frac{2}{\sqrt{\pi t_H}}\left\{[B]^{-1}[\Gamma]\right\}^{1/2} \tag{3.44}$$

The $[B]$ is the matrix of inverted diffusivity with the following elements:

$$B_{ii} = \frac{x_i}{\mathbf{D}_{in}} + \sum_{\substack{k=1 \\ k \neq i}}^{n} \frac{x_k}{\mathbf{D}_{ik}}, \quad \overset{i=1,2,\dots,n-1}{B_{ij} = -x_i\left(\frac{1}{\mathbf{D}_{ij}} - \frac{1}{\mathbf{D}_{in}}\right),} \quad i,j=1,2,\dots,n-1,i\neq j$$

The $[X]$ is the correction matrix with the following elements:

$$[X] = \frac{\exp\left\{-N_t^2/\left(\left(\pi c_t^2\right)\right)[k]^{-2}\right\}}{[I] + \mathrm{erf}\left\{N_t/(\sqrt{\pi}c_t)[k]^{-1}\right\}}$$

The diffusion flux in liquid phase N_i^L is obtained as follows

$$\left(N_i^L\right) = c_t^L\left[\beta^L\right]\left[k^L\right]\left[X^L\right](x_b - x_0) \tag{3.45}$$

Also in vapor phase

$$\left(N_i^V\right) = c_t^V\left[\beta_0^V\right]\left[k^V\right]\left[X^V\right](y_0 - y_b) \tag{3.46}$$

3.7.2.5 Remarks

The difference between the foregoing two solution of Maxwell–Stefan equation, i.e., Eqs. (3.40) and (3.43), are:

(a) k_{ij} in the matrix $[R]$ of Eq. (3.40) is calculated by using $k_{ij} = \frac{D_{ij}}{\delta}$ accordingly, while employing $k_{ij} = 2\sqrt{\frac{D_{ij}}{\pi t_H}}$ in Eq. (3.40) is only a substitute pending on confirmation.

(b) Equation (3.40) involves the contribution of non-ideality by matrix $[\Gamma]$, while Eq. (3.43) involves not only the contribution by matrix $[\Gamma]$ but also the contribution of mass transport N_t by matrix $[X]$.

Nevertheless, the calculated results using Eqs. (3.41) and (3.45) display no substantial difference, and all are confirmed with experimental data.

3.8 Model System of CMT Process Computation

Generally speaking, most of the existing mass transfer processes involve fluid flow, heat, and mass transfer. Thus, the process simulation using CMT should comprise momentum, heat, and mass transfer model equation sets for coupling computation as given below.

(I) **CFD equation set**: It consists of overall mass conservation equation, momentum conservation equation, and its closure equations. It aims to find the velocity distribution (velocity profile) and other flow parameters.

(II) **CHT equation set**: It consists of energy conservation equation and its closure equations. It aims to find the temperature distribution (temperature profile) and other heat parameters.

(III) **CMT equation set**: It consists of species mass conservation equation and its closure equations. It aims to find the concentration distribution (concentration profile) and other mass transfer parameters.

The equations in the foregoing equation set are depending on what model is being used. The corresponding equations for fluid dynamic model are given in Chap. 1, while those for heat and mass transfer model are summarized in Chap. 2 and this chapter.

The model system of process computation in CMT in this book can be shown schematically in Fig. 3.9.

3.9 Summary

Besides the computation of velocity distribution by CFD and temperature distribution by CHT as presented in previous chapters, the computation of concentration distribution in a process equipment so far receives less attention, but it is the basis of evaluating the process efficiency and should be much concerned. The challenge
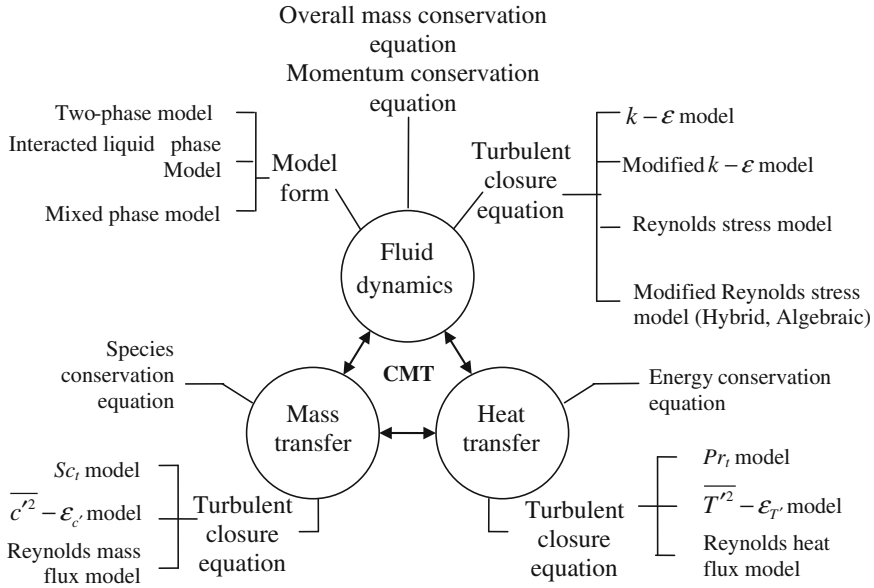
Fig. 3.9 Model system of CMT process computation

of this problem is the closure of the differential species conservation equation. The recently investigated $\overline{c'^2} - \varepsilon_{c'}$ model, and Reynolds mass flux model are found to be successful in fulfilling the need.

1. $\overline{c'^2} - \varepsilon_{c'}$ model, in which the unknown Reynolds mass flux $-\rho\overline{u_i'c'}$ is calculated by Eq. (3.4) involving a new parameter of turbulent mass transfer diffusivity D_t. The D_t can be calculated by Eq. (3.6) where the $\overline{c'^2}$ and $\varepsilon_{c'}$ equations are given by Eqs. (3.1) and (3.17), respectively. Note that, the molded $\varepsilon_{c'}$ equation has different forms, but they give comparable simulated results each other. Although this model is convenient to be used and give good simulated results in many cases, it is isotropic and its accuracy of simulation is less than that by Reynolds mass flux model.

2. Reynolds mass flux model, or standard Reynolds mass flux model, in which the unknown $-\rho\overline{u_i'c'}$ is calculated directly using model equation either Eq. (3.25a) or Eq. (3.25b). This model is rigorous and applicable to anisotropic case with mass and heat transfer. The model equations comprises the following equation sets:

   - Mass transfer equation set, i.e., Eqs. (3.3) and (3.25a);
   - Fluid dynamic (CFD) equation set, i.e., Eqs. (3.26), (3.27), and (1.23a);
   - Heat transfer equation set, i.e., Eqs. (2.3a) and (2.13).

The weakness of this model is requiring heavy computer work. For simplifying the computation, the complicated equations Eq. (3.25a) can be replaced by Eq. (1.8), which is called hybrid mass flux model. Another simplification is made by letting Eq. (3.31) to replace Eq. (3.25a) for calculating $\overline{u'_i c'}$, called algebraic Reynolds mass flux model. These simplified models are able to give similar simulated results in comparision with the standard model.

The Reynolds (turbulent) mass flux $\overline{u'_i c'}$ is the variance of $u'_i c'$ created from the turbulent mass flux uc; the transport of which is by both uc flow and fluctuated concentration diffusion. If both are in the same direction, the process is promoted (enhanced). Inversely, if they are in opposite direction, the counteraction of diffusion causes reduction of uc by mutual mixing. Thus, the $\overline{u'_i c'}$ initiated from turbulent effect is influential to the mass transfer.

References

1. Liu BT (2003) Study of a new mass transfer model of CFD and its application on distillation tray. Ph.D. dissertation, Tianjin University, Tianjin, China (in Chinese)
2. Sun ZM (2005) Study on computational mass transfer in chemical engineering. Ph.D. dissertation, Tianjin University, Tianjin, China (in Chinese)
3. Sun ZM, Liu BT, Yuan XG, Yu KT (2005) New turbulent model for computational mass transfer and its application to a commercial-scale distillation column. Ind Eng Chem Res 44(12):4427–4434
4. Sun ZM, Yu KT, Yuan XG, Liu CJ (2007) A modified model of computational mass transfer for distillation column. Chem Eng Sci 62:1839–1850
5. Liu GB (2006) Computational transport and its application to mass transfer and reaction processes in pack-beds. Ph.D. dissertation, Tianjin University, Tianjin, China (in Chinese)
6. Liu GB, Yu KT, Yuan XG, Liu CJ, Guo QC (2006) Simulations of chemical absorption in pilot-scale and industrial-scale packed columns by computational mass transfer. Chem Eng Sci 61:6511–6529
7. Liu GB, Yu KT, Yuan XG, Liu CJ (2006) New model for turbulent mass transfer and its application to the simulations of a pilot-scale randomly packed column for CO_2–NaOH chemical absorption. Ind Eng Chem Res 45:3220–3229
8. Liu GB, Yu KT, Yuan XG, Liu CJ (2008) A computational transport model for wall-cooled catalytic reactor. Ind Eng Chem Res 47:2656–2665
9. Liu GB, Yu KT, Yuan XG, Liu CJ (2009) A numerical method for predicting the performance of a randomly packed distillation column. Int J Heat Mass Tran 52:5330–5338
10. Li WB, Liu BT, Yu KT, Yuan XG (2011) A rigorous model for the simulation of gas adsorption and its verification. Ind Eng Chem Res 50(13):361–370 (8)
11. Sun ZM, Liu CJ, Yu GC, Yuan XG (2011) Prediction of distillation column performance by computational mass transfer method. Chin J Chem Eng 19(5):833–844
12. Lemoine F, Antoine Y, Wolff M et al (2000) Some experimental investigations on the concentration variance and its dissipation rate in a grid generated turbulent flow. Int J Heat Mass Tran 43(7):1187–1199
13. Spadling DB (1971) Concentration fluctuations in a round turbulent free jet. Chem Eng Sci 26:95
14. Launder BE, Samaraweera SA (1979) Application of a second-moment turbulence closure to heat and mass transport in thin shear flows—two-dimensional transport. Int J Heat Mass Tran 22:1631–1643

15. Sommer TP, So MRC (1995) On the modeling of homogeneous turbulence in a stably stratified flow. Phys Fluids 7:2766–2777
16. Sherwood TK, Pigford RL, Wilke CR (1975) Mass transfer. McGraw Hill, New York
17. Cai TJ, Chen GX (2004) Liquid back-mixing on distillation trays. Ind Eng Chem Res 43(10):2590–2597
18. Comini G, Del Giudice S (1985) A k–e model of turbulent flow. Numer Heat Transf 8:299–316
19. Patankar SV, Sparrow EM, Ivanovic M (1978) Thermal interactions among the confining walls of a turbulent recirculating flow. Int J Heat Mass Tran 21(3):269–274
20. Tavoularis S, Corrsin S (1981) Experiments in nearly homogenous turbulent shear-flow with a uniform mean temperature-gradient. J Fluid Mech 104:311–347 (MAR)
21. Ferchichi M, Tavoularis S (2002) Scalar probability density function and fine structure in uniformly sheared turbulence. J Fluid Mech 461:155–182
22. Sun ZM, Liu CT, Yuan XG, Yu KT (2006) Measurement and numerical simulation of concentration distribution on sieve tray. J Chem Ind Eng (China) 57(8):1878–1883
23. Chen CJ, Jaw SY (1998) Fundamentals of turbulence modeling. Taylor and Francis, London
24. Jone CJ, Launder BE (1973) The calculation of low-reynolds-number phenomena with a two-equation model of turbulence. Int J Heat Mass Tran 16:1119–1130
25. Khalil EE, Spalading DB, Whitelaw JH (1975) Calculation of local flow properties in 2-dimensional furnaces. Int J Heat Mass Transfer 18:775–791
26. Li WB, Liu BT, Yu KT, Yuan XG (2011) A new model for the simulation of distillation column. Chin J Chem Eng 19(5):717–725
27. Li WB (2012) Theory and application of computational mass transfer for chemical engineering processes. Ph.D. dissertation, Tianjin University, Tianjin
28. Gesit G, Nandakumar K, Chuang KT (2003) CFD modeling of flow patterns and hydraulics of commercial-scale sieve trays. AIChE J 49:910
29. Krishna R, van Baten JM, Ellenberger J (1999) CFD simulations of sieve tray hydrodynamics. Trans IChemE 77 Part A 10:639–646
30. Solari RB, Bell RL (1986) Fluid flow patterns and velocity distribution on commercial-scale sieve trays. AIChE J 32:640
31. Wang XL, Liu CT, Yuan XG, Yu KT (2004) Computational fluid dynamics simulation of three-dimensional liquid flow and mass transfer on distillation column trays. Ind Eng Chem Res 43(10):2556–2567
32. Auton TR, Hunt JCR, Prud'homme M (1988) The force exerted on a body in inviscid unsteady non-uniform rotational flow. J Fluid Mech 197:241
33. Krishna R, Urseanu MI, Van Baten JM et al (1999) Rise velocity of a swarm of large gas bubbles in liquids. Chem Eng Sci 54:171–183
34. Yu KT, Yuan XG, You XY, Liu CJ (1999) Computational fluid-dynamics and experimental verification of two-phase two-dimensional flow on a sieve column tray. Chem Eng Res Des 77A:554
35. Colwell CJ (1979) Clear liquid height and froth density on sieve trays. Ind Eng Chem Proc Des Dev 20:298
36. Bennet DL, Agrawal R, Cook PJ (1983) New pressure drop correlation for sieve tray distillation columns. AIChE J 29:434–442
37. Higbie R (1935) The rate of absorption of a pure gas into a still liquid during short periods of exposure. Trans Am Inst Chem Eng 35:360–365
38. Doan HD, Fayed ME (2000) Entrance effect and gas-film mass-transfer coefficient in at large diameter packed column. Ind Eng Chem Res 39:1039–1047
39. Gostick J, Doan HD, Lohi A, Pritzkev MD (2003) Investigation of local mass transfer in a packed bed of pall rings using a limiting current technique. Ind Eng Res 42:3626–3634
40. Yih SM, Chen KY (1982) Gas absorption into wavy and turbulent falling liquid films in a wetted-wall. Chem Eng Commun 17(1–6):123–136
41. Gostick J, Doan HD, Lohi A, Pritzkev MD (2003) Investigation of local mass transfer in a packed bed of pall rings using a limiting current technique. Ind Eng Chem Res 42:3626–3634

42. Chen YM, Sun CY (1997) Experimental study on the heat and mass transfer of a combined absorber evaporator exchanger. Int J Heat Mass Tran 40:961–971
43. Krupiczka R, Rotkegel A (1997) An experimental study of diffusional cross-effect in multicomponent mass transfer. Chem Eng Sci 52(6):1007–1017
44. Vasquez G, Antorrena G, Navaza JM, Santos V, Rodriguez T (1993) Adsorption of CO_2 in aqueous solutions of various viscosities in the presence of induced turbulence. Int Chem Eng 33(4):649–655
45. Sterinberger N, Hondzo M (1999) Diffusional mass transfer at sediment water interface. J Environ Eng 125(2):192–200
46. Carberry JJ (1960) A boundary-layer model of fluid-particle mass transfer in mixed beds. AIChE J 4:460
47. Nielsen CHE, Kiil S, Thomsen HW, Dam-Johansen K (1998) Mass transfer in wetted-wall columns: correlations at high Reynolds numbers. Chem Eng Sci 53(3):495–503
48. Yang MC, Cussler EL (1986) Designing hollow-fiber contactors. AIChE J 32(11):1910–1916
49. Hichey PJ, Gooding CH (1994) Mass transfer in spiral wound pervaporation modules. J Membr Sci 92(1):59–74
50. Sekino M (1995) Study of an analytical model for hollow fiber reverse osmosis module systems. Desalination 100(1):85–97
51. Erasmus AB, Nieuwoudt I (2001) Mass transfer in structured packing: a wetted-wall study. Ind Eng Chem Res 40:2310–2321
52. Cussler EL (1989) Diffusion. Cambridge University Press, New York
53. Baerns M, Hofmann H, Renken A (1987) Chemische Reaktionstechnik Stuttgart. Thieme
54. Jordan U, Schumpe A (2001) The gas density effect on mass transfer in bubble columns with organic liquids. Chem Eng Sci 56(21):6267–6272
55. Yang W, Wang J, Jin Y (2001) Mass transfer characteristics of syngas components in slurry system at industrial conditions. Chem Eng Technol 24(6):651–657
56. Hameed MS, Saleh Muhammed M (2003) Mass transfer into liquid falling film in straight and helically coiled tubes. Int J Heat Mass Transf 46(10):1715–1724
57. Shulman HL, Ullrich CF, Proulx AZ et al (1955) Performance of packed columns. Wetted and effective interfacial areas, gas- and liquid-phase mass transfer rates. AIChE J 1(2):253–258
58. Onda K, Takeuchi H, Okumoto Y (1968) Mass transfer coefficients between gas and liquid phases in packed columns. J Chem Eng Jpn 1(1):56–62
59. Billet R, Schultes M (1992) Advantage in correlating packing column performance. Inst Chem Eng Symp Ser 128(2):B129–B136
60. Bravo JL, Rocha JA, Fair JR (1985) Mass transfer in gauze packings. Hydrocarb Process 64(1):91–95
61. Olujic Z, Kamerbeek AB, De Graauw J (1999) A corrugation geometry based model for efficiency of structured distillation packing. Chem Eng Process 38(4–6):683–695
62. Zuiderweg FJ (1892) Sieve trays: a view on state of art. Chem Eng Sci 37:1441–1464
63. Akita K, Yoshida F (1973) Gas holdup and volumetric mass transfer coefficient in bubble column. Ind Eng Chem Process Des Dev 12(1):76–80
64. Zhou CF (2005) Study on the influence of Marangoni effect and other factor on the mass transfer coefficients. M.S. dissertation, Tianjin University, Tianjin, China (in Chinese)
65. Wang GQ, Yuan XG, Yu KT (2005) Review of mass-transfer correlations for packed columns. Ind Eng Chem Res 44:8715–8729
66. Krishna R, Wesselingh JA (1997) The Maxwell-Stefan approach to mass transfer. Chem Eng Sci 52(6):861–911
67. Krishna R (1985) Model for prediction of point efficiencies for multicomponent distillation. Chem Eng Res Des 63(5):312–322
68. Song HW, Wang SY, Han JC, Wu JW (1996) A new model for predicting distillation point efficiencies of non-ideal multicomponent mixture. CIESC J 47(5):571
69. Wang ZC (1997) Non-ideal multicomponent mass transfer and point efficiencies on a sieve tray. PhD dissertation, Tianjin University, Tianjin, China (in Chinese)

Chapter 4
Application of Computational Mass Transfer (I): Distillation Process

Abstract In this chapter, the application of computational mass transfer (CMT) method in the forms of two-equation model and Rayleigh mass flux model as developed in previous chapters to the simulation of distillation process is described for tray column and packed column. The simulation of tray column includes the individual tray efficiency and the outlet composition of each tray of an industrial-scale column. Methods for estimating various source terms in the model equations are presented and discussed for the implementation of the CMT method. The simulated results are presented and compared with published experimental data. The superiority of using standard Reynolds mass flux model is shown in the detailed prediction of circulating flow contours in the segmental area of the tray. In addition, the capability of using CMT method to predict the tray efficiency with different tray structures for assessment is illustrated. The prediction of tray efficiency for multicomponent system and the bizarre phenomena is also described. For the packed column, both CMT models are used for the simulation of an industrial-scale column with success in predicting the axial concentrations and HETP. The influence of fluctuating mass flux is discussed.

Nomenclature

A	Surface area per unit volume of packed column, m^{-1}
c_1, c_2, c_3	Model parameters in transport equation for the turbulent mass flux
C	Concentration, $\mathrm{kg\ m}^{-3}$
$\overline{C}$	Average concentration, $\mathrm{kg\ m}^{-3}$
$C_\mu, C_{1\varepsilon}, C_{2\varepsilon}, C_{3\varepsilon}$	Model parameters in k–ε model equations
c'	Fluctuating concentration, $\mathrm{kg\ m}^{-3}$
$\overline{c'^2}$	Variance of fluctuating concentration, $\mathrm{kg^2\ m}^{-6}$
D	Molecular diffusivity, $\mathrm{m^2\ s}^{-1}$
D_t	Turbulent mass diffusivity, $\mathrm{m^2\ s}^{-1}$

d_e	Equivalent diameter of random packing, m
d_H	Hydraulic diameter of random packing, m
d_p	Nominal diameter of the packed particle, m
E_o	Overall efficiency
E_{MV}	Murphree tray efficiency on gas basis
E_{ML}	Murphree tray efficiency on liquid basis
F	F factor, $U_G\sqrt{\rho_G}$, m s^{-1} (kg m^{-3})$^{0.5}$
g	Acceleration due to gravity, m s^{-2}
G	Production term
H	Height of packed bed measured from column bottom, m
h_f	Height of the liquid layer in tray column, m
h_w	Weir height in tray column, m
K_{OL}	Overall liquid-phase mass transfer coefficient in tray column, m s^{-1}
k	Turbulent kinetic energy, m^2 s^{-2}
k_G	Gas-phase mass transfer coefficient in packed column, kg m^{-2} s^{-1}
k_L	Liquid-phase mass transfer coefficient in packed column, kg m^{-2} s^{-1}
L	Liquid flow rate per unit cross-sectional area, kg m^{-2} s^{-1}
l_w	Weir width, m
m	Distribution coefficient
r	Position in radial direction, m
R	Radius of the column, m
S_C	Source term in species conversation equation, kg m^{-3} s^{-1}
S_m	Source term in momentum equation, N m^{-3}
t	Time, s
U	Superficial velocities, m s^{-1}
U	Interstitial velocity vector, m s^{-1}
u_i'	Fluctuating velocity, m s^{-1}
W	Weir length, m
x	Distance in x direction, m; mole fraction in liquid phase
y	Distance in y direction, m; mole fraction in gas phase
z	Distance in z direction, m
Z	Total height of packed bed, m
β_L, β_V	Volume fraction of liquid phase and vapor phase
α_{re}	Relative volatility
ε	Turbulent dissipation rate, m^2 s^{-3}
$\varepsilon_{c'}$	Turbulent dissipation rate of concentration fluctuation, kg^2 m^{-6} s^{-1}
γ	Porosity distribution of the random packing bed
μ, μ_G	Liquid- and gas-phase viscosities, kg m^{-1} s^{-1}
ρ, ρ_G	Liquid- and gas-phase densities, kg m^{-3}
σ	Surface tension of liquid, N m^{-1}

σ_k, σ_ε	Correction factor in k–ε model equations
χ	Characteristic length of packing, m
Φ	Enhancement factor

Subscripts

G	Gas
i	Coordinates in different directions; component in solution
in	Inlet
L	Liquid
0	Interface
b	Bulk

Distillation is a vapor–liquid separation process widely employed in petrochemical, chemical, and allied industries nowadays. The simulation of distillation has long been investigated since the 1930s of the last century.

There are two basic types of distillation equipment: column with tray structure (tray column) and column with packing (packed column).

For the tray column, the early approach of simulation is based on the concept of equilibrium tray where the thermodynamic equilibrium between liquid and vapor phases is achieved; and it converts to actual tray by means of empirical tray efficiency. The later advance is to use the rate equation to account for the mass transfer instead of using empirical efficiency and equilibrium relationships. These methods are on the overall basis with the assumption that the flow and concentration are uniform on the column tray.

In the 1990s of the last century, the application of CFD to a column tray enables us to calculate the velocity distribution (velocity profile), yet the calculation of concentration distribution is still lacking. Nevertheless, the concentration distribution is even more important and interested by the chemical engineers as it is the deciding factor for predicting the tray efficiency. The recently developed computational mass transfer (CMT) enables us to overcome this insufficiency and provides a rigorous basis for predicting all transport quantities, including the concentration distribution, of a distillation column.

The status of packed column simulation is similar to that of tray column.

The efficiency of distillation process is very important in optimal design and operation as it is closely related to the column size needed and heat energy consumed. The accurate modeling of distillation process enables us to show the non-ideal distribution of concentration as well as the fluid flow, and the designer and operator can take steps to overcome such non-ideality, so as to improve the separation ability of the distillation process.

4.1 Tray Column

The tray column simulation involves mainly the following aspects:

- Velocity distribution to show the deviation from ideal flow: It can be calculated by using CFD as described in Chap. 1;
- Concentration distribution for the calculation of tray efficiency: As stated in Chap. 3, the conventional way of using turbulent Schmidt number Sc_t model for predicting the concentration distribution is not dependable for the reason that the correct Sc_t is not only hard to guess but also it is varying throughout the process. Hence the recently developed $\overline{c'^2} - \varepsilon_{c'}$ two-equation model and the Reynolds mass flux model are recommended to use as described in the subsequent sections.

4.1.1 $\overline{c'^2} - \varepsilon_{c'}$ Two-Equation Model

Interacted liquid-phase form (see Sect. 3.6) of two-equation model is employed in this section for process simulation.

4.1.1.1 Model Equations

1. **The CFD equation set ($k - \varepsilon$ model, see Chap. 1)**

   Overall mass conversation

$$\frac{\partial(\rho_L \beta_L U_{Li})}{\partial x_i} = S_m \tag{1.3a}$$

   Momentum conversation

$$\frac{\partial(\rho_L \beta_L U_{Li} U_{Lj})}{\partial x_i} = -\beta_L \frac{\partial P}{\partial x_j} + \frac{\partial}{\partial x_i}\left[\beta_L \mu_L \left(\frac{\partial U_{Lj}}{\partial x_i}\right) - \beta_L \rho_L \overline{u_i' u_j'}\right] + \beta_L \rho_L S_{Li} \tag{1.4a}$$

$$-\rho_L \overline{u_{Li}' u_{Lj}'} = \mu_{Lt}\left(\frac{\partial U_{Li}}{\partial x_j} + \frac{\partial U_{Lj}}{\partial x_i}\right) - \frac{2}{3}\rho_L \delta_{ij} k_L \tag{1.8}$$

   k_L *equation*

$$\begin{aligned}
\frac{\partial \rho_L \beta_L U_{Li} k_L}{\partial x_i} &= \frac{\partial}{\partial x_i}\left[\beta_L\left(\mu_L + \frac{\mu_{Lt}}{\sigma_k}\right)\frac{\partial k_L}{\partial x_i}\right] \\
&\quad - \mu_{Lt}\beta_L\left(\frac{\partial U_{Li}}{\partial x_j} + \frac{\partial U_{Lj}}{\partial x_i}\right)\frac{\partial U_j}{\partial x_i} - \rho_L \beta_L \varepsilon_L
\end{aligned} \tag{1.11b}$$

ε_L *equation*

$$\frac{\partial \rho_L \beta_L U_{Li} \varepsilon_L}{\partial x_i} = \frac{\partial}{\partial x_i}\left[\beta_L\left(\mu_L + \frac{\mu_{Lt}}{\sigma_\epsilon}\right)\frac{\partial \varepsilon_L}{\partial x_i}\right]$$
$$- C_{\epsilon 1}\beta_L\frac{\varepsilon_L}{k_L}\mu_{Lt}\left(\frac{\partial U_L j}{\partial x_i} + \frac{\partial U_L i}{\partial x_j}\right)\frac{\partial U_L j}{\partial x_i} - C_{\epsilon 2}\beta_L\rho_L\frac{\varepsilon_L^2}{k_L} \tag{1.13a}$$

In foregoing equations, the subscript L denotes the liquid phase.

2. **Heat transfer equation set($\overline{T'^2} - \varepsilon_{T'}$ model, see** Chap. 2):

Energy conservation equation

$$\frac{\partial \rho \beta_L T}{\partial t} + U_{Li}\frac{\partial \rho \beta_L T}{\partial x_i} = \frac{\lambda}{C_p}\beta_L\frac{\partial^2 T}{\partial x_i \partial x_i} + \beta_L\frac{\partial\left(-\rho\overline{u'_{Li}T'}\right)}{\partial x_i} + \rho_L\beta_L S_T \tag{2.3}$$

or written as

$$\frac{\partial \beta_L T}{\partial t} + U_i\frac{\partial \beta_L T}{\partial x_i} = \frac{\lambda}{\rho C_p}\beta_L\frac{\partial^2 T}{\partial x_i \partial x_i} + \beta_L\frac{\partial\left(-\overline{u'_{Li}T'}\right)}{\partial x_i} + \beta_L S_T$$
$$= \alpha\beta_L\frac{\partial^2 T}{\partial x_i \partial x_i} + \beta_L\frac{\partial\left(-\overline{u'_{Li}T'}\right)}{\partial x_i} + \beta_L S_T \tag{2.3a}$$

$$-\overline{u'_{Li}T'} = \alpha_{Lt}\frac{\partial T}{\partial x_i} \tag{2.4}$$

$\overline{T'^2}$ *equation*

$$\frac{\partial \rho_L \beta_L \overline{T'^2}}{\partial t} + \frac{\partial \rho_L \beta_L U_i \overline{T'^2}}{\partial x_i} = \frac{\partial}{\partial x_i}\beta_L\rho_L\frac{\partial \overline{T'^2}}{\partial x_i}\left(\frac{\alpha_{Lt}}{\sigma_{T'}} + \alpha\right)$$
$$- 2\beta_L\rho_L\alpha_{Lt}\frac{\partial T}{\partial x_i}\frac{\partial T}{\partial x_i} - 2\beta_L\rho_L\varepsilon_{T'} \tag{2.7a}$$

$\varepsilon_{T'}$ *equation*

$$\frac{\partial \rho_L \beta_L \varepsilon_{T'}}{\partial t} + \frac{\partial \rho_L \beta_L U_{Li} \varepsilon_{T'}}{\partial x_i} = \frac{\partial}{\partial x_i}\left[\rho_L\beta_L\left(\frac{\alpha_t}{\sigma_{\varepsilon_{T'}}} + \alpha\right)\frac{\partial \varepsilon_{T'}}{\partial x_i}\right]$$
$$- C_{T1}\beta_L\rho_L\frac{\varepsilon_{T'}}{\overline{T'^2}}\overline{u'_i T'}\frac{\partial T}{\partial x_i}$$
$$- C_{T2}\beta_L\rho_L\frac{\varepsilon_{T'}^2}{\overline{T'^2}} - C_{T3}\beta_L\rho_L\frac{\varepsilon_L\varepsilon_{T'}}{k_L} \tag{2.10}$$

α_t *equation*

$$\alpha_{Lt} = C_{T0}k_L\left(\frac{k_L}{\varepsilon_L}\frac{\overline{T'^2}}{\varepsilon_{T'}}\right)^{\frac{1}{2}} \tag{2.6}$$

Model constant are: $C_{T0} = 0.11$, $C_{T1} = 1.8$, $C_{T3} = 2.2$, $C_{T2} = 0.8$, $\sigma_{T'} = 1.0$, $\sigma_{\varepsilon_{T'}} = 1.0$.

If the latent heat of vaporization of the component species in distillation process is approximately equal, the conservation equation of energy (heat) can be omitted and the mathematical model comprises with only CFD and mass transfer equation sets. Otherwise, the heat transfer equation set should be involved.

3. **Mass transfer equation set ($\overline{c'^2} - \varepsilon_{c'}$ model, see Chap. 3):**

Species mass conservation

$$\frac{\partial \beta_L U_{Lj} C}{\partial x_i} = \frac{\partial}{\partial x_i} \beta_L \left(D \frac{\partial C}{\partial x_i} - \overline{u'_{Lj} c'} \right) + \beta_L S_n \tag{3.3}$$

$$\overline{u'_{Lj} c'} = -D_{Lt} \frac{\partial C}{\partial x_j}$$

$\overline{c'^2_L}$ *equation*

$$\frac{\partial \beta_L U_{Li} \overline{c'^2_L}}{\partial x_i} = \frac{\partial}{\partial x_i} \left[\beta_L \left(D + \frac{D_{Lt}}{\sigma_{c'^2}} \right) \frac{\partial \overline{c'^2_L}}{\partial x_i} \right] - 2\beta_L D_{Lt} \left(\frac{\partial C}{\partial x_i} \right)^2 - 2\beta_L \varepsilon_{c'_L} \tag{3.10}$$

$\varepsilon_{Lc'}$ *equation*

$$U_{Li} \beta_L \frac{\partial \varepsilon_{Lc'}}{\partial x_i} = \frac{\partial}{\partial x_i} \beta_L \left[\left(D + \frac{D_{Lt}}{\sigma_{\varepsilon_c}} \right) \frac{\partial \varepsilon_{Lc'}}{\partial x_i} \right] - C_{c1} \beta_L D_t \frac{\varepsilon_{Lc'}}{\overline{c'^2_L}} \left(\frac{\partial C}{\partial x_i} \right)^2$$
$$- C_{c2} \beta_L \frac{\varepsilon^2_{Lc'}}{\overline{c'^2_L}} - C_{c3} \beta_L \frac{\varepsilon_{Lc'} \varepsilon_{Lc'}}{k_L} \tag{3.17}$$

D_{Lt} *equation*

$$D_{Lt} = C_{c0} k_L \left(\frac{k_L \overline{c'^2_L}}{\varepsilon_L \varepsilon_{Lc'}} \right)^{\frac{1}{2}} \tag{3.6}$$

Model constants are as follows: $C_{c0} = 0.14$, $C_{c1} = 1.8$, $C_{c2} = 2.2$, $C_{c3} = 0.8$, $\sigma_{c^2} = 1.0$, $\sigma_{\varepsilon_{c'}} = 1.0$.

In the foregoing equations, the fraction of liquid β_L in the liquid–vapor mixture for tray column can be calculated by the following correlation [1]:

$$\beta_L = \exp \left[-12.55 \left(U_G \sqrt{\frac{\rho_G}{\rho_L - \rho_G}} \right)^{0.91} \right] \tag{4.1}$$

Usually, the net amount of interfacial mass transfer exchange between liquid to vapor and vapor to liquid phases on a tray is small, ρ_L and ρ_G can be considered practically unchanged, so that β_L is substantially constant. It should be noted that
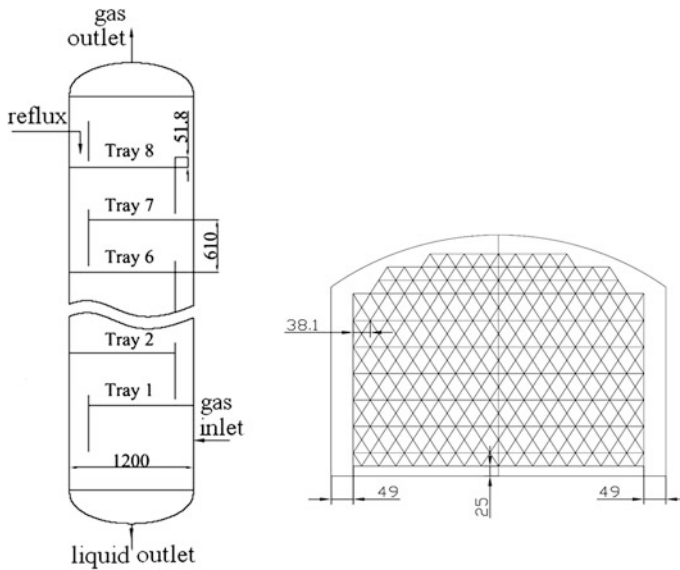
Fig. 4.1 Structure of simulated sieve tray [17]

in the case of packed column, the β_L is varying because the porosity of the packing is non-uniformly distributed, especially in the near-wall region as described in Sect. 4.2.

4.1.1.2 Evaluation of Source Terms

The present simulated object is an industrial-scale sieve tray column of FRI, which is 4 ft in diameter with six sieve trays for (1) separation of n-heptane and methylcyclohexane [2] and (2) stripping of toluene from dilute water solution [3]. They reported the outlet composition and the tray efficiency of each tray under different operating conditions. The details of this column are given in Fig. 4.1 and Table 4.1 [2]. The operating pressure is 165 kPa.

In the numerical computation, the model equations should be firstly discrete into a large number of small finite elements and solved by algebraic method. Thus, the empirical correlations can be applied to the discrete elements under their local conditions, such as velocity, concentration, and temperature obtained in the course of numerical computation. Note that the local conditions should be within the applicable range of the correlation.

Since the latent heat of vaporization and condensation as well as the density of n-heptane and methylcyclohexane is practically equal, the amount of n-heptane transferred from liquid phase to the vapor phase is almost equal to the amount of methylcyclohexane transferred from vapor phase to the liquid phase; thus, no material is accumulated or depleted on the tray, and the liquid density is kept

Table 4.1 Dimension of simulated sieve tray

Item	Value
Column diameter, m	1.2
Tray spacing, mm	610
Hole diameter and spacing, mm × mm	12.7 × 38.1
Outlet weir, (height × length) mm × mm	51 × 940
Clearance under downcomer, mm	38
Downcomer area, m^2	0.14
Effective bubbling area, m^2	0.859
Hole area, m^2	0.118

substantially constant. For this separating system, it can be letting the source term $S_m = 0$.

Sun et al. [4–6] and Li et al. [7] simulated this column using interacted liquid-phase modeling form with the assumption that the liquid density on a simulated single tray is constant, but for the multitray simulation, the density should be changed tray by tray.

The source term S_{Li} in the momentum conservation equation can be calculated by one of the following modes.

(a) Based on superficial vapor velocity: For the *x, y* directions [8]

$$S_{Li} = \frac{\rho_G U_G}{\rho_L h_L} U_{Li}, \quad i = x, y \tag{4.2}$$

where h_L is given by [9]

$$h_L = 0.0419 + 0.189\, h_w - 0.0135\, F_s + 2.45\, L/W$$

For the *z* direction [10]

$$S_{Lz} = \frac{(1 - \beta_L)^3}{U_G^2} g(\rho_L - \rho_G)|U_G - U_L|(U_G - U_{Lz})$$

(b) Based on sieve hole vapor velocity

As the vapor velocity leaving the sieve holes is much higher than the superficial and sometimes even forming jet flow, such influential effect cannot be ignored, especially under the condition of high *F* factor. Referring to Fig. 4.2, the three-dimensional vapor velocities leaving the sieve hole can be expressed as follows [11]:
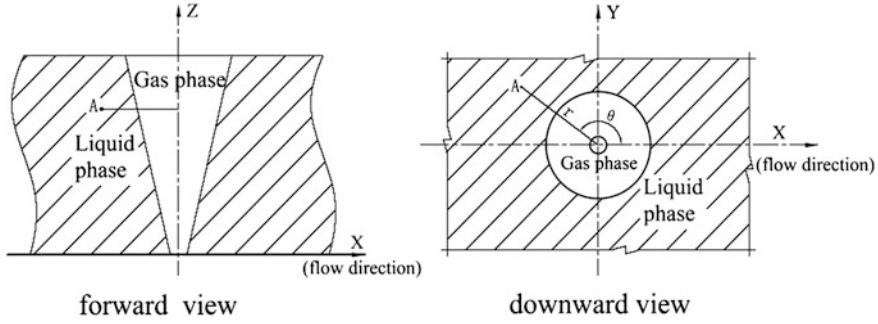
Fig. 4.2 Coordinate of a sieve [17]

$$U_{Gz} = 4.0 \, U_h \frac{D_h}{z} \exp\left[\left(\frac{d}{0.1z}\right)^2\right]$$

$$U_{Gx} = U_{Gr} \cos\theta$$
$$U_{Gy} = U_{Gr} \sin\theta$$

$$U_{Gr} = \frac{1}{4}\sqrt{\frac{3}{\pi}}\sqrt{\frac{M_0}{\rho_G}}\frac{1}{z}\frac{\eta - \eta^3/4}{(1 + \eta^2/4)^2}$$

$$\eta = \sigma\frac{d}{z}$$

where M_0 is the momentum of the gas phase flowing out the sieve hole.

The source term S_{Li} in the momentum equation involves the drag force by the jetting vapor F_{drag} and the resistance F_p created by the liquid–vapor cross-flow. The F_{drag} is given by [12]

$$F_{drag} = C_T\rho_G(U_{Gi} - U_{Li})|U_G - U_L|/h_f \quad i = x, y, z$$

The F_p in the x direction is calculated by [11]

$$F_p = -C_p\rho_L U_x^2/h_f$$

where $C_p = 0.4$; $h_f = \frac{h_L}{\beta_L}$.

The source term S_{Li} is given as follows:

$$S_x = F_{drag} + F_p$$
$$S_j = F_{drag,j} \ (j = y, z)$$

(c) Comparison between two modes

Sun computed the velocity distribution of experimental simulator (Sect. 3.9 for details) by using foregoing two modes to show their difference. The result is shown in Fig. 4.3.
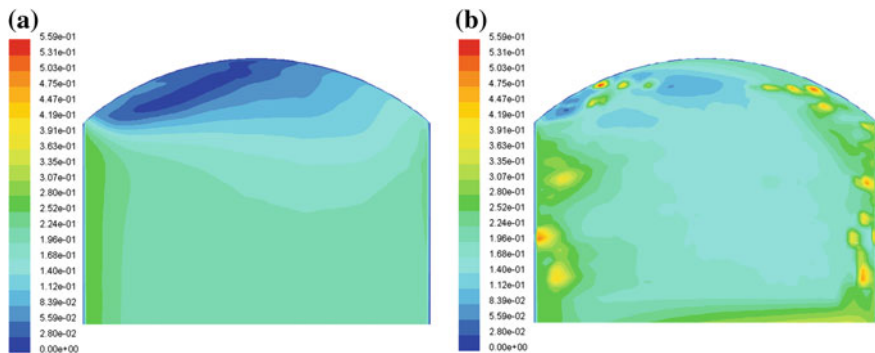
Fig. 4.3 Liquid velocity profiles obtained by using different modes, operation condition: $z = 38$ mm, $F_S = 1.464$ m/s $(kg/m^3)^{0.5}$, $L = 6.94 \times 10^{-3}$ m^3/s **a** based on superficial vapor velocity mode and **b** based on sieve hole vapor velocity [17]

As shown from Fig. 4.3, the velocity in mode A is more uniformly distributed than that in mode B except in the region near the column wall. Moreover, the average velocity in the main flow region of mode B is slightly higher than that in mode A but lower locally near the wall. Computation further reveals that, for a large diameter sieve tray with large number of uniformly distributed sieve holes, the simulated results show no substantial difference by using either mode. In subsequent calculation, mode B is used.

The source term S_n in the species mass conservation equation represents the component species transferred from one phase to the other, which can be calculated by the conventional mass transfer equation:

$$S_n = K_{OL}a(C_L^* - C_L) \tag{4.3}$$

where K_{OL} (m^2 s^{-1}) is the overall mass transfer coefficient; a (m^2 m^{-3}) is the effective interfacial vapor liquid contacting area; C_L^* (kg m^{-3}) is the average liquid mass concentration in equilibrium with the vapor flowing through the tray; K_{OL} can be given by

$$K_{OL} = \frac{1}{\frac{1}{k_L} + \frac{1}{mk_G}} \tag{4.4}$$

where k_L and k_G are the film coefficients of mass transfer on liquid side and gas (vapor) side, respectively, and m is the coefficient of distribution between two phases, which is conventionally called Henry's constant. The value of m is dependent on the concentration of the species concerned. If the concentration change on a tray is not large, the value of m might be taken at the average concentration. However, for the simulation of a multitray column, where the change of concentration in the column is appreciable, the value of m should be redetermined for each tray. The k_L, k_G, and a can be calculated by the empirical equation given by Zuiderweg [13]:

Fig. 4.4 Diagram of
boundary conditions [16]
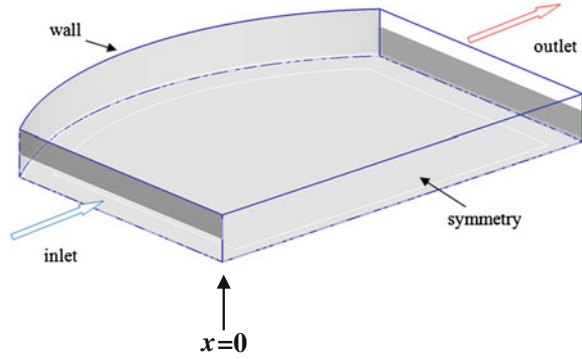
$$k_G = \frac{0.13}{\rho_G} - \frac{0.065}{\rho_G{}^2} \quad (1.0 < \rho_G < 80 \, \text{kg/m}^3) \tag{4.5}$$

$$k_L = \left(\frac{1}{0.37} - 1\right) m k_G \tag{4.6}$$

The effective vapor–liquid interfacial area a is calculated by $a = \frac{a'}{h_f}$, where h_f is the height of liquid level, a' is given by [13]:

$$a' = \frac{43}{F^{0.3}} \left(\frac{F_{bba}^2 h_L FP}{\sigma}\right)^{0.53}$$

where F_{bba} is the F factor based on the vapor velocity passing through the bubbling area; $h_L = 0.6 h_w^{0.5} p^{0.25} b^{-0.25} (FP)^{0.25}$ $\quad (25 \, \text{mm} < h_w < 100 \, \text{mm})$, $FP = \frac{U_L}{U_G}\left(\frac{\rho_L}{\rho_G}\right)^{0.5}$, b is the weir length per unit bubbling area (Fig. 4.4).

4.1.1.3 Boundary Conditions

Inlet (inlet weir, $x = 0$): The liquid velocity and concentration are considered as uniformly distributed, so that $U_L = U_{L,\text{in}}$, $C = C_{\text{in}}$.

For the k–ε equations, the conventional boundary conditions are adopted [14]: $k_{\text{in}} = 0.003 U_{x,\text{in}}^2$ and $\varepsilon_{\text{in}} = 0.09 k_{\text{in}}^{3/2} / \left(0.03 \times \frac{W}{2}\right)$.

The inlet conditions of $\overline{c'^2} - \varepsilon_{c'}$ equations, as presented by Sun et al. [4], are

$$\overline{c_{L,\text{in}}'^2} = [0.082 \cdot (C^* - C_{\text{in}})]^2$$

$$\varepsilon_{Lc',\,in} = 0.9 \left(\frac{\varepsilon_{L,\text{in}}}{k_{L,\text{in}}}\right) \overline{c'^2}_{\text{in}}$$

Outlet (outlet weir overflow): We let $\frac{\partial C}{\partial x} = 0$.

Solid border (tray floor, inlet weir wall, outlet weir wall, and column wall): The boundary conditions for the mass flux are equal to zero. The wall surface is considered to be no-slip of liquid flow.

Interface of the vapor and liquid: We set $\frac{\partial U_x}{\partial z} = 0$, $\frac{\partial U_y}{\partial z} = 0$, and $U_z = 0$.

4.1.1.4 Simulated Results and Verification (I): Separation of *n*-Heptane and Methylcyclohexane

The model equations were solved numerically by using the commercial software FLUENT 6.2 with finite volume method. The SIMPLEC algorithm was used to solve the pressure–velocity coupling problem in the momentum equations. The second-order upwind spatial discretization scheme was employed for all differential equations.

As samples of the computed results, Fig. 4.5a, b show, respectively, the computed concentration distribution on tray 8 and tray 6. Unfortunately, no experimental data on the concentration field of the tray are available in the literature for the comparison. However, we may compare indirectly by means of the outlet concentration of each tray.

From the concentration distribution on a tray as shown in Fig. 4.5a, b, the outlet composition of each tray can be obtained as shown in Fig. 4.6a and also compared with the experimental data.

As shown from Fig. 4.6a, the computed outlet concentration of each tray is in good agreement with the experimental measurement except for the tray 4. As we understand, for the total reflux operation, the outlet concentration should form a smooth curve on the plot. The deviation on tray 4 is obvious and likely to be due to experimental error or some other unknown reasons. The average deviation of the outlet composition is 3.77 %.

Another way of comparison is by means of individual tray efficiency. The common expression of tray efficiency is the gas-phase Murphree efficiency which is defined by

$$E_{\text{MV}} = \frac{y_n - y_{n+1}}{y_n^* - y_{n+1}} \tag{4.7}$$

where y_n^* is the species concentration (mole fraction) of gas phase in equilibrium with the liquid-phase concentration x_n (mole fraction); y_n and y_{n+1} are, respectively, the gas concentration in mole fraction leaving and entering the tray. The comparison between simulated results and experimental data is shown in Fig. 4.6b, in which disagreement in tray numbers 3 and 4 reveals the experimental error in the outlet concentration from tray 4 because the tray efficiency cannot be as high as 150 % for tray 3 and as low as 20 % for tray 4.

The overall tray efficiency of all trays in the column is commonly used for distillation column evaluation in order to reduce the error of individual tray efficiency. Figure 4.7 shows the simulated overall tray efficiency versus experiment
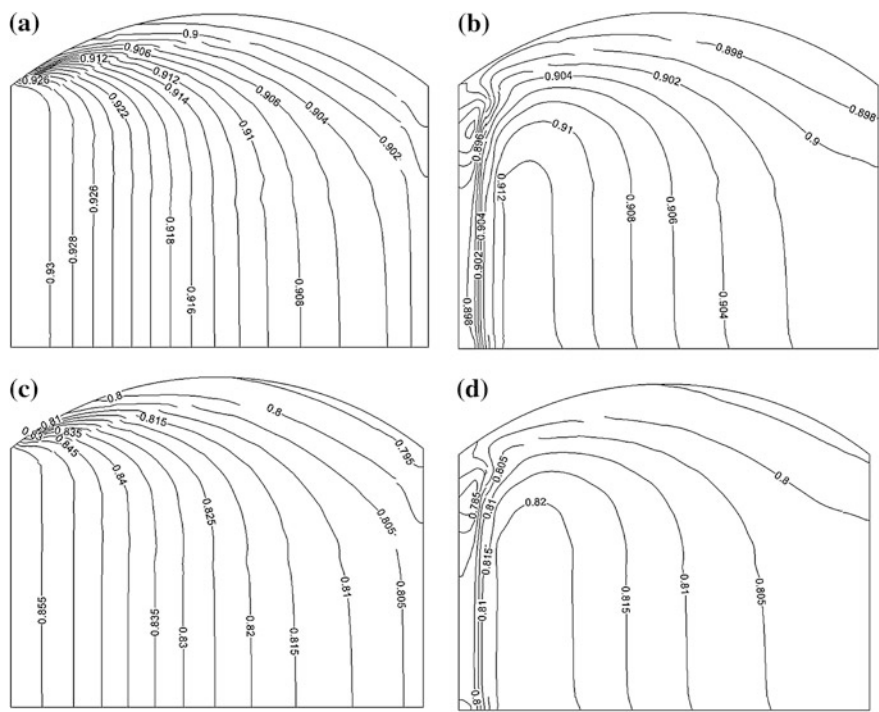
Fig. 4.5 C_6 concentration distribution on trays [17] **a** at 20 mm above the floor of tray number 8, **b** 70 mm above the floor of tray number 8, **c** at 20 mm above the floor of tray number 6, and **d** 70 mm above the floor of tray number 6
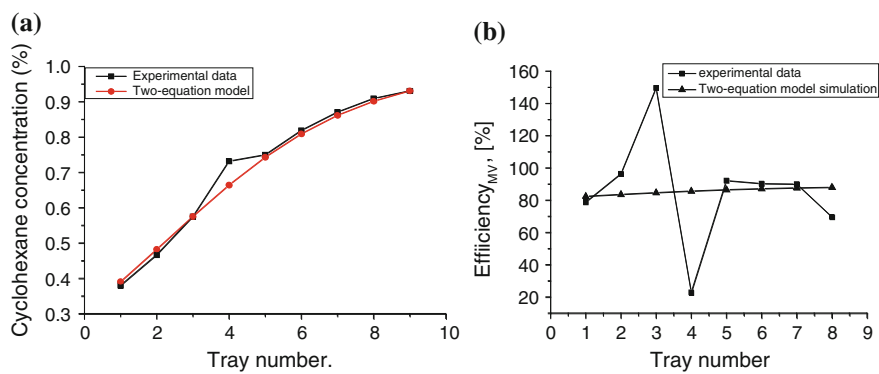
Fig. 4.6 Simulation results and experimental data **a** outlet concentration and **b** Murphree tray efficiency (reprinted from Ref. [4], Copyright 2005, with permission from American Chemical Society)
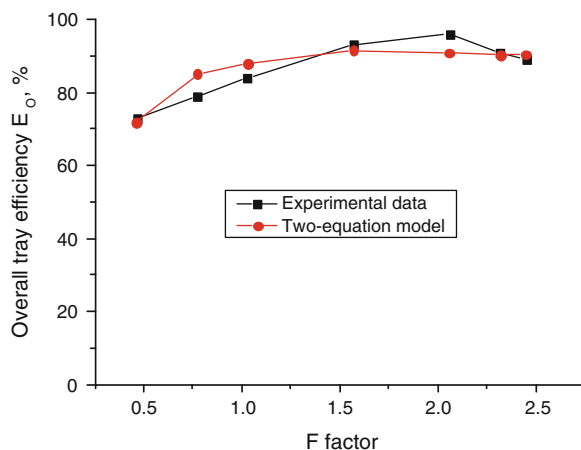
measurement under different vapor rates expressed as F factor $\left(F = U_{\mathrm{G}}\sqrt{\rho_{\mathrm{G}}}\right)$. The simulation can be seen to be confirmed.

A feature of CMT is able to predict the liquid turbulent mass diffusivity D_{t}, which is commonly regarded as representing the extent of back-mixing (non-ideal flow), and thus, it is an influential factor to the tray efficiency. Figure 4.8 displays the distribution of D_{Lt} on tray number 8 at the depth z of 50 and 100 mm, respectively, apart from tray floor. As shown from the figure, the D_{Lt} is non-uniformly distributed, which reflexes the effectiveness or efficiency of mass transfer is varying with position on a tray.

The volume average of D_{Lt} calculated is compared with experimental data reported by Cai and Chen [15] for the same tray column under different vapor rates (F factor) as shown in Fig. 4.9. Although the experimental measurement is performed by using inert tracer technique and the comparison is only approximate, it demonstrates that the prediction of D_{Lt} is feasible by using the method of CMT without doing tedious experimental work.

4.1.1.5 Simulated Results and Verification (II): Stripping of Toluene from Dilute Water Solution

Kunesh et al. [3] reported the experimental data for the column as shown in Fig. 4.1 for the stripping of toluene from dilute water solution. They gave the outlet composition and the tray efficiency of each tray under different operating conditions.

Sun et al. [6] simulated the outlet concentration of each tray, expressed in area-weighted average, versus tray number for a typical run 16552 is shown in Fig. 4.10 and compared with the experimental data. According to the Fenske–Underwood equation under constant relative volatility and low concentration, a plot of logarithmic concentration versus tray number should yield a straight line. In Fig. 4.10,
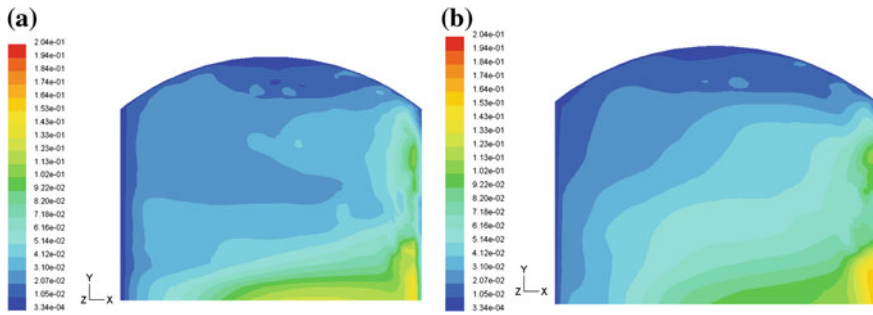
Fig. 4.8 Distribution of liquid turbulent mass diffusivity on tray number 8, **a** tray number 8, 50 mm above tray floor, $p = 165$ kPa, $L = 30.66$ m^3/h and **b** tray number 8, 100 mm above tray floor $p = 165$ kPa, $L = 30.66$ m^3/h [17]

Fig. 4.9 Simulated turbulent mass diffusivity and experimental data [17]
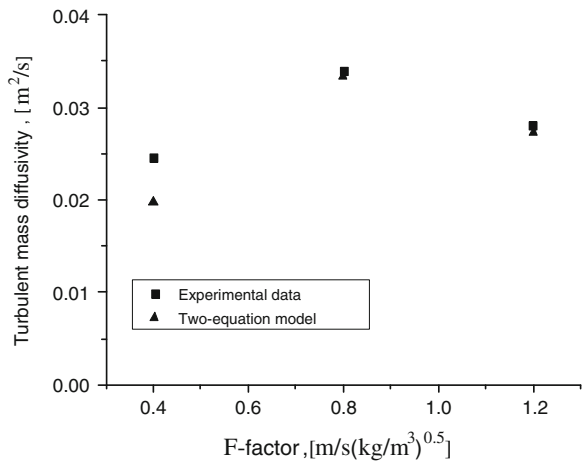
both simulated and experimental points are shown closely to a line with agreement each other. The conventional method of assuming constant turbulent Schmidt number, Sc_t, for instance equal to 0.7, is also shown in Fig. 4.10, and the deviation of arbitrary assuming a constant Sc_t can be clearly seen.

The simulated concentration distribution on a sieve tray is given in Fig. 4.11, in which the stripping action on the tray can be seen to be unevenly progressed.

Based on the simulated concentration distribution as shown in Fig. 4.11, the local tray efficiencies can be obtained. The simulated tray efficiency by area average for run 16552 is 33.4 % in comparison with the experimental value of 36 %. More simulated tray efficiencies at different mV/L are compared with the experimental measurements as shown in Fig. 4.12, in which reasonable agreement can be seen between them.

As another example of illustration, the simulated distribution of D_{Lt} across the tray for run 16552 is shown in Fig. 4.13. The diverse distribution of D_{Lt} is chiefly

Fig. 4.10 Simulated outlet concentration and experimental measurement, run 16552 $Q_L = 76.3$ m^3/h, $F_s = 1.8$ (m/s) (kg/m^3)$^{0.5}$ (reprinted from Ref. [6], Copyright 2011, with permission from Elsevier)
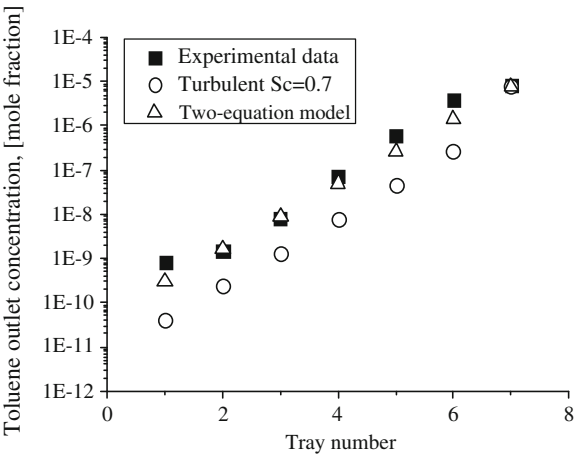
Fig. 4.11 Simulated concentration distribution, tray 6, run 16552 $Q_L = 76.3$ m^3/h, $Fs = 1.8$ (m/s) (kg/m^3)$^{0.5}$ 20 mm above tray floor (reprinted from Ref. [6], Copyright 2011, with permission from Elsevier)
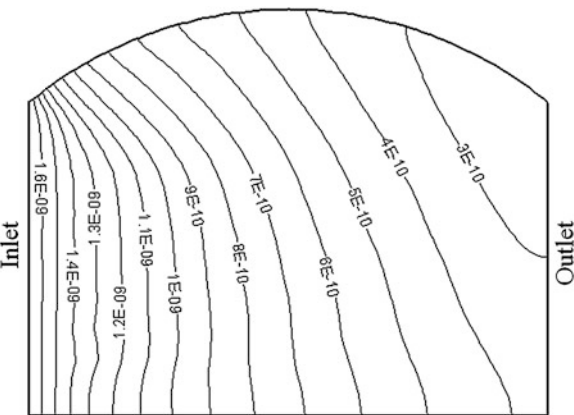
Fig. 4.12 Simulated and experimental tray efficiency under different $m\frac{V}{L}$ $Q_L = 76.3$ m^3/h, $Fs = 1.8$ (m/s) (kg/m^3)$^{0.5}$ (reprinted from Ref. [6], Copyright 2011, with permission from Elsevier)
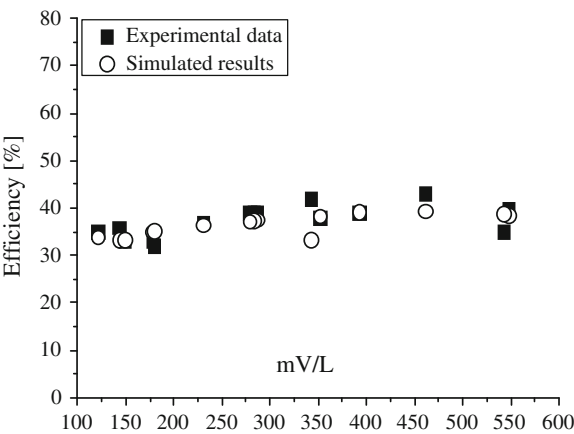
Fig. 4.13 Distribution of
turbulent mass transfer
diffusivity, tray 6, run 16552
$Q_L = 76.3$ m^3/h,
$Fs = 1.8$ (m/s) (kg/m^3)$^{0.5}$
20 mm above tray floor
(reprinted from Ref. [6],
Copyright 2011, with
permission from Elsevier)
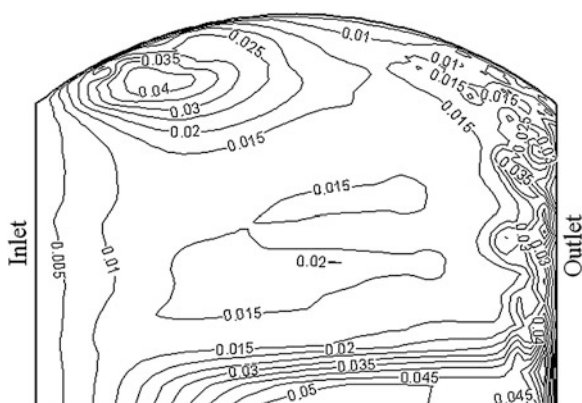
due to the complicated non-uniform flow and concentration distributions on the
tray. In practice, the mass transfer diffusivity is expressed macroscopically by the
volume average. For instance, the predicted volume average values of D_{Lt} for three
runs under different operations are 0.035, 0.030, and 0.021 m^2/s, respectively,
which are within the reasonable range reported by Cai and Chen [15].

4.1.1.6 Prediction of Tray Efficiency for Different Tray Structures

By means of the simulated concentration distribution on a tray, the influence of
tray structure on the tray efficiency can be calculated. Sun et al. [6] simulated
foregoing sieve tray distillation column as shown in Sect. 4.1.1.3 for separating
cyclohexane (C_6) and n-heptane (n-C_7) mixture with different tray structures,
including sieve hole arrangement and heights of inlet weir and outlet weir. As an
example of illustration, the tray efficiency with different heights of outlet weir is
predicted and compared each other. The simulated concentration distributions on
the same sieve tray with different outlet weir heights h_w are shown in Fig. 4.14.

The inlet concentration of C_6 to both trays was 0.482 in mole fraction; the
simulated outlet concentrations for outlet weir height h_w equal to 20 and 100 mm
were found to be 0.393 and 0.383, respectively. Higher outlet concentration of C_6
on the $h_w = 100$ tray may be due to deeper liquid layer resulting more interacting
area and time between vapor and liquid and therefore enhance the mass transfer.
The corresponding Murphree tray efficiencies obtained were 86.7 and 89.5 % for
h_w equal to 20 and 100 mm, respectively. The simulated D_{Lt} for both cases are
shown in Fig. 4.15, in which different profiles can be clearly seen. However, such
simulated results do not mean that higher outlet weir is a good choice, as the
higher tray efficiency achieved is on the expense of higher pressure drop which
means to require more energy of operation. However, it demonstrates that the
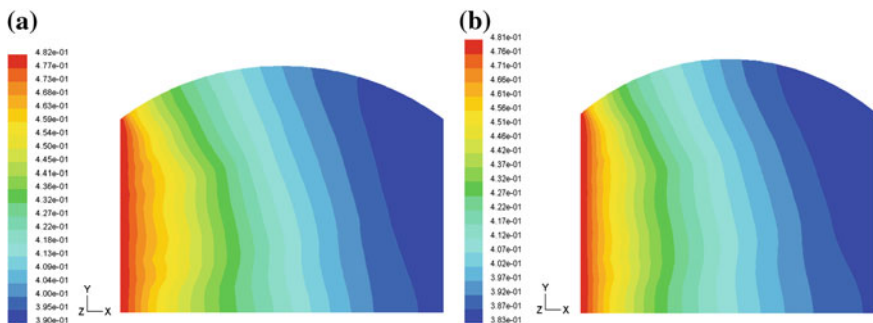
Fig. 4.14 Simulated concentration profile of a sieve trays number 1 at different outlet weir heights h_w $x_{in} = 0.482$ $Q_L = 30.66$ m^3 h^{-1}, $G = 5.75$ Kgs^1, $P = 165$ kPa total reflux 20 mm above tray floor **a** $h_w = 20$ mm and **b** $h_w = 100$ mm (reprinted from Ref. [6], Copyright 2011, with permission from Elsevier)
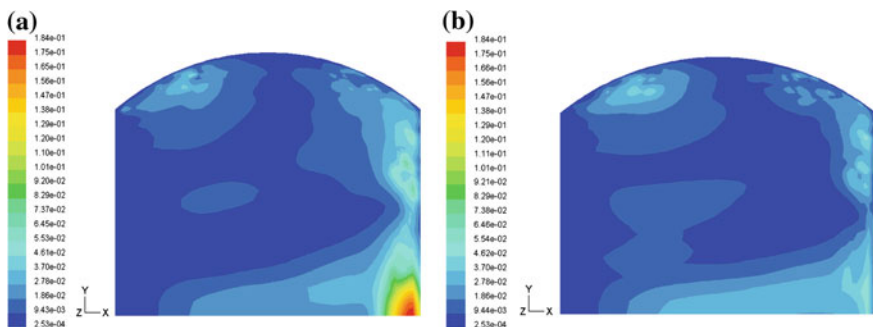
Fig. 4.15 Simulated turbulent mass transfer diffusivity profile of sieve trays number 1 $x_{in} = 0.482$, $Q = 30.66$ m^3 h^{-1}, $P = 165$ kPa, total reflux, 20 mm above tray floor **a** $h_w = 20$ mm and **b** $h_w = 100$ mm (reprinted from Ref. [6], Copyright 2011, with permission from Elsevier)

application of CMT to evaluate the mass transfer efficiency of different tray structures is feasible, which is helpful in designing new column and assessing existing column.

4.1.2 Reynolds Mass Flux Model

The interacted liquid-phase modeling form is employed for present simulation. The simplified assumptions of constant liquid fraction β_L and density ρ_L on a tray are applied.

4.1.2.1 Standard Reynolds Mass Flux Model

Model equations

1. The CFD equation set (k-ε model)

   Overall mass conversation

   $$\frac{\partial(\rho_L \beta_L U_{Li})}{\partial x_i} = S_m \tag{1.3}$$

   Momentum conversation

   $$\frac{\partial\left(\rho_L \beta_L U_{Li} U_{Lj}\right)}{\partial x_i} = -\beta_L \frac{\partial P}{\partial x_j} + \frac{\partial}{\partial x_i}\left[\beta_L \mu_L \left(\frac{\partial U_{Lj}}{\partial x_i}\right) - \beta_L \rho_L \overline{u'_{Li} u'_{Lj}}\right] + S_{Li} \tag{1.4}$$

   where $\overline{u'_{Li} u'_{Lj}}$ is given by

   $$
   \begin{aligned}
   \frac{\partial \rho \beta_L \overline{u'_{Li} u'_{Lj}}}{\partial t} + U_{Lk}\frac{\partial \rho_L \overline{\beta_L u'_{Li} u'_{Lj}}}{\partial x_k} = & \frac{\partial}{\partial x_k}\left(\rho\beta_L C_k \frac{k_L^2}{\varepsilon}\frac{\partial \overline{u'_{Li} u'_{Lj}}}{\partial x_k} + \mu_L \frac{\partial \overline{u'_{Li} u'_{Lj}}}{\partial x_k}\right) \\
   & - \rho_L \beta_L \left(\overline{u'_{Li} u'_{Lk}}\frac{\partial U_{Lj}}{\partial x_k} + \overline{u'_{Lj} u'_{Lk}}\frac{\partial U_{Li}}{\partial x_k}\right) \\
   & - C_1 \rho_L \beta_L \frac{\varepsilon_L}{k_L}\left(\overline{u'_{Li} u'_{Lj}} - \frac{2}{3} k_L \delta_{ij}\right) \\
   & - C'_2 \rho_L \beta_L \left(\overline{u'_{Li} u'_{Lk}}\frac{\partial U_{Lj}}{\partial x_k} + \overline{u'_{Lj} u'_{Lk}}\frac{\partial U_{Li}}{\partial x_k} - \frac{2}{3}\delta_{ij}\overrightarrow{u'_{Li} u'_{Lj}}\frac{\partial U_{Li}}{\partial x_j}\right) \\
   & - \frac{2}{3}\rho_L \beta_L \varepsilon_L \delta_{ij}
   \end{aligned}
   \tag{1.23}
   $$

   where the constants are as follows: $C_k = 0.09$, $C_1 = 2.3$, $C'_2 = 0.4$ [10].

2. The mass transfer equation set (Reynolds mass flux model)

   Species mass conservation

   $$\frac{\partial \beta_L U_{Lj} C}{\partial x_i} = \frac{\partial}{\partial x_i}\beta_L\left(D_L \frac{\partial C}{\partial x_i} - \overline{u'_{Lj} c'}\right) + S_n \tag{3.3}$$

   Fluctuating mass flux $\overline{u'_i c'}$

   $$
   \begin{aligned}
   \frac{\partial \overline{\beta_L u'_{Li} c'}}{\partial t} + \frac{\partial \beta_L U_j \overline{u'_{Li} c'}}{\partial x_j} = & \frac{\partial}{\partial x_j}\left[\left(C_{c1}\rho_L \beta_L \frac{k_L^2}{\varepsilon_L} + \frac{\mu_L}{\rho_L}\right)\frac{\partial \overline{u'_{Li} c'}}{\partial x_j}\right] - \left(\overline{u'_i u'_j}\frac{\partial C}{\partial x_j}\right) \\
   & - C_{c2}\beta_L \frac{\varepsilon}{k}\overline{u'_{Li} c'} + C_{c3}\beta_L \overline{u'_{Lj} c'}\frac{\partial U_{Li}}{\partial x_j}
   \end{aligned}
   \tag{3.25a}
   $$

   where the constants are as follows: $C_{c1} = 0.09$, $C_{c2} = 3.2$, $C_{c3} = 0.55$.

Auxiliary equations
k_L equation

$$\frac{\partial \rho \beta_L U_{Li} k_L}{\partial x_i} = \frac{\partial}{\partial x_i}\left[\beta_L\left(\mu_L + \frac{\mu_{Lt}}{\sigma_k}\right)\frac{\partial k_L}{\partial x_i}\right]$$
$$- \mu_{Lt}\beta_L\left(\frac{\partial U_{Li}}{\partial x_j} + \frac{\partial U_{Lj}}{\partial x_i}\right)\frac{\partial U_{Lj}}{\partial x_i} - \rho_L\beta_L\varepsilon_L \tag{1.11a}$$

ε_L equation

$$\frac{\partial \rho_L \beta_L U_{Li}\varepsilon_L}{\partial x_i} = \frac{\partial}{\partial x_i}\left[\beta_L\left(\mu_L + \frac{\mu_{Lt}}{\sigma_{L\epsilon}}\right)\frac{\partial \varepsilon_L}{\partial x_i}\right]$$
$$- C_{\epsilon 1}\beta_L\frac{\varepsilon}{k}\mu_{Lt}\left(\frac{\partial U_{Lj}}{\partial x_i} + \frac{\partial U_{Li}}{\partial x_j}\right)\frac{\partial U_{Lj}}{\partial x_i} - C_{\epsilon 2}\beta_L\rho_L\frac{\varepsilon_L^2}{k_L} \tag{1.13a}$$

The boundary conditions are the same as given in Sect. 4.1.1.3.

Verification of simulated result and comparison

The simulated column tray is shown in Sect. 4.1.1.1 for separating *n*-heptane and methylcyclohexane. Li et al. [7] and Li [16] simulated the concentration profiles for all trays at different levels from the tray floor, among which the tray numbers 8 and 6 are shown in Fig. 4.16a, b, respectively.

4.1.2.2 Hybrid Reynolds Mass Flux Model

The model equations are the same as the standard Reynolds mass flux model except that the $\overline{u'_{Li}u'_{Lj}}$ term is simplified by using Eq. (1.8) as follows:

$$-\rho\overline{u'_{Li}u'_{Lj}} = \mu_{Lt}\left(\frac{\partial U_{Li}}{\partial x_j} + \frac{\partial U_{Lj}}{\partial x_i}\right) - \frac{2}{3}\rho_L\delta_{ij}k_L \tag{1.8}$$

The hybrid Reynolds mass flux model and algebraic Reynolds mass flux model, which only need to solve simpler Eq. (1.8) instead of complicated Eq. (1.23), may be a proper choice for multiple tray computation if their simulated results are very close to the standard Reynolds mass flux model. For comparison, the simulated column trays in Sect. 4.1.1.1 for separating *n*-heptane and methylcyclohexane are used. Li [17] simulated concentration profiles of all trays at different levels above the tray floor, among which the tray number 8 and tray number 6 are shown in Fig. 4.17a and b.

It is found that by comparing Figs. 4.16a versus 4.17a and Figs. 4.6b versus 4.17b, the simulated results between standard and hybrid Reynolds mass flux models are practically the same except at the very small region near the end of the inlet weir and the neighboring segmental wall. Such difference is coming from the fact that the standard mass flux model is anisotropic enabling to give more precise three-dimensional flow and mass transfer simulation, while the hybrid Reynolds
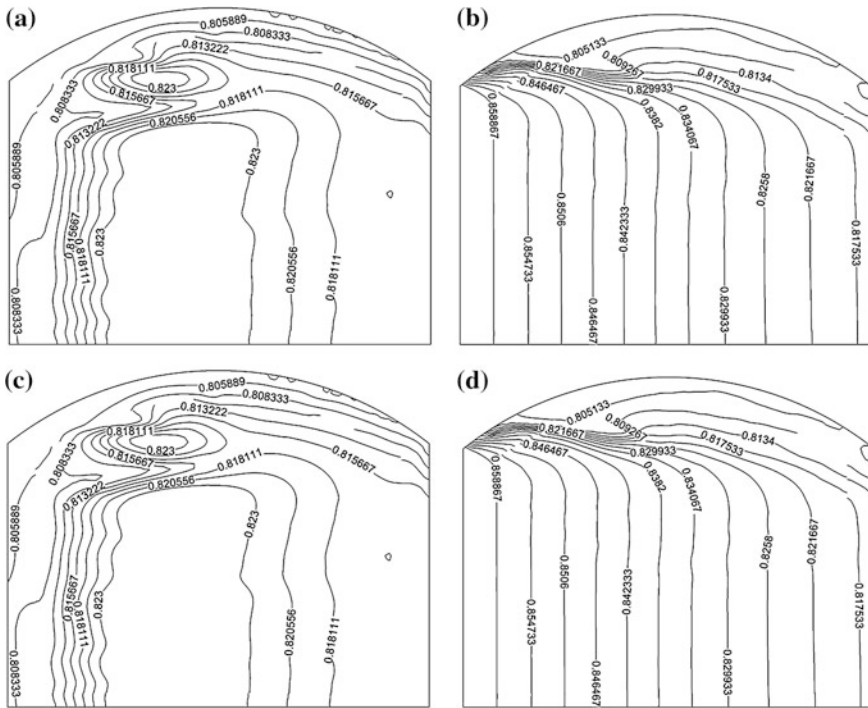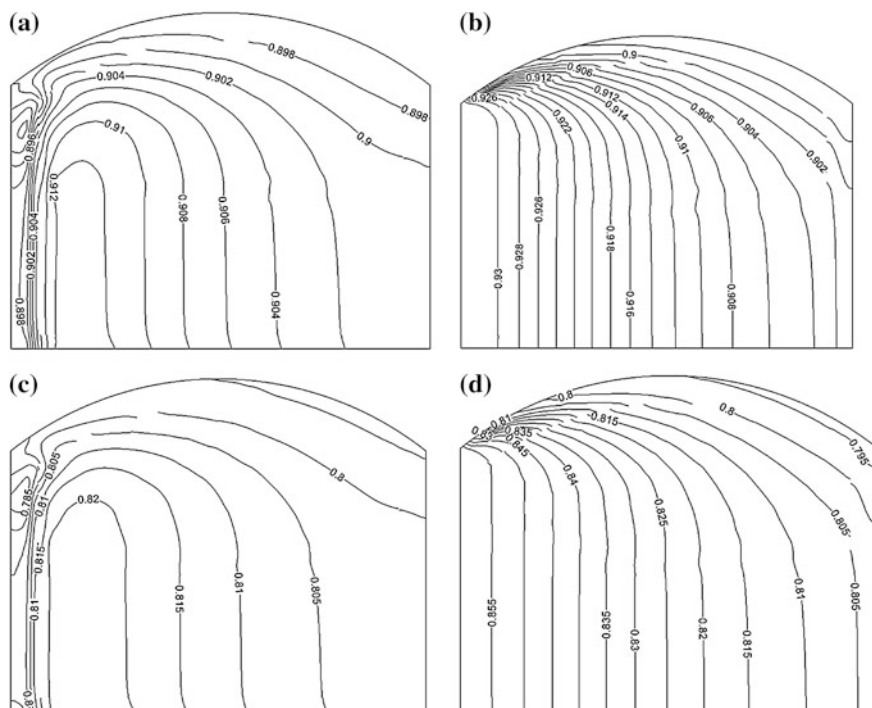
Fig. 4.16 Concentration contour of *x–y* plan on trays by standard Reynolds mass flux model, **a** 20 mm above tray floor of tray number 8, **b** 70 mm above tray floor of tray number 8, **c** 20 mm above tray floor of tray number 6, and **d** 70 mm above tray floor of tray number 6 [16]

mass flux model is isotropic and cannot show the detailed three-dimensional behaviors in that region. However, if overlooking the difference in this small region, it indicates that the hybrid Reynolds mass flux model can be used for overall simulation instead of using the complicated standard Reynolds mass flux model for the simulation of all trays in a multitray column with less computer work.

The simulated result by using hybrid Reynolds mass flux model can also compared with that obtained by using two-equation model as shown in Fig. 4.17, in which the agreement between them can be seen except in the region near inlet weir and column wall where the hybrid Reynolds mass flux model gives more detailed concentration distribution than the two-equation model.

The verification of hybrid Reynolds mass flux model can also be made by comparing with the experimental outlet concentration of each tray as shown in Figs. 4.18 and 4.19, in which the result by using two-equation model is also presented. It can be seen that the hybrid Reynolds mass flux model gives closer outlet concentration to the experimental measurement than the two-equation model, although both of them are considered to be verified by experiment.

Fig. 4.17 Concentration contour of x–y plan on trays by hybrid Reynolds mass flux model, **a** 20 mm above tray floor of tray number 8, **b** 70 mm above tray floor of tray number 8, **c** 20 mm above tray floor of tray number 6, and **d** 70 mm above tray floor of tray number 6 [16]
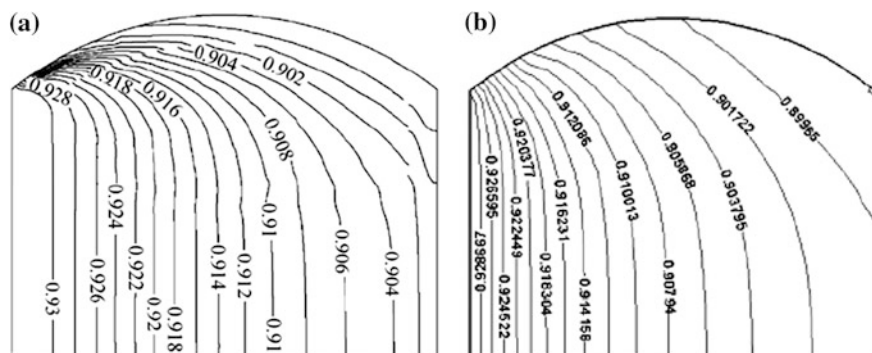
Fig. 4.18 Comparison between hybrid Reynolds mass flux model and two-equation model by simulated concentration contours of 20 mm above tray floor on tray number 8. **a** Hybrid Reynolds mass flux model (reprinted from Ref. [7], Copyright 2011, with permission from Elsevier) and **b** $\overline{c'^2} - \varepsilon_{c'}$ two-equation model (reprinted from Ref. [4], Copyright 2005, with permission from American Chemical Society)
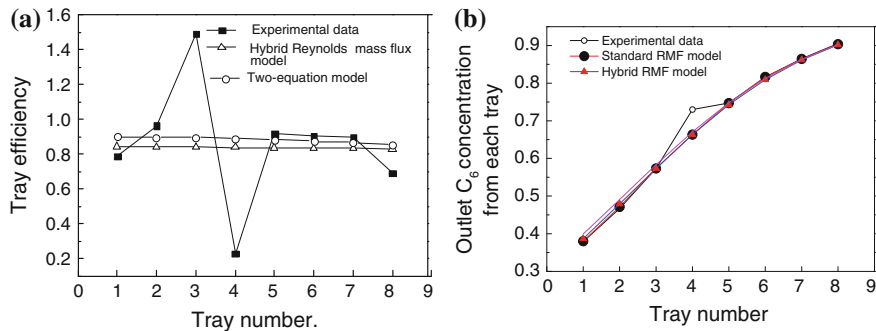
Fig. 4.19 a Comparisons of simulated results by different models with experimental data [16] tray efficiency and outlet C_6 concentration. **b** Comparisons of the outlet C_6 concentration between standard and hybrid Reynolds mass flux model simulations and experimental data [16]

The verifications of simulated Murphree tray efficiencies by using hybrid Reynolds mass flux models and two-equation model can also be checked by comparing with experimental data as shown in Fig. 4.19a. The comparison of outlet C_6 from each tray between standard and hybrid Reynolds mass flux models is given in Fig. 4.19b, in which the agreement between them can be seen.

Generally speaking, the overall simulated result of a distillation tray column by using two-equation model and different Reynolds mass flux models is very close each other and checked with experimental measurements, but if detailed mass transfer and flow information on the trays are needed, the standard Reynolds mass flux model is the better choice.

Reynolds mass flux

In this section for convenience, the fluctuating mass flux $\overline{u'_{Li}c'}$, which is the negative Reynolds mass flux $-\overline{u'_{Li}c'}$, is used for illustration instead of using Reynolds mass flux.

In the course of solving the model equation, the fluctuating mass flux $\overline{u'_x c'}$, $\overline{u'_y c'}$, $\overline{u'_z c'}$ can be obtained simultaneously [16]. The radial distributions of them at different axial positions of tray 8 are given in Fig. 4.20a. The sum of fluctuating mass flux in all directions, $\overline{u'_{Li}c'} = \overline{u'_x c'} + \overline{u'_y c'} + \overline{u'_z c'}$, is shown in Fig. 4.20b.

As shown in Fig. 4.20b, the fluctuating mass flux $\overline{u'_x c'}$ is greater near the inlet weir region ($x = 0.2$) than that around the outlet weir region ($x = 0.6$) because c as well as c' is decreased with x (main flow) direction in distillation process. In the r direction, which is perpendicular to the main flow, all the $\overline{u'_x c'}$, $\overline{u'_y c'}$, and $\overline{u'_z c'}$ contours are almost unchanged up to about $0.3r$, then slightly increasing until about $r = 0.45r$ reaching the maximum. This tendency is shown in Fig. 4.19b, c, and d. Such maximum point indicates the appearance of greatest mass flux transport as well as turbulent diffusion and vortical mixing there due to the impact with the reversed flow (large-scale vortex) created in the segmental region of the

(a)

(b)

(c)

(d)

(e)

x axial distance from the inlet weir
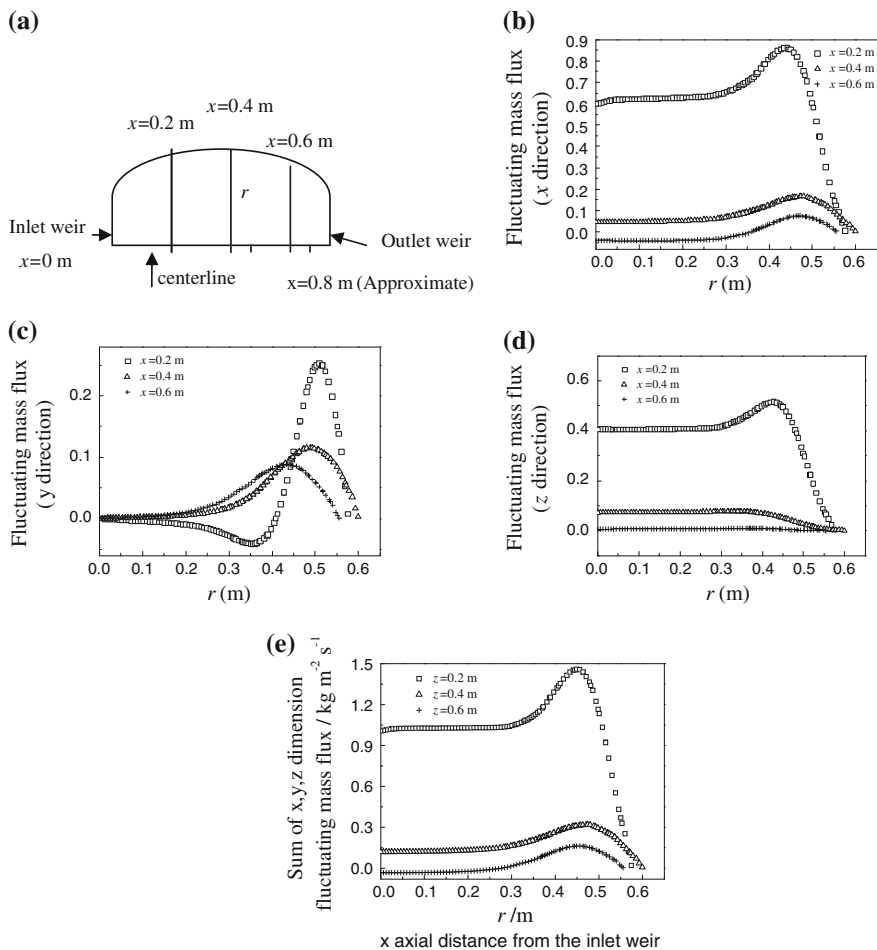
Fig. 4.20 Simulation results of fluctuating mass flux on tray number 8 by standard Rayleigh mass flux model [16] **a** the tray for simulation, **b** x direction (*main flow*), **c** r direction (*perpendicular to main flow*), **d** z direction (*depth*), and **e** profiles of $\overline{u'_{Li}c'} = \overline{u'_x c'} + \overline{u'_y c'} + \overline{u'_z c'}$ at different axial distances of tray

column. Such simulated result is consistent with many experimental works that the reversed flow was observed around this region. In Figs. 4.20 and 4.19b, the $\overline{u'_i c'}$ and $\overline{u'_x c'}$ contours along r (radial) direction showing almost zero gradient from $r = 0$ to about 0.3 indicates that the turbulent (fluctuating) mass flux flow remains constant, i.e., the turbulent effect is kept steady in this region (see Sect. 3.6.1.3). However, the foregoing-mentioned variation of concentration is very small and cannot be found clearly in the profile of concentration contour.
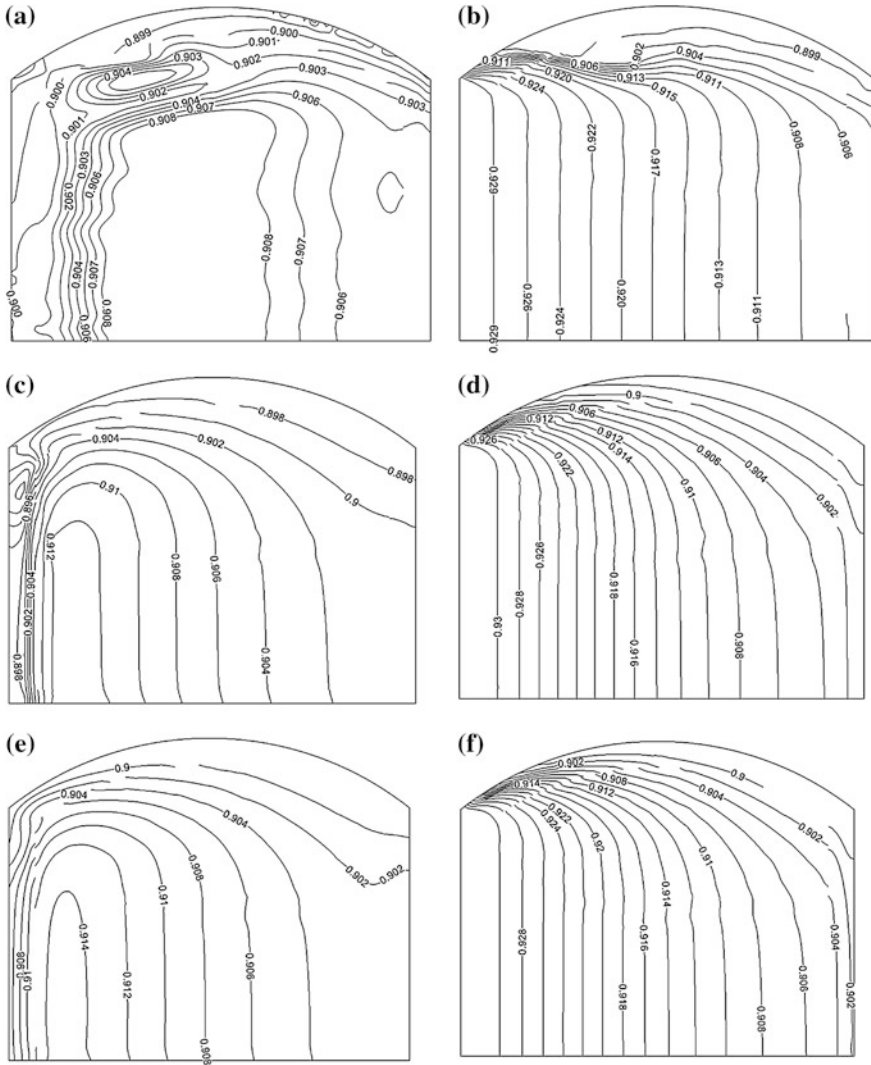
Fig. 4.21 Simulated results of the C_6 concentration profiles of the x–y plane on tray number 8 simulated by different Reynolds flux models for $F = 2.44$ m s^{-1} (kg m^3)$^{0.5}$ [16]. **a** Standard Reynolds mass flux model at 70 mm above the tray floor, **b** standard Reynolds mass flux model at 20 mm above the tray floor, **c** hybrid Reynolds mass flux model at 70 mm above the tray floor, **d** hybrid Reynolds mass flux model at 20 mm above the tray floor, **e** algebraic Reynolds mass flux model at 70 mm above the tray floor, and **f** algebraic Reynolds mass flux model at 20 mm above the tray floor

4.1.2.3 Algebraic Reynolds Mass Flux Model

The hybrid Reynolds mass flux model can be further reducing the complexity of model equations by setting the convection term on the left side of Eq. (3.26a) equal to the turbulent and molecular diffusions term on the right side under steady condition to obtain Eq. (3.27) as shown below.

$$\overline{u_i'c'} = -\frac{k}{C_{c2}\gamma\beta_{L}\varepsilon}\left(\overline{u_i'u_j'}\frac{\partial C}{\partial x_j} + \overline{u_i'c'}\frac{\partial U_i}{\partial x_j}\right) + \frac{C_{c3}k}{C_{c2}\varepsilon}\overline{u_i'c'}\frac{\partial U_i}{\partial x_j} \qquad (3.27)$$

The algebraic Reynolds mass flux model is using Eq. (3.27) to replace Eq. (3.26a); all other model equations are the same as the hybrid Reynolds mass flux model.

To testify this model, Li [16] simulated the sieve tray column as mentioned in Sect. 4.1.1.1. The concentration profile on tray number 8 are simulated and compared with the simulated results by using different Reynolds mass flux models as shown in Fig. 4.21, from which it can be seen that the standard give more detailed information than the other two simplified models although generally speaking their simulated profiles are similar.

The comparison can also be made by the outlet concentration and Murphree efficiency of each tray as shown in Figs. 4.22 and 4.23. The simulated outlet concentrations by using algebraic Reynolds mass flux model are slightly higher than that by the hybrid model, while in Fig. 4.23 the simulated Murphree tray efficiencies by using algebraic Reynolds mass flux mode are slightly lower, although both of them are seen to be sufficiently confirmed by experimental data except tray 4 where experimental error is obvious.

4.1.3 Prediction of Multicomponent Point Efficiency

4.1.3.1 Difference Between Binary and multicomponent Point Efficiency

The separation efficiency in multicomponent distillation is quite different with that in binary (two components) distillation in the following aspects:

1. In binary system, the diffusion flux between liquid and vapor phases is proportional to the negative concentration gradient, while it is not true in multicomponent system.
2. In binary system, the diffusion coefficient for components i and j is equal, while in multicomponent it is not equal.
3. In binary system, the range of point efficiency is from 0 to 1, while it is ranging from $-\infty$ to $+\infty$ for multicomponent system.

Fig. 4.22 Comparison of simulated results for outlet concentrations of each tray by different models with experimental data [16]
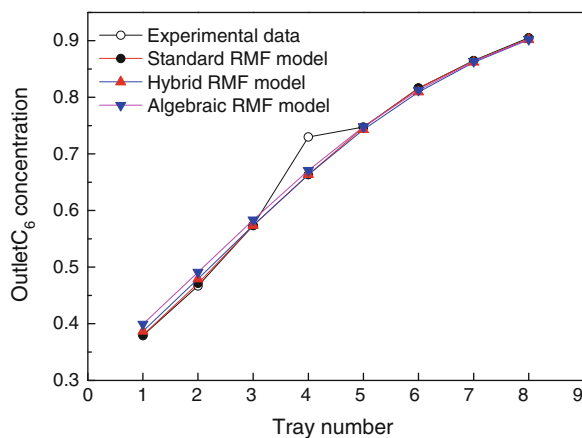
Fig. 4.23 Comparison of simulated results for tray efficiencies by different models with experimental data [16]
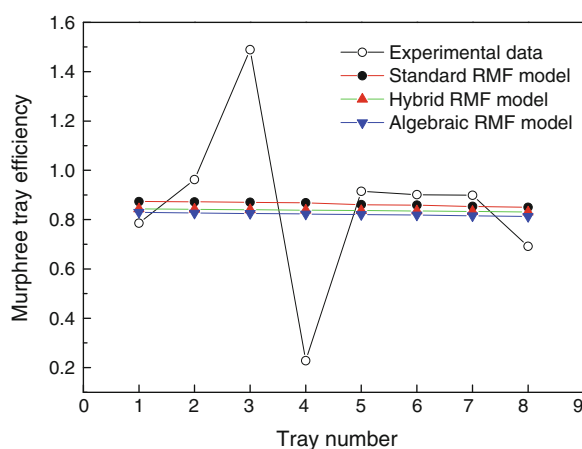
The complication appeared in multicomponent system is chiefly due to the complex nature of molecular interaction to form non-ideal solution and may appear bizarre behaviors (see Sect. 4.1.3.6).

The point efficiency is an essential information in distillation design and operation. The tray efficiency can be calculated by the CMT models presented in this chapter; it shows that the tray efficiency is in connection with the tray structure, flow pattern, and operating conditions, and thus, it is only referred to a specific distillation column under specific condition. On the other hand, the point efficiency, which depends on only the local condition of vapor–liquid contact and the physical properties of the system, is the better way to evaluate the feasibility of using distillation tray column for the separation.

The research on point efficiency has been undertaken over many decades and developed different expressions under the name of the author, such as Murphree [18], Hausen [19], Standard [20], and Holland and McMahon [21]. Among them,
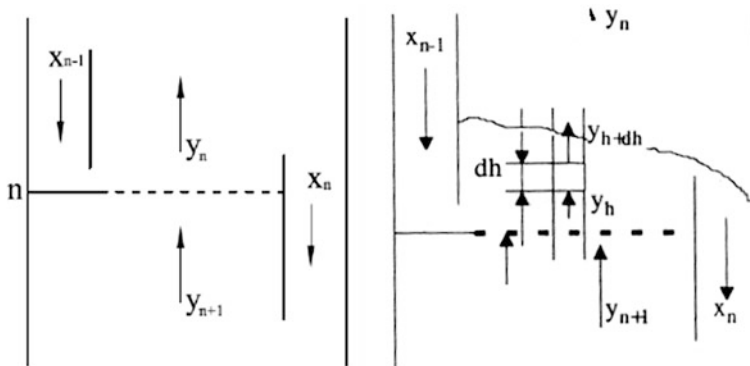
Fig. 4.24 Microelement (cell) taken on sieve tray

the Murphree point efficiency E_{MV} is commonly used, which is defined for tray column as the ratio of the concentration decrease in vapor between entering and leaving the tray and that if the leaving vapor is in thermodynamic equilibrium with the liquid on the tray. Mathematically, it can be expressed as follows:

$$E_{MV} = \frac{y_{i,n} - y_{i,n+1}}{y_{i,n}^* - y_{i,n+1}} \tag{4.8}$$

where subscript n denotes the tray number; y_{n+1} and y_n are, respectively, the concentration (component i) of vapor entering and leaving the tray; $y_{i,n}^*$ is the vapor concentration in equilibrium with the liquid at this local point. Note that the subscripts i and j in this section refer to the components i and j, respectively, but not the coordinate direction of flow. The nomenclature can be shown clearly from Fig. 4.24.

Murphree point efficiency can be also expressed in terms of liquid concentration as follows:

$$E_{ML} = \frac{x_{i,n-1} - x_{i,n}}{x_{i,n-1} - x_{i,n}^*} \tag{4.9}$$

The vapor-phase Murphree point efficient E_{MV} is frequently used especially in distillation, while the liquid-phase point efficient E_{ML} is suitable for the liquid-phase control processes, such as absorption and desorption processes.

Precisely, the mass transfer undertaken in the vertical direction above the tray deck is complicated as shown typically in Fig. 4.25, involving jetting, dispersed bubbles, splashing as well as the generation of liquid drops as entrainment in the tray spacing. Usually, it is divided into three zones, i.e.

- *froth zone* (jetting),
- *bubble dispersing zone* (free bubbling), and
- *bubble breaking zone* (liquid drops splashing as entrainment in tray space).

Fig. 4.25 Formation of vapor bubbles from sieve holes in different zones
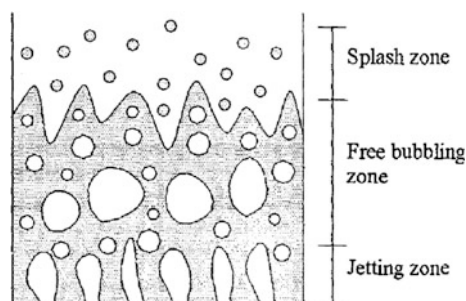
Table 4.2 Main construction parameters of Oldershaw sieve tray

Parameter	Value
Tray diameter (mm)	38
Diameter of tray spacing (mm)	64
Sieve hole diameter (mm)	1.25
Thickness of tray floor (mm)	1.2
Perforation (%)	6.38
Height of outlet weir (mm)	15–38

Since the bubble breaking (splash) zone has very small contribution to the mass transfer, the first two zones, in which the liquid as continuous phase and the vapor as dispersed phase, are dominant and have been established as two-zone model in the literature.

4.1.3.2 The Oldershaw Sieve Tray

The sieve tray developed by Oldershaw [22, 23] is recognized as the common distillation tray to be used for representing the point efficiency. The construction parameters are given in Table 4.2, and the column is shown in Fig. 4.26. The simulation of which is the convenient way to find the point efficiency of the corresponding separating system.

Wang [24] simulated the Oldershaw sieve tray [24] with consideration of using two zones model for the liquid on the tray. The distillation is three-component non-ideal solution (ethanol, isopropanol, and water) for the purpose of investigating the bizarre phenomenon of multicomponent distillation.

For the non-ideal multicomponent vapor–liquid system, the Maxwell–Stefan equation is usually employed to evaluate the mass transfer behaviors. The fundamentals of Maxwell–Stefan equation is briefly introduced in Sect. 3.4.2.
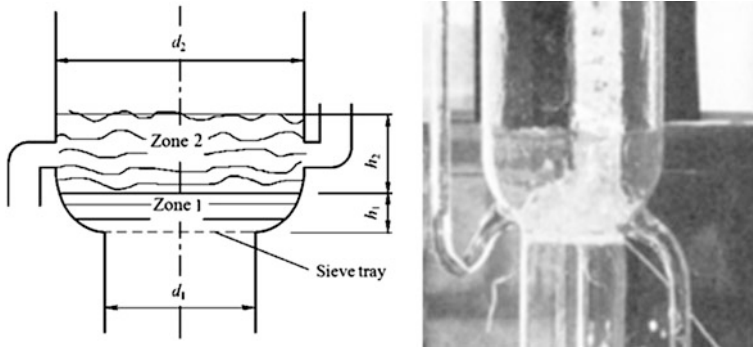
Fig. 4.26 Construction and operation of Oldershaw sieve tray (reprinted from Ref. [23], Copyright 1987, with permission from American Chemical Society)

4.1.3.3 Experimental Work on Multicomponent Tray Efficiency

Wang [24] performed the following experimental works to verify the simulation. Experiment was conducted in Oldershaw sieve tray as shown in Fig. 4.27. Two multicomponent systems are used for testing the point efficiency, i.e., three-component system (ethanol, isopropanol, and water) and four-component system (ethanol, isopropanol, tert-butyl alcohol, and water). The initial composition of three-component system in sequence is as follows:

$$(x_b) = (0.4477, 0.2209, 0.3314)^T$$

The composition of entering vapor is

$$(y_F) = (0.4447, 0.2214, 0.3339)^T$$

The operating conditions are as follows: temperature $T = 351.4$ K, $Q_V = 1.652 \times 10^{-4}$ m^3 s^{-1}, $h_L = 11.28$ mm. The experimental setup is shown schematically in Fig. 4.27.

4.1.3.4 Simulation Model for Point Efficiency

For calculating Murphree tray efficiency, we need to know the composition of vapor leaving the tray y_{out}, which can be obtained as follows. Since the range of composition change on a tray is small, we may assume the vapor–liquid equilibrium relationship to be linear, i.e.

$$(y^*) = [K^{eq}][\Gamma](x_b) \tag{4.10}$$

where $[K^{eq}]$ is $(n - 1)$ rank diagonal matrix, representing the equilibrium constant of the binary pairs. Also at the interface,

Fig. 4.27 Experimental setup (1 column, 2 Oldershaw tray, 3 downcomer, 4 reboiler, 5 heating pot, 6 flow meter, 7 reflux tube, 8 cooling water meter, 9 condenser, P pressure measuring point, T temperature measuring point, and S sampling point)
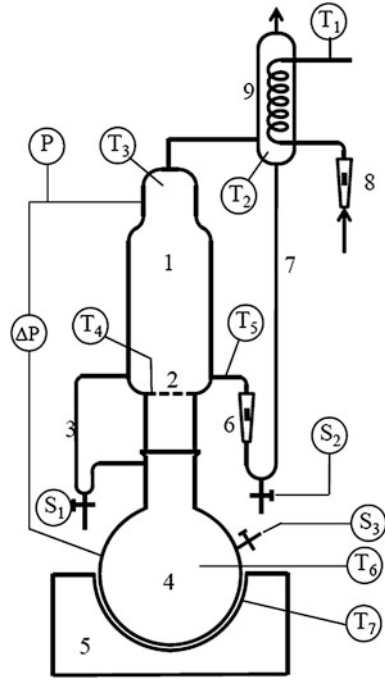
$$(y_0) = [K^{eq}][\Gamma](x_0) \tag{4.11}$$

where y_0 is the vapor concentration at interface. Then, we have

$$(y^* - y_0) = [K^{eq}][\Gamma](x_b - x_0)$$

The mass flux transferred can be calculated by (see Sect. 3.7.2)

$$N_i^L = -c_t[\boldsymbol{\beta}^L][R^L]^{-1}[\boldsymbol{\Gamma}^L](x_b - x_0) \tag{3.41}$$

$$N_i^V = -c_t[\boldsymbol{\beta}^V][R^V]^{-1}[\boldsymbol{\Gamma}^V](x_b - x_0) \tag{3.42}$$

In the calculation, the liquid bulk concentration x_b is known. Equation set (3.41) and (3.42) can be solved by stepwise iteration as given below to obtain the mass flux being transferred between liquid and vapor phases N_i ($N_i = N_i^L = N_i^V$).

For the vapor passing through the liquid on the tray, the vapor concentration is changing from y_{in} to y_{out} and should be calculated by differential method. Take a differential element Δh on the sieve tray as shown in Fig. 4.28, we have

$$dG_i = N_i \alpha A dh$$

and

$$dG_i = c_t^V u_s \alpha A dy$$

Fig. 4.28 Differential
element on the tray
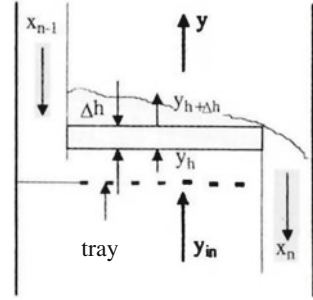
where G_i is the vapor flow rate; A is the area of the bubbling zone on the tray; α is the surface area of the bubbles. Combine foregoing equations to yield

$$dy_i = \left(\frac{N_i a}{c_t^V \alpha u_s}\right) dh$$

Integrating consecutively above equation from $h = 0$ at the tray deck to $h = h_1$ for the bubble formation zone and from h_1 to h_2 for the dispersed bubble zone, the y_{out} can be found for calculating the point efficiency. The trial and error method for stepwise calculation is employed to obtain the solution. The equations needed for computation of each zone are given below.

Bubble formation zone

Experimental work shows that the main form of vapor in this layer is jetting. The diameter of the vapor jet d_j, which is related to the liquid height h_L and the diameter of sieve hole d_h, was correlated by Hai [25]:

$$d_j = 1.1 d_h + 0.25 h_L$$

Thus, the surface area of the jet column is

$$\alpha = \frac{4\varphi d_j}{(d_h)^2}$$

where φ is the fraction of hole area. As the vapor flow through the jet column is similar to its flow through the falling film column, the mass transfer coefficient k^V can be calculated by the following relationship for two-component system [26]:

$$k^V = 2.0\sqrt{\frac{D^V}{\pi t_V}} = 0.046\left(\frac{D^V}{d_j}\right)(Re)^{0.96}(Sc)^{0.44}$$

$$Re = \frac{d_j u_j \rho_V}{\mu_V}, \quad Sc = \frac{\mu_V}{\rho_V D^V}$$

$$u_j = \frac{Q_V}{[(\pi/4)(d)^2]\varphi} \cdot \left(\frac{d_h}{d_j}\right)^2 = u_h\left(\frac{d_h}{d_j}\right)^2, \quad t_V = \frac{h_j}{u_j}$$

where d_j is the diameter of the vapor jet; u_j and u_h are, respectively, the vapor velocity based on jet diameter and sieve hole diameter.

Bubble dispersion zone

The vapor column reaching to this zone is broken into bubbles of different sizes and distributed diversely. The average diameter of the bubble can be estimated by the following equation [27]:

$$d_{\max} = (0.5We_c)^{0.6}\left(\frac{\sigma}{\rho_L}\right)^{0.6}(u_sg)^{-0.4}\left(\frac{\rho_V}{\rho_L}\right)^{-0.2}$$

$$We_c = \left(\frac{\tau d_{\max}}{\sigma}\right)\left(\frac{\rho_V}{\rho_L}\right)^{1/3}$$

where We_c is Weber group; σ is the surface tension; τ is the residence time, which is given by [27]

$$\tau = 2\rho_L(u_sgd_{\max})^{4/3}$$

It was reported [28, 29] that the ratio of average and maximum bubble diameters is a constant, i.e.

$$\frac{d_{av}}{d_{\max}} = 0.62$$

The reliability of foregoing estimation can be seen to be confirmed by some experimental data from the literature as shown in Table 4.3.

The vapor fraction β_V in this layer for sieve hole smaller than 2 mm can be estimated by equation below

$$\frac{\beta_V}{1 - \beta_V} = 8.5Fr^{0.5}, \quad Fr \leq 4.68 \times 10^{-4}\varphi^{-0.56}$$

$$\frac{\beta_V}{1 - \beta_V} = 1.25\varphi^{-0.14}Fr^{0.25}, \quad Fr > 4.68 \times 10^{-4}\varphi^{-0.56}$$

$$Fr = \frac{(u_s)^2}{gh_L}$$

where φ is the fraction of sieve perforation on the tray. By the iteration of foregoing equations, the d_{av} can be obtained as well as the surface area of the bubble by

$$a = \frac{6}{d_{av}} \cdot \beta_V$$

The mass transfer coefficient between bubble and the liquid on the tray was measured for binary system by Zaritsky and Calvelo [30] and correlated by Prado and Fair [31] as follows:

Table 4.3 Calculated bubble diameter compared with experimental measurements

Sieve hole (m/s)	Calculated d_{av} (mm)	Experimental value by Sharma and Gupta [29] (mm)	Experimental value by Raper et al. [43] (mm)	Experimental value by Geary [27] (mm)
1.70	3.35			
1.94	3.60			
2.01	3.60	4.0	2.0–5.0	2.0–4.0
2.24	3.55			
2.26	4.05			

$$k^{V} = Sh\frac{D^{V}}{d_{av}}$$

$$Sh = -11.878 + 25.879(\lg Pe) - 5.640(\lg Pe)^{2}$$

$$Pe = \frac{d_{av}u_{b}}{D^{V}}, \ u_{b} = \frac{Q_{V}}{\frac{\pi}{4}(d)^{2}\beta_{V}\rho_{V}}$$

where D^{V} is the molecular diffusivity of component i in the vapor phase.

Steps of calculation

As shown in Fig. 4.29, let the height of the two liquid zones on the tray be h ($h = h_{1} + h_{2}$), take a differential element Δh on the tray, where $y_{in} = y_{h}$ and $y_{out} = y_{h+\Sigma\Delta h}$. The mass flux of component i in the element can be calculated as follows:

1. Let $y_{in} = y_{bh}$ and assume $y_{out} = y_{bh+\Delta h}^{0}$, the average concentration of component i is $y_{av} = \frac{1}{2}(y_{bh} + y_{bh+\Delta h})$.
2. Calculate the mass flux to be transferred by aforementioned method so as to obtain the concentration of vapor leaving from the differential element. If it is close enough to the assumed value, then proceed to the next differential element above until reaching to the top of the liquid zone to obtain the outlet vapor concentration from the tray.

As an example, Wang [24] give the calculated result along liquid height h as shown in Table 4.4.

As seen, the mass transfer is high at low liquid level and decreases as the vapor goes up to the top of the froth. It indicates the bubble formation zone is dominant in the mass transfer process.

4.1.3.5 Simulated Results and Comparison with Experimental Data

The comparisons between simulated and experimental Murphree point efficiencies of three-component and four-component systems are given, respectively, in Tables 4.5 and 4.6. The error in most cases is less than few percent, which is acceptable for estimation purpose.

Fig. 4.29 Vapor column
from sieve hole
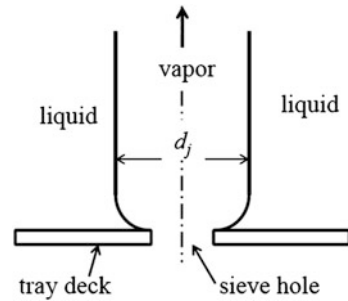
4.1.3.6 The Bizarre Phenomena of Multicomponent System

The bizarre phenomena of multicomponent system can be illustrated by the case of three-component system as calculated by Wang given in preceding section. The simulated diffusion flux of isopropanol is plotted versus driving force of mass transfer $(y_0 - y)$ as shown in Fig. 4.30.

As shown in the figure that the driving force $(y_0 - y)$ is positive between A and B, the direction of mass transfer is from y_0 (vapor) to y (liquid). At point B, although the driving force is positive, the mass flux of isoprenol transferred is zero; such phenomenon is regarded as *diffusion barrier*, which is not happened in binary system. From points B to C, the driving force is still positive, yet the isoprenol transferred is negative, i.e., the direction of mass transfer is reversed and such phenomenon is regarded as *reversed diffusion*. Moreover, as shown in Fig. 4.31, at the liquid height about $h = 25$, the driving force is approaching zero, but the isopropanol still able to undertake mass transfer between phases; such phenomenon is regarded as *osmotic diffusion*. It should be mentioned that such *bizarre phenomena* is only happened for isopropanol in the three-component system, but not for ethanol and water. Thus, the complication of non-ideal multicomponent system depends on many factors and still under investigation. The plot of simulated results is also given in Fig. 4.31.

4.2 Packed Column

The simulation of packed column by CMT methodology has been made by Liu et al. [32] and Li et al. [7] as given in the following sections.

The model assumptions are the same as the tray column except that axially symmetrical condition is applied for the packed column.

The packed column to be simulated are that reported by Sakata and Yanagi [2], it is 1.22 m in diameter packed with 50.8-mm carbon steel Pall ring of 3.66-m height for separating *n*-heptane and methylcyclohexane under 165.5 kPa and total reflux operation.

Table 4.4 Calculated result of mass flux transferred along liquid height

Liquid height h from tray deck (mm)	Vapor concentration, mole fraction			Mass flux transferred N (mol m^{-2} s^{-1})		
	Ethanol	Isopropanol	Water	Ethanol	Isopropanol	Water
1.30	0.4461	0.2216	0.3323	12.36×10^{-6}	1.663×10^{-5}	-11.68×10^{-5}
2.60	0.4474	0.2218	0.3308	11.95×10^{-6}	1.566×10^{-5}	-11.27×10^{-5}
3.89	0.4488	0.2219	0.3293	11.56×10^{-6}	1.473×10^{-5}	-10.86×10^{-5}
5.19	0.4500	0.2221	0.3279	11.18×10^{-6}	1.384×10^{-5}	-10.48×10^{-5}
6.49	0.4513	0.2222	0.3265	10.81×10^{-6}	1.300×10^{-5}	-10.10×10^{-5}
7.79	0.4524	0.2224	0.3252	10.46×10^{-6}	1.220×10^{-5}	-9.743×10^{-5}
9.09	0.4536	0.2225	0.3239	10.12×10^{-6}	1.143×10^{-5}	-9.396×10^{-5}
10.38	0.4547	0.2226	0.3227	9.876×10^{-6}	1.070×10^{-5}	-9.061×10^{-5}
11.68	0.4558	0.2228	0.3215	9.466×10^{-6}	1.001×10^{-5}	-8.739×10^{-5}
12.98	0.4568	0.2229	0.3203	9.158×10^{-6}	0.935×10^{-5}	-8.428×10^{-5}
14.18	0.4621	0.2234	0.3145	8.625×10^{-6}	0.815×10^{-5}	-7.887×10^{-5}
15.38	0.4665	0.2237	0.3098	7.144×10^{-6}	0.517×10^{-5}	-6.410×10^{-5}
16.59	0.4702	0.2239	0.3060	5.926×10^{-6}	0.296×10^{-5}	-5.214×10^{-5}
17.79	0.4732	0.2239	0.3029	4.924×10^{-6}	0.135×10^{-5}	-4.246×10^{-5}
18.99	0.4757	0.2239	0.3003	4.096×10^{-6}	0.020×10^{-5}	-3.460×10^{-5}
20.19	0.4778	0.2239	0.2983	3.413×10^{-6}	-0.062×10^{-5}	-2.822×10^{-5}
21.39	0.4796	0.2238	0.2966	2.847×10^{-6}	-0.116×10^{-5}	-2.304×10^{-5}
22.60	0.4810	0.2237	0.2952	2.378×10^{-6}	-0.152×10^{-5}	-1.882×10^{-5}
23.80	0.4823	0.2236	0.2941	1.989×10^{-6}	-0.172×10^{-5}	-1.539×10^{-5}
25.00	0.4833	0.2235	0.2932	1.666×10^{-6}	-0.183×10^{-5}	-1.259×10^{-5}

Table 4.5 Comparison of simulated point efficiency with experimental data (I)

Expt. No.	Component	Liquid concentration on tray, mole fraction	Experimental point efficiency	Simulated point efficiency	Error = Sim. − Exp.
1	1	0.1247	0.9888	0.8155	−0.1733
	2	0.6434	0.9924	0.9430	−0.0494
	3	0.2319	0.9932	0.9709	−0.0223
2	1	0.0859	0.8529	0.8280	−0.0249
	2	0.7434	0.9710	0.9494	−0.0216
	3	0.1707	0.9903	0.9695	−0.0208
3	1	0.4477	0.8679	0.8745	−0.0066
	2	0.2209	2.8615	2.8842	0.0227
	3	0.3314	0.8558	0.9072	0.0514
4	1	0.2589	0.6976	0.6771	−0.205
	2	0.4210	0.0846	0.1044	0.198
	3	0.3201	0.7732	0.7526	−0.0027
5	1	0.2115	0.7807	0.8338	0.0531
	2	0.4510	1.1921	1.1591	−0.0330
	3	0.3375	0.8625	0.8984	0.0359

System 1 ethanol, *2* isopropanol, and *3* water

4.2.1 $\overline{c'^2}$-ε_c *Two-Equation Model*

4.2.1.1 Modeling Equations

The model equation for packed column comprises CFD equation set and mass transfer equation set. Unlike the tray column, the porosity of packed column is non-uniformly distributed, and the liquid fraction β_L should be retained in the model equations. The interacted liquid-phase model equations are as follows:

Overall mass conservation

$$\frac{\partial(\rho_L \gamma \beta_L U_{Li})}{\partial x_i} = S_m \tag{4.12}$$

where γ is the porosity of the packed bed.

Momentum conservation

$$\frac{\partial \rho_L \gamma \beta_L U_{Li} U_{Lj}}{\partial x_i} = -\gamma \beta_L \frac{\partial P}{\partial x_j} + \gamma \beta_L \frac{\partial}{\partial x_i}\left[\mu_L \frac{\partial U_{Li}}{\partial x_i} - \rho_L \overline{u'_{Li} u'_{Lj}}\right] + \gamma \beta_L S_{Li} \tag{4.13}$$

where $\overline{u'_{Li} u'_{Lj}}$ by

$$-\rho_L \overline{u'_{Li} u'_{Lj}} = \mu_{Lt}\left(\frac{\partial U_{Li}}{\partial x_j} + \frac{\partial U_{Lj}}{\partial x_i}\right) - \frac{2}{3}\rho_L \delta_{ij} k_L \tag{1.8}$$

Table 4.6 Comparison of simulated point efficiency with experimental data (II)

Expt. No.	Component	Liquid concentration on tray, mole fraction	Point efficiency		Error
			Experimental	Simulated	
1	1	0.3436	0.9035	0.8225	−0.0343
	2	0.2679	0.8087	0.8238	0.0186
	3	0.0640	0.7242	0.7801	0.0773
	4	0.3245	0.9706	0.9070	−0.0655
2	1	0.2313	0.9625	0.8154	−0.1528
	2	0.4694	0.9977	0.9279	−0.0699
	3	0.1231	0.7667	0.9163	0.1951
	4	0.1763	0.9292	0.9682	0.0419
3	1	0.4866	0.9108	0.9341	0.0256
	2	0.0781	1.2949	0.8274	−0.3611
	3	0.0788	1.5687	1.6066	0.0241
	4	0.3566	0.8928	0.9507	0.0648
4	1	0.0507	0.9027	0.8939	−0.0097
	2	0.0465	0.9100	0.8466	−0.0697
	3	0.3963	0.8686	0.8968	0.0324
	4	0.5065	0.8659	0.9092	0.0500
5	1	0.3488	0.8741	0.8282	−0.0525
	2	0.3534	0.8702	0.9133	0.0496
	3	0.0809	0.9261	0.9019	−0.0262
	4	0.2170	0.9384	0.9972	0.0627
6	1	0.3717	0.9891	0.9444	−0.0452
	2	0.1339	5.2322	7.3893	0.4123
	3	0.0669	0.8891	0.9618	0.0818
	4	0.4275	0.9882	0.9620	−0.0265
7	1	0.8658	0.7967	0.7867	−0.0125
	2	0.0145	0.8643	0.9694	0.1216
	3	0.0396	0.9631	0.9190	−0.0458
	4	0.0801	1.0429	1.0323	−0.0102
8	1	0.1360	0.9437	0.9491	0.0057
	2	0.1102	0.7173	0.5346	−0.2547
	3	0.2214	0.8633	0.8590	−0.0050
	4	0.5344	0.8813	0.9165	0.0400

System 1 ethanol, *2* isopropanol, *3* tert-butyl alcohol, and *4* water

k_L *equation*

$$\frac{\partial \rho_L \gamma \beta_L U_{Li} k_L}{\partial x_i} = \frac{\partial}{\partial x_i}\left[\gamma \beta_L \left(\mu_L + \frac{\mu_{Lt}}{\sigma_{k_L}}\right)_L \frac{\partial k_L}{\partial x_j}\right] + \gamma \beta_L (G_{Lk} - \varepsilon_L) \quad (4.14)$$

ε_L *equation*

$$\frac{\partial \rho_L \gamma \beta_L U_{Li} \varepsilon_L}{\partial x_i} = \frac{\partial}{\partial x_i}\left[\gamma \beta_L \left(\mu_L + \frac{\mu_{Lt}}{\sigma_{\epsilon_L}}\right) \frac{\partial \varepsilon_L}{\partial x_i}\right] + \gamma \beta_L (C_{1\epsilon} G_{Lk} - C_{2\epsilon} \rho_L \varepsilon_L)\frac{\varepsilon_L}{k_L} \quad (4.15)$$

Fig. 4.30 Diffusion mass flux of isopropanol in three-component system versus driving force of mass transfer
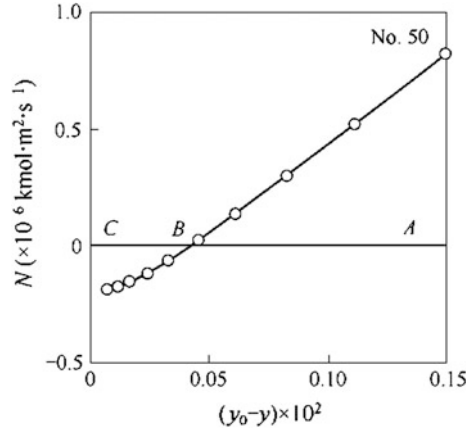
Fig. 4.31 Mass transfer flux and driving force of isopropanol in three-component system versus liquid height
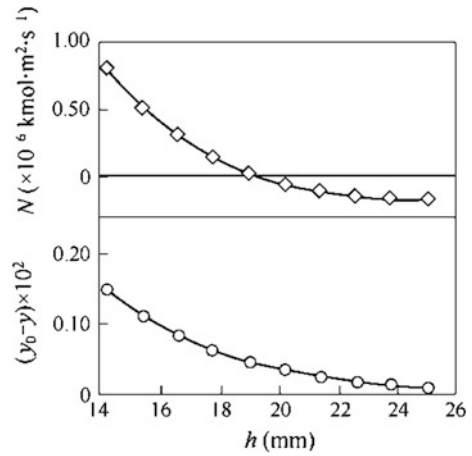
The model constants are: $c_\mu = 0.09$, $\sigma_k = 1.0$, $\sigma_\epsilon = 1.3$, $C_{1\epsilon} = 1.44$, $C_{2\epsilon} = 1.92$.

Species mass conservation equation

$$\frac{\partial \gamma \beta_L U_{Li} C}{\partial x_i} = \frac{\partial}{\partial x_i} \gamma \beta_L \left(D_{Lt} \frac{\partial C}{\partial x_i} - \overline{u'_{Li} c'} \right) + S_n \quad (4.16)$$

$\overline{c'^2}$ *equation*

$$\frac{\partial \gamma \beta_L U_{Li} \overline{c'^2}}{\partial x_i} = \frac{\partial}{\partial x_i} \left[\gamma \beta_L \left(D_L + \frac{D_{Li}}{\sigma_{c'^2}} \right) \frac{\partial \overline{c'^2}}{\partial x_i} \right] - 2\gamma \beta_L D_{Lt} \left(\frac{\partial C}{\partial x_i} \right)^2 - 2\gamma \beta_L \varepsilon_{c'} \quad (3.10)$$

$\varepsilon_{c'}$ *equation*

$$U_i \gamma \beta_L \frac{\partial \varepsilon_{c'}}{\partial x_i} = \frac{\partial}{\partial x_i} \left[\gamma \beta_L \left(D_L + \frac{D_{Lt}}{\sigma_{\varepsilon_c}} \right) \frac{\partial \varepsilon_{c'}}{\partial x_i} \right] - C_{c1} \gamma \beta_L D_{Lt} \frac{\varepsilon_{c'}}{\overline{c^2}} \left(\frac{\partial C}{\partial x_i} \right)^2$$
$$- C_{c2} \frac{\varepsilon_{c'}^2}{\overline{c'^2}} - C_{c3} \gamma \beta_L \frac{\varepsilon_{c'} \varepsilon_{c'}}{k_L}$$

(3.17)

D_t *equation*

$$D_{Lt} = C_{c0} k_L \left(\frac{k_L \overline{c'^2}}{\varepsilon_L \varepsilon_{c'}} \right)^{\frac{1}{2}}$$

(3.6)

Model constants are as follows: $C_{c0} = 0.14$, $C_{c1} = 1.8$, $C_{c2} = 2.2$, $C_{c3} = 0.8$, $\sigma_{c2} = 1.0$.

4.2.1.2 Boundary Conditions

Inlet (reflux at column top $x = 0$): $U_L = U_{in}$, $V_L = 0$, $C_i = C_{i,in}$. For the other parameters, we may set to be [1, 33]

$$k_{L,in} = 0.003 \, U_{L,\,in}^2$$
$$\varepsilon_{L,in} = 0.09 \, \frac{k_{L,in}^{1.5}}{d_H}$$
$$\overline{c'^2} = (0.082 \, C_{in})^2 = 0.0067 C_{in}^2$$
$$\varepsilon_{c'} = 0.4 \left(\frac{\varepsilon_{in}}{k_{in}} \right) \overline{c_{in}'^2}$$

Outlet (column bottom): Fully developed turbulent condition is assumed so that the gradients of all parameters Φ except pressure are set to be zero:

$$\frac{\partial \Phi}{\partial x} = 0$$

Column symmetrical axis ($r = 0$): The radial gradients of all parameters Φ except pressure are equal to zero.

$$\frac{\partial \Phi}{\partial r} = 0$$

Column wall ($r = R$): The relevant flux is equal to zero.
Near column wall region: Standard wall function is employed.

4.2.1.3 Evaluation of Source Term

As stated in Sect. 4.1, considering the latent heat of both species is almost equal, so that $S_n = 0$.

The source term S_{Li} is expressed by

$$S_{Li} = \rho_L g + F_{LS,i} + F_{LG}$$

where F_{LS} is the flow resistance created by random packing, and F_{LG} is the interface drag force between liquid and vapor phases. The F_{LS} can be evaluated by using following correlation [34]:

$$F_{LS} = -\left[A\mu_L \frac{(1-\gamma)^2}{\gamma^2 d_e^2} + B\rho_L \frac{(1-\gamma)}{\gamma d_e}|U_L|\right]U_L$$

where U is interstitial velocity vector; γ is the porosity; d_e is the equivalent diameter of the packing; constants $A = 150$, $B = 1.75$.

The F_{LG} is calculated by

$$F_{LG} = \frac{\Delta p_L}{|U_{slip}|}U_{slip}$$

where Δp_L is the wet-bed pressure drop; U_{slip} is slip velocity vector between vapor and liquid and equal to

$$U_{slip} = U_G - U_L$$

The S_n in species equation, similar to the tray column, can be calculated by

$$S_n = K_{OL}a\left(C_G^* - C_L\right)$$

$$K_{OL} = \frac{1}{\frac{1}{k_L} + \frac{1}{mk_G}}$$

The gas and liquid film coefficients k_L, k_G and the volumetric effective surface area a are obtained from the correlation by Wagner et al. [33] as follows:

$$k_L = \left(\frac{4\Phi_L D_L U_L}{\pi h \gamma \chi}\right)^{0.5}$$

$$k_G = \left(\frac{4\Phi_G D_G U_G}{\pi(\gamma - h\gamma)\chi}\right)^{0.5}$$

where the enhancement factors Φ_L and Φ_G are set equal to 1 under experimental condition; χ is characteristic length depending on bed height Z:

$$\chi = C_{pk}^2 Z$$

The coefficient C_{pk} for 50.8-mm Pall ring packing is equal to 0.031.

The vapor liquid contacting area a is calculated by [33]

$$\frac{a}{a_T} = \frac{h\gamma}{1.0 - \gamma}$$

where a_T is the specific area of the packing; γ is the porosity; h is the total liquid holdup of the packing, which comprises static holdup h_s and dynamic holdup h_d. For 50.8-mm Pall ring packing, h_s is calculated by [35]

$$h_s = 0.033 \exp\left(-0.22 \frac{g\rho_L}{\sigma_L a_T^2}\right)$$

and h_d by [36]

$$h_d = 0.555 \left(\frac{a_T U_L^2}{g\gamma^{4.65}}\right)^{1/3}$$

4.2.1.4 Simulated Result and Verification: Separation of Methylcyclohexane and *n*-Heptane

Average axial concentration along column height and verification

The simulated radial averaged axial concentration along radial direction at different column heights as shown in Fig. 4.32. The plot is made by $\ln\left(\frac{x}{1-x}\right)$ versus column height z (z is the height of the packed bed measured from the column bottom) because according to the Fenske equation such plot should be in a straight line at constant relative volatility, which is applicable to the present case. The simulated curve is nearly a straight line and in good agreement with the experimental data.

HETP and verification

The separation efficiency of packed column is usually expressed in terms of height equivalent of theoretical plate (HETP). According to the Fenske equation, the slop of $\ln\left(\frac{x}{1-x}\right)$ versus Z plot is equal to $\frac{\ln \alpha_{re}}{HETP}$, where α_{re} is the relative volatility of the separating system. The simulated HETP can be obtained from Fig. 4.32 by smoothing the computed curve to a straight line and find the slop. As shown in Fig. 4.33, the simulated HETP is confirmed by the experimental data.

Turbulent mass diffusivity distribution

The volume average turbulent mass diffusivity D_{Lt} computed by the two-equation model is shown in Fig. 4.34 at different F factors, and more detailed distributions are given in Fig. 4.35. These figures show that the turbulent mass diffusivity is higher in the upper part of the column and lower in the near-wall region. The reason is higher concentration around the upper column in distillation process so as to undertaking more quantity of mass transfer. At the same time, the wall effect accounts for the mass transfer lower down in the near-wall region.
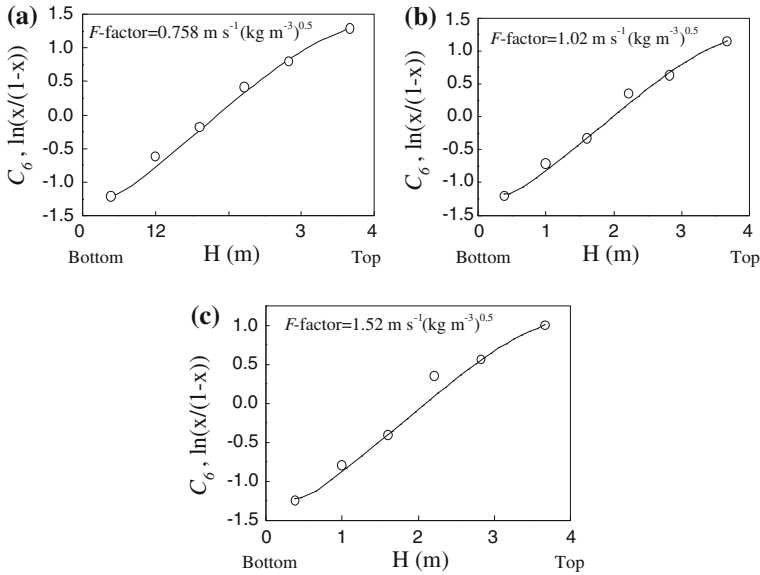
Fig. 4.32 Comparisons of the concentration profiles in liquid phase between two-equation model predictions (*solid lines*) and experimental data (*circles*) (*H* is height of packed) **a** *F* factor = 0.758 m s^{-1} (kg m^{-3})$^{0.5}$, **b** *F* factor = 1.02 m s^{-1} (kg m^{-3})$^{0.5}$, and **c** *F* factor = 1.52 m s^{-1} (kg m^{-3})$^{0.5}$ (reprinted from Ref. [32], Copyright 2009, with permission from Elsevier)

Fig. 4.33 HETP comparison between predictions and measurements (reprinted from Ref. [32], Copyright 2009, with permission from Elsevier)
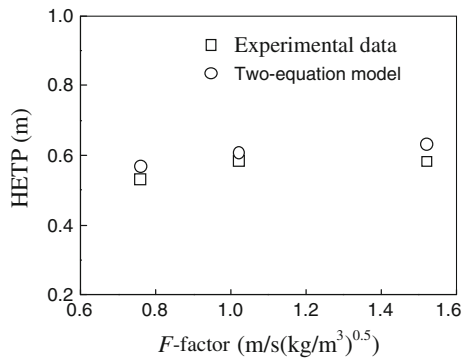
4.2.2 Reynolds Mass Flux Model

Li [7] simulated the packed column as described in Sect. 4.2.1 by using Reynolds mass flux model instead of two-equation model and compared their difference. The simulated results for three forms of Reynolds mass flux model (standard, hybrid, and algebraic) are given in subsequent sections.
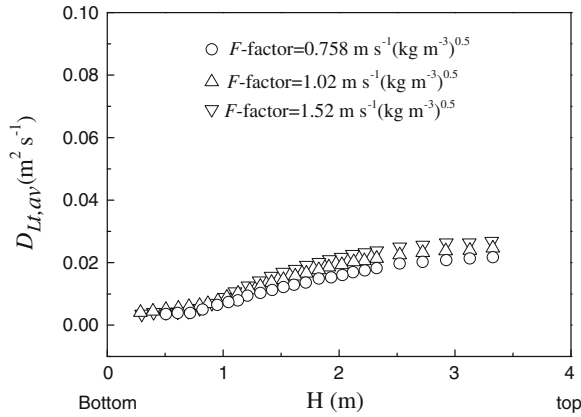
Fig. 4.34 Average turbulent mass diffusivity along the column height at different F factors (reprinted from Ref. [32], Copyright 2009, with permission from Elsevier)
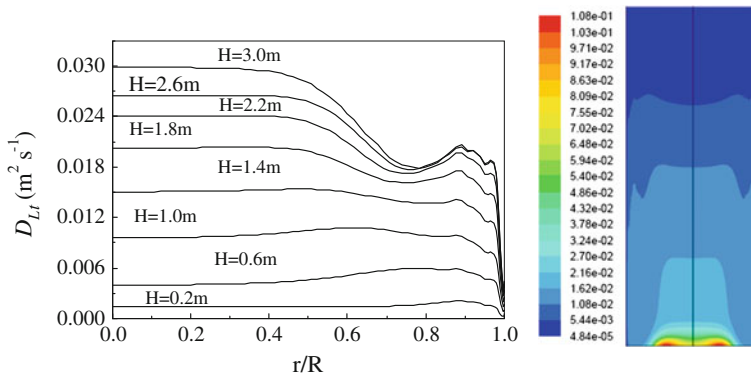
Fig. 4.35 Distribution of turbulent mass diffusivity in the column F = 1.02 m s^{-1} (kg m^{-3})$^{0.5}$, H height of packed bed ($H = 0$ at the column bottom) (reprinted from Ref. [32], Copyright 2009, with permission from Elsevier)

4.2.2.1 Standard Reynolds Mass Flux Model

Interacted liquid-phase model with constant fluid density ρ and constant liquid fraction β is employed for simulation. The model equations are as follows:

Overall mass conservation

$$\frac{\partial \rho \gamma \beta_L U_{Li}}{\partial x_i} = S_m \tag{4.17}$$

Momentum conservation

$$\frac{\partial \rho \gamma \beta_L U_{Li} U_{Lj}}{\partial x_i} = -\gamma \beta_L \frac{\partial P}{\partial x_j} + \frac{\partial}{\partial x_i} \gamma \beta_L \left[\mu_L \frac{\partial U_{Li}}{\partial x_i} - \rho \overline{u'_{Li} u'_{Lj}} \right] + \gamma \beta_L S_{Li} \qquad (4.18)$$

where $\overline{u'_{Li} u'_{Lj}}$ is calculated by

$$\frac{\partial \overline{u'_{Li} u'_{Lj}}}{\partial t} + U_k \frac{\partial \overline{u'_{Li} u'_{Lj}}}{\partial x_k} = \frac{\partial}{\partial x_k} \left(C_k \frac{k}{\varepsilon} \overline{u'_i u'_j} \frac{\partial \overline{u'_{Li} u'_{Lj}}}{\partial x_k} + \frac{\mu}{\rho} \frac{\partial \overline{u'_{Li} u'_{Lj}}}{\partial x_k} \right)$$
$$- \left(\overline{u'_{Li} u'_{Lk}} \frac{\partial U_{Lj}}{\partial x_k} + \overline{u'_{Lj} u'_{Lk}} \frac{\partial U_{Li}}{\partial x_k} \right) - C_1 \frac{\varepsilon}{k} \left(\overline{u'_{Li} u'_{Lj}} - \frac{2}{3} k_L \delta_{ij} \right)$$
$$- C_2 \left(\overline{u'_{Li} u'_{Lk}} \frac{\partial U_j}{\partial x_k} + \overline{u'_{Lj} u'_{Lk}} \frac{\partial U_{Li}}{\partial x_k} - \frac{2}{3} \delta_{ij} \overrightarrow{u'_{Li} u'_{Lk}} \frac{\partial U_{Li}}{\partial x_k} \right) - \frac{2}{3} \varepsilon_L \delta_{ij}$$
$$(1.23)$$

where the constants are as follows: $C_k = 0.09$, $C_1 = 2.3$, $C_2 = 0.4$.

Species mass conservation equation

$$\frac{\partial \gamma \beta_L U_{Li} C}{\partial x_i} = \frac{\partial}{\partial x_i} \lambda \beta_L \left(D_L \frac{\partial C}{\partial x_i} - \overline{u'_{Li} c'} \right) + \gamma \beta_L S_{Ln} \qquad (3.3)$$

Fluctuating mass flux equation

$$\frac{\partial \overline{u'_{Li} c'}}{\partial t} + \frac{\partial U_{Lj} \overline{u'_{Li} c'}}{\partial x_j} = \frac{\partial}{\partial x_j} \left[\left(C_{c1} \frac{k_L}{\varepsilon_L} \overline{u'_{Li} u'_{Lj}} + \frac{\mu}{\rho} \right) \frac{\partial \overline{u'_{Li} c'}}{\partial x_j} \right]$$
$$- \left(\overline{u'_{Li} u'_{Lj}} \frac{\partial C}{\partial x_j} \right) - C_{c2} \frac{\varepsilon}{k} \overline{u'_{Li} c'} + C_{c3} \overline{u'_{Lj} c'} \frac{\partial U_{Li}}{\partial x_j}$$
$$(3.26a)$$

where $C_{c1} = 0.09$, $C_{c2} = 3.2$, $C_{c3} = 0.55$.

Auxiliary equations

k_L *equation*

$$\frac{\partial \rho \gamma \beta_L U_{Li} k_L}{\partial x_i} = \frac{\partial}{\partial x_i} \left[\gamma \beta_L \left(\mu_L + \frac{\mu_{Lt}}{\sigma_k} \right) \frac{\partial k_L}{\partial x_i} \right]$$
$$- \mu_t \gamma \beta_L \left(\frac{\partial U_{Li}}{\partial x_j} + \frac{\partial U_{Lj}}{\partial x_i} \right) \frac{\partial U_{Lj}}{\partial x_i} - \rho_L \gamma \beta_L \varepsilon_L \qquad (1.11a)$$

ε_L *equation*

$$\frac{\partial \rho_L \gamma \beta_L U_{Li} \varepsilon_L}{\partial x_i} = \frac{\partial}{\partial x_i} \left[\gamma \beta_L \left(\mu_L + \frac{\mu_{Lt}}{\sigma_\epsilon} \right) \frac{\partial \varepsilon_L}{\partial x_i} \right]$$
$$- C_{\varepsilon 1} \gamma \beta_L \frac{\varepsilon_L}{k_L} \mu_{Lt} \left(\frac{\partial U_{Lj}}{\partial x_i} + \frac{\partial U_{Li}}{\partial x_j} \right) \frac{\partial U_{Lj}}{\partial x_i} - C_{\varepsilon 2} \gamma \beta_L \rho_L \frac{\varepsilon_L^2}{k_L} \qquad (1.13a)$$

(a)   **(b)**   **(c)**

Fig. 4.36 Concentration profile of C_6 by standard Reynolds mass flux model, **a** $F = 0.758$ m s^{-1} (kg m^3)$^{0.5}$, **b** $F = 1.02$ m s^{-1} (kg m^3)$^{0.5}$, and **c** $F = 1.52$ m s^{-1} (kg m^3)$^{0.5}$ [16]

The model constants are as follows: $c_\mu = 0.09$, $\sigma_k = 1.0$, $\sigma_\epsilon = 1.3$, $C_{1\epsilon} = 1.44$, $C_{2\epsilon} = 1.92$.

The boundary conditions and the evaluation of source terms are the same as given in Sects. 4.1.2.2 and 4.1.2.3.

Simulated result and verification

The simulated C_6 concentration profile of the whole column at different F factors is shown in Fig. 4.36. In comparison with Fig. 4.22 simulated by using two-equation model, the concentration in the main flow area is almost the same but in the near-wall region is somewhat difference. The volume average axial concentration distribution is given in Fig. 4.37, in which the simulated curve can be seen to be in agreement with the experimental data.

Reynolds mass flux

The fluctuating mass flux (negative Reynolds mass flux) in axial and radial directions and their sum are given in Figs. 4.38 and 4.39.

In the distillation column tray, the species concentration is decreasing from inlet to the outlet weir, i.e., under negative gradient. The positive $\overline{u'_x c'}$ means that the diffusion of turbulent mass flux $\overline{u'_x c'}$ is consistent with the bulk mass flow and promotes the mass transfer in x direction.

As shown in Fig. 4.38a, most of the $\overline{u'_{L,i} c'}$ gradient in y (radial) directions is almost zero around the column centerline ($r/R = 0$) of the lower part of the column ($H < 1.9$ m) indicating only molecular diffusion is existed. At the upper part of the column ($H > 2.3$ m), $\overline{u'_x c'}$ contour is increasing from $r/R = 0$ to about
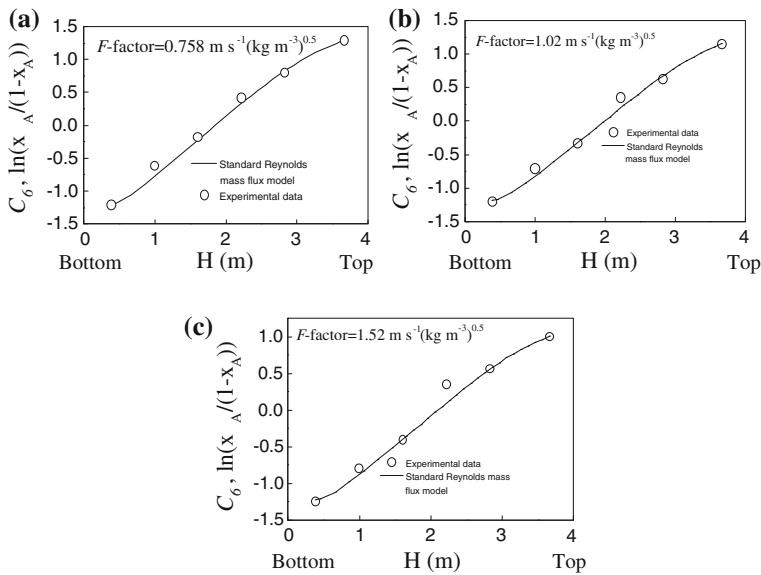
Fig. 4.37 Average C_6 concentration along column height at different F factors [16]
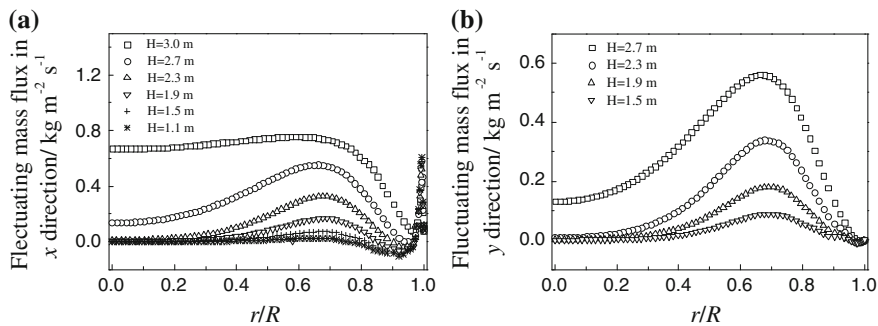
Fig. 4.38 Simulated fluctuating mass flux in axial (x) and radial (y) directions at different bed heights H **a** $\overline{u'_x c'}$ and **b** $\overline{u'_y c'}$ [16]

$r/R = 0.7$, indicating that the turbulent diffusion $\overline{u'_x c'}$ is promoted with increasing rate (see Sect. 3.5.1.4). Afterward, from $r/R = 0.7$, the slope is turning to negative, which means the diffusion rate is decreasing until about $r/R = 0.95$. Thus, the diffusion of $\overline{u'_x c'}$ in radial direction displays wavy changes and follows the pattern of   decreasing $\rightarrow$ increasing $\rightarrow$ decreasing $\rightarrow$ increasing   sharply $\rightarrow$ decreasing sharply near the column wall.

Fig. 4.39 Profiles of $\overline{u_x'c'} + \overline{u_y'c'}$ at different packed heights H (H is measured from column bottom) [16]
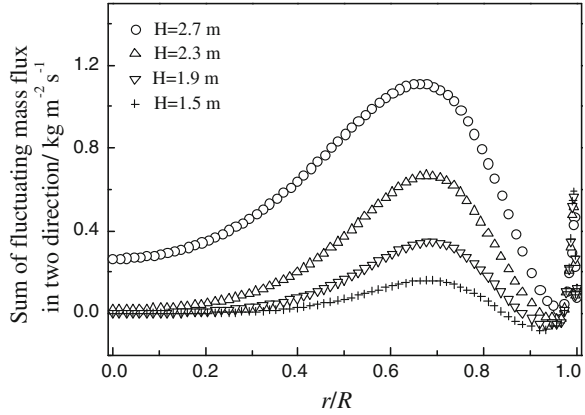
In Fig. 4.38b, the $\overline{u_y'c'}$ contours behave similar to the $\overline{u_x'c'}$, indicating that the radial $\overline{u_y'c'}$ diffusion varies with the pattern of decreasing → increasing → decreasing sharply to the column wall.

As shown in Fig. 4.39, the overall tendency of $\overline{u_{Li}'c'}$ (equal to $\overline{u_x'c'} + \overline{u_y'c'}$) is similar to both $\overline{u_x'c'}$ and $\overline{u_y'c'}$. It is noted that $\overline{u_x'c'}$ is much greater than $\overline{u_y'c'}$ in this case, that means the $\overline{u_{Li}'c'}$ diffusion is dominated by $\overline{u_x'c'}$.

It should be noted that the radial variation in concentration is small and may not be seen clearly in the concentration profile of the whole column. However, the detailed information about the mass transfer, which can be obtained by using Rayleigh mass flux model, is helpful to the column design and the evaluation of process efficiency.

4.2.2.2 Hybrid Reynolds Mass Flux Model

The model equations are the same as the standard Reynolds mass flux model except that the calculation of $\overline{u_{Li}'u_{Lj}'}$ is by Eq. (1.8) instead of Eq. (1.23).

Simulated result and verification

The simulated C_6 concentration profile of whole column is shown in Fig. 4.40, which is almost identical with Fig. 4.36.

The simulated radial averaged axial concentration distribution is compared with experimental data and the simulated result by using standard Reynolds mass flux model as shown in Fig. 4.41. These figures display no substantial difference between hybrid and standard Reynolds mass flux models.

The comparison of simulated result on radial averaged axial concentration between hybrid Reynolds mass flux model and two-equation model is given in
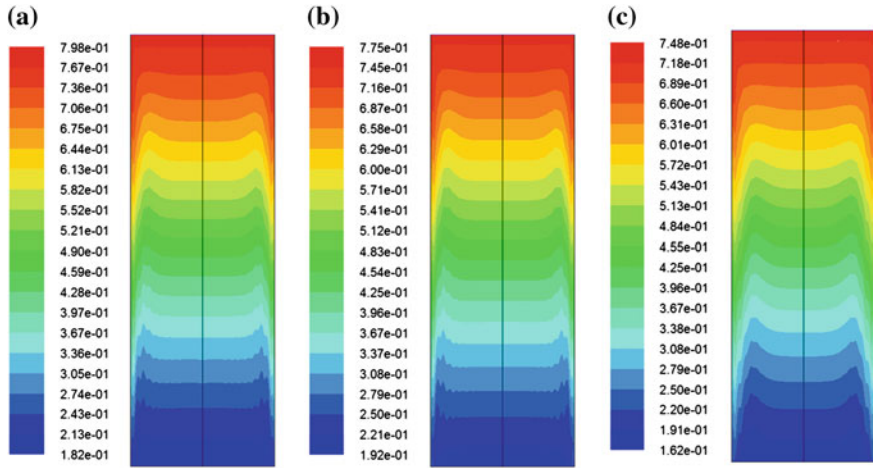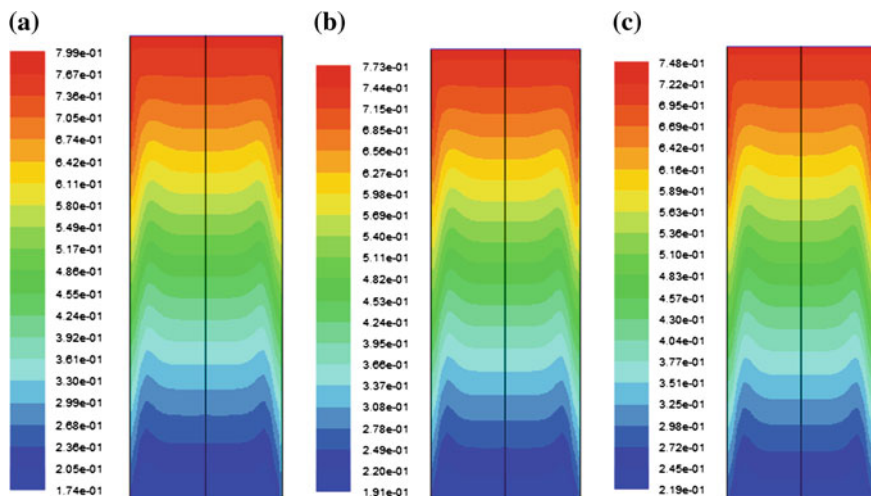
Fig. 4.40 Concentration profiles by hybrid Reynolds mass flux model **a** $F = 0.758$ m s^{-1} (kg m^{-3})$^{0.5}$, **b** $F = 1.02$ m s^{-1} (kg m^{-3})$^{0.5}$, and **c** $F = 1.52$ m s^{-1} (kg m^{-3})$^{0.5}$ (reprinted from Ref. [7], Copyright 2011, with permission from Elsevier)
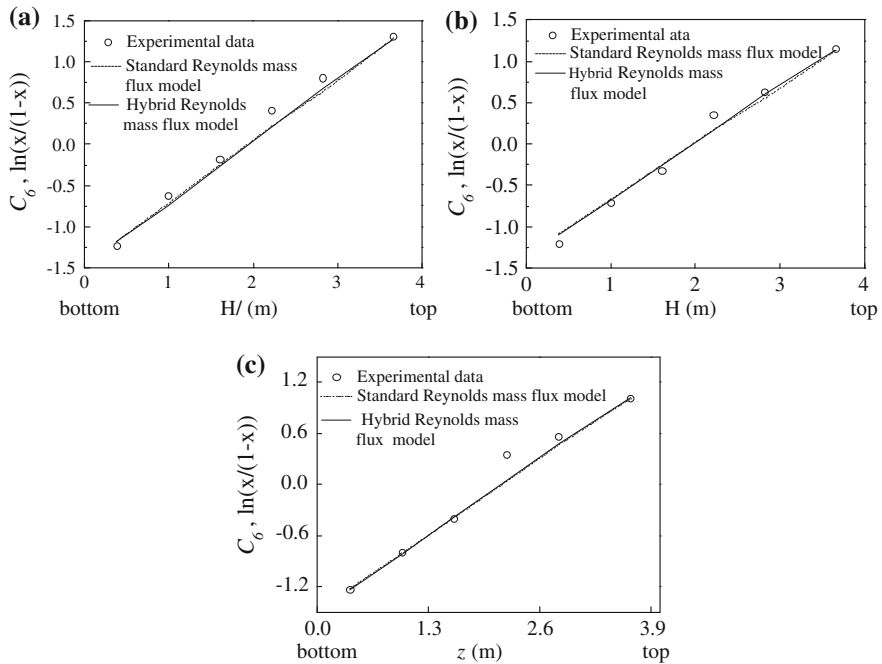
Fig. 4.41 Comparison between standard and hybrid Reynolds mass flux models with experimental data [16]. **a** $F = 0.758$ m s^{-1} (kg m^3)$^{0.5}$, **b** $F = 1.02$ m s^{-1} (kg m^3)$^{0.5}$, and **c** $F = 1.52$ m s^{-1} (kg m^3)$^{0.5}$
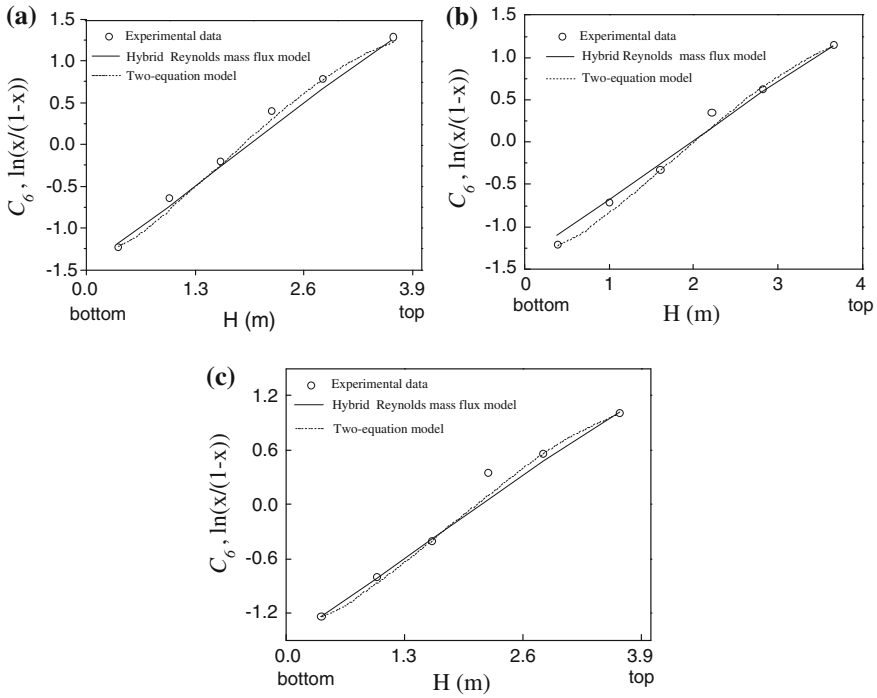
Fig. 4.42 Comparison of hybrid Reynolds model and two-equation model with experimental data. **a** $F = 0.758$ m s^{-1} (kg m^{-3}), **b** $F = 1.02$ m s^{-1} (kg m^{-3}), and **c** $F = 1.52$ m s^{-1} (kg m^{-3}) (reprinted from Ref. [7], Copyright 2011, with permission from Elsevier)

Fig. 4.42. As shown from the figures, both show close to the experimental data and the one better than the other only in upper or lower part of the column.

The simulated HETP by hybrid Reynolds model is compared with that by two-equation model as shown in Fig. 4.43. The prediction by hybrid Reynolds model is better than two-equation model for low and high F factors, but not in the intermediate range.

4.2.2.3 Algebraic Reynolds Mass Flux Model

The model equations are the same as the standard Reynolds mass flux except $\overline{u'_{Li}u'_{Lj}}$ and $\overline{u'_{Li}c'}$ equations are changed to the following algebraic form:

Fig. 4.43 HETP by hybrid Reynolds mass flux model and two-equation model (reprinted from Ref. [7], Copyright 2011, with permission from Elsevier)
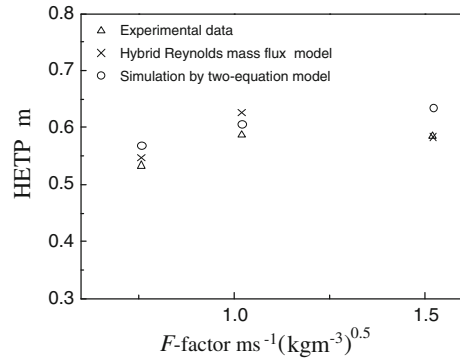
$$\overline{u'_{\mathrm{L}i}u'_{\mathrm{L}j}} = -\frac{k}{C_1\varepsilon}\left(\overline{u'_{\mathrm{L}j}u'_{\mathrm{L}k}}\frac{\partial U_{\mathrm{L}j}}{\partial x_k} + \overline{u'_{\mathrm{L}j}u'_{\mathrm{L}k}}\frac{\partial U_{\mathrm{L}i}}{\partial x_k}\right)$$
$$-\frac{k_{\mathrm{L}}C_2}{C_1\varepsilon_{\mathrm{L}}}\left(\overline{u'_{\mathrm{L}i}u'_{\mathrm{L}k}}\frac{\partial U_{\mathrm{L}j}}{\partial x_k} + \overline{u'_{\mathrm{L}j}u'_{\mathrm{L}k}}\frac{\partial U_i}{\partial x_k} - \frac{2}{3}\overline{u'_{\mathrm{L}i}u'_{\mathrm{L}k}}\frac{\partial U_{\mathrm{L}i}}{\partial x_k}\delta_{ij}\right) \quad (1.24)$$
$$+\frac{2}{3}\frac{1}{C_1}k_{\mathrm{L}}\delta_{ij}$$

where $C_k = 0.09$, $C_1 = 2.3$, $C_2 = 0.4$.

$$\overline{u'_{\mathrm{L}i}c'} = -\frac{k}{C_{c2}\varepsilon}\left(\overline{u'_{\mathrm{L}i}u'_{\mathrm{L}j}}\frac{\partial C}{\partial x_j} + \overline{u'_{\mathrm{L}i}c'}\frac{\partial U_{\mathrm{L}i}}{\partial x_j}\right) + \frac{C_{c3}k_{\mathrm{L}}}{C_{c2}\varepsilon_{\mathrm{L}}}\overline{u'_{\mathrm{L}i}c'}\frac{\partial U_{\mathrm{L}i}}{\partial x_j} \quad (3.27)$$

where $C_2 = 3.2$, $C_3 = 0.55$.

The simulated C_6 concentration profiles of the whole column are shown in Fig. 4.44, which is substantially identical with Fig. 4.40 by hybrid Reynolds mass flux model simulation.

The verification of algebraic Reynolds mass flux model as well as the comparison with hybrid model is shown in Fig. 4.45. At low F factor, these two models are in agreement with experiment, but at high F factor the algebraic Reynolds mass flux model shows greater deviation from the experimental data.

4.3 Separation of Benzene and Thiophene by Extractive Distillation

Extractive distillation is frequently employed for the separation of mixture with close boiling point. It features by adding an extractive agent to increase the relative volatility of the mixture concerned so as to make the separation easier with less number of theoretical plates or transfer unit required. Liu et al. [37] employed this process for the separation of benzene (boiling point 80.09 °C) and thiophene (boiling point 84.16 °C) in a packed column with N-methyl-2-pyrrolidone (NMP) as the extractive agent. The flow sheet is shown schematically in Fig. 4.46.

Fig. 4.44 Concentration profiles by using algebraic Reynolds mass flux model **a** $F = 0.758$ m s^{-1} (kg m^3)$^{0.5}$, **b** $F = 1.02$ m s^{-1} (kg m^3)$^{0.5}$, and **c** $F = 1.52$ m s^{-1} (kg m^3)$^{0.5}$ [16]
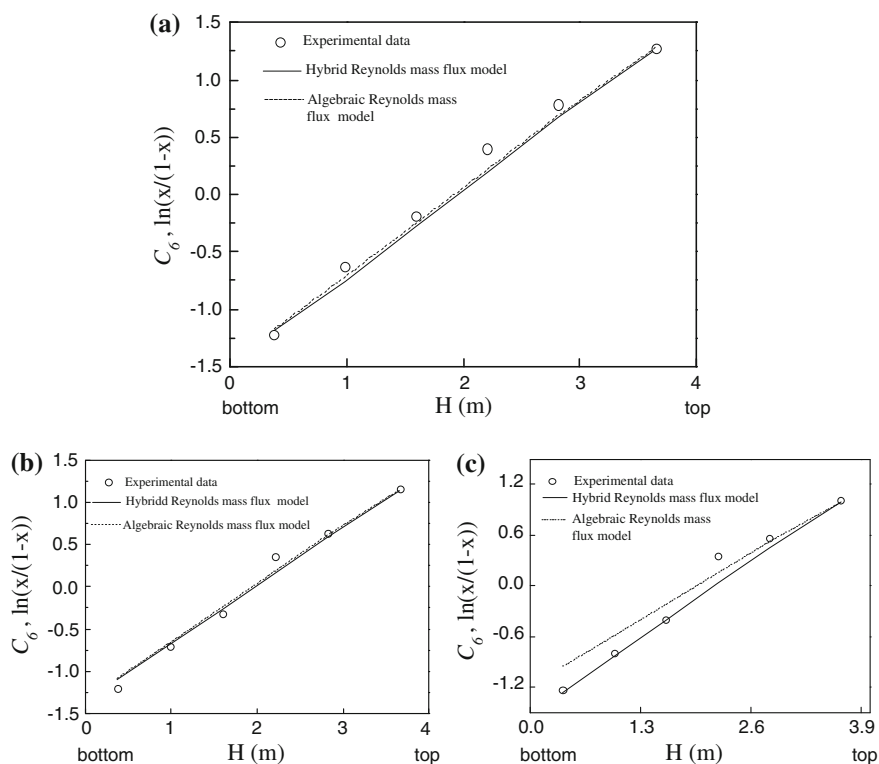
Fig. 4.45 Comparison of algebraic and hybrid Reynolds mass flux models with experimental data, **a** F factor $= 0.758$ m s^{-1} (kg m^{-3})$^{0.5}$, **b** F factor $= 1.02$ m s^{-1} (kg m^{-3})$^{0.5}$, and **c** F factor $= 1.52$ m s^{-1} (kg m^{-3})$^{0.5}$ [16]
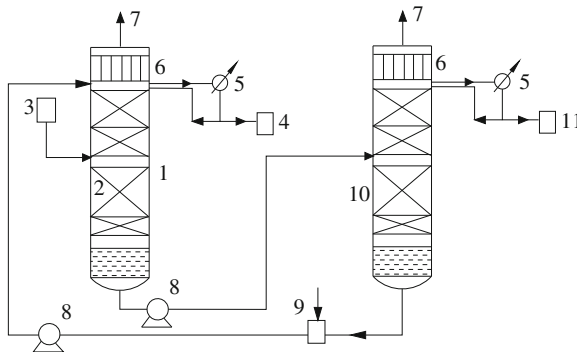
Fig. 4.46 Experimental installation of extractive distillation (*1* extractive distillation column, *2* packing, *3* feed tank, *4* product tank, *5* condenser, *6* partial condenser, *7* vent, *8* pump, *9* extractive agent tank, *10* extractive agent recovery column, and *11* recovered extractive agent tank) (reprinted from Ref. [16], Copyright 2011, with permission from CIESC)

The extractive column was 0.19 m in diameter, packed with 2×2 mm stainless θ rings packing. The column consisted four sections of 700, 600, 1,000, and 4,000 mm packing, respectively, in sequence from the column top. The operating pressure was 101.325 kPa. The extractive agent, NMP, was introduced at the column top at 2.4 ml/min, and the feed containing 90 % benzene and 10 % NMP was entered between sections 2 and 3 at 0.4 ml/min. The operating reflux ratio was 20:1 where about 99 % benzene was drawn as top product at 0.4 ml per min and the bottom product was about 5 % thiophene.

Model equations

The model equations and boundary conditions are the same as given in Sect. 4.1.1.1 except the source terms should be revaluated.

1. The source term S_m

Since the molecular weight of benzene (78) is close to that of thiophene (84), the mass transfer in distillation do not change substantially the amount of liquid phase in the process, we may let

$$S_m = 0$$

2. Source term S_n

The rate of mass transfer for benzene can be calculated by the following equations:

$$S_{n,B} = k_L a_{eff} M_B X (x_B - x_{B,i})$$
$$S_{n,B} = k_G a_{eff} M_B Y (y_{B,i} - y_B)$$

Table 4.7 Antoine constants

Material	Const.				
	a_1	a_2	a_3	a_4	a_5
Benzene	31.772	−2725.4	−8.4443	-5.3534×10^{-09}	2.7187×10^{-06}
Thiophene	36.602	−2979.4	−10.104	1.1445×10^{-09}	3.2472×10^{-06}

where subscript B refers to benzene and subscript i refers to interface; M_B is kg per mole of benzene; X and Y are the total moles of mixture in liquid and vapor phases, respectively; x and y are the mole fractions; the interfacial $x_{B,i}$ and $y_{B,i}$ are in equilibrium obeying the relationship at constant relative volatility α_{re}:

$$y_{B,i} = \frac{\alpha_{re}x_{B,i}}{1 + (\alpha_{re} - 1)x_{B,i}}$$

Since the system concerned is non-ideal, the α_{re} is calculated by thermodynamics as follows:

$$\alpha_{re} = \frac{y_B/x_B}{y_T/x_T} = \frac{\gamma_B p_B^0}{\gamma_T p_T^0}$$

where γ and p^0 are, respectively, the activity coefficients and vapor pressures; subscripts B and T refer to benzene and thiophene, respectively. The vapor pressure p^0 is calculated by Antoine equation [38] as follows:

$$\log_{10} p^0 = a_1 + a_2/T + a_3 \log_{10} T + a_4 T + a_5$$

The constants are given in Table 4.7.

The activity coefficients γ_A and γ_B are calculated using Wilson model [39]:

$$\ln \gamma_i = 1 - \ln\left(\sum_j A_{ij}x_j\right) - \sum_j \frac{A_{ij}x_j}{\sum_k A_{jk}x_k}$$
$$\ln A_{ij} = a_{ij} + b_{ij}/T$$

where a_{ij} and b_{ij} are given in Table 4.8.

After combining foregoing equations, we yield the equation for S_n as follows:

$$m_0 S_{n,B}^2 + m_1 S_{n,B} + m_2 = 0 \tag{A}$$

where m_0, m_1, and m_2 are

$$m_0 = \frac{\alpha_{re} - 1}{k_L k_G M_B^2 a_{eff}^2 XY}$$
$$m_1 = \frac{(\alpha_{re} - 1)y_B - \alpha_{re}}{k_L a_{eff} M_B X} - \frac{(\alpha_{re} - 1)x_B + 1}{k_G a_{eff} M_B Y}$$
$$m_2 = \alpha_{re}x_B - ((\alpha_{re} - 1)x_B + 1)y_B$$

Table 4.8 Wilson parameters

Term	Value		
Component i	Benzene	Benzene	Thiophene
Component j	Thiophene	NMP	NMP
a_{ij}	7.0499	2.5723	0
a_{ji}	−4.6713	−2.7964	0
b_{ij}	−2452.1033	−1041.9158	−290.8908
b_{ji}	1610.3286	1002.4481	146.9923

where the mass transfer coefficients k_L, k_G can be calculated by the correlations by Wagner [33] as shown in Sect. 4.2.1.3; the effective interfacial area a_{eff} is obtained by using Onda correlation given in Sect. 4.1.1.1.

In finding k_L and k_G, the molecular diffusivity of benzene in gas and liquid phases are calculated by the correlations given by Fuller and Perkins, respectively [40]. The viscosities of benzene and thiophene are obtained from Perry Handbook [41].

Then, the source term $S_n(S_{nB})$ can be calculated by solving the aforementioned Eq. (A).

Interacting force FLG between two phases

The vapor liquid interacting force can be measured by the pressure drop Δp of the vapor through the packing. For the 2×2 stainless θ rings, Chang et al. [42] proposed a correlation for the Δp_w of gas flowing through wetted packing as follows:

$$\frac{\Delta p_w}{Z} = 300 \times 10^{90 U_{L,s}} \left(\frac{a_T}{\gamma^3}\right)^{0.3} \left(\sqrt{\rho_G U_{G,s}^2}\right)^{1.5}$$

Under the condition of no liquid flow, the Δp of gas flowing through dry packing Δp_d is

$$\frac{\Delta p_d}{Z} = 300 \left(\frac{a_T}{\gamma^3}\right)^{0.3} \left(\sqrt{\rho_G U_{G,s}^2}\right)^{1.5}$$

Thus, the Δp_L due to the vapor liquid interaction can be

$$\frac{\Delta p_L}{Z} = 300 \times \left(10^{90 U_{L,s}} - 1.0\right) \left(\frac{a_T}{\gamma^3}\right)^{0.3} \left(\sqrt{\rho_G U_{G,s}^2}\right)^{1.5}$$

Consequently the vapor–liquid interacting force can be expressed as

$$\mathbf{F}_{LG} = \frac{\Delta p_L}{\left|\mathbf{U}_{slip}\right|} \mathbf{U}_{slip}$$
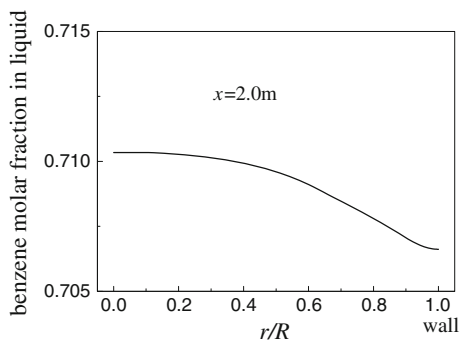
where the slip velocity $\mathbf{U}_{slip}$ is equal to the difference between the average gas velocity $\mathbf{U}_G$ and liquid velocity $\mathbf{U}$:

$$\mathbf{U}_{slip} = \mathbf{U}_G - \mathbf{U}$$

Simulation results and verification

Under the reflux ratio of 20:1, the simulated concentration distribution of benzene at $x = 0.2$ m (measured from column top) is given in Fig. 4.47. As shown in these figures, the concentrations of benzene are gradually lowering toward the column wall due to the velocity is decreased and the boundary condition is set zero mass flux at the wall, while the concentration of NMP is increasing (Fig. 4.47).

The radial concentrations of benzene were averaged at each x to obtain the average benzene concentrations along the column height as shown in Fig. 4.48.

In Fig. 4.48, the benzene concentration is suddenly increase at about $x = 1.3$ m due to adding the feed at this point with 90 % benzene. The simulated result is roughly in agreement with the experimental data although the former shows about half percent higher than the latter. Such discrepancy is probably due to the inaccuracy of α_{re} predicted by thermodynamic model.

4.4 Summary

The simulation of distillation process is described for tray column and packed column by using CMT models. The simulated results are presented and compared with published experimental data.

1. Tray column. Both $\overline{c'^2}$-$\varepsilon_{c'}$ model and Reynolds mass flux model are used for simulating an industrial-scale tray distillation column to obtain the outlet concentration of each tray and the individual tray efficiency. Both simulated results are in agreement with the experimental measurement. Precisely, only the standard Reynolds mass flux model can give the details of circulating flow contours in the segmental area of the tray. It indicates the superiority of the anisotropic standard Reynolds mass flux model over the others. Furthermore, the prediction of tray efficiency with different tray structures by CMT model as illustrated in this chapter is helpful for selecting the optimal one by the designer. The prediction of tray efficiency for multicomponent system and the bizarre phenomena is also described.
2. Packed column. The simulated packed column is 1.22 m in diameter and 3.66-m height packed with Pall ring. Both $\overline{c'^2}$-$\varepsilon_{c'}$ model and Reynolds mass flux model (including standard, hybrid, and algebraic model forms) give satisfactory results in comparison with published experimental data in axial concentration distribution and HETP.

References

1. Bennet DL, Agrawal R, Cook PJ (1983) New pressure drop correlation for sieve tray distillation columns. AIChE J 29(434):442
2. Sakata M, Yanagi T (1979) Performance of a commercial scale sieve tray. In: Institution of chemical engineers symposium series, (3.2):21–34
3. Kunesh JG, Ognisty TP, Sakata M, Chen GX (1996) Sieve tray performances for steam stripping toluene from water in a 4-ft diameter column. Ind Eng Chem Res 35:2660–2671
4. Sun ZM, Liu BT, Yuan XG, Yu KT (2005) New turbulent model for computational mass transfer and its application to a commercial-scale distillation column. Ind Eng Chem Res 44(12):4427–4434
5. Sun ZM, Yu KT, Yuan XG, Liu CJ (2007) A modified model of computational mass transfer for distillation column. Chem Eng Sci 62:1839–1850
6. Sun ZM, Liu CJ, Yu GC, Yuan XG (2011) Prediction of distillation column performance by computational mass transfer method. Chin J Chem Eng 19(5):833–844
7. Li WB, Liu BT, Yu KT, Yuan XG (2011) A new model for the simulation of distillation column. Chin J Chem Eng 19(5):717–725
8. Zhang MQ, Yu KT (1994) Simulation of two dimensional liquid phase flow on a distillation tray. Chin J of Chem Eng 2(1):63–71
9. AIChE Research Committee (1958) Bubble tray design manual. AIChE, New York
10. Krishna R, van Baten JM, Ellenberger J, Higler AP, Taylor R (1999) CFD simulations of sieve tray hydrodynamics. Chem Eng Res Des, Trans Inst Chem Eng Part A 77:639–646

11. Dai GC, Chen MH (1988) Fluid dynamics in chemical engineering. Chemical Industry Press, Beijing
12. Leboeuf F, Huang GP, Kulisa P et al (1991) Model and computation of discrete jets in crossflow. Eur J Mech B-fluid 10(6):629–650
13. Zuiderweg FJ (1982) Sieve tray: a view on the state of the art. Chem Eng Sci 37:1441–1464
14. Nallasamy M (1987) Turbulence models and their applications to the prediction of internal flows: a review. Comput Fluids 15(2):151–194
15. Cai TJ, Chen GX (2004) Liquid back-mixing on distillation trays. Ind Eng Chem Res 43(10):2590–2597
16. Li WB (2012) Theory and application of computational mass transfer for chemical engineering processes. PhD dissertation, Tianjin University
17. Sun ZM (2005) Study on computational mass transfer in chemical engineering. PhD dissertation, Tianjin University
18. Murphree EV (1925) Rectifying column calculations. Ind Eng Chem 17(7):747–750
19. Hausen H (1953) A definition of exchange efficiency of rectifying plates for binary and ternary mixtures. Chem Ind Tech 25:595
20. Standard G (1965) Studies on distillation-V: generalized definition of a theoretical plate or stage of contacting equipment. Chem Eng Sci 20(6):611–622
21. Holland CD, McMahon KS (1970) Comparison of vaporization efficiencies with Murphree-type efficiencies in distillation-I. Chem Eng Sci 25(3):431–436
22. Oldershaw C (1941) Perforated plate columns for analytical batch distillations. Ind Eng Chem Anal Ed 13(4):65–268
23. Kalbassi MA, Biddulph MW (1987) A modified Oldershaw column for distillation efficiency measurements. Ind Eng Chem Res 26(6):1127–1132
24. Wang ZC (1997) Non-ideal multi-component mass transfer and point efficiency on a sieve tray. PhD dissertation, Tianjin University
25. Hai NT (1980) PhD dissertation, The University of New South Wales, Australia
26. Calderbank PH, Moo-Young M (1960) The mass transfer efficiency of distillation and gas absorption plate columns. Part 2. Inst Chem Eng Symp Ser 6:59
27. Geary NW, Rice RG (1991) Bubble size prediction for rigid and flexible spargers. AIChE J 37(2):161–168
28. Hesketh RP, Fraser Russell TW, Etchells AW (1987) Bubble size in horizontal pipelines. AIChE J 33(4):663–667
29. Sharma MM, Gupta RK (1967) Mass transfer characteristics of plate columns without downcomer. Trans Inst Chem Eng 45(1):T169–T175
30. Zaritsky NE, Calvelo A (1979) Internal mass transfer coefficient within single bubbles. Theory and experiment. Can J Chem Eng 57:58–64
31. Prado M, Fair JR (1990) Fundamental model for the prediction of sieve tray efficiency. Ind Eng Chem Res 29(6):1031–1042
32. Liu GB, Yu KT, Yuan XG, Liu CJ (2009) A numerical method for predicting the performance of a randomly packed distillation column. Int J Heat Mass Tran 52:5330–5338
33. Wagner I, Stichlmair J, Fair JR (1997) Mass transfer in beds of modern, high-efficiency random packings. Ind Eng Chem Res 36:227–237
34. Ergun S (1952) Fluid flow through packed columns. Chem Eng Prog 48:89–94
35. Engel V, Stichmair J, Geipel W (1997) A new model to predict liquid holdup in packed columns-using data based on capacitance measurement techniques. In: Institution of chemical engineers symposium series, pp 939–947
36. Stichlmair J, Bravo JL, Fair JR (1989) General model for prediction of pressure drop and capacity of countercurrent gas/liquid packed columns. Gas Separ Purif 3(3):19–28
37. Liu GB, Liu BT, Yuan XG, Zeng AW, Yu KT (2010) Computational mass transfer simulation of extractive distillation and its experimental confirmation. CIESC J 61(7):1809–1814
38. Zhang SQ (1986) Chemical engineering handbook. Shandong Science and Technology Press

39. Wilson GM (1964) Vapor-liquid equilibrium. XI. A new expression for the excess free energy of mixing. J Am Chem Soc 86(2):127–130
40. Poling BE, Prausnitz JM, Connell JT (2001) The properties of gases and liquids. McGraw Hill, New York
41. Perry RH, Green DW (2001) Perry's chemical engineers handbook. McGraw Hill, New York
42. Chang YL, Feng QH, Kun Z (2004) Hydromechanical performance measurement and comparison of four species of mini type packings. Chin J Process Eng 4(6):496–501
43. Raper JA, Kearney MS, Burgess JM et al (1982) The structure of industrial sieve tray froths. Chem Eng Sci 37(4):501–506

Chapter 5
Application of Computational Mass Transfer (II): Chemical Absorption Process

Abstract In this chapter, the two CMT models, i.e., $\overline{c'^2} - \varepsilon_{c'}$ model and Reynolds mass flux model (in standard, hybrid, and algebraic forms) are used for simulating the chemical absorption of CO_2 in packed column by using MEA, AMP, and NaOH separately and their simulated results are closely checked with the experimental data. It is noted that the radial distribution of D_t is similar to α_t but quite different from μ_t. It means that the conventional assumption on the analogy between the momentum transfer and the mass transfer in turbulent fluids is unjustified, and thus, the use of CMT method for simulation is necessary. In the analysis of the simulation results, some transport phenomena are interpreted in terms of the co-action or counteraction of the turbulent mass flux diffusion.

Nomenclature

a	Surface area per unit volume of packed bed, m^{-1}
a_{eff}	Effective area for mass transfer between the gas phase and liquid phase, 1/m
a_w	Wetted surface area, m^{-1}
$\overline{c^2}$	Concentration variance, $kg^2 \, m^{-6}$
$\overline{C}$	Average concentration of mass fraction, $kg \, m^{-3}$
C_μ, c_1, c_2	Model parameters in $k - \varepsilon$ model equations, dimensionless
$C_{c0}, C_{c1}, C_{c2}, C_{c3}$	Model parameters in $\overline{c^2} - \varepsilon_c$ model equations, dimensionless
C_p	Liquid-phase specific heat, J/kg/K
$C_{t0}, C_{t1}, C_{t2}, C_{t3}$	Model parameters in $\overline{t^2} - \varepsilon_t$ model equations, dimensionless
D	Molecular diffusivity, $m^2 \, s^{-1}$
D_{eff}	Effective diffusivity, $m^2 \, s^{-1}$
D_G	Molecular diffusivity of CO_2 in gas phase, $m^2 \, s^{-1}$
D_t	Turbulent diffusivity for mass transfer, $m^2 \, s^{-1}$
d_e	Equivalent diameter of random packing, m

d_H	Hydraulic diameter of random packing, m
d_p	Nominal diameter of the packed particle, m
E	Enhancement factor, dimensionless
G	Gas-phase flow rate per unit cross-sectional area, kg m^2 s^{-1}
H_A	Physical absorption heat of mol CO_2 absorbed, J kmol^{-1}
H_R	Chemical reaction heat of mol CO_2 absorbed, J kmol^{-1}
H_s	Static holdup, dimensionless
H_t	Total liquid holdup, dimensionless
k	Turbulent kinetic energy, m^2/s^2
k_2	Second-order reaction rate constant, m^3 kmol s^{-1}
k_G	Gas-phase mass transfer coefficient, kmol m s kPa^{-1}
k_L	Liquid-phase mass transfer coefficient without chemical reaction, m s^{-1}
$k_{R,L}$	Liquid-phase mass transfer coefficient with chemical reaction, m s^{-1}
L	Liquid flow rate per unit cross-sectional area, kg m^2 s^{-1}
R	Position in radial direction, m
Rc	The rate of reaction, kmol m^3 s^{-1}
r	Radius of the column, m
$\overline{t^2}$	Temperature variance, dimensionless
T	Liquid temperature, K
U	Liquid superficial velocity, m s^{-1}
X	Molar concentration in the liquid bulk, kmol m^{-3}
X_i	Molar concentration at interface, kmol m^{-3}
x	Distance measured from column top ($x = 0$ at the column top), m
α, α_{eff}, α_t	Molecular, turbulent, and effective thermal diffusivities, respectively, m^2 s^{-1}
β	Volume fraction of liquid phase based on pore space, dimensionless
ε	Turbulent dissipation rate, m^2 s^{-3}
ε_c	Turbulent dissipation rate of concentration fluctuation, kg^2 m^{-6} s^{-1}
ε_t	Turbulent dissipation rate of temperature fluctuation, s^{-1}
Φ	Variable, dimensionless
v_t	Turbulent diffusivity, m^2 s^{-1}
ρ	Liquid density, kg/m^3
ρ_G	Gas-phase density, kg/m^3
σ	Surface tension of aqueous solutions, dynes/cm, or N/m
σ_c, σ_{ε_c}	Model parameters in $\overline{c^2} - \varepsilon_c$ model equations, dimensionless
σ_t, σ_{ε_t}	Model parameters in $\overline{t^2} - \varepsilon_t$ model equations, dimensionless
σ_k, σ_ε	Model parameters in $k - \varepsilon$ model equations, dimensionless

Gas absorption is an important separation process commonly employed in chemical production. The processing gas usually is a mixture containing absorbate (component species) which is being absorbed by a liquid absorbent. If the absorbent and the absorbate are undergoing chemical reaction, it is chemical absorption; otherwise, it is physical absorption.

The absorption of CO_2 from flue gas is a typical chemical absorption, which has been becoming the focus of research nowadays by scientists and chemical engineers due to the environmental consideration. Many absorbents can be used for CO_2 absorption, among them the derivatives of amine are commonly used in the industries, such as monoethanolamine (MEA), 2-amino-2-methyl-1-propanol (AMP), diethanolamine (DEA), and methyldiethanolamine (MDEA). The reaction between CO_2 and the amine is reversible, and the CO_2 absorbed by amine can be easily desorbed by heating or other means to make the amine easily to be reused in a recycling process.

The operation of gas absorption is mostly countercurrent, that is, the gas entering to the bottom of the column and the liquid flowing down from the top. There are two usual kinds of equipment for absorption: packed column and tray column. The former is most frequently used in industries, and thus, it will be the object of simulation in this chapter.

Chemical reaction is accompanied with heat effect, and the model equation sets should involve the heat transfer besides the mass transfer and fluid flow.

Over the last decades, the application of computational fluid dynamics (CFD) to study the velocity and temperature profiles in packed column has been frequently reported [1–5]. However, for the prediction of concentration profile, the method commonly employed is by guessing an empirical turbulent Schmidt number Sc_t or by using experimentally determined turbulent mass diffusivity D_t obtained by using the inert tracer technique under the condition of no mass transfer [6, 7]. Nevertheless, the use of such empirical methods of computation, as pointed out in Chap. 3, is unreliable and not always possible. To overcome these drawbacks, the development of rigorous mathematical model is the best choice.

In this chapter, the work by Liu et al. [8, 9], Li [10] on the absorption of CO_2 by the aqueous solution of MEA, AMP, and NaOH is used as an example to show the prediction of absorption behaviors by using computational mass transfer model, and also the model predictions are tested by comparing with the published experimental data.

5.1 $\overline{c'^2} - \varepsilon_c$ Two-Equation Model

The interacted liquid-phase $\overline{c'^2} - \varepsilon_c$ two-equation model (abbreviated as two-equation model hereafter) under steady operating condition is employed for the simulation of CO_2 absorption by aqueous absorbent with the following assumptions:

1. Only the CO_2 component in the gas phase is absorbed by the aqueous solution, and the water in aqueous absorbent does not vaporize to gas phase.
2. The heat of absorption and heat of reaction are all absorbed instantaneously by liquid phase. The heat conduction by the packing is negligible.
3. The heat loss to the environment is neglected.
4. The packed column for absorption is axially symmetrical.

The model equations involve fluid dynamics, heat transfer, and mass transfer equation sets as given below.

a. The CFD equation set

Overall mass conversation

$$\frac{\partial(\rho_L \gamma \beta_L U_{Li})}{\partial x_i} = S_m \tag{1.3b}$$

where γ is the porosity of the packed bed and β_L is the volume fraction of liquid in the porous space. Note that in absorption process, the mass of absorbent is changed due to the absorption of absorbate (species); therefore, $S_m \neq 0$ and ρ is not a constant. The liquid faction β_L is considered constant in the column.

Momentum conversation

$$\frac{\partial\left(\rho_L \gamma \beta_L U_{Li} U_{Lj}\right)}{i} = -\gamma\beta_L \frac{\partial P}{j} + \frac{\partial}{\partial x_i}\left[\gamma\beta_L\mu_L\left(\frac{\partial U_{Lj}}{\partial x_i}\right) - \gamma\beta_L\rho_L\overline{u_i'u_j'}\right] + S_{Li}$$

$$-\rho_L\overline{u_i'u_j'} = \mu_t\left(\frac{\partial U_{Li}}{\partial x_j} + \frac{\partial U_{Lj}}{\partial x_i}\right) - \frac{2}{3}\rho\delta_{ij}k_L \tag{1.4b}$$

$$\mu_t = \mu\frac{k_L^2}{\varepsilon_L}$$

K_L *equation*

$$\frac{\partial(\rho_L \gamma \beta_L U_{Li} k_L)}{\partial x_i} = \frac{\partial}{\partial x_i}\left(\gamma\beta_L\left(\mu_L + \frac{\mu_t}{\sigma_k}\right)\frac{\partial k_L}{\partial x_i}\right) + \rho_L\gamma\beta_L G_k - \rho_L\gamma\beta_L\varepsilon_L$$

$$G_k = \mu_t\left(\frac{\partial U_{Lj}}{\partial x_i} + \frac{\partial U_{Li}}{j}\right)\frac{\partial U_{Li}}{\partial x_k}$$

ε_L *equation*

$$\frac{\partial\rho_L\gamma\beta_L U_i\varepsilon_L}{\partial x_i} = \frac{\partial}{\partial x_i}\left[\gamma\beta_L\left(\mu + \frac{\mu_t}{\sigma_\varepsilon}\right)_L\frac{\partial\varepsilon_L}{\partial x_i}\right] + \gamma\beta_L(C_{1\varepsilon}G_{Lk} - C_{2\varepsilon}\rho_L\varepsilon_L)\frac{\varepsilon_L}{k_L}$$

Model constants are the following [11]: $c_\mu = 0.09$, $\sigma_k = 1.0$, $\sigma_\varepsilon = 1.3$, $C_1 = 1.44$, and $C_2 = 1.92$.

b. The heat transfer equation set

Energy conservation

$$\frac{\partial(\rho_L\gamma\beta_L C_p U_{Li} T)}{\partial x_i} = \frac{\partial}{\partial x_i}\left(\rho_L\gamma\beta_L C_p(\alpha + \alpha_t)\frac{\partial T}{\partial x_i}\right) + S_T$$

where C_p is the specific heat of the fluid; S_T is the source term; α and α_t are, respectively, the molecular diffusivity and turbulent thermal diffusivity. The source term S_T represents heat of solution and reaction as well as other thermal effects. The unknown α_t is obtained by using $\overline{T'^2} - \varepsilon_{T'}$ model, in which

$$\alpha_t = C_{T0}k\left[\frac{k}{\varepsilon}\frac{\overline{T'^2}}{\varepsilon_{T'}}\right]^{1/2}$$

$\overline{T'^2}$ *equation*

$$\frac{\partial\left(\rho_L\gamma\beta_L U_{Li}\overline{T'^2}\right)}{\partial x_i} = \frac{\partial}{\partial x_i}\left[\rho_L\gamma\beta_L\left(\alpha + \frac{\alpha_t}{\sigma_{T'}}\right)\frac{\partial\overline{T'^2}}{\partial x}\right] - 2\rho_L\alpha_t\left(\frac{\partial T}{\partial x_i}\right)^2 - 2\rho_L\gamma\beta_L\varepsilon_{T'}$$

$\varepsilon_{T'}$ *equation*

$$\frac{\partial(\rho_L\gamma\beta_L U_{Li}\varepsilon_{T'})}{\partial x_i} = \frac{\partial}{\partial x_i}\left[\rho_L\gamma\beta_L\left(\alpha + \frac{\alpha_t}{\sigma_{\varepsilon_{T'}}}\right)\frac{\partial\varepsilon_{T'}}{\partial x_i}\right] - C_{T1}\rho_L\alpha_t\left(\frac{\partial T}{\partial x_i}\right)^2\frac{\varepsilon_{T'}}{\overline{T'^2}} - C_{T2}\gamma\beta_L\frac{\varepsilon_{T'}^2}{\overline{T'^2}}$$
$$- C_{T3}\gamma\beta_L\frac{\varepsilon\varepsilon_{T'}}{k}$$

Model constants are the following: $C_{T0} = 0.10$, $C_{T1} = 1.8$, $C_{T2} = 2.2$, $C_{T3} = 0.8$, and $\sigma_t = 1.0$.

c. The mass transfer equation set

Species mass conservation

$$\frac{\partial(\rho_L\gamma\beta_L U_{Li} C)}{\partial x_i} = \frac{\partial}{\partial x_i}\left(\rho_L\gamma\beta_L(D_L + D_t)\frac{\partial C}{\partial x_i}\right) + S_n$$

For finding turbulent mass diffusivity D_t, the $\overline{c'^2} - \varepsilon_{c'}$ two-equation model is employed.

$$D_t = c_{c0}k\left(\frac{k}{\varepsilon}\frac{\overline{c'^2}}{\varepsilon_{c'}}\right)$$

$\overline{c'^2}$ *equation*

$$\frac{\partial\left(\rho_L\gamma\beta_L U_{Li}\overline{c'^2}\right)}{\partial x_i} = \frac{\partial}{\partial x_i}\left[\rho_L\gamma\beta_L\left(D_L + \frac{D_t}{\sigma_c}\right)\frac{\partial\overline{c'^2}}{\partial x_i}\right] - 2\rho_L\gamma\beta_L D_t\left(\frac{\partial C}{\partial x_i}\right)^2 - 2\rho_L\gamma\beta_L\varepsilon_{c'}$$

$\varepsilon_{c'}$ *equation*

$$\frac{\partial\rho_L\gamma\beta_L U_{Li}\varepsilon_{c'}}{\partial x_i} = \frac{\partial}{\partial x_i}\left[\rho_L\gamma\beta_L\left(D_L + \frac{D_t}{\sigma_{\varepsilon_{c'}}}\right)\frac{\partial\varepsilon_{c'}}{\partial x_i}\right] - C_{c1}\rho_L\gamma\beta_L D_t\left(\frac{\partial C}{\partial x_i}\right)^2\frac{\varepsilon_{c'}}{\overline{c'^2}}$$
$$- C_{c2}\gamma\beta_L\frac{\varepsilon_{c'}^2}{\overline{c'^2}} - C_{c3}\gamma\beta_L\frac{\varepsilon\varepsilon_{c'}}{k}$$

Model constants are the following: $C_{c0} = 0.11$, $C_{c1} = 1.8$, $C_{c2} = 2.2$, $C_{c3} = 0.8$, and $\sigma_c = 1.0$.

The volume fraction β_L of the liquid phase is based on porous space, which can be expressed by $\beta_L = H_t/\gamma$ from the total liquid holdup H_t and the unevenly distributed porosity γ under the operating condition concerned. The total liquid holdup H_t is defined as the sum of the static holdup H_s and the operating holdup H_{op}, i.e., $H_t = H_s + H_{op}$. The correlations for estimating H_s and H_{op} for metal Pall rings are [12, 13]

$$H_s = 0.033\exp\left(-0.22\frac{g\rho}{\sigma a^2}\right)$$
$$H_{op} = 0.555\left(\frac{a\mu^2}{g\gamma^{4.55}}\right)^{1/3}$$

The porosity γ of randomly packed bed is a constant around the center and increases to a maximum in the neighborhood of the wall region, which had been observed by many experimental investigations [14–16]. Thus, the uneven porosity distribution is being considered and calculated by the following correlation reported by Liu [2]:

$$\gamma = \gamma_\infty + \frac{(1 - \gamma_\infty)}{2}\mathrm{Er}\left\{(1 - 0.3p_d) \times \cos\left(\frac{2\pi}{c_\gamma + 1.6\,\mathrm{Er}^2}\frac{R - r}{p_d d_p}\right) + 0.3p_d\right\}$$

where γ_∞ is the porosity of an unbounded packing, R is the radius of the column, r is the position in radial direction, and Er is the exponential decaying function as given by Wellek et al. [17]:

$$\mathrm{Er} = \exp\left[-1.2p_d\left(\frac{R - r}{d_p}\right)^{3/4}\right]$$

where p_d is the period of oscillation normalized by the nominal particle size and $p_d = 0.94 \times (2 + 1.414)/3$ for Pall rings; c_γ is a constant depending on the ratio of the particle size to column size as follows:

$$c_\gamma = \frac{2R}{n_\gamma p_d d_p} - 1.6 \exp\left[-2.4 p_d \left(\frac{R}{d_p}\right)^{3/4}\right]$$

where

$$n_\gamma = \text{int}\left\{\frac{2}{1 + 1.6 \exp\left[-2.4 p_d \left(R/d_p\right)^{3/4}\right]} \frac{R}{p_d d_p}\right\}$$

Boundary condition
Inlet (column top, $x = 0$):
For fluid flow, $U = U_{\text{in}}$, $V = 0$, $T = T_{\text{in}}$, and $C_i = C_{i,\text{in}}$

$$k_{\text{in}} = 0.003\, U_{\text{in}}^2$$

$$\varepsilon_{\text{in}} = 0.09 \frac{k_{\text{in}}^{1.5}}{d_H}$$

For $\overline{T'^2}$, the work by Ferchichi and Tavoularis [18] is adopted:

$$\overline{T_{\text{in}}'^2} = (0.082\, \Delta T)^2 = 0.0067 (\Delta T)^2$$

where $\Delta T = 0.1 K$ is set as initial value.

For $\overline{c'^2}$, the analogy to heat transfer is applied:

$$\overline{c'^2} = \left(0.082 C_{i,\text{in}}\right)^2 = 0.0067 C_{i,\text{in}}^2$$

For $\varepsilon_{c'}$ and $\varepsilon_{T'}$, it is set to be

$$\varepsilon_{c'} = 0.4 \left(\frac{\varepsilon_{\text{in}}}{k_{\text{in}}}\right) \overline{c_{\text{in}}'^2}$$

$$\varepsilon_{T'} = 0.4 \left(\frac{\varepsilon_{\text{in}}}{k_{\text{in}}}\right) \overline{T_{\text{in}}'^2}$$

Outlet (column bottom): Assuming the fluid is fully developed to the turbulent state, the gradients of all parameters Φ along x direction is equal to zero except pressure:

$$\frac{\partial \Phi}{\partial x} = 0$$

Axial symmetry: At the center of the column ($y = 0$), symmetrical condition is set:

$$\frac{\partial \Phi}{\partial y} = 0$$

Column wall ($r = R$): No slip condition is set, and all parameters are equal to zero except pressure.

Near wall region: The standard wall function is applied.

5.1.1 Absorption of CO$_2$ by Aqueous MEA in Packed Column

5.1.1.1 Chemical Reaction Between CO$_2$ and Aqueous MEA

When CO_2 is being absorbed and reacts with aqueous MEA solutions, the following reactions are taking place:

$$CO_{2,g} \rightarrow CO_{2,L} + H_A \tag{R1}$$

$$CO_{2,L} + 2BNH_2 \xrightarrow{k_2} BNHCOO^- + BNH_3^+ + H_R \tag{R2}$$

$$CO_{2,L} + BNHCOO^- + 2H_2O \xrightarrow{k_2} BNH_3^+ + 2HCO_3^- \tag{R3}$$
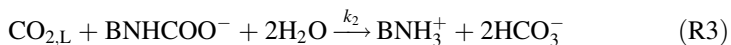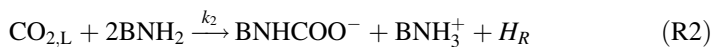
Letter B denotes the group $HOCH_2.CH_2^-$ and step (R1) represents the physical absorption of CO_2 by water, accompanied by the heat of solution H_A. At very short time of exposure in industrial practice, the effect of reaction (R3) can be neglected, and only reaction (R2) affects the absorption rate of CO_2. Reaction (R2) can be resolved to two steps:

$$CO_{2,L} + BNH_2^- \longrightarrow BNHCOO^- + H^+ \tag{R4}$$

$$BNH_2 + H^+ \longrightarrow BNH_3^+ \tag{R5}$$
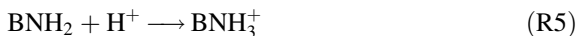
Reaction (R4) can be considered as second order, which is the rate-controlling step, because reaction (R5) is a proton-transfer reaction and virtually instantaneous. Therefore, the absorption of CO_2 in MEA solutions can be regarded as gas absorption accompanied by a second-order reaction, and the overall reaction is represented by reaction (R2). The rate of reaction Rc can be expressed by the following equation:

$$Rc = k_2 \, [CO_2] \, [MEA]$$

where k_2 is the second-order reaction rate constant, which is given by Hikita et al. [19]

$$\log \ k_2 = 10.99 - \frac{2152}{T}$$

5.1.1.2 Evaluation of Source Terms

The source terms F_{LS} and F_{LG} in S_{Li} as well as β_L have been given in Sect. 4.2.1.

The source term S_m(Kg m^{-3}s^{-1}) represents the rate of CO_2 absorbed by the liquid phase, which can be calculated by the following mass transfer equation:

$$S_m = k_L a_e E \left(C^*_{CO_2} - C_{CO_2} \right)$$

where k_L is the liquid-phase mass transfer film coefficient (m^2 s^{-1}); a_e is the effective mass transfer area per unit volume (m^2 m^{-3}); E is the enhancement factor because of accompanying with chemical reaction; and $C^*_{CO_2}$ and C_{CO_2} are, respectively, the concentration of CO_2 in the interface and bulk liquid (kg m^{-3}). Enhancement factor E can be calculated by the correlation [17]

$$E = 1 + \left[\frac{1}{(E_i - 1)^{-1.35} + (E_1 - 1)^{-1.35}} \right]^{1/1.35}$$

$$E_i = 1 + \frac{D_{MEA,L} X_{MEA}}{2 D_{CO_2,L} X_{i,CO_2}}$$

$$Ha = \frac{D_{CO_2,L} k_2 X_{MEA}}{(k_L)^2}$$

$$E_1 = \frac{\sqrt{Ha}}{\tanh \sqrt{Ha}}$$

where X_{MEA} is the mole fraction of MEA in liquid phase (kmol m^{-3}); $D_{MEA,L}$ is the molecular diffusivity of MEA; k_2 is the second-order reaction rate constant; and k_L is the liquid-phase mass transfer coefficient without chemical reaction (m^2 s^{-1}).

The k_L and a_e can be obtained by the following correlation [20]:

$$k_L = 0.0051 \left(\frac{\mu g}{\rho} \right)^{1/3} \left(\frac{L}{a_w \mu_L} \right)^{2/3} \left(\frac{\mu_L}{\rho D_{CO_2,L}} \right)^{-1/2} (ad_p)^{0.4}$$

$$\frac{a_w}{a} = 1 - \exp \left\{ -1.45 \left(\frac{\sigma_{ct}}{\sigma} \right)^{0.75} \left(\frac{L}{a\mu_L} \right)^{0.1} \left(\frac{L^2 a}{\rho^2 g} \right)^{-0.05} \left(\frac{L^2}{\rho a \sigma} \right)^{0.2} \right\}$$

where a and a_w are, respectively, the dry and wet surface area of packing per unit bed volume (m^2/m^3), and a_e is considered to be equal to a_w. The calculation of the parameters in foregoing equations is given in Ref. [8].

The source term S_n represents the rate of MEA consumed due to reacting with CO_2, which can be obtained from the rate of CO_2 absorbed S_m and reaction (2) by stoichiometric calculation as follows:

$$S_n = -\frac{S_m}{44} \times 61 \times 2$$

The source term S_T represents the heat generated by absorption H_A and by reaction H_R, which can be calculated by

$$S_T = \frac{S_m}{M_{CO_2}}(H_A + H_R)$$

where M_{CO_2} (kg mol^{-1}) is the molar mass of CO_2; H_A is the heat of physical absorption, $H_A = 1.9924 \times 10^7$ (J kmol^{-1} CO_2 absorbed) [21]; and H_R is the heat of chemical reaction, $H_R = 8.4443 \times 10^7$ (J kmol^{-1} CO_2 reacted) [22].

5.1.1.3 Simulated Results and Verification

1. Industrial column

The object of simulation is an industrial absorber of 1.9 m in diameter packed with 2″ Pall rings and 14.1 m in packing height for removing CO_2 from natural gas by using aqueous MEA solutions. Fifteen runs of experimental data of the absorption column reported by Pintola et al. [23] are the concentration and temperature at the top and bottom of the column.

Axial and radial concentration and temperature distributions along the column

Liu employed two-equation model for simulating [8] the axial and radial concentration as well as the temperature profiles as shown in Fig. 5.1 including gas-phase CO_2 concentration, CO_2 absorbed (CO_2 loading) in MEA, liquid-phase temperature, and free MEA concentration. As seen in this figure, the absorption takes place mainly at the bottom of the tower.

The distribution of simulated average axial MEA concentration along the column is shown in Fig. 5.2. As seen in the figure, the simulated top and bottom concentrations by using two-equation model are closely checked by the experimental measurement.

Axial distribution of turbulent diffusivities D_t, α_t, and v_t

The use of present two-equation model enables to find the distribution of diffusivities D_t, α_t, and v_t in the whole column as shown in Fig. 5.3, and their average at different height of the column is given in Fig. 5.4.

As shown in the figure, both D_t and α_t are found to be almost constant around the center region of the packed bed until about $r/R = 0.8$ and suddenly increased to a maximum then decreased sharply toward the wall surface. Such simulated phenomenon is consistent with the experimental results using inert tracer technique. It is also clearly seen that the shape of the v_t curve is not similar to that of D_t and α_t throughout the column, which means the similarity between D_t or α_t and v_t is not justified; thus, the Schmidt number $\left(Sc = \frac{v}{D_t}\right)$ and Prandtl number $\left(Pr = \frac{v_t}{\alpha_t}\right)$ cannot be a constant and are varying locally with the position.
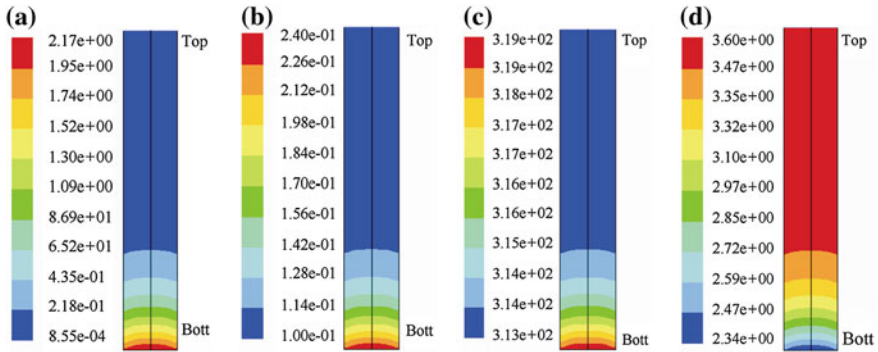
Fig. 5.1 Simulated profiles for Run 115 by two-equation model. **a** Gas-phase CO_2 concentration. **b** CO_2 absorbed. **c** Liquid-phase temperature. **d** Free MEA concentration (Reprinted from Ref. [8], Copyright 2006, with permission from Elsevier)
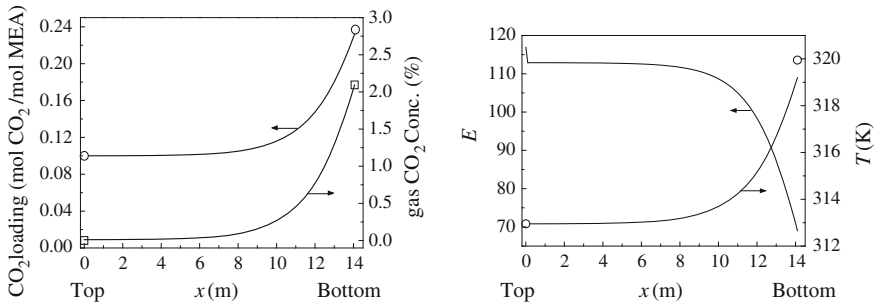
Fig. 5.2 Simulation by two-equation model (*solid curve*) and experimental data (*circle and square*) for Run T115 by two-equation model (*x is measured from column top*) (Reprinted from Ref. [8], Copyright 2006, with permission from Elsevier)

2. **Pilot-scale column**

The object of simulation is a pilot-scale column reported by Tontiwachwuthikul et al. [24] for the absorption of CO_2 from air mixture by aqueous MEA solution. The column is 0.1 m in diameter and packed with $1/2''$ ceramic Berl saddles with a total packing height of 6.55 m. The column consisted of six equal-height sections, and the samples were taken at the inlet and outlet of each section for analyzing the concentration. Ten sets of experimental data were reported including the variation of radial averaged carbonation reaction (CO_2 loading or CO_2 absorbed), the temperature in the liquid phase, and the radial averaged CO_2 concentration in the gas phase along the column height.

The simulated average axial gas-phase CO_2 concentrations and CO_2 absorbed (CO_2 loading) are compared with the experimental data as shown in Fig. 5.5, in which agreement between them is seen. The simulated distribution of diffusivities D_t, α_t, and v_t are given in Fig. 5.6.
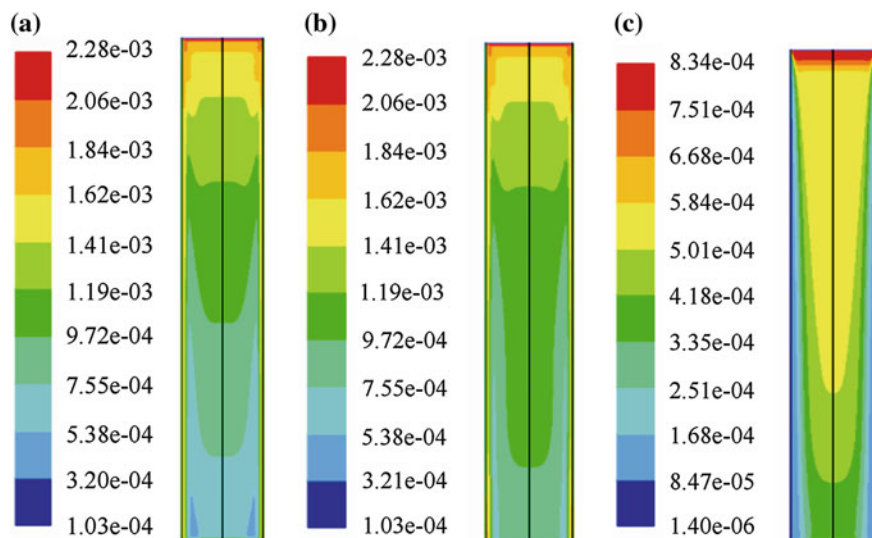
Fig. 5.3 Simulated diffusivities distributions for Run T115 by two-equation model [10]. **a** D_t. **b** α_t. **c** v_t
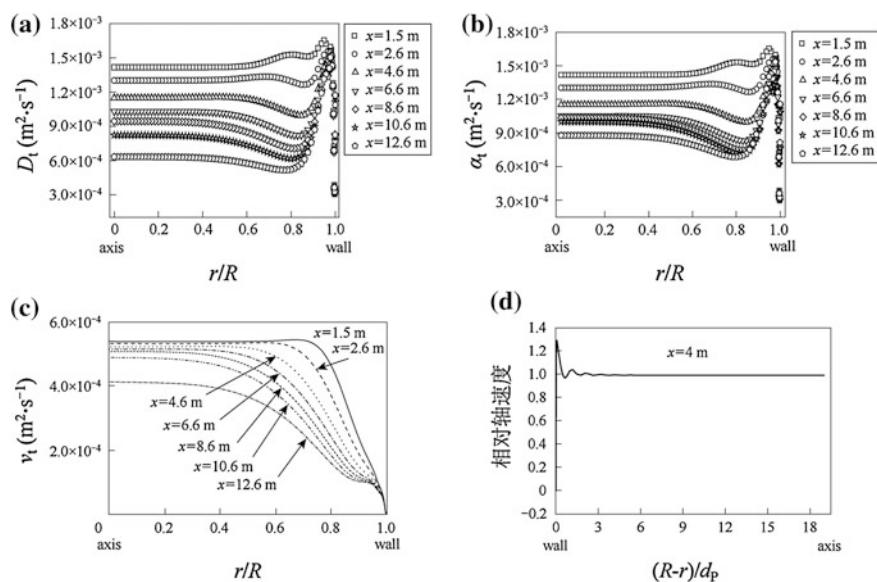
Fig. 5.4 Simulated diffusivities and relative radial liquid velocity at different column height for Run T115 by two-equation model (*x is measured from column top*). **a** D_t. **b** α_t. **c** v_t. **d** Relative velocity (Reprinted from Ref. [8], Copyright 2006, with permission from Elsevier)
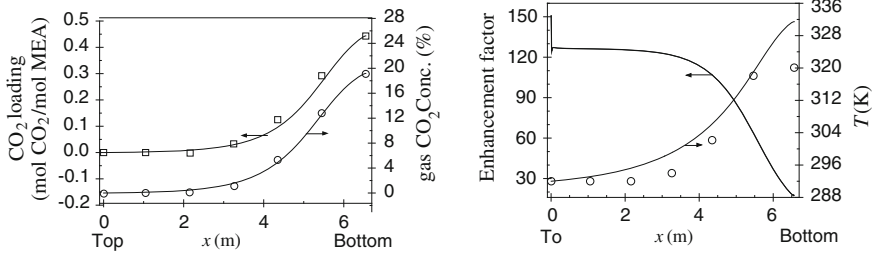
Fig. 5.5 Comparison between simulation by two-equation model (*solid curve*) and experimental data (*circle and square*) for Run T22 (*x is measured from column top*) (Reprinted from Ref. [8], Copyright 2006, with permission from Elsevier)
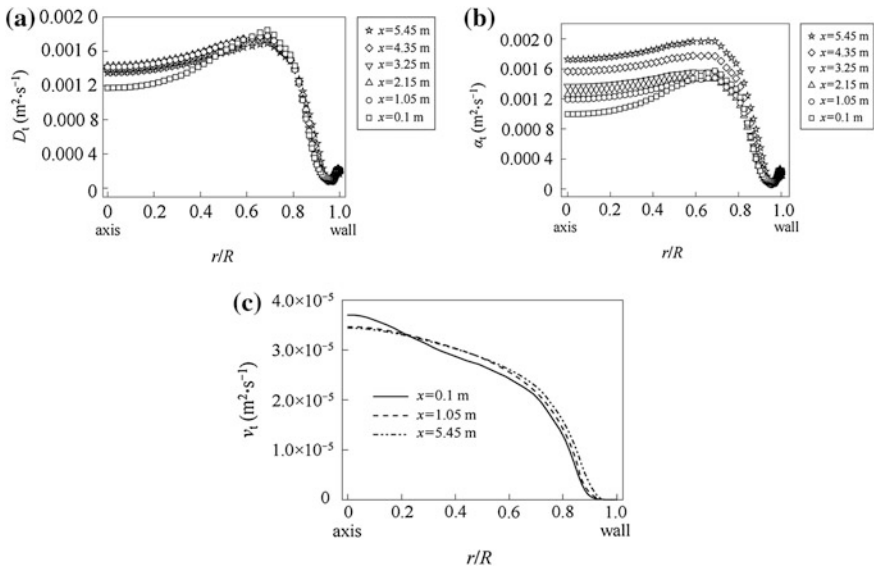
Fig. 5.6 Simulated diffusivities at different height of column by two-equation model for Run T22 (*x is measured from column top*). **a** D_t. **b** α_t. **c** v_t (Reprinted from Ref. [8], Copyright 2006, with permission from Elsevier)

Again from Fig. 5.6, the similarity between D_t and α_t and dissimilarity with v_t are also clearly seen. The sharp decrease in all diffusivities at about $r/R = 0.6$ is related with the velocity decreasing due to wall effect.

Axial distribution of average concentration and temperature

Take Run T17 as an example; the simulated gas CO_2 concentration, CO_2 loading, liquid-phase temperature, and the enhancement factor are shown in Fig. 5.7.
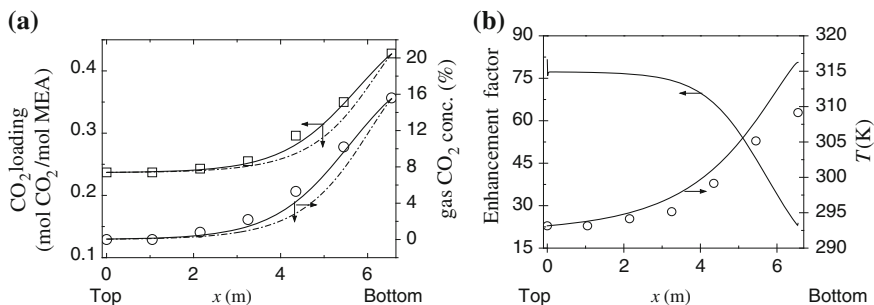
Fig. 5.7 Comparisons of experimental data, the simulation by two-equation model and by conventional model for Run T17 (*dash dot lines* one-dimensional model with mass diffusivity obtained by inert tracer technique, *solid curve* two-equation model, and *circle and square* experimental data). **a** CO_2 loading. **b** Enhancement factor (Reprinted from Ref. [8], Copyright 2006, with permission from Elsevier.)

In Fig. 5.7a, it is interested to note the difference in simulated results between using the two-equation model without knowing the diffusivity in advance and using the conventional one-dimensional model with published experimental diffusivity obtained by employing the inert tracer technique [12]. The simulated results by the conventional model on gas CO_2 concentration and liquid CO_2 loading profiles along the axial direction are shown in Fig. 5.7a by the dash dot lines. It should be pointed out that the column is taller than it is needed as seen in Fig. 5.1; thus, the liquid-phase concentration in the upper part of the column is very small and hardly distinguished the difference in the figure regardless of what model is being used for simulation. However, the difference is clearly seen at the lower part of the column, in which the simulation by using the two-equation model is better than the conventional.

In Fig. 5.7b, the simulated radial averaged axial temperature is somewhat higher than the experimental temperature and deviate obviously at the bottom of the column. The error may come from (1) the cooling of outlet liquid by the incoming gas at the column bottom is neglected; (2) the heat consumed by the evaporation of water in the liquid phase is ignored; and (3) the heat loss to the environment is not considered.

5.1.2 Absorption of CO_2 by Aqueous AMP in Packed Column

The advantages of using AMP as absorbent for the absorption of CO_2 is the high rate of absorption, less corrosion, and low energy of recovery, also low stability of the absorbed amino product which is easy to hydrolyze to liberate free AMP.

5.1.2.1 Chemical Reaction Between AMP and CO_2

The reaction between AMP and CO_2 can be represented by the following steps with liberation of heat of solution and reaction:

$$CO_{2,G} \longrightarrow CO_{2,L} + H_A \tag{R1}$$

$$CO_{2,L} + RR'NH \rightarrow RR'NH^+COO^- + H_R \tag{R2}$$

$$RR'NH^+COO^- + RR'NH \longrightarrow RR'NCOO^- + RR'NH_2^+ \tag{R3}$$

$$RR'NCOO^- + H_2O \rightarrow RR'NH + HCO_3^- \tag{R4}$$

$$RR'NH + CO_2 + H_2O \rightarrow RR'NH_2^+ + HCO_3^- \tag{R5}$$
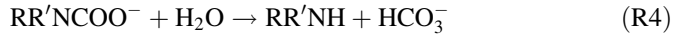
where R and R' denote, respectively, $HOCH_2C(CH_3)_2^-$ and H. The step (R3) is unstable and easily turn to step (R4) for hydrolysis. From the overall step (R5), one mole of AMP can absorb one mole of CO_2, and the reaction can be considered as second order. The rate of chemical absorption R_c can be expressed as

$$R_c = k_2 \, [CO_2] \, [AMP]$$

where the coefficient k_2 is given by Saha et al. [25]

$$\ln k_2 = 23.69 - 5\,176.49/T$$

5.1.2.2 Simulated Results and Verification

The object of simulation, a pilot-scale packed column, is the same as given in Sect. 5.1.1.3 (2). Ten sets of experimental data for absorption of CO_2 by AMP aqueous solution were reported by Tontiwachwuthikul et al. [24], in which three sets are taken as examples for comparison with present simulation.

The determination of source terms in the modeling equations is similar to Sect. 5.1.1.2 except the physical parameters should be reevaluated. Refer to Ref. [26] for details.

Distribution of average radial concentration and temperature along column height

The simulated radial averaged axial concentration and temperature of the aqueous AMP are shown by the curves in Fig. 5.8 for Run T27 and Fig. 5.9 for Run T29. In these figures, the experimental points are also given for comparison. Agreement is seen between simulation and experimental measurement.

The influence of inlet boundary condition of $\overline{c'^2_{in}}$ and $\overline{T'^2_{in}}$ on the simulated result

In previous simulation, the inlet boundary conditions of $\overline{c'^2_{in}}$ and $\overline{T'^2_{in}}$ are set as $\overline{c'^2} = \left(0.082 C_{i,in}\right)^2$ and $\overline{T'^2_{in}} = (0.082 \Delta T)^2$. The influence of boundary condition
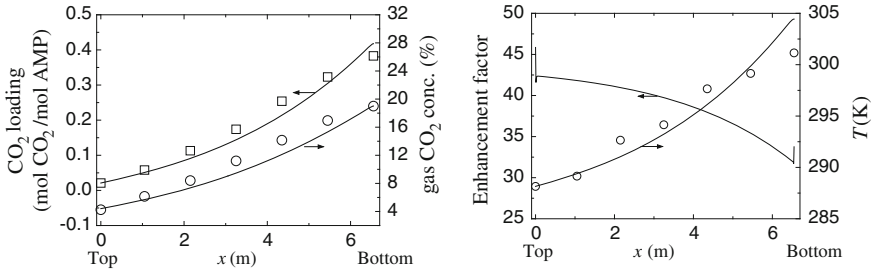
Fig. 5.8 Comparison between simulation by two-equation model (*curve*) and experimental data (*circle and square*) for Run T27 (*x is measured from column top*) [26]. *x*—distance measured from column top
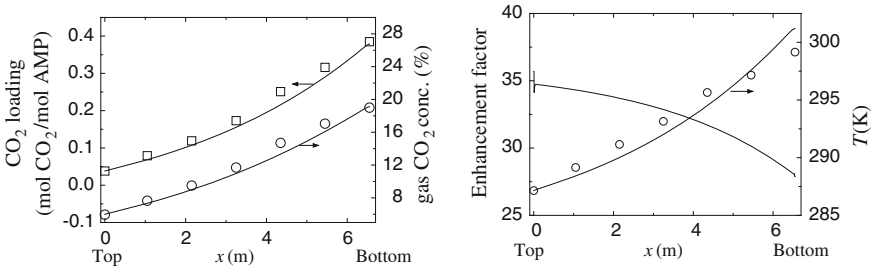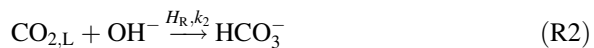

Fig. 5.9 Comparison between simulation by two-equation model (*solid line*) and experimental data (*circle and square*) for Run T29 [26]

was investigated by changing the condition to $\overline{T'^2_{in}} = 0.003(\Delta T)^2$ and $\overline{c'^2} = 0.003C^2_{in}$. As given in Fig. 5.10, the simulated results for T30 by using these two boundary settings are substantially the same and can only be represented by a unique curve. However, it is true for the example T30; the influence of boundary condition in general is yet to be further investigated.

Variation of D_t and α_t in radial directions

The turbulent mass diffusivity D_t and turbulent thermal diffusivity α_t can be obtained by present model computations as shown in Fig. 5.11. Once again, it demonstrates that the choice of different boundary conditions of $\overline{c'^2_{in}}$ and $\overline{T'^2_{in}}$ do not affect substantially the simulated result in this case. Comparing Fig. 5.11 with Fig. 5.6, the shape of D_t and α_t along radial direction for T30 and T22 is highly similar, even their values are very close each other.
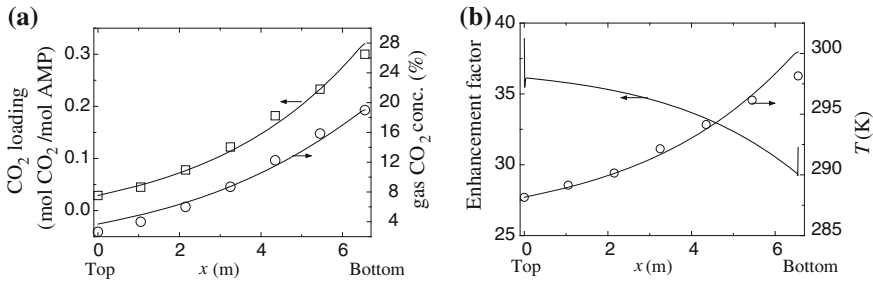
Fig. 5.10 Simulation by two-equation model (*curve*) and experimental data (*circle*) for Run T30 [26]
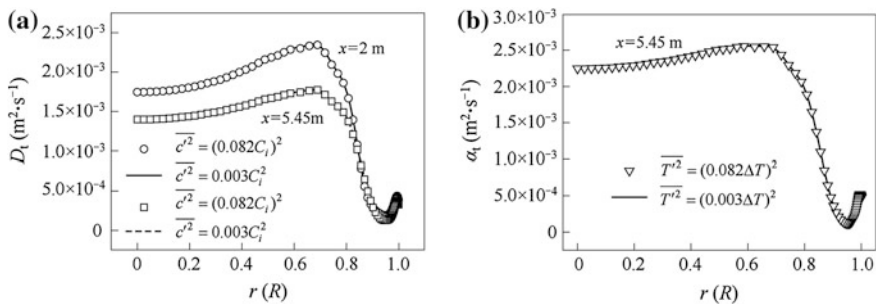
Fig. 5.11 Distribution of D_t and α_t in radial direction for Run T30 by two-equation model at different inlet boundary conditions (*x is measured from column top*). **a** Distribution of D_t. **b** Distribution of α_t [26]

5.1.3 Absorption of CO_2 by Aqueous NaOH in Packed Column

5.1.3.1 Chemical Reaction Between NaOH and CO_2

The absorption of CO_2 and the reaction between CO_2 and NaOH in the aqueous solution are undertaken by the following steps:

$$CO_{2,g} \xrightarrow{H_A} CO_{2,L} \tag{R1}$$

$$CO_{2,L} + OH^- \xrightarrow{H_R, k_2} HCO_3^- \tag{R2}$$

$$HCO_3^- + OH^- \rightarrow CO_3^{2-} + H_2O \tag{R3}$$

$$CO_{2,L} + 2OH^- \rightarrow CO_3^{2-} + H_2O \tag{R4}$$
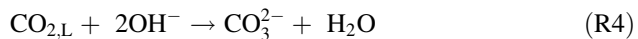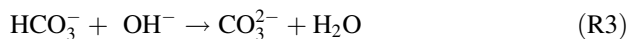
Reaction (R1) expresses the physical absorption of CO_2 by water, accompanied with the evolution of heat of solution H_A. Reaction (R2) is known as the rate-controlling step because reaction (R3) is a proton-transfer reaction and is very faster than reaction (R2). Thus, the absorption of CO_2 by aqueous NaOH solution can be regarded as a gas absorption accompanied with second-order reaction (R2), and the overall reaction is represented by (R4).

The second-order reaction rate constant k_2 for CO_2–NaOH reaction was correlated by Pohorecki [27] as a function of temperature and ionic strengths I_c of aqueous electrolyte solutions as follows:

$$\log k_2 = 11.895 - \frac{2382}{T} + 0.221I_c - 0.016I_c^2$$

The model equations are given in Sect. 5.1; the determination of source terms in the modeling equations is similar to Sect. 5.1.2 except the physical parameters should be reevaluated as given in Ref. [9].

5.1.3.2 Simulated Results and Verification

The object of simulation and verification is a randomly packed column reported by Tontiwachwuthikul et al. [24]; the structure of this pilot-scale column has been described in Sect. 5.1.1.3 (2). Twelve sets of experimental data for the absorption of CO_2 by NaOH were presented by the authors, among which six sets are taken to check the validity of the present simulated results.

Distributions of radial averaged concentration and temperature in the liquid phase along the column height

The simulated distributions of average radial OH^- concentration in liquid phase, C_{OH}^- and CO_2 concentration in gas phase, as well as the temperature along the column height are shown in Figs. 5.12, 5.13, 5.14, 5.15, 5.16, and 5.17 with experimental data for comparison.

As seen in these figures, the agreement between the simulations and experimental results for OH^- concentration in liquid phase and CO_2 concentration in gas phase is satisfactory. However, the predicted temperature profiles along the column by simulation show somewhat lower than the experimental measurement, especially near the bottom of the column. As stated in previous section, there are several reasons for such deviation: Firstly, in the assumption, the cooling of descending liquid by the entering gas is ignored; secondly, the evaporation of solvent water in liquid phase is neglected, leading to overestimate the liquid temperature; and thirdly, the assumption of adiabatic operation means the neglect of heat exchange between the column and environment.

Also as seen in these figures, the enhancement factor, E, increases from column bottom to the top. Take T11 as an example shown in Fig. 5.16; the enhancement
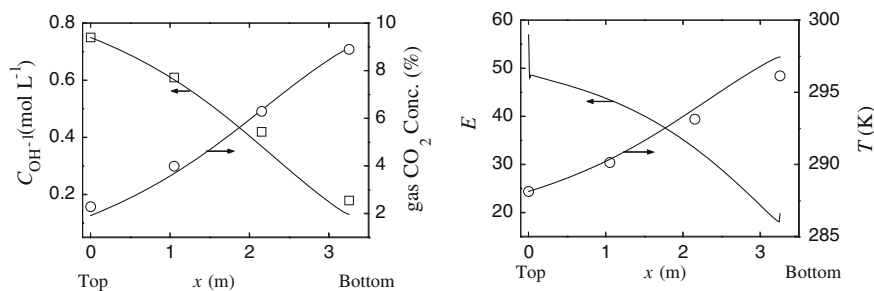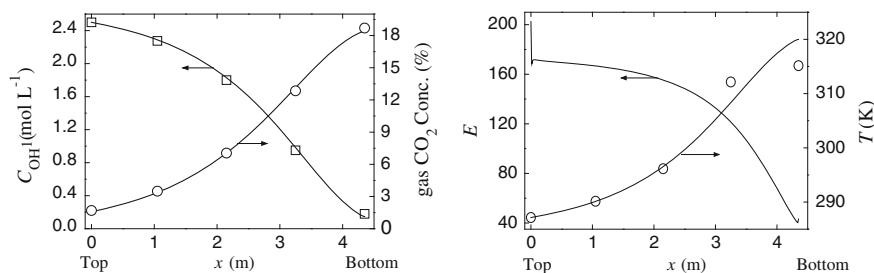
Fig. 5.12 Comparison of simulated results by two-equation model (*solid line*) with experimental data (*circle and square*) for RunT1 (Reprinted from Ref. [9], Copyright 2006, with permission from American Chemical Society)
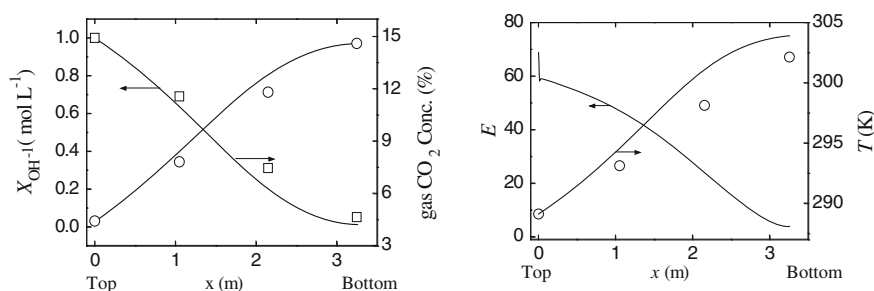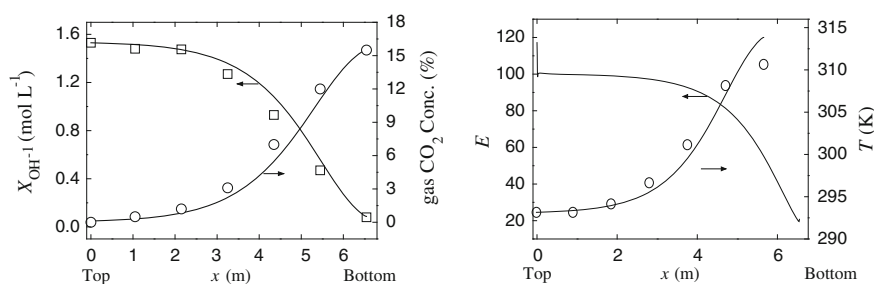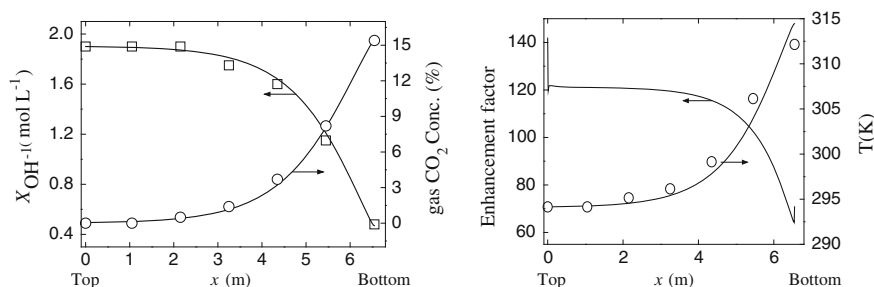

Fig. 5.13 Comparison of simulated results by two-equation model (*solid line*) with experimental data (*circle and square*) for RunT2 (Reprinted from Ref. [9], Copyright 2006, with permission from American Chemical Society)
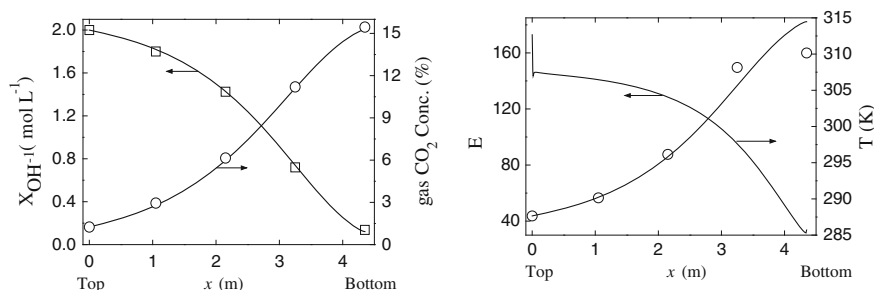
Fig. 5.14 Comparison of simulated results by two-equation model (*solid line*) with experimental data (*circle and square*) for RunT7 (Reprinted from Ref. [9], Copyright 2006, with permission from American Chemical Society)

factor E increases from about 20 at the column bottom to about 100 at the column top, which means the rate of chemical absorption is about 20–100 times higher than that of physical absorption.

Fig. 5.15 Comparison of simulated results by two-equation model (*solid line*) with experimental data (*circle and square*) for RunT8 (Reprinted from Ref. [9], Copyright 2006, with permission from American Chemical Society)

Fig. 5.16 Comparison of simulated results by two-equation model (*solid line*) with experimental data (*circle and square*) for RunT11 (Reprinted from Ref. [9], Copyright 2006, with permission from American Chemical Society)

Fig. 5.17 Comparison of simulated results by two-equation model (*solid line*) with experimental data (*circle and square*) for RunT12 (Reprinted from Ref. [9], Copyright 2006, with permission from American Chemical Society)

Liquid Velocity Profile along the Radial Direction

Due to the non-uniformly distributed porosity especially higher porosity near the wall region, the fluid flow seriously deviates from the plug flow. As seen from Fig. 5.18a and b, serious "wall flow" is appeared, and the flow becomes relatively
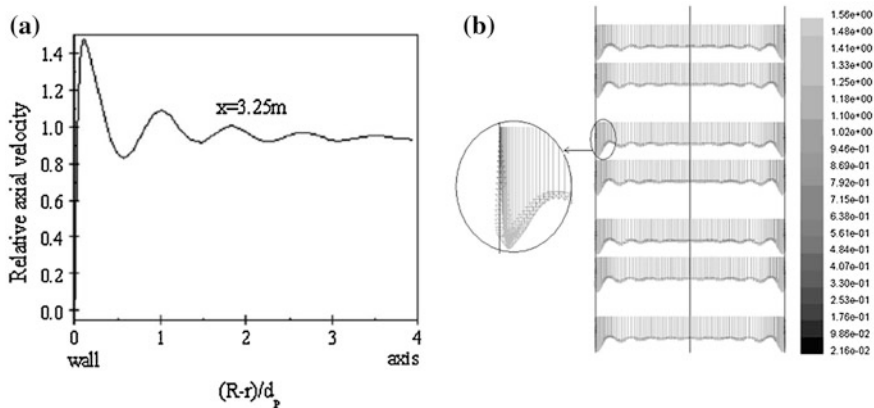
Fig. 5.18 Relative axial velocity profile two-equation model for T12. **a** Axial velocity profile. **b** Schematic distribution (Reprinted from Ref. [9], Copyright 2006, with permission from American Chemical Society)

uniform only about $2d_p$ apart from the wall. Similar result has been observed by many investigators.

Distributions of D_t, α_t, and α_t along column height

The simulated profiles of D_t, α_t, and α_t obtained along the whole column are displayed in Fig. 5.19.

The radial distributions of D_t, α_t, and v_t at different height of the column are displayed in Figs. 5.19, 5.20, 5.21, and 5.22. These figures show the non-uniform distribution of diffusivity and the similarity between the shape of D_t and α_t. The dissimilarity of v_t with D_t and α_t is seen obviously, which indicates once again the Schmidt number and Prandtl number are not a constant throughout the column.

5.2 Reynolds Mass Flux Model

In this section, the standard Reynolds mass flux model (abbreviated as RMF model) is employed for simulation.

The assumptions of Reynolds mass flux model as applied to the chemical absorption column are the same as the $c'^2 - \varepsilon_{c'}$ two-equation model in Sect. 5.1.

The mathematical model in interacted liquid-phase form is given below.

1. The mass transfer equation set

Species mass conservation equation

$$\frac{\partial}{\partial x_i}(\gamma \beta_L U_{Li} C) = \frac{\partial}{\partial x_i}\left[\gamma \beta_L \left(D\frac{\partial C}{\partial x_i} - \overline{u_i' c'}\right)\right] + S_n$$
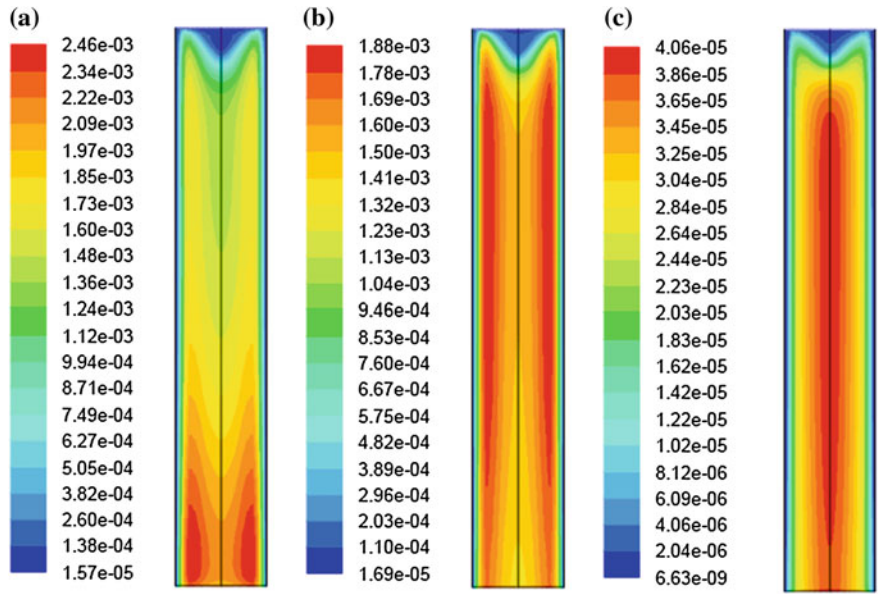
Fig. 5.19 Simulated diffusivities (m^2 s^{-1}) by two-equation model. **a** α_t. **b** D_t. **c** ν_t [26]

Fig. 5.20 Radial distribution of D_t at different column height for T12 (*x is measured from column top*) (Reprinted from Ref. [9], Copyright 2006, with permission from American Chemical Society)
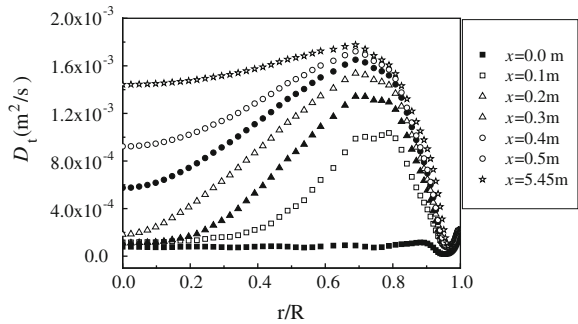
Fig. 5.21 Radial distribution of α_t at different column height for T12 (*x is measured from column top*) [26]
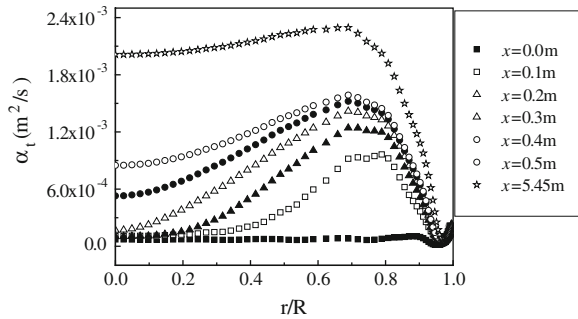
Fig. 5.22 Radial distribution of v_t at different column height for T12 (*x is measured from column top*) [26]
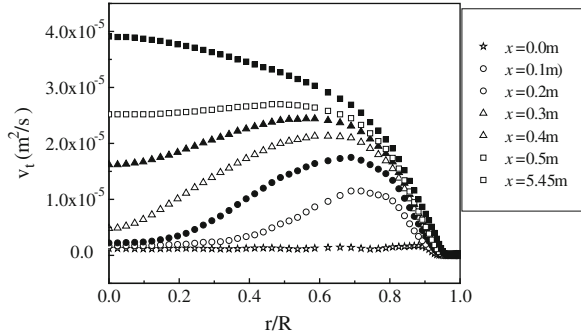
where γ is the porosity of the packed bed; β_L is the volume fraction of liquid in the vapor–liquid mixture based on pore space; $\overline{C}$ and c' are, respectively, the average and the fluctuated mass concentration (kg m^{-3}); and D is the molecular diffusivity of absorbent in the liquid phase.

Fluctuating mass flux $\overline{u_i'c'}$ equation

$$\frac{\partial \overline{u_i'c'}}{\partial t} + \frac{\partial U_j \overline{u_i'c'}}{\partial x_j} = \frac{\partial}{\partial x_j}\left[\left(C_{c1}\frac{k}{\varepsilon}\overline{u_i'u_j'} + \frac{\mu}{\rho}\right)\frac{\partial \overline{u_i'c'}}{\partial x_j}\right] - \left(\overline{u_i'u_j'}\frac{\partial C}{\partial x_j}\right) - C_{c2}\frac{\varepsilon}{k}\overline{u_i'c'}$$
$$+ C_{c3}\overline{u_j'c'}\frac{\partial U_{Li}}{\partial x_j} \tag{3.25a}$$

where $C_{c1} = 0.09$, $C_{c2} = 3.2$, $C_{c3} = 0.55$; k and ε equations are given by Eqs. (1.11a) and (1.13a), respectively.

2. Accompanied CFD equation set

Overall mass conservation:

$$\frac{\partial(\rho\gamma\beta_L U_{Li})}{\partial x_i} = S_m$$

Momentum conservation:

$$\frac{\partial(\rho\gamma\beta_L U_{Li}U_{Lj})}{\partial x_j} = -\gamma\beta_L\frac{\partial p}{\partial x_i} + \frac{\partial}{\partial x_j}\gamma\beta_L\left(\frac{\mu}{\rho}\frac{\partial(\rho U_{Li})}{\partial x_j} - \rho\overline{u_i'u_j'}\right) + S_{LF}$$

where S_F is the source term of the liquid flow, $\overline{u_i'u_j'}$ is calculated according to Eq. (1.23) as follows.

$$\frac{\partial \overline{u_i'u_j'}}{\partial t} + U_k \frac{\partial \overline{u_i'u_j'}}{\partial x_k} = \frac{\partial}{\partial x_k}\left(C_k \frac{k}{\varepsilon} \overline{u_i'u_j'} \frac{\partial \overline{u_i'u_j'}}{\partial x_k} + \frac{\mu}{\rho}\frac{\partial \overline{u_i'u_j'}}{\partial x_k}\right)$$
$$- \left(\overline{u_i'u_k'}\frac{\partial U_{Lj}}{\partial x_k} + \overline{u_j'u_k'}\frac{\partial U_{Li}}{\partial x_k}\right) - C_1 \frac{\varepsilon}{k}\left(\overline{u_i'u_j'} - \frac{2}{3}k\Delta_{ij}\right)$$
$$- C_2\left(\overline{u_i'u_k'}\frac{\partial U_{Lj}}{\partial x_k} + \overline{u_j'u_k'}\frac{\partial U_{Li}}{\partial x_k} - \frac{2}{3}\Delta_{ij}\overrightarrow{u_i'u_k'}\frac{\partial U_{Li}}{\partial x_k}\right) - \frac{2}{3}\varepsilon\delta_{ij}$$

$$(1.23a)$$

k_L equation

$$\frac{\partial \rho\gamma\beta_L U_{Li} k_L}{\partial x_i} = \frac{\partial}{\partial x_i}\left[\gamma\beta_L\left(\mu + \frac{\mu_t}{\sigma_k}\right)\frac{\partial k}{\partial x_i}\right] - \mu_t\gamma\beta_L\left(\frac{\partial U_{Li}}{\partial x_j} + \frac{\partial U_{Lj}}{\partial x_i}\right)\frac{\partial U_{Lj}}{\partial x_i} - \rho\gamma\beta_L\varepsilon_L$$

$$(1.11b)$$

ε_L equation

$$\frac{\partial \rho\gamma\beta_L U_{Li}\varepsilon_L}{\partial x_i} = \frac{\partial}{\partial x_i}\left[\gamma\beta_L\left(\mu + \frac{\mu_t}{\sigma_\varepsilon}\right)\frac{\partial \varepsilon_L}{\partial x_i}\right] - C_{\varepsilon 1}\gamma\beta_L\frac{\varepsilon_L}{k}\mu_t\left(\frac{\partial U_{Lj}}{\partial x_i} + \frac{\partial U_{Li}}{\partial x_j}\right)\frac{\partial U_{Lj}}{\partial x_i}$$
$$- C_{\varepsilon 2}\gamma\beta_L\rho_L\frac{\varepsilon_L^2}{k}$$

$$(1.13b)$$

3. Accompanied CHT equation set

Energy conservation:

$$\frac{\partial(\rho\gamma\beta_L c_p U_{Li} T)}{\partial x_i} = \frac{\partial}{\partial x_i}\left[\rho\gamma\beta_L c_p\left(\alpha\frac{\partial C}{\partial x_i} - \overline{u_i'T'}\right)\right] + S_T$$

where T is the average temperature of liquid phase, c_p is the specific heat of liquid phase, S_T is the thermal source term including the heat of solution, heat of reaction, and others; and α is the molecular thermal diffusivity.

Fluctuating heat flux $\overline{u_i'T'}$:

$$\frac{\partial \overline{u_i'T'}}{\partial t} + U_i \frac{\partial \overline{u_i'T'}}{\partial x_k} = \frac{\partial}{\partial x_k}\left[\left(C_{T1}\frac{k}{\varepsilon}\overline{u_i'u_j'} + \alpha\right)\frac{\partial \overline{u_i'T'}}{\partial x_k}\right]$$
$$- \left(\overline{u_i'u_k'}\frac{\partial T}{\partial x_k} + \overline{u_k'T'}\frac{\partial U_j}{\partial x_k}\right) - C_{T2}\frac{\varepsilon}{k}\overline{u_i'T'} + C_{T3}\overline{u_k'T'}\frac{\partial U_i}{\partial x_k}$$

$$(2.13)$$

where $C_{T1} = 0.07$, $C_{T2} = 3.2$, $C_{T3} = 0.5$.

The auxiliary k and ε equations are given in (2) CFD equation set.

Boundary Conditions

1. **Inlet Condition (column top, $x = 0$)**

At the top of the column, the boundary condition for the liquid phase is set to be [28]

$$U = U_{\text{in}}, \; C = C_{\text{in}}, \; k = 0.003U_{\text{ln}}^2, \; \varepsilon_{\text{in}} = 0.09\frac{k_{\text{in}}^{1.5}}{d_{\text{H}}}$$

where d_{H} is the hydraulic diameter of random packing, which can be calculated by

$$d_{\text{H}} = \frac{4\gamma_\infty}{a(1 - \gamma_\infty)}$$

Since no experimental measurements reported or empirical correlations available from the literature for determining the inlet condition of the fluctuating mass flux $\overline{u_i'c'}_{\text{in}}$ and fluctuating heat flux $\overline{u_i'T'}_{\text{in}}$, the following conditions for $\overline{u_i'c'}$ and $\overline{u_i'T'}$ are adopted based on the best fitting of experimental data [10, 13]:

$$\left(\overline{u_i'c'}\right)_{\text{in}} = -0.7(\partial C/\partial x_i)|_{\text{in}} \; \left(\overline{u_i'T'}\right)_{\text{in}} = -0.9(\partial T/\partial x_i)|_{\text{in}}$$

It is found that the foregoing inlet condition is applicable to many other simulation with satisfactory results.

Outlet Condition (column bottom)

The flow in the packed column at the outlet is considered as fully developed in turbulent state; the zero normal gradients are applied for all variables Φ except pressure.

2. **Axis Condition**

Under the assumption that all variables Φ in the packed column are axially symmetrical, we have $\partial\Phi/\partial x = 0$ at $y = 0$ of the column central axis.

3. **Wall Conditions**

The no-slip condition of flow is applied to the wall, and the zero-flux condition at the wall is adopted.

Evaluation of Source Terms

The object of simulation and the evaluation of source terms S_{m}, S_F, S_{T}, and S_n are the same as in Sect. 5.1.

(a)

(b)
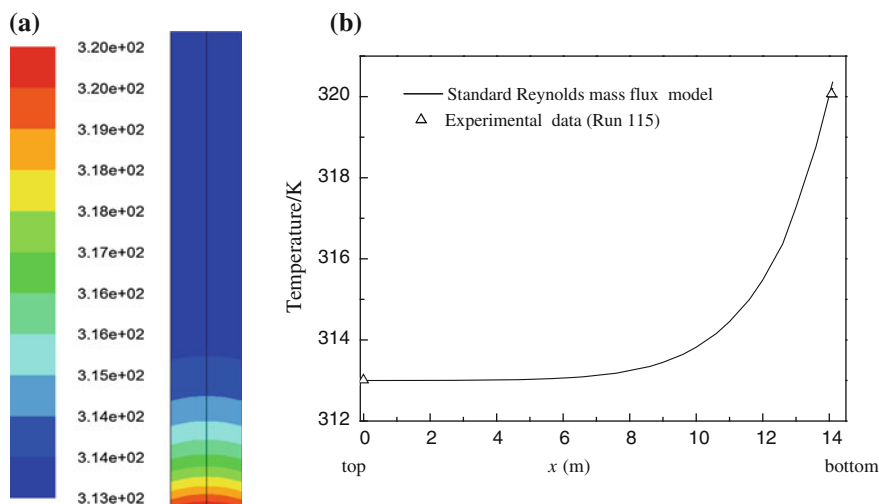
Fig. 5.23 Simulated temperature profiles of liquid phase in the column of absorption of CO_2 into aqueous MEA (Run 115) by RMF model [10]. **a** Profile of liquid-phase temperature in the column. **b** Comparison of axial distribution of radial average temperature in the column with experimental data

5.2.1 Absorption of CO₂ by Aqueous MEA in Packed Column

5.2.1.1 Simulated Results and Verification

The liquid-phase temperature profile

The simulated profile of liquid-phase temperature in the packed column is given in Fig. 5.23a. The axial distribution of liquid-phase temperature after radial average is shown in Fig. 5.23b.

Since the reported experimental measurements are only inlet and outlet temperature of liquid phase, the validity of the present model can only be checked by comparing with such limited data. As seen from Fig. 5.23b, the simulated outlet temperature is a little higher than the experimental measurement (about 0.3 K). This error may be due to the neglect of heat loss to the environment in the assumption, which results in somewhat increase in the fluid temperature; other sources of error are similar to the absorption by MEA and AMP as given in previous sections.

The axial and radial liquid-phase velocity distributions

The simulated axial velocity distribution along radial direction is shown in Fig. 5.24a. As seen, the axial liquid velocity is almost constant from column center
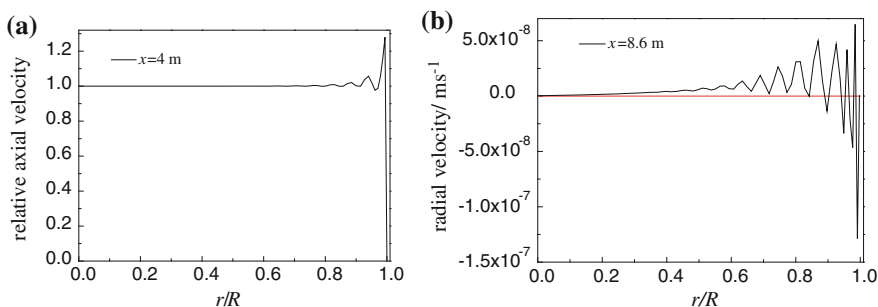
Fig. 5.24 Simulated velocity profiles of the liquid in the column of absorption of CO_2 into aqueous MEA (Run 115) by RMF model [10]. **a** Axial velocity profile of the liquid along radial direction. **b** Radial velocity profiles of the liquid along radial direction

to about $r/R = 0.8$ due to relatively uniform porosity in this region of the column. The obvious up and down variation of velocity near the wall region is mainly due to the non-uniform porosity. The simulated radial velocity along radial direction is shown in Fig. 5.24b, in which the radial velocity increases slowly from $r/R = 0$ to about 0.4. From 0.4 to the column wall, the wavy variation of the radial velocity is intensified sharply, especially around $r/R = 0.9$. It shows that the influence of non-uniform porosity is appreciable especially near the wall.

The profile of CO_2 loading

Figure 5.25a gives the distribution of CO_2 loading in the packed column. It can be seen from this figure that most absorptions take place at the bottom part of the column, while at the top part, only trace of CO_2 is removed. As shown in Fig. 5.25b, the simulated CO_2 loading at the bottom of the column is closely checked by the published outlet data.

The profile of CO_2 concentration in gas phase is given in Fig. 5.26a. The average radial concentration along axial direction is given in Fig. 5.26b. As seen in the figure, the prediction on outlet concentration is confirmed by experimental data.

The MEA concentration profile

As shown in Fig. 5.27a and b, the free MEA molar concentration in the liquid phase increases from column center to the wall at different height of the column. It can be explained that the liquid velocity is slow down near the wall in the randomly packed column (see Fig. 5.24), resulting in worse contact with the gas phase and consequently less CO_2 to be absorbed. This is also the reason why the CO_2 loading in liquid phase decreases with the distance away from the column center at a given height near the bottom, as shown in Fig. 5.25a.

(a)

(b)
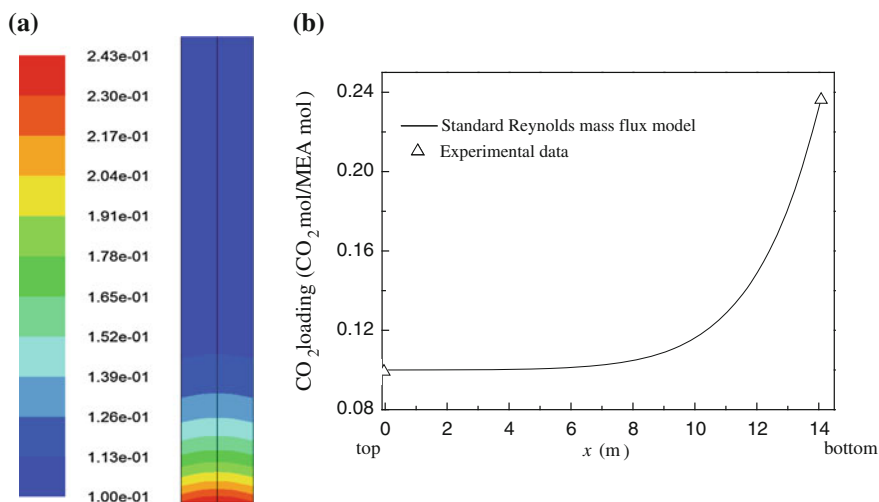
Fig. 5.25 Simulated profiles of CO_2 loading in the packed column of absorption of CO_2 into aqueous MEA (Run 115) by RMF model [10]. **a** Profile of CO_2 loading in the packed column. **b** Comparison of axial profile of average CO_2 loading with experimental data
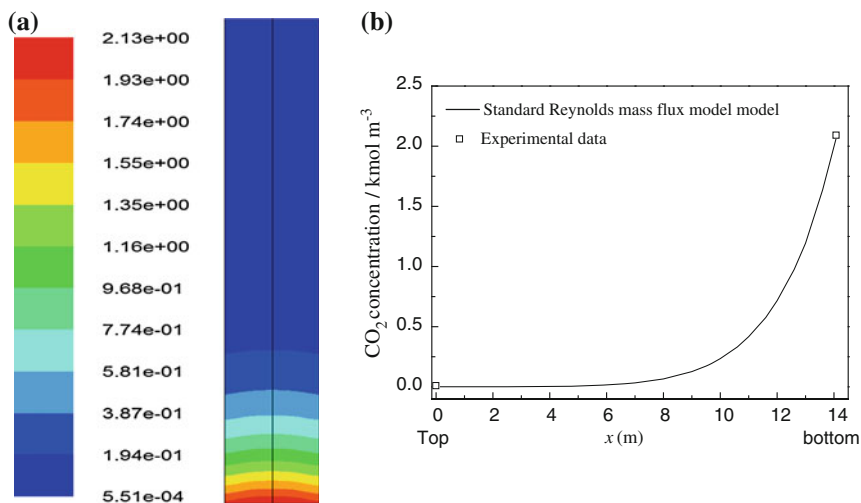
(a)

(b)

Fig. 5.26 Simulated profiles of CO_2 concentration in gas phase in the packed column of absorption of CO_2 into aqueous MEA (Run115) by RMF model [10]. **a** Profile of CO_2 concentration in gas phase. **b** Profile of average CO_2 concentration along radial direction
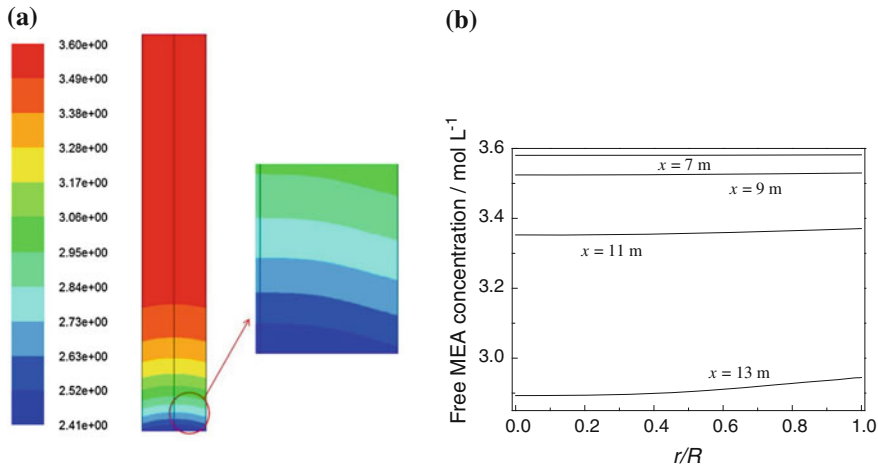
Fig. 5.27 Simulated Profile of MEA concentration in the column for absorption of CO_2 into aqueous MEA (Run 115) by RMF model [10]. **a** Profile of MEA concentration in the column. **b** Distribution of MEA concentration in radial direction

5.2.1.2 Anisotropic Mass Diffusivity

The axial turbulent (fluctuating) mass flux $\overline{u'_x c'}$

As seen from Fig. 5.28a, the $\overline{u'_x c'}$ is increasing rapidly at the lower part of the column ($x > 8$ m); it indicates that the $\overline{u'_x c'}$ increasing profile is consistent with the decreasing MEA concentration profile as seen in Fig. 5.27a, so that the axial mass transfer is enhanced (see Sect. 3.6.1.3 for reference hereafter). Also the positive slope of $\overline{u'_x c'}$ in the plot implies the rate of enhancement is much greater at the bottom than at the top. In Fig. 5.28b, $\overline{u'_x c'}$ is almost constant at the upper part of the column ($x < 6$) and increases rapidly toward the column bottom; it means that the turbulent effect is kept unchanged at the column top and advances intensely along the lower part of the bottom.

In the radial direction as shown in Fig. 5.28a, $\overline{u'_x c'}$ also remained unchanged from column center to about $r/R = 0.6$, indicating molecular diffusion is dominant in this region. From $r/R = 0.6$ to the column wall, although the positive $\overline{u'_x c'}$ gradually lowers down with low rate (negative slope), it counteracts with the axial MEA concentration increasing profile (see $x = 11$ and 13 in Fig. 3.27b), so that the axial MEA concentration is being suppressed to some extent in this region.

The axial mass transfer diffusivity $\mathbf{D_{t,x}}$

Figure 5.29 gives the concentration gradient of MEA along the x direction. From Eq. (3.37) and Figs. 5.28a and 5.29, the axial turbulent mass diffusivity $\mathbf{D_{t,x}}$ can be obtained as given in Fig. 5.30. As seen in Fig. 5.30b, the $\mathbf{D_{t,x}}$ is decreasing

(a)

(b)
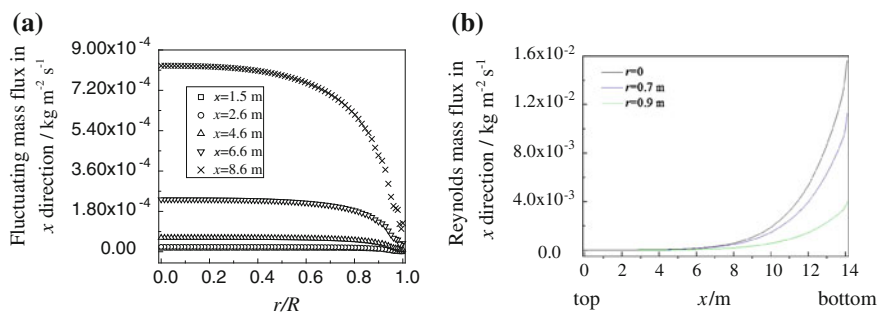
Fig. 5.28 Simulated profiles of $\overline{u'_x c'}$ of MEA in the absorption of CO_2 into aqueous MEA (Run115) [10]. **a** Profiles of $\overline{u'_x c'}$ along radial direction. **b** Profiles of $\overline{u'_x c'}$ along axial direction

Fig. 5.29 Simulated profile of average MEA concentration gradient along axial direction in the absorption of CO_2 into aqueous MEA (Run 115) [10]
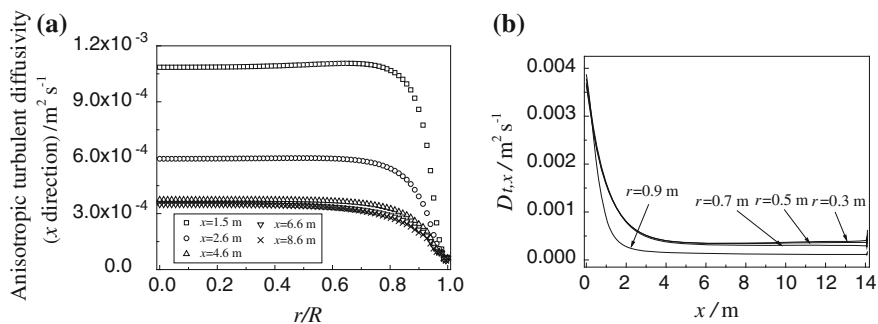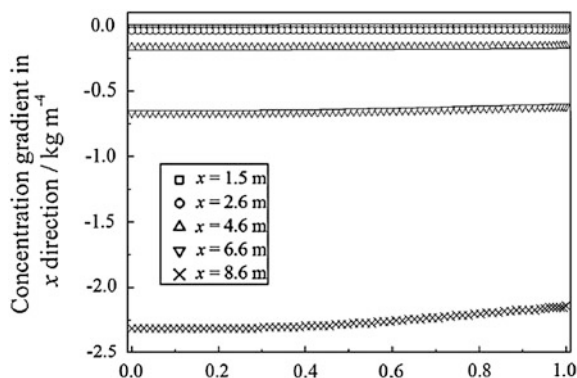

(a)

(b)

Fig. 5.30 Simulated profiles of $\mathbf{D_{t,x}}$ for MEA in the absorption of CO_2 into aqueous MEA (Run 115), (*x is measured from column top*) [10]. **a** $\mathbf{D_{t,x}}$ along radial direction and **b** $\mathbf{D_{t,x}}$ along axial directions

along the upper part of the column ($x < 4$); it means the mass transfer is not active in the radial direction, the $\mathbf{D_{t,x}}$ is almost constant from column center to about $r/R = 0.8$ and gradually down to zero with negative slope, which implies the $\overline{u'_x c'}$ diffusion remains steady until $r/R = 0.8$ and falls to zero at the wall with slow rate. It is also noted that although $\mathbf{D_{t,x}}$ is high at the column top ($x = 1.5$ m), yet the MEA concentration gradient there is very low (see Fig. 5.29) to make the fluctuating mass flux $\overline{u'_x c'}$ very small. At the lower part of the column (e.g. $x = 8.6$), although $\mathbf{D_{t,x}}$ is low, the concentration gradient (absolute value) is high, and so the product $\overline{u'_x c'}$ becomes higher toward the bottom as shown in Fig. 5.28b.

The radial mass transfer diffusivity $\mathbf{D_{t,y}}$

The profile of $\overline{u'_y c'}$ is given in Fig. 5.31. The negative $\overline{u'_y c'}$ means its diffusion is under negative gradient of C (see Sect. 3.6.1.3), which suppresses the increasing MEA concentration in radial direction. In Fig. 5.33, the $\mathbf{D_{t,y}}$ contour displays a sudden increase to very high value near the column center. But the radial concentration gradient around the column center is nearly zero according to the axial symmetrical assumption, as shown in Fig. 5.32, so that very small value of denominator in $D_{t,y} = -\overline{u'_y c'} \big/ \frac{\partial C}{\partial y}$ makes high $\mathbf{D_{t,y}}$.

As stated in Sect. 3.5.1.4 , the anisotropic diffusivities $\mathbf{D_{t,x}}$ and $\mathbf{D_{t,y}}$ obtained by Reynolds mass flux model are not comparable with the D_t from two-equation model, but it is interesting to see the difference between anisotropic $\mathbf{D_{t,x}}$ as shown in Fig. 5.30 and the isotropic D_t as shown in Fig. 5.6a. Both $\mathbf{D_{t,x}}$ and D_t are in the same order of magnitude, although $\mathbf{D_{t,x}}$ is somewhat lower than D_t. Their tendency is similar as their values are high at the column top and low at the column bottom.

Note that the dissimilarity between $\mathbf{D_{t,x}}$ and $\mathbf{D_{t,y}}$ demonstrates the anisotropy of the absorption packed column.

The total fluctuating mass flux

The total fluctuating mass fluxes $\overline{u'_x c'} + \overline{u'_y c'}$ along the radial direction at different bed height for Run 115 are shown in Fig. 5.34. Note that the profile of $\overline{u'_x c'} + \overline{u'_y c'}$ in this simulation is practically equal to that of $\overline{u'_x c'}$ in Fig. 5.28a because in the present case, the $\overline{u'_x c'}$ is much greater than the $\overline{u'_y c'}$, as seen by comparing Figs. 5.28a and 5.31a. Thus, $\overline{u'_x c'}$ diffusion is the main contribution to the turbulent effect.
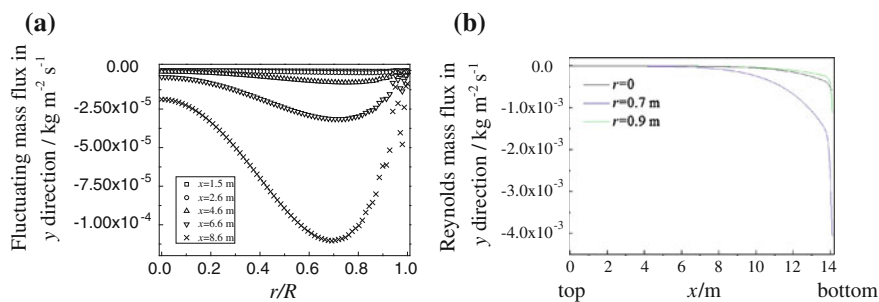
Fig. 5.31 Simulated profiles of $\overline{u'_y c'}$ for MEA in the absorption of CO_2 into aqueous MEA (Run 115) [10]. **a** $\overline{u'_y c'}$ along radial direction and **b** $\overline{u'_y c'}$ along axial direction

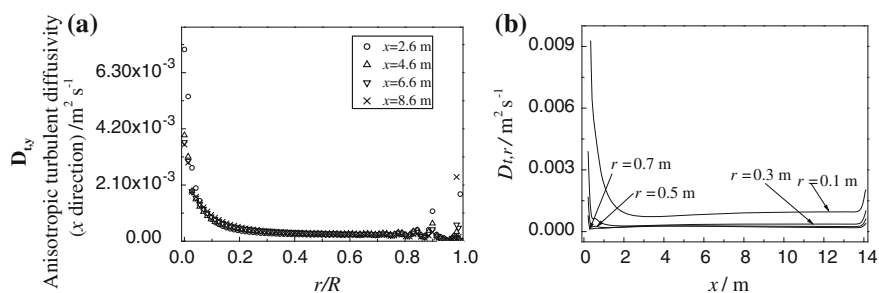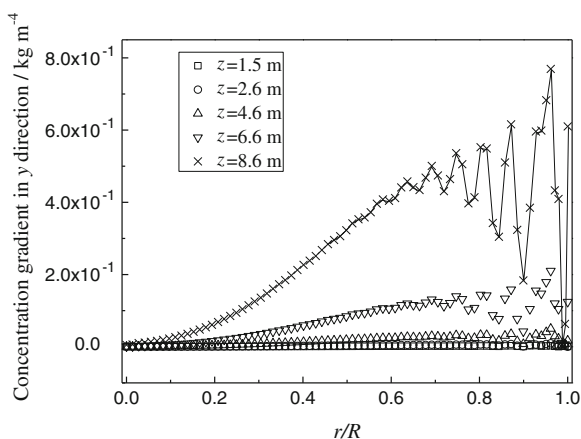**Fig. 5.32** Simulated profiles of MEA concentration gradient along radial direction (Run 115)

Fig. 5.33 Simulated profiles of $\mathbf{D_{t,y}}$ (*x is measured from column top*) for MEA in the absorption of CO_2 into aqueous MEA (Run 115) [10]. **a** $\mathbf{D_{t,y}}$ along radial direction. **b** $\mathbf{D_{t,y}}$ along axial direction

Fig. 5.34 Simulated profile of $\overline{u'_x c'} + \overline{u'_y c'}$ at different packed height (Run 115), (*x is measured from column top*) [10]
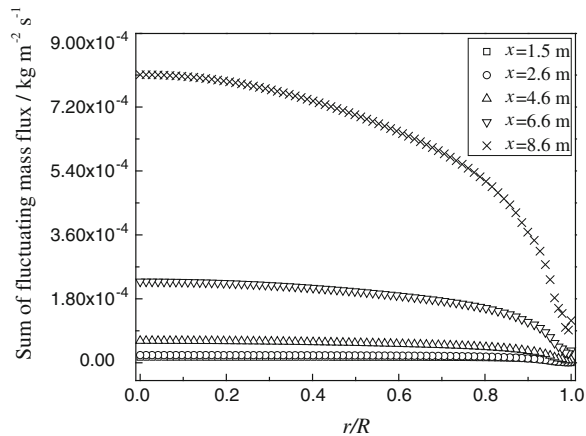
5.2.2 The Absorption of CO_2 by Aqueous NaOH in Packed Column

The simulation is by using standard Reynolds mass flux model; the model equation sets, the boundary conditions, and the evaluation of source terms are the same as given in Sect. 5.1.3. The simulated results are given in the following sections.

5.2.2.1 The Simulated Results and Verification

The liquid-phase temperature profile

The simulated profile of liquid-phase temperature for experiment T11 is shown in Fig. 5.35 and compared with experimental data. The simulated temperature at the column bottom is somewhat higher than the experimental measurement due to the same reason for the case of MEA absorption as stated in Sect. 5.2.1.1.

The NaOH concentration profile

The simulated profile of OH^- for T11 is given in Fig. 5.36. The simulated radial averaged axial concentration is seen to be confirmed by the experimental data.

5.2.2.2 The Anisotropic Mass Diffusivity

The radial distribution of axial liquid-phase velocity

The radial averaged axial liquid-phase velocity is shown in Fig. 5.37. As seen in the figure, wavy fluctuating of axial velocity in this case may be due to the
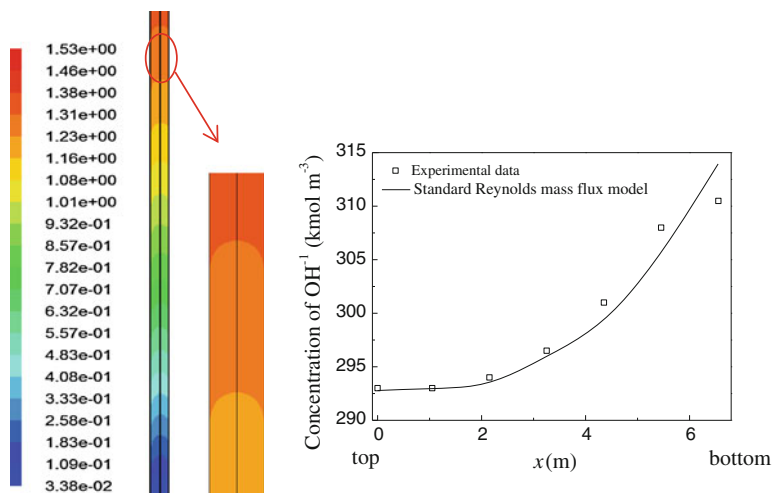
Fig. 5.35 Simulated profile of liquid-phase temperature in the column for CO_2 absorption into aqueous NaOH (T11) [10]
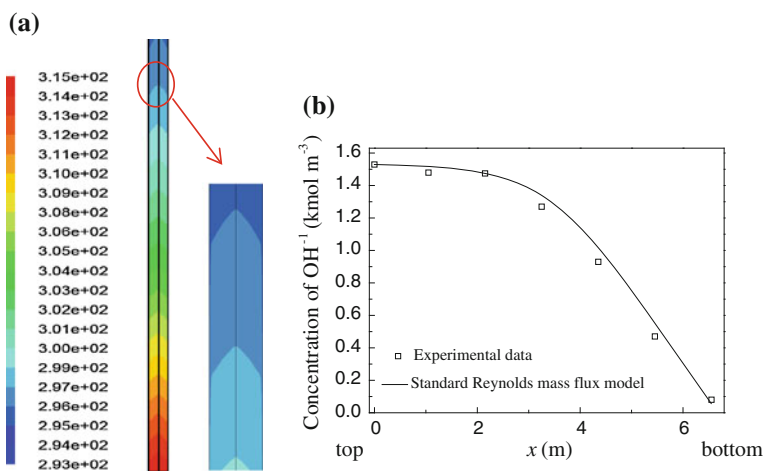

Fig. 5.36 Simulated profile of average OH^- concentration in the column for CO_2 absorption into aqueous NaOH (T11) [10]. **a** Profile of average OH^- concentration. **b** Average OH^- along axial direction

uneven porosity of the packing, and the ratio of column diameter to packing size is only about eight. Such wavy velocity affects significantly the shape of the anisotropic Reynolds mass flux and the mass diffusivities as seen in Figs. 5.38 and 5.39.
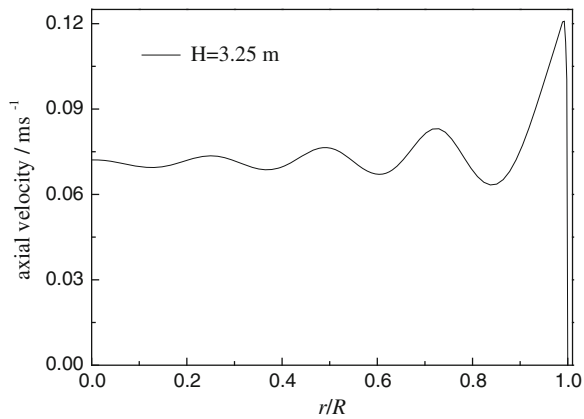
Fig. 5.37 Simulated radial profile of axial velocity at $z = 3.25$ m in the column for CO_2 absorption into aqueous NaOH (T11) [10]
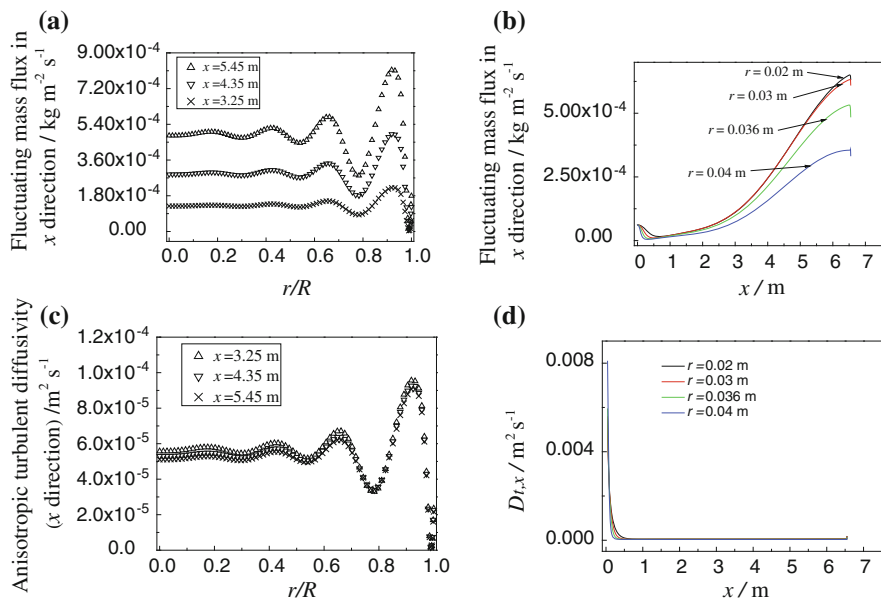
Fig. 5.38 Simulated axial fluctuating mass flux, concentration gradient, and axial mass diffusivity of OH^- in the column for CO_2 absorption into aqueous NaOH (T11), x—distance measured from column top (*x is measured from column top*) [10]. **a** $\overline{u'_x c'}c$ in radial direction. **b** $\overline{u'_x c'}$ in axial direction. **c** $\mathbf{D_{t,x}}$ in radial direction. **d** $\mathbf{D_{t,x}}$ in axial direction
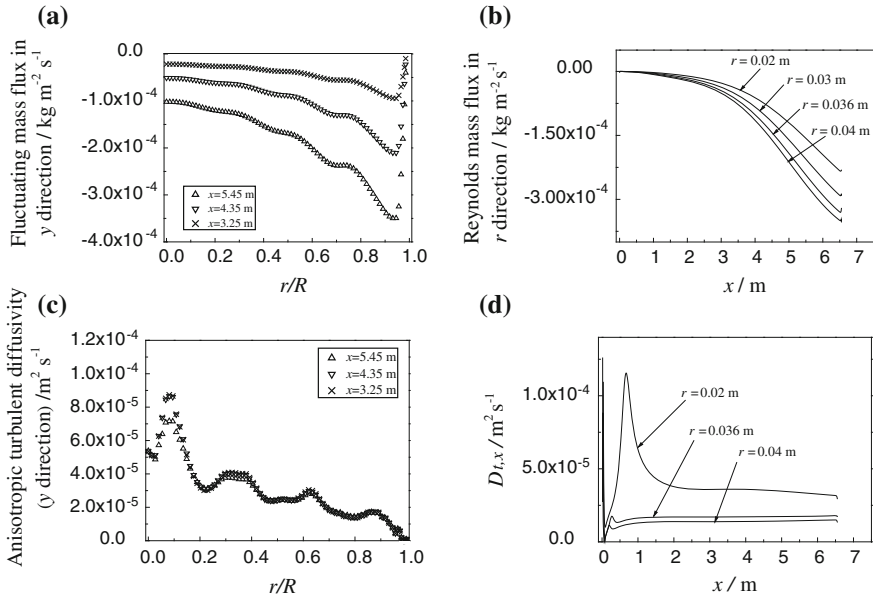
Fig. 5.39 Simulated fluctuating mass flux and mass diffusivity of OH^- in the column for CO_2 absorption into aqueous NaOH (T11), x—distance measured from column top (*x is measured from column top*) [10]. **a** $\overline{u'_y c'}$ in radial direction. **b** $\overline{u'_y c'}$ in axial direction. **c** $D_{t,y}$ in radial direction. **d** $D_{t,y}$ in axial direction

The anisotropic mass diffusivity

1. *The axial mass diffusivity*

The anisotropic mass diffusivity $\mathbf{D_{t,x}}$ is calculated using Eq. (3.37); the axial mass diffusivity is given in Fig. 5.38. Note that the wavy shape of $\overline{u'_x c'}$ and $\mathbf{D_{t,x}}$ contours is as the result of existing intense wavy axial velocity distribution along radial direction as seen in Fig. 5.37.

Similar to the absorption by MEA, the $\overline{u'_x c'}$ diffusion (turbulent effect) is small along the upper part of the column and becomes intense along the lower part of the column as shown in Fig. 5.38b.

2. *The radial mass diffusivity*

As seen in Fig. 5.39, the negative $\overline{u'_y c'}$ suppresses the NaOH radial decreasing concentration profile with decreasing rate toward the column bottom. The wavy shape of radial velocity and $\overline{u'_y c'}$ also affects the $\mathbf{D_{t,y}}$ to be waving.

5.3 Summary

In this chapter, the two CMT models, i.e., $\overline{c'^2} - \varepsilon_{c'}$ model and Reynolds mass flux model (standard, hybrid, and algebraic forms) are used for simulating the chemical absorption of CO_2 in packed column by MEA, AMP, and NaOH separately, and their simulated results are closely checked with the experimental data. It is noted that the radial distribution of D_t is similar to α_t but quite different from μ_t. It means the conventional assumption that $Sc_t\left(= \frac{\mu_t}{\rho D_t}\right)$ and $Pr_t\left(= \frac{\mu_t}{\rho \alpha_t}\right)$ are constant throughout the column is unjustified. Also the appearance of negative $\overline{u'_y c'}$ in MEA and NaOH absorption indicates the increasing tendency of their radial concentrations because lower absorption is promoted by the co-action of the turbulent mass flux diffusion.

References

1. Yin FH, Sun CG, Afacan A, Nandakumar K, Chuang KT (2000) CFD modeling of mass-transfer processes in randomly packed distillation columns. Ind Eng Chem Res 39(5):1369–1380
2. Liu SJ (2001) A continuum model for gas-liquid flow in packed towers. Chem Eng Sci 56:5945–5953
3. Hjertager LK, Hjertager BH, Solberg T (2002) CFD modelling of fast chemical reactions in turbulent liquid flows. Com and Chem Eng 26(4–5):507–515
4. Jiang Y, Khadilkar MR, Al-Dahhan MH, Dudukovic AP (2002) CFD of multiphase flow in packed-bed reactors: I. k-fluid modeling issues. AIChE J 48(4):701–715
5. Jiang Y, Khadilkar MR, Al-Dahhan MH, Dudukovic MP (2002) CFD of multiphase flow in packed-bed reactors: II. Results and applications. AIChE J 48(4):716–730
6. Yin FH, Afacan A, Nandakumar K, Chuang KT (2002) Liquid holdup distribution in packed columns: gamma ray tomography and CFD simulation. Chem Eng Process 41(5):473–483
7. de Lemos MJS, Mesquita MS (2003) Turbulent mass transport in saturated rigid porous media. Int J Heat Mass Transfer 30(1):105–113
8. Liu GB, Yu KT, Yuan XG, Liu CJ (2006) Simulations of chemical absorption in pilot-scale and industrial-scale packed columns by computational mass transfer. Chem Eng Sci 61(19):6511–6529
9. Liu GB, Yu KT, Yuan XG, Liu CJ (2006) New model for turbulent mass transfer and its application to the simulations of a pilot-scale randomly packed column for CO_2-NaOH chemical absorption. Ind Eng Chem Res 45(9):3220–3229
10. Li WB (2012) Theory and applications of computational mass transfer, PhD dissertation, Tianjin University, Tianjin, China
11. Chen CJ, Jaw SY (1998) Fundamentals of turbulence modeling. Taylor and Francis, Washington, DC
12. Sater VE, Levenspiel O (1966) Two-phase flow in packed beds. Ind Eng Chem Fundam 5:86–92
13. Engel V, Stichmair J, Geipel W (1997) A new model to predict liquid holdup in packed columns—using data based on capacitance measurement techniques. Institute Chemical Engineering Symposium Series, Part 2, p. 939–947

14. Giese M, Rottschafer K, Vortmeyer D (1998) Measured and modeled superficial flow profiles in packed beds with liquid flow. AIChE J 44:484–490
15. Roblee LHS, Baird RM, Tierney JW (1958) Radial porosity variations in packed beds. AIChE J 4:460–464
16. de Klerk A (2003) Voidage variation in packed beds at small column to particle diameter ratio. AIChE J 49:022–2029
17. Wellek RM, Brunson RJ, Law FH (1978) Enhancement factors for gas absorption with 2nd-order irreversible chemical-reaction. Can J Chem Eng 56:181–186
18. Ferchichi M, Tavoularis S (2002) Scalar probability density function and fine structure in uniformly sheared turbulence. J Fluid Mech 461:155–182
19. Hikita H, Asai S, Katsu Y, Ikuno S (1979) Absorption of carbon-dioxide into aqueous monoethanolamine solutions. AIChE J 25:793–800
20. Onda K, Takeuchi H, Okumoto Y (1968) Mass transfer coefficients between gas and liquid phases in packed columns. J Chem Eng Japan 1:56–62
21. Danckwerts PV (1979) Reaction of CO_2 with ethanolamines. Chem Eng Sci 34(4):443–446
22. Kohl AL, Nielsen RB (1997) Gas purification. Gulf Publishing Company, Houston
23. Pintola T, Tontiwachwuthikul P, Meisen A (1993) Simulation of pilot plant and industrial CO_2-MEA absorbers. Gas Sep Purif 7:47–52
24. Tontiwachwuthikul P, Meisen A, Lim CJ (1992) CO_2 absorption by NaOH, monoethanolamine and 2-Amino-2-Methyl-1-Propanol Solutions in a packed-column. Chem Eng Sci 47(2):381–390
25. Saha AK, Bandyopadhyay SS, Biswas AK (1995) Kinetics of absorption of CO_2 into aqueous-solutions of 2-Amino-2-Methyl-1-Propanol. Chem Eng Sci 50(22):3587–3598
26. Liu GB (2006) Computational transport and its application to mass transfer and reaction processes in packed beds. PhD dissertation, Tianjin University, Tianjin, China
27. Pohorecki R, Moniuk W (1988) Kinetics of reaction between carbon-dioxide and hydroxyl ions in aqueous-electrolyte solutions. Chem Eng Sci 43(7):1677–1684
28. Jones WP, Launder BE (1973) The calculation of low-Reynolds-number phenomena with a two-equation model of turbulence. Int J Heat Mass Transfer 16:1119–1130

Chapter 6
Application of Computational Mass Transfer (III): Adsorption Process

Abstract In this chapter, adsorption process is simulated by using computational mass transfer (CMT) models as presented in Chap. 3. As the adsorption process is unsteady and accompanied with heat effect, the time parameter and the energy equation as presented in Chap. 2 are involved in the model equations. The simulated concentration profile of the column at different times enables to show the progress of adsorption along the column as an indication of the process dynamics. The simulated breakthrough curve and regeneration curve for adsorption and desorption by the two CMT models, i.e., the $\overline{c'^2} - \varepsilon_{c'}$ model and the Reynolds mass flux model, are well checked with the experimental data. Some issues that may cause discrepancies are discussed.

Keywords Simulation of adsorption · Concentration profile · Breakthrough curve · Regeneration curve

Nomenclature

a_{p}	Surface area per unit volume of packed column, m^{-1}
c	Mass concentration, $\mathrm{kg\ m}^{-3}$
$c_{\mathrm{pg}},\ c_{\mathrm{ps}}$	Specific heat of gas phase and solid phase, respectively, $\mathrm{J\ kg}^{-1}\ \mathrm{K}^{-1}$
$C_{\mu},\ C_{1\varepsilon},\ C_{1\varepsilon}$	Turbulence model constants for the velocity field
$C_{c0},\ C_{c1},\ C_{c2},\ C_{c3}$	Turbulence model constants for the concentration field
$C_{t0},\ C_{t1},\ C_{t2},\ C_{t3}$	Turbulence model constants for the temperature field
$\overline{c^2}$	Concentration variance, $\mathrm{kg}^2\ \mathrm{m}^{-6}$
D	Molecular diffusivity, $\mathrm{m}^2\ \mathrm{s}^{-1}$
D_{t}	Turbulent mass diffusivity, $\mathrm{m}^2\ \mathrm{s}^{-1}$
d_{H}	Hydraulic diameter of packing, m
d_{p}	Nominal packing diameter, m
Er	Exponential decaying function
F	Flow rate, $\mathrm{L\ min}^{-1}$
g	Gravity acceleration, $\mathrm{m\ s}^{-2}$
Gr	Grashof number ($Gr = \rho^2 g\beta\ (T_g - T_0)\ d_{\mathrm{col}}^3/\mu^2$)

H	Packing height measured from column bottom ($H = 0$ at column bottom), m
h	Heat transfer coefficient from gas phase to packing, W m^{-2} K^{-1}
h_{w}	Heat transfer coefficient from gas phase to ambient, W m^{-2} K^{-1}
h_{w1}	Heat transfer coefficient from gas phase to column wall, W m^{-2} K^{-1}
h_{w2}	Heat transfer coefficient from column to ambient, W m^{-2} K^{-1}
ΔH	Heat of adsorption of adsorbate, J mol^{-1}
k	Turbulent kinetic energy, m^2 s^{-2}
K_{G}	Mass transfer coefficient of gas phase and intra-particle, m s^{-1}
k_{G}	Mass transfer coefficient of gas phase, m s^{-1}
k_{g}	Thermal conductivity of gas, W m^{-1} K^{-1}
k_{p}	Intra-particle mass transfer coefficient, m s^{-1}
k_{s}	Thermal conductivity of adsorbent particle, W m^{-1} K^{-1}
M	Molecular weight of adsorbate, kg mol^{-1}
Nu	Nusselt number ($Nu = hR_{\mathrm{p}}/k_{\mathrm{g}}$)
P	Total pressure of gas phase in the column, atm
Pr	Prandtl number ($Pr = C_{\mathrm{pg}}\mu/k_{\mathrm{g}}$)
q	Adsorbate concentration in solid phase, respectively, mol kg^{-1}
r	Radial distance from the axis of the column, m
R	Inner radius of the column, m
R_{τ}	Velocity to concentration time scale ratio
R_{p}	Packing radius, m
Re_{p}, Re_{col}	Reynolds number base on packing and column diameter, respectively $\left(Re_{\mathrm{p}} = \rho|u|d_{\mathrm{p}}/\mu, Re_{\mathrm{col}} = \rho|u|d_{\mathrm{col}}/\mu\right)$
Sc, Sc_{t}	Schmidt number base on molecular and turbulent diffusivity, respectively ($Sc = \mu/\rho D$, $Sc_{\mathrm{t}} = \mu/\rho D_{\mathrm{t}}$)
S_{c}	Source term of mass transfer, kg m^{-3} s^{-1}
S_{m}	Source term of momentum transfer, N m^{-3}
S_{Tg}	Thermal source term of the gas phase, J m^{-3} s^{-1}
S_{Ts}	Thermal source term of the solid phase, J m^{-3} s^{-1}
t	Time, min
T_{g}	Gas phase temperature, K
$T_{\mathrm{g, in}}$	Inlet temperature of the gas phase, K
T_{s}	Solid phase temperature, KT_{w1}, T_{w2} temperature of the inner and outer wall, K
T_0	Ambient temperature and initial temperature of the solid phase, K
$\overline{T'^2}$	Temperature variance, t^2

u	Gas interstitial velocity vector, m s^{-1}
u'	Gas fluctuating velocity, m s^{-1}
x	Axial distance from column top ($x = 0$ at column top), m
y_w	Distance from the column wall, m
z	Height of packing measured from the gas phase inlet of the column, m
Z	Total packing height of the column, m
α, α_t	Molecular, turbulent thermal diffusivity, respectively, m^2 s^{-1}
ε	Turbulent dissipation, m^2 s^{-3}
ε_c	Turbulent dissipation of the concentration fluctuation, kg^2 m^{-6} s^{-1}
ε_t	Turbulent dissipation rate of temperature fluctuation, s^{-1}
γ	Local column porosity
γ_∞	Porosity in an unbounded packing
γ_p	Particle porosity
δ_{ij}	Kronecker delta
ρ	Gas density, kg m^{-3}
ρ_g	Total gas concentration, mol m^{-3}
ρ_s	Apparent density of the solid adsorbent, kg m^{-3}
μ, μ_t	Gas molecular, turbulent viscosity, respectively, kg m^{-1} s^{-1}
σ_k, σ_ε, σ_c, $\sigma_{\varepsilon c}$, σ_t, $\sigma_{\varepsilon t}$	Turbulence model constants for diffusion of k, ε, $\overline{c^2}$, ε_c, $\overline{t^2}$, ε_t

Adsorption process has been widely used in many chemical and related industries, such as the separation of hydrocarbon mixtures, the desulfurization of natural gas, and the removal of trace impurities in fine chemical production. Most of the adsorption researches in the past are focused on the experimental measurement of the breakthrough curve for studying the dynamics. The conventional model used for the adsorption process is based on one-dimensional or two-dimensional dispersion, in which the adsorbate flow is either simplified or computed by using computational fluid dynamics (CFD), and the distribution of adsorbate concentration is obtained by adding dispersion term to the adsorption equation with unknown turbulent mass diffusivity D_t. Nevertheless, the usual way to find the D_t is either by employing empirical correlation obtained from inert tracer experiment or by guessing a Schmidt number applied to the whole process. As stated in Chap. 3, such empirical method is unreliable and lacking theoretical basis.

Theoretically, the unknown diffusivity can be obtained directly by the closure of the mass transfer differential equation by a proper method in order to solve at once all unknown parameters in the equation. In the following sections, the

two-equation $\overline{c'^2} - \varepsilon_{c'}$ model and Rayleigh mass flux model are used for this purpose as presented by Li et al. [1].

6.1 $\overline{c'^2} - \varepsilon_c$ Two-Equation Model for Gas Adsorption

Assumptions
1. The gas flow in the randomly packed adsorption column is axially symmetrical and in turbulent state.
2. The concentration of adsorbate in the gas phase is very low.
3. The driving force of adsorption is the concentration difference between gas phase and outer surface of the solid adsorbent, and thus, the mass transfer calculation is based on the surface area and the surface concentration of the solid adsorbent.
4. The column has no insulation, and the heat is lost from the column outer surface to the environment.

6.1.1 Model Equations

The $\overline{c'^2} - \varepsilon_{c'}$ two-equation model equations for adsorption are similar to those of absorption except that adsorption is an unstable process and the time parameter should be involved. On the other hand, the gas adsorption process consists of gas and solid phases, and the corresponding equations should established for each phase

1. The CFD equation set

   Mass conversation for gas phase

   $$\frac{\partial(\rho_G\gamma)}{\partial t} + \frac{\partial(\rho_G\gamma U_i)}{\partial x_i} = S_{mG}$$

   Momentum conversation for gas phase

   $$\frac{\partial(\rho_G\gamma U_i)}{\partial t} + \frac{\partial\left(\rho_G\gamma U_i U_j\right)}{\partial x_i} = -\gamma\frac{\partial P}{\partial x_j} + \frac{\partial}{\partial x_i}\left(\gamma\mu\frac{\partial U_j}{\partial x_i} - \gamma\rho_G\overline{u_i'u_j'}\right) + S_{FG}$$

   $$-\rho_G\overline{u_i'u_j'} = \mu_t\left(\frac{\partial U_i}{\partial x_j} + \frac{\partial U_j}{\partial x_i}\right) - \frac{2}{3}\delta_{ij}\rho_G k$$

   $$\mu_t = C_\mu\rho_G\frac{k^2}{\varepsilon}$$

k equation

$$\frac{\partial(\rho_G\gamma k)}{\partial t} + \frac{\partial(\rho_G\gamma U_i k)}{\partial x_i} = \frac{\partial}{\partial x_i}\left[\gamma\left(\mu + \frac{\mu_t}{\sigma_k}\right)\frac{\partial k}{\partial x_i}\right] + \gamma G_k - \rho_G\gamma\varepsilon$$

ε equation

$$\frac{\partial(\rho_G\gamma\varepsilon)}{\partial t} + \frac{\partial(\rho_G\gamma U_i\varepsilon)}{\partial x_i} = \frac{\partial}{\partial x_i}\left[\gamma\left(\mu + \frac{\mu_t}{\sigma_\varepsilon}\right)\frac{\partial\varepsilon}{\partial x_i}\right] + C_{1\varepsilon}\gamma\frac{\varepsilon}{k}G_k - C_{2\varepsilon}\gamma\rho_G\frac{\varepsilon^2}{k}$$

$$G_k = \mu_t\left(\frac{\partial U_i}{\partial x_j} + \frac{\partial U_j}{\partial x_i}\right)\frac{\partial U_j}{\partial x_i}$$

(1.15c)

where γ is the porosity of the packed bed; model constants are as follows [2]: $C_\mu = 0.09$, $C_{1\varepsilon} = 1.44$, $C_{2\varepsilon} = 1.92$, $\sigma_k = 1.0$, $\sigma_\varepsilon = 1.3$.

2. The heat transfer equation set

Energy conservation for adsorbate in gas phase

$$\frac{\partial(\rho_G\gamma C_{pG}T_G)}{\partial t} + \frac{\partial(\rho_G\gamma C_{pG}U_i T_G)}{\partial x_i} = \frac{\partial}{\partial x_i}\left[\rho_G\gamma C_{pG}(\alpha + \alpha_t)\frac{\partial T_G}{\partial x_i}\right] + S_{TG}$$

where T_G is the temperature of the gas phase; C_{pG} is the specific heat of the gas phase.

Energy conservation for solid adsorbent

$$\frac{\partial\left[\rho_s(1-\gamma)C_{ps}T_s\right]}{\partial t} = \frac{\partial}{\partial x_i}\left[(1-\gamma)\lambda_s\frac{\partial T_s}{\partial x_i}\right] + S_{TS}$$

where C_{ps} is specific heat of the solid adsorbent.

Energy conservation for the column wall

$$\frac{\partial(\rho_w C_{pw}T_w)}{\partial t} = \frac{\partial}{\partial x_i}\left(\lambda_w\frac{\partial T_w}{\partial x_i}\right) + S_{TW}$$

where C_{pw} is the specific heat of the wall material;

$\overline{T'^2}$ *equation*

$$\frac{\partial\left(\rho_G\gamma\overline{T'^2}\right)}{\partial t} + \frac{\partial\left(\rho_G\gamma U_i\overline{T'^2}\right)}{\partial x_i} = \frac{\partial}{\partial x_i}\left[\rho_G\gamma\left(\frac{\alpha_t}{\sigma_T} + \alpha\right)\frac{\partial\overline{T'^2}}{\partial x_i}\right] + 2\rho_G\gamma\alpha_t\frac{\partial T_G}{\partial x_j}\frac{\partial T_G}{\partial x_j}$$
$$- 2\rho_G\gamma\varepsilon_{T'}$$

$\varepsilon_{T'}$ equation

$$\frac{\partial(\rho_G \gamma \varepsilon_{T'})}{\partial t} + \frac{\partial(\rho_G \gamma U_i \varepsilon_{T'})}{\partial x_i} = \frac{\partial}{\partial x_i}\left[\rho_G \gamma \left(\frac{\alpha_t}{\sigma_{\varepsilon_{T''}}} + \alpha\right)\frac{\partial \varepsilon_{T'}}{\partial x_i}\right]$$

$$+ C_{T1}\rho_G \gamma \alpha_t \frac{\varepsilon_{T'}}{T'^2}\left(\frac{\partial T_G}{\partial x_i}\right)^2 - C_{T2}\gamma \rho_G \frac{\varepsilon_{T'}^2}{T'^2} - C_{T3}\rho_G \gamma \frac{\varepsilon \varepsilon_{T'}}{k}$$

α_t equation

$$\alpha_t = C_{T0}k\left(\frac{k\overline{T'^2}}{\varepsilon \varepsilon_{T'}}\right)^{\frac{1}{2}}$$

Model constants are as follows [3]:
$C_{T0} = 0.11$, $C_{T1} = 1.8$, $C_{T2} = 2.2$, $C_{T3} = 0.8$, $\sigma_{T'} = 1.0$, $\sigma_{\varepsilon_{T'}} = 1.0$.

3. The mass transfer equation set

   Species mass conservation for gas phase

   $$\frac{\partial(\gamma C)}{\partial t} + \frac{\partial(\gamma U_i C)}{\partial x_i} = \frac{\partial}{\partial x_i}\left[\gamma D \frac{\partial C}{\partial x_i} - \overline{u_i' c'}\right] + S_{CG}$$

   $$\overline{u_i' c'} = D_t \frac{\partial C}{\partial x_i}$$

where C is the mass concentration (kg m^{-3}) of adsorbate in the gas phase.

$\overline{c'^2}$ equation

$$\frac{\partial\left(\overline{\gamma c'^2}\right)}{\partial t} + \frac{\partial\left(\gamma U_i \overline{c'^2}\right)}{\partial x_i} = \frac{\partial}{\partial x_i}\left[\gamma\left(\frac{D_t}{\sigma_c} + D\right)\frac{\partial \overline{c'^2}}{\partial x_i}\right] + 2\gamma D_t\left(\frac{\partial C}{\partial x_i}\right)^2 - 2\gamma \varepsilon_{c'}$$

$\varepsilon_{c'}$ equation

$$\frac{\partial(\gamma \varepsilon_{c'})}{\partial t} + \frac{\partial(\gamma U_i \varepsilon_{c'})}{\partial x_i} = \frac{\partial}{\partial x_i}\left[\gamma\left(\frac{D_t}{\sigma_{\varepsilon_{c'}}} + D\right)\frac{\partial \varepsilon_{c'}}{\partial x_i}\right] + C_{c1}\rho_G \gamma D_t \frac{\varepsilon_{c'}}{\overline{c'^2}}\left(\frac{\partial C}{\partial x_i}\right)^2 - C_{c2}\gamma\frac{\varepsilon_{c'}^2}{\overline{c'^2}}$$

$$- C_{c3}\gamma\frac{\varepsilon \varepsilon_{c'}}{k}$$

D_t equation

$$D_t = C_{c0}k\left(\frac{k\overline{c'^2}}{\varepsilon \varepsilon_{c'}}\right)^{\frac{1}{2}}$$

Model constants are as follows [4]:
$C_{c0} = 0.11$, $C_{c1} = 1.8$, $C_{c2} = 2.2$, $C_{c3} = 0.8$, $\sigma_{c'} = 1.0$, $\sigma_{\varepsilon_{c'}} = 1.3$.

6.1.2 Boundary Conditions

Inlet (column bottom, $x = 0$): Similar to the absorption column in Chap. 5:

$$u = u_{in}, \quad C = C_{in}, \quad T = T_{in}$$

$$k_{in} = 0.003 u_{in}^2, \quad \varepsilon_{in} = 0.09 \frac{k_{in}^{1.5}}{d_H},$$

$$\overline{c_{in}'^2} = (0.082 C_{in})^2, \quad \varepsilon_{c',in} = R_\tau \left(\frac{\varepsilon_{in}}{k_{in}}\right) \overline{c_{in}'^2}.$$

$$\overline{T_{in}'^2} = (0.082 \Delta T)^2, \quad \varepsilon_{t',in} = R_{\tau,t} \left(\frac{\varepsilon_{in}}{k_{in}}\right) \overline{T_{in}'^2}.$$

where d_H is the hydraulic diameter of the particle, which is calculated by:

$$d_H = \frac{4\gamma_\infty}{a_p(1 - \gamma_\infty)}$$

where γ_∞ is the average porosity of the unbounded packed bed; a_p is the volumetric packing surface, which is given by:

$$a_p = \frac{6(1 - \gamma_\infty)}{d_p}$$

where R_τ represents the time scale, $R_\tau = \left(C_{c0} \frac{k_{in}^2}{\varepsilon_{in}} \frac{1}{D_t}\right)^2$.

Outlet (column top): Consider as fully developed turbulence.

Column wall: No slip condition is adopted. Zero flux condition is not satisfied for the present model, and the boundary conditions of $\overline{c_w'^2}$ and $\overline{T_w'^2}$ are set as follows:

$$\overline{c_w'^2} = \left(0.082 \overline{C_{in}}\right)^2, \quad \varepsilon_{c',w} = R_{\tau,w} \frac{\varepsilon_w}{k_w} \overline{c'^2}$$

$$\overline{T_w'^2} = (0.082 \Delta T)^2, \quad \varepsilon_{T',w} = R_{\tau,t,w} \frac{\varepsilon_w}{k_w} \overline{T_w'^2}$$

where $R_{\tau,w} = \left(C_{c0} \frac{k_w^2}{\varepsilon_w} \frac{1}{D_t}\right)^2$, which should be calculated by the method of trial and error as the D_t is known only after the simulation. However, if D_t is greater than 10^{-3}, the $R_{\tau,w}$ is substantially equal to one. The k_w and ε_w can be obtained from the standard wall function of k–ε model.

6.1.3 Evaluation of Source Terms

Determination of S_{FG}

The source term S_{FG} in the momentum equation represents the resistance of gas flow by the solid adsorbent (packing particles), which can be calculated by [5]:

$$S_{FG} = \gamma(F_{GS} + \rho g)$$

$$F_{GS} = \frac{150\mu_G}{d_p^2}\frac{(1-\gamma)^2}{\gamma^3}U + \frac{1.75\rho_G}{d_p}\frac{(1-\gamma)}{\gamma^3}U^2$$

where γ is calculated by [6]:

$$\gamma = \gamma_\infty + \frac{1-\gamma_\infty}{2}\mathrm{Er}\left[(1-0.3P_d)\times\cos\left(\frac{2\pi}{a_\gamma + 1.6\mathrm{Er}^2}\frac{R-r}{P_d d_p}\right) + 0.3P_d\right]$$

where γ_∞ is the porosity in an unbounded packed bed; R is the radius of the packed bed; r is the radial position concerned; a_γ is a constant depending on the ratio of the particle size to the column size:

$$a_\gamma = \frac{2R}{n_\gamma P_d d_p} - 1.6\exp\left[-2.4P_d\left(\frac{R}{d_p}\right)^{3/4}\right]$$

$$n_\gamma = \mathrm{int}\left\{\frac{2}{1+1.6\exp\left[-2.4P_d\left(\frac{R}{d_p}\right)3/4\right]}\frac{R}{P_d d_p}\right\}$$

The Er is the exponential decaying function, which is given by:

$$\mathrm{Er} = \exp\left[-1.2P_d\left(\frac{R-r}{d_p}\right)^{3/4}\right]$$

where P_d is the period of oscillation normalized by the nominal particle size and $P_d = 0.94$ for sphere particle.

Determination of S_{TG}

The source term S_{TG} in the adsorbate conservation equation for gas phase can be expressed by:

$$S_{TG} = h_s(1-\gamma)a_p(T_s - T_G) - h_w a_{w1}(T_G - T_{w1})$$

The first term on the right-hand side of foregoing equation represents the transfer of heat of adsorption from the outer surface of solid adsorbent particle to the gas phase; the second term represents the heat transfer from the gas phase to the column wall. In the equation, h_s is heat transfer film coefficient between solid adsorbent surface and the gas phase; a_p is the outer surface of the solid adsorbent; T_s is the outer temperature of the solid adsorbent; T_G is the temperature of the gas

phase; h_w is the heat transfer film coefficient between gas phase and the inner wall of the column; a_{w1} is the inner area of the column wall; T_{w1} is the temperature of the inner wall.

Determination of S_{TS}

The source term S_{TS} in the equation of energy conservation for solid adsorbent can be written as follows:

$$S_{TS} = \Delta H \rho_s (1 - \gamma) \frac{\partial q}{\partial t} - h_s (1 - \gamma) a_p (T_s - T_G)$$

where ΔH is the heat of adsorption; q is the concentration of adsorbate in the solid surface; $\frac{\partial q}{\partial t}$ is the rate of adsorption, equal to S_{mG}; h_s is the film coefficient of heat transfer. h_s can be calculated by [7]:

$$h_s = \frac{h_G}{R_p} Nu, \qquad Nu = \frac{0.357}{2\gamma} Re_p^{0.641} Pr^{1/3}$$

where Re_p is the Reynolds number based on particle diameter.

Determination of S_{TW}

The source term S_{TW} in the energy conservation equation for the column wall is given by:

$$S_{TW} = h_{w1} a_{w1} (T_G - T_{w1}) - h_{w2} a_{w2} (T_{w2} - T_0)$$

The first term on the right side of the equation represents the heat transfer from gas phase to the inner wall of the column; the second term represents the heat transfer from outer wall of the column to the environment. The T_{w1} and T_{w2} are, respectively, the temperature of the inner and outer wall of the column; T_0 is environmental temperature; h_{w1} is the film coefficient of heat transfer between gas and inner column wall; h_{w2} is the film coefficient of heat transfer between outer column wall and the environment; a_{w1} and a_{w2} are, respectively, the inner and outer area of the column wall. Considering the high thermal conductivity of the column wall, T_{w1} and T_{w2} is practically equal, and the difference between a_{w1} and a_{w2} is very small, the foregoing equation can be written as follows:

$$h_{w1} a_{w1} (T_G - T_{w1}) = h_{w2} a_{w2} (T_{w2} - T_0) = h_w a_w (T_G - T_0) = Q_w$$

where Q_w is the heat loss from outer surface of the adsorption column to the environment; h_w is the film coefficient of heat transfer, which is equal to:

$$h_w = \frac{h_{w1} h_{w2}}{h_{w1} + h_{w2}}$$

where h_{w1} and h_2 can be calculated by [8]:

$$h_{w1} = 0.023 \frac{k_G}{d_{col}} (Re_{col})^{0.8} (Pr)^{0.3}$$

$$h_{w2} = b_h \frac{k_G}{Z} (Gr \, Pr)^n$$

where k_G is the thermal conductivity of the gas phase, d_{col} is the column inner diameter, Re_{col} is the Reynolds number based on the column diameter, Pr is the Prandtl number, Z is the height of the packed bed, Gr is the Grashof number, and b_h and n are heat convection parameters.

Determination of S_{mG}

Source term S_{mG} (kg m^{-3} s^{-1}) in the species conservation equation represents the rate of mass adsorbed, which can be expressed by:

$$S_{mG} = K_G a_p \left(c_A - c_A^* \right)$$

where c_A is the mass concentration of adsorbate in the gas phase (kg m^{-3}); c_A^* is the c_A in equilibrium with the solid adsorbent surface; K_G is the mass transfer coefficient (m^2 s^{-1}) based on the gas phase driving force $\left(c_A - c_A^* \right)$ and includes the intra-particle mass transfer; a_p is the volumetric surface area of the packing particle (m^2 m^{-3}). K_G is given by [9]:

$$\frac{1}{K_G} = \frac{1}{k_G} + \frac{1}{\gamma_p k_p}$$

where γ_p is the porosity of the particle; k_G is the film coefficient of mass transfer between gas phase and the outer surface of the particle; k_p is the intra-particle mass transfer coefficient of the particle, which can be calculated by [10]:

$$k_p = \frac{5D_p}{R_p}$$

where R_p is the particle radius; D_p is the pore diffusivity as given by Yang [11]. The k_G can be calculated by the following correlation [12]:

$$\frac{k_G d_p}{D} = 2.0 + 1.1 Re_p^{0.6} Sc^{0.33}$$

where Re_p is the Reynolds number based on particle diameter.

Table 6.1 Properties of the adsorption column and the adsorbent particles

Term (unit)	Value
Inside diameter R (m)	0.41
Packed column height Z (m)	0.20
Average particle size d_p (m)	0.002
Bulk density ρ_s (kg m^{-3})	420
Particle porosity γ_p	0.67
Average column porosity γ_∞	0.42
Specific heat of gas C_{pg} [J (kg K)$^{-1}$]	970
Specific heat of adsorbent C_{ps} [J (kg K)$^{-1}$]	836
Ambient temperature T_0 (K)	298
Thermal conductivity of adsorbent k_s [W (m K)$^{-1}$]	0.3
Heat of adsorption of adsorbate ΔH (J mol^{-1})	28,020

6.1.4 Simulated Results and Verification

The object of simulation is the adsorption of methylene chloride vapor in air on an activated carbon column, and the simulated results were compared with published experimental data [13]. The details of adsorption column and adsorbent particle properties are given in Table 6.1

Since the adsorption process is unsteady, a convenient method of solution is to dividing the process time into a large number of time intervals Δt for stepwise computation. The Δt in present case is set to be 1 min, which is about 1/140 of the total adsorption time.

The simulated results and comparison with experimental data are given below.

Concentration profile along the column at different times

The simulated profiles of adsorbate, methylene chloride, at different times are given in Fig. 6.1, in which the development of the concentration profiles in the column with time is seen. The concentration profiles enable us to provide detailed inside information of the breakthrough curve. For instance, although Y_{out}/Y_{in} is almost approach to zero at 15 and 45 min, large amounts of methylene chloride have been adsorbed in the column as shown in the concentration profile. From 105 to 135 min, the adsorption in the column is substantially being saturated, but Y_{out}/Y_{in} is still less than 1.0. As shown in the figure, the methylene chloride concentration distributions along radial direction are unevenly in parabolic shape. It is due to the existence of flow dispersion, non-uniform porosity, and the wall effect; these influential factors have been considered and modeled in the present simulation. Besides, Fig. 6.1 also shows more details of the progress of the adsorption in the column at different times. The rate of adsorption in the column from 15 to 45 min is seen much faster than from 105 to 135 min. This result is helpful to understand the process dynamics and the optimization of the adsorption process.
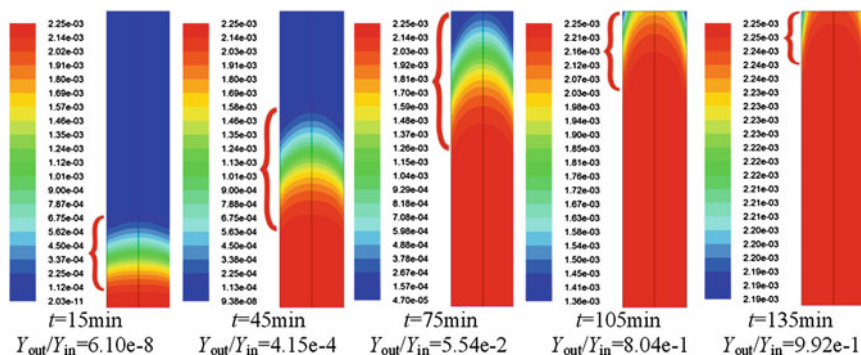
Fig. 6.1 Simulated sequences of concentration profiles along the column at different times by two-equation model [14]

Fig. 6.2 Comparison between simulated breakthrough curve and experimental data (*Y is the mole fraction of adsorbate in gas phase*) (Reprinted from Ref. [1], Copyright 2011, with permission from American Chemical Society)
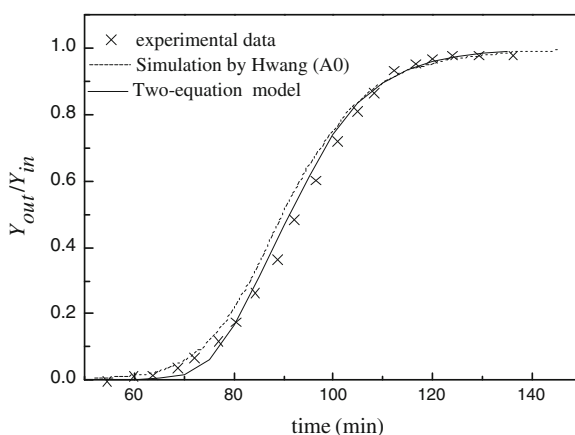
In the adsorption column, the adsorption is taken place only in certain part of column height as represented by the red bracket shown in Fig. 6.1. The parabolic form of concentration distribution is obvious due to the wall effect.

Breakthrough curve

From the radial average of Y_{out} and Y_{in} at different times as given in Fig. 6.1, the simulated breakthrough curve can be obtained as shown in Fig. 6.2. The simulated curve matches closely the experimental data. In this figure, the simulation by Hwang [13] is also given. Their simulation was based on assuming the turbulent mass diffusivity D_t to be separately 1.5×10^{-2}, 1.5×10^{-3}, and 1.5×10^{-4}, and the best fitting to the experimental data was found to be 1.5×10^{-3}; such simulation is shown in Fig. 6.1. The advantage of present model is avoiding the use of any empirical or guessing means to estimate the D_t.
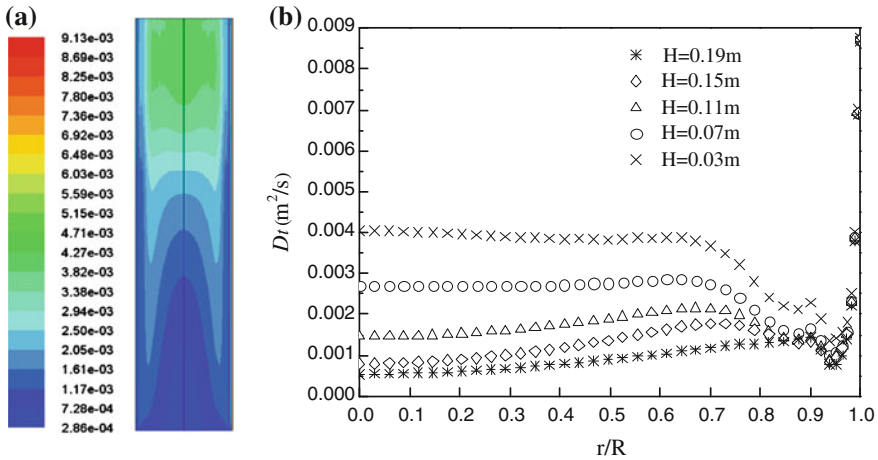
Fig. 6.3 Simulated profiles of D_t at 75 min (*H is the height of the packed bed measured from column bottom*). **a** Distribution along column and **b** radial distribution (Reprinted from Ref. [1], Copyright 2011, with permission from American Chemical Society)
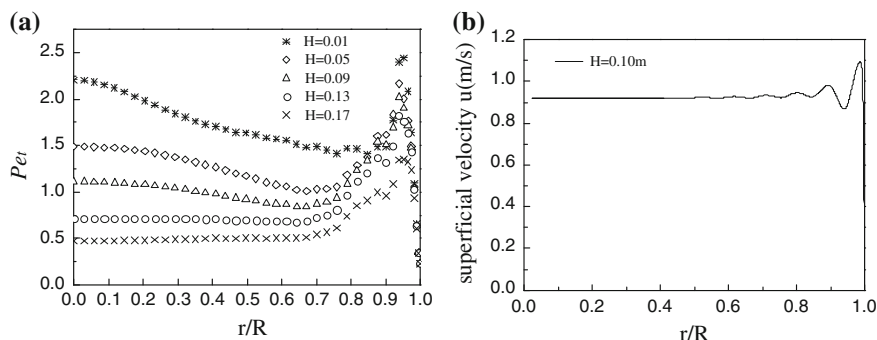

Fig. 6.4 Simulated radial distribution of μ_t at 75 min (*H is the height of the packed bed measured from column bottom*) (Reprinted from Ref. [1], Copyright 2011, with permission from American Chemical Society)
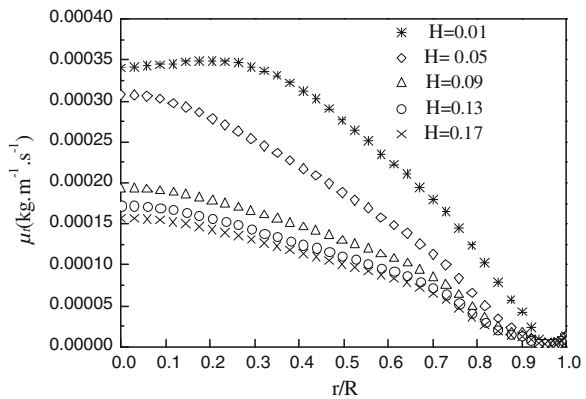
Distribution of the turbulent diffusivities

Figure 6.3 shows the profile of turbulent mass diffusivity D_t in the adsorption column at $t = 75$ min. It is clearly seen that the distribution of D_t is complicated and cannot be much simplified as a constant as usually done. Moreover, D_t is determined by many factors, such as the type and the shape of solid adsorbent, operating condition, adsorption system, and thus, only the simulated profile can show the distribution of D_t so that the inside picture of mass transfer can be further understood. More details on the radial variation at different heights of the column for D_t and μ_t are given in Figs. 6.3 and 6.4. The turbulent Schmidt number Sc_t can be calculated by $Sc_t = \mu_t/D_t$ as shown in Fig. 6.5, in which Sc_t is seen changing
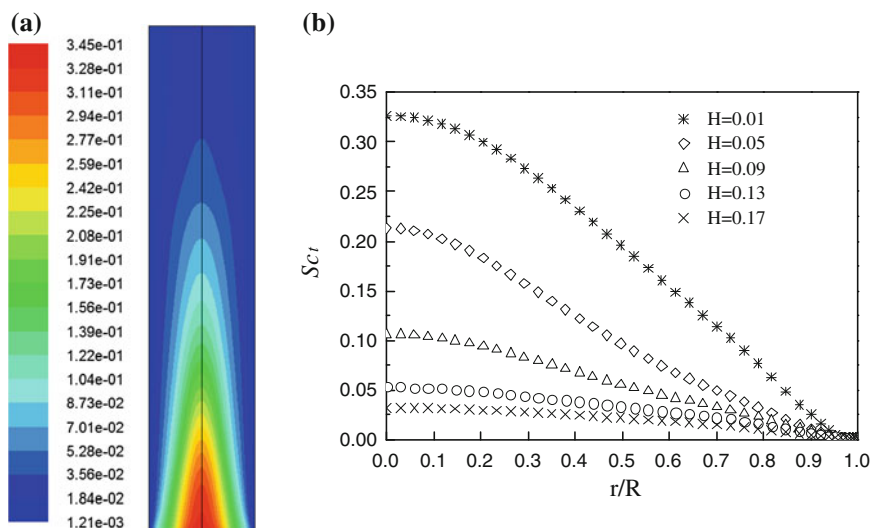
Fig. 6.5 Simulated profiles of Sc_t at 75 min (*H is the height of the packed bed measured from column bottom*). **a** Distribution along column and **b** radial distribution (Reprinted from Ref. [1], Copyright 2011, with permission from American Chemical Society)

Fig. 6.6 Simulated radial distribution of Pe_t and gas velocity at 75 min (*H is the height of the packed bed measured from column bottom*). **a** Radial distribution of Pe_t and **b** radial distribution of gas velocity (Reprinted from Ref. [1], Copyright 2011, with permission from American Chemical Society)

sharply in axial and radial directions. The value of Sc_t in the main flow region is changing significantly from 0.035 to 0.01.

Similarly, the radial distribution of turbulent Peclet number Pe_t can be calculated as shown in Fig. 6.6a, in which its variation throughout the column is seen. It is interested to compare Figs. 6.5 and 6.6 with the radial distribution of velocity as shown in Fig. 6.6b. The velocity drops sharply near the column wall is the main cause of making Sc_t and Pe_t approach zero toward the wall.
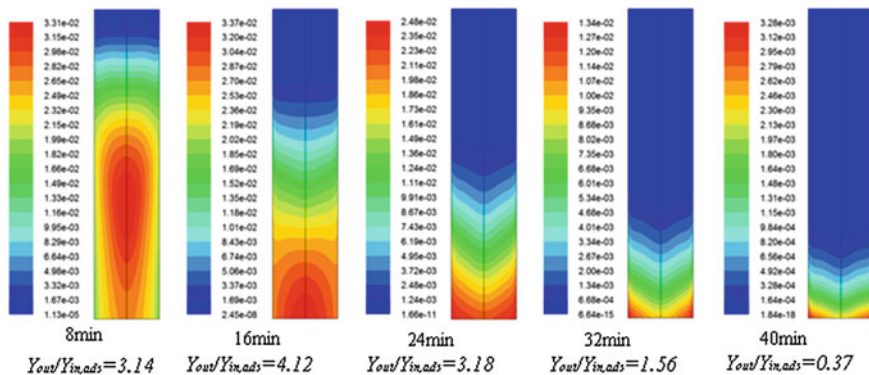
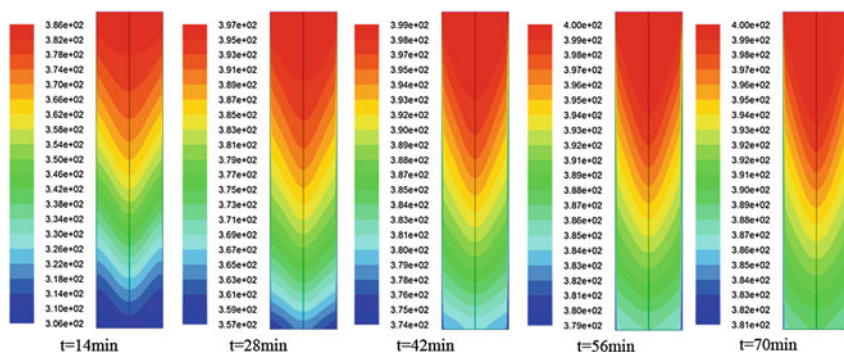**Fig. 6.7** Simulated concentration profiles of the purge gas at different times by two-equation model (Reprinted from Ref. [1], Copyright 2011, with permission from American Chemical Society)

6.1.5 Simulation for Desorption (Regeneration) and Verification

The model equations for desorption are the same as in Sect. 6.1. The object of simulation is also the experimental desorption of methylene chloride by Hwang [13] in the same column as adsorption. The purge gas is nitrogen at the inlet temperature of 298 K.

Concentration profiles of the purge gas along the column

The serial concentration profiles of the purge gas at different times are given in Fig. 6.7, which shows the details of the progress of the regeneration in the column.

Regeneration curve

The simulated regeneration curve can be obtained by the radial average of Y_{out} and Y_{in} of the purge gas at different times (Fig. 6.7) as plotted in Fig. 6.8, in which comparison is made with experimental data. It shows that the ratio Y_{in}/Y_{out} of methylene chloride increases rapidly at the initial stage, reaches maximum about 4.1 at 16 min, then decreases to 1.0 at 35 min, and gradually drops to zero. The simulated curve is in agreement with the experimental measurement. In Fig. 6.8, the simulation curve by Hwang [13] is also given; it was done by preassuming different values of D_t and found the best-fitted curve. The serial concentration profiles of the purge gas along the column are given in Fig. 6.7, which shows the details of the behaviors of the regeneration in the column.

Temperature distribution of the purge gas

The simulated profiles of the purge gas temperature along the column at different times are given in Fig. 6.9 showing the uneven axial and radial temperature distribution.
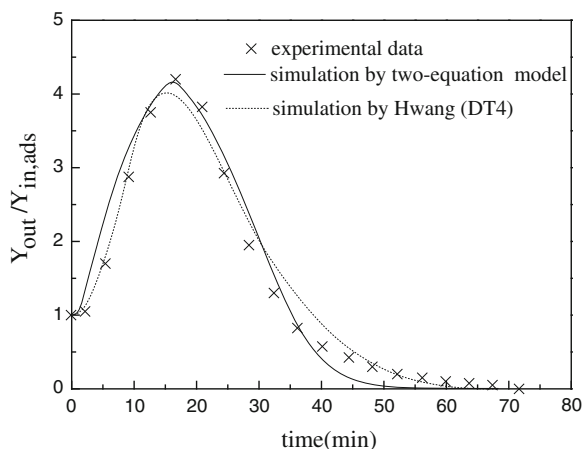
Fig. 6.8 Comparison between simulated regeneration curve with experimental data (Reprinted from Ref. [1], Copyright 2011, with permission from American Chemical Society)

Fig. 6.9 Simulated temperature profiles of purge gas along column at different times by two-equation model (Reprinted from Ref. [1], Copyright 2011, with permission from American Chemical Society)

In order to compare the simulated result with experimental data, the radial average of purge gas temperatures at different times and at different heights ($z = 0$, 0.1, 0.2 m of the column) are calculated as shown in Fig. 6.10.

As shown from Fig. 6.10, each temperature curve consists of an ascending part and a relatively steady part. The initial entering purge gas temperature is 299 K, and it is gradually heated up to 399 K by a preheater. Following the progress of regeneration, the heat supply by incoming hot purge gas is greater than the heat needed for desorption and environmental loss; therefore, the gas temperatures at different column heights are raised sharply forming the ascending part of the temperature curve. When most of the methylene chloride have been desorbed and

Fig. 6.10 Comparison of purge gas temperature and experimental data (*H is the height of the packed bed measured from column bottom*) (Reprinted from Ref. [1], Copyright 2011, with permission from American Chemical Society)
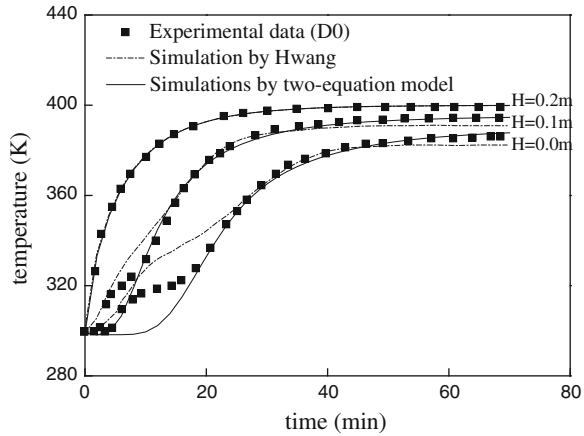
only a smaller part of the sensible heat of the purge gas is sufficient to balance the heat needed for remaining desorption and the heat loss, so that the purge gas temperature is maintained almost constant, forming the relatively steady part of the temperature curve. In Fig. 6.10, some deviations could be seen in the region of the ascending part profiles for the $z = 0.1$ and 0.2 m the curves; it may be due to the assumption that the heat of desorption is equal to the heat of adsorption in magnitude but opposite in sign in the ascending part is overestimated, so that the measured temperatures of purge gas are higher than the simulated temperatures at $H = 0.1$ m before 10 min and $H = 0.2$ m before 20 min. After those times, the regeneration approaching to the end and the heat needed for desorption gradually drop to zero; thus, the simulated temperatures are closely checked by the measurements. As mentioned previously, the simulated curve by Hwang is obtained by setting three values of D_t and to find the best one to fit the experimental data.

6.2 Reynolds Mass Flux Model

In this section, the standard Reynolds mass flux model (abbreviated as standard RMF model) is employed. The assumptions are the same as in Sect. 6.1.

6.2.1 Model Equations

1. The CFD equation set

   Mass conversation for gas phase

   $$\frac{\partial(\rho_G \gamma)}{\partial t} + \frac{\partial(\rho_G \gamma U_i)}{\partial x_i} = S_{mG}$$

Momentum conversation for gas phase

$$\frac{\partial(\rho_G \gamma U_i)}{\partial t} + \frac{\partial(\rho_G \gamma U_i U_j)}{\partial x_i} = -\gamma \frac{\partial P}{\partial x_j} + \frac{\partial}{\partial x_i}\left(\gamma\mu\frac{\partial U_j}{\partial x_i} - \gamma\rho_G\overline{u_i'u_j'}\right) + S_{FG}$$

where $\overline{u_i'u_j'}$ is given by:

$$\frac{\partial\overline{u_i'u_j'}}{\partial t} + U_k\frac{\partial\overline{u_i'u_j'}}{\partial x_k} = \frac{\partial}{\partial x_k}\left(C_0\frac{k}{\varepsilon}\overline{u_i'u_j'}\frac{\partial\overline{u_i'u_j'}}{\partial x_k} + \frac{\mu}{\rho}\frac{\partial\overline{u_i'u_j'}}{\partial x_k}\right) - \left(\overline{u_i'u_k'}\frac{\partial U_j}{\partial x_k} + \overline{u_j'u_k'}\frac{\partial U_i}{\partial x_k}\right)$$
$$- C_1\frac{\varepsilon}{k}\left(\overline{u_i'u_j'} - \frac{2}{3}k\delta_{ij}\right) \tag{1.23}$$
$$- C_2\left(\overline{u_i'u_k'}\frac{\partial U_j}{\partial x_k} + \overline{u_j'u_k'}\frac{\partial U_i}{\partial x_k} - \frac{2}{3}\delta_{ij}\overrightarrow{u_i'u_k'}\frac{\partial U_i}{\partial x_k}\right) - \frac{2}{3}\varepsilon\delta_{ij}$$

The constants are as follows:
$C_0 = 0.09$, $C_1 = 2.3$, $C_2 = 0.4$. The k and ε in foregoing equation are given by:

$$\frac{\partial(\rho_G\gamma k)}{\partial t} + \frac{\partial(\rho_G\gamma U_i k)}{\partial x_i} = \frac{\partial}{\partial x_i}\left[\gamma\left(\mu + \frac{\mu_t}{\sigma_k}\right)\frac{\partial k}{\partial x_i}\right] + \gamma G_k - \rho_G\gamma\varepsilon$$

$$\frac{\partial(\rho_G\gamma\varepsilon)}{\partial t} + \frac{\partial(\rho_G\gamma U_i\varepsilon)}{\partial x_i} = \frac{\partial}{\partial x_i}\left[\gamma\left(\mu + \frac{\mu_t}{\sigma_\varepsilon}\right)\frac{\partial\varepsilon}{\partial x_i}\right] + C_{1\varepsilon}\gamma\frac{\varepsilon}{k}G_k - C_{2\varepsilon}\rho_G\gamma\frac{\varepsilon^2}{k}$$

$$G_k = \mu_t\left(\frac{\partial U_i}{\partial x_j} + \frac{\partial U_j}{\partial x_i}\right)\frac{\partial U_i}{\partial x_k}$$

where γ is the porosity of the packed bed; model constants are as follows [2]:
$C_{1\varepsilon} = 1.44$, $\quad C_{2\varepsilon} = 1.92$, $\quad \sigma_k = 1.0$, $\quad \sigma_\varepsilon = 1.3$.

2. The heat transfer equation set

Energy conservation for adsorbate in gas phase

$$\frac{\partial(\rho_G\gamma C_{pG}T_G)}{\partial t} + \frac{\partial(\rho_G\gamma C_{pG}U_iT_G)}{\partial x_i} = \frac{\partial}{\partial x_i}\left[\rho_G\gamma C_{pG}\alpha\frac{\partial T_G}{\partial x_i} - \overline{u'T'}\right] + S_{TG}$$

where $\overline{u_i'T'}$ is given by:

$$\frac{\partial\overline{u_i'T'}}{\partial t} + U_i\frac{\partial\overline{u_i'T'}}{\partial x_k} = \frac{\partial}{\partial x_k}\left[\left(C_{T1}\frac{k}{\varepsilon}\overline{u_i'u_j'} + \alpha\right)\frac{\partial\overline{u_i'T'}}{\partial x_k}\right]$$
$$- \left(\overline{u_i'u_k'}\frac{\partial T}{\partial x_k} + \overline{u_k'T'}\frac{\partial U_j}{\partial x_k}\right) - C_{T2}\frac{\varepsilon}{k}\overline{u_i'T'} + C_{T3}\overline{u_k'T'}\frac{\partial U_i}{\partial x_k} \tag{2.13}$$

The constants are as follows: $C_{t1} = 0.07$, $\quad C_{t2} = 3.2$, $\quad CL_{T3} = 0.5$.
Energy conservation for solid adsorbent

$$\frac{\partial[\rho_s(1-\gamma)C_{ps}T_s]}{\partial t} = \frac{\partial}{\partial x_i}\left[(1-\gamma)\lambda_s\frac{\partial T_s}{\partial x_i}\right] + S_{TS}$$

Energy conservation for the column wall

$$\frac{\partial(\rho_w C_{pw} T_w)}{\partial t} = \frac{\partial}{\partial x_i}\left(\lambda_w \frac{\partial T_w}{\partial x_i}\right) + S_{TW}$$

3. The mass transfer equation set

Species mass conservation for gas phase

$$\frac{\partial(\gamma C)}{\partial t} + \frac{\partial(\gamma U_i C)}{\partial x_i} = \frac{\partial}{\partial x_i}\left[\gamma D \frac{\partial C}{\partial x_i} - \overline{u_i' c'}\right] + S_{nG}$$

where $\overline{u_i' c'}$ is calculated by:

$$\begin{aligned}
\frac{\partial \overline{u_i' c'}}{\partial t} + U_j \frac{\partial \overline{u_i' c'}}{\partial x_i} &= \frac{\partial}{\partial x_i}\left[\left(C_{c1} \frac{\varepsilon}{k} \overline{u_i' u_j'} + \frac{\mu}{\rho}\right)\frac{\partial \overline{u_i' c'}}{\partial x_j}\right] \\
&\quad - \left(\overline{u_i' u_j'}\frac{\partial C}{\partial x_j} + \overline{u_j' c'}\frac{\partial U_i}{\partial x_j}\right) - C_{c2}\frac{\varepsilon}{k}\overline{u_i' c'} + C_{c3}\overline{u_j' c'}\frac{\partial U_i}{\partial x_j}
\end{aligned}$$

(3.26)

The model constants are as follows: $c_1 = 0.09$, $c_2 = 1.8$, $c_3 = 0.6$.
Boundary condition and evaluation of source terms
Inlet ($x = 0$): Similar to the absorption column in Chap. 5:

$$u = u_{in}, \quad C = C_{in}, \quad T = T_{in}$$

Outlet ($x = Z$): Consider as fully developed turbulence.
Column wall: No slip condition is adopted.
Evaluation of source terms: The evaluation is the same as in Sect. 6.1

6.2.2 Simulated Results and Verification

The object of simulation is the adsorption of methylene chloride vapor in air on an activated carbon column as described in Sect. 6.1.2.

Concentration profile along the column at different times

The simulated profiles of adsorbate, methylene chloride, at different times are given in Fig. 6.11, in which the development of the concentration profiles in the column with time is seen. In comparison with Fig. 6.1, it is found that the simulation is closely similar. Yet after careful comparison, the shape of concentration distribution in the adsorption section (represented by the red brackets) is somewhat different. The parabolic shape of purge gas concentration distribution is more obvious by using standard Reynolds mass flux model due to better simulation near the column wall.
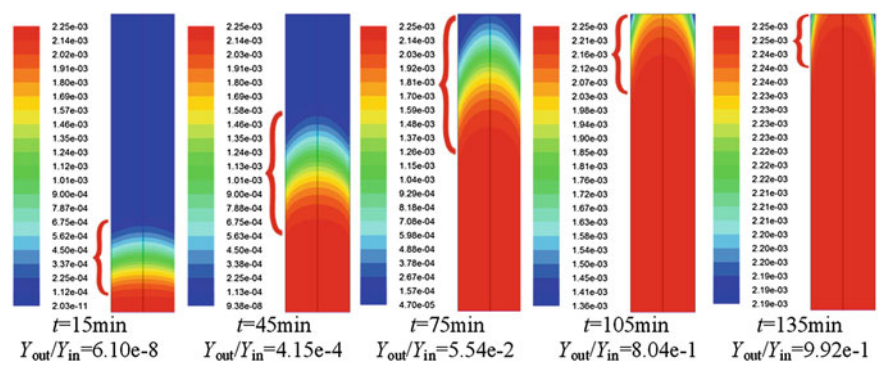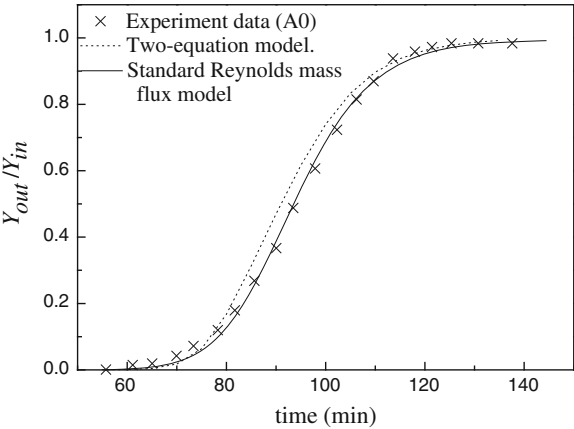
Fig. 6.11 Simulated sequence of concentration profiles along adsorption column in mole fraction at different times by standard Reynolds mass flux model [14]

Fig. 6.12 Comparison of simulated breakthrough curve with experimental data (*Y is the mole fraction of adsorbate in gas phase*) [14]

Breakthrough curve

The simulated breakthrough curve and experimental data are shown in Fig. 6.12, in which the simulation is in agreement with experimental data.

Concentration profile along column

The simulated concentration profiles along the column at different times by employing standard RMF model and hybrid RMF model are given in Fig. 6.13. As seen, the simulated profiles by these two models are similar and the difference between them is small. It demonstrates that the hybrid RMF model can give good simulation at less computer work.
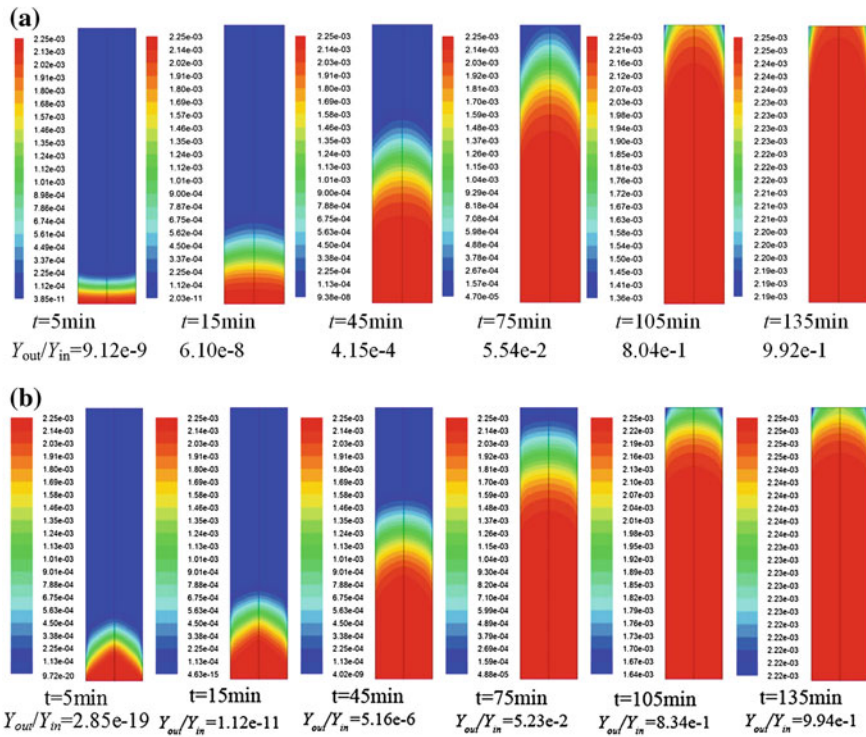
Fig. 6.13 Simulated sequence of concentration profiles along column at different times $Y_{in} = 2.25 \times 10^{-3}$, $T_{in} = 298$ K, $P = 1.10$ atm, $F = 33.5$ L min^{-1}. **a** Predicted by standard Reynolds mass flux model and **b** predicted by hybrid Reynolds mass flux model [14]

Fluctuating Mass flux

The fluctuating mass flux can be obtained in the course of simulation computation. The distribution of $\overline{u'_x c'}$ along axial and radial directions is given in Fig. 6.14.

As shown in Fig. 6.14b, all $\overline{u'_x c'}$ are positive; it implies the direction of $\overline{u'_x c'}$ diffusion is consistent with the decreasing concentration of methylene chloride along the column which can enhance the adsorption. The $\overline{u'_x c'}$ curve in axial direction decreases slightly from column top to about $x = 0.1$ and then increases rapidly toward bottom; it indicates more turbulent effect appears at the column bottom than at the top. The numerical value of axial $\overline{u'_x c'}$ is much larger than $\overline{u'_y c'}$ and dominates the dominated turbulent effect in axial direction.

The radial and axial distribution of $\overline{u'_y c'}$ is given in Fig. 6.15, in which all $\overline{u'_y c'}$ are positive; the negative gradient of $\overline{u'_y c'}$ diffusion is consistent with the decreasing radial gradient of methylene chloride, which is helpful to the adsorption.
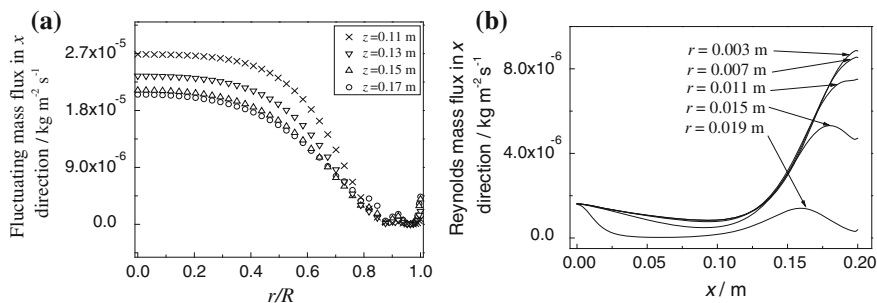
Fig. 6.14 Simulated profile of fluctuating mass flux $\overline{u'_x c'}$ for Yin $= 2.25 \times 10-3$, Tin $= 298$ K, P $= 1.10$ atm, F $= 33.5$ L min-1, t $= 75$ min [14]. a Radial direction and b axial direction
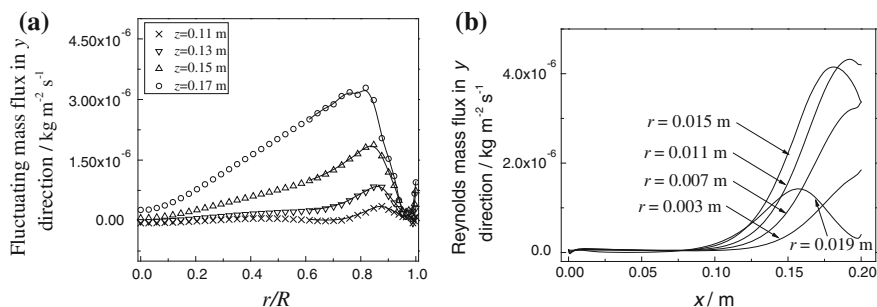
Fig. 6.15 Simulated profile of fluctuating mass flux $\overline{u'_y c'}$ for $Y_{\mathrm{in}} = 2.25 \times 10^{-3}$, $T_{\mathrm{in}} = 298$ K, $P = 1.10$ atm, $F = 33.5$ L min^{-1}, $t = 75$ min [14]. **a** Radial direction and **b** axial direction

Anisotropic diffusivities

The methylene chloride concentration gradients along radial and axial directions are shown in Fig. 6.16. According to Eq. (3.37), the anisotropic diffusivities $D_{t,x}$ and $D_{t,y}$ can be obtained as given in Fig. 6.17.

As shown in Fig. 6.17a, $D_{t,x}$ is high at $x = 0.11$ and very low at $x = 0.17$ indicates the turbulent diffusion rate is low at the vicinity of column bottom and soon rapidly increases toward column top. Such tendency is kept in radial direction from column center to about $r/R = 0.8$ and then diminishes to almost zero toward the column wall. The $D_{t,y}$ around column center ($r/R < 0.1$) fluctuates obviously may be due to $\partial \overline{C} / \partial y$ there is almost zero so as to affect the inlet boundary condition. After $r/R < 0.1$, $D_{t,y}$ is almost zero means the turbulent effect in radial direction is negligible.
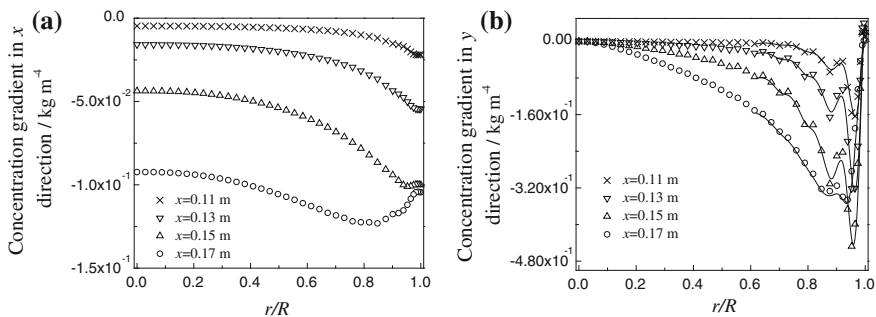
Fig. 6.16 Simulated concentration gradient of methylene chloride for $Y_{in} = 2.25 \times 10^{-3}$, $T_{in} = 298$ K, $P = 1.10$ atm, $F = 33.5$ L min^{-1}, $t = 75$ min [14]. **a** $\partial\overline{C}/\partial x$ and **b** $\partial\overline{C}/\partial y$
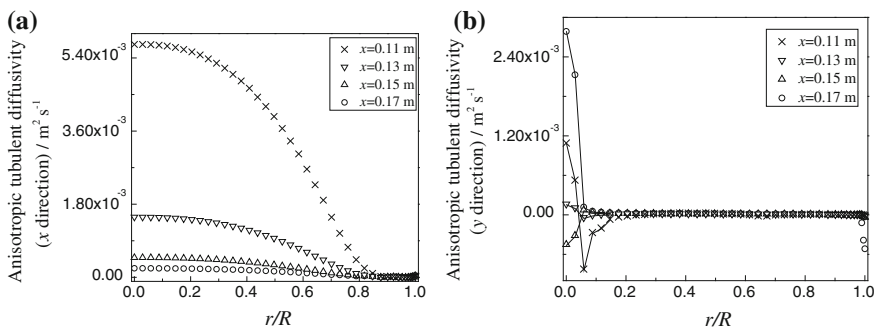

Fig. 6.17 Simulated anisotropic diffusivities for $Y_{in} = 2.25 \times 10^{-3}$, $T_{in} = 298$ K, $P = 1.10$ atm, $F = 33.5$ L min^{-1}, $t = 75$ min [14]. **a** $\mathbf{D_{t,x}}$ and **b** $\mathbf{D_{t,y}}$

6.2.3 The Simulation for Desorption (Regeneration) and Verification

The model equations for desorption are the same as in Sect. 6.2, and the object of simulation is the same as in Sect. 6.1.5, i.e., experimental desorption of methylene chloride from solid adsorbent by Hwang [13].

Concentration profiles of the purge gas along the column

The concentration profiles of the regeneration (desorption) column at different times are shown in Fig. 6.18.

8min   16min   24min   32min   40min

$Y_{out}/Y_{in,ads}=2.65$ $Y_{out}/Y_{in,ads}=4.20$ $Y_{out}/Y_{in,ads}=2.96$ $Y_{out}/Y_{in,ads}=1.52$ $Y_{out}/Y_{in,ads}=0.64$
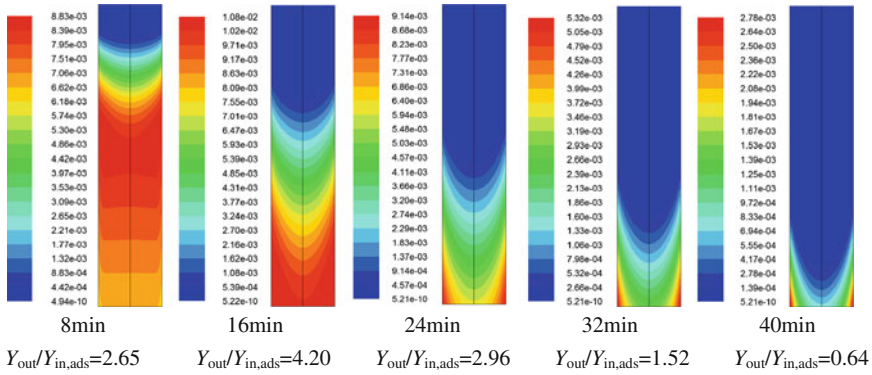
Fig. 6.18 Simulated sequences of concentration distribution along regeneration column in mole fraction at different times by standard Reynolds mass flux model for $Y_{in,ads} = 2.50 \times 10^{-3}$, $T_{g,in} = 365–365 \exp (-0.352t^{0.666}-1.654)$K, $P = 1.09$ atm, $F = 33.5$ L min^{-1} [14]

Fig. 6.19 Comparison between different simulated regeneration curves with experimental data [14]
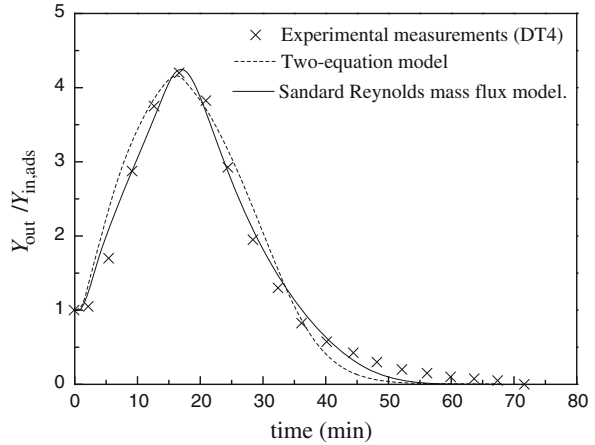
Regeneration curve

The simulated regeneration curve by using standard Reynolds mass flux model is shown in Fig. 6.19.

As shown in Fig. 6.19, the simulated curve by using standard Reynolds mass flux model is better than that by two-equation model.

Temperature distribution of the purge gas

The simulated profiles of the purge gas temperature along the column at different times are given in Fig. 6.20.

The radial average of purge gas temperatures at different times and at different heights ($H = 0, 0.1, 0.2$ m of the column) are calculated as shown in Fig. 6.10.
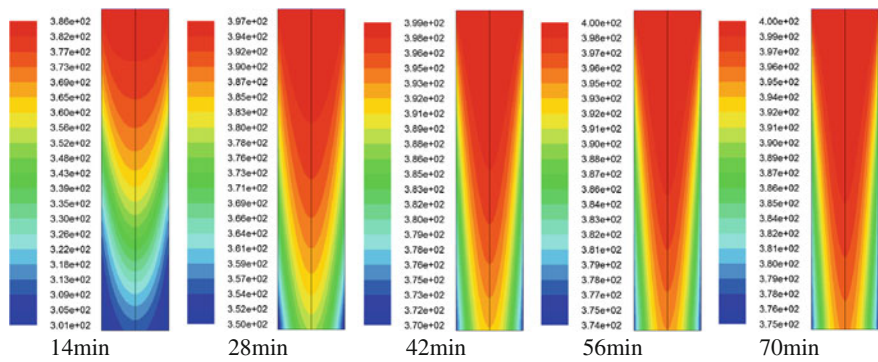
Fig. 6.20 Simulated temperature distributions of purge gas along column at different times by Standard Reynolds mass flux model [14]

Fig. 6.21 Comparison of simulated purge gas temperature with experimental data (*H is the height of the packed bed measured from column bottom*) [14]
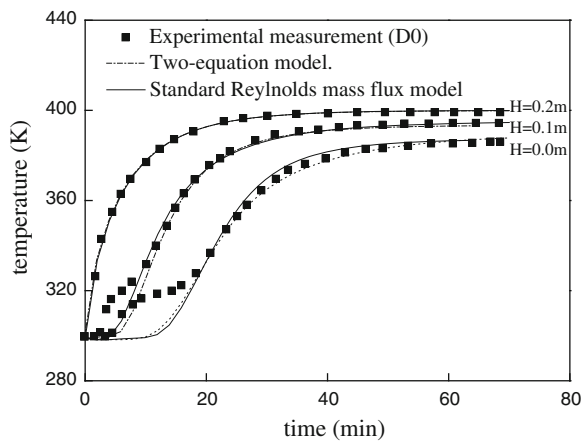
As shown in Fig. 6.21, the deviation of experimental data is obvious in $H = 0.1$ and 0.2 and the simulations are in agreement with the rest of experimental data.

6.3 Summary

As the adsorption process is unsteady and accompanied with heat effect, the time parameter is involved in the model equations. The simulated concentration profile of the column at different times enables us to show the progress of adsorption along the column as an indication of the process dynamics. The simulated breakthrough curve for adsorption and regeneration curve for desorption by the two computational mass transfer (CMT) models are well checked with the experimental data except some deviation on the regeneration curve at the inlet of purge gas. This discrepancy may be due to incorrect assumption on the heat of desorption.

References

1. Li WB, Liu BT, Yu KT, Yuan XG (2011) A rigorous model for the simulation of gas adsorption and its verification. Ind Eng Chem Res 50(13):8361–8370
2. Launder BE, Spalding DB (1972) Lectures in mathematical models of turbulence. Academic Press, London
3. Jone WP, Launder BE (1973) The calculation of low-reynolds-number phenomena with a two-equation model of turbulence. Int J Heat Mass Transfer 16:1119–1130
4. Elghobashi SE, LaRue JG (1983) The effect of mechanical stream on the dissipation rate of a scalar variance. In: 4th Symposium on turbulent shear flows, Karlsruhe, Germany, pp 1–5
5. Ergun S (1952) Fluid flow through packed columns. Chem Eng Prog 48(2):89–94
6. Liu S, Long J (2000) Gas-liquid countercurrent flows through packed towers. J Porous Media 3(2):99–113
7. Butt JB (1980) Reaction kinetics and reactor design. Prentice-Hall, NJ
8. Levenspiel O (1993) Engineering flow and heat exchange. Plenum Press, New York
9. Silva JAC, Rodrigues AE (1997) Fixed-bed adsorption of n-pentane/isopentane mixtures in pellets of 5A zeolite. Ind Eng Chem Res 36:3769–3777
10. Glueckauf E (1955) Formulae for diffusion into spheres and their application to chromatography. J Chem Soc 51:1540
11. Yang RT (1987) Gas separation. Adsorption process. Butterworth, Stoneham
12. Wakao N (1978) Particle-to-fluid transfer coefficients and fluid diffusivities at low flow rate in packed beds. Chem Eng Sci 31:1115
13. Hwang KS (1997) Adsorption and thermal regeneration of methylene chloride vapor on an activated carbon bed. Chem Eng Sci 52(7):1111–1123
14. Li WB (2012) Theory and application of computational mass transfer for chemical engineering processes. Ph.D. dissertation, Tianjin University, Tianjin, China

Chapter 7
Application of Computational Mass Transfer (IV): Fixed-Bed Catalytic Reaction

Abstract In this chapter, an exothermic catalytic reaction process is simulated by using computational mass transfer (CMT) models as presented in Chap. 3. The difference between the simulation in this chapter from those in Chaps. 4, 5, and 6 is that chemical reaction is involved. The source term S_n in the species conservation equation represents not only the mass transferred from one phase to the other, but also the mass created or depleted by a chemical reaction. Thus, the application of the CMT model is extended to simulating the chemical reactor. The simulation is carried out on a wall-cooled catalytic reactor for the synthesis of vinyl acetate from acetic acid and acetylene by using both $\overline{c'^2} - \varepsilon_{c'}$ model and Reynolds mass flux model. The simulated axial concentration and temperature distributions are in agreement with the experimental measurement. As the distribution of μ_t shows dissimilarity with D_t and α_t, the Sc_t or Pr_t are thus varying throughout the reactor. The anisotropic axial and radial turbulent mass transfer diffusivities are predicted where the wavy shape of axial diffusivity $\mathbf{D_{t,x}}$ along the radial direction indicates the important influence of catalysis porosity distribution on the performance of a reactor.

Keywords Simulation of chemical reactors · Exothermic catalytic reaction · Concentration profile · Turbulent mass transfer diffusivity profile

Nomenclature

a	Surface area, m
C	Mass concentration, kg m^{-3}
$\overline{c^2}$	Concentration variance, kg^2 m^{-6}
C_μ, c_1, c_2	Model parameters in $k - \varepsilon$ model equations
$C_{c0}, C_{c1}, C_{c2}, C_{c3}$	Model parameters in $\overline{c^2} - \varepsilon_c$ model equations
$C_{D0}, C_{D1}, C_{D2}, C_{D3}, C_{D4}$	Model parameters in $\overline{t^2} - \varepsilon_t$ model equations
C_p	Specific heat, J kg^{-1} K^{-1}
C_{si}^s	Mass concentration of reactive species at the surface of catalyst
d_e	Effective diameter of catalyst particle, m
D_e	Effective turbulent mass diffusivity, m^2 s^{-1}

D_s	Intra-diffusivity of the catalyst, m2 s−1
D_t	Turbulent mass diffusivity, $m^2\ s^{-1}$
G	Gas-phase flow rate per unit cross-sectional area, $kg\ m^{-2}\ s^{-1}$
h	Film coefficient of mass transfer, $m\ s^{-1}$
H	Axial distance measured from column bottom ($H = 0$ at column bottom), m
ΔH_r	Heat of reaction, $kJ\ mol^{-1}$
k	Turbulent kinetic energy, $m^2\ s^{-2}$
M	Molar mass, $kg\ mol^{-1}$
Pe_t	Turbulent Peclet number
r	Position in radial direction, m
R	Radius of the column
m	Molar reaction rate mol/kg catalyst
s	Apparent reaction rate
R_0	The resistant coefficient of porous media
R_s	Apparent reaction rate, $kmol\ kg^{-1}$ (cat) s^{-1}
Sc	Turbulent Schmidt number
t_0	Fluid inlet temperature, °C
$\overline{t^2}$	Temperature variance, K^2
T	Temperature, K
U	Fluid superficial velocity, $m\ s^{-1}$
x	Axial position, m
z	Dimensionless distance, $z = (R-r)/d_e$
$\alpha,\ \alpha_t$	Molecular and turbulent thermal diffusivities, respectively, $m^2\ s^{-1}$
ε	Turbulent dissipation rate, $m^2\ s^{-3}$
ε_c	Turbulent dissipation rate of concentration fluctuation, $kg^2\ m^{-6}\ s^{-1}$
ε_t	Turbulent dissipation rate of temperature fluctuation, $K^2\ s^{-1}$
Φ	Variable
γ	Porosity distribution of the random packing bed
γ_∞	Porosity in an unbounded packing
λ	Thermal conductivity, $KJ\ m^{-1}\ K^{-1}\ s^{-1}$
μ_t	Turbulent viscosity, $kg\ m^{-1}\ s^{-1}$
ρ	Density, $kg\ m^{-3}$
ρ_b	Bulk density of catalyst, kg/m^3
v_t	Turbulent kinetic viscosity, $m^2\ s^{-1}$
$\sigma_c, \sigma_{\varepsilon_c}$	Model parameters in $\overline{c^2} - \varepsilon_c$ model equations
σ_t	Model parameter in $\overline{t^2} - \varepsilon_t$ model equations
$\sigma_k,\ \sigma_\varepsilon$	Model parameters in $k - \varepsilon$ model equations

Subscripts

c   Coolant
G   Gas phase
i   Interface
s   Catalyst; reactive species
w   Reactor wall
1   Inner
2   Outer

Superscripts

s   Surface

The methodology of computational mass transfer (CMT) is not only applicable to the process involving mass, heat, and momentum transfer accompanied with chemical reaction as presented in previous chapters but also to the catalytic reaction process. In this chapter, a fixed-bed catalytic reactor with cooling jacket is used as an example for illustration.

The fixed-bed reactors are the most commonly used for undertaking industrial heterogeneous catalytic reactions in the basic chemical, petrochemical, and allied industries, such as the carbon monoxide conversion and ammonia synthesis, the ethylene oxide and vinyl acetate synthesis, and many other reactive processes. The design and performances of such kind of reactors have been extensively reported.

The one-dimensional plug-flow model is used early for reactor design and analysis, where the concentration and temperature gradients were assumed only to occur in the axial direction. Later, the flow model with axial mixing is introduced to take into account the mixing effect, which is influential to the temperature and concentration gradients as well as the reactor performances. Afterward, the uneven radial concentration distribution was considered by using empirical correlations. At the same time, some researchers used the two-dimensional pseudo-homogeneous model with the consideration of the radial velocity distribution. The advancement of applying pseudo-homogeneous CFD model to reactor design enabled us to calculate the velocity profile, whereas the temperature and concentration distributions were obtained by using either the turbulent Prandtl number (Pr_t) and turbulent Schmidt number (Sc_t) or the empirical correlations obtained by using inert tracer technique for predicting the unknown diffusivities of heat and mass transfer [1]. In fact, such empirical correlations, even available, are unreliable as stated in Chap. 3. The use of CMT model can overcome such drawback as the turbulent mass and thermal diffusivities need not knowing in advance. In this chapter, the two-equation model and Reynolds mass flux model of CMT are used for illustrative simulation.

7.1 $\overline{c'^2} - \varepsilon_c$ Two-Equation Model for Catalytic Reactor

Liu [2] used the CMT $\overline{c'^2} - \varepsilon_c$ two-equation model (abbreviated as two-equation model) for simulating a catalytic reactor with cooling jacket for producing vinyl acetate from acetic acid and acetylene as described below.

7.1.1 Model Equation

Assumptions

1. Both the reactant and product are in homogeneous fluid phase, and the operation is steady.
2. The fluid-phase flow is axially symmetrical in the catalytic reactor (packed column) and in turbulent state.
3. The temperature of outer catalyst surface is equal to the fluid temperature.
4. The temperature at the outer wall of the cooling jacket is constant.
5. The heat created by the friction between catalysis and the fluid is neglected.
6. The activity of the catalyst remains unchanged.

The mass and volume of the fluid phase are changing in the course of chemical reaction, the source term S_m in the overall mass conservation equation is not equal to zero, and the fluid density is not a constant.

In the model equations, the variables U_i, k, ε, ρ, etc., are referred to the gaseous fluid phase (reactant and product) without subscript. Subscripts s and w refer the conditions at the solid phase (catalyst) and reactor wall, respectively.

(I) CFD equation set

(a) *Overall mass conservation*

$$\frac{\partial(\rho\,\gamma U_i)}{\partial x_i} = S_m$$

(b) *Momentum conservation*

$$\frac{\partial(\rho\,\gamma U_i U_j)}{\partial x_i} = -\gamma\frac{\partial P}{\partial x_j} + \frac{\partial}{\partial x_i}\left[\gamma\mu\left(\frac{\partial U_j}{\partial x_i}\right) - \gamma\rho\,\overline{u_i'u_j'}\right] + \gamma(\rho\,g + R_0 U_i)$$

$$-\rho\,\overline{u_i'u_j'} = \mu_t\left(\frac{\partial U_i}{\partial x_j} + \frac{\partial U_j}{\partial x_i}\right) - \frac{2}{3}\Delta_{ij}\rho k$$

$$\mu_t = \rho C_\mu \frac{k^2}{\varepsilon}$$

(c) *k equation*

$$\frac{\partial(\rho\,\gamma U_i k)}{\partial x_i} = \frac{\partial}{\partial x_i}\left(\gamma\left(\mu + \frac{\mu_t}{\sigma_k}\right)\frac{\partial k}{\partial x_i}\right) + \gamma G_k - \rho\,\gamma\varepsilon$$

$$G_k = \mu_t\left(\frac{\partial U_i}{\partial x_j} + \frac{\partial U_j}{\partial x_i}\right)\frac{\partial U_j}{\partial x_i}$$

(d) *ε equation*

$$\frac{\partial(\rho\,\gamma U_i \varepsilon)}{\partial x_i} = \frac{\partial}{\partial x_i}\left(\gamma\left(\mu + \frac{\mu_t}{\sigma_\varepsilon}\right)\frac{\partial\varepsilon}{\partial x_i}\right) + C_1\gamma G_k\frac{\varepsilon}{k} - C_2\gamma\rho\,\frac{\varepsilon^2}{k}$$

where γ is the porosity of the catalytic bed; R_0 is the coefficient of resistance created by the fluid flow through the catalyst; μ_t is the turbulent diffusivity of the fluid. The model constants are as follows [3]: $C_\mu = 0.09$, $\sigma_k = 1.0$, $\sigma_\varepsilon = 1.3$, $C_1 = 1.44$, $C_2 = 1.92$.

(II) **Heat transfer equation set**

Energy Conservation Equations:

(a) *Energy conservation of gas phase*

$$\frac{\partial(\gamma\rho\,C_p U_i T)}{\partial x_i} = \frac{\partial}{\partial x_i}\left(\gamma\rho\,C_p(\alpha + \alpha_t)\frac{\partial T}{\partial x_i}\right) + Q_1 - Q_2$$

$$= \frac{\partial}{\partial x_i}\left(\gamma\rho\,C_p\alpha_e\frac{\partial T}{\partial x_i}\right) + h_s a_s\left(T_s^s - T\right) - h_w a_{w1}(T - T_{w1})$$

where T is the temperature of the gas phase; α_t is the thermal diffusivity; α_e is the effective thermal diffusivity $(= \alpha + \alpha_t)$; a_s is the outer surface area of the catalyst $(m^2\ m^{-3})$; T_s^s is the outer temperature of the catalyst; h_s is the gas film mass transfer coefficient between catalyst and the gas phase $(kJ\ m^{-2}\ K^{-1})$; a_{w1} is the inner surface area of the reactor wall $(m^2\ m^{-3})$; T_{w1} is the temperature at the inner wall of the reactor; h_{w1} is the gas film mass transfer coefficient between gas phase and inner wall of the reactor. The terms on the right side of the equation $Q_1 = h_s a_s\left(T_s^s - T\right)$ represents the heat transfer from the catalyst to the gas phase and $Q_2 = h_{w1} a_{w1}(T - T_{w2})$ represents the heat transfer from the gas phase to the inner wall of the reactor.

(b) *Energy conservation of catalyst*

$$\frac{\partial}{\partial x_i}\left((1-\gamma)\lambda_s\frac{\partial T_s}{\partial x_i}\right) + (1-\gamma)\rho_s(\Delta HR) - h_s a_s\left(T_s^s - T\right) = 0$$

where T_s, ρ_s, λ_s are, respectively, the inner temperature of the catalyst, density of catalyst, and thermal conductivity of the catalyst (kJ m^{-1} K^{-1} s^{-1}); R is the apparent reaction rate (mol kg^{-1} s^{-1}); ΔH is the molar heat of reaction (kJ mol^{-1}); h_s is the film coefficient of mass transfer between catalyst and fluid.

(c) *Energy conservation of reactor wall*

$$\frac{\partial}{\partial x_i}\left(\lambda_w \frac{\partial T_w}{\partial x_i}\right) + h_{w1}a_{w1}(T - T_{w1}) - h_{w2}a_{w2}(T_{w2} - T_c) = 0$$

where T_w, λ_w is, respectively, the temperature and the thermal conductivity of the reactor wall; h_{w1} is the gas film coefficient of mass transfer coefficient between gas phase and the inner wall surface of the reactor; h_{w2} is the liquid film coefficient of mass transfer coefficient between the outer wall surface of the reactor and the liquid coolant; a_{w1}, a_{w2} are, respectively, the inner and outer surface of the reactor wall; T_{w1}, T_{w2} are, respectively, the temperature of the inner wall surface and the temperature of liquid coolant at the outer wall surface of the reactor; T_c is the average temperature of the coolant.

The turbulent thermal diffusivity

The turbulent thermal diffusivity α_t is calculated by using the $\overline{T'^2} - \varepsilon_{T'}$ two-equation model:

$$\alpha_t = C_{T0}k\left(\frac{k}{\varepsilon}\frac{\overline{T'^2}}{\varepsilon_{T'}}\right)$$

$\overline{T'^2}$ *equation*

$$\frac{\partial}{\partial x_i}\left(\rho\,\gamma U_i\overline{T'^2}\right) = \frac{\partial}{\partial x_i}\left(\rho\,\gamma\left(\alpha + \frac{\alpha_t}{\sigma_T}\right)\frac{\partial\overline{T'^2}}{\partial x_i}\right) + 2\rho\,\gamma\alpha_t\left(\frac{\partial T}{\partial x_i}\right)^2 - 2\gamma\varepsilon_{T'}$$

$\varepsilon_{T'}$ *equation*

$$\frac{\partial\rho\,\gamma U_i\varepsilon_{T'}}{\partial x_i} = \frac{\partial}{\partial x_i}\left[\rho\,\gamma\left(\alpha + \frac{\alpha_t}{\sigma_{T'}}\right)\frac{\partial\varepsilon_{T'}}{\partial x_i}\right]$$
$$+ C_{T1}\frac{\varepsilon_{T'}}{\overline{T'^2}}\rho\,\gamma\alpha_t\left(\frac{\partial T}{\partial x_i}\right)^2 - C_{T2}\rho\,\frac{\varepsilon_{T'}}{\overline{T'^2}}\varepsilon_{T'} - C_{T3}\rho\,\gamma\frac{\varepsilon}{k}\varepsilon_{T'}$$

The model constants are as follows [4]: $C_{T0} = 0.10$, $C_{T1} = 1.8$, $C_{T2} = 2.2$, $C_{T3} = 0.8$, $\sigma_t = 1.0$.

(III) Mass transfer equation set

(a) *Mass conservation of reactive species (gas phase)*

$$\frac{\partial(\gamma U_i C)}{\partial x_i} = \frac{\partial}{\partial x_i}\left(\gamma D_e \frac{\partial C}{\partial x_i}\right) + h\,a_s\left(C_{si}^s - C\right)$$

where C is the mass concentration of the gaseous reactive species (kg m^{-3}), D_e is the effective thermal diffusivity $D_e = D + D_t$; h is the film coefficient of mass transfer between gas phase and the surface of the catalyst; C_{si}^s is the mass concentration of reactive species at the surface of catalyst; a_s is the outer surface area of the catalyst.

(b) *Mass conservation of the solid phase*

$$\frac{\partial}{\partial x_i}\left(D_s \frac{\partial T_s}{\partial x_i}\right) + (1-\gamma)\rho_s(MR) - ha_s\left(C_s^s - C\right) = 0$$

where D_s is the intra-diffusivity of the catalyst; M is the molar mass of the reactive species (kg mol^{-1}); R is the molar reaction rate (mol/kg catalyst. s); ρ_s is the density of the catalyst. If the resistance of intra-diffusion is neglected, the foregoing equation can be simplified to:

$$k_G a_s\left(C_{si}^s - C\right) = \rho_s(1-\gamma)M\,R$$

The turbulent mass diffusivity

The turbulent mass diffusivity of the reactive species D_t can be obtained according to $\overline{c'^2} - \varepsilon_{c'}$ model as follows:

$$D_t = C_{T0}k\left(\frac{k\,\overline{c'^2}}{\varepsilon\,\varepsilon_{c'}}\right)^{1/2}$$

$\overline{c'^2}$ *equation*

$$\frac{\partial(U_i \gamma \overline{c'^2})}{\partial x_i} = \frac{\partial}{\partial x_i}\left(\gamma\left(D_L + \frac{D_t}{\sigma_{c'}}\right)\frac{\partial(\overline{c'^2})}{\partial x_i}\right) + 2D_t\gamma\left(\frac{\partial C}{\partial x_i}\right)^2 - 2\gamma\varepsilon_{c'}$$

$\varepsilon_{c'}$ *equation*

$$\frac{\partial(\gamma U_i \varepsilon_{c'})}{\partial x_i} = \frac{\partial}{\partial x_i}\left(\gamma\left(D_L + \frac{D_t}{\sigma_{\varepsilon_{c'}}}\right)\frac{\partial(\varepsilon_{c'})}{\partial x_i}\right) + C_{c1}\gamma D_t\left(\frac{\partial C}{\partial x_i}\right)^2\frac{\varepsilon_{c'}}{\overline{c'^2}} - C_{c2}\gamma\frac{\varepsilon_{c'}^2}{\overline{c'^2}} - C_{c3}\gamma\frac{\varepsilon_{c'}\varepsilon}{k}$$

The model constants are as follows [5]: $C_{c0} = 0.11$, $C_{c1} = 1.8$, $C_{c2} = 2.2$, $C_{c3} = 0.8$, $\sigma_c = 1.0$, $\sigma_{\varepsilon_c} = 1.0$.

7.1.2 Boundary Conditions

Inlet (column bottom, $x = 0$): $U = U_{in}$, $V = 0$, $k = 0.003U_{in}^2$, $\varepsilon = 0.09k^{3/2}/d_e$

$$T = T_{in} = T_w, \quad \overline{T'^2} = (0.082\Delta T)^2, \quad \varepsilon_{T'} = 0.4\frac{\varepsilon}{k}\overline{t^2}$$

$$C_{AC} = C_{AC,in}, \quad C_{HAc} = C_{HAc,in}, \quad \overline{c_i^2} = (0.082C_{i,in})^2, \quad \varepsilon_{c_i} = 0.4\frac{\varepsilon}{k}\overline{c_i^2}$$

Outlet (column top, $x = Z$): The fluid flow is considered as fully developed, the gradient of all parameters Φ except pressure is equal to zero.

Axis: All of the variables Φ have a zero gradient due to the assumption of axial symmetry.

Wall: No slip condition is applied; all parameters related to flow are equal to zero.

$$U = V = k = \varepsilon = \overline{T'^2} = \varepsilon_t = \overline{c'^2} = \varepsilon_{c'} = 0$$

Near-wall region: The method of standard wall function is employed and the mass flux $\frac{\partial C}{\partial r} = 0$.

7.1.3 Determination of the Source Terms

Porosity of the catalyst bed
For the reactor filled with catalyst of small cylindrical particle, the porosity γ can be represented by the following correlations [5]:

$$\gamma = 2.14z^2 - 2.53z + 1, \quad z \leq 0.637$$
$$\gamma = \gamma_\infty + 0.29\exp(-0.6z)\cos(2.3\pi(z - 0.16)) + 0.15\exp(-0.9z), \quad z > 0.637$$

where γ_∞ is the porosity with unbounded boundary; z is the dimensionless distance from the wall, defined as follows:

$$z = (R - r)/d_e$$

where d_e is the equivalent diameter of the catalyst.

Coefficient of flow resistance R_0
When fluid phase flowing through the catalyst, the frictional resistance is created. The coefficient of the frictional force R_0 can be calculated by the modified Ergun equation [6]:

$$R_0 = 150\mu_L\frac{(1 - \gamma)^2}{\gamma^2 d_e^2} + 1.75\rho_G\frac{(1 - \gamma)}{\gamma^2 d_e}|\mathbf{U}|.$$

Table 7.1 Reaction mixture specifications [7]

Case no.	t_0 (°C)	Molar ratio	Average molar weight (kg/kmol)	G (kg/ m²s)	μ 10^{-5} (Ns/m²)	Re_p	c_p (J/ kg K)	k_L (J/ m K s)
1	176.1	1.5	39.6	0.242	1.372	58	1,680	0.0333
2	176.0	1.5	39.6	0.186	1.369	45	1,680	0.0333
3	186.4	1.5	39.6	0.242	1.376	58	1,710	0.0344
4	176.1	4.0	32.8	0.200	1.375	48	1,800	0.0380

Source term S_i

The source term S_i representing the mass of component i generated by the chemical reaction and can be calculated from the reaction rate:

$$S_i = \pm M_i R_s F_b$$

where M_i is the molar weight of component i; R_s is the apparent reaction rate, which will be given in the subsequent section; F_b is the bulk density of catalyst. In the equation, negative and positive signs refer to the reactant and product components, respectively.

7.1.4 The Simulated Wall-Cooled Catalytic Reactor

Simulation is made for a wall-cooled fixed-bed catalytic reactor reported by Valstar [7], in which the synthesis of vinyl acetate from acetic acid and acetylene is untaken with zinc acetate on activated carbon as catalyst. The internal and external diameters of the tubular reactor are, respectively, 0.041 and 0.0449 m, and the reactor length is 1 m. The gaseous mixture is flowing upward from the bottom of the reactor. The reactor tube is surrounded by a jacketed tube with an internal diameter of 0.0725 m. Cooling oil is pumped through the annular space between the reactor and the cooling tube. The oil temperature is controlled to within ±0.5 °C. The radial average conversions and the temperature profiles along the radial direction at different axial positions are measured. The properties of reaction mixture are listed in Table 7.1, and the catalyst specification is listed in Table 7.2.

The overall chemical reaction of vinyl acetate synthesis is as follows:

$$CH_3COOH + CH \equiv CH \longrightarrow Zn(Ac)_2 CH_3COOCH = CH_2 + \Delta H_r$$
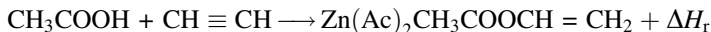
The apparent reaction rate of foregoing reaction is given below [7]:

$$R_s = \frac{k_\infty \exp(-E/R_g T)p_{AC}}{1 + \exp(-\Delta H_1/R_g T)\exp(-\Delta S_1/R_g)p_{HAc} + C_r p_{VA}}$$

where $k_\infty = 5,100$ (kmol kg (cat)$^{-1}$ s^{-1} atm^{-1}), $E = 85,000$ (kJ kmol^{-1}), $\Delta H_1 = (31,500$ kJ kmol$^{-1})$, $\Delta S_1 = -71,000$ (kJ kmol^{-1} K^{-1}); $C_r = 2.6$ (atm^{-1}) for molar ratio of acetylene to acetic acid equal to 1.5; $C_r = \exp\left(-\frac{70,000}{R_g T}\right)\exp\left(\frac{170}{R_g}\right)$

Table 7.2 Catalyst specification [7]

Term, unit	Value
Average length, mm	5.4
Average diameter, mm	2.8
Effective diameter d_e, mm	3.3
Specific external surface, m^2/g	0.00217
Specific external surface, m^2/g	350
Bed porosity	0.36
Bulk density, kg/m^3	570–600
Particle density, kg/m^3	910
Thermal conductivity, J/m K s	0.184

Table 7.3 Coefficients for heat of reaction [8]

Component	A	B	C
Vinyl acetate	−298.36	−6.9870E−02	3.9316E−05
Acetic acid	−417.91	−5.8243E−02	3.3466E−05
Acetylene	228.04	1.5754E−03	−3.5319E−06

(atm^{-1}) for a molar ratio of acetylene to acetic acid equal to 4. The heat of reaction, ΔH_r is function of temperature:

$$\Delta H_r = \Delta_f H_{VA,m} - \Delta_f H_{HAc,m} - \Delta_f H_{AC,m} \Delta_f H_{i,m} = A + BT + CT^2$$

where subscripts VA, HAc, and AC denote, respectively, vinyl acetate, acetic acid, and acetylene; their coefficients A, B, and C are listed in Table 7.3.

7.1.5 Simulated Result and Verification

The species concentration distribution along the whole reactor

Following the progress of the reaction from the bottom ($H = 0$) to the top ($H = 1$) of the reactor, the concentration of acetic acid is gradually decreasing and the product, vinyl acetate, is increasing; that means the conversion is consequently increasing along the reactor from bottom to the top. From the simulated concentration profile of acetic acid in the whole column, its concentration in radial direction is averaged at different heights and at different operating conditions of the reactor in order to obtain the average acetic acid conversion along the axial direction. The simulated conversion curve is shown in Fig. 7.1 and compared with the experimental data [8]; satisfactory agreement between them is seen.

The radial temperature profile

As an example, one of the temperature profiles along the whole reactor is shown in Fig. 7.2. The radial temperatures are averaged at different reactor heights and under different operating conditions as shown in Fig. 7.3, in which the
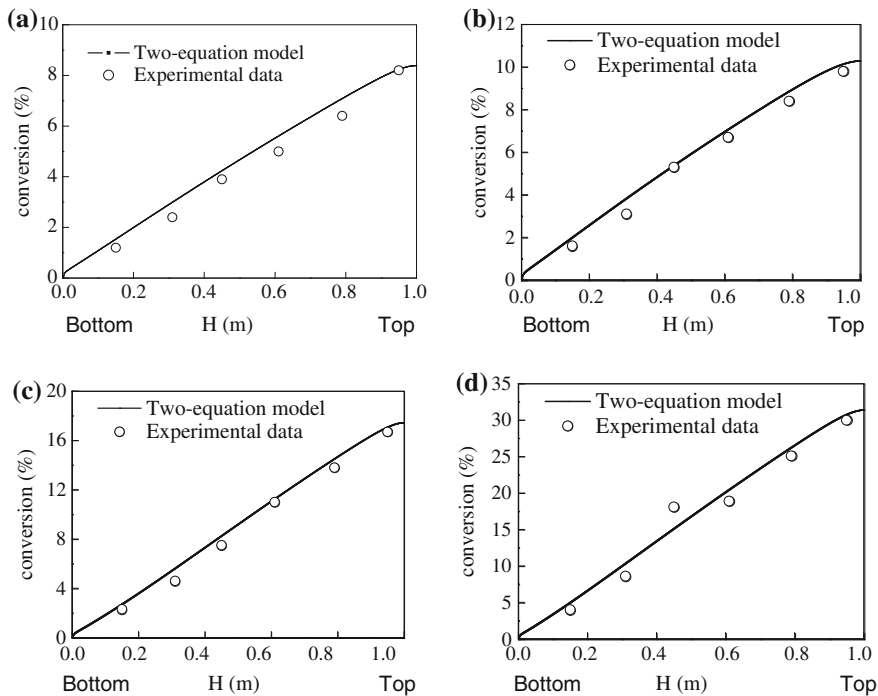
Fig. 7.1 Simulated and measured conversion profiles along reactor axis. **a** Case 1, molar ratio = 1.5, t_0 = 176.1 °C, G = 0.242 kg m^{-2} s^{-1}, **b** Case 2, molar ratio = 1.5, t_0 = 176.0 °C, G = 0.186 kg m^{-2} s^{-1}, **c** Case 3, molar ratio = 1.5, t_0 = 186.4 °C, G = 0.242 kg m^{-2} s^{-1}, **d** Case 4, molar ratio = 4.0, t_0 = 176.1 °C, G = 0.200 kg m^{-2} s^{-1} (reprinted from Ref. [2], copyright 2008, with permission from American Chemical Society)

experimental measurements by Valstar et al. [8] and their prediction are also given for comparison. It is seen that the simulated temperature profiles by the present model are closer to the experimental measurements than that by Valstar [8].

The distribution of turbulent mass diffusivity D_t
By using present two-equation model, both the diffusivity profiles of acetylene and acetic acid along the reactor can be obtained as shown in Fig. 7.4. As shown in the figure, the turbulent mass diffusivity of acetylene $D_{t,AC}$ in axial direction becomes steady after traveling from inlet to a distance about 20-fold of effective catalyst diameter d_e (d_e in present case is 3.3 mm). As shown in Fig. 7.4b, the distribution of $D_{t,AC}$ in radial direction in the main flow region increases gradually to a maximum until to about $r/R = 0.8$ and then decreases sharply toward the column wall. Such tendency is in consistent with the experimental measurement. It is as a result of the uneven distribution of porosity, velocity, temperature, and concentration near the wall region.

The turbulent mass diffusivity of acetic acid $D_{t,HAc}$ is also given in Fig. 7.4c, and the tendency of its axial and radial distributions is similar to those of acetylene

Fig. 7.2 Simulated temperature profile along the reactor for Case 1, molar ratio = 1.5, $t_0 = 176.1$ °C, $G = 0.242$ kg m^{-2} s^{-1} (reprinted from Ref. [2], copyright 2008, with permission from American Chemical Society)
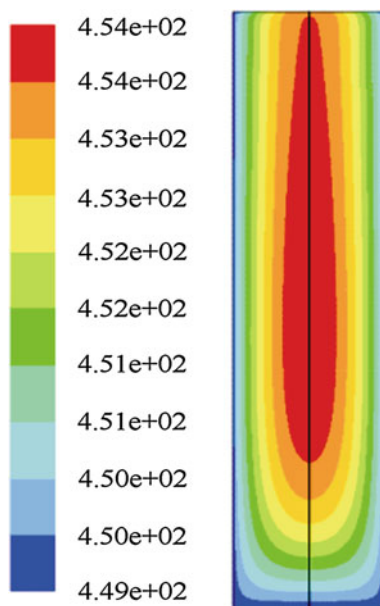
because both of them are in the same temperature and velocity fields although the concentration field is different.

The distribution of turbulent thermal diffusivity α_t

The turbulent thermal diffusivity α_t can also be calculated by using two-equation model as shown in Fig. 7.5, in which, similar to the turbulent mass diffusivity D_t, the α_t reaches almost steady condition after traveling a distance about 50-fold of the effective catalyst diameter from the entrance and decreases sharply afterward.

The distribution of turbulent diffusivity ν_t

For the comparison purpose, the simulated turbulent diffusivity (kinematic viscosity) ν_t is also given in Fig. 7.6. On careful study, the tendency of axial and radial distributions of ν_t is similar to that of D_t, and α_t only appears not far from the entrance ($H \leq 0.1$ in the figure), although they are all drop down almost to zero at the wall. The comparison again displays that the $\frac{\nu_t}{D_t}$ ratio (Sc_t) and $\frac{\nu_t}{\alpha_t}$ ratio (Pr_t) are complicated and cannot be simply to be considered as a constant.

7.2 Reynolds Mass Flux Model for Catalytic Reactor

Li [9] employed standard Reynolds mass flux model to simulate the water-cooled reactor as described in Sect. 7.1.3.
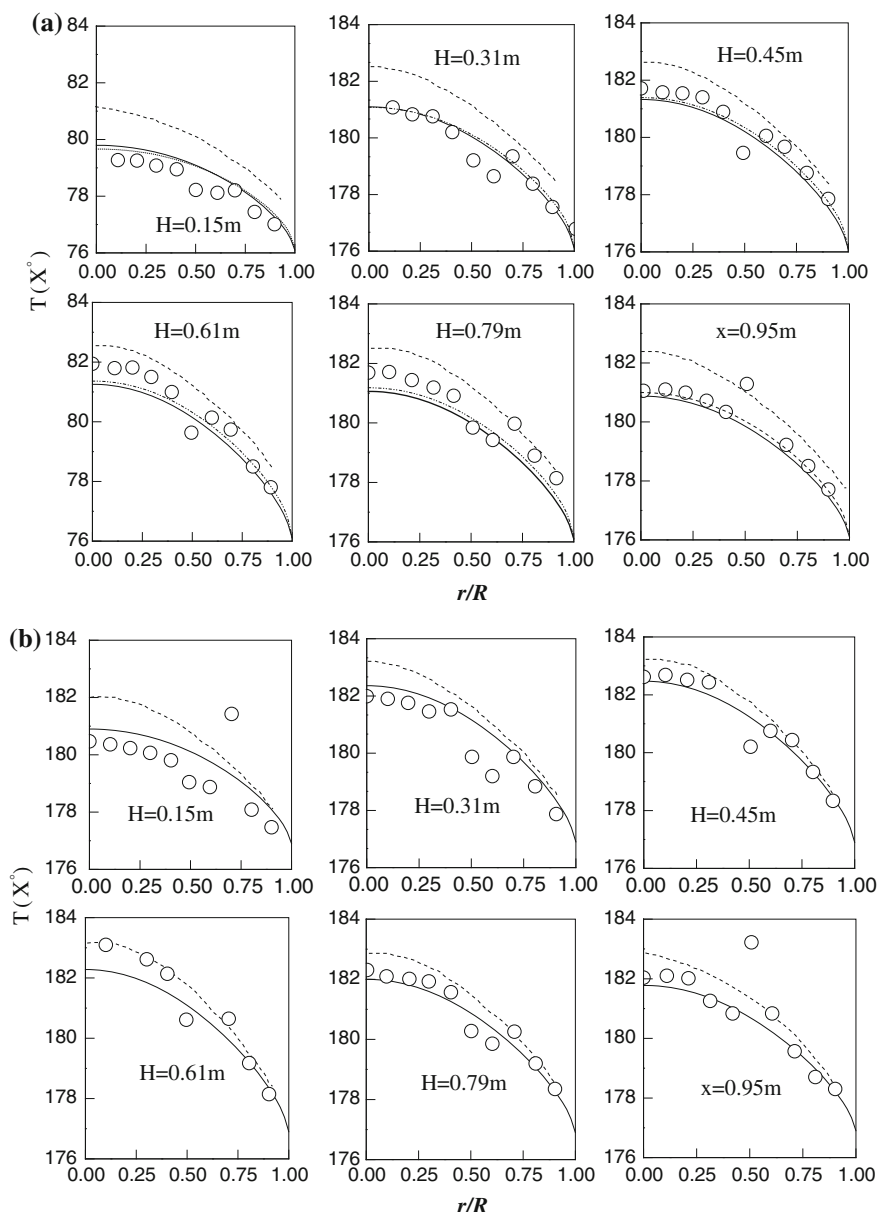
Fig. 7.3 Radial temperature distribution along reactor (*dash* simulated by two-equation model, *line* simulated by Valstar, *circle* experimental data, *H*-bed height measured from bottom, $H = 0$ at the reactor bottom). **a** Case 1, molar ratio = 1.5, $t_0 = 176.1$ °C, $G = 0.242$ kg m^{-2} s^{-1}, **b** Case 2, molar ratio = 1.5, $t_0 = 176.0$ °C, $G = 0.186$ kg m^{-2} s^{-1}, **c** Case 3, molar ratio = 1.5, $t_0 = 186.4$ °C, $G = 0.242$ kg m^{-2} s^{-1}, **d** Case 4, molar ratio = 4.0, $t_0 = 176.1$ °C, $G = 0.200$ kg m^{-2} s^{-1} (reprinted from Ref. [2], copyright 2008, with permission from American Chemical Society)

Fig. 7.3 (continued)

(a)

(b)

(c)
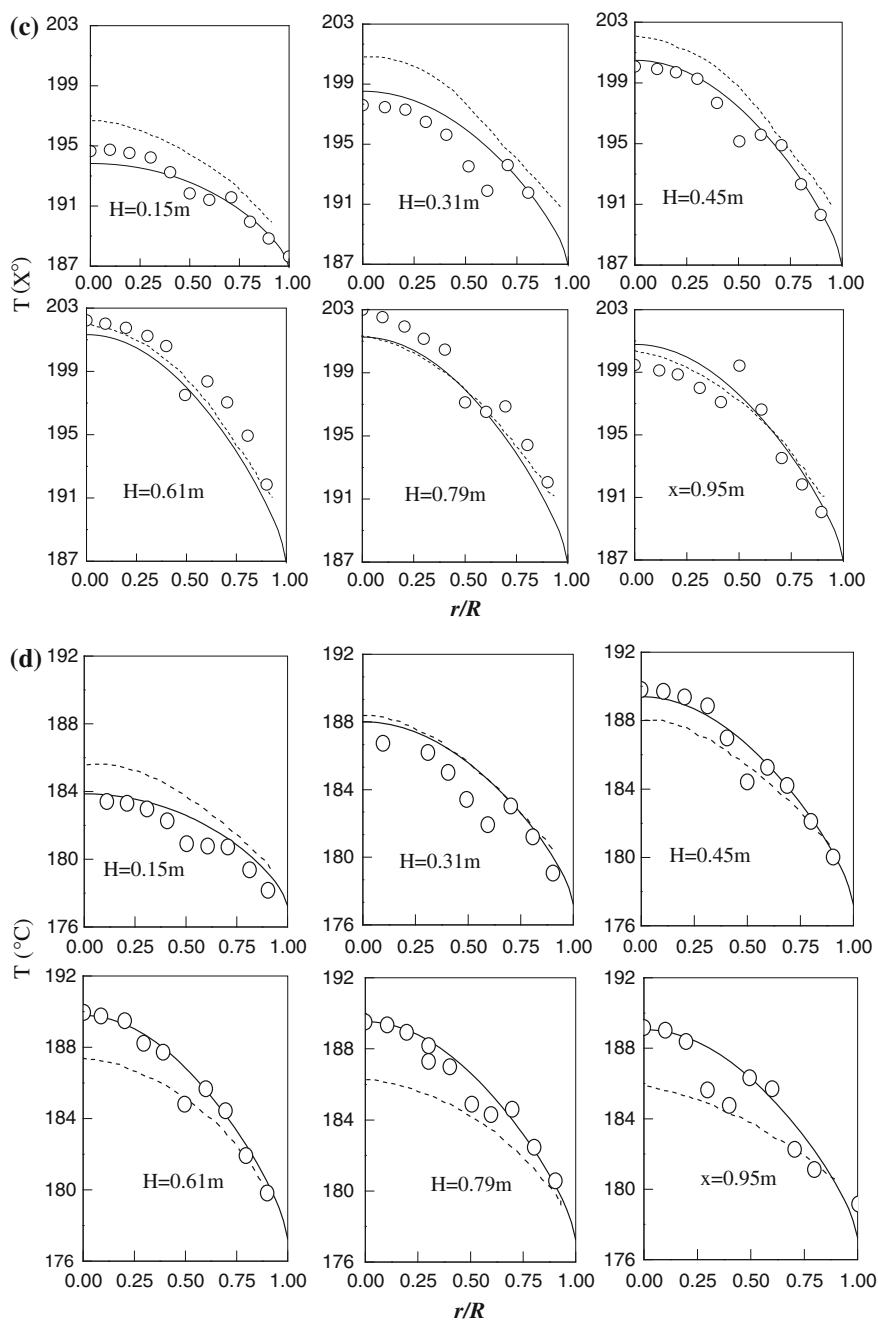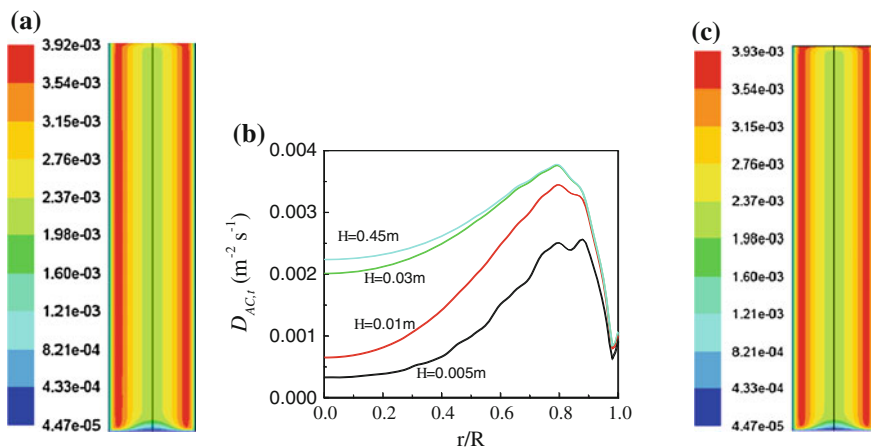
Fig. 7.4 Simulated axial and radial distributions of turbulent mass diffusivity for Case 1. **a** Acetylene, **b** acetylene, and **c** acetic acid (reprinted from Ref. [2], copyright 2008, with permission from American Chemical Society)
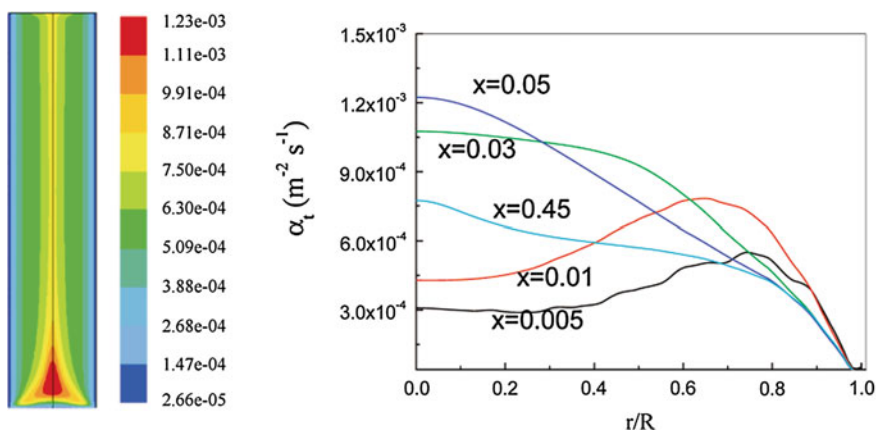
Fig. 7.5 Simulated axial and radial distributions of turbulent thermal diffusivity for Case 1 (reprinted from Ref. [2], copyright 2008, with permission from American Chemical Society)

7.2.1 Model Equations

The model equations are similar to the $\overline{c'^2} - \varepsilon_c$ two-equation model except that the parameters, $\overline{u_i' u_j'}$, $\overline{u_i' T'}$ and $\overline{u_i' c'}$, are not solved by diffusivity method but are calculated directly using Reynolds stress, Reynolds heat flux, and Reynolds mass flux equations.

(a)
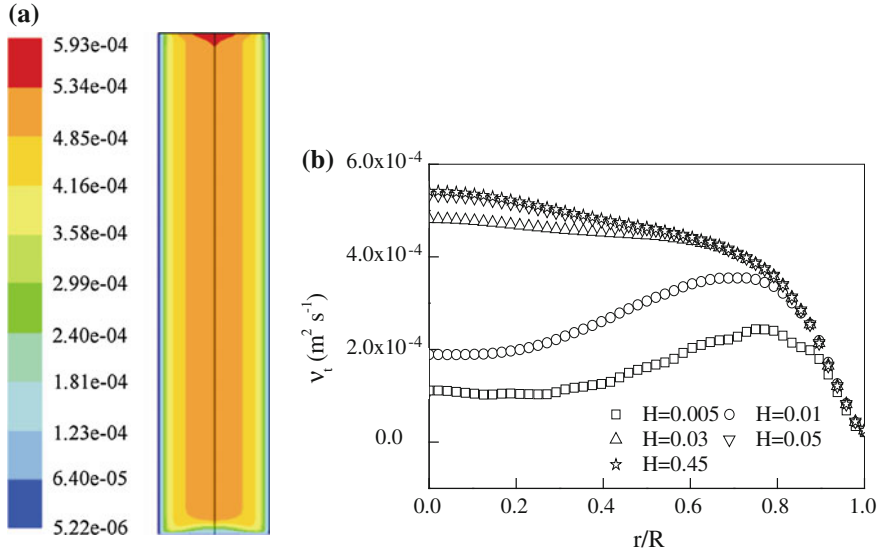
Fig. 7.6 Simulated axial and radial distributions of turbulent diffusivity for Case 1 (reprinted from Ref. [2], copyright 2008, with permission from American Chemical Society)

1. **CFD equation set**

   Overall mass conservation

$$\frac{\partial(\rho\,\gamma U_i)}{\partial x_i} = S_m$$

   Momentum conservation

$$\frac{\partial\left(\rho_G\gamma U_iU_j\right)}{\partial x_i} = -\gamma\frac{\partial P}{\partial x_j} + \frac{\partial}{\partial x_i}\left[\gamma\mu\left(\frac{\partial U_j}{\partial x_i}\right) - \gamma\rho_G\overline{u_i'u_j'}\right] + \gamma(\rho_G g + R_0 U_i)$$

where $\overline{u_i'u_j'}$ is calculated by:

$$\frac{\partial\overline{u_i'u_j'}}{\partial t} + U_k\frac{\partial\overline{u_i'u_j'}}{\partial x_k} = \frac{\partial}{\partial x_k}\left(C_0\frac{k}{\varepsilon}\overline{u_i'u_j'}\frac{\partial\overline{u_i'u_j'}}{\partial x_k} + \frac{\mu}{\rho}\frac{\partial\overline{u_i'u_j'}}{\partial x_k}\right) - \left(\overline{u_i'u_k'}\frac{\partial U_j}{\partial x_k} + \overline{u_j'u_k'}\frac{\partial U_i}{\partial x_k}\right)$$
$$- C_1\frac{\varepsilon}{k}\left(\overline{u_i'u_j'} - \frac{2}{3}k\Delta_{ij}\right) - C_2\left(\overline{u_i'u_k'}\frac{\partial U_j}{\partial x_k} + \overline{u_j'u_k'}\frac{\partial U_i}{\partial x_k} - \frac{2}{3}\Delta_{ij}\overrightarrow{u_i'u_k'}\frac{\partial U_i}{\partial x_k}\right) - \frac{2}{3}\varepsilon\Delta_{ij}$$

$$(1.23)$$

   The constants are as follows: $C_0 = 0.09$, $C_1 = 2.3$, $C_2 = 0.4$. The k and ε in foregoing equation are given by:

$$\frac{\partial\rho\,U_i k}{\partial x_i} = \frac{\partial}{\partial x_i}\left[\left(\mu + \frac{\mu_t}{\sigma_k}\right)_L\frac{\partial k}{\partial x_j}\right] + (G_k - \varepsilon) \qquad (1.11c)$$

$$\frac{\partial \rho\, U_i \varepsilon}{\partial x_i} = \frac{\partial}{\partial x_i}\left[\left(\mu + \frac{\mu_t}{\sigma_\varepsilon}\right)_L \frac{\partial \varepsilon}{\partial x_i}\right] + \rho(C_{1\varepsilon}G_{Lk} - C_{2\varepsilon}\varepsilon)\frac{\varepsilon}{k} \tag{1.13b}$$

The model constants are as follows: $c_\mu = 0.09$, $\sigma_k = 1.0$, $\sigma_\varepsilon = 1.3$, $C_{1\varepsilon} = 1.44$, $C_{2\varepsilon} = 1.92$.

2. Heat transfer equation set

(a) *Energy conservation of gas phase*

$$\frac{\partial(\gamma\rho\, C_p U_i T)}{\partial x_i} = \frac{\partial}{\partial x_i}\left[\gamma\rho\, C_p\left(\alpha\frac{\partial \overline{C}}{\partial x_i} - \overline{u_i'T'}\right)\right] + S_T$$

$$S_T = Q_1 - Q_2 = h_s a_s\left(T_s^s - T\right) - h_w a_{w1}(T - T_{w1})$$

where $Q_1 = h_s a_s\left(T_s^s - T\right)$ represents the heat transfer from the catalyst to the gas phase; $Q_2 = h_{w1}a_{w1}(T - T_{w2})$ represents the heat transfer from the gas phase to the inner wall of the reactor. The $\overline{u_i'T'}$ is calculated by Reynolds heat flux equation as follows:

$$\frac{\partial \overline{u_i'T'}}{\partial t} + U_i\frac{\partial \overline{u_i'T'}}{\partial x_k} = \frac{\partial}{\partial x_k}\left[\left(C_{T1}\frac{k}{\varepsilon}\overline{u_1'u_j'} + \alpha\right)\frac{\partial \overline{u_i'T'}}{\partial x_k}\right]$$
$$- \left(\overline{u_i'u_k'}\frac{\partial T}{\partial x_k} + \overline{u_k'T'}\frac{\partial U_j}{\partial x_k}\right) - C_{T2}\frac{\varepsilon}{k}\overline{u_i'T'} + C_{T3}\overline{u_k'T'}\frac{\partial U_i}{\partial x_k} \tag{2.13}$$

where the constants are as follows: $C_{t1} = 0.07$, $C_{t2} = 3.2$, $C_{t1} = 0.5$.

(b) *Energy conservation of catalyst*

$$\frac{\partial}{\partial x_i}\left((1 - \gamma)\lambda_s\frac{\partial T_s}{\partial x_i}\right) + (1 - \gamma)\rho_s(\Delta HR) - h_s a_s\left(T_s^s - T\right) = 0$$

(c) *Energy conservation of reactor wall*

$$\frac{\partial}{\partial x_i}\left(\lambda_w\frac{\partial T_w}{\partial x_i}\right) + h_{w1}a_{w1}(T - T_{w1}) - h_{w2}a_{w2}(T_{W2} - T_c) = 0$$

3. Mass transfer equation set

(a) *Mass conservation of reactive species (gas phase)*

$$\frac{\partial \beta_L U_i C}{\partial x_i} = \frac{\partial}{\partial x_i}\beta_L(D\frac{\partial C}{\partial x_i} - \overline{u_i'c'}) + \beta_L S_n$$
$$S_n = h\, a_s\left(C_{si}^s - C\right) \tag{3.3b}$$

where $\overline{u_i'c'}$ is given by Reynolds mass flux equation as follows:

$$\frac{\partial \overline{u_i'c'}}{\partial t} + \frac{\partial U_j \overline{u_i'c'}}{\partial x_j} = \frac{\partial}{\partial x_j}\left[\left(C_{c1}\frac{k}{\varepsilon}\overline{u_i'u_j'} + \frac{\mu}{\rho}\right)\frac{\partial \overline{u_i'c'}}{\partial x_j}\right] - \left(\overline{u_i'u_j'}\frac{\partial C}{\partial x_j}\right) - C_{c2}\frac{\varepsilon}{k}\overline{u_i'c'}$$
$$+ C_{c3}\overline{u_j'c'}\frac{\partial U_i}{\partial x_j} \tag{3.33a}$$

The constants are as follows: $C_{c1} = 0.09$, $C_{c2} = 3.2$, $C_{c3} = 0.55$.

(b) *Mass conservation of the solid phase*

$$\frac{\partial}{\partial x_i}\left(D_s\frac{\partial T_s}{\partial x_i}\right) + (1-\gamma)\rho_s(MR) - k_G a_s\left(C_s^s - C\right) = 0$$

If the resistance of intra-diffusion is neglected, the foregoing equation can be simplified to:

$$k_G a_s\left(C_{si}^s - C\right) = \rho_s(1-\gamma)M\,R$$

Boundary conditions and determination of source terms

The boundary conditions and determination of source terms are the same as in Sects. 7.1.1 and 7.1.2.

7.2.2 Simulated Result and Verification

The reactor simulated is a wall-cooled fixed-bed catalytic reactor reported by Valstar [7] for the synthesis of vinyl acetate from acetic acid and acetylene with zinc acetate on activated carbon as catalyst as given in Sect. 7.1.2.

Simulated concentration profiles of the species in the reactor

As an example, the profiles of acetic acid, acetylene, and vinyl acetate along the whole column are shown in Fig. 7.7, in which the radial concentration distribution is clearly seen.

Simulated acetic acid conversion

From the simulated radial concentration distribution along the column, the conversion of acetic acid can be found as shown in Fig. 7.8. The simulated radial conversion is averaged at different heights of reactor to find the average conversion along the axial direction under different operating conditions as given in Fig. 7.9. The simulated curve is confirmed by the measured data reported by Valstar [7]. In this figure, the simulation by using two-equation model is also plotted for comparison; it can be seen that the simulation is better by using Reynolds mass flux model than by using two-equation model.
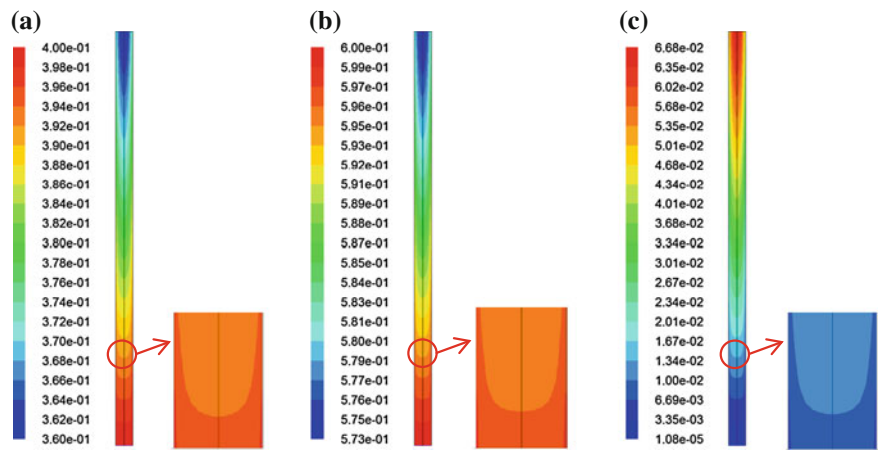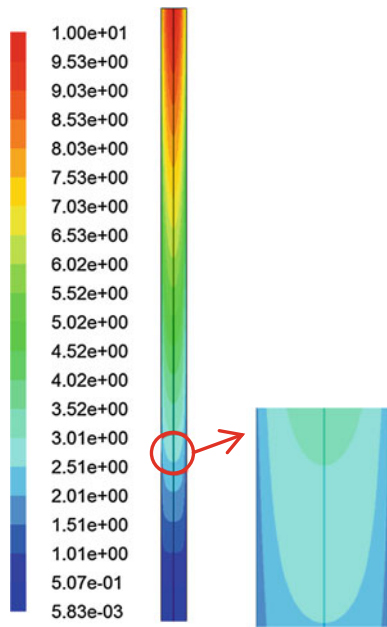
Fig. 7.7 Simulated profiles of molar fraction. **a** Acetic acid, **b** acetylene, and **c** vinyl acetate [9]

Fig. 7.8 Simulated profiles of acetic acid conversion (%) in the fixed bed [9]

Simulated temperature profiles of the gas phase

An example of the simulated temperature profile of gas phase in the reactor is shown in Fig. 7.10.

Fig. 7.9 Simulated
comparison of acetic acid
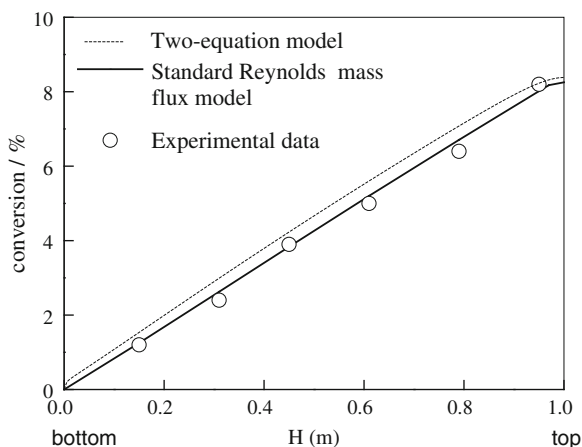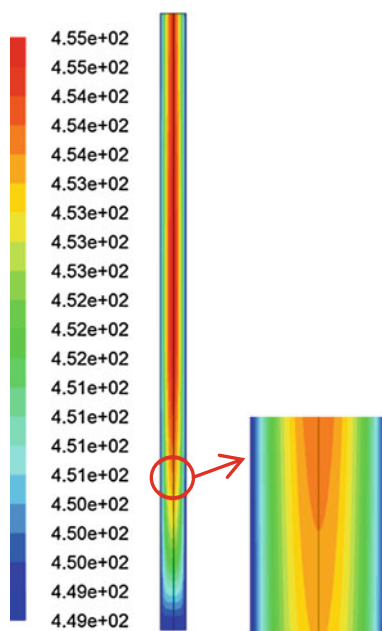conversion along axial
direction between simulation
and experimental data for
Case 1 [9]

Fig. 7.10 Simulated profiles
of temperature (K) in the
reactor [9]

Comparison with experimental data and two-equation model

The radial temperature is averaged at different heights along the axial direction is
given in Fig. 7.11 and compared with the experimental data and the simulation by
using two-equation model. As shown in the figure, the simulation by using Rey-
nolds mass flux model is better than that by two-equation model although both of
them are considered in agreement with the experimental data.
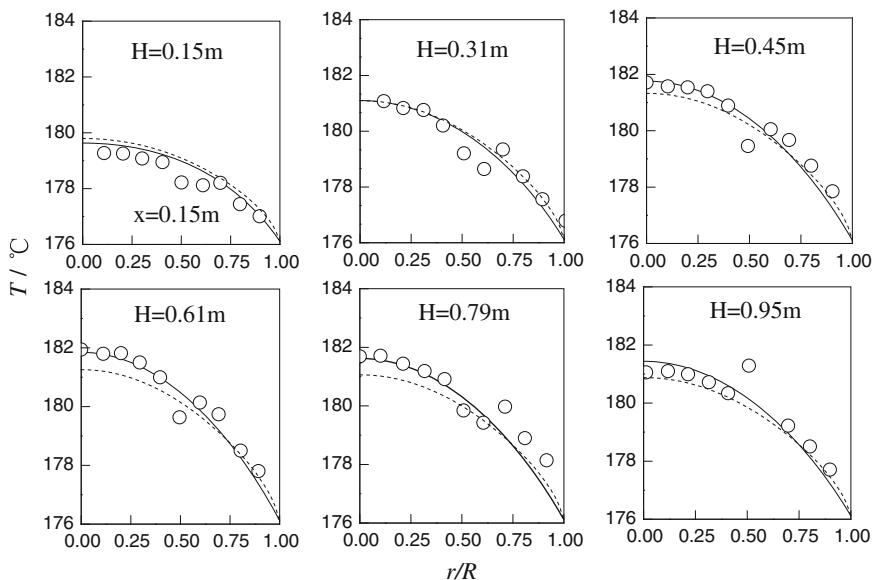
Fig. 7.11 Comparison of radial temperature profiles at different packed heights between simulation obtained by the standard Reynolds mass flux model (*line*), two-equation model (*dash*), and experimental data (*circle*) for Case 1 (*H*-distance of bed height measured from column bottom) [9]

7.2.3 The Anisotropic Mass Diffusivity

(1) *The axial mass diffusivity*

Figure 7.12a shows the wavy shape profile of $\overline{u'_x c'}$ in radial direction with alternating positive and negative slope, but its tendency is likely to be gradually increasing, which is consistent with the increasing profile of vinyl acetate as shown in Fig. 7.7 so as to enhance the reaction in axial direction. Also in Fig. 7.12b, the positive $\overline{u'_x c'}$ is seen decreasing around the column top ($x < 1$), while it turns to increasing rapidly over the remaining part of the column. It indicates that the $\overline{u'_x c'}$ diffusion is in co-action with the axial increasing profile of vinyl acetate (Fig. 7.7), so that the reaction in axial direction is enhanced by turbulent diffusion.

From Eq. (3.37) and Figs. 7.12a and 7.13a, the axial turbulent mass diffusivity $\mathbf{D_{t,x}}$ can be obtained as given in Fig. 7.14. As shown in the figure, $\mathbf{D_{t,x}}$ is in the wavy shape and fluctuated strongly beyond $r/R = 0.6$. It is mainly due to the high fluctuation of gas-phase velocity in both axial and radial directions as shown in Fig. 7.15. However, the tendency of turbulent effect looks increasing toward the column bottom.
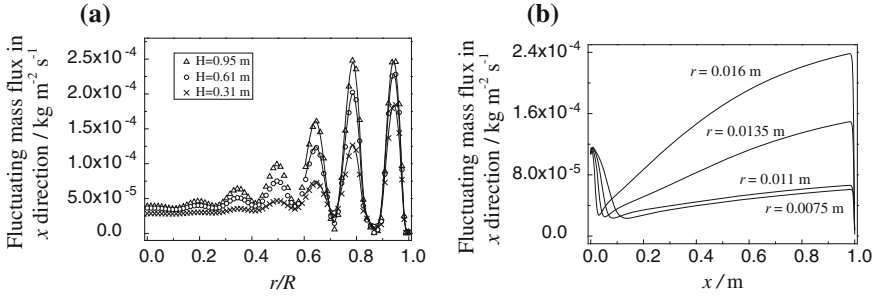
Fig. 7.12 Simulated $\overline{u'_x c'}$ profiles [9]. **a** $\overline{u'_x c'}$ in radial direction and **b** $\overline{u'_x c'}$ in axial direction
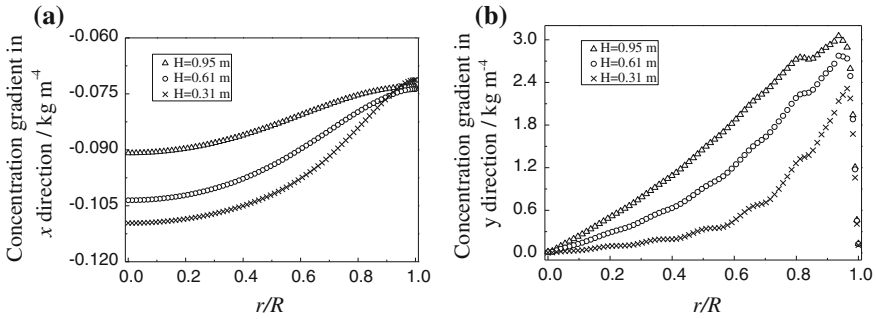

Fig. 7.13 Simulated concentration gradients of vinyl acetate [9]. **a** Axial $\frac{\partial C}{\partial x}$ gradient of vinyl acetate and **b** radial $\frac{\partial C}{\partial y}$ gradient
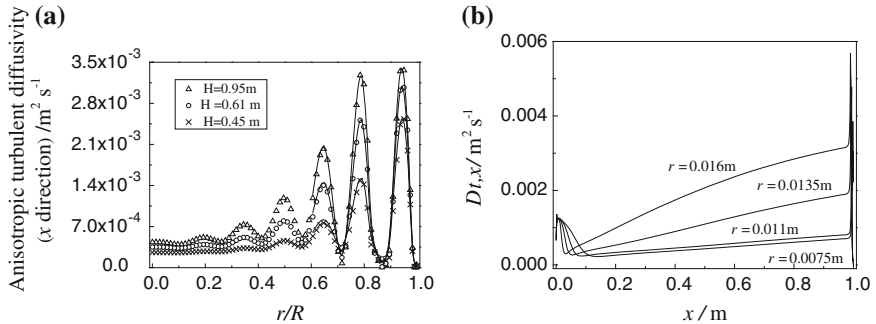

Fig. 7.14 Simulated $\mathbf{D_{t,x}}$ [9]. **a** $\mathbf{D_{t,x}}$ in radial direction and **b** $\mathbf{D_{t,x}}$ in axial direction

(2) *The radial mass diffusivity*

The profile of $\overline{u'_y c'}$ is given in Fig. 7.16, in which all $\overline{u'_y c'}$ is negative. It indicates that the negative gradient of $\overline{u'_y c'}$ diffusion is in contradiction with the positive
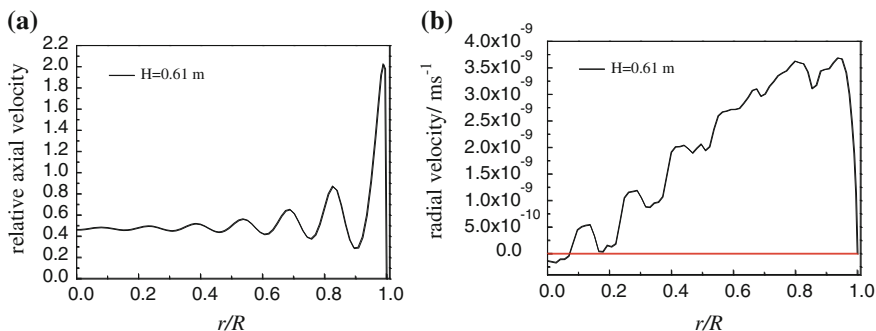
Fig. 7.15 Simulated profiles of axial and radial velocities along radial direction at $H = 0.61$ m [9]. **a** Axial velocity and **b** radial velocity
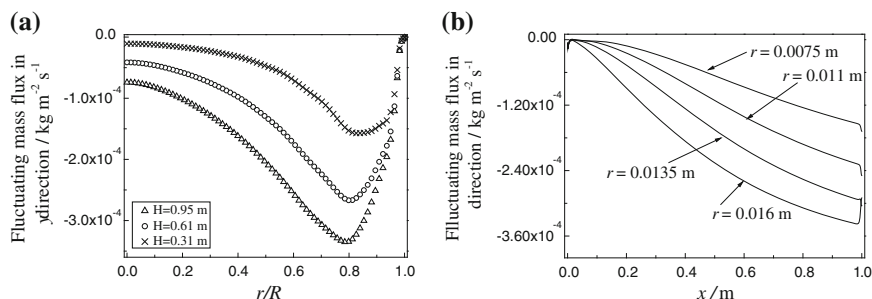

Fig. 7.16 Simulated $\overline{u'_y c'}$ [9]. **a** $\overline{u'_y c'}$ in radial direction and **b** $\overline{u'_y c'}$ in axial direction

process gradient $(\partial C/\partial y)$ of vinyl acetate as shown in Fig. 7.7, so that the reaction in radial direction is suppressed.

From Eq. (3.37) and Figs. 7.16 and 7.13, the radial turbulent mass diffusivity $\mathbf{D_{t,y}}$ can be obtained as given in Fig. 7.17. As shown in the figure, $\mathbf{D_{t,y}}$ is very high near the column center; it is due to very low $(\partial C/\partial y)$ gradient there as the concentration is assumed to be symmetrical to the centerline.

The profile of $\overline{u'_i c'}$ (sum of $\overline{u'_x c'}$ and $\overline{u'_y c'}$) is given in Fig. 7.16. The wavy shape and negative $\overline{u'_i c'}$ are noted. The negative $\overline{u'_i c'}$ indicates the axial turbulent diffusion is overwhelmed by the radial diffusion.

The radial turbulent mass diffusivity $\mathbf{D_{t,y}}$ are shown in Fig. 7.17, and the sum of the fluctuating mass flux is given in Fig. 7.18.
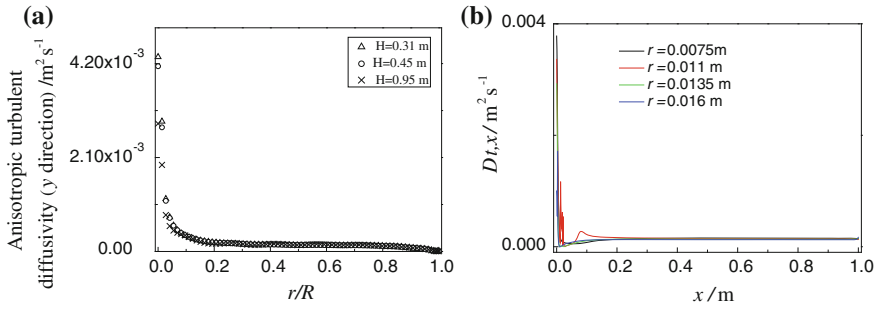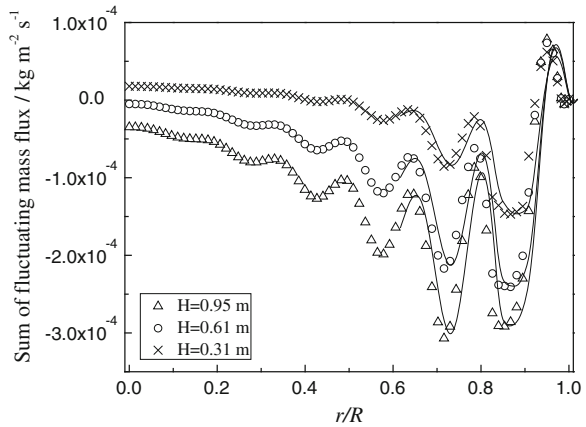
Fig. 7.17 Simulated profiles of $\mathbf{D_{t,y}}$ [9]. **a** $\mathbf{D_{t,x}}$ in radial direction and **b** $\mathbf{D_{t,x}}$ in axial direction

Fig. 7.18 Simulated profile of $\overline{u_i'c'}$ (sum of $\overline{u_x'c'}$ and $\overline{u_y'c'}$) [9]

7.3 Summary

The source term S_n in the species conservation Eq. (3.1) can represent the mass created or depleted by a chemical reaction besides the mass transferred from one phase to the other. Thus, CMT model can be used for simulating the chemical reactor. A catalytic reactor with water-cooled jacket is chosen as typical example for illustration. The CMT model equations are regularly comprises mass transfer equation set and the accompanied fluid-dynamic equation set and heat transfer equation set. Note that the source term S_n is calculated in terms of reaction rate. The simulated results of a wall-cooled catalytic reactor for the synthesis of vinyl acetate from acetic acid and acetylene by both $\overline{c'^2} - \varepsilon_{c'}$ model and Reynolds mass flux model for simulating the axial concentration and temperature distributions are in agreement with the experimental measurement. As the distribution of μ_t shows dissimilarity with D_t and α_t, the Sc_t or Pr_t are varying throughout the reactor. The wavy shape of axial diffusivity $\mathbf{D_{t,x}}$ along the radial direction indicates the important influence of porosity distribution on the performance of a reactor.

References

1. Froment GF, Bischoff KB (1990) Chemical reactor analysis and design. Wiley, New York
2. Liu GB, Yu KT, Yuan XG, Liu CJ (2008) A computational transport model for wall-cooled catalytic reactor. Ind Eng Chem Res 47:2656–2665
3. Launder BE, Spalding DB (1972) Lectures in mathematical models of turbulence. Academic Press, London
4. Elghobashi SE, Launder BE (1983) Turbulent time scales and the dissipation rate of temperature variance in the thermal mixing layer. Phys Fluids 26(9):2415–2419
5. de Klerk A (2003) Voidage variation in packed beds at small column to particle diameter ratio. AIChE J 49(8):2022–2029
6. Ergun S (1952) Fluid flow through packed columns. Chem Eng Prog 48:89–94
7. Valstar JM, van den Berg PJ, Oyserman J (1975) Comparison between twodimensional fixed bed reactor calculations and measurements. Chem Eng Sci 30(7):723–728
8. Yaws CL (2003) Yaws' handbook of thermodynamic and physical properties of chemical compounds. Knovel, New York
9. Li WB (2012) Theory and application of computational mass transfer. PhD Dissertation, Tianjin University, Tianjin

Chapter 8
Simulation of Interfacial Effect on Mass Transfer

Abstract The mass transferred from one phase to the adjacent phase must diffuse through the interface and subsequently may produce interfacial effect. In this chapter, two kinds of important interfacial effects are discussed: Marangoni effect and Rayleigh effect. The theoretical background and method of computation are described including origin of interfacial convection, mathematical expression, observation, theoretical analysis (interface instability, on-set condition), experimental and theoretical study on enhancement factor of mass transfer. The details of interfacial effects are simulated by using CMT differential equations.

Keywords Interfacial mass transfer · Marangoni effect · Rayleigh effect · Interfacial concentration gradient · Interfacial convection · Mass transfer enhancement

Nomenclature

Bi	Biot number
c	Mass concentration, kg m^{-3}
$c^{\mathbf{i}}$	Interfacial concentration, kg m^{-3}
c^*	Interfacial concentration in equilibrium with the bulk concentration, kg m^{-3}
Cr	Crispation number
d	Liquid layer thickness, m
D	Diffusivity of solute, m^2 s^{-1}
F	Enhancement factor
g	Acceleration of gravity, m s^{-2}
j	Mass transfer flux, mol s^{-1} m^{-2}
k	Coefficient of mass transfer, m s^{-1}; wave number
k_{H}	Coefficient of mass transfer calculated by penetration theory, m s^{-1}
l, L	Characteristic length, m
Le	Lewis number
Ma	Marangoni number

N	Mass transfer flux, mol s^{-1} m^{-2}
P	Pressure, kg m^{-1} s^{-2}
Ra	Rayleigh number
Re	Reynolds number
S	Source term
Sc	Schmidt number
Sh	Sherwood number
t	Time, s
T	Temperature, K
$\overline{T}$	Residence time of fluid cell, s
u, v, w	Velocity component, m s^{-1}
U, V, W	Dimensionless velocity component
U_s	Velocity at interface, m s^{-1}
x, y, z	Coordinate
X, Y, Z	Dimensionless distance
β_c	Concentration gradient in x direction, $\frac{\partial c}{\partial x}$
β'_c	Concentration gradient in z direction, $\frac{\partial c}{\partial z}$
β_T	Temperature gradient in x direction, $\frac{\partial T}{\partial x}$
β'_T	Temperature gradient in z direction, $\frac{\partial T}{\partial z}$
R_T	Coefficient of surface tension change with temperature, $\frac{\partial \sigma}{\partial T}$
R_c	Coefficient of surface tension change with concentration, $\frac{\partial \sigma}{\partial c}$
α	Thermal diffusivity, m^2 s^{-1}
μ	Viscosity, kg m^{-1} s^{-1}
v	Kinematic viscosity, m^2 s^{-1}
σ	Surface tension, kg s^{-2}
τ	Dimensionless time
ψ	Amplitude of velocity disturbance
$\varPhi$	Amplitude of concentration disturbance
$\varTheta$	Amplitude of temperature disturbance
ρ	Density, kg m^{-3}
ω	Increasing rate of disturbance

Superscript

$'$	Disturbance
-	Average

Subscript

cr	Critical
exp	Experimental
h	Heat transfer
G	Gas phase
log	Logarithmic average

L   Liquid phase
surf   Surface
theo   Theoretical

The mass transfer between two fluid phases must go through the interface. Due to the existence of surface tension gradient on the interface and the density gradient between the interface and the main fluid, the fluid dynamic instability or bifurcation may appear under certain conditions, which can significantly influence the process efficiency.

8.1 The Interfacial Effect

In the course of interfacial mass transfer, from molecular point of view, the process is stochastic, that means some local molecules may undergo the mass transfer in advance than the others, so that small concentration gradient $\frac{\partial c}{\partial x_i}$ (where $i = x, y, z$) is established at the interface. As the surface tension σ is function of concentration, it follows that the surface tension gradient $\frac{\partial \sigma}{\partial x_i}$ is also created at the interface. If $\frac{\partial \sigma}{\partial x_i}$ is increased up to a critical point, the fluid dynamic instability will appear to induce the interfacial convection as well as the formation of orderly structure at the interface. At the same time, the rate of mass transfer may be enhanced or suppressed depending on the properties of the mass transfer system concerned; such phenomena is generally regarded as interfacial effect.

In the middle of eighteenth century, Marangoni described and investigated such interfacial convection [1], which afterward was called Marangoni convection and its effect was also regarded as Marangoni effect.

Further increase in $\frac{\partial \sigma}{\partial x_i}$ after the critical point will continue to magnify (if not to depress) the interfacial effect until the interface structure becomes blurred and the orderly structure gradually turns to the disordered or chaotic state. At this time, the process is approaching to the turbulent state of mass transfer.

The Marangoni convection, induced by surface tension gradient $\frac{\partial \sigma}{\partial x_i} = \frac{\Delta \sigma}{\Delta x}\big|_{\Delta x \to 0}$ or by concentration gradient $\frac{\partial c}{\partial x_i} = \frac{\Delta c}{\Delta x}\big|_{\Delta x \to 0}$ and at the same time can be represented by a dimensionless group, denoted as Marangoni number Ma, as given below. The greater Ma number means more intense interfacial convection:

$$Ma = \frac{R_c \Delta c L}{\mu D} \tag{8.1}$$

where $R_c \left(R_c = \frac{\partial \sigma}{\partial c}\right)$ is the rate of surface tension increase with respect to the concentration of the transferred species; D and μ are, respectively, the diffusivity and viscosity of the transferred species; L is the characteristic length. In the literature, L and Δc can be expressed in specified form according to the process concerned.

When Ma number reaches its critical value Ma_{cr} and beyond, i.e., $Ma \geq Ma_{cr}$, the mass transfer system is under instability and Marangoni convection is induced; when $Ma < Ma_{cr}$, the system is stable and the convection is suppressed.

The Marangoni number Ma may be positive or negative dependent on the value of R_c and Δc. For instance, if CO_2 is absorbed by ethanol, the Δc of CO_2 in ethanol is positive but R_c is negative, then Ma is negative. Otherwise, if CO_2 is desorbed from CO_2-saturated ethanol, both R_c and Δc are negative, thus Ma is positive. In multicomponent mass transfer process, since more than one component is transferred, the sign of Ma is dependent on their coupling result.

According to the sign of Ma, the mass transfer processes can be classified into the following:

(1) Positive Ma process ($Ma > 0$): Marangoni convection is promoted.
(2) Negative Ma process ($Ma < 0$): Marangoni convection is inhibited.
(3) Neutral Ma process ($Ma = 0$): Marangoni convection is absent. Generally, this class also refers to the case that $\Delta\sigma$ is less than 1–2 dyn/cm.

Marangoni convection is also influential to many other transfer processes, such as crystallization, metallurgical and drug productions as well as the transport behaviors in the space [2].

Since Marangoni convection is induced by surface tension gradient on the interface, the creation of such gradient is caused not only by having concentration gradient but also by temperature gradient $\frac{\partial T}{\partial x_i}$. The intensity of Marangoni convection created due to the temperature gradient on interface can be represented by Ma_h as follows:

$$Ma_h = \frac{R_h \Delta T d}{\mu D} \tag{8.2}$$

where R_h represents the rate of surface tension increase with respect to the temperature, $R_h = \frac{\partial \sigma}{\partial T} = \frac{\Delta\sigma}{\Delta T}\big|_{\Delta T \to 0}$; ΔT and d are, respectively, the temperature difference and the characteristic length, which are usually specified by different investigators to suit different processes.

Furthermore, the interfacial convection and the renewal of interface can also be promoted by the vertical convective circulation between interface and main fluid due to the density difference. Such convection is called Rayleigh convection [3, 4] or Rayleigh-Bénard convection. The intensity of Rayleigh convection can be represented by the Rayleigh number Ra as follows:

$$Ra = \frac{g \Delta\rho L^3}{D\mu} \tag{8.3}$$

where L is the characteristic length and generally refers to the distance from interface to the bulk fluid; g is the acceleration of gravity. Similar to Ma, the Rayleigh convection appears only after reaching its critical value.

Table 8.1 The sign of *Ma* and *Ra* for the absorption and desorption of CO_2 by different absorbents

Absorbent	CO_2 absorption		CO_2 desorption	
	Ma	*Ra*	*Ma*	*Ra*
Methanol	−	+	+	−
Ethanol	−	+	+	−
Chlorobenzene	−	−	+	+
Trichloroethylene	−	−	+	+

In short, the Marangoni convection induced by surface tension gradient and the Rayleigh convection induced by density gradient are the two main interfacial effects. Marangoni convection displays on the interface and underneath (the depth of Marangoni convection underneath is about 10^{-4} m in our observation); and the Rayleigh convection appears vertically from interface to the bulk fluid with accompanied action of interfacial renewal. When the critical point of each convection is reached, the interfacial effect will be initiated.

In fact, the gradients of concentration, temperature, and density are all giving contributions to the interfacial convection and forming coupling effect. For instance, when CO_2 is desorbed from CO_2-saturated ethanol, the Marangoni convection is positive ($Ma > 0$), but if the Rayleigh convection is negative ($Ra < 0$), it will depress the Marangoni convection. On the contrary, when CO_2 is desorbed from CO_2-saturated chlorobenzene, both *Ma* and *Ra* are positive, the Marangoni convection will be strengthened. The sign of *Ma* and *Ra* for the absorption and desorption of CO_2 by different absorbents are listed in Table 8.1.

8.2 Experimental Observation of Interfacial Structure Induced by Marangoni Convection

Since last century, many researchers have undertaken the observation of Marangoni convection, especially using the laser Schlieren technique. In this section, some results of our experimental study on interface structure are presented for illustration [5–9]. The experimental installation is shown in Fig. 8.1. The experiment was undertaken at constant temperature so that the temperature-induced Marangoni convection can be eliminated. The liquid–gas contactor can be placed in horizontal position for horizontal liquid–gas flow, or in vertical position for falling liquid film and uprising gas flow. The mass transfer process to be study is either absorption or desorption of CO_2 by various kinds of absorbent. Nitrogen is served as CO_2 carrier. The liquid phase can be in either stagnant or countercurrent flow with the gas phase.
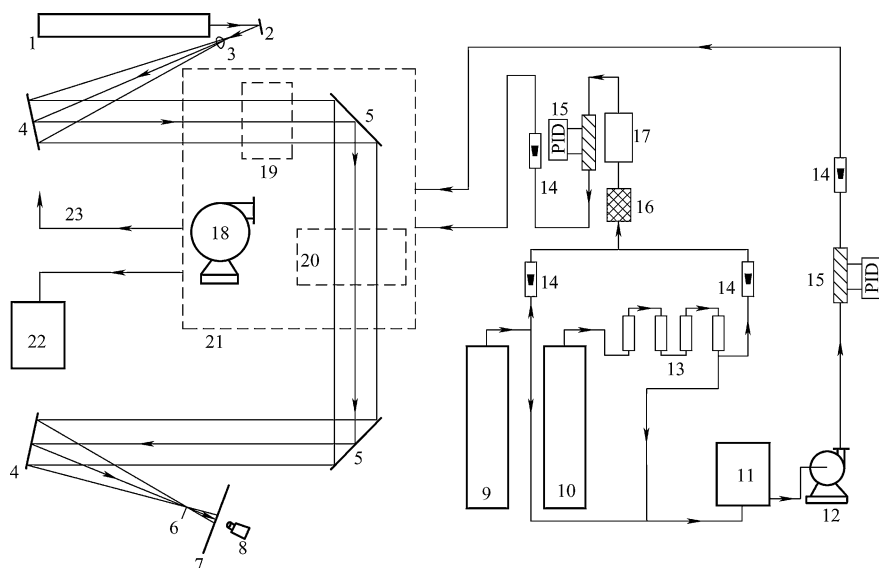
Fig. 8.1 Experimental installation for the observation of interfacial structure (*1*—He–Ne laser, *2*—reflecting mirror, *3*—expanding lens, *4*—concave mirror, *5*—mirror, *6*—blade, *7*—screen, *8*—CCD camera, *9*—N_2 cylinder, *10*—CO_2 cylinder, *11*—absorbent vessel, *12*—pump, *13*—CO_2 purifier, *14*—rotameter, *15*—PID controlled heater, *16*—mixer, *17*—bubbling vessel, *18*—blower, *19*—falling film liquid–gas contactor, *20*—horizontal flow liquid–gas contactor, *21*—air-conditioning zone, *22*—solvent recovery vessel, *23*—flue gas exit) [1]

8.2.1 Stagnant Liquid and Horizontal Gas Flow

1. *Desorption of CO_2 from CO_2saturated ethyl acetate*

In this case, $Ma > 0$, $Ra < 0$, the Marangoni convection is induced after the surface tension gradient is reaching to the critical value. The interface was photographed for the whole desorption process until stable picture was obtained. The liquid–gas contactor is schematically shown in Fig. 8.2a.

Under the condition of 17 °C, nitrogen flow rate 0.1 m^3/h, and liquid thickness 5 mm, the interface image displayed not so clear roll structure at the beginning as shown in Fig. 8.3a, afterward turned to polygonal-like structure (b), and finally reached stable clear polygonal cell structure (c).

2. *Absorption of CO_2 by ethyl acetate*

In this case, $Ma < 0$, $Ra > 0$, although the Marangoni convection is negative, yet the density gradient between interface and the bulk liquid induced the Rayleigh convection to renew the interface so as to establish concentration gradient with the depleted local point and formed interfacial convection as shown in Fig. 8.4. As shown in this figure, when the liquid thickness is 2 mm, the interface displayed
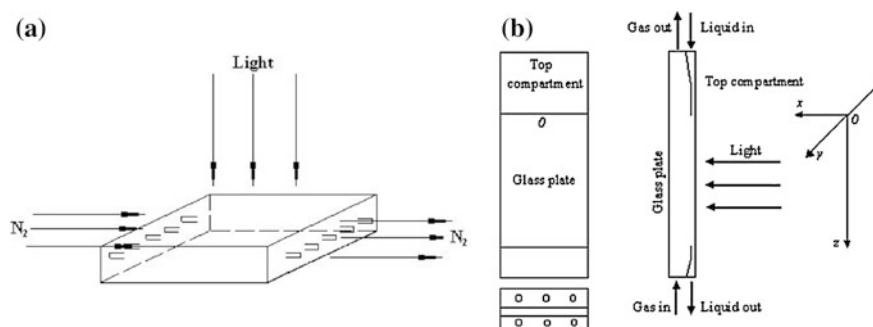
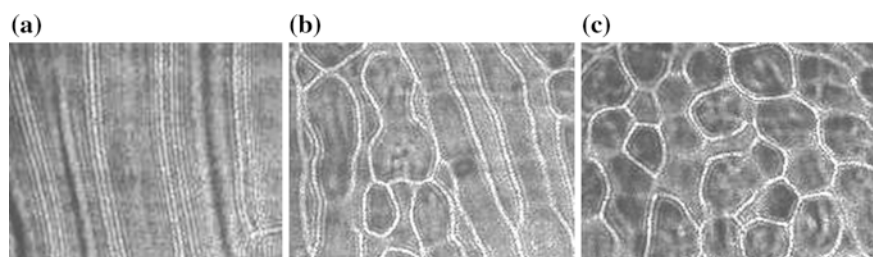**Fig. 8.2** Liquid–gas contactors. **a** Horizontal contactor, **b** vertical (falling film) contactor

Fig. 8.3 Interfacial structure of CO_2 desorption from stagnant ethyl acetate at 17 °C and N_2 rate of 0.1 m^3/h [1]. **a** Beginning of formation. **b** Development. **c** Stable structure
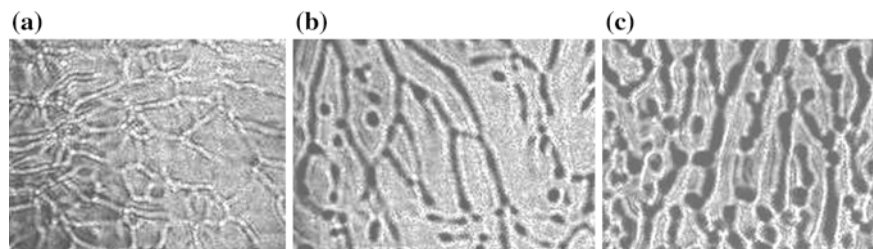

Fig. 8.4 Interfacial structure of CO_2 absorption by stagnant ethyl acetate at 17 °C and gas rate of 0.04 m^3/h [1]. **a** Liquid thickness 2 mm. **b** Liquid thickness 5 mm. **c** Liquid thickness 10 mm

polygonal-like structure but without order. When thickness of liquid was increased to 5 mm, mixed roll and cellular structure was appeared. Further increased in liquid thickness to 10 mm, the interface showed the enlargement of the mixed structure and more intense convection. It demonstrated that the Rayleigh effect was strengthened by deeper liquid thickness to increase the density gradient. It is also shown that the interfacial structure is dependent on the coupling effect of Marangoni and Rayleigh convections.

Fig. 8.5 Image of convection perpendicular to the interface for the absorption of CO_2 by stagnant ethyl acetate [1]

The Rayleigh convection was also photographed from vertical view (perpendicular to the interface) as shown in Fig. 8.5. The inverted mushroom shape of convection penetrates from the interface to the main body of liquid.

8.2.2 Horizontal Concurrent Flow of Liquid and Gas

1. **Desorption of CO_2 from CO-saturated ethanol**
   In this case ($Ma > 0$, $Ra < 0$), under the condition of liquid thickness 4.6 mm, ethanol velocity 6.9×10^{-3} m s^{-1}, and nitrogen rate 0.12 m^3 h^{-1}, Marangoni convection was induced as shown in Fig. 8.6a in the form of parallel roll structure. When nitrogen rate was increased to 0.16 m^3 h^{-1}, the roll became finer and smaller as shown in Fig. 8.6b.

2. **Diffusion of aqueous ethanol to nitrogen in countercurrent flow**
   In this case, two component, water and ethanol, was diffused to nitrogen in the liquid–gas concurrent flow and induced interfacial structure ($Ma > 0$, $Ra > 0$). Under the condition of liquid thickness 5.3 mm, aqueous ethanol rate 8.7×10^{-6} m s^{-1}, and nitrogen rate 0.1 m^3 h^{-1}, the interface displayed clear cellular structure as shown in Fig. 8.7a. Under another condition of liquid thickness 4.3 mm, aqueous ethanol rate 1.1×10^{-5} m s^{-1}, and nitrogen rate 0.16 m^3 h^{-1}, the cellular structure was not so clear and likely to have tendency of becoming roll as shown in Fig. 8.7b. Thus, the interfacial structure is also affected by the flowing condition of liquid and gas.

8.2.3 Vertical (Falling-Film) Countercurrent Flow of Liquid and Gas

Two cases of chemical absorption are taken for illustration.

1. **CO_2 absorption by aqueous diethanolamine**
   In this case, 28 mol% of aqueous diethanolamine was used to absorb CO_2 ($Ma > 0$, $Ra > 0$) in the falling-film liquid–gas countercurrent contactor as
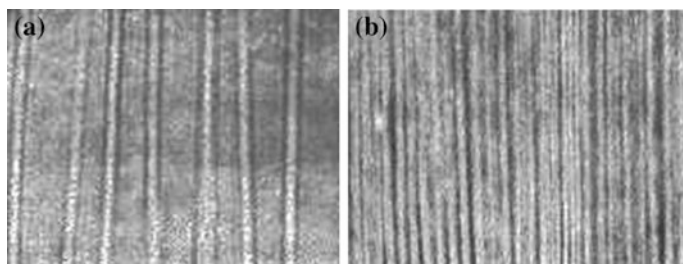
Fig. 8.6 Desorption of CO_2 in horizontal concurrent liquid–gas flow [1]. **a** Nitrogen rate 0.12 m³/h. **b** Nitrogen rate 0.16 m³/h

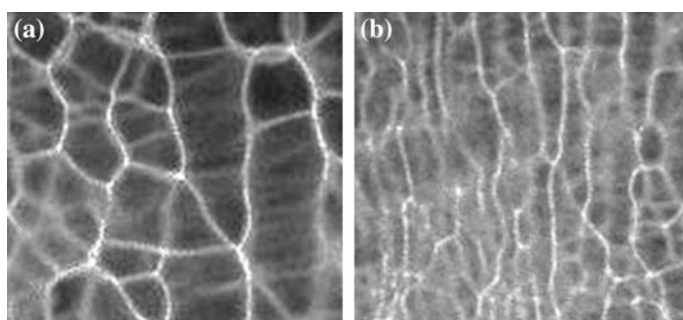**Fig. 8.7** Diffusion of aqueous ethanol to nitrogen in concurrent flow. **a** Nitrogen rate 0.12 m³/h. **b** Nitrogen rate 0.16 m³/h (reprinted from Ref. [8], Copyright 2002, with permission from CIESC)
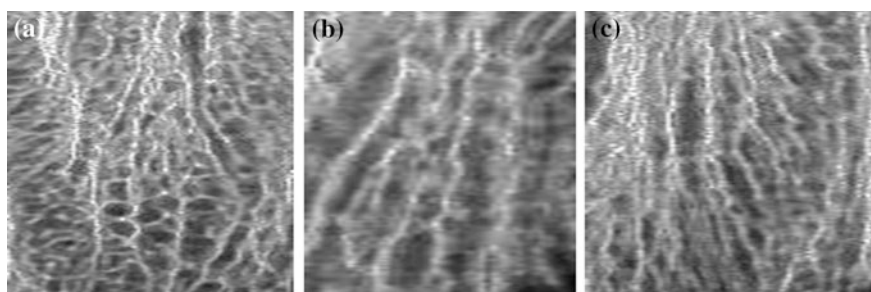
Fig. 8.8 Falling-film absorption of CO_2 by diethanolamine [1]. **a** CO_2 flow rate 0.016 m³ h⁻¹. **b** CO_2 flow rate 0.1 m³ h⁻¹. **c** CO_2 flow rate 0.2 m³ h⁻¹

shown in Fig. 8.2b. Under the condition of liquid thickness 0.12 mm, liquid rate 3.22×10^{-2} m s⁻¹, and CO_2 rate 0.016 m³ s⁻¹, the interface displayed mixed structure of roll and cell as shown in Fig. 8.8a. At higher CO_2 rate of 0.1 and 0.2 m³ s⁻¹, the roll structure was dominated although some cells were appeared locally as shown in Fig. 8.8b and c.
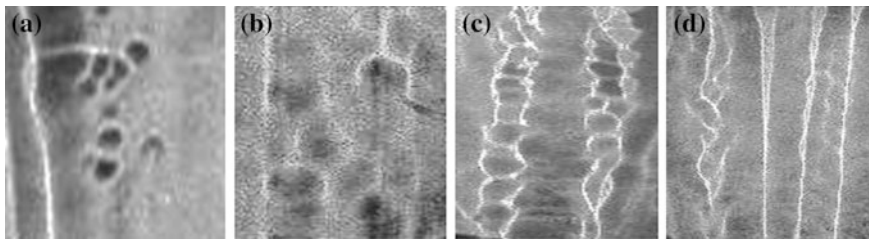
Fig. 8.9 Falling-film absorption of CO_2 by NaOH [1]. **a** CO_2 rate 0.08 m^3 h^{-1}. **b** CO_2 rate 0.1 m^3 h^{-1}. **c** CO_2 rate 0.16 m^3 h^{-1}. **d** CO_2 rate 0.3 m^3 h^{-1}

2. ***CO_2 absorption by aqueous NaOH***

   In this case, under the condition of falling-film thickness 0.13 mm, liquid rate 2.76×10^{-2} m s^{-1}, and the countercurrent CO_2 rate, respectively, 0.08, 0.1, 0.16, and 0.3 m^3 s^{-1}, the interface structure is shown in Fig. 8.9a–d. At low gas rate, cellular structure appeared locally; while at higher gas rate, the roll structure involving cells was developed with tendency to becoming all roll structure.

8.3 The Condition for Initiating Marangoni Convection

The appearance of Marangoni convection in the liquid–gas interface means that the system cannot retain the stable state and turn to induce interfacial flow and accompany with the formation of orderly structure. In other words, the Marangoni convection initiates at the point where the stability of a mass transfer process is broken down and led to the non-equilibrium phase transition to the orderly structure.

   The condition of initiating Marangoni convection can be found by analyzing the stability of a mass transfer process, i.e., answering the question: under what condition the stable state is interrupted. The process chosen for this study is desorption of falling-film desorbent (aqueous acetone) by the countercurrent flowing gas (nitrogen) as shown in Fig. 8.10.

   Sha [10, 11] simulated and analyzed this process with the following model:

Assumptions

(1) The thickness of falling film is small; the density difference between interface and the film in the direction perpendicular to the interface is negligible so that the effect of Rayleigh convection can be neglected. Also the process is isothermal, and the Marangoni convection is only due to interfacial concentration difference.

Fig. 8.10 Mass transfer
model of falling-film and
countercurrent gas flow
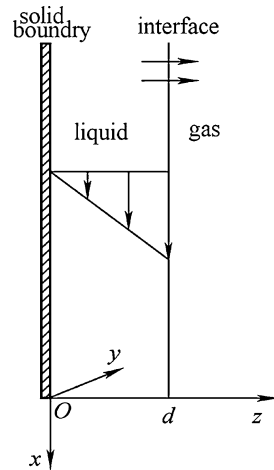
(2) The interface is flat, no deformation.
(3) All physical properties are constant except surface tension.
(4) Both the rate of falling film and uprising gas flow are low, and the frictional
force between liquid and gas is neglected.
(5) The amount of desorbed species (acetone) transferred is small, so that the
density of desorbent is practically remained constant.

8.3.1 Model Equations

The mass transfer process is desorption where desorbed species (acetone) is
transferred from aqueous liquid phase to the gas phase. The surface tension is
changed linearly with the concentration as follows:

$$\sigma = \sigma_0 + R_c(c - c_0)$$

where σ_0 is the surface tension at the interfacial desorbent (aqueous acetone)
concentration, c_0; $R_c = \frac{\partial \sigma}{\partial c}$ is the rate of surface tension change with respect to the
concentration; c is the desorbent concentration in aqueous liquid phase.

For the desorption of aqueous acetone to the nitrogen, the concentration of
acetone is decreased as the liquid phase flowing down, the concentration gradient
$\frac{\partial c}{\partial x}$ is negative. Since R_c is negative in this case, thus $R_c \Delta c$ as well as Ma is positive
and Marangoni convection can be induced under appropriate condition. The fol-
lowing interacted liquid-phase (aqueous acetone) model can be established:

$$\frac{\partial u}{\partial x_i} = 0$$

$$\frac{\partial u}{\partial t} + u\frac{\partial u}{\partial x_i} = -\frac{1}{\rho}\frac{\partial p}{\partial x_j} + \frac{\mu}{\rho}\frac{\partial^2 u}{\partial x_i^2} + S$$

$$\frac{\partial c}{\partial t} + u\frac{\partial u}{\partial x_i} = D\frac{\partial^2 c}{\partial x_i}$$

$$S = -\left(0, \frac{\rho' g}{\rho}\right)$$

$$u = (u, v, w)$$

where c is the mass concentration of the desorbed species (acetone) in desorbent (kg m^{-3}); D is the molecular diffusivity (m^2 s^{-1}); S is the source term (gravity); and t is the time.

The boundary conditions are as follows:

At $z = 0$ (wall), $u = v = w = 0$, $\frac{\partial c}{\partial z} = 0$.

At $z = d$ (liquid–gas interface), solute is diffused from liquid phase to the gas phase, the rate of which can be represented by the following equation:

$$-D\frac{\partial c}{\partial z} = k_L(c - c_I)$$

where k_L is the liquid film coefficient of mass transfer; c_I is the solute concentration at the interface.

Dimensionless model equations

For the convenience of solving the model equation, the method of dimensionless is used to reduce the number of variables. Let d, $\beta_c R_c d/\mu$, $\beta_c R_c$, $\beta_c d$, $\mu/\beta_c R_c$ are respectively the dimensionless length, velocity, pressure, concentration, and time, i.e.,

$$U = \frac{u\mu}{\beta_c R_c d}, \quad V = \frac{v\mu}{\beta_c R_c d}, \quad W = \frac{w\mu}{\beta_c R_c d}, \quad X = \frac{x}{d}, \quad Y = \frac{y}{d},$$

$$Z = \frac{z}{d}, \quad C = \frac{c}{\beta_c d}, \quad \tau = \frac{t\beta_c R_c}{\mu}, \quad P = \frac{p}{\beta_c R_c}$$

Substitute the foregoing dimensionless variables to the model equations to yield the following equations:

$$\frac{\partial U}{\partial x_i} = 0$$

$$Re\left[\frac{\partial U}{\partial \tau} + U\frac{\partial U}{\partial x_i}\right] = -\frac{\partial P}{\partial x_j} + \frac{\partial^2 U}{\partial x_i}$$

$$Ma\left[\frac{\partial C}{\partial \tau} + U\frac{\partial C}{\partial x_i}\right] = \frac{\partial^2 C}{\partial x_i^2}$$

$$U = (U, V, W)$$

The dimensionless boundary conditions are as follows:
At $Z = 0$,

$$U = V = W = \partial C/\partial Z = 0$$

At $Z = 1$,

$$W = 0$$

$$\frac{\partial U}{\partial Z} = -\frac{\partial C}{\partial X}$$

$$\frac{\partial V}{\partial Z} = -\frac{\partial C}{\partial Y}$$

$$-\frac{\partial C}{\partial Z} = Bi(C - C_{\mathrm{I}}) + S$$

where the dimensionless group are as follows:

$$Re = \frac{\rho \beta_c R_c d^2}{\mu^2}, \quad Sc = \frac{\mu}{\rho D}, \quad Bi(M, L) = \frac{k_L d}{D}, \quad Ma = \frac{\beta_c R_c d^2}{\mu D},$$

$$C - C_{\mathrm{I}} = \frac{c - c_{\mathrm{I}}}{\beta_c d}, \quad C = \frac{c - c_0}{\beta_c d}, \quad S = \frac{S_G}{\beta_c D}$$

where $Bi(M, L)$ is the Biot number for liquid phase and the (M, L) is omitted in subsequent section.

8.3.2 Stability Analysis

Since the inhomogeneity of surface tension at the interface is the cause of initiating the Marangoni convection, the surface tension gradient $\frac{\partial \sigma}{\partial x_i}$ can be considered as an external force acting to the system. When this external force is not great enough to overcome the viscous shearing force of the fluid, the system remains stable. If this external force is just equal to the viscous shearing force of the fluid, the system is said to be in the critical condition. The Marangoni number at this point is denoted as critical Marangoni number Ma_{cr}. Thus, we may apply a small disturbance as external force to study the stability of the system.

The small disturbance acting on the variables concerned can be represented as follows:

$$(U, V, W, P, C) = (\bar{U}, \bar{V}, \bar{W}, \bar{P}, \bar{C}) + (\delta u, \delta v, \delta w, \delta p, \delta c)$$

where superscript "−" denotes stable state. If the disturbance system follows single normal mode, the disturbance term $(\delta u, \delta v, \delta w, \delta p, \delta c)$ is expressed by two-dimensional (x, y) exponential form as follows:

$$(\delta u, \delta v, \delta w, \delta p, \delta c) = (\hat{u}(Z), \hat{v}(Z), \hat{w}(Z), \hat{p}(Z), \hat{c}(Z)) \exp\left[ik_x x + ik_y y + \omega t\right]$$

where k_x and k_y are, respectively, the wave number in x and y direction; ω is the increasing rate of disturbance; superscript $\wedge$ represents the amplitude of the disturbed variable; x, y are the dimensionless coordinates.

Under neutral condition, ω is equal to 0. If the disturbance appears in x direction, $k_y = 0$. Substituting the disturbance expression to the dimensionless model equation and the boundary condition, we have the following:

$$
\begin{aligned}
(\tilde{D}^2 - k_x^2)\hat{u} &= MaSc^{-1}\hat{w} \\
(\tilde{D}^2 - k_x^2)^2\hat{w} &= 0 \\
(\tilde{D}^2 - k_x^2)\hat{C} &= -Ma(\hat{u} + MaZ^2\hat{w}/2)
\end{aligned}
\tag{8.4}
$$

At $Z = 0$, $\hat{u} = \hat{w} = \hat{D}\hat{w} = \hat{D}\hat{C} = 0$

At $Z = 1$, $\tilde{D}\hat{u} = \hat{w} = \tilde{D}^2\hat{w} + k_x^2\hat{C} = \tilde{D}\hat{C} + Bi\hat{C} = 0$

where $\tilde{D}$ is differential operator.

If the system is stable, the foregoing dimensionless equations have zero solution; if the system is unstable, there should have solution. Direct integration of foregoing dimensionless equations yield the solutions for $\hat{u}, \hat{w}$ and $\hat{C}$ with eight unknown integration constants in which the Ma, Bi, Sc, k_x are involved. Substituting to the boundary condition, eight linear equations are obtained. In this equation set, if the coefficients of 8×8 determinant equal to zero, the dimensionless equations can be solved. Mathematically speaking, the necessary and sufficient condition of system under instability is the foregoing 8×8 determinant is equal to zero. It follows that we have the following:

$$
f(Ma, Bi, Sc, k_x) = 0
$$

The left-hand side of the equation represents the relationship between Ma, Bi, Sc, k_2 obtained by setting the 8×8 determinant equal to zero. In other words, the foregoing system is unstable if its reasonable values of Ma, Bi, Sc, k_x are fulfill the condition of $f(Ma, Bi, Sc, k_x) = 0$.

By setting different Sc and Bi, the relationship between Ma and k_x can be obtained from $f(Ma, Bi, Sc, k_x) = 0$ as shown by the curves in Figs. 8.11 and 8.12. In these figures, any points above the curve are unstable and induce Marangoni convection, while any points below are stable without Marangoni convection. The minimum point of the curve represents the critical Marangoni number Ma_{cr}. It is also shown in Figs. 8.13 and 8.14 that Ma_{cr} is affected by both Sc and Bi of the process.

Sha performed the experiment on the falling-film desorption of acetone from its aqueous solution [10, 11] and found the Ma_{cr} as given in Table 8.2. In comparison with the calculated Ma_{cr}, the error is less than 10 %.

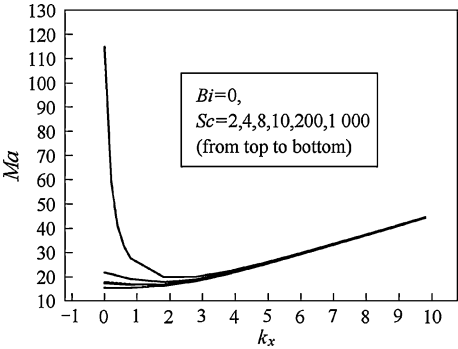**Fig. 8.11** *Ma* and
k relationship at $Bi = 0$ and
different *Sc*

Box: *Bi*=0,
Sc=2,4,8,10,200,1 000
(from top to bottom)

Fig. 8.12 *Ma* and
k relationship at $Sc = 1,000$
and different *Bi*

Box: *Sc*=1 000
Bi=10, 5, 2, 1, 0.6, 0.3, 0
(from top to bottom)
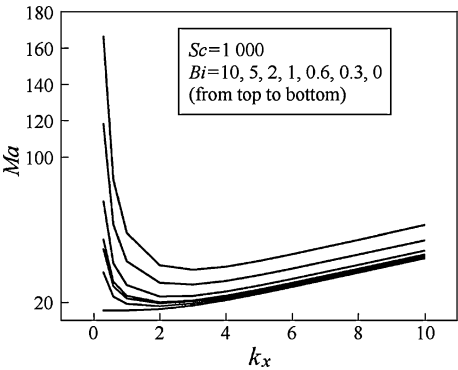
Fig. 8.13 Ma_{cr} and *Sc*
relationship at $Bi = 2, 0$

Box: *Bi*=2, 0
(from top to bottom)
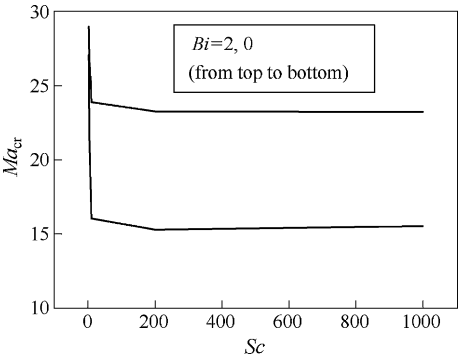
Fig. 8.14 Ma_{cr} and Bi relationship at $Sc = 2, 1000$
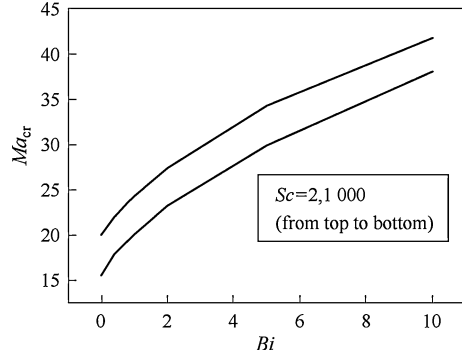
Table 8.2 Comparison of calculated and experimental Ma_{cr} (gas-phase N_2, $Re = 446$)

Liquid rate $\times 10^5$ ($m^3\ s^{-1}$)	Film thickness $\times 10^4$ (m)	Bi	Sc	Experimental Ma_{cr}	Calculated Ma_{cr}	Error (%)
1.11	2.78	1.655	714	26.92	24.86	8.29
1.67	3.18	2.168	714	28.67	26.24	9.26
2.22	3.5	2.62	714	29.86	27.43	8.97
2.78	3.77	3.05	714	31.24	28.56	9.4

8.4 Mass Transfer Enhancement by Marangoni Convection

As stated in previous section, the mass transfer process can be enhanced by the presence of Marangoni convection. Xiao analyzed the mass transfer condition under $Ma > Ma_{cr}$ to find the enhancement factor as follows [12].

Starting from the equation of steady diffusion,

$$u\frac{\partial c}{\partial x} + w\frac{\partial c}{\partial x} = D\frac{\partial^2 c}{\partial z^2} \tag{8.5}$$

and the direct integration of continuity equation:

$$w = -z\frac{\partial u}{\partial x} \tag{8.6}$$

Substituting Eq. (8.6) to Eq. (8.5), we have the following:

$$u\frac{\partial c}{\partial x} - z\frac{\partial u}{\partial x}\frac{\partial c}{\partial z} = D\frac{\partial^2 c}{\partial z^2} \tag{8.7}$$

The boundary conditions are as follows:

$$\begin{cases} z = d & c = c_{\mathrm{I}} \\ z = 0 & c = c_0 \\ x = 0 & c = c_0 \end{cases}$$

where c_{I} and c_0 are, respectively, the concentration at the interface and bulk fluid. If the thickness of the boundary layer at point x is $h(x)$, let

$$\eta = \frac{z}{h(x)}$$

Substituting to Eq. (8.7) yields the following:

$$\frac{1}{D}\left(\frac{u}{2}\frac{\mathrm{d}h^2}{\mathrm{d}x} + h^2\frac{\mathrm{d}u}{\mathrm{d}x}\right)\eta\frac{\mathrm{d}c}{\mathrm{d}\eta} + \frac{\mathrm{d}^2 c}{\mathrm{d}\eta} + \frac{\mathrm{d}^2 c}{\mathrm{d}\eta^2} = 0 \tag{8.8}$$

Let

$$\frac{1}{D}\left(\frac{u}{2}\frac{\mathrm{d}h^2}{\mathrm{d}x} + h^2\frac{\mathrm{d}u}{\mathrm{d}x}\right) = l \tag{8.9}$$

Equation (8.8) becomes

$$l \cdot \eta\frac{\mathrm{d}c}{\mathrm{d}\eta} + \frac{\mathrm{d}^2 c}{\mathrm{d}\eta^2} = 0 \tag{8.10}$$

From the boundary condition, at $x = 0$, $h = 0$, integrating Eqs. (8.9) and (8.10) and combining with the boundary condition, we get the following:

$$c = c_0 - \sqrt{\frac{2l}{\pi}}(c_{\mathrm{I}} - c_0)\int_0^n e^{-\frac{1}{2}\eta^2}\mathrm{d}\eta \tag{8.11}$$

or

$$\frac{\partial c}{\partial z} = \frac{\partial c}{\partial \eta}\frac{\partial \eta}{\partial z} = \frac{1}{h}\sqrt{\frac{2l}{\pi}}(c_0 - c_{\mathrm{I}})e^{-\frac{1}{2}\eta^2} \tag{8.12}$$

Let N be the mass flux transferred, which is given by the following:

$$N = D\frac{\partial c}{\partial z}\bigg|_{z=0} = \mathbf{k_p}(c_0 - c_{\mathrm{I}})$$

In connection with Eqs. (8.11) and (8.12), we have the following:

$$\mathbf{k_p} = \sqrt{\frac{D}{\pi}}\frac{u}{\left(\int_0^x u\mathrm{d}x\right)^{\frac{1}{2}}}$$

where k_p is the local mass transfer coefficient at point p. Thus, the liquid-phase mass transfer coefficient covering the length x_0 of the process can be considered as the averaged k_p:

$$
k = \frac{1}{x_0} \int_0^x k_p dx = \sqrt{\frac{D}{\pi}} \frac{1}{x_0} \int_0^{x_0} \frac{u}{\left(\int_0^x u dx \right)^{\frac{1}{2}}} dx
$$

$$
= 2 \sqrt{\frac{D}{\pi x_0}} \left[\frac{1}{x_0} \int_0^{x_0} u dx \right]^{\frac{1}{2}}
$$

(8.13)

If u in the foregoing equation is replaced by the average velocity u_0, it becomes Higbie penetration model. Here, we considered a disturbance velocity δu is added to u_0 as follows:

$$
u = u_0 + \delta u
$$

and

$$
\delta u = - \int \frac{\partial \delta w}{\partial z} dx = - \int DW \exp(ik_x x + \omega t) dx
$$

The W can be expressed as function of z as follows:

$$
W = Af(z)
$$

where A is a constant to be determined. Then, we have the following:

$$
\delta u = \frac{i}{k_1} Af(z) \exp(ik_x x + \omega t)
$$

Substituting ∂u to the force balance equation at the interface gives as follows:

$$
\frac{\partial \sigma}{\partial x} = \mu \left(\frac{\partial \delta u}{\partial z} + \frac{\partial \delta w}{\partial x} \right)
$$

$$
= \mu A \left[\frac{i}{k_2} f(z) + ikf(z) \right] \exp(ik_x x + \omega t)
$$

Integrating foregoing equation from 0 to x_0 yields the following:

$$
\Delta \sigma = \mu A \left[\frac{1}{k^2} f(z) + f(z) \right] \exp(ik_x x + \omega t)_0^{x_0} = \theta A
$$

where $\Delta \sigma$ is the liquid-phase surface tension difference of the element in contact with the gas phase at the interface after traveling through distance x_0. Substituting $\Delta \sigma$ to the definition of Ma and rearranging, we have the following:

$$
A = \frac{\Delta \sigma}{\theta} = \frac{\mu D}{d^2 \theta} Ma = BMa
$$

Substitute δu and A to the following velocity equation yields the following:

$$u = u_0 + \delta u = u_0 + \frac{i}{k}BMaf'(z)\exp(ik_x x + \omega t)$$

Then, we have the following:

$$\mathbf{k} = 2\sqrt{\frac{D}{\pi x_0}}\left[u_0 + \frac{1}{k_x^2}BMaf'(z)\exp(ik_x x + \omega t)|_0^{x_0}\right]^{\frac{1}{2}}$$

$$= 2\sqrt{\frac{D}{\pi(x_0/u_0)}}\left[1 + \frac{1}{u_0 k_x^2}BMaf'(z)\exp(ik_x x + \omega t)|_0^{x_0}\right]^{\frac{1}{2}}$$

$$= \mathbf{k_H}[1 + EMa]^{\frac{1}{2}}$$

Obviously, $\mathbf{k_H}$ is the mass transfer coefficient given by penetration theory; E can be considered as a constant. Then we have the ratio of the mass transfer coefficients with surface disturbance to that of penetration theory as follows:

$$F = \frac{\mathbf{k}}{\mathbf{k_H}} = (1 + EMa)^{\frac{1}{2}} = \left(\frac{1}{Ma} + E\right)^{\frac{1}{2}}Ma^{\frac{1}{2}}$$

where the ratio F is the enhancement factor. When Ma is sufficient large, the foregoing equation can be simplified to as follows:

$$F = E^{\frac{1}{2}}Ma^{\frac{1}{2}}$$

The F is proportional to square root of the Ma. As shown from foregoing equation, the mass transfer can be enhanced by Marangoni convection, although it should be verified by experimental evidence as shown in subsequent section.

Sun [13, 14] derived from dimensionless disturbance equation to obtain F to be:

$$F = \left[1 + a\left(\frac{Ma - Ma_{cr}}{Ma_{cr}}\right)\right]^{\frac{1}{2}}$$

where a is a constant. When Ma is sufficient large, it becomes

$$F = a^{\frac{1}{2}}\left(\frac{Ma}{Ma_{cr}}\right)^{\frac{1}{2}}$$

When $Ma = Ma_{cr}$, $F = 1$, we obtain $a = 1$; the equation also takes in the form of the following equation:

$$F = \left(\frac{Ma}{Ma_{cr}}\right)^{\frac{1}{2}}$$

For a mass transfer process, the Ma_{cr} is a fixed value, the foregoing equation can be written as $F = b(Ma)^{\frac{1}{2}}$.

8.5 Experiment on the Mass Transfer Enhancement by Interfacial Marangoni Convection

8.5.1 Absorption of CO₂ by Horizontal Stagnant Solvent

Sun [13, 14] performed the experiment of CO_2 absorption by methanol, toluene, and chlorobenzene in a horizontal liquid–gas contactor at different liquid thickness h as shown in Fig. 8.16 for investigating the progress of Marangoni effect. The development of enhancement factor F with time of the unsteady absorption is given in Fig. 8.15.

As shown from Fig. 8.15, the enhancement factor F at the beginning is increased with time where the rate of absorption by ethanol is faster than that by toluene. While the absorption by chlorobenzene shows no enhancement effect ($F = 1$) due to both the Ma and Ra numbers are negative. Figure 8.16 shows the F–t curve of CO_2 absorption by isopropanol at different liquid thickness.

As shown in Fig. 8.16, the F increases with increasing liquid thickness because the higher the liquid thickness the more intense Rayleigh effect. It demonstrates that the coupling effect of Rayleigh and Marangoni makes greater increase in the enhancement factor.

Sun proposed that the F–t curve is composed with three stages [14]: (1) ascending stage where the interfacial disturbance is gradually intensified and F is increased; (2) transition stage where the interfacial disturbance and F becomes relatively stable; and (3) descending state where the absorption is approaching saturation so that the driving force of mass transfer is lowered and F is gradually declined.

In the ascending stage, the F factor can be regressed by the following equation:

$$F = \left(\frac{Ma}{Ma_{cr}}\right)^n.$$

8.5.2 Desorption of CO₂ by Falling-Film Solvent

Zhou performed the experiment of steady falling-film mass transfer process to investigate the effect of Marangoni convection on the mass transfer coefficient [5, 7, 15]. The choice of falling film is to eliminate the Rayleigh effect. The experimental setup is the same as shown in Figs. 8.1 and 8.2b. The process is desorption of aqueous desorbent by nitrogen. The inlet composition of aqueous desorbent was changed for every run in order to study the influence of mass transfer coefficient on the effect of Marangoni convection. Pure nitrogen was used as gas absorbent for desorption. The composition of desorbent in the outlet gas phase can be calculated by the following:

$$c_{\text{Gout}} = \frac{Q_{\text{L}}(c_{\text{Lin}} - c_{\text{Lout}})}{Q_{\text{G}}}$$

where c_{Lin} is the desorbent concentration at the inlet (mol m^{-3}); c_{Lout} and c_{Gout} are, respectively, the desorbate (species to be desorbed, called solute hereafter) concentration at the outlet liquid and gas phases; Q_{L} and Q_{G} are, respectively, the volumetric flow of liquid and gas phases.

The overall coefficient of mass transfer can be calculated by the following equation:

$$K_{\text{Lexp}} = \frac{Q_{\text{L}}(c_{\text{Lin}} - c_{\text{Lout}})}{A(c_{\text{L}} - c_{\text{L}}^{*})_{\text{log}}}$$

$$(c_{\text{L}} - c_{\text{L}}^{*})_{\text{log}} = \frac{(c_{\text{Lin}} - c_{\text{Gout}}/m) - c_{\text{Lout}}}{\log \frac{c_{\text{Lin}} - c_{\text{Gout}}/m}{c_{\text{Lout}}}}$$

where A is the liquid–gas contacting area; $(c_{\text{L}} - c_{\text{L}}^{*})_{\text{log}}$ is the logarithmic average driving force of mass transfer between liquid inlet and outlet; c_{L}^{*} is the desorbate (solute) concentration in liquid phase in equilibrium with that in gas phase;

$m = c_G^*/c_L$; c_G^* is the solute concentration in equilibrium with the partial pressure of solute concentration c_L in the bulk liquid phase.

In this case, the Δc in Marangoni number, which represents the intensity of Marangoni convection, can be expressed by the interfacial solute concentration difference per unit length of interface as follows:

$$\Delta c = \frac{\Delta c_{Lf}}{l} = \frac{c_{Lf\,(out)} - c_{Lf\,(in)}}{l}$$

where c_{Lf} is the solute concentration at interface. The $\frac{\Delta c_{Lf}}{l}$ can be regarded as the driving force per unit interfacial length. The $c_{Lf\,(in)}$ and $c_{Lf\,(out)}$ can be calculated as follows [16]:

$$c_{Lf\,(in)} = \frac{c_{Gout} + c_{Lin}\sqrt{\frac{D}{D_G}}}{m + \sqrt{\frac{D}{D_G}}}$$

$$c_{Lf\,(out)} = \frac{c_{Lout}\sqrt{\frac{D}{D_G}}}{m + \sqrt{\frac{D}{D_G}}}$$

where D and D_G are, respectively, the diffusivity of solute in liquid phase and gas phase.

Under the condition of no Marangoni convection, the mass transfer on falling film is only by diffusion. Zhang et al. [16] and Bird et al. [17] derived the following equation of overall mass transfer coefficient K_{Ltheo} based on the penetration theory:

$$\frac{1}{K_{Ltheo}} = (\pi T)^{0.5}\left(D^{-0.5} + D_G^{-0.5} \times m\right)/2$$

Under the condition of existing Marangoni convection, the enhancement factor F can be expressed as follows:

$$F = \frac{K_{Lexp}}{K_{Ltheo}}$$

From the experimental F factor obtained under different $\frac{\Delta c_{Lf}}{l}$, we can judge the intensity of Marangoni effect.

1. *The Increase in K_{Lexp} with $\frac{\Delta c_{Lf}}{l}$*

(A) *Desorption of ethyl ether in nitrogen stream*

Under the condition of N_2 1.5 m^3 h^{-1}, aqueous ethyl ether 10 L h^{-1}, the overall liquid-phase mass transfer coefficient K_{Lexp} versus driving force per unit interfacial length $\frac{\Delta c_{Lf}}{l}$, is shown in Fig. 8.17. Different $\frac{\Delta c_{Lf}}{l}$ are established by changing the inlet composition of aqueous ethyl ether.
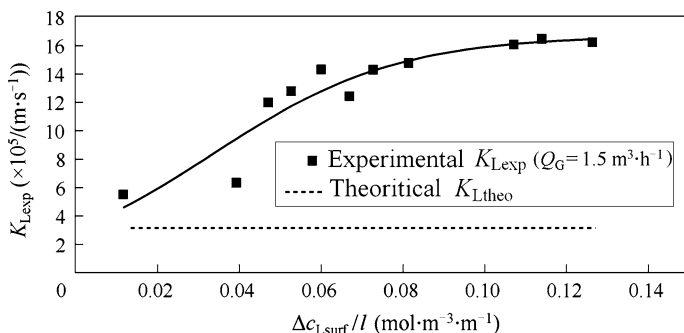
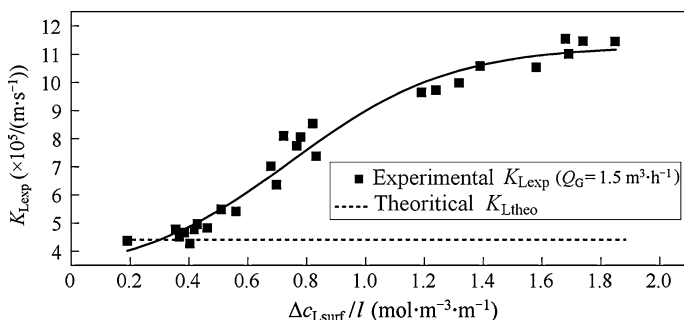**Fig. 8.17** The K_{Lexp} versus $\Delta c_{Lf}/l$ *curve* for the desorption of aqueous diethyl ether

Fig. 8.18 The K_{Lexp} versus $\Delta c_{Lf}/l$ *curve* for the desorption of aqueous ethanol

(B) *Desorption of ethanol in nitrogen stream*

Under the condition of N_2 1.5 m^3/h, aqueous ethanol 10 L/h, the overall liquid-phase mass transfer coefficient K_{Lexp} versus driving force unit length $\frac{\Delta c_{Lf}}{l}$ is shown in Fig. 8.18.

As shown from Figs. 8.17 and 8.18, the overall mass transfer coefficient K_{Lexp} is increased with increasing $\frac{\Delta c_{Lf}}{l}$ because the Marangoni convection is intensified. When $\frac{\Delta c_{Lf}}{l}$ is further increased, the Marangoni convection is strong to approaching turbulence, and desorption is gradually turning to the stable turbulent mass transfer. The enhancement factor is found about 1.5–4.0.

2. *The Increase in enhancement factor F with Ma number*
   The $\Delta c_{Lsurf}/l$ can be converted to the *Ma* number by Eq. (8.1). The increase in *F* with *Ma* number at different liquid and gas rates is shown in Fig. 8.19 [9]. As shown in figure, the liquid rate is much influential on *F* factor than the gas rate.
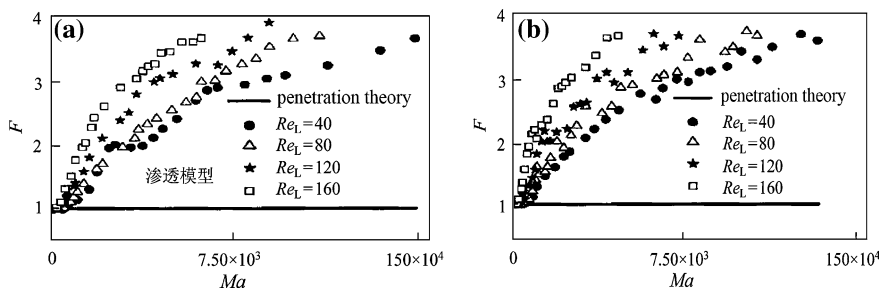
Fig. 8.19 The F versus Ma curve for the desorption of aqueous ethanol, **a** $Re_G = 230$, **b** $Re_G = 460$ (reprinted from ref [9], Copyright 2006, with permission from Tianjin University)

8.6 The Transition of Interfacial Structure from Order to Disorder

For the falling-film mass transfer process as shown in Fig. 8.3, when the Ma number exceeds the critical value Ma_{cr}, the linear stability analysis is not valid, and the nonlinear disturbance should be considered. Xiao [12] solved the following non-linear disturbance equation for the process with heat and mass transfer as follows:

$$\frac{\partial \delta u}{\partial t} + \delta u \cdot \frac{\partial \delta u}{\partial x_i} = -\frac{1}{\rho}\frac{\partial \delta P}{\partial x_j} + v\frac{\partial^2 \delta u}{\partial x_i}$$

$$\frac{\partial \delta T}{\partial t} + \delta u \frac{\partial \Delta T}{\partial x_i} = \delta w + \alpha \frac{\partial^2 \delta T}{\partial x_i^2}$$

$$\frac{\partial \delta C}{\partial t} + \delta u \frac{\partial \delta C}{\partial x_i} = \delta w + D \frac{\partial^2 \delta C}{\partial x_i^2}$$

$$\frac{\partial \delta u}{\partial x_i} = 0$$

The foregoing equation set involves unknown δu, δw, δp, δT, and δC. Eliminating δp from the velocity equation, we have the following:

$$\frac{\partial \varphi}{\partial t} + \delta \boldsymbol{u} \cdot \nabla \varphi = v \nabla^2 \varphi$$

where $\varphi = \frac{\partial \delta u}{\partial z} - \frac{\partial \delta w}{\partial x}$.

The boundary conditions are as follows:

At $z = 0$ (wall surface):

$$\delta u = 0$$

$$\frac{\partial \delta C}{\partial z} = Bi_m^0 \delta C$$

$$\frac{\partial \delta T}{\partial z} = Bi_h^0 T \delta T$$

where $Bi_m^0 = \frac{k_L^0 d}{D}$ is the Biot number for mass transfer; $Bi_h^0 = \frac{h_L^0 d}{\alpha}$ is the Biot number for heat transfer; superscript 0 denotes at the solid wall.

At $z = 1$ (interface):

$$\delta w = 0$$

$$\frac{\partial \delta T}{\partial z} = Bi_h^I \delta T$$

$$\frac{\partial \delta C}{\partial z} = Bi_m^I \delta C$$

$$\frac{\partial \delta u}{\partial z} + \frac{\partial \delta w}{\partial x} = \frac{Ma_h}{Le} \frac{\partial \delta T}{\partial x} + Ma \frac{\partial \delta C}{\partial x}$$

where the superscript I denotes the interface.

For solving the unknown δu, δw, δT, and δC, the tau method developed from Gelerkin method was used. The energy spectrum function P is defined as [18] follows:

$$P(f) = \sum_{k=1}^{N} C_k \exp\left(2\pi f\, k\sqrt{-1}/N\right)$$

where f is the frequency; k is the wave number; N is the number of terms taken in the expansion series of disturbance. Figures 8.19 (no heat transfer, $Ma_h = 0$) and 8.20 (with heat transfer, $Ma_h = 34$) show the energy spectrum for desorption of aqueous methanol at different Ma/Ma_{cr} and Ma_h.

From the energy spectrum at different Ma/Ma_{cr}, it is shown that when Ma/Ma_{cr} between 3 and 12, clear peak is found indicating periodic motion (ordered convection); but when Ma/Ma_{cr} up to about 13, obvious noise is appeared indicating the periodic motion being interrupted and turned to disorder (chaos). Thus, the transition point, which can be found from interfacial order to disorder structure, is about $Ma/Ma_{cr} = 13$. Nevertheless, upon careful study of Figs. 8.20 and 8.21, some small noise yet to be seen; it means that some small disorder is always accompanied with the major part of the ordered interfacial structure.

From the solution of foregoing differential equation set, Xiao [12] also obtained the relationship between mass flux (represented by Sherwood number Sh, $\left(Sh = \frac{k_c l}{D} = \frac{j_c l}{D \Delta c}\right)$ and Ma/Ma_{cr}. The calculated results are compared with experimental data on desorption of aqueous methanol and acetone under nitrogen stream as shown in Figs. 8.22 and 8.23. When Ma exceed critical value ($Ma/Ma_{cr} = 1$), Sh goes up sharply and then slow down as Ma further increases. Finally, Sh becomes almost constant which indicates that the chaos or turbulent state is reached.
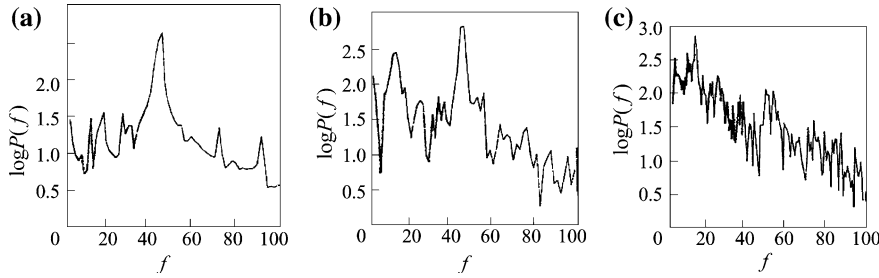
Fig. 8.20 Energy spectrum of aqueous methanol desorption ($Ma_h = 0$), **a** $Ma/Ma_{cr} = 2$, **b** $Ma/Ma_{cr} = 12$, **c** $Ma/Ma_{cr} = 13$
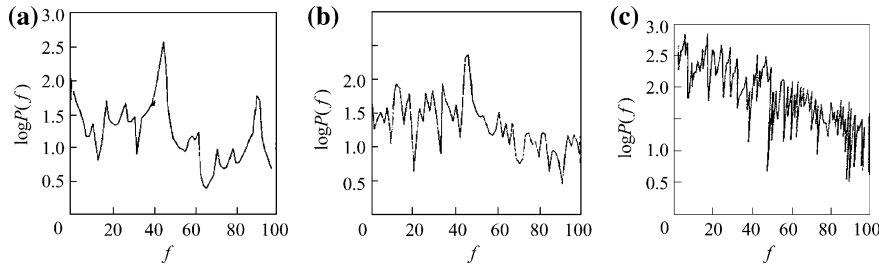

Fig. 8.21 Energy spectrum of aqueous methanol desorption ($Ma_h = 34$), **a** $Ma/Ma_{cr} = 2$, **b** $Ma/Ma_{cr} = 12$, **c** $Ma/Ma_{cr} = 13$

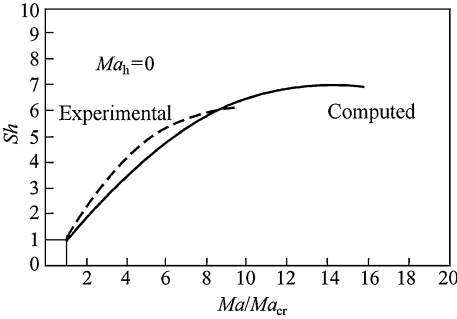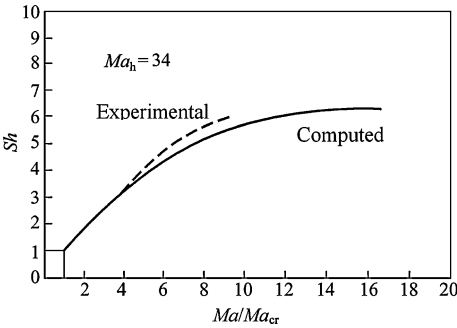**Fig. 8.22** Sh versus Ma/Ma_{cr} for aqueous methanol desorption

Fig. 8.23 Sh versus Ma/Ma_{cr} for aqueous acetone desorption

8.7 Theory of Mass Transfer with Consideration of Marangoni Effect

In the study of mass transfer, the fluid element (microcell) can be used to describe the behaviors of the process. Under the condition of no Marangoni effect, according to the penetration theory, the fluid element flows randomly from fluid phase to the interface and stays there within residence time $\overline{T}$ for unsteady mass transfer and then go back to the bulk fluid. The liquid-phase mass transfer coefficient k_H is given by the following:

$$k_H = 2\sqrt{\frac{D}{\pi \overline{T}}}$$

When Marangoni convection appears, the interfacial flow and accompanied underneath circulation promotes the renewal of interface. The residence time of fluid element is then shortened.

Based on this viewpoint, Sha modified the penetration theory [10, 19] with consideration that the residence time of fluid element should be changed to t instead of $\overline{T}(t < \overline{T})$ when Marangoni convection occurs. The mass transfer coefficient k_c at the presence of Marangoni convection becomes

$$k_c = 2\sqrt{\frac{D}{\pi t}}$$

The enhancement factor F can be calculated by the following ratio:

$$F = \frac{k_c}{k_H} = \sqrt{\frac{\overline{T}}{t}} \ (t < \overline{T})$$

Since the F factor is generally about 2–5, the residence time of fluid element is then reduced by 4–25 folds. The shorter residence time means the faster the fluid circulation and quicker the interfacial mass renewal. The circulations of the fluid element without Marangoni convection and with Marangoni convection are shown schematically in Fig. 8.24. It is shown that by the help of Marangoni convection, the path of circulation is smaller ($l < L$) and the residence time is shorten ($t < \overline{T}$) because the renewal of interfacial concentration is faster. Nevertheless, the l and t are statistic average length and time, which are still unknown.

Sha postulated that the dimensionless time $\frac{t}{\overline{T}}$ and length $\frac{l}{L}$ satisfy the exponential relationship as follows:

$$\frac{t}{\overline{T}} = \left(\frac{l}{L}\right)^m \tag{8.14}$$

where $0 < \frac{t}{\overline{T}} < 1$ and $0 < \frac{l}{L} < 1$ as shown in Fig. 8.25; m is a constant and $0 < m < 1$. The value of m will be given later.

Fig. 8.24 Renewal of interfacial fluid element. **a** No Marangoni convection. **b** With Marangoni convection (reprinted from Ref. [19], Copyright 2003, with permission from CIESC)
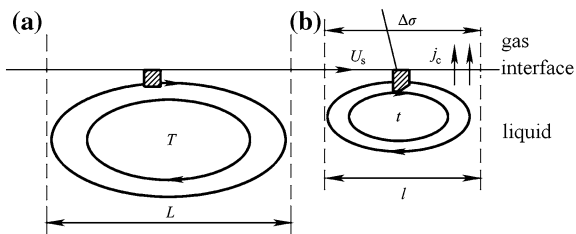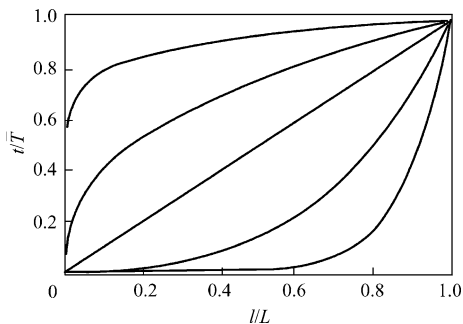

Fig. 8.25 $t/\bar{T}$ versus l/L at different m (From *upper* to *lower curves* in sequence $m = 0.2, 0.4, 1, 3, 8$) (reprinted from Ref. [19], Copyright 2003, with permission from CIESC)

At the critical point of initiating Marangoni convection $(Ma = Ma_{cr})$, the interfacial flow is a result of establishing the following force balance at the interface:

$$\mu \frac{\partial u}{\partial y} = \frac{\partial \sigma}{\partial c} \frac{\partial c}{\partial x}$$

Let the local interfacial velocity u be the average convective velocity at interface U_s, the vertical distance y be the penetration depth of the Marangoni convection δ_y, the following approximated relationship is obtained from foregoing equation:

$$\mu \frac{U_s}{\delta_y} \sim \frac{\partial \sigma}{\partial c} \frac{\Delta c}{l}$$

Substituting $U_s \sim l/t$, $\delta_y \sim \sqrt{vt}$, where v is the kinematic viscosity, one yields:

$$\frac{l^2}{t^{\frac{3}{2}}} \sim \frac{1}{\mu} \frac{\partial \sigma}{\partial c} \Delta c v^{1/2}$$

Combining with Eq. (8.14),

$$\frac{L^2}{\bar{T}^{\frac{2}{m}}} \frac{1}{t^{\frac{3m-4}{2m}}} \sim \frac{1}{\mu} \frac{\partial \sigma}{\partial c} v^{1/2} \Delta c$$

and after simplifying, the residence time t can be expressed by the following equation:

$$\frac{1}{t^{\frac{3m-4}{2m}}} \sim \frac{1}{\mu}\frac{\partial\sigma}{\partial c}v^{1/2}\Delta c\frac{\bar{T}_m^2}{L^2}$$

or

$$\frac{1}{t^{\left(-\frac{1}{2}\right)\frac{4-3m}{m}}} \sim \frac{1}{\mu}\frac{\partial\sigma}{\partial c}\Delta c\frac{L}{D}\frac{D_L}{L}v^{1/2}\frac{\bar{T}_m^2}{L^2}$$

Substituting the definition of Ma,

$$Ma = \frac{1}{\mu}\frac{\partial\sigma}{\partial c}\Delta c\frac{L}{D}$$

the following relationship is obtained:

$$\frac{1}{t^{\left(-\frac{1}{2}\right)\frac{4-3m}{m}}} \sim MaDv^{1/2}\frac{\bar{T}_m^2}{L^3}$$

$$t^{-\frac{1}{2}} \sim \left(MaDv^{1/2}\frac{\bar{T}_m^2}{L^3}\right)^{\frac{m}{3m-4}}$$

For unsteady diffusion, the mass flux j_c can be expressed by penetration theory:

$$j_c \sim \Delta c\sqrt{\frac{D}{t}}$$

Substitute the expression for t to have

$$j_c \sim \Delta cD^{\frac{1}{2}}\left(MaDv^{1/2}\frac{\bar{T}_m^2}{L^3}\right)^{\frac{m}{3m-4}}$$
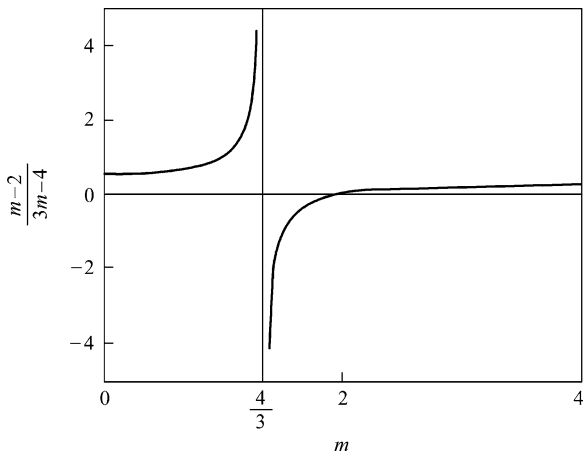
The Sherwood number Sh is defined as follows:

$$Sh = \frac{k_c l}{D} = \frac{j_c l}{D\Delta c}$$

Substitute j_c to yield

$$Sh \sim D^{-\frac{1}{2}}\left(MaDv^{1/2}\frac{\bar{T}_m^2}{L^3}\right)^{\frac{m}{3m-4}}l$$

and eliminate l by Eq. (8.14), the following relationship is obtained:

$$Sh \sim D^{-\frac{1}{2}}\left(MaDv^{1/2}\frac{\bar{T}_{m}^{2}}{L^{3}}\right)^{\frac{m-2}{3m-4}}\frac{L}{\bar{T}_{m}^{\frac{1}{m}}}$$

As all variables are constant except Sh, Ma, and Sc $\left(Sc = \frac{v}{D}\right)$ in the foregoing equation, it can be simplified as follows:

$$Sh \propto Ma^{\frac{m-2}{3m-4}}Sc^{\frac{1}{2}\left(\frac{m-2}{3m-4}\right)}$$

or

$$Sh \propto Ma^{n}Sc^{\frac{1}{2}n}, \quad n = \frac{m-2}{3m-4}$$

The exponent $\frac{m-2}{3m-4}$ is not continuous as shown in Fig. 8.26.

According to Eq. (8.14), m should be greater than 0 and less than 1; therefore, the exponent n is between 0.5 and 1.

At the critical point, where $t = \bar{T}$, $l = L$ and $m = 0$, the Sh and Ma relationship becomes

$$Sh = Ma^{0.5}Sc^{0.25}$$

Or express generally as

$$Sh = Ma^{n}Sc^{a}$$

It indicates that the exponent n of Ma is 0.5 at the beginning of Marangoni convection appearance, and n is gradually increased with increasing Ma as t and l becoming smaller to make m larger. Note that the extent of n increase is dependent on the nature of the process concerned.

The exponent n is affected by many factors, such as Re_{L} of liquid phase, Re_{G} of gas phase, physical property of the system, structure of the equipment, depth of the

liquid (Ra effect), concentration and temperature (Ma and Ma_h effect). For instance, the falling-film experiment of desorption by Yu indicated that the value of n is varied with the Reynolds number Re_L of the flowing liquid [18]. Thus, different values of n were reported in literature by different authors under their specific experimental conditions.

Zhou gave $n = 0.452$ [15] for desorption of falling aqueous isopropanol, ether and acetone in uprising nitrogen; Sun reported $n = 0.5 \pm 0.05$ [13, 14]; Imaishi et al. obtained $n = 0.6$ [20] for acetone desorption under short liquid–gas contacting time and $Re = 80$. Brian reported $n = 0.5$, $n = 1.01$ [21] and also n between 0.25 and 0.5 [22, 23] under different conditions. Hozawa et al. presented $n = 0.4 \pm 0.1$ [24] for desorption of aqueous methanol, ether, acetone, and triethanolamine. Golovin considered n was between 1/3 and 1 [25, 26]. Fujinawa et al. obtained $n = 1.05$ [27] in agitation system with $Re = 10,000$. Olander and Reddy [28] and Sawistowski and Goltz [30] reported $n = 1$ from their experiment of extraction with agitation.

Although the exponent n reported is quite different, it can be considered that n is about $0.45 \sim 0.6$ for desorption process. In the process with agitation, n can be around 1 as it is in the chaos (highly turbulent) condition.

Sun gave the following relationship by solving the dimensionless disturbance equation [13, 30] for the roll cell convection at interface:

$$Sh = 1 + 2AI\left(\frac{Ma - Ma_{cr}}{Ma_{cr}}\right)$$

and for the hexagonal cell convection:

$$Sh = 1 + 12B^2I\left[1 + \frac{A}{B^2}\left(\frac{Ma - Ma_{cr}}{Ma_{cr}}\right)\right]^{\frac{1}{2}} + 12B^2I\left[1 + \frac{A}{2B^2}\left(\frac{Ma - Ma_{cr}}{Ma_{cr}}\right)\right]$$

where the parameters A, B and I are function of Bi and $\frac{Ma}{Ma_{cr}}$, which can be obtained by the regression of experimental data.

8.8 Simulation of Rayleigh Convection

8.8.1 Mathematical Model

As observed from experimental work, the mass transfer through horizontal interface is affected by the Rayleigh convection created by the density difference between interface and the main fluid.

Sha established the mathematical model and analyzed the results of simulation for the gas absorption with Rayleigh effect [10, 31]. The simulated object is shown in Fig. 8.27.

Fig. 8.27 Rayleigh
convection simulation
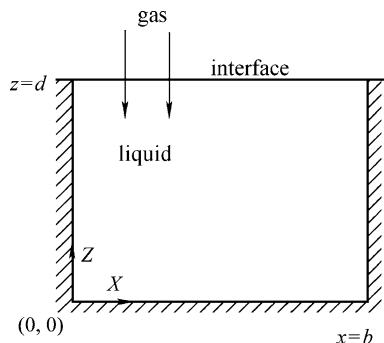
Assumptions

(1) The Marangoni number of the liquid–gas mass transfer is negative, $Ma < 0$;
(2) All physical properties except density are constant;
(3) Linear relationship between absorbed species (solute) concentration and density;
(4) The interface is flat, no deformation;
(5) The rate of mass transfer is small.

Model equations

$$\frac{\partial u}{\partial x_i} = 0$$

$$\frac{\partial u}{\partial t} + u\frac{\partial u}{\partial x_i} = -\frac{1}{\rho}\frac{\partial p}{\partial x_j} + \frac{\mu}{\rho}\frac{\partial^2 u}{\partial x_i^2} + S$$

$$\frac{\partial c}{\partial t} + u\frac{\partial u}{\partial x_i} = D\frac{\partial^2 c}{\partial x_i}$$

$$\boldsymbol{u} = (u, w)$$

$$\boldsymbol{S} = -\left(0, \frac{\rho' g}{\rho}\right)$$

$$\rho' = \rho\big(1 + R_\rho(c - c_0)\big)$$

where u and w are, respectively, the liquid velocity (liquid element or cluster motion) component in x (horizontal, parallel to the interface) and z directions (vertical, perpendicular to the interface); D is the diffusivity of solute in liquid phase; c is the solute concentration in liquid phase; c_0 is the solute concentration in main liquid; g is gravitational acceleration; ρ' and ρ are, respectively, the density of liquid with concentration c and c_0; $R_\rho = \frac{1}{\rho}\left(\frac{\partial \rho}{\partial c}\right)_{p,T}$ is a constant.

Combining the static pressure of the fluid to the pressure term, the following two-dimensional flow and mass transfer equation set is established:

$$\frac{\partial u}{\partial x} + \frac{\partial w}{\partial z} = 0$$

$$\frac{\partial u}{\partial t} + u\frac{\partial u}{\partial x} + w\frac{\partial u}{\partial z} = -\frac{1}{\rho}\frac{\partial p}{\partial x} + v\left(\frac{\partial^2 u}{\partial x^2} + \frac{\partial^2 u}{\partial z^2}\right)$$

$$\frac{\partial w}{\partial t} + u\frac{\partial w}{\partial x} + w\frac{\partial w}{\partial z} = -\frac{1}{\rho}\frac{\partial p}{\partial z} + \frac{\mu}{\rho}\left(\frac{\partial^2 w}{\partial x^2} + \frac{\partial^2 w}{\partial z^2}\right) - gR_\rho(c - c_0)$$

$$\frac{\partial c}{\partial t} + u\frac{\partial c}{\partial x} + w\frac{\partial c}{\partial z} = D\left(\frac{\partial^2 c}{\partial x^2} + \frac{\partial^2 c}{\partial z^2}\right)$$

The initial and boundary conditions are as follows:

At $t = 0$, $u = w = 0$, $c = c_0$;
When $t > 0$, no slip and solute penetration conditions are applied to the solid wall:
At $x = 0, u = w = 0, \frac{\partial c}{\partial x} = 0$
At $x = b, u = w = 0, \frac{\partial c}{\partial x} = 0$
At $z = 0, u = w = 0, \frac{\partial c}{\partial z} = 0$
At interface, $z = d$, $w = 0$, $\frac{\partial u}{\partial z} = 0$.

The solute transferred from gas phase to liquid phase should go through Gibbs adsorption layer (see Sect. 8.11), and the boundary condition is as follows:

$$-D\frac{\partial c}{\partial z} = k_G(p_c - mc_I) + S_{\text{Gibbs}}$$

where k_G is the gas-phase film mass transfer coefficient; p_c is the partial pressure of solute in gas phase; c^I is the solute concentration at interface; m is the Henry constant ($m = \frac{p_c^*}{c_I}$, p_c^* is the partial pressure of the solute in equilibrium with c_I); S_{Gibbs} is the source term representing the influence of Gibbs adsorption layer to the mass transfer, which can be neglected due to small rate of mass transfer.

The foregoing equation set can be generalized to dimensionless for the convenience of solution and analysis.

Let d, $\frac{\mu}{\rho d}, \frac{c_\infty}{m} - c_0, \frac{d^2\rho}{\mu}, \frac{\mu^2}{\rho d^2}$ be the scalar length, velocity, concentration, time pressure; the following dimensionless parameters can be formed:

$$U = \frac{ud\rho}{\mu}, \quad W = \frac{wd\rho}{\mu}, \quad X = \frac{x}{d}, \quad Z = \frac{z}{d}, \quad C = \frac{c}{(c_I/m)},$$

$$\tau = \frac{t\mu}{\rho d^2} \quad P = \frac{pd^2\rho}{\mu^2}, \quad P_c = \frac{p_c d^2\rho}{\mu^2}$$

The dimensionless equation set and boundary conditions are obtained as follows:

$$\frac{\partial U}{\partial X} + \frac{\partial W}{\partial Z} = 0$$

$$\frac{\partial U}{\partial \tau} + U\frac{\partial U}{\partial X} + W\frac{\partial U}{\partial Z} = -\frac{\partial P}{\partial X} + \left(\frac{\partial^2 U}{\partial X^2} + \frac{\partial^2 U}{\partial Z^2}\right)$$

$$\frac{\partial W}{\partial \tau} + u\frac{\partial W}{\partial X} + w\frac{\partial W}{\partial Z} = -\frac{\partial P}{\partial Z} + \left(\frac{\partial^2 W}{\partial X^2} + \frac{\partial^2 W}{\partial Z^2}\right) - \frac{Ra}{Sc}C$$

$$\frac{\partial C}{\partial \tau} + U\frac{\partial C}{\partial X} + W\frac{\partial C}{\partial Z} = \frac{1}{Sc}\left(\frac{\partial^2 C}{\partial X^2} + \frac{\partial^2 C}{\partial Z^2}\right)$$

The initial and boundary conditions are as follows:

At $\tau = 0, U = W = 0, C = 0$

At $\tau > 0, X = 0, U = W = 0, \dfrac{\partial C}{\partial X} = 0$

$$X = b/d, U = W = 0, \frac{\partial C}{\partial X} = 0$$

$$Z = 0, U = W = 0, \frac{\partial C}{\partial Z} = 0$$

$$Z = 1, W = 0, \frac{\partial U}{\partial Z} = 0 - \frac{\partial C}{\partial Z} = Bi_{\mathrm{m}}(P_{\mathrm{c}} - mC^*) + S$$

The dimensionless groups *Ra, Sc,* and *Bi* in the equation set are as follows:

$$Ra = \frac{g(c^* - c_0)\beta_{\mathrm{c}}d^3}{vD}, Sc = \frac{\mu}{\rho D}, Bi_{\mathrm{m}} = \frac{k_{\mathrm{G}}d}{D}$$

where Bi_{m} is the *Bi* for mass transfer in gas phase, the subscript *m* will be omitted in subsequent Sect. 8.8.2.

8.8.2 Result of Simulation and Analysis

The dimensionless equation set involves three dimensionless groups *Ra, Sc,* and *Bi*. By designating the values of these three dimensionless groups for a specific mass transfer process, the Rayleigh convective flow and the solution of model equations can be obtained [10, 31]. In industrial equipment, the corresponding *Ra* number is usually large and far from the critical Ra_{cr}. Thus, we chose larger *Ra* for investigation. As the mass transfer is also affected by the condition of gas phase, different *Bi* is adopted for study its effect.

1. **Rayleigh convection and interface renewal**
   Take the absorption of CO_2 by ethanol as an example. The dimensionless groups chosen are $Bi = 1$, $Sc = 200$ and $Ra = 10^8$ which is far from Ra_{cr}. The simulated results are shown in Figs. 8.28 and 8.29, the former displays dimensionless CO_2 contours at different dimensionless time, and the latter displays the dimensionless velocity contours at different dimensionless time.
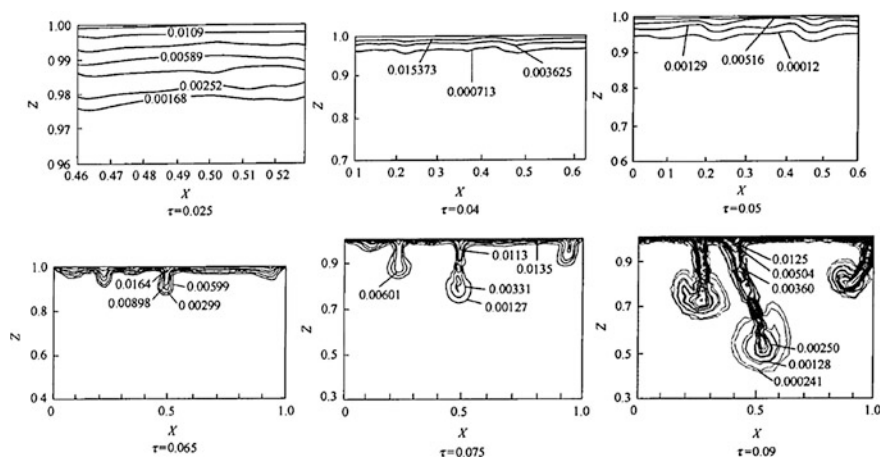
Fig. 8.28 The solute concentration contour at different time for the absorption of CO_2 by ethanol $(Bi = 1, Ra = 10^8, Sc = 200)$ (reprinted from Ref. [31], Copyright 2002, with permission from CIESC)
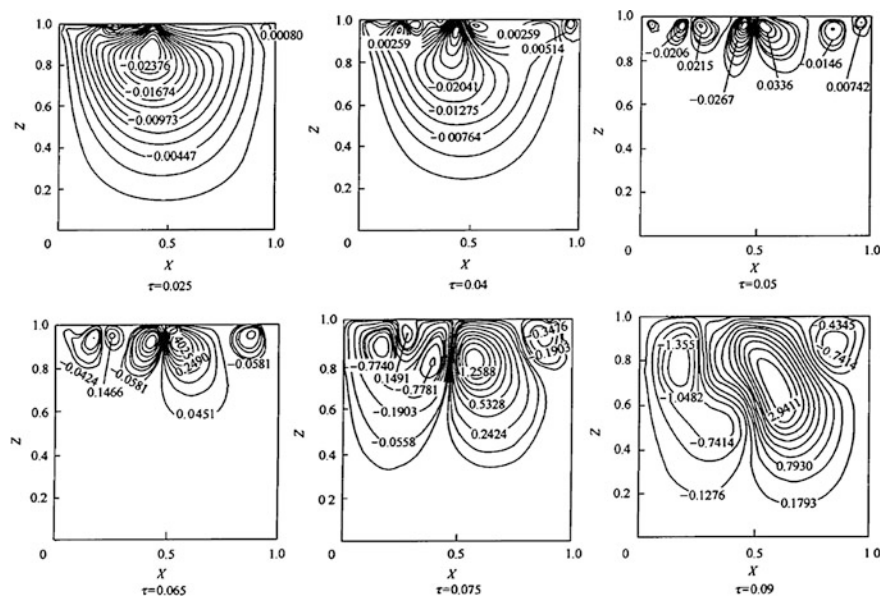

Fig. 8.29 The contour of liquid cell moving velocity at different time for the absorption of CO_2 by ethanol $(Bi = 1, Ra = 10^8, Sc = 200)$ (reprinted from Ref. [31], Copyright 2002, with permission from CIESC)

As shown from Fig. 8.28, at the beginning $(\tau < 0.005)$ of mass transfer, the concentration contour is almost flat as the mass transfer is only by molecular diffusion. At $\tau = 0.065$, sudden change is shown at the interface due to the formation of individual Rayleigh convection to force some local interfacial fluid cells moving downward. The corresponding velocity contour of individual Rayleigh convection is shown in Fig. 8.29 $(\tau < 0.005)$. As shown in Fig. 8.29, the couples of opposite eddy flow (small Rayleigh convection) carry the local aqueous solute cells apart from interface; the vacancy at the interface is refilled instantly by the flash bulk fluid cells. The moving downward interfacial cells are interacting with the Rayleigh fluid convection to form inverted mushroom shape of concentration vortex as shown in Fig. 8.28 at $\tau = 0.09$. Compared with Fig. 8.5, the simulated result is similar with the Schlieren picture where the line of reflective index is equivalent to the concentration contour.

The renewal of interfacial cells demonstrates the effect of Rayleigh convection in enhancing the mass transfer and promoting the mixing of the interfacial fluid with the bulk liquid. Obviously, the enhancement factor F of mass transfer is increased with increasing Rayleigh convection or Ra number.

2. **Analysis of interfacial concentration**

Under the condition of $Bi = 1$, $Sc = 200$, $Ra = 10^8$, the variation of dimensionless concentration with time at the central point of interface is given in Fig. 8.30.

At the beginning of CO_2 absorption by ethanol $(\tau = 0)$, the solute absorbed is accumulated at the interface to raise the interfacial concentration $(\tau = 0.06)$. Following the initiation of Rayleigh convection, some interfacial cells are carrying down to the bulk liquid by the convection stream so as to lower the interfacial concentration as shown Fig. 8.30 at $\tau = 0.06$. At this time, the supplement of fresh fluid to renew the interface is insufficient. The lowering of interfacial concentration means the greater driving force of transferring solute, and then the interfacial concentration is raised again slightly. After $\tau = 0.08$, the Rayleigh convection is gradually established to increase the renewal of interfacial cells but not yet sufficient to compensate the solute depletion. At $\tau = 0.1$, the interface is almost renewed and the interfacial concentration lowering is suppressed or even begin to raise up. Thus, the interfacial concentration is oscillating up and down.

The oscillating variation of interfacial concentration by the action of Rayleigh convection is stochastic; thus, at different positions of interface, the $C-\tau$ curve (concentration–time) is different. Figure 8.31 give the solute concentration at different position of interface and at different time. It demonstrates that the interfacial concentration in non-uniform in position and changing with time.

The transfer of solute from gas to liquid depends on the resistance of both sides which can be represented by the Biot number $\left(Bi = \frac{k_G d}{D}\right)$. The influence of interfacial concentration by Bi number is shown in Fig. 8.32 by the $C-\tau$ curve at the center of interface under $Bi = 5$, 10, 20, and 50. As shown in Fig. 8.32 that maximum interfacial concentration is lowered with increasing Bi number,

Fig. 8.30 Variation of solute concentration at the center of interface for CO_2 absorption by ethanol [10]
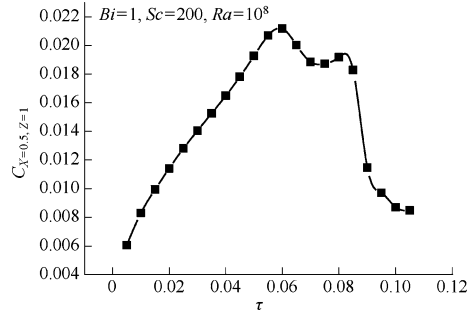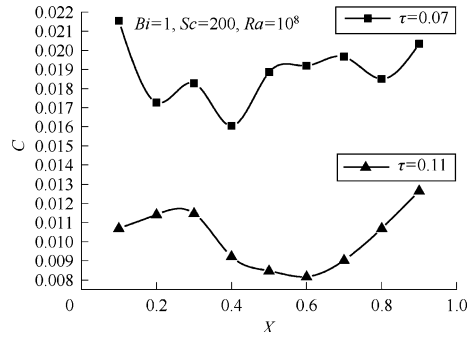

Fig. 8.31 Solute concentration at different position of interface and at different time for CO_2 absorption by ethanol (reprinted from Ref. [31], Copyright 2002, with permission from CIESC)

although their concentration oscillating shape is similar. For more detailed comparison, the $C-\tau$ curve is drawn for $Bi = 20, 50$ in the same coordinate as shown in Fig. 8.33. At high Bi, the gas-phase resistance is low to facilitate the solute transfer, so that the average interfacial concentration is higher.

The intensity of Rayleigh convection, which is represented by Ra number, is another influential factor to the interfacial concentration. Figures 8.34 and 8.35 show the variation of solute concentration at the center of interface with different Ra number. With increasing Ra, the intense Rayleigh convection promotes the interface renewal so that the solute concentration at the interface is increased with increasing Ra. In Fig. 8.34, the point representing $Ra = 6,000$ at $\tau = 30$, is obviously in error.

3. Rayleigh Convection at $Bi = \infty$

For the case of $Bi \to \infty$, it is worthy to mention. Under such condition, the mass transfer from gas phase to the interface will be no resistance; thus, the interfacial concentration will remain at constant and in equilibrium with the partial pressure of gas phase. For this case, the boundary conditions of the model equations in Sect. 8.8.1 for mass transfer should be changed to $c = c^*$ at $z = d$, where c^* is the interfacial solute concentration in equilibrium with the partial pressure of gas phase. The simulated results of dimensionless solute concentration and convection velocity at $Ra = 10^8$ and $Sc = 200$ are shown, respectively, in Figs. 8.36
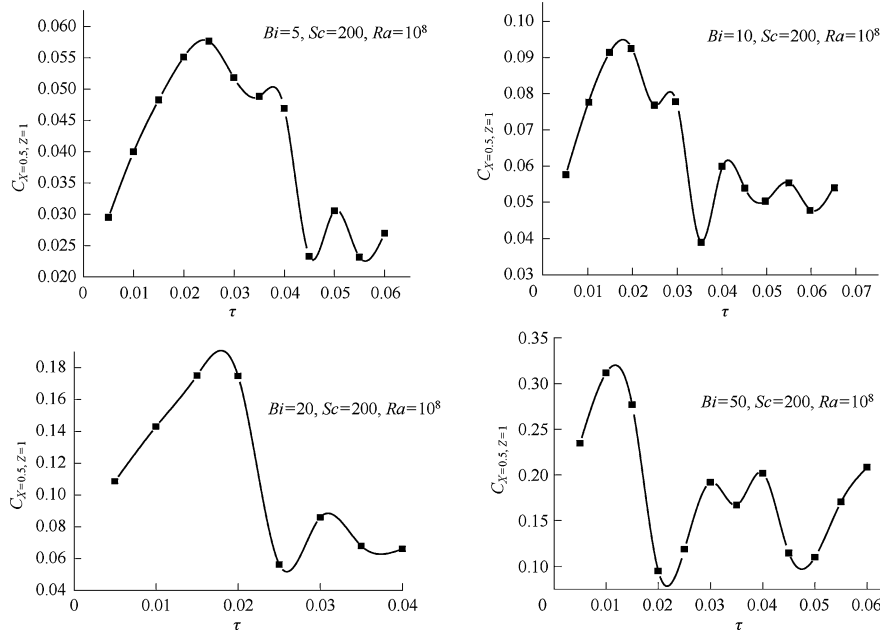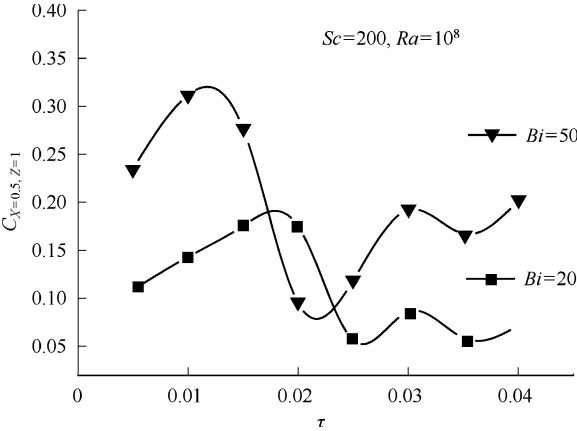
Fig. 8.32 Solute concentration at the center of interface and at different Bi for CO_2 absorption by ethanol [10]

Fig. 8.33 Solute concentration at the center of interface and $Bi = 20, 50$ for CO_2 absorption by ethanol (reprinted from Ref. [31], Copyright 2002, with permission from CIESC)

and 8.37. They are similar to Figs. 8.34 and 8.35 except the early appearance of Rayleigh convection because the interfacial concentration at the beginning is c^* and not need any time for transferring solute from gas phase to the interface. Besides, small Rayleigh convection is also appear near the wall due to the wall effect.

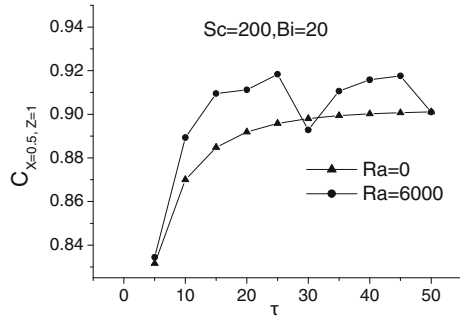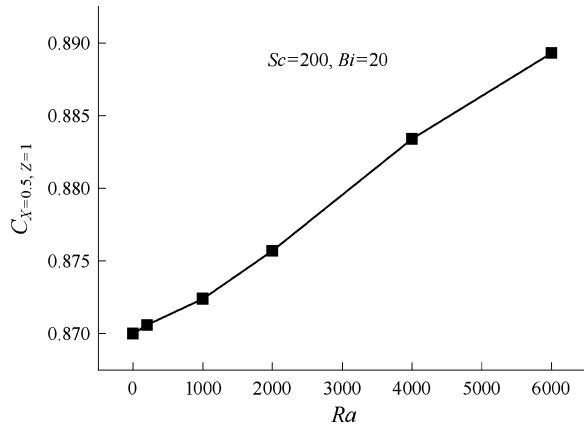**Fig. 8.34** Solute concentration at center of interface at different Ra number for CO_2 absorption by ethanol

Fig. 8.35 Solute concentration at center of interface versus Ra number for CO_2 absorption by ethanol

8.9 Experimental Measurement of Rayleigh Convection

Chen used particle image velocimeter (PIV) to measure and study Rayleigh convection [32]. The experimental setup is shown in Fig. 8.38.

The PIV system used in this study were made by a double-cavity Nd-YAG laser with a maximum energy of 200 mJ and a wavelength of 532 nm as the light source. The laser beam, with a 10-ns duration of the pulsed illumination, had a variable pulse frequency up to 15 Hz. The laser was also equipped with a lens system to produce a diverging laser sheet with a thickness not exceeding 1 mm. A CCD camera with resolution of $1376 \times 1,040$ pixels was used to capture the images and was equipped with a filter with a wavelength of 532 nm to capture only the light scatted from the laser-lightened particles. Hollow glass microspheres with diameters of 8–12 μm were seeded in the liquid as tracer particles. The laser was run at 4 Hz and the measurement time was 30 s. The PIV system grabbed and processed the digital particle images utilizing the cross-correlation approach of the FlowMaster software to give the measured velocity vector.
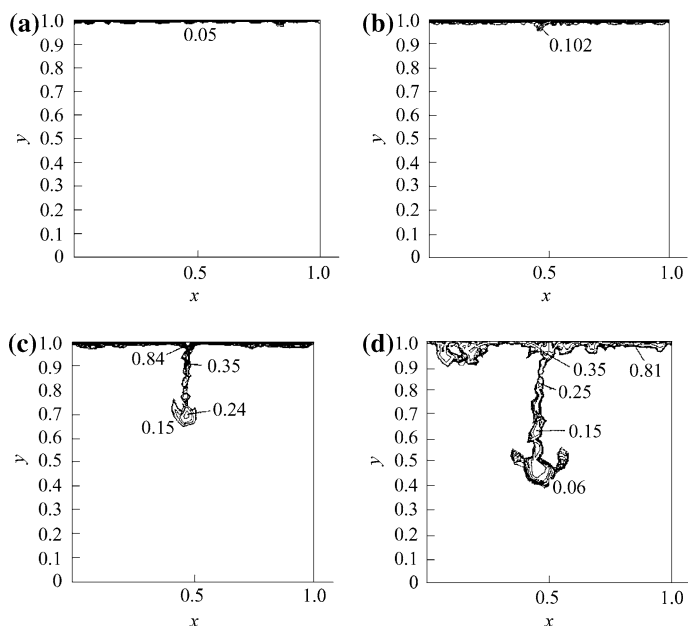
Fig. 8.36 Contour of solute concentration at different time for CO_2 absorption by ethanol ($Ra = 10^8$, $Sc = 200$, $Bi = \infty$) **a** $\tau = 0.002$, **b** $\tau = 0.0075$, **c** $\tau = 0.018$, **d** $\tau = 0.023$

Fig. 8.37 Contour of liquid-phase convection velocity at different time for CO_2 absorption by ethanol ($Ra = 10^8$, $Sc = 200$, $i = \infty$) **a** $\tau = 0.002$, **b** $\tau = 0.0075$, **c** $\tau = 0.018$, **d** $\tau = 0.023$
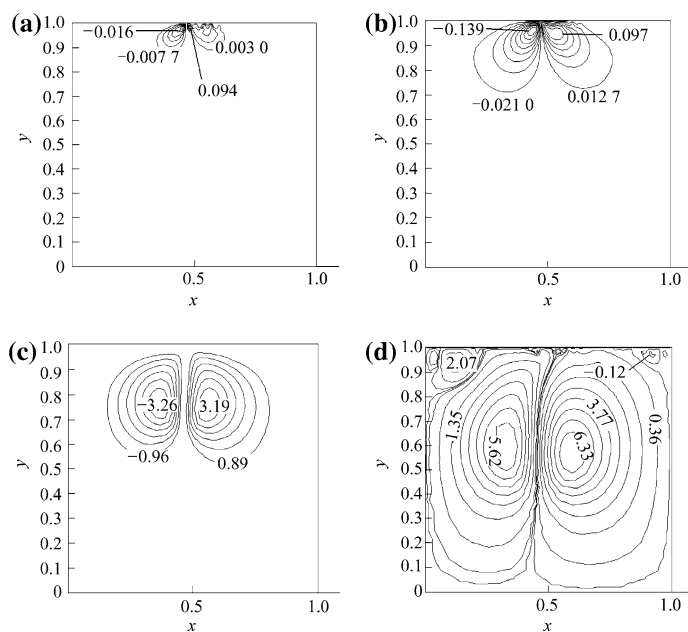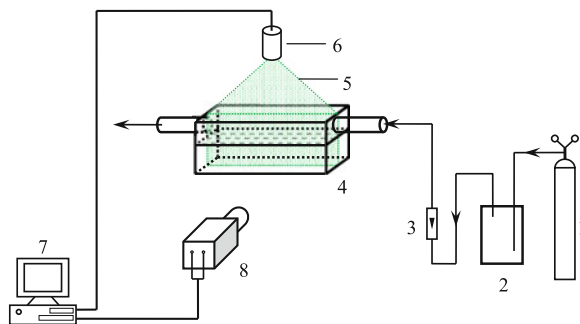
Fig. 8.38 Experimental setup for the measurement of Rayleigh convection (*1*—nitrogen vessel, *2*—gas purifier and presaturator, *3*—rotameter, *4*—interfacial mass transfer simulator, *5*—laser sheet, *6*—laser head, *7*—computer, *8*—CCD camera)

The interfacial mass transfer simulator was made of quartz glass with an inner size of 200 mm in length, 20 mm in width, and 40 mm in height. The liquid was initially quiescent in the simulator with a thickness of 10 mm. Nitrogen gas successively passed through activated carbon, silica gel, and molecular sieve to remove the impurities and water, and then presaturated by the solvent in a tank in order to reduce the influence of solvent evaporation. The liquid was likewise presaturated by nitrogen gas to avoid the gas absorption into the liquid. The liquid concentrations near the gas inlet and outlet positions of the simulator were measured by the gas chromatography.

The experimental system is desorption of acetone from the binary solution of acetone and ethyl acetate under nitrogen stream. Parts of the experimental results are given below [32]:

1. **Velocity vector of Rayleigh convection**

The convection velocity can be obtained by measuring the velocity of tracer particle by the PIV installation at different time as shown in Figs. 8.39 and 8.40.

Figures 8.39 and 8.40 display the velocity distributions perpendicular to the interface of the liquid at different time, Re_L and Re_G of the acetone desorption process. As shown in figures at $t = 5$ s, two-cell symmetrical convection is clearly formed near the interface (Fig. 8.39a). Following at $t = 15$ s, the convection cells are developed and merged into the bulk liquid. At $t = 25$ s, the large convection cells are dissipated, and new smaller convection cells are generated.

Comparing (a)–(c) in Fig. 8.40, it is shown that following the increase in Ra and Re_G, the scale of velocity vortex becomes larger and the convective vortexes turn to slightly chaos. The convection patterns shown in Fig. 8.40 are found to be in good agreement with the simulated result for Rayleigh convection in previous section.

The velocity distributions shown in Figs. 8.39 and 8.40 are not only due to the Rayleigh convection but also imply the bulk flow convection from the incoming liquid, i.e., the small surface flow induced by gas sweeping over the interface and the influence by Marangoni convection. In other words, the Rayleigh convection from interface to the bulk liquid is always accompanied with the convection induced by incoming liquid flow, gas sweeping, and the Marangoni convection.
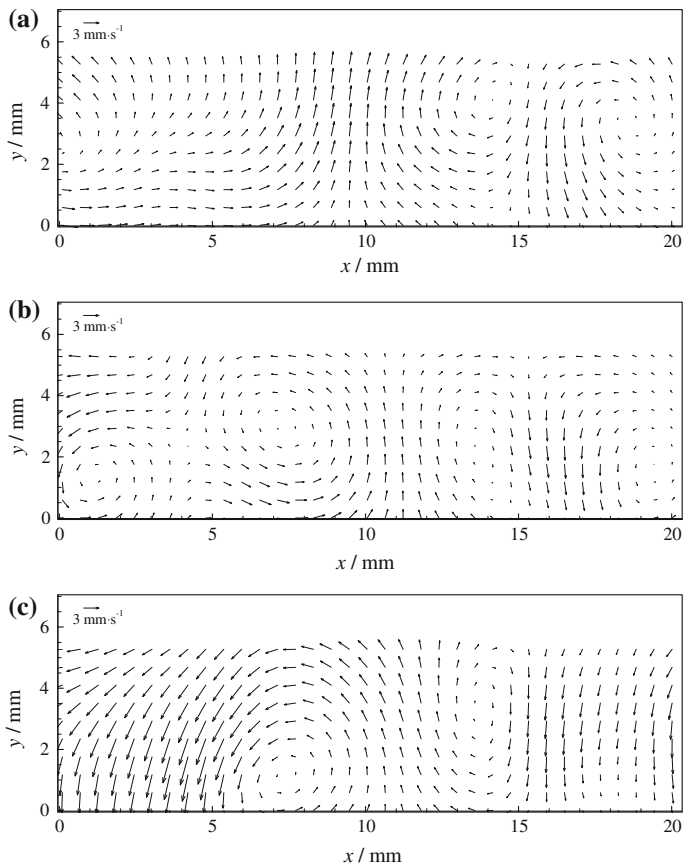
Fig. 8.39 Velocity vector distributions at different times measured by PIV for $Ra = 2.66 \times 10^8$, $Re_G = 13.78$ at different time for the desorption of acetone. **a** 5 s, **b** 15 s, **c** 25 s

However, Rayleigh convection is dominant in the large-scale convective flow between interface and the bulk liquid; the other effects are relatively small and uninfluential.

According to the concept of convective flow, the large vortexes formed from the bulk flow and carried the flow energy are soon convert to small-scale vortexes (eddies) which dissipate afterward in counteracting with the viscous force of the fluid. Thus, large eddy simulation (LES) decomposition [33] was employed to filter out the velocity of smaller scale. According to LES decomposition, the measured velocity can be decomposed into a filtered average velocity u_{avg} that forms large eddies and velocity u' that forms small eddies, i.e., $u = u_{avg} + u'$, as shown in Fig. 8.41.
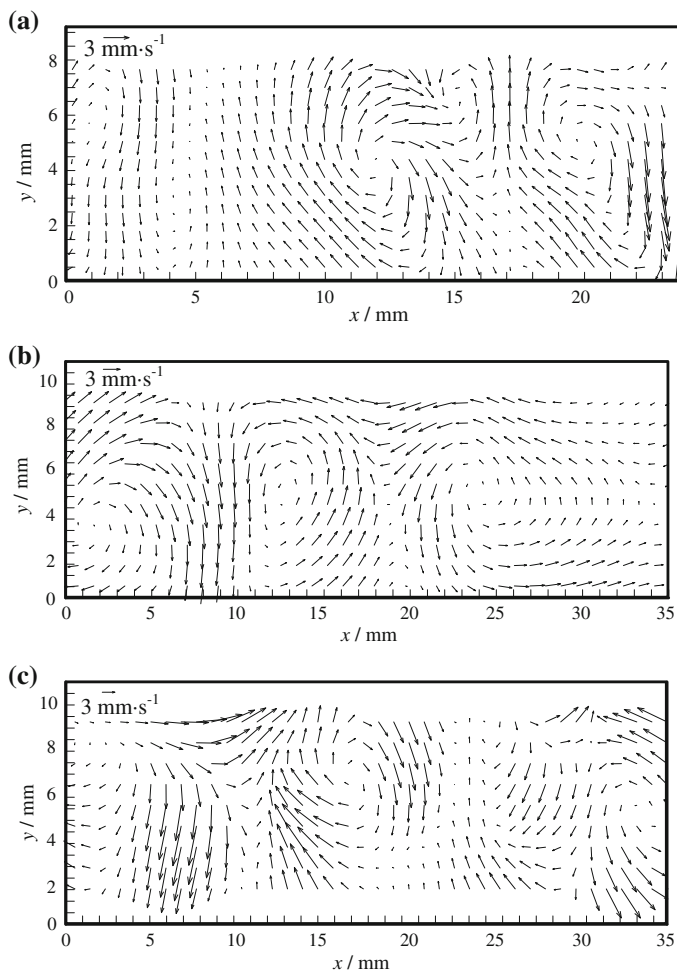
Fig. 8.40 The measured velocity vector by PIV under different conditions for the desorption of acetone. **a** $Ra = 8.6 \times 10^6$, $Re_G = 86.25$, **b** $Ra = 8.3 \times 10^7$, $Re_G = 86.25$, **c** $Ra = 8.3 \times 10^7$, $Re_G = 172.5$

Average convection velocity

Rayleigh convection caused by the density gradient plays the dominant role in the gravitational direction (y direction). Therefore, the time–space averaged velocity in y direction is employed to characterize the Rayleigh convection.

Figure 8.42 shows the time–space averaged vertical velocity u_{avg} versus Ra with different Re_G. The reason that u_{avg} is increased with increasing Re_G is due to the gas flow can renew the solute concentration of gas phase at the interface and promote the convection. Therefore, both high liquid concentration and gas flow rate can enhance the volatilization of acetone.
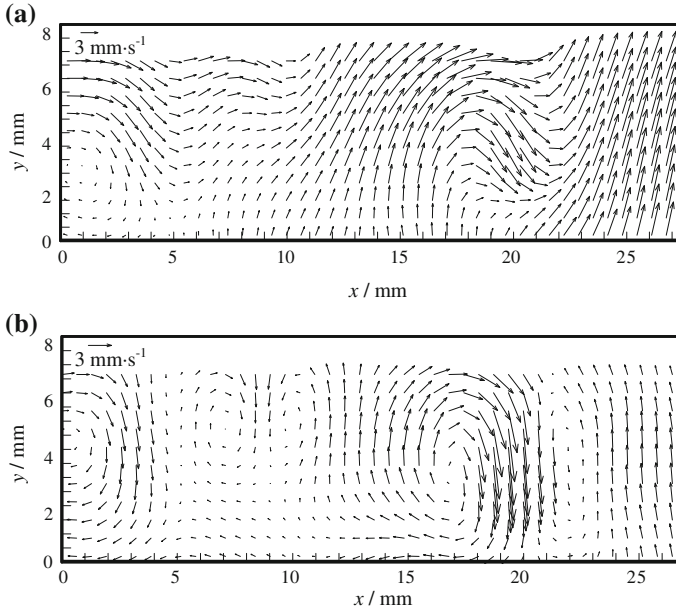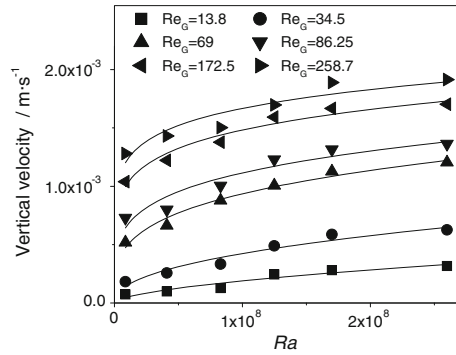
(a)

(b)

Fig. 8.41 LES decomposition of the velocity field for the desorption of acetone. **a** Velocity vector field of large-scale velocity u_{avg}. **b** Velocity vector field of small-scale velocity u'

Fig. 8.42 Time–space averaged vertical velocity under different conditions

Average characteristic length

The characteristic scale can be defined as the size of the largest Rayleigh vortex which can be obtained by velocity vector measurement as shown in Fig. 8.40. The characteristic scale L can be decompounded into $L_{u,x}$, $L_{v,x}$, $L_{u,y}$ and $L_{v,y}$, where the first subscript is the u or v velocity components and the second subscript means along the x or y coordinates [33]. Finally, L can be calculated by orthogonal synthesis of $L_{u,x}$, $L_{v,x}$, $L_{u,y}$ and $L_{v,y}$. The time–space averaged characteristic scale L_{avg} is obtained under different Ra and Re_G as shown in Fig. 8.43.

Fig. 8.43 Characteristic scale of Reyleigh vortex under different conditions
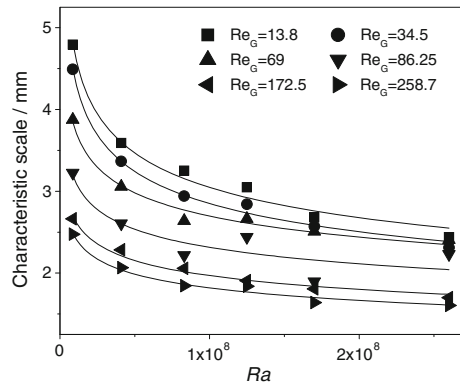
From Fig. 8.43, it is found that L_{avg} is decreased exponentially with the increasing of Ra and also decreased with the increasing Re_G. Besides, the calculated characteristic scale of the system could be further used to compute the surface residence time for the penetration mass transfer model.

The enhancement factor by Rayleigh convection

The mean mass transfer coefficient during 30s interval can be obtained for the acetone desorption from acetone–ethyl acetate solution. The measured average mass transfer coefficient $K_{L,exp}$ can be calculated by the following equation:

$$K_{L,exp} = \frac{V_L(C_{L,0} - C_{L,t})/t}{A\left(\overline{C_L - C_L^i}\right)_{log}}$$

where V_L is the liquid volume; $C_{L,0}$ is the initial solute concentration of the solution at $t = 0$; $C_{L,t}$ is the solute concentration at $t = 30$ s which is estimated by averaging the solute concentrations at the inlet and outlet of the simulator; A is the mass transfer area; $\overline{(C_L - C_L^i)}_{log}$ is the logarithmic average mass transfer-driven force between $t = 0$ s and $t = 30$ s, i.e.,

$$\left(C_L - C_L^i\right)_{log} = \frac{\left(C_{L,in} - C_{L,in}^i\right) - \left(C_{L,out} - C_{L,out}^i\right)}{\ln\frac{\left(C_{L,in} - C_{L,in}^i\right)}{\left(C_{L,out} - C_{L,out}^i\right)}}$$

where superscript i represents the interfacial condition.

For mass transfer process, Zhang derived a model for the overall liquid-phase mass transfer coefficient $K_{L,theo}$ based on the Higbie penetration theory [28]:

$$\frac{1}{K_{L,theo}} = \frac{1}{2}(\pi\tau)^{0.5}\left(D_L^{-0.5} + mD_G^{-0.5}\right)$$

where τ is the surface residence time.

Fig. 8.44 Enhancement factors F for different conditions. **a** $Re_G = 13.78$, **b** $Re_G = 34.45$, **c** $Re_G = 68.90$, **d** $Re_G = 86.12$, **e** $Re_G = 172.25$, **f** $Re_G = 258.4$

In the actual mass transfer process, the liquid mass transfer coefficient is enhanced by the interfacial convection, usually represented by the enhancement factor F as described in Sect. 8.8.2. The F factor calculated by Chen [32] for acetone desorption at different Ra and Re_G as given in Fig. 8.44. As shown in figure, the F factor increases with increasing Ra and Re_G. The corresponding critical Ra (Ra_{cr} at $F = 1$) is seen around 10^7 at $Re_G = 13.78$.

Figure 8.44 displays the relationship between enhancement factor F and Ra at different Re_G. It is shown that F increased firstly with Ra and Re_G and became flat when F was up to about 4. This result indicates that the Rayleigh convection can promote the liquid surface renewal and intensify the mass transfer significantly only to a certain limit, which is in consistent with the experimental measurement in Sect. 8.5.2.

The simulated (predicted) mass transfer coefficient

It is difficult to obtain the surface residence time of the liquid for mass transfer processes by experimental measurement. Yet we may consider that the resident time of a solute particle at the interface equals to the traveling time of a solute particle from bulk fluid to the interface in order to avoid solute accumulation or depletion and keep constant solute concentration at the interface. Thus, the interfacial residence time of the solute can be computed by the average interfacial velocity and the average characteristic scale. Characteristic scale was referred to the largest turbulent eddy in the fluid as defined in Sect. 8.8.2. On the assumption that the interfacial solute renewal is controlled by the large-scale vortex ranging from bulk liquid to the interface, the surface residence time can be obtained by the following relationship:

$$\tau = L_{avg}/u_{avg}$$

where u_{avg} and L_{avg} are given, respectively, in Figs. 8.42 and 8.43.

With the computed surface residence time by foregoing equation, the liquid mass transfer coefficient of liquid phase can also be obtained by applying the Higbie penetration theory as follows:

$$k_L = \sqrt{\frac{4D_L}{\pi\tau}}$$

The computed mass transfer coefficient [32] is shown in Fig. 8.45.

The predicted mass transfer coefficients by applying Higbie penetration theory are seen to be in rough agreement with the experimental data. As shown in Fig. 8.45, the computed mass transfer coefficients based on the calculated surface residence time are well in agreement with the experimental data for low Re_G number, but the deviations became greater with the increasing Re_G. For low Re_G, the sweeping effect of the gas flow on the liquid surface is weak, and the solute resident time at liquid surface is mainly attributed by Rayleigh convection. While for high Re_G, the gas flow might promote the removal of the solute acetone so that the Rayleigh convection becomes faster to fill up the solute depletion. Thus, the simulated results deviate from experimental data at high Re_G is due to ignoring the gas sweeping effect.

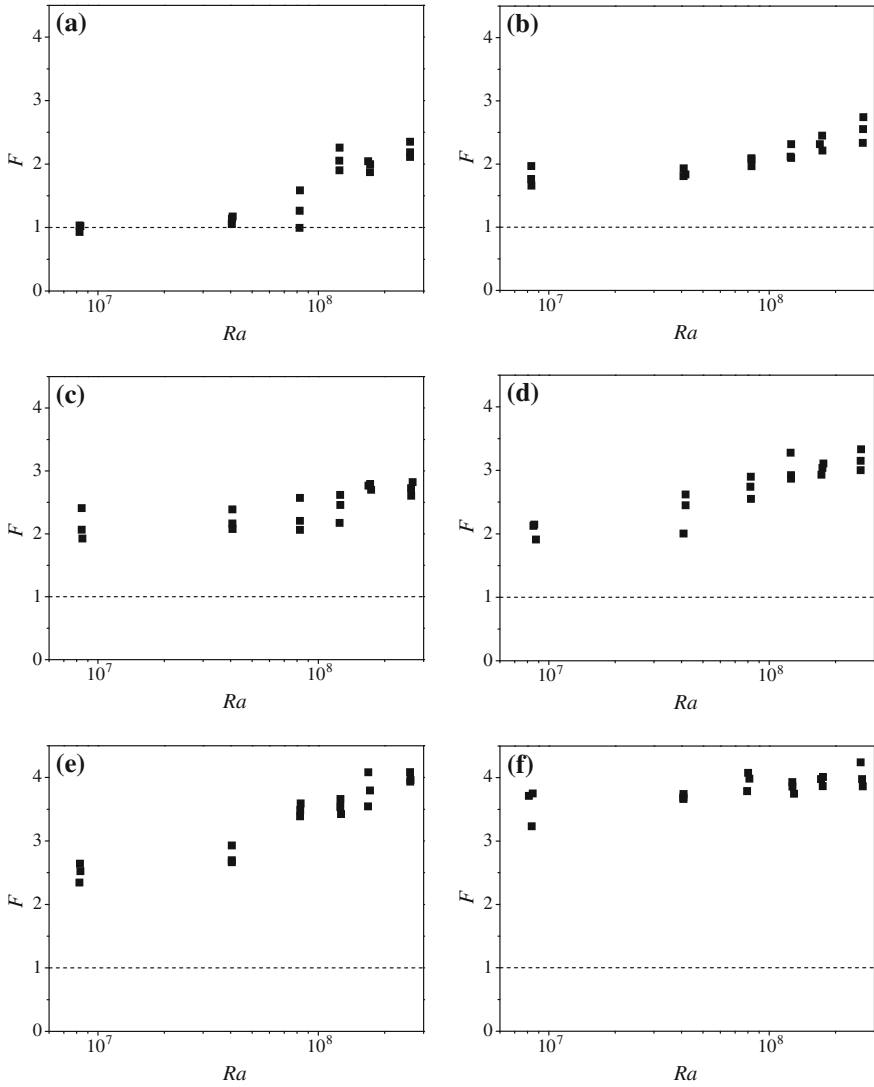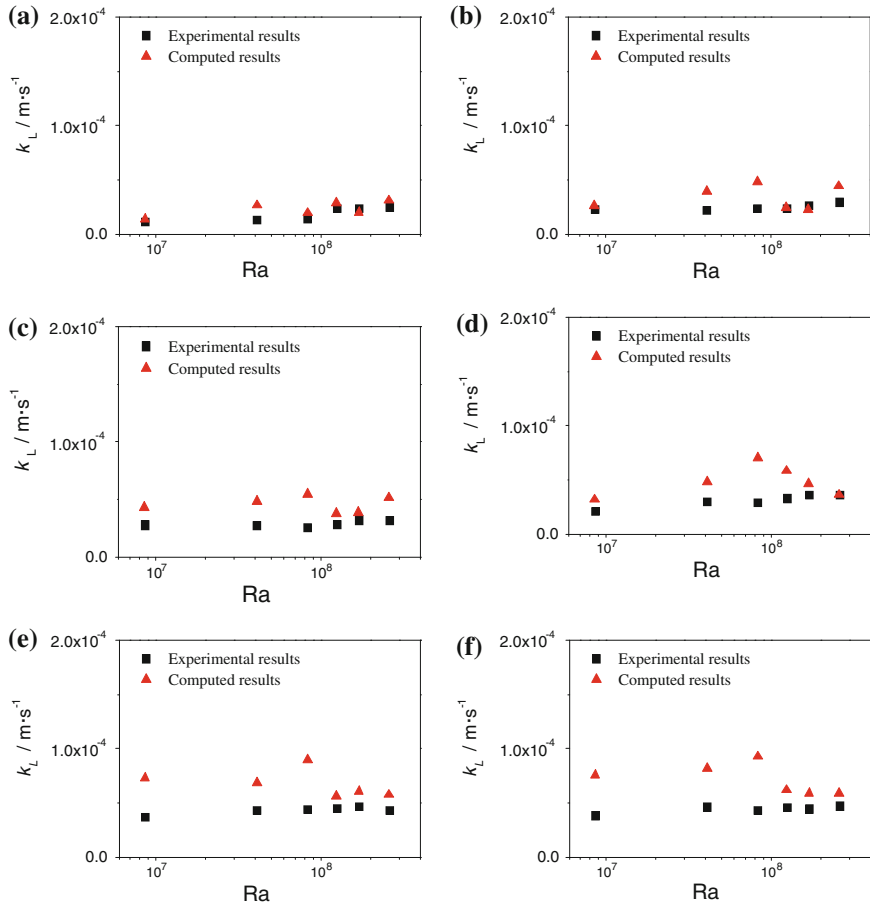**Fig. 8.45** Predicted and measured value of mass transfer coefficient under different conditions. **a** $Re_G = 13.78$, **b** $Re_G = 34.45$, **c** $Re_G = 68.90$, **d** $Re_G = 86.12$, **e** $Re_G = 172.25$, **f** $Re_G = 258.4$

8.10 Simulation and Observation of Two-Dimensional Solute Convection at Interface

8.10.1 Simulation of Two-Dimensional Interfacial Concentration

In the foregoing sections, the analysis of interfacial concentration is based on the x–z plane where x and z are, respectively, the coordinates of interface and perpendicular to the interface. That means the study is on a cross section of the interface in x direction with no concern on y direction. In this section, the study on interface is considered two-dimensional in x and y directions.

Fig. 8.46 Desorption model of horizontal stagnant liquid by gas stream
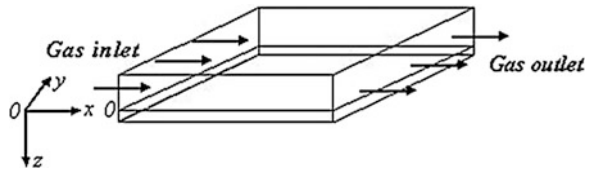
Yu simulated the desorption of aqueous ethanol in horizontal manner and the physical model is as shown in Fig. 8.46, with unsteady three-dimensional model [7] to obtain the solute distribution on x–y and x–z planes. Some of the simulated results are given below:

8.10.1.1 Model Equations

The assumption of model simulation is similar to that in Sect. 8.8.1. The model equations are as follows:

$$\frac{\partial \boldsymbol{u}}{\partial x_i} = 0, \boldsymbol{u} = (u, v, w)$$

$$\frac{\partial \boldsymbol{u}}{\partial t} + \boldsymbol{u}\frac{\partial \boldsymbol{u}}{\partial x_i} = \frac{1}{\rho_L}\left[-\frac{\partial p}{\partial x_j} + \mu_L\left(\frac{\partial^2 \boldsymbol{u}}{\partial x_i}\right) + S_F\right]$$

$$S_F = (F_{LG}, F_{LG} + g)$$

$$\frac{\partial c}{\partial t} + \boldsymbol{u}\frac{\partial c}{\partial x_i} = D\frac{\partial^2 c}{\partial x_i}$$

where S_F is the source term representing the liquid–gas interfacial shearing force in x, y, z directions.

In order to transform the model equation to dimensionless, let length, velocity, time, and concentration be d_L, D/d_L, d_L^2/D, and C, where d_L is the thickness of the liquid layer (10 mm in present simulation).

The initial and boundary conditions as well as the calculation of source term can be found from Ref. [7].

The object of simulation is the desorption of ethanol (solute) from aqueous ethanol by nitrogen stream. It is an unsteady process. For the convenience of expression, dimensionless time $\tau' = t\frac{D}{d_L^2}$ is adopted in the subsequent figures. The simulation is ranging from very short time at the beginning ($\tau' = 1.0 \times 10^{-8}$) to the very long time ($\tau' = 3.5 \times 10^{-2}$).

8.10.1.2 Simulated Results

(A) **Interfacial velocity and solute concentration distributions**

Figures 8.47 and 8.48 display, respectively, the simulated distributions of liquid velocity and solute concentration on x–y plane.
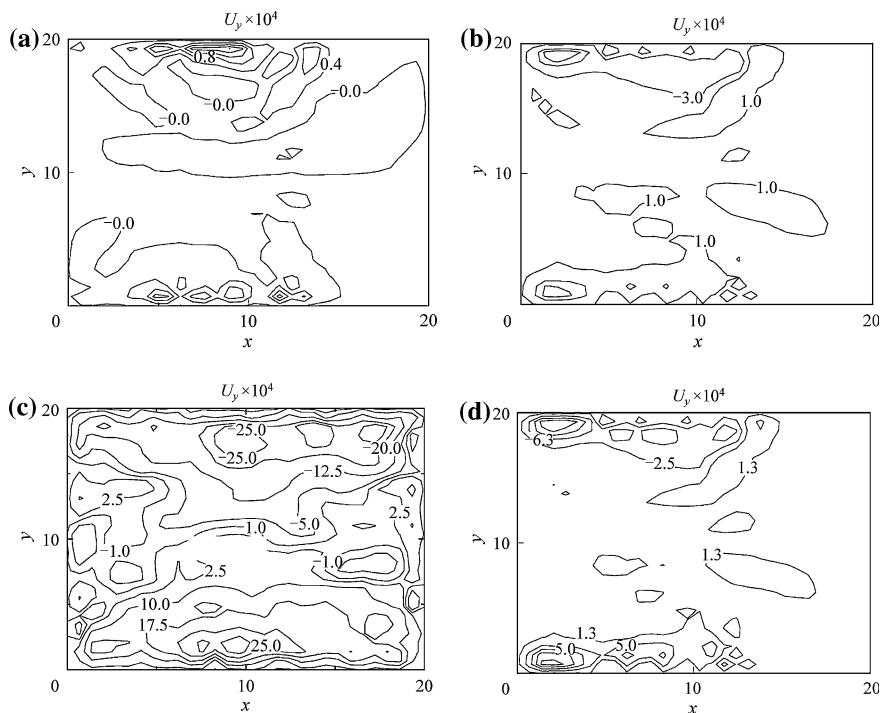
Fig. 8.47 Interfacial liquid velocity contours for horizontal desorption of aqueous ethanol ($Re_G = 20$, $c_0 = 0.5$ mol m^{-3}). **a** $\tau' = 1.5 \times 10^{-8}$, **b** $\tau' = 3.0 \times 10^{-7}$, **c** $\tau' = 2.5 \times 10^{-5}$, **d** $\tau' = 1.2 \times 10^{-2}$ (reprinted from Ref. [34], Copyright 2008, with permission from Elsevier)

At the beginning of desorption ($\tau' = 1.0 \times 10^{-8}$), few small-scale velocity eddies appear and no appreciable vortex is formed. It follows that only few concentration eddies are displayed, indicating that the surface tension difference established at the interface is not sufficient to initiate Marangoni convection.

Following the time progress to $\tau' = 3.0 \times 10^{-7}$, some local circular convection is formed by the combination of neighboring small eddies, indicating the evolution of local disturbance. Further development of the local disturbance will promote the formation of Marangoni convection.

At $\tau' = 2.5 \times 10^{-5}$, the local convection grows up to form large circular flow indicating the appearance of Marangoni convection and interfacial structure. The concentration eddies are in different scale distributed at the interface.

After sufficient long time, $\tau' > 2.5 \times 10^{-2}$, the ethanol in the stagnant liquid is depleted by desorption, the interfacial ethanol concentration as well as the local Δc is decreased so that the Marangoni convection is depressed and gradually vanished.
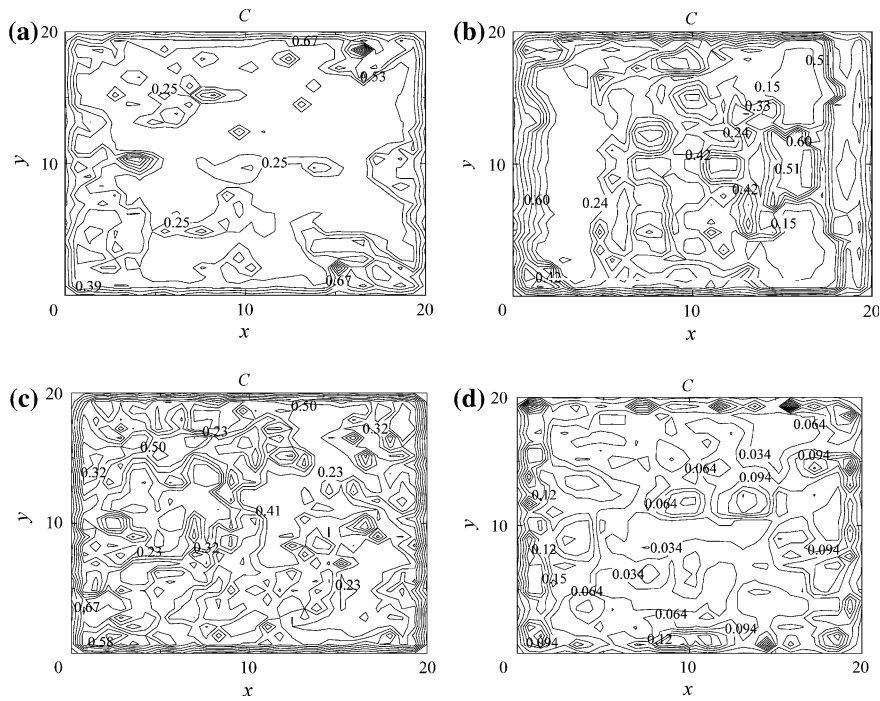
Fig. 8.48 Interfacial solute concentration contours for horizontal desorption of aqueous ethanol ($Re_G = 20$, $c_0 = 0.5$ mol m^{-3}). **a** $\tau' = 1.5 \times 10^{-8}$, **b** $\tau' = 3.0 \times 10^{-7}$, **c** $\tau' = 2.5 \times 10^{-5}$, **d** $\tau' = 1.2 \times 10^{-2}$

Fig. 8.49 Enhancement factor at different time for the desorption of stagnant aqueous ethanol
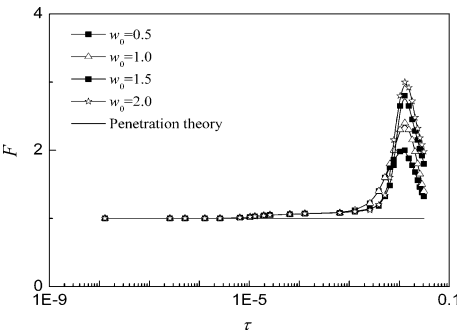
(B) Enhancement factor

The calculated enhancement factor F at different time for the desorption of stagnant aqueous ethanol in nitrogen stream is shown in Fig. 8.49.

At the beginning stage before dimensionless time $\tau' = 1 \times 10^{-5}$, the local surface tension difference Δc is not great enough to create Marangoni convection

and therefore $F = 1$. The critical point is seen to appear around $\tau' = 1 \times 10^{-5}$ and F is increased afterward until reaching the maximum at $\tau' = 1 \times 10^{-2}$. Then, due to the continuous depletion of ethanol to make the interfacial ethanol concentration decreasing, which tends to lowering the Δc and dropping the F factor, such tendency is in agreement with the works published in literature [35, 36].

8.10.2 Experimental Observation of Interfacial Concentration Gradient

Besides mathematical simulation, Liu et al. [34] obtained the interfacial concentration gradient by analyzing the light intensity distribution of the Schlieren image on x–y plane for the desorption of acetone from its aqueous solution under nitrogen stream as shown in Fig. 8.50.

As shown from Fig. 8.50, at the beginning period of desorption, the interface displays instantly some disordered concentration gradients in small scale which are not great enough to induce Marangoni convection. Following the progress of desorption, the concentration gradient is increased to form some larger concentration vortex, although these figures are not so clear.

In brief, both simulation and observation in this section indicate that, for the $Ma > 0$ liquid–gas mass transfer process, the velocity and concentration gradients always occur at the interface to form velocity and concentration eddies in large or smalls scales; they are developed and vanished in alternation until sufficient surface tension is established to initiate the interfacial Marangoni convection.

8.11 Marangoni Convection at Deformed Interface Under Simultaneous Mass and Heat Transfer

In the foregoing sections, the interface is considered as a horizontal or vertical plane without deformation. Actual observation reveals that in the liquid–gas flowing process the contacting interface is always in wavy or ripply form. Such condition is considered in this section.

For simplifying the problem, the simulated object is the liquid–gas contacting falling film with wavy interface as shown in Fig. 8.51. The simulation is on the two-dimensional x–z plane. Xiao [12] established the model equation and give the simulated results as follows.
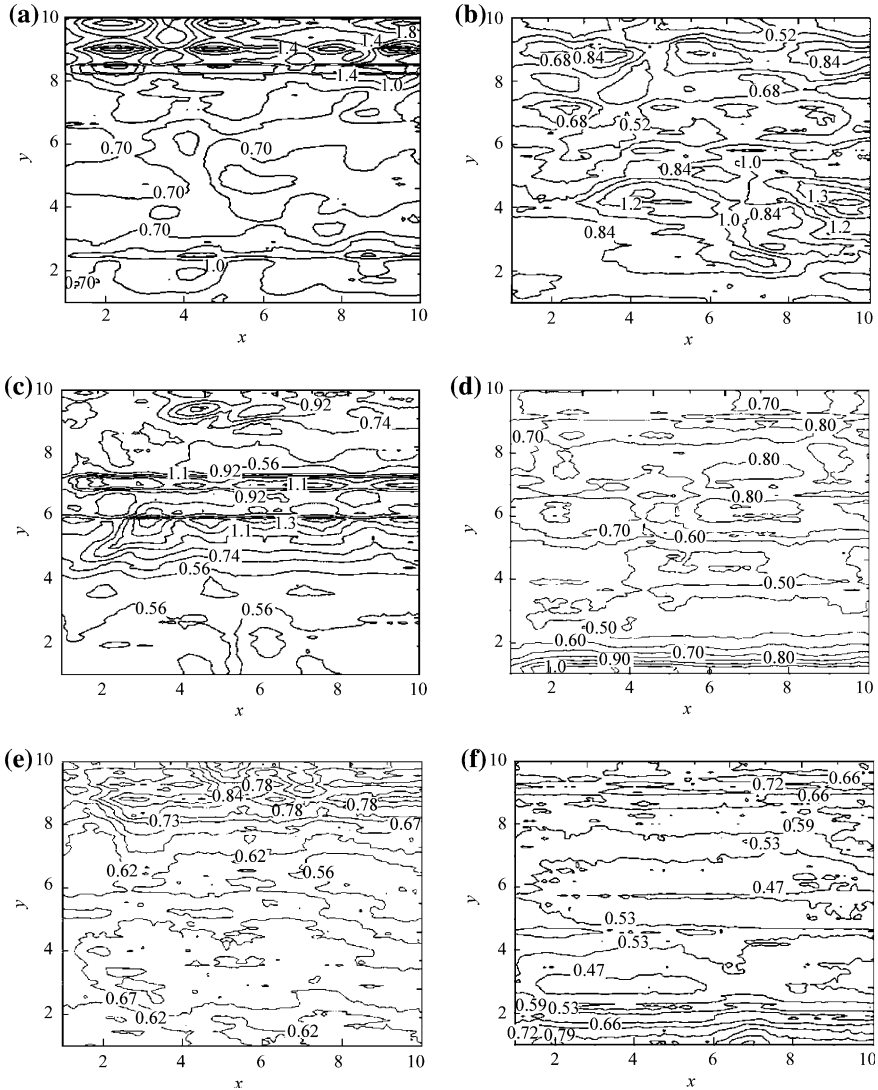
Fig. 8.50 Experimental observation of interfacial solute concentration gradient for aqueous acetone desorption at different time. **a** ~0 s, **b** 30 s, **c** 60 s, **d** 90 s, **e** 120 s, **f** 150 s (reprinted from Ref. [34], Copyright 2008, with permission from Elsevier)

8.11.1 Model Equations

Assumptions

- The mass and heat transfer are taken place simultaneously in the direction between the wall and the interface (z direction in figure) in order to avoid the

Fig. 8.51 Falling film with
wavy interface

$d' = d + \xi\,(x,t)$
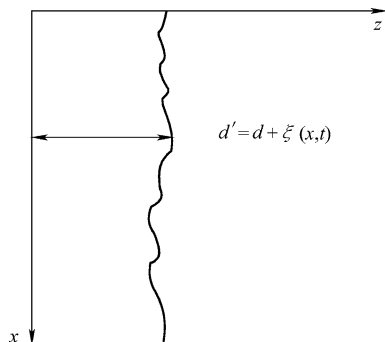
Rayleigh convection. Thus, the gravitational influence (Rayleigh convection) can be ignored;
- The velocity of both liquid and gas is low so that the drag force between gas and falling liquid is neglected;
- The mass of liquid phase is substantially constant as the amount of mass transfer is small.

1. **Basic equations**

$$\frac{\partial \boldsymbol{u}}{\partial x_i} = 0$$

$$\frac{\partial \boldsymbol{u}}{\partial t} + \boldsymbol{u}\frac{\partial \boldsymbol{u}}{\partial x_i} = \frac{1}{\rho} - \frac{\partial p}{\partial x_i} + \frac{\mu}{\rho}\frac{\partial^2 \boldsymbol{u}}{\partial x_i^2} + \boldsymbol{S}$$

$$\frac{\partial T}{\partial t} + \boldsymbol{u}\frac{\partial T}{\partial x_i} = \alpha\frac{\partial^2 T}{\partial x_i^2}$$

$$\frac{\partial c}{\partial t} + \boldsymbol{u}\frac{\partial c}{\partial x_i} = D\frac{\partial^2 c}{\partial x_i^2}$$

where $\boldsymbol{u} = (u, w)$ and source term $\boldsymbol{S}$ (gravity) is neglected by assumption.

Since the mass and heat transfer is considered in horizontal (z) direction, the change in liquid temperature and solute concentration with respect to the liquid thickness in z direction can be represented by the following equation:

$$T = T_0 - \beta'_T z$$

$$c = c_0 - \beta'_c z$$

where subscript 0 denotes the condition at $z = 0$, β'_T and β'_c represent, respectively, the temperature gradient $\left(\frac{\partial T}{\partial z}\right)$ and concentration gradient $\left(\frac{\partial c}{\partial z}\right)$.

2. **Disturbance equations**

Let $\delta\boldsymbol{u}(\delta u, \delta w), \delta T, \delta c, \delta p$ are the infinitesimal small disturbance of velocity, temperature, concentration, and pressure, we have after disturbance,

$$\boldsymbol{u}' = \boldsymbol{u} + \delta\boldsymbol{u}$$
$$T' = T + \delta T$$
$$c' = c + \delta c$$
$$p' = p + \delta p$$

Substituting $\boldsymbol{u}', T', c'$ and p' to the model equation and neglecting the nonlinear term, the following linear disturbance equations are obtained:

$$\frac{\partial \delta\boldsymbol{u}}{\partial x_i} = 0$$
$$\frac{\partial \delta\boldsymbol{u}}{\partial t} = -\frac{1}{\rho}\frac{\partial \delta p}{\partial x_j} + \frac{\mu}{\rho}\frac{\partial^2 \delta\boldsymbol{u}}{\partial x_i^2}$$
$$\frac{\partial \delta T}{\partial t} = \alpha\frac{\partial^2 \delta T}{\partial x_i^2} + \beta_T \delta w \qquad (8.15)$$
$$\frac{\partial \delta c}{\partial t} = D\frac{\partial^2 \delta c}{\partial x_i^2} + \beta' \delta w$$

Eliminating δp from Eq. (8.15) and after rotational transformation, we have in z direction,

$$\frac{\partial}{\partial t}\left(\frac{\partial^2 \delta w}{\partial x_i^2}\right) = \frac{\mu}{\rho}\frac{\partial^4 \delta w}{\partial x_i^4}.$$

3. **The effect of interface deformation**

Under the condition of interface deformation, the surface tension σ can be represented by the following:

$$\sigma = \sigma_f + \frac{\partial \sigma}{\partial T}\left(T - T_f\right) + \frac{\partial \sigma}{\partial c}\left(c - c_f\right) \qquad (8.16)$$

where subscript f denotes the condition of no deformation.

Suppose the quantity of interfacial deformation is $\xi(x, t)$, the thickness of the liquid layer is changed from d to d'; then we have the following:

$$d' = d + \xi(x, t)$$

The temperature and concentration at interface after disturbance become

$$T' = T + \delta T = T_0 - \beta'_T d' + \delta T = T_0 - \beta'_T (d + \xi) + \delta T = T_f - \beta_T \xi + \delta T$$
$$c' = c + \delta c = c_f - \beta'_c \xi + \delta c$$

Substituting to Eq. (8.16) yields

$$\sigma = \sigma_f + \frac{\partial \sigma}{\partial T}(\delta T - \beta'_T \xi) + \frac{\partial \sigma}{\partial c}(\delta c - \beta'_c \xi). \qquad (8.17)$$

4. **Boundary conditions**
(a) At $z = 0$ (solid wall), the condition of no slip is applied

$$\delta w = 0$$

and from continuity equation gives

$$\frac{\partial \delta w}{\partial z} = 0$$

Take heat balance to yield

$$\lambda \frac{\partial \delta T}{\partial z} = h_L^S \delta T$$

The left-hand side of above equation represents the heat transferred by conduction to the solid wall surface at $z = 0$; the right-hand side represent the heat transferred between solid wall surface and the bulk liquid; λ is the thermal conductivity; h_L^S is the film coefficient of heat transfer between solid wall surface and bulk liquid.

As no mass is transferred between solid wall and the liquid, it is obvious that $\frac{\partial \delta c}{\partial z} = 0$.

(b) At $z = 1$ (liquid–gas interface), since the interface is deformed, the disturbance velocity should satisfy the following relationship:

$$\delta w = \frac{\partial \xi}{\partial t}$$

In normal direction, the force causing interfacial deformation is equal to the force acting by the bulk liquid to the interface [37], that is,

$$\sigma \frac{\partial^2 \xi}{\partial x^2} = -\delta p + 2\mu \frac{\partial \delta w}{\partial z}$$

Substituting Eq. (8.15) to eliminate δp, we get

$$\frac{\partial \delta u}{\partial t} = \frac{\sigma}{\rho} \frac{\partial^3 \xi}{\partial x^3} + \frac{\mu}{\rho}\left(\frac{\partial^2 \delta u}{\partial z^2} - 3\frac{\partial^2 \delta w}{\partial x \partial z}\right)$$

Similarly, in tangential direction when interfacial convection is initiated, the surface tension is equal to shearing force acting to the interface by the bulk liquid as follows

$$\frac{\partial \sigma}{\partial x} = \mu\left(\frac{\partial \delta u}{\partial z} + \frac{\partial \delta w}{\partial x}\right)$$

where σ can be obtained from Eq. (8.17).

Take heat balance at the interface and consider the deformation ξ, we yield

$$\lambda\frac{\partial \delta T}{\partial z} = -h_{L}(\delta T - \beta\xi)$$

where h_{L} is the film coefficient of heat transfer.

(c) At interface, according to thermodynamics, the interfacial liquid concentration c_{L}^{*} and the interfacial gas concentration c_{G}^{*} are coexisted and in equilibrium. For the explanation of interfacial behaviors, Gibbs in 1878 proposed the theory of adsorption layer by considering the interface was an imaginary layer with no thickness.

Take desorption as an example, the quantity of mass transferred from bulk liquid to the interface is undergoing the following steps in sequence:

1. Solute diffuse to the interface from bulk liquid.
2. Accumulation of solute in the adsorption layer.
3. Diffusion of solute in the adsorption layer.
4. Diffusion of solute from the interface (adsorption layer) to the gas phase.

Mathematically, the mass balance of foregoing steps can be expressed as follows:

$$-D\frac{\partial c}{\partial Z} = k_{L}\Delta c + \frac{\partial \Gamma}{\partial t} - \left[\frac{\partial u\Gamma}{\partial x} + \frac{\partial w\Gamma}{\partial z} - D_{S}\left(\frac{\partial^2\Gamma}{\partial x^2} + \frac{\partial^2\Gamma}{\partial z^2}\right)\right] = k_{L}\Delta c + S_{G}$$

where k_{L} and Δc are, respectively, the film coefficient of mass transfer and solute concentration difference between bulk liquid and interface; Γ is the excess quantity in the adsorption layer, that is the accumulated solute per unit interfacial area; D_{S} is the solute diffusivity in adsorption layer, which is considered equal to the diffusivity of solute in bulk liquid D.

The excess quantity (solute) Γ can be expressed as the sum of fixed Γ and disturbance quantity $\delta\Gamma$:

$$\Gamma = \Gamma + \delta\Gamma$$

Substituting to the mass balance equation and considering the disturbance of concentration and velocity as well as the interfacial deformation, the following equation is obtained after neglecting the high-order infinitesimal terms:

$$-D\frac{\partial c}{\partial Z} = k_{\mathrm{L}}\left(\delta c - \beta'_c\xi\right) + \frac{\partial\delta\Gamma}{\partial t} - D\left(\frac{\partial^2\delta\Gamma}{\partial x^2} + \frac{\partial^2\delta\Gamma}{\partial z^2}\right)$$

From Gibbs theory, we have the following relationship:

$$\Gamma = -\frac{1}{RT}\left(\frac{\partial\sigma}{\partial c}\right)c = d_{\mathrm{G}}c$$

If surface tension σ is linear with concentration, then $d_{\mathrm{G}} = -(1/RT)(\partial\sigma/\partial c)$ becomes a constant and having the dimension of length, which is commonly defined as "adsorption layer thickness."

Combining the foregoing equations, we have the boundary condition at interface to be

$$-D\frac{\partial\delta c}{\partial z} = k_{\mathrm{L}}(\delta c - \beta'\xi) + d_{\mathrm{G}}\frac{\partial(\delta c - \beta'_c\xi)}{\partial t} - d_{\mathrm{G}}D\left[\frac{\partial^2(\delta c - \beta'_c\xi)}{\partial x^2} + \frac{\partial^2(\delta c - \beta'_c\xi)}{\partial z^2}\right]$$

If the mass transfer process is absorption, similar boundary condition is also established.

8.11.2 Generalization to Dimensionless

For the generalization of foregoing equations and boundary conditions to dimensionless, let the bulk liquid thickness d be the length scale, d^2/D be the time scale, $\beta'_{\mathrm{T}}d$ be the temperature scale, $\beta'_c d$ be the concentration scale, i.e.,

$$t = \frac{d^2}{D}\tau$$
$$\boldsymbol{u} = \frac{D}{d}U$$
$$(\xi, x, z) = d(\xi_1, x_1, z_1)$$
$$T = \beta'_T d\,\bar{T}$$
$$c = \beta'_c d\,C$$

where $\tau, \boldsymbol{U}, \bar{T}, C$ are dimensionless. Substituting to the foregoing model equations, we have the following:

$$\frac{\partial}{\partial \tau}\left(\frac{\partial^2 \delta w}{\partial x_i^2}\right) = \frac{\mu}{\rho D}\left(\frac{\partial^4 \delta w}{\partial x_i^4}\right)$$

$$\frac{\partial \delta U}{\partial x_i} = 0$$

$$\frac{\partial \delta C}{\partial \tau} = \frac{\partial^2 \delta C}{\partial x_i^2} + \delta w$$

$$\frac{\partial \delta \bar{T}}{\delta \tau} = \frac{\alpha}{D}\frac{\partial^2 \delta \bar{T}}{\partial x_i^2} + \delta w$$

Boundary conditions:

At $z = 0$ (wall)

$$\frac{\partial \delta \mathbf{U}}{\partial x_i} = 0$$

$$\frac{\partial \delta W}{\partial z} = 0$$

$$\frac{\partial \delta C}{\partial z} = Bi^0 \delta C$$

$$\frac{\partial \delta \bar{T}}{\partial z} = Bi_h^0 \delta \bar{T}$$

where $Bi^0 = k_\mathrm{L}d/D_\mathrm{L}$ is the liquid-phase Biot number for mass transfer; $Bi_\mathrm{h}^0 = h_\mathrm{L}d/\alpha$ is the Biot number for heat transfer; superscript 0 denotes the value at $z = 0$.

At $z = 1$ (interface)

$$\delta W = \frac{\partial \xi}{\partial \tau}$$

$$\frac{\partial \delta \bar{T}}{\partial z} = Bi_\mathrm{h}^1(\delta \bar{T} - \xi)$$

$$\frac{\partial \delta C}{\partial z} = Bi^1(\partial C - \xi) - G\frac{\partial(\partial C - \xi)}{\partial \tau} + \hat{S}\frac{\partial^2}{\partial x_i^2}(\delta C - \xi)$$

$$\frac{\partial \delta U}{\partial \tau} = \frac{Sc}{Cr}\frac{\partial^3 \xi}{\partial x^3} + Sc\left(\frac{\partial^2 \delta U}{\partial z^2} - 3\frac{\partial^2 \delta W}{\partial x \partial z}\right)$$

$$\frac{\partial \delta U}{\partial z} + \frac{\partial \delta W}{\partial x} = \frac{Ma_\mathrm{h}}{Le}\left(\frac{\partial \delta \bar{T}}{\partial x} - \frac{\partial \xi}{\partial x}\right) + Ma\frac{\partial(\delta C - \xi)}{\partial x}$$

where $Sc = \frac{\mu}{\rho D}$; $Le = \frac{D_\mathrm{L}}{\alpha}$; $\hat{S} = Bi^1\frac{d_\mathrm{G}c^*}{d^2\beta_c'}$; $Ma = \frac{\partial \sigma}{\partial c}\frac{\beta'd^2}{\mu D}$; $Ma_\mathrm{h} = \frac{\partial \sigma}{\partial T}\frac{\beta d^2}{\mu \alpha}$; $G = \frac{d_\mathrm{G}}{d}$; d_G is the adsorption layer thickness; c^* is the interfacial solute concentration; β_c' is the concentration gradient in the bulk liquid, and superscript 1 denotes the value at $z = 1$. Dimensionless group $Cr = \mu D/(\sigma d)$ represents the influence of surface tension to the interfacial deformation and is called crispation number [38].

8.11.3 Stability Analysis

Similar to the stability analysis in Sect. 8.3, let the small disturbance follows the following form:

$$\delta W = \Psi(z) \exp(ik_x x + \omega t)$$
$$\delta T = \Theta(z) \exp(ik_x x + \omega t)$$
$$\delta c = \Phi(z) \exp(ik_x x + \omega t)$$

where Ψ, Θ, and Φ are, respectively, the disturbance amplitude of velocity, temperature, and concentration; k_x is the wave number in direction x; and ω is the increasing rate of disturbance.

Similar to the Sect. 8.3, let

$$\frac{\partial^2}{\partial x^2} = -k_x^2$$

$$\nabla^2 = \frac{\partial^2}{\partial x^2} + \frac{\partial^2}{\partial z^2} = \frac{d^2}{dz^2} - k_x^2 = \tilde{D}^2 - k_x^2$$

The dimensionless disturbance equation can be written in the following form:

$$\left(\tilde{D}^2 - k_x^2\right)^2 \psi = 0$$
$$\left(\tilde{D}^2 - k_x^2\right)^2 \Theta = -Le\,\Psi$$
$$\left(\tilde{D}^2 - k_x^2\right) \Phi = -\Psi$$

The boundary conditions are as follows:
At $z = 0$,

$$\Psi = 0 \quad \tilde{D}\Psi = 0$$
$$\tilde{D}\Theta - Bi_h^0 \Theta = 0$$
$$\tilde{D}\Phi - Bi^0 \Phi = 0$$

At $z = 1$,

$$\Psi = 0$$
$$\tilde{D}\Theta + Bi_h^1(\Theta - \eta) = 0$$
$$\tilde{D}\Phi + Bi^1(\Phi - \eta) - \hat{S}\left(\tilde{D}^2 - k_x^2\right)(\Phi - \eta) = 0$$
$$\left(\tilde{D}^2 + k_x^2\right)\Psi + \frac{Ma_h}{Le}k^2(\Theta - \eta) + Mak_x^2(\Phi - \eta) = 0$$

where dimensionless group $\hat{S} = Bi^1 \frac{d_G c^*}{d^2 \beta_c'}$, β' is the temperature gradient in bulk liquid.
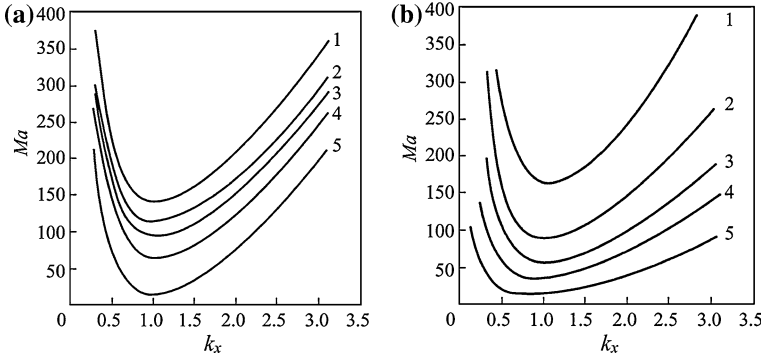
Fig. 8.52 The Ma–k curves at different Ma_h. **a** $Cr = 0$, $\hat{S} = 0$, $Bi_h^0 = Bi^0 = 0$, $Bi_h^1 = Bi^1 = 10$, **b** $Cr = 0.001$, $\hat{S} = 0.01$, $Bi_h^0 = Bi^0 = 5$, $Bi_h^1 = Bi_l^1 = 15$ (*Curve 1—$Ma_h = -50$; 2—$Ma_h = 0$; 3—$Ma_h = 20$; 4—$Ma_h = 50$; 5—$Ma_h = 100$*)

Simulated results

In order to find the instability of foregoing model equations enabling to induce interfacial convection, no zero solution is necessary. Similar to the method used in Sect. 8.3.2, by letting the coefficients of the corresponding determinant equal to zero, the following equation can be established:

$$f\left(Ma, Ma_h, k_x, Cr, Bi_h^1, Bi^1, Bi_h^0, Bi^0, \hat{S}\right) = 0$$

If reasonable value of $Cr, Bi_h^1, Bi^1, \hat{S}$, Ma_h are given, the relationship between Ma and k_x is obtained, from which the critical Ma number, Ma_{cr}, can be found.

1. **The influence of Ma_h on Ma_{cr}**

Figure 8.52 shows the Ma–k_x curves calculated under designated conditions at different Ma_h. The area underneath a curve represents the system in stable state and that above the curve is in the unstable state for the corresponding condition. The minimum point of the curve represents the smallest Ma which is the bordering point between the system in stable state and unstable state, in other words, it represents the critical Ma number, or Ma_{cr}. If Ma_{cr} plotted against Ma_h as shown from Fig. 8.53, the Ma_{cr} is shown to decrease with increasing Ma_h. Figure 8.53 demonstrates clearly the effect of Ma_h on Ma_{cr}.

2. **The influence of Cr on Ma_{cr}**

The dimensionless crispation number, $Cr = \mu D/(\sigma d)$, represents the influence of surface tension on interface deformation. Figure 8.54 shows the Ma_{cr} at different Cr for various systems. The influence of Cr on Ma_{cr} is obvious as shown at higher Cr.

Fig. 8.53 Critical Ma_{cr} at different Ma_h for simultaneous mass and heat transfer (line a—$Cr = 0$, $\hat{S} = 0, Bi_h^0 = Bi^0 = 0, Bi_h^1 = Bi^1 = 10$, line b—$Cr = 0.001, \hat{S} = 0.01, Bi_h^0 = Bi^0 = 5, Bi_h^1 = Bi_l^1 = 15$)

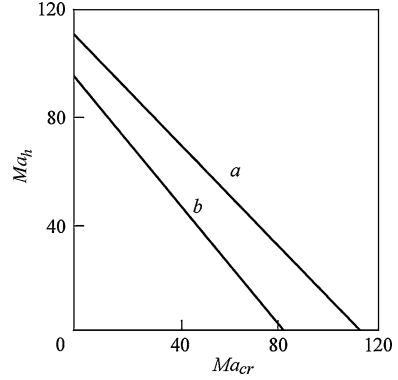**Fig. 8.54** The influence of Cr on Ma_{cr} (1—$Ma_h = -20, B_h^0 = 20, B_h^1 = Bi^1 = 100, \dot{S} = 0, 2$—$Ma_h = 0, Bi_m^1 = 100, \dot{S} = 0, 3$—$Ma_h = 40, B_h^0 = 20, B_h^1 = Bi^1 = 100, \dot{S} = 0.01, 4$—$Ma_h = 100, B_h^0 = 20, B_h^1 = Bi^1 = 100, \dot{S} = 0.05$)
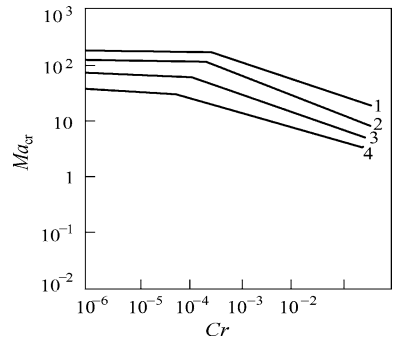
Fig. 8.55 The influence of $\hat{S}$ on Ma_{cr} (1—$Ma_h = -20, B_h^0 = 20, B_h^1 = Bi^1 = 10, Cr = 0, 2$—$Ma_h = 0, Bi^1 = 10, Cr = 0, 3$—$Ma_h = 50, B_h^0 = 20, B_h^1 = Bi^1 = 10, Cr = 0.01$)
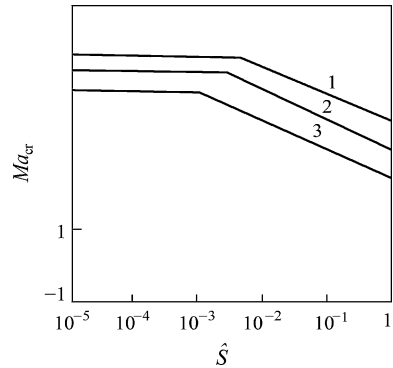
3. **The influence of interfacial adsorption on Ma_{cr}**

The effect of interfacial adsorption can be represented by the dimensionless group [22] $\hat{S} = Bi^1 \frac{d_G c^*}{d^2 \beta_c'}$ where d_G is the thickness of adsorption layer. The $\hat{S}$ is also reflected the influence of Bi^1. Figure 8.55 shows that Ma_{cr} is lowered at higher $\hat{S}$, it

means the appearance of Marangoni convection can be promoted earlier by interfacial adsorption.

From the simulated results of foregoing sections, the interfacial effect is influenced by many factors, such as Marangoni convection, Rayleigh convection, heat transfer, interface deformation, physical properties of the process, and others. Each factor may be positive or negative; the overall effect depends on their coupling result. For the flowing system, it is also in connection with the behaviors of fluid dynamics.

8.12 Summary

The mass transferred from one phase to the adjacent phase must diffuse through the interface and subsequently produces interfacial effect. The behaviors of interfacial effect can be summarized briefly as follows:

1. From the molecular viewpoint, the transfer of mass at the interface is stochastic and subsequently produces local concentration difference Δc from which the surface tension difference $\Delta \sigma$ is also established so as to induce interfacial circulation; it is called Marangoni convection. Furthermore, due to the density at the interface is different from that of the bulk fluid by $\Delta \rho$, circulation between interface and the bulk fluid is also induced, which is called Rayleigh convection. Nevertheless, the creation of $\Delta \sigma$ may be also due to the interfacial local temperature difference ΔT and the $\Delta \rho$ may be achieved due to the temperature difference between interface and the bulk. Thus, there are ΔT-based besides Δc-based Marangoni convection and Rayleigh convection.
2. Generally speaking, the Marangoni convection exists at the interface and slightly underneath, while the Rayleigh convection appears between interface and the bulk. The coupling effect of these two convections may be positive (enhance mass transfer) or negative (suppress mass transfer). The enhancement factor may be up to above 5.
3. The intensity of Marangoni convection and Rayleigh convection can be represented by the Marangoni number Ma and Rayleigh number Ra. The onset of convection and orderly interfacial structure only when Ma and Ra reach its critical value Ma_{cr} and Ra_{cr}. When Ma and Ra number further increase to a certain extent, the system turns to stable at fully turbulence or chaos state.
4. The interface in most cases is not flat but deformed. Thus, the effect of crispation number Cr should be considered.

References

1. Marangoni C (1871) Ueber die ausbreitung der tropfeneiner flüssigkeit auf der oberflächeeineranderen. Ann Phys-Berlin 219(7):337–354
2. Sha Y, Cheng C, Yu KT (2003) Interfacial effect of mass and heat transfer. Prog Chem 15(1):9–11

3. Rayleigh L (1916) On the convection currents in a horizontal layer of fluid when the higher temperature is on the under side. Phil Mag 32:529–535

4. Bénard H (1901) Les tourbillons cellulaires dans une nappeliquide. Rerue Gén Sci Pures Appl 11:1261–1271

5. Yu YH (2003) Interfacial disturbance in gas liquid mass transfer process. MS dissertation, Tianjin University, Tianjin, China (in Chinese)

6. Yu YH, Sha Y, Cheng H (2003) Observation of interfacial structure on single component diffusion. Chem Eng J Chinese Univ 17(2):212–215 (in Chinese)

7. Yu LM (2005) The study of Marangoni effect on the gas liquid mass transfer process. PhD dissertation, Tianjin University, Tianjin, China (in Chinese)

8. Yu YH, Sha Y, Cheng H (2002) Observation of interfacial structure on binary mass transfer process. Chem Eng Prog 137–141 (in Chinese)

9. Yu LM, Zeng AW, Yu GC (2006) The effect of Marangoni convection in gas-liquid system. Trans Tianjin Univ 12(6):391–398

10. Sha Y (2002) Study on Rayleigh-Benard-Marangoni convection driven by the mass transfer, PhD dissertation, Tianjin University, Tianjin, China (in Chinese)

11. Sha Y, Chen H, Yu LH (2003) Stability analysis of falling film mass transfer process. Chem Eng J 54(10):1361–1368 (in Chinese)

12. Xiao FZ (1991) Stability of heat and mass transfer on a deformable gas-liquid interface. PhD dissertation, Tianjin University, Tianjin, China (in Chinese)

13. Sun ZF (1998) Study on the non-equilibrium phase transition in mass transfer process. PhD dissertation, Tianjin University, Tianjin, China (in Chinese)

14. Sun ZF, Yu KT (2002) Absorption and desorption of carbon dioxide in and from organic solvent: effects of Rayleigh and Marangoni instability. Ind Eng Chem Res 41:1905–1913

15. Zhou CF (2005) The influence of Marangoni effect on the mass transfer coefficient. MS dissertation, Tianjin University, Tianjin, China (in Chinese)

16. Zhang SH, Wang ZM, Su YF (1990) Mass transfer and interfacial turbulence in a laminar film/Study of transferring two solutes separately and simultaneously through liquid–liquid interface. Trans IChemE 68:84–92

17. Bird RB, Stewart WE, Lightfoot EN (1994) Transport phenomena. Wiley, New York

18. Yuen CK, Fraser D (1986) Digital spectral analysis. CSIRO/Pitman, Melbourne

19. Sha Y, Cheng H, Yuan XG, Yu KT (2003) Dynamics of mass transfer with Marangoni effect. Chem Eng J 54(11):1518–1523 (in Chinese)

20. Imaishi N, Suzuki Y, Hozawa M, Fujinawa K (1982) Interfacial turbulence in gas–liquid mass transfer. Intern Chem Eng 22:659–665

21. Brian PLT, Vivian JE, Mayr ST (1971) Cellular convection in desorbing surface tension-lowering solutes from water. Ind Eng Chem Fundam 10:75–83

22. Brian PLT, Ross JR (1972) The effect of Gibbs adsorption on Marangoni Instability in penetration mass transfer. AIChE J 18:582–591

23. Brian PLT, Smith KA (1972) Influence of Gibbs adsorption on oscillatory Marangoni instability. AIChE J 18:231–233

24. Hozawa M, Komatsu N, Imaishi N, Fujinawa K (1984) Interfacial turbulence during the physical absorption of carbon dioxide into non-aqueous solvents. J Chem Eng Japan 17:173–179

25. Golovin AA (1992) Mass transfer under interfacial turbulence: kinetic regularities. Chem Eng Sci 47:2069–2080

26. Golovin AA, Nepomnyashchy AA, Pismen LM (1995) Pattern formation in large-scale Marangoni convection with deformable interface. Physica D 81:117–147

27. Fujinawa K, Hozawa M, Imaishi N (1978) Effects of desorption and absorption of surface tension lowering solutes on liquid phase mass transfer coefficients at a turbulent gas-liquid interface. J Chem Eng Japan 11:107–111

28. Olander DR, Reddy LB (1964) The effect of concentration driving force on liquid–liquid mass transfer. Chem Eng Sci 19:67–73

29. Sawistowski H, Goltz GE (1963) The effect of interface phenomena on mass transfer rates in liquid–liquid extraction. Trans Instn Chem Engrs 41:174–181
30. Sun ZF, Yu KT (2006) Rayleigh-Bénard-Marangoni convection: expressions for heat and mass transfer rate. Chem Eng Res Des 84(A3):185–191
31. Sha Y, Hong C, Yu Y (2002) The numerical analysis of the gas-liquid absorption process accompanied by Rayleigh convection. Chin J Chem Eng 10(5):539–544
32. Chen W (2010) Experimental measurement of gas–liquid interfacial Rayleigh-Bénard-Marangoni convection and mass transfer. Ph.D. Thesis, Tianjin University, Tianjin, China
33. Zhang ZS, Cui GX, Xu CX (2005) Theory and modeling of turbulence. Tsinghua University Press, Beijing
34. Liu CX, Zeng AW, Yuan XG, Yu GC (2008) Experimental study on mass transfer near gas–liquid interface through quantitative Schlieren method. Chem Eng Res Des 86(2):201–207
35. Agble D, Mendes-Tatsis MA (2000) The effect of surfactants on interfacial mass transfer in binary liquid–liquid systems. Int J Heat Mass Tran 43(6):1025–1034
36. Agble D, Mendes-Tatsis MA (2001) The prediction of Marangoni convection in binary liquid–liquid systems with added surfactants. Int J Heat Mass Transfer 44:1439–1449
37. Scriven LE, Sternling CV (1964) On cellular convection driven by surface-tension gradients: Effects of mean surface tension and surface viscosity. J Fluid Mech 19(3):321–340
38. Scriven LE (1960) Dynamics of a fluid interface equation of motion for Newtonian surface fluids. Chem Eng Sci 12(2):98–108

Chapter 9
Simulation of Interfacial Behaviors by Lattice Boltzmann Method

Abstract In this chapter, the mesoscale computational methodology, Lattice Boltzmann Method (LBM), is introduced for the simulation of the interfacial Marangoni and Rayleigh effects as described and discussed in Chap. 8. The fundamentals of LBM are briefly introduced and discussed. By the simulation using the LBM, some mechanisms and phenomena of the interfacial effect are studied, including the patterns of the interfacial disturbance for inducing the interfacial convections, conditions of initiating interfacial instability and interfacial convection as well as the effect on interfacial mass transfer.

Keywords Lattice Boltzmann method · Simulation of interfacial mass transfer · Solutal-induced interfacial convection · Marangoni convection · Rayleigh convection

Nomenclature

A_i	Interfacial area, m^2
b	Number of particle streaming directions; number of discrete particle velocities
c	Lattice velocity, m/s
C	Solute concentration, kg/m^3
C_i	Interfacial solute concentration, kg/m^3
C_S	Saturation concentration, kg/m^3
C_0	Initial concentration of solute, kg/m^3
C_s	Sound velocity of simulated object, m/s
c_s	Sound speed of lattice model, m/s
c_k	Solute concentration of component k, kg/m^3
D_k	Mass diffusivity of component k, m^2/s
E	Internal energy, J
$\boldsymbol{e}_\alpha$	Discrete velocity ($\alpha = 1, 2, 3, …, b$), m/s
F	Volumetric external force, $kg\ m/s^2$
f_α	Distribution function
f_α^{eq}	Equilibrium distribution function

G_α	Concentration distribution function
G_α^{eq}	Equilibrium concentration distribution function
g	Internal energy density distribution function
$\boldsymbol{g}_0$	Gravitational force, kg m/s^2
H	Thickness of liquid, m
L	Characteristic length of simulated object, m
l	Characteristic length of lattice model, m
Ma	Marangoni number
n_α	Number of particles along direction α, 0, or 1
R	Gas constant, J/mol k
Ra	Rayleigh number
Re	Reynolds number
S	Source term
Sc	Schmidt number
T	Temperature, K
T_i	Temperature distribution function
T_i^{eq}	Equilibrium temperature distribution function
t	Time, s
U	Characteristic velocity of the simulated object, m/s
u^*	Macroscopic velocity in equilibrium distribution function, m/s
u	Macroscopic velocity, m/s
V	Volume of liquid, m^3
x	Space position
α	Thermal diffusivity, m^2/s
μ	Viscosity, kg/m s
μ_{t}	Turbulent viscosity, kg/m s
v	Kinematic viscosity, m^2/s
v^*	Kinematic viscosity of the simulated object, m^2/s
ρ	Macroscopic density, kg/m
σ	Ratio of specific heat between solid wall and fluid
τ	Single relaxation time
τ_0	Relaxation time, s
τ_{e}	Single relaxation time in internal energy distribution function
τ_{h}	Single relaxation time in heat transfer model
τ_{k}	Single relaxation time in mass transfer model
Ω	Collision operator
ω	Weight coefficient

In the foregoing chapters, the simulation is based on the macroscopic point of view that the fluid is continuous medium and its physical properties, such as density, velocity, and pressure, are functions of time and space. Thus, the Navier–Stokes equation can be employed as modeling equation in the mathematical simulation. In this chapter, we turn to the mesoscopic point of view and use the lattice Boltzmann

method (LBM) for simulating the interfacial phenomena. The LBM is based on such postulation that the fluid is composed of large number of particles which obey the law of mechanics and exhibit the macroscopic behaviors by means of statistical methodology. This method has been applied to various fields since the 1980s of last century.

In 1986, Frisch simulated the two-dimensional Navier–Stokes equation by using lattice gas automation and called it as lattice gas method [1]. At the same time, Wolfram used this method for simulating the flowing fluid behaviors [2]. Chen et al. [3] and Qian et al. [4] further developed this method by combining with the work of Bhatnager et al. [5] to establish a new method called lattice Boltzmann BGK method (LBGK), or simply LBM. This method has been received wide attention by the researchers and applied to multiphase flow, heat transfer, convection, reaction, and many other fields. The LBM is still developing and serving as a new method in the computational methodology.

In this chapter, the LBM is used for simulating the interfacial behaviors of mass transfer. The fundamentals of LBM are briefly introduced in subsequent section as the basic knowledge for understanding this method.

9.1 Fundamentals of Lattice Boltzmann Method

9.1.1 From Lattice Gas Method to Lattice Boltzmann Method

The lattice gas method was developed from cellular automaton for simulation purpose. Cellular automaton is a method that automatically repeats the designated process to approaching the desired goal. The simulation of flow field by lattice gas method is based on the viewpoint that the fluid is composed of large amount of microparticles with mass and zero volume. The macroscopic motion of the fluid is the result of the collective behaviors of the microparticles. The detail of mutual interaction of particles is not important as it influences only the fluid parameters and does not affect the mass, momentum, and energy conversation laws of the fluid. Thus, the lattice gas method is employing the model of simple regular particle motion for simulating the complicated real process.

The basic idea of lattice gas method is to discrete the fluid and its occupied space into lattices. The microparticle of fluid at the nodes of the lattice is moving synchronously to the neighboring node with velocity e_α ($\alpha = 1, 2, 3, \ldots, b$), where b represents the number of possible moving directions, including stationary (no direction). In each moving direction, either one particle or no particle is allowed. Since the particles at the neighboring nodes are moving toward the other nodes, collision of particles happens. Therefore, at the time interval Δt_1, the following events are appeared:

1. Streaming of particles: The particles at a node are moving to the neighboring nodes with velocity e_α;
2. Collision of particles: When different particles reach to the same node, collision happens and the moving direction is changed; such collision obeys the conservation laws of mass, momentum, and energy.

Following the next time interval Δt_2, the propagation of particle and collision are repeated; such cyclic evolution goes on again and again for all particles at increasing time intervals to realize the simulation of the fluid motion.

Let $n_\alpha(x, t)$ denote the number of particles at node x moving along α direction with velocity e_α within time interval Δt, the whole process can be expressed mathematically as follows:

$$n_\alpha(x + e_\alpha \Delta t, t + \Delta t) - n_\alpha(x, t) = \Omega_\alpha(x, t), \quad \alpha = 1, 2, 3, \ldots, b \tag{9.1}$$

where $\Omega_\alpha(x, t)$ is the collision term representing the rate of change of the particle distributions due to collisions. Some researchers, such as McNamara, used Fermi–Dirac distribution function f_α to replace n_α for simulating the flow pattern [6].

9.1.2 Basic Equations of Lattice Boltzmann Method

1. **The model equation**

The LBM is established on the basis of lattice gas method. The difference between them is that the LBM is dealing with average character of the particles in the system instead of single particle.

The Boltzmann equation, derived from molecular motion and collision, expresses the relationship between distribution function of molecular density f, time t, molecular velocity e, and space position x. In LBM, the molecule is considered to be the particle and the molecular velocity is identical with the particle velocity, and then, the Boltzmann equation can be written as follows:

$$\frac{\partial f}{\partial t} + e \cdot \nabla f = \Omega_C + \Phi \tag{9.2a}$$

where f is the distribution function of particles; e is the particle velocity; Ω_C is the collision term; and Φ represents the influence of external force (such as gravitational force) on f.

According to the H theorem and BGK model, the non-equilibrium system always tends to approach the state of equilibrium. Thus, the collision of particles can be considered as a process intended to reach the equilibrium state; the rate of the process approaching equilibrium is proportional to $\left[f_\alpha(x, t) - f_\alpha^{eq}(x, t)\right]$. The Ω_C can be expressed as follows:

$$\Omega_C(\pmb{x}, t) = -\frac{1}{\tau_0}\left[f_\alpha(\pmb{x}, t) - f_\alpha^{\text{eq}}(\pmb{x}, t)\right], \quad \alpha = 1, 2, 3, \ldots, b$$

where $f_\alpha(\pmb{x}, t)$ is the distribution function of single molecule, or the probability of a particle at node $\pmb{x}$ and time t moving along α direction with velocity $\pmb{e}_\alpha$; $f_\alpha^{\text{eq}}(\pmb{x}, t)$ is the f_α when equilibrium is reached; τ_0 is a proportionality constant with dimension of time, called relaxation time. In the LBM, Chen et al. [3, 7] and Qian et al. [4] employed Maxwell–Boltzmann distribution function to replace the Fermi–Dirac distribution function. Substituting foregoing equation to Eq. (9.2a) under the condition of no external force ($\Phi = 0$), the following equation is obtained:

$$\frac{\partial f}{\partial t} + \pmb{e} \cdot \nabla f = -\frac{1}{\tau_0}\left[f_\alpha(\pmb{x}, t) - f_\alpha^{\text{eq}}(\pmb{x}, t)\right] \tag{9.2b}$$

After discretization at Δt and distance x, the foregoing equation becomes

$$f_\alpha(\pmb{x} + \pmb{e}_\alpha \Delta t, t + \Delta t) - f_\alpha(x, t) = -\frac{1}{\tau_0/\Delta t}\left[f_\alpha(\pmb{x}, t) - f_\alpha^{\text{eq}}(\pmb{x}, t)\right]$$

or

$$f_\alpha(\pmb{x} + \pmb{e}_\alpha \Delta t, t + \Delta t) - f_\alpha(\pmb{x}, t) = -\frac{1}{\tau}\left[f_\alpha(\pmb{x}, t) - f_\alpha^{\text{eq}}(\pmb{x}, t)\right] \tag{9.3}$$

where τ is dimensionless proportional constant, $\tau = \frac{\tau_0}{\Delta t}$, called single relaxation time, which controls the rate of approach to equilibrium. Equation (9.3) is commonly called LBGK equation.

2. **The lattice model**

For the implementation of LBM to the simulation of fluid behavior, the simulated object should be firstly divided into lattice. The objective fluid is discrete and represented by the particles at the nodes. The two-dimensional (denoted by 2D) 9-direction (denoted by Q9) square lattice model is shown in Fig. 9.1.

The particle at the node may be moving toward any one of the nine directions as indicated in the figure including zero direction (stationary). At time interval Δt, the particle moves with velocity $\pmb{e}_\alpha$ ($\alpha = 0, 1, 2, 3, \ldots, 8$) to the neighboring nodes and collision happens. Let Δx be the length of the square lattice, and the ratio of $\frac{\Delta x}{\Delta t} = c$ is called lattice velocity. The ratio c can be letting $c = 1$ or $c = \sqrt{3RT} = \sqrt{3}c_s$ where R is gas constant, T is the absolute temperature, and $c_s = \sqrt{RT}$ is customarily called speed of sound (see Appendix 3). The particle velocity in the diagonal directions is $\sqrt{2}$ times that in x direction, the nine particle velocity $\pmb{e}_\alpha$ is given below:

$$\pmb{e}_\alpha = \begin{cases} (0, 0), & \alpha = 0 \\ \left[\cos\left(\frac{\alpha-1}{2}\pi\right)c, \ \sin\left(\frac{\alpha-1}{2}\pi\right)c\right], & \alpha = 1, 2, 3, 4 \\ \left[\sqrt{2}\cos\left(\frac{\alpha-5}{2}\pi + \frac{\pi}{4}\right)c, \ \sqrt{2}\sin\left(\frac{\alpha-5}{2}\pi + \frac{\pi}{4}\right)c\right], & \alpha = 5, 6, 7, 8 \end{cases} \tag{9.4}$$

Fig. 9.1 D2Q9 lattice model
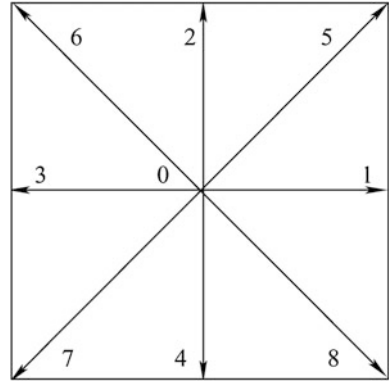
From statistical mechanics, the Maxwell–Boltzmann distribution function for single particle in equilibrium state can be expressed as follows:

$$f^{\text{eq}} = \frac{\rho}{(2\pi RT)^{D/2}} \exp\left[-\frac{(\boldsymbol{e} - \boldsymbol{u})^2}{2RT}\right] \tag{9.5}$$

where $\boldsymbol{u}$ is the macroscopic fluid velocity (vector) and ρ is the macroscopic density. Using Taylor expansion and Chapman–Enskog expansion technique, the equilibrium distribution function of single particle for D2Q9 lattice model is obtained as follows (see Appendix 2 or Ref. [4]).

$$f^{\text{eq}} = \rho\omega_\alpha\left[1 + \frac{\boldsymbol{e}_\alpha \cdot \boldsymbol{u}}{c_s^2} + \frac{(\boldsymbol{e}_\alpha \cdot \boldsymbol{u})^2}{2c_s^4} - \frac{\boldsymbol{u}^2}{2c_s^2}\right] \tag{9.6a}$$

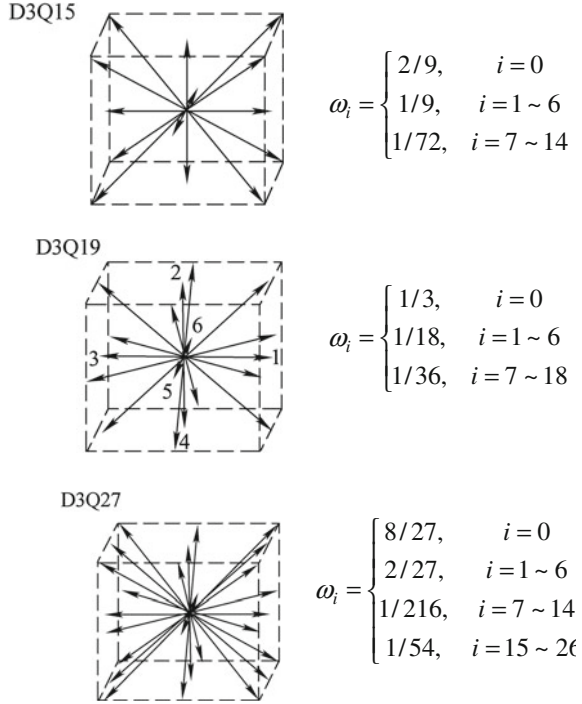where the weight coefficient ω_α is

$$\omega_\alpha = \begin{cases} \frac{4}{9}, & \alpha = 0 \\ \frac{1}{9}, & \alpha = 1, 2, 3, 4 \\ \frac{1}{36}, & \alpha = 5, 6, 7, 8 \end{cases}$$

The relationship between macroscopic quantities and f_α is as follows:

$$\rho = \sum_{\alpha=0}^{8} f_\alpha(\boldsymbol{x}, t)$$

$$\rho\boldsymbol{u} = \sum_{\alpha=0}^{8} \boldsymbol{e}_\alpha f_\alpha(\boldsymbol{x}, t) \tag{9.6b}$$

Besides two-dimensional lattice, there are many three-dimensional lattice models can be chosen as shown in Fig. 9.2 [8]. Three-dimensional lattice model has more discrete velocity to give more accurate simulation, yet the computer load becomes heavy and requires parallel computation.

Fig. 9.2 Several three-dimensional lattice models

D3Q15

$$\omega_i = \begin{cases} 2/9, & i = 0 \\ 1/9, & i = 1 \sim 6 \\ 1/72, & i = 7 \sim 14 \end{cases}$$

D3Q19

$$\omega_i = \begin{cases} 1/3, & i = 0 \\ 1/18, & i = 1 \sim 6 \\ 1/36, & i = 7 \sim 18 \end{cases}$$

D3Q27

$$\omega_i = \begin{cases} 8/27, & i = 0 \\ 2/27, & i = 1 \sim 6 \\ 1/216, & i = 7 \sim 14 \\ 1/54, & i = 15 \sim 26 \end{cases}$$

The suitability of using LBM to the simulation of fluid flow can be proofed by converting Eq. (9.3) to Navier–Stokes equation under some specified conditions (see Appendix 3 or Ref. [4, 9]). In other words, any fluid process, which can be modeled by Navier–Stokes equation, is suitable to use LBM for process simulation.

For D2Q9 lattice model, the following specified condition should be satisfied for applying LBM (see Appendix 3):

$$v = \frac{c^2 \Delta t}{3} \left(\tau - \frac{1}{2} \right) \tag{9.7}$$

where v is the kinematic viscosity and $v = \frac{\mu}{\rho}$ for lamina flow and $v = \frac{\mu + \mu_t}{\rho} \approx \frac{\mu_t}{\rho}$ for turbulent flow; $c = \sqrt{3RT}$. If v is known for the fluid concerned, the unknown parameter τ can be obtained by Eq. (9.7). Obviously, τ cannot be less than $\frac{1}{2}$.

3. **Boundary conditions**

There are several boundary conditions that can be chosen for the distribution function f under different conditions. The details can be found in Ref. [10–13].

(1) Bounce-back boundary condition
    This is the simplest condition by considering that the particle impacts the solid wall and bounces back with the same velocity but in opposite direction. If f and
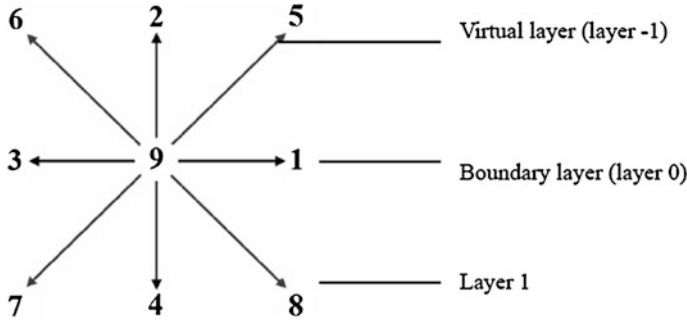
Fig. 9.3 Extended boundary layer

f' denote, respectively, the distribution function before and after the impact, then $f' = f$. This boundary condition is easy to apply, but the degree of accuracy is low.

(2) No slip boundary condition

Since the slip of particle appears during the impact to the wall, a negative distribution function f_{-1} is introduced to eliminate the effect of slip. The accuracy of simulation by this method is better than that by bounce-back.

(3) Extended boundary condition

Refer to Fig. 9.3, if the boundary of simulation is located on the line 391 (denoted as layer 0) and the underneath neighboring nodes of the fluid are 748 (denoted as layer 1), an virtual (extended) layer with nodes 625 (denoted as layer −1) is imagined, and then, the boundary nodes 391 are considered as the nodes of the fluid in the computation. The condition of the imaginary nodes may be bounce-back or others. Satisfactory accuracy is obtained by this method.

(4) Periodic boundary condition

In case of simulating flowing fluid, the periodic boundary condition is frequently used by considering that the distribution function in the inlet and outlet is equal.

4. **Procedure of computation**

(1) Select lattice model, for instance, D2Q9 and evaluate τ, Δx, Δt according to Eq. (9.7);

(2) Give the initial value of distribution function f_α, ρ, and u;

(3) Calculate equilibrium distribution function f_α^{eq} by Eq. (9.6a);

(4) Calculate the distribution function $f_\alpha(\boldsymbol{x}, t)$ for all nodes at time t and direction α;

(5) Calculate the new distribution function $f_\alpha(\boldsymbol{x} + \boldsymbol{e}_\alpha \Delta t,\ t + \Delta t)$ at $t + \Delta t$ by Eq. (9.3);

(6) According to the boundary conditions chosen, calculate the distribution function at the boundary;

(7) Renew ρ and u according to Eq. (9.6b) to be the initial value for next iteration. Go back to step (3) and repeat the procedure again and again until the simulation is satisfied.

5. **The lattice Boltzmann equation with external force**

In the presence of external force, its action on the molecules should be considered, and the Boltzmann equation can be expressed by one of the following form:

(1) Retaining the source term Φ

The Φ term in Eq. (9.2a) is retained and written as S_F in more general sense, that is,

$$\frac{\partial f}{\partial t} + \boldsymbol{e} \cdot \nabla f = \Omega_C + \boldsymbol{S}_F \tag{9.8a}$$

where $\boldsymbol{S}_F$ is the source term representing the action of external force in general. After discretization, Eq. (9.8b) becomes

$$f_\alpha(\boldsymbol{x} + \boldsymbol{e}_\alpha \Delta t, \ t + \Delta t) - f_\alpha(\boldsymbol{x}, t) = \Omega_\alpha(\boldsymbol{x}, t) + S_\alpha(\boldsymbol{x}, t), \quad \alpha = 1, 2, 3, \ldots, b \tag{9.8b}$$

Substituting the expression for $\Omega(\boldsymbol{x}, t)$, one yields

$$\begin{aligned} &f_\alpha(\boldsymbol{x} + \boldsymbol{e}_\alpha \Delta t, \ t + \Delta t) - f_\alpha(\boldsymbol{x}, t) \\ &= -\frac{1}{\tau} \left[f_\alpha(\boldsymbol{x}, t) - f_\alpha^{eq}(\boldsymbol{x}, t) \right] + S_\alpha(\boldsymbol{x}, t), \quad \alpha = 1, 2, 3, \ldots, b \end{aligned} \tag{9.9}$$

The source term $\boldsymbol{S}_F$ is evaluated for the specified object of simulation. For instance, He et al. [14] proposed a lattice Boltzmann model for simulating the influence of gravity on the non-ideal fluid, $\boldsymbol{S}_F$ was given below:

$$\boldsymbol{S}_F = -\frac{(\boldsymbol{e} - \boldsymbol{u}) \cdot (\boldsymbol{F}_e + \boldsymbol{g}_0)}{\rho RT} f^{eq}$$

where $\boldsymbol{F}_e$ is the effective intermolecular acting force; $\boldsymbol{g}_0$ is the gravitational force and R is a gas constant.

Another example is the model proposed by Dixit for simulating the high Reynolds number convection created by heating, where the source term $\boldsymbol{S}_F$ is given below [15]:

$$\boldsymbol{S}_F = \frac{\boldsymbol{F} \cdot (\boldsymbol{e} - \boldsymbol{u})}{RT} f^{eq}$$

where $\boldsymbol{F}$ is the external force acting on the system per unit mass, which is related to many factors, such as density, coefficient of thermal expansion, and local and average temperature of the system concerned.

(2) Modifying the particle velocity

The external force per unit volume $\left(\frac{1}{m^3} \frac{kg\,m}{s^2}\right)$ acting on the particle can be expressed by $F = \rho \frac{u^*-u}{\tau_0} = \rho \frac{u^*-u}{\tau \Delta t}$, where u^* and u are, respectively, the particle velocity in the equilibrium distribution function after and before modification and ρ is the density of the particle. The modified u^* is expressed as follows:

$$u^* = u + \frac{F\tau}{\rho}\Delta t$$

6. **The scale-up of lattice Boltzmann model**

The simulated object generally is in large scale, such as the fluid behaviors in industrial equipment. Nevertheless, the dimension of lattice Δx is very small, and the number of lattices for the full-scale simulation is tremendous to make the computer load too heavy. In practice, the model equations are established aiming to the reduced size of the equipment and then use the principle of similarity to adjust the parameters in the model so that the simulated results are applicable to the large dimension equipment.

For example, let L, U, and v^* are, respectively, the characteristic length, velocity, and turbulent viscosity of the large simulated object, and l, u, and v are the corresponding parameters of the small-scale lattice model. The Reynolds number for the simulated object (large scale) is then given by $Re = \frac{LU}{v^*}$. By letting the corresponding Reynolds number of the lattice Boltzmann model (small scale) Re' be equal to Re, or $\frac{LU}{v^*} = \frac{lu}{v}$, then we have $v = v^* \frac{l}{L} \cdot \frac{u}{U}$, in which the velocity ratio $\frac{u}{U}$ can be considered equal to the ratio of sound speeds $\frac{c_s}{C_s}$, and then the viscosity of lattice Boltzmann simulation model should be modified to:

$$v' = v^* \frac{l}{L} \cdot \frac{c_s}{C_s}$$

where c_s and C_s are, respectively, the speed of sound at lattice Boltzmann model and that at the actual object; the ratio C_s/c_s can be set equal to 1. By using v' instead v in the lattice Boltzmann model, the simulated results are applicable to the behaviors of the large object at the Reynolds number Re.

It should be emphasized that the similarity principle is not applicable to more than one dimensionless group. For instance, under the condition of Re, it is equal for both the object and model simulation, and the corresponding dimensionless group Eu may not be equal. Therefore, only the dominated dimensionless group is used to modify the scaling-up simulation. Obviously, the application of such method of scale-up is restricted.

9.1.3 Lattice Boltzmann Method for Heat Transfer Process

1. Scalar temperature model

The discrete LBGK equation for heat transfer can be expressed below if the source term is ignored [16]:

$$T_\alpha(\boldsymbol{x} + \boldsymbol{e}_\alpha \Delta t, t + \Delta t) - T_\alpha(\boldsymbol{x}, t) = -\frac{1}{\tau_h}\left[T_\alpha(\boldsymbol{x}, t) - T_\alpha^{\text{eq}}(\boldsymbol{x}, t)\right] \tag{9.10}$$

where T_α is the temperature distribution function and τ_h is the single relaxation time for heat transfer. The equilibrium T_α is given below:

$$T_\alpha^{\text{eq}} = \omega_\alpha T \left[\frac{\boldsymbol{e}_\alpha \cdot \boldsymbol{u}}{c_s^2} + \sigma\right]$$

where $\boldsymbol{e}_\alpha$ and ω_α for D2Q9 model are referred to Eq. (9.6a) with lattice velocity $c = \frac{\Delta x}{\Delta t} = \sqrt{3RT} = \sqrt{3}c_s$. The τ_h is calculated by

$$\alpha = \sigma c_s^2 \left(\tau_h - \frac{1}{2}\right)\Delta t$$

where α is thermal diffusivity. The simulated temperature and velocity distributions of the process can be obtained by solving simultaneously Eq. (9.10) with fluid dynamic Eqs. (9.9) and (9.6a).

2. Heat energy model

He proposed a model considering the heat energy, and heat flux can be expressed in terms of internal energy distribution function [17]. On this basis, Dixit suggested a simplified model [15], in which the internal energy distribution function is given by

$$g(\boldsymbol{x}, \boldsymbol{e}, t) = \frac{(\boldsymbol{e} - \boldsymbol{u})^2}{2} f$$

The internal energy is calculated by

$$E(\boldsymbol{x}, t) = \frac{1}{\rho(\boldsymbol{x}, t)} \int g(\boldsymbol{x}, \boldsymbol{e}, t)\mathrm{d}\boldsymbol{e}$$

Similar to the Boltzmann equation, the equation of internal energy can be expressed in the form of approaching to the equilibrium as follows:

$$\frac{\partial g}{\partial t} + \boldsymbol{e} \cdot \nabla g = -\frac{g - g^{\text{eq}}}{\tau_e}$$

where τ_e is the single relaxation time for internal energy distribution function.

The foregoing equation can be discrete as follows:

$$g_\alpha(\boldsymbol{x} + \boldsymbol{e}_\alpha \Delta t, t + \Delta t) - g_\alpha(\boldsymbol{x}, t) = -\frac{1}{\tau_e} \left[g_\alpha(\boldsymbol{x}, t) - g_\alpha^{\text{eq}}(\boldsymbol{x}, t) \right] \tag{9.11}$$

For D2Q9 model, the g_α^{eq} is given by

$$g_\alpha^{\text{eq}} = \begin{cases} -\frac{2}{3} \rho E \frac{\boldsymbol{u}^2}{RT}, & \alpha = 0 \\ \frac{\rho E}{9} \left[\frac{3}{2} + \frac{3 \boldsymbol{e}_\alpha \cdot \boldsymbol{u}}{2RT} + \frac{9 (\boldsymbol{e}_\alpha \cdot \boldsymbol{u})^2}{4(RT)^2} - \frac{3 \boldsymbol{u}^2}{2RT} \right], & \alpha = 1, 2, 3, 4 \\ \frac{\rho E}{36} \left[3 + 6 \frac{\boldsymbol{e}_\alpha \cdot \boldsymbol{u}}{RT} + \frac{9 (\boldsymbol{e}_\alpha \cdot \boldsymbol{u})^2}{2(RT)^2} - \frac{3 \boldsymbol{u}^2}{2RT} \right], & \alpha = 5, 6, 7, 8 \end{cases}$$

The macroscopic quantities are calculated by

$$\rho = \sum_\alpha f_\alpha$$

$$\rho \boldsymbol{u} = \sum_\alpha \boldsymbol{e}_\alpha f_\alpha$$

$$\rho E = \sum_\alpha g_i$$

For the calculation of τ_e, He and Dixit gave the following equation [15] for D2Q9 lattice model:

$$\alpha = \frac{2}{3} c^2 \left(\tau_e - \frac{1}{2} \right) \Delta t = 2 c_s^2 \left(\tau_e - \frac{1}{2} \right) \Delta t$$

where $c = \sqrt{3RT}$; $c_s = \sqrt{RT}$.

The simulated temperature and velocity distributions of the heat transfer process can be obtained by simultaneous solution of Eq. (9.11) and fluid dynamic Eqs. (9.9) and (9.6a).

9.1.4 Lattice Boltzmann Method for Mass Transfer Process

The following mass transfer (species conservation) equation can be derived from lattice Boltzmann equation after Chapman–Enskog expansion [18] (also see Appendix 3).

$$\frac{\partial c_k}{\partial t} + \boldsymbol{u} \frac{\partial c_k}{\partial x_i} = \frac{\partial}{\partial x_i} \left(D_k \frac{\partial c_k}{\partial x_i} \right)$$

where c_k is the concentration of component species k and D_k is the diffusivity of species k. Thus, the LBM is applicable to the simulation of mass transfer process.

The foregoing equation can be discrete as follows:

$$G_\alpha^k(\boldsymbol{x} + \boldsymbol{e}_\alpha \Delta t, t + \Delta t) - G_\alpha^k(\boldsymbol{x}, t) = -\frac{1}{\tau_k}\left[G_\alpha^k(\boldsymbol{x}, t) - G_\alpha^{k,\mathrm{eq}}(\boldsymbol{x}, t)\right] + \boldsymbol{S}_\alpha^k \qquad (9.12)$$

where G_α^k is the concentration distribution function of component species k; τ_k is the single relaxation time for the mass transfer; and $\boldsymbol{S}_\alpha^k$ is the source term for component species k. It is noted that the foregoing equation can be written for each component species.

For the mass transfer process accompanied with chemical reaction, each mode can be considered as a complete mixing reactor, and the concentration change in component species k at Δt can be calculated from the equation of reaction kinetics. The $G_\alpha^{k,\mathrm{eq}}$ is given below for D2Q9 model:

$$G_\alpha^{k,\mathrm{eq}} = \omega_\alpha c_n \left[1 + \frac{\boldsymbol{e}_\alpha \cdot \boldsymbol{u}}{RT} + \frac{(\boldsymbol{e}_\alpha \cdot \boldsymbol{u})^2}{2(RT)^2} - \frac{u^2}{2RT}\right]$$

The concentration of component species k is calculated by

$$c_k = \sum_\alpha G_\alpha^k$$

The relaxation time τ_k, which is related to D_k, can be determined by the relationship:

$$D_k = c_s^2 \left(\tau_k - \frac{1}{2}\right)\Delta t$$

The concentration distributions of component species k and the fluid velocity can be obtained by the simultaneous solution of Eq. (9.12) and fluid dynamic Eqs. (9.9) and (9.6a).

9.2 Simulation of Solute Diffusion from Interface to the Bulk Liquid

The simulated object is the absorption of CO_2 through horizontal interface in a container by the ethanol as shown in Fig. 9.4.

The density difference between interface and the bulk liquid is considered as external force F. The influence of the external force on the simulation by LBM is realized by modifying macroscopic velocity $\boldsymbol{u}$ by $\boldsymbol{u}^*$ as follows:

$$\boldsymbol{u}^* = \boldsymbol{u} + \frac{\boldsymbol{F}\tau}{\rho}\Delta t = \boldsymbol{u} + \frac{\left(\frac{\partial \rho}{\partial c_k}\right)(c_{k,i} - c_k)\boldsymbol{g}}{\rho}\tau\Delta t$$
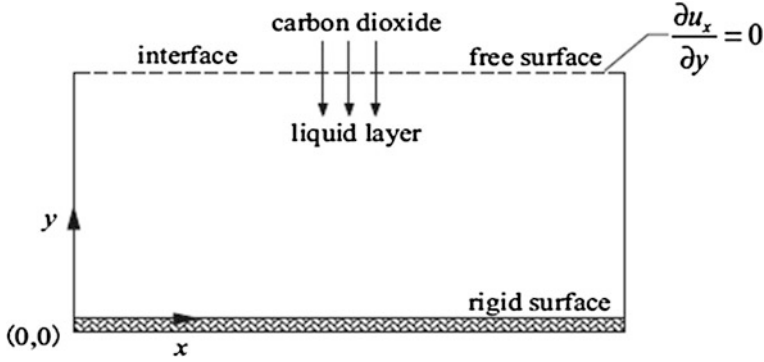
Fig. 9.4 Simulation domain of Rayleigh convection

where $c_{k,i}$ and c_k are, respectively, the concentration of component species k at the interface and in the bulk liquid.

The model equations are shown below:

The LBGK equation for solvent particles:

$$f_\alpha(\boldsymbol{x} + \boldsymbol{e}_a \Delta t, t + \Delta t) - f_\alpha(\boldsymbol{x}, t) = -\frac{1}{\tau}\left[f_\alpha(\boldsymbol{x}, t) - f_\alpha^{eq}(\boldsymbol{x}, t)\right], \quad \alpha = 0, 1, 2, \ldots, 8$$

$$f_\alpha^{eq} = \omega_\alpha \rho \left[1 + \frac{\boldsymbol{e}_\alpha \cdot \boldsymbol{u}^*}{RT} + \frac{(\boldsymbol{e}_\alpha \cdot \boldsymbol{u}^*)^2}{2(RT)^2} - \frac{\boldsymbol{u}^{*2}}{2RT}\right]$$

$$\rho = \sum_{\alpha=0}^{8} f_\alpha(\boldsymbol{x}, t)$$

$$\rho \boldsymbol{u}^* = \sum_{\alpha=0}^{8} \boldsymbol{e}_\alpha f_\alpha(\boldsymbol{x}, t) + \tau_0 \boldsymbol{F}$$

$$v = c_s^2 \left(\tau - \frac{1}{2}\right) \Delta t$$

The LBGK equation for solute particles:

$$G_\alpha^k(\boldsymbol{x} + \boldsymbol{e}_\alpha \Delta t, t + \Delta t) - G_\alpha^k(\boldsymbol{x}, t) = -\frac{1}{\tau_n}\left[G_\alpha^k(\boldsymbol{x}, t) - G_\alpha^{k,eq}(\boldsymbol{x}, t)\right], \quad \alpha = 0, 1, 2, \ldots, 8$$

$$G_\alpha^{k,eq} = \omega_\alpha c_n \left[1 + \frac{\boldsymbol{e}_\alpha \cdot \boldsymbol{u}^*}{RT} + \frac{(\boldsymbol{e}_\alpha \cdot \boldsymbol{u}^*)^2}{2(RT)^2} - \frac{\boldsymbol{u}^{*2}}{2RT}\right]$$

$$c^k = \sum_\alpha G_\alpha^k$$

$$D_k = c_s^2 \left(\tau_k - \frac{1}{2}\right) \Delta t$$

The profiles of concentration and velocity of the gas–liquid interfacial diffusion process can be obtained by the simultaneous solution of the model equations.

Boundary conditions

The bounce-back boundary condition is applied to the solid bottom of the container, and the bounce-back or periodic boundary conditions can be employed to the left and right walls according to the model condition.

In the gas–liquid mass transfer process, such as absorption, the interface can be considered as composed of numerous numbers of local solute concentration points. Due to the fluctuation of solute concentration and stochastic local absorption, the interfacial solute concentration cannot be remained uniform and inevitably appear as some local points with higher solute concentration. For instance, in the gas absorption process, some solvent points at the gas–liquid contacting interface may absorb the solute prior to the others to form higher solute concentration so as to create solute concentration gradient. The higher solute concentration point diffuses instantly from interface to the bulk liquid, and at the same time, the solute concentration is being lowered. If the depleted solute is not renewed in time, the priority of diffusion will shift to the neighboring point with higher solute concentration. The diffusion of interfacial local solute points is thus competitive and stochastic.

The appearance of solute concentration gradient at interface (as well as the accompanied surface tension, density, and temperature gradients) may produce interfacial instability or disturbance, by which Marangoni and Rayleigh convections are induced; the former is acting mainly around the interface and the latter between the interface and the bulk liquid. Thus, the description of concentration distribution at interface, which may be regarded as interface model, should be designated, for which the following models are given in subsequent sections.

- Fixed point interfacial disturbance model
- Random point interfacial disturbance model
- Self-renewable interface model

9.3 Fixed Point Interfacial Disturbance Model

The gas–liquid mass transfer process of CO_2 absorbed by quiescent ethanol is Rayleigh unstable ($Ra > 0$) and Marangoni stable ($Ma < 0$). The absorption process is initiated at some local points to create concentration gradient at the interface and also establish the density gradient between interface and the bulk liquid. Thus, the condition of specified disturbance points (higher concentration points) at the interface is necessary as shown in the following sections.

Table 9.1 Physical properties of solute and solvent

$v/(m^2\ s^{-1})$	$D_k/(m^2\ s^{-1})$	$\rho/(kg\ m^{-3})$	$c_{sat}/(kg\ m^{-3})$	$\partial\rho/\partial C$	Sc	Ra
1.52×10^{-6}	3.42×10^{-9}	788.9	5.15	0.214	444.44	3.19×10^5

Note v is the kinematic viscosity of ethanol; D_k is the diffusivity of CO_2 in ethanol; C is the concentration of CO_2 in ethanol; c_{sat} is the saturated concentration of CO_2 in ethanol; ρ is the density of ethanol

9.3.1 Single Local Point of Disturbance at Interface

The study of local single point diffusion is helpful to understand the development of mass transfer from gas to the liquid phase. Fu employed LBM to investigate the point diffusion process of solute from interface to the bulk liquid and the influence by Rayleigh convection [19]. The object of simulation is the absorption of CO_2 (solute) by ethanol (solvent) in a container (Table 9.1).

Assumptions:

1. The gas-phase resistance of mass transfer is neglected, and the diffusion is liquid film control. The liquid phase is pure ethanol;
2. The absorption is low, and the heat of absorption can be neglected;
3. The interface is horizontal and flat without deformation.

The simulated domain is 5×5 mm square flow field with 100×100 grids. Extended boundary condition is applied to the upper gas–liquid interface; periodic and bounce-back boundary conditions are chosen, respectively, for the two side walls and solid bottom. The simulated scale is $\Delta x = 5 \times 10^{-5}$ m and $\Delta t = 5 \times 10^{-5}$ s. An uniform distributed higher solute concentration is set in the width of 1 mm at the interface at $t = 0$. During the diffusion process, both Marangoni and Rayleigh convections are simultaneously coupling; the former is created at the surface, and the latter is formed perpendicular to the interface. Figure 9.5 shows the simulated results at different times:

Figure 9.5 shows at $t = 1$ and $t = 5$ s the solute diffuse freely from the concentrated point, and no Rayleigh convection is found in the vertical direction. At $t = 10$ s, the solute diffusion cell is squeezed by the newborn Rayleigh convection to form cylindrical shape. Later at $t = 20$ s, the further influence by the two symmetrical Rayleigh convections (see Fig. 9.6) is obvious, which squeeze the diffusion cell to the shape of inverted mushroom with long rod. Afterward, the circulating Rayleigh convections become stronger and lead the mushroom top to be in anchor shape. Figure 9.6 displays clearly the symmetrical Rayleigh convection, and it moves gradually downward with stronger circulation.
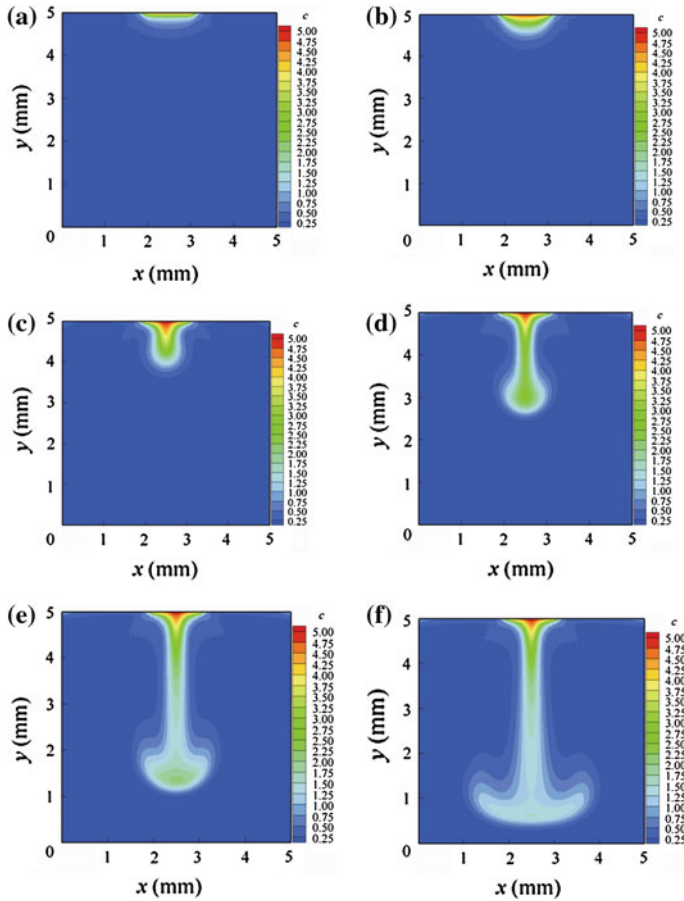
Fig. 9.5 Solute distribution profile at different times **a** $t = 1.0$ s, **b** $t = 5.0$ s, **c** $t = 10$ s, **d** $t = 15$ s, **e** $t = 20$ s, and **f** $t = 25$ s

9.3.2 Influence of Physical Properties on the Solute Diffusion from Interface

Under the conditions of fixed interfacial local point of disturbance and linear relationship between concentration and density, the influence of kinematic viscosity and diffusivity of solute on the interfacial diffusion was studied by Fu et al. [20].

The simulated conditions (size of simulated object, grid network, and interfacial concentration) are identical with Sect. 9.3.1 except the physical properties as given in Table 9.2. The simulated profiles of solute concentration at $t = 20$ s and $t = 30$ s for various physical properties of solvent are shown in Figs. 9.7 and 9.8.

Figures 9.7 and 9.8 indicate that at constant v and increasing D_k, the solute diffusion is intensified by Rayleigh convection. At constant D_k and increasing v,
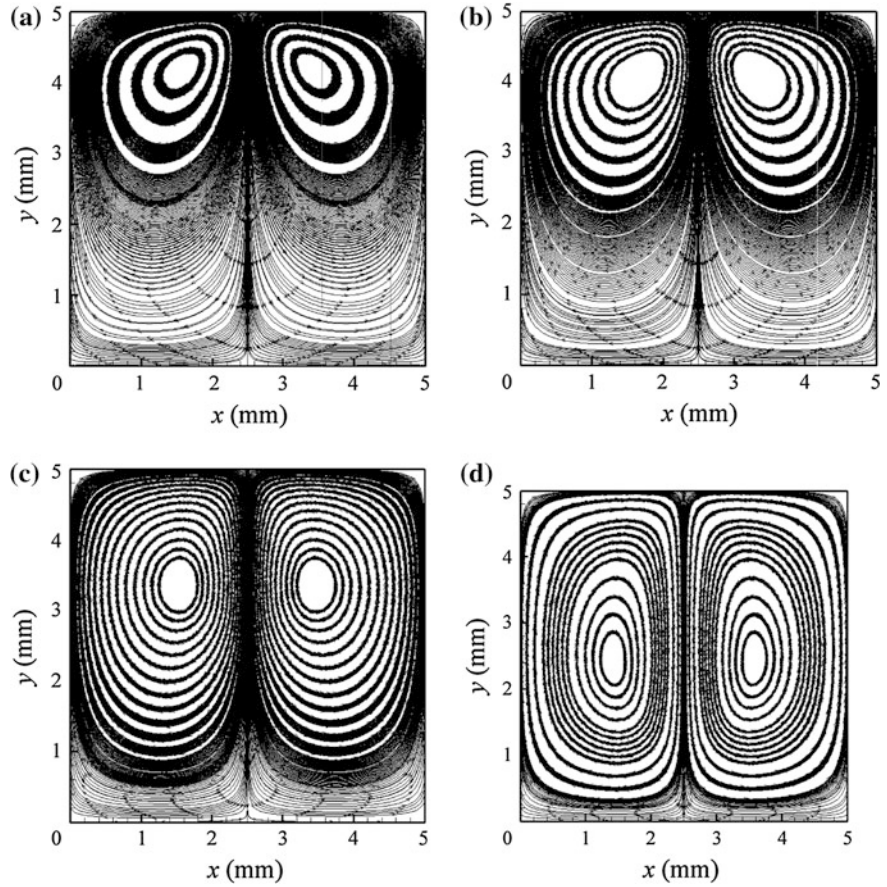
Fig. 9.6 Contours of Rayleigh convection at different times. **a** $t = 5$ s, **b** $t = 10$ s, **c** $t = 15$ s, and **d** $t = 20$

Table 9.2 Different conditions of simulation

Serial marks	v (m^2/s)	D_k (m^2/s)	$\partial\rho/\partial C$	ρ (kg/m^3)	Sc	Ra
a	2×10^{-6}	1×10^{-9}	0.214	1,000	2,000.0	6.55×10^5
b	2×10^{-6}	2×10^{-9}	0.214	1,000	1,000.0	3.28×10^5
c	2×10^{-6}	3×10^{-9}	0.214	1,000	666.7	2.18×10^5
d	2×10^{-6}	4×10^{-9}	0.214	1,000	500.0	1.64×10^5
e	1×10^{-6}	2×10^{-9}	0.214	1,000	500.0	6.55×10^5
f	3×10^{-6}	2×10^{-9}	0.214	1,000	1,500.0	2.18×10^5
g	4×10^{-6}	2×10^{-9}	0.214	1,000	2,000.0	1.64×10^5

the Rayleigh convection is depressed. Also, in Fig. 9.8, by comparing (d, $Sc = 500$) and (g, $Sc = 2,000$) at constant Ra, the solute diffusion is stronger at smaller Sc number. On the other hand, by comparing (a, $Ra = 6.55 \times 10^5$) and
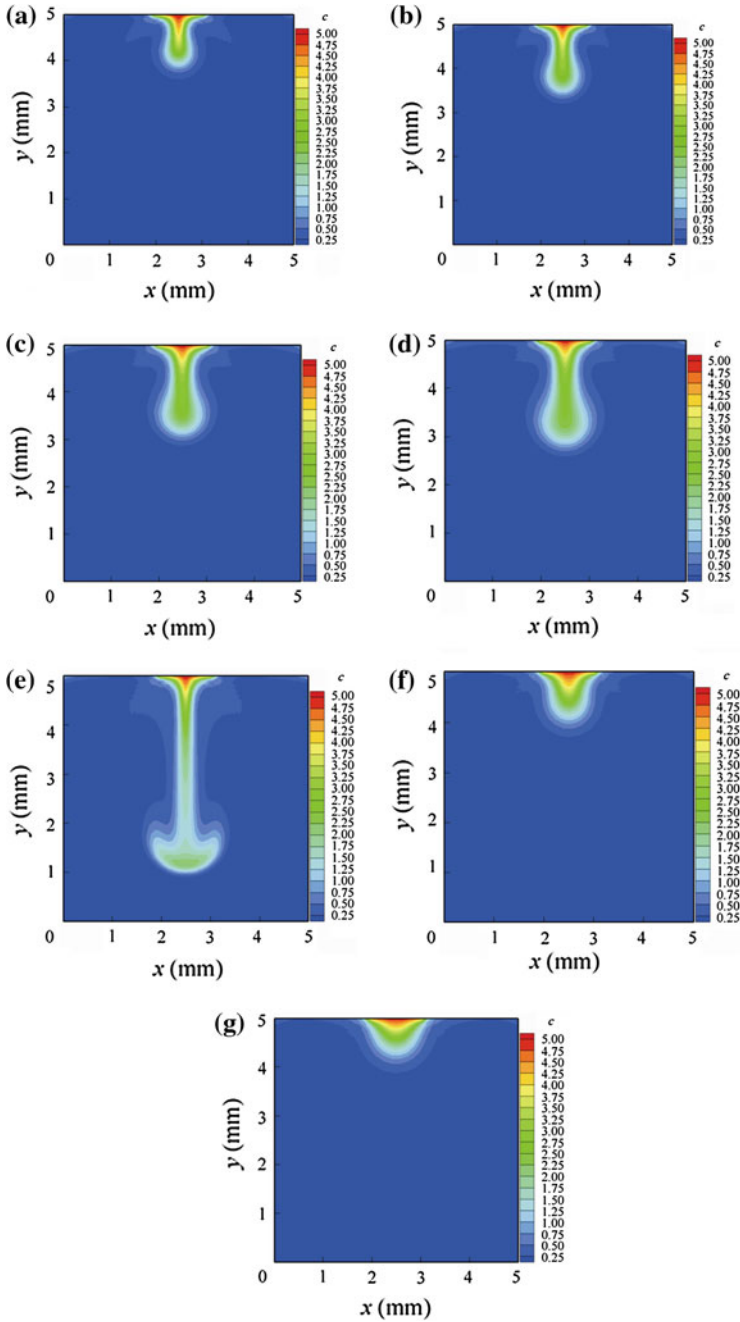
Fig. 9.7 The solute concentration profiles under different diffusivities (**a–d**) and kinematic viscosities (**e–g**) at $t = 20$ s **a** $v = 2 \times 10^{-6}$ m^2 s^{-1} $D_k = 1 \times 10^{-9}$ m^2 s^{-1}, **b** $v = 2 \times 10^{-6}$ m^2 s^{-1}, $D_k = 2 \times 10^{-9}$ m^2 s^{-1}, **c** $v = 2 \times 10^{-6}$ m^2 s^{-1}, $D_k = 3 \times 10^{-9}$ m^2 s^{-1}, **d** $v = 2 \times 10^{-6}$ m^2 s^{-1}, $D_k = 4 \times 10^{-9}$ m^2 s^{-1}, **e** $v = 1 \times 10^{-6}$ m^2 s^{-1}, $D_k = 2 \times 10^{-9}$ m^2 s^{-1}, **f** $v = 3 \times 10^{-6}$ m^2 s^{-1}, $D_k = 2 \times 10^{-9}$ m^2 s^{-1}, and **g** $v = 4 \times 10^{-6}$ m^2 s^{-1}, $D_k = 2 \times 10^{-9}$ m^2 s^{-1}

Fig. 9.8 The solute concentration profiles under different diffusivities (**a–d**) and kinematic viscosities (**e–g**) at $t = 30$ s **a** $v = 2 \times 10^{-6}$ m^2 s^{-1} $D_k = 1 \times 10^{-9}$ m^2 s^{-1}, **b** $v = 2 \times 10^{-6}$ m^2 s^{-1}, $D_k = 2 \times 10^{-9}$ m^2 s^{-1}, **c** $v = 2 \times 10^{-6}$ m^2 s^{-1}, $D_k = 3 \times 10^{-9}$ m^2 s^{-1}, **d** $v = 2 \times 10^{-6}$ m^2 s^{-1}, $D_k = 4 \times 10^{-9}$ m^2 s^{-1}, **e** $v = 1 \times 10^{-6}$ m^2 s^{-1}, $D_k = 2 \times 10^{-9}$ m^2 s^{-1}, **f** $v = 3 \times 10^{-6}$ m^2 s^{-1}, $D_k = 2 \times 10^{-9}$ m^2 s^{-1}, and **g** $v = 4 \times 10^{-6}$ m^2 s^{-1}, $D_k = 2 \times 10^{-9}$ m^2 s^{-1}

Fig. 9.9 The transient contours of solute concentration at $t = 30$ s for different n ($P = 10^{-4}$, $\beta = 10^{-8}$) **a** $n = 2$, **b** $n = 3$, **c** $n = 4$, **d** $n = 6$, **e** $n = 7$, **f** $n = 8$, **g** $n = 13$, **h** $n = 15$, and **i** $n = 19$

(g, $Ra = 1.64 \times 10^5$) at constant Sc, the Rayleigh convection is promoted by greater Ra number.

9.3.3 Uniformly Distributed Multipoints of Disturbance at Interface

Similar to Sect. 9.3.1, Fu simulated the absorption of CO_2 by ethanol with 19 points of disturbance at the interface [20]. The periodic boundary condition is employed for the left and right sides of the container with $\Delta x = 1 \times 10^{-4}$ m and $\Delta t = 1 \times 10^{-4}$ s. Figure 9.9 shows the solute distribution profiles at $t = 30$ s for $n = 1, 2, 3, 4, 5, 7, 9, 19$.

In Fig. 9.9, when the number of concentration points is small ($n < 5$), the concentration profile is clearly in anchor shape. When the number of concentration points is larger ($n < 5$), the diffusion at the center of interface is suppressed and restricted to a small region by the strong upward symmetrical Rayleigh convection as shown in Fig. 9.8d. When the concentration point is further increased ($n = 19$), the diffusion at the central part of interface is almost stopped by the Rayleigh convection and only appeared round the region near the wall.

Figure 9.10 displays the velocity vector diagram of $n = 5$ at different times. At $t = 1$ s, small convection is seen at every designated interfacial points.
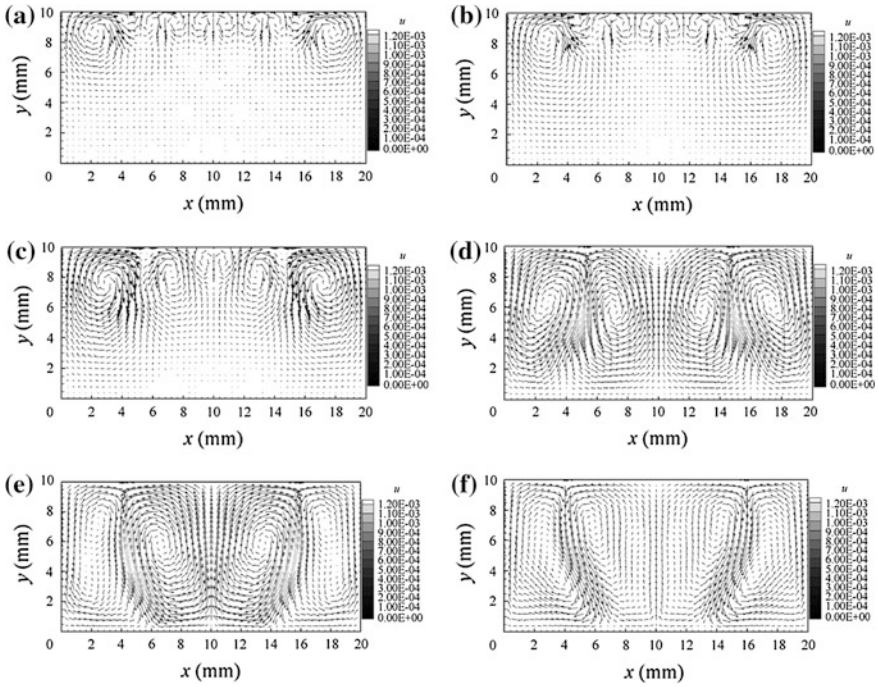
Fig. 9.10 Velocity vector diagram for $n = 5$ at different times. **a** $t = 1$ s, **b** $t = 10$ s, **c** $t = 20$ s, **d** $t = 30$ s, **e** $t = 40$ s, and **f** $t = 50$ s

At $t = 10$ s, Rayleigh convection structure is appeared. At $t = 30$ s, strong Rayleigh convection is clearly seen with the tendency to develop large convection.

If n is very large to approach infinity, which means the solute concentration is remained constant at interface, the progress of diffusion is shown in Fig. 9.11.

As shown in Fig. 9.11a and b, the interfacial disturbance starts firstly around the two sides of container wall, and it may be due to the numerical perturbation in model computation. However, following the Rayleigh convection, the solute concentration there is being lowered, and concentration gradient is created with the neighboring points so as to induce more Rayleigh convections as shown in Fig. 9.11c. After that, four mushroom-type convections are formed toward the bottom and soon combined to large convective flow as shown in Fig. 9.11h–l. It demonstrates that the large Rayleigh convection is created from the mutual interaction between small convections; such phenomenon is consistent with the experimental observation.
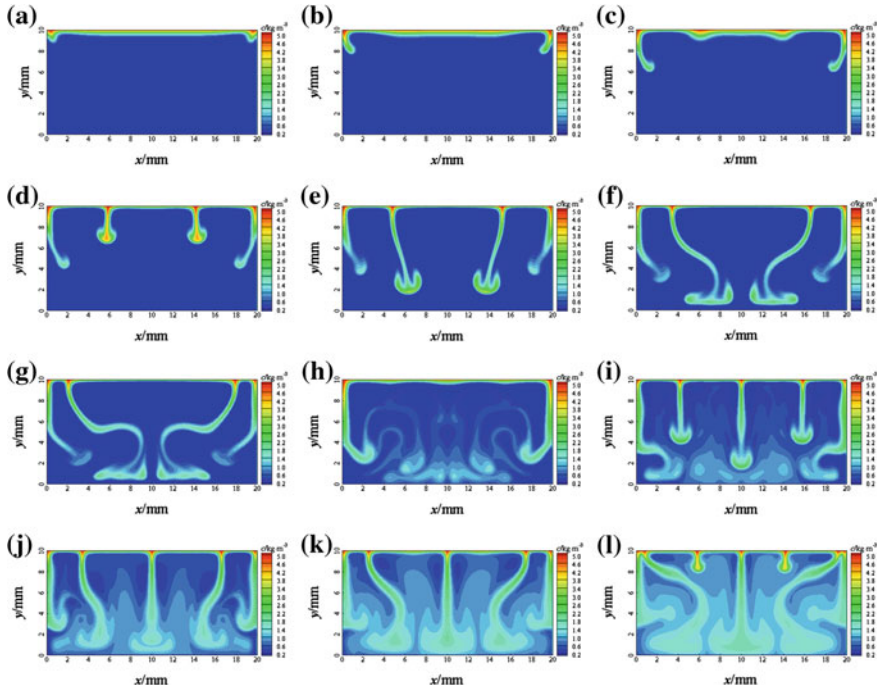
Fig. 9.11 The transient contours of solute concentration for $n = \infty$ at different times **a** $t = 40$ s, **b** $t = 20$ s, **c** $t = 30$ s, **d** $t = 35$ s, **e** $t = 40$ s, **f** $t = 45$ s, **g** $t = 50$ s, **h** $t = 70$ s, **i** $t = 90$ s, **j** $t = 110$ s, **k** $t = 130$ s, and **l** $t = 150$ s

9.3.4 Non-uniformly Distributed Multipoints of Disturbance at Interface

In the case that the distribution of local disturbance points is non-uniform, Figs. 9.12 and 9.13 show separately the concentration and velocity profiles for $n = 1$ and unevenly distributed $n = 2$ and $n = 3$ at $t = 35$ s.

As shown in Fig. 9.12, similar to the previous section, the shape of concentration profile is significantly influenced by the position of local points as well as Rayleigh convection and the wall effect. In Fig. 9.12c and d, the position of the three local points is different, so as to show different concentration profiles. The influence of Rayleigh convection and wall effect on the concentration profiles is also clearly seen by the velocity profiles as shown in Fig. 9.13. The renewal of interfacial concentration is demonstrated in these figures by the convective circulation of the outer velocity contour of Rayleigh convection.
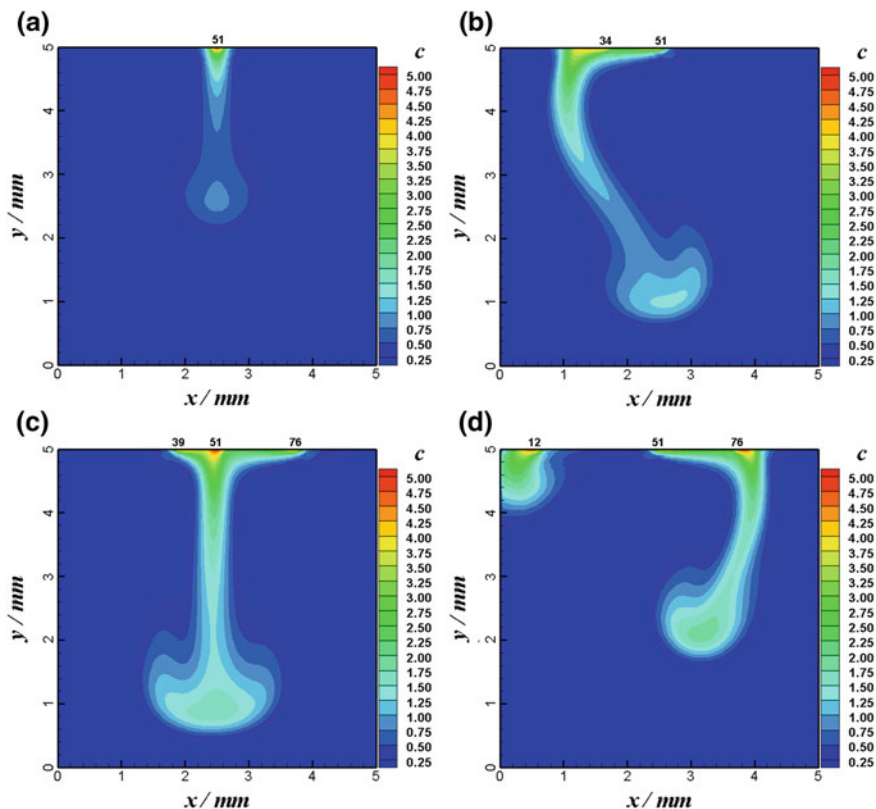
Fig. 9.12 Solute concentration profile for $n = 1$ and unevenly distributed $n = 2$ and $n = 3$ at $t = 35$ s **a** $n = 1$, **b** $n = 2$, **c** $n = 3$, and **d** $n = 3$
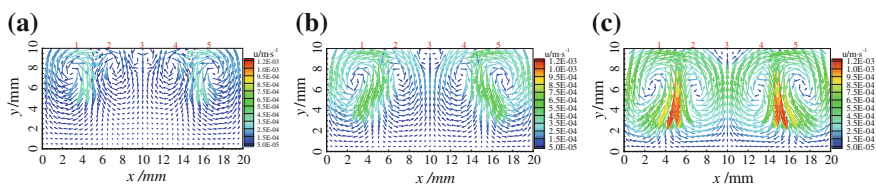

Fig. 9.13 The transient velocity vector distributions of flow field for $n = 5$ (uniformly distributed) at different times **a** $t = 20$ s, **b** $t = 25$ s, and **c** $t = 30$ s

9.4 Random Disturbance Interfacial Model

Fu [21] proposed a random disturbance model by using P to represent the probability of concentration point at the interface with concentration higher than the average, denoted by C_D, and their suitable values are $0.05 \leq P < 0.3$ and

$10^{-15} < C_D \leq 10^{-9}$ kg m^{-3}. For instance, let $P = 0.06$ and concentration $C_D = 10^{-12}$ kg m^{-3}. For instance, $P = 0.06$ means that there are 6 % randomly distributed concentration points out of every 100 points at the interface with concentration higher than the average interfacial concentration by 10^{-12} kg m^{-3}. For the absorption of CO_2 by ethanol as shown in Sect. 9.3.1, the concentration contours at $P = 0$ (no high concentration point) and $P = 0.06$ are given in Figs. 9.14 and 9.15 for comparison.

As shown in Fig. 9.14, if no disturbance at the interface ($P = 0$), no Rayleigh convection is found in spite of having concentration (density) difference between interface and the bulk liquid, and in the meanwhile, only molecular diffusion of solute from interface occurs. Under the condition of disturbance at the interface with $P = 0.06$ and $C_D = 10^{-12}$ kg m^{-3}, a slight deformation of the concentration contours is found at the left side near the wall at about $t = 50$–54 s, from where the Rayleigh convection initiates. The concentration cell is fully developed at $t = 65$ s, and it is squeezed by two symmetrical Rayleigh convective fluid vortexes on both sides (not shown in the figure) so as to form the inverted mushroom shape.

By this model, the simulated results of the transient fields of concentration and velocity vector under $P = 0.06$, $C_D = 10^{-12}$ are shown in Figs. 9.16 and 9.17.

As shown in Fig. 9.16, the interface displays some unstable indication at 52 s (a) and then develops randomly to nearby local points. At the same time, the developed concentration cells move downward to the bulk liquid. At 62 s, as shown in Fig. 9.17a, the velocity cell by Rayleigh convection has been formed to squeeze the concentration cell to become mushroom shape until reaching the bottom turning to anchor shape. It is noted that the circulating velocity of the velocity cell is about 10^{-3}–10^{-4} m s^{-1}, which is consistent with the experimental measurement by Chen [23] and Fu et al. [24]. The foregoing simulation demonstrates that the velocity circulation promotes the renewal of concentration around interface so as to enhance the mass transfer by Rayleigh convection.

To test the effect of P on mass transfer, the quantity of instantaneous mass transferred N (kg m^{-2} s^{-1}) can be calculated for comparison. During the gas–liquid contacting time Δt, the instantaneous simulated $N_{ins,t}$ can be calculated by the following equation between t and $t + \Delta t$:

$$N_{ins,t} = \frac{[C(t + \Delta t) - C(t)] \cdot V}{\Delta t \cdot A_i} = \frac{[C(t + \Delta t) - C(t)] \cdot H}{\Delta t} \qquad (9.13)$$

where C is the solute mass concentration; V is the volume of the liquid; A_i is the area of the flat gas–liquid contacting interface; and H is the thickness of the liquid.

Under the condition of no Rayleigh convection, the unsteady interfacial mass transferred N_{pen} can be calculated from penetration theory by the following equation:

$$N_{pen} = (C_i - C_0)\sqrt{\frac{D}{\pi t}} \qquad (9.14)$$

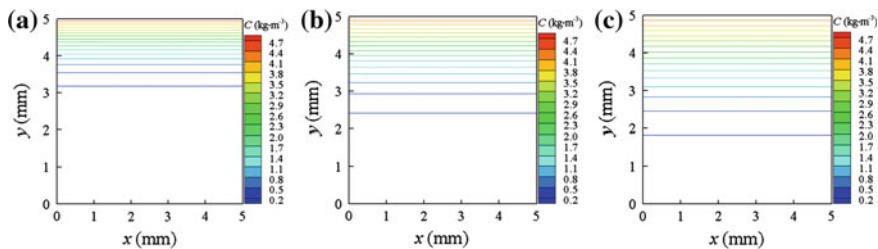**Fig. 9.14** Concentration profiles of CO_2 concentration without interfacial disturbance ($P = 0$, $C_D = 0$) at different times for CO_2 absorption by ethanol **a** $t = 100$ s, **b** $t = 200$ s, and **c** $t = 200$ s (reprinted from Ref. [22], copyright 2013, with permission from Elsevier)
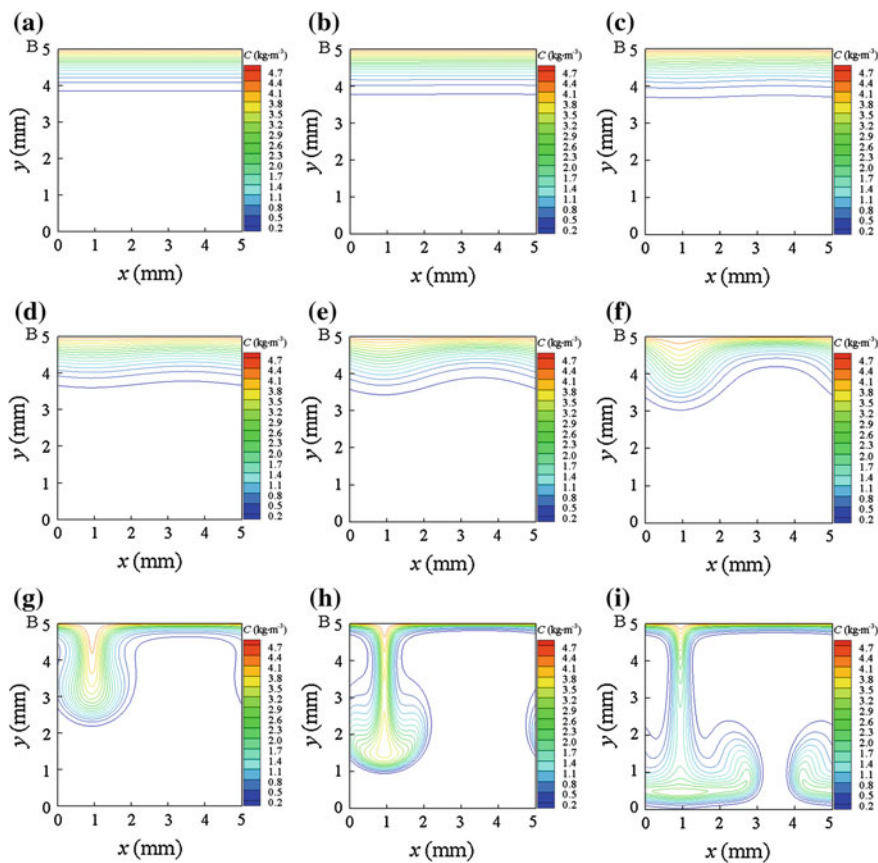

Fig. 9.15 CO_2 concentration profiles under $P = 0.06$, $C_D = 10^{-12}$ kg m^{-3} at different times for the process of CO_2 absorption by ethanol **a** $t = 40$ s, **b** $t = 45$ s, **c** $t = 50$ s, **d** $t = 52$ s, **e** $t = 54$ s, **f** $t = 56$ s, **g** $t = 58$ s, **h** $t = 60$ s, and **i** $t = 65$ s (reprinted from Ref. [22], copyright 2013, with permission from Elsevier)

Fig. 9.16 Transient concentration fields of CO_2 at 52 s (**a**) 58 s (**b**), 62 s (**c**), and 66 s (**d**) for CO_2 absorption by ethanol ($P = 0.06$, $C_D = 10^{-12}$) (reprinted from Ref. [22], copyright 2013, with permission from Elsevier)
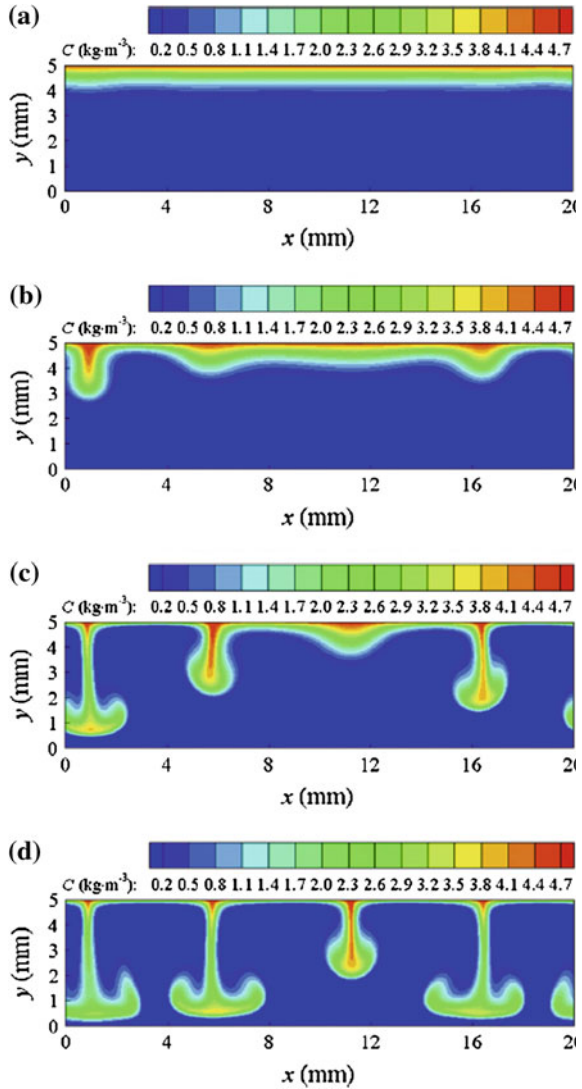

where C_i is the interfacial concentration and C_0 is the solute concentration in the solvent.

With consideration of the Rayleigh convection, the simulated concentration profiles of CO_2 absorption by ethanol at interfacial solute concentration of 5 kg m^{-3} are shown in Fig. 9.15. From such profile, the values of $N_{ins,t}$ during $C(t)$ and $C(t + \Delta t)$ are obtained by the summation of solute concentration counting in each lattice (discrete elements in computation) at time t and $t + \Delta t$. The calculated $N_{ins,t}$, denoted by N_{sim}, is given in Fig. 9.18, in which the N_{pen} by

Fig. 9.17 Transient velocity vector field at 62 s (**a**) and 66 s (**b**) for CO_2 absorption by ethanol ($P = 0.06$, $C_D = 10^{-12}$) (reprinted from Ref. [22], copyright 2013, with permission from Elsevier)
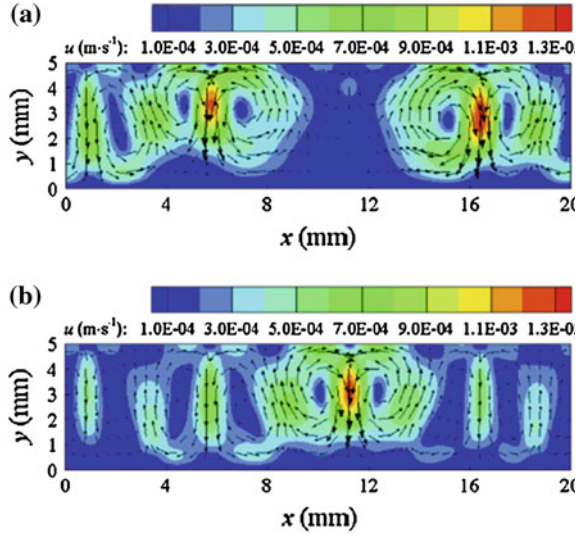
Fig. 9.18 Simulated N_{sim} by random disturbance model ($P = 0.06$, $C_D = 10^{-12}$ kg m^{-3}) and N_{pen} by penetration theory at different times (reprinted from Ref. [22], copyright 2013, with permission from Elsevier)
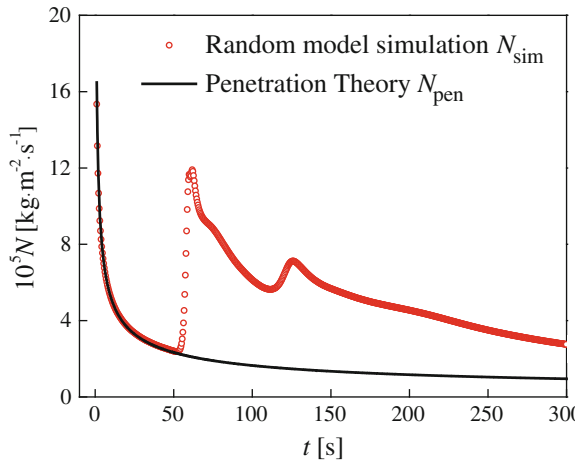
penetration theory is also shown for comparison. In this figure, the onset of Rayleigh convection is found at about 50–54 s so that the mass flux N is increased sharply. After that, the wavy fluctuation of N_{sim} is due to the alternative action of depletion and renewal of solute at the interface as a result of Rayleigh convection. Following the accumulation of solute in the liquid bulk by absorption, the driving force of mass transfer $(C_i - C_0)$ is gradually lowered to reduce both N_{sim} and N_{pen}. When the depletion of solute is compensated and renewed by Rayleigh convection, the N_{sim} goes up again. Such action keeps on alternatively, forming a wavy curve.

Fig. 9.19 Influence of P on N at $C_D = 10^{-12}$ kg m^{-3} in CO_2 absorption by ethanol
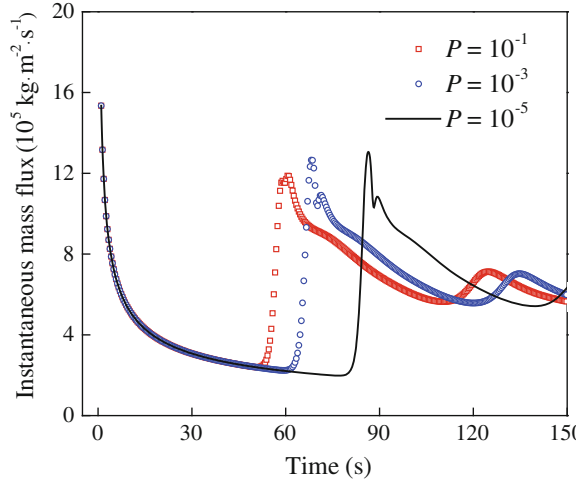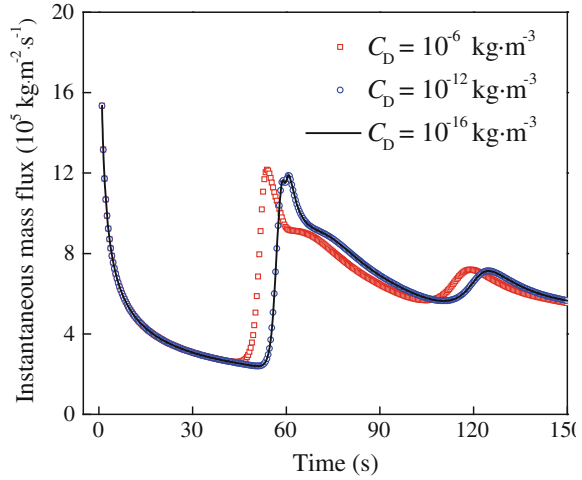

Fig. 9.20 Influence of C_D on N at $P = 0.1$ for CO_2 absorption by ethanol

The influence of parameter P on the mass flux N_{sim} is given in Fig. 9.19 where the onset time of Rayleigh convection is faster for greater P. After 120 s, the N_{sim} is almost independent of P.

The influence of C_D on the mass flux N_{sim} is also given in Fig. 9.20 where the onset time of Rayleigh convection is faster for smaller C_D; the difference in simulations at different C_D is not obvious.

The instantaneous mass transfer enhancement factor $F_{ins,t}$ can also be calculated from the N curve by the equation:

$$F_{ins,t} = \frac{N_{ins,t}}{N_{pen,t}}$$

where $N_{\text{pen},t}$ is the N by penetration theory.

The instantaneous mass transfer coefficient at time t, denoted by $k_{\text{ins},t}$, can be computed by the following equation:

$$k_{\text{ins},t} = \frac{(C_{t+\Delta T} - C_t)V}{A_i \Delta T (C_i - C_0)_{\text{av}}} = \frac{(C_{t+\Delta T} - C_t)H}{\Delta T (C_i - C_0)_{\text{av}}} \tag{9.15}$$

where C_i is the interfacial solute concentration; $(C_i - C_0)_{\text{av}}$ is the average of the driving force of mass transfer during Δt; and Δt is the time interval which is set to be 0.1 s. The computed enhancement factor $F_{\text{ins},t}$ at different interfacial solute concentrations for different absorption processes are given in Figs. 9.21 and 9.22. As indicated in the figures, the onset time (the durations for $F = 1$) is quite different for different solvents.

As shown from Fig. 9.23, the variations in $k_{\text{ins},t}$ for different interfacial concentrations of C_i have similar trend with those of the enhancement factor.

Fu further proposed more precise random disturbance model [21] by considering the position, size, and duration of concentration disturbance that should be randomly varying in the real gas–liquid mass transfer process. In this model, a probability P and a coefficient of disturbance size β are introduced to express randomness of concentration disturbance at the liquid surface. The probability P at any point in the interface represents the probability of the occurrence of concentration disturbance at that point. The distribution size C_R is proportional to the degree approach (denoted by β) of interfacial concentration C_i to the concentration of saturated liquid C_S as follows:

$$C_R = \beta(C_S - C_i)$$

Figure 9.24 is an example where the solute points with higher concentration are changing randomly at different times. As shown in the figure, the evolution of the concentration contour is stochastic without definite pattern.

As shown in Fig. 9.25, the velocity of Rayleigh convection and mutual interaction is increased with time. The random characters of both velocity and concentration are obvious.

9.5 Self-Renewable Interface Model

For the self-renewable interface model, the simulated domain as shown in Fig. 9.25 consists of two parts: the quiescent gas and liquid phases. The evolutions of concentration distributions in both gas and liquid phases are simulated, and the disturbance is maintained by the evolution of the interfacial concentration distribution. For this purpose, a zone of gas phase is imposed between the liquid and gas phases as shown in Fig. 9.25 where both gas and liquid phases are quiescent and the mass transfer in gas phase is only by molecular diffusion.

Fig. 9.21 Instantaneous mass transfer enhancement factor for different interfacial concentrations for the process of CO_2 absorption by ethanol
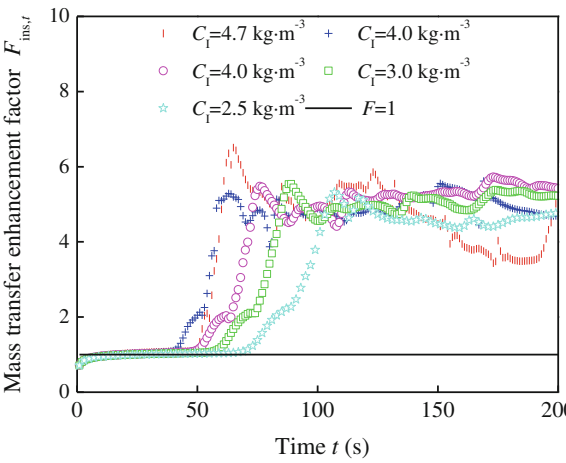

Fig. 9.22 Variation in instantaneous mass transfer enhancement factor with time for the process of CO_2 absorption by various solvents
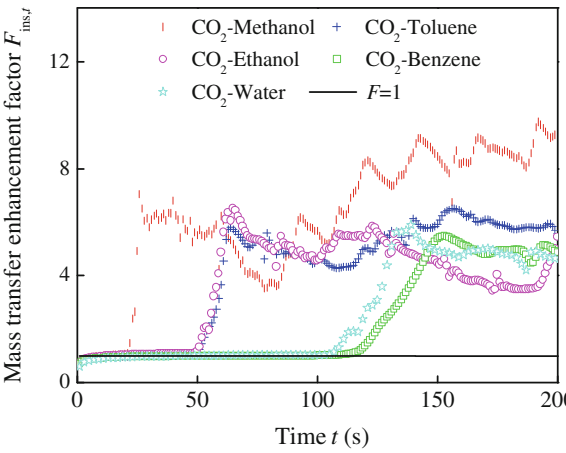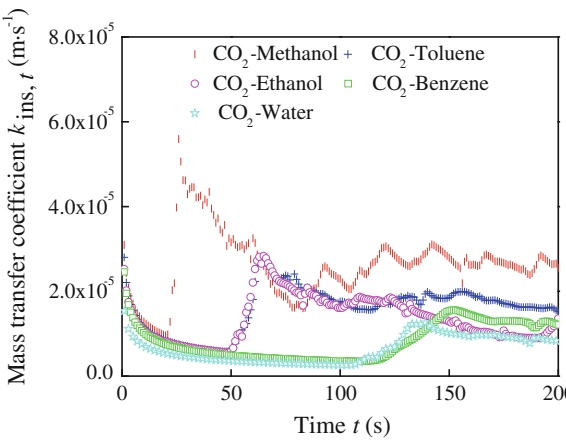

Fig. 9.23 Variation in instantaneous mass transfer coefficient with time for CO_2 absorption by various solvents
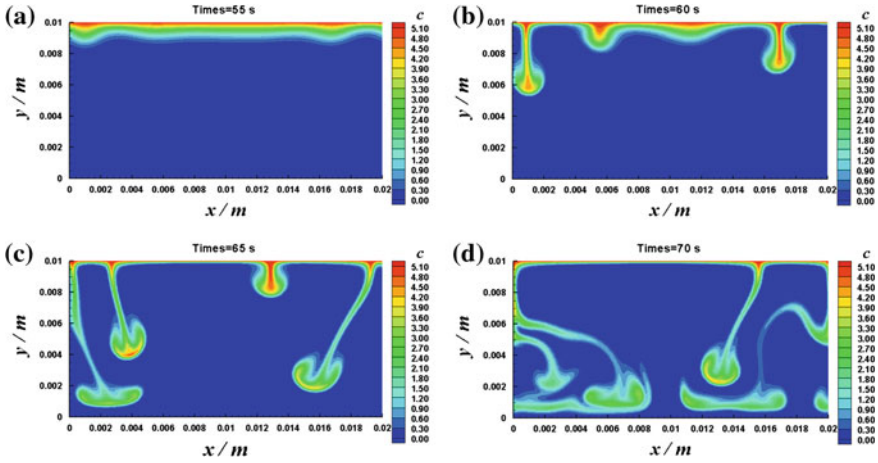
Fig. 9.24 Concentration profiles of random disturbance interfacial diffusion at different times ($P = 10^{-4}$, $\beta = 10^{-8}$) **a** $t = 55$ s, **b** $t = 60$ s, **c** $t = 65$ s, and **d** $t = 70$ s
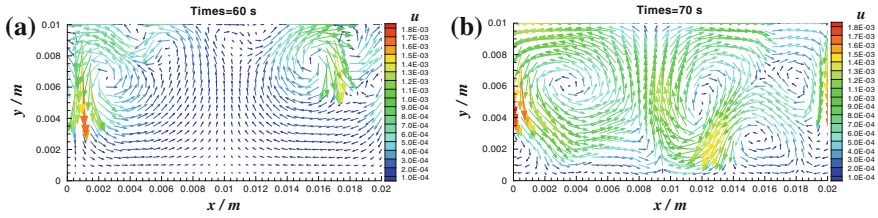

Fig. 9.25 Velocity vector of random interfacial diffusion at different times. **a** $t = 60$ s and **b** $t = 70$ s

Chen et al. [25] implemented this model by considering an instantaneous non-uniform concentration distribution of gas phase at the interface due to the localizing mass transfer from the interface to be the source of disturbance. The non-uniform distribution of concentration in the gas phase at the interface leads to different driving forces of mass transfer, and the instantaneous depletion of solute enhances the non-uniformity of the interfacial concentration so as to promote the Rayleigh convection. Moreover, in LBM, the numerical accuracy and stability are strongly dependent on the relaxation time τ (see section 9.1.4), which should be greater than 0.5. Nevertheless, as Servan-Camas [26] pointed out that the computed accuracy drops down after $\tau \approx 0.789$. In CO_2 absorption, the liquid phase Sc is in the order of 10^2, and therefore, the τ_c is out of the 0.5–0.789 satisfactory range. To overcome this difficulty, Chen employed a hybrid model for computation in which the velocity field is computed according to BGK equation and the concentration field is calculated by using finite different method (FDM).

Fig. 9.26 Schematic computational domain (reprinted from Ref. [27], copyright 2012, with permission from American Chemical Society)
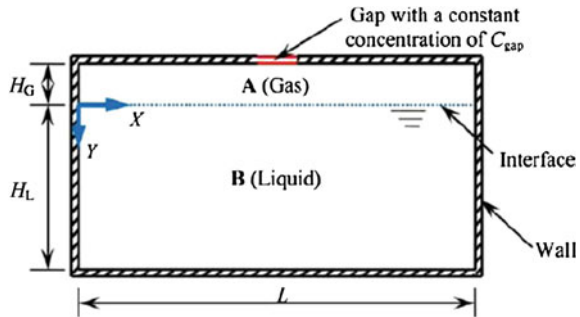
The governing equation of concentration field C_k is as follows:

$$\frac{\partial C_k}{\partial t} + \mathbf{u}\frac{\partial C^k}{\partial x} = D_k \frac{\partial^2 C_k}{\partial x^2}$$

In order to simplify the model, the following assumptions are made:

a. The mass transfer in the gas phase is only by means of molecular diffusion;
b. Gas and liquid phases are in equilibrium at the interface;
c. No mass is accumulated at the interface.

For the boundary conditions, bounce-back is applied for the solid walls. Constant concentration is implemented at the gap of upper wall as shown in Fig. 9.26. The sizes of domains A (gas) and B (liquid) in the figure are 100 mm × 5 mm ($L \times H_G$) and 100 mm × 30 mm ($L \times H_L$), respectively, and the gap of the upper wall has a width of 4 mm.

The initial condition for CO_2 absorption is $C_{0,G} = 0\,\text{kg m}^{-5}$, $C_{0,L} = 0\,\text{kg m}^{-5}$, $C_{gap} = 1.7\,\text{kg m}^{-3}$, $u_L = 0\,\text{m s}^{-1}$. The hybrid LBM-FDM method is used.

The hybrid LBM-FDM method is used for the simulation, the convection term is discretized by upwind weighted scheme, and the diffusion term is discretized by central difference scheme. Runge–Kutta scheme is employed for time stepping.

For testing the accuracy of simulation, Chen also performed the experiment under the simulated condition. The experimental setup is shown in Fig. 9.27.

The experimental results are shown in Fig. 9.28a. As shown, in the beginning, one pair of vortex is found around the center of the interface and then further develops and influences the fluid near the wall. This pattern may be as a result of faster absorption at the center of interface due to higher concentration at the gap of the upper wall so that the concentration around the center of interface is higher than the others by faster absorption. Figure 9.28b shows similar pattern by simulation as well as in (c) where concentration development from two interfacial points and penetration to the bulk liquid are seen. In Fig. 9.29, symmetric peaks in average velocity distributions along the x direction are found in both experimental and simulated results, which are corresponding to the vortex shown in Fig. 9.28.
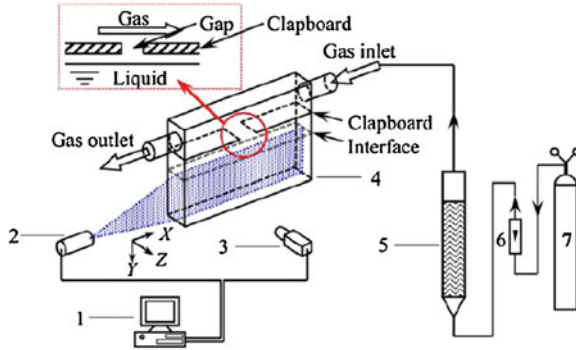
Fig. 9.27 Schematic diagram of the experimental setup (*1* computer; *2* laser source; *3* camera; *4* optical cell; *5* presaturator; *6* rotameter; *7* gas cylinder) (reprinted from Ref. [27], copyright 2012, with permission from American Chemical Society)
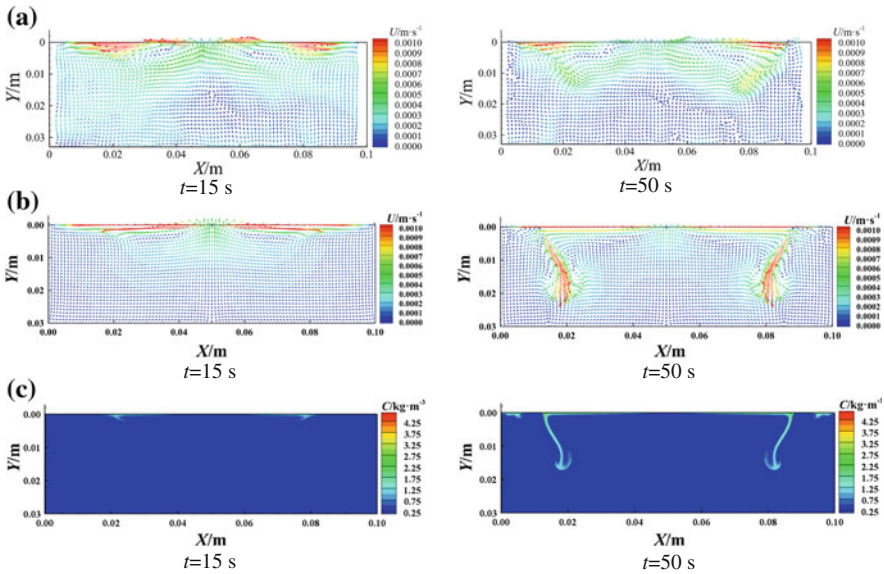

Fig. 9.28 Results of CO_2 absorption at $t = 15$ and 50 s for CO_2 absorption **a** experimental velocity distribution, **b** simulated velocity distribution, and **c** simulated concentration distribution (reprinted from Ref. [27], copyright 2012, with permission from American Chemical Society)

The peaks move toward the left and right walls with time before 50 s due to the diverging flow induced by surface concentration gradient.

From Figs. 9.28 and 9.29, it can be found that both the simulated and experimental results show the following tendency:
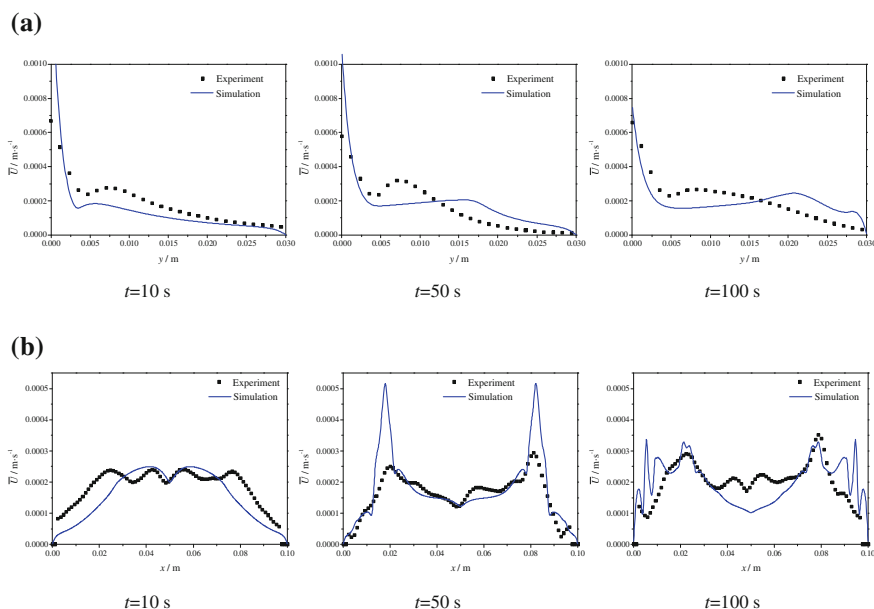
(a)

t=10 s   t=50 s   t=100 s

(b)

t=10 s   t=50 s   t=100 s

Fig. 9.29 Simulated and experimental results on average velocity distributions for CO_2 absorption at different times **a** along Y (vertical) direction and **b** along X (horizontal) direction (reprinted from Ref. [27], copyright 2012, with permission from American Chemical Society)

a. The maximum velocity appears at the liquid surface, and the average velocity decreased rapidly in the direction perpendicular to the liquid surface;
b. The convection was centered in a region of $Y = 0$–0.01 m. The simulated average velocity at the liquid surface is higher than the experimental measurement. The deviation may be due to the fact that the simulation is two-dimensional, and the experiment is under three-dimensional performance.

As shown in Fig. 9.29, the velocity of Rayleigh convection and mutual interaction is increased with time. The random characters of both velocity and concentration are obvious.

9.6 Summary

In short, any disturbance on concentration or temperature at interface may create interfacial surface tension gradient and also the density difference between interface and the bulk fluid is the cause to initiate Marangoni and Rayleigh convections; the former is mainly acting around interface, and the latter is circulated between interface and the bulk fluid. The influence of Marangoni convection and Rayleigh convection on the mass transfer is significant as seen by the increase in

enhancement factor by simulations and experimental measurement as described in this chapter and Chap. 8. The necessary conditions for initiating both Rayleigh and Marangoni convections are as follows: Firstly, the Ra and Ma numbers should exceed the critical value, and secondly, the interface should be disturbed at least one point to initiate the instability. Based on the conditions of the disturbed points, different interfacial models are proposed, such as

- Fix point interfacial disturbance model, in which the disturbed points are presented.
- Random disturbance interfacial model, in which the disturbed points are stochastic.
- Self-renewable interface model, in which the non-uniform distribution of absorbed solute concentration in gas phase leads to have local mass transfer at the interface so that non-uniform solute concentration is established there as the sources of disturbance. In simulation, the velocity field is computed according to BGK equation and the concentration field is calculated by using finite difference method (FDM) in order to ensure the numerical stability.

Remarks are made for the simulation that in the course of computation, the numerical disturbance may affect the simulated result. For instance, in the absorption process as shown in Fig. 9.13, since the bounce-back boundary condition is applied, numerical disturbance is arising from the two sides of the container wall to make the Rayleigh convection appeared primo near the wall as shown in Figs. 9.10 and 9.24. Such convection promotes the instability of neighboring interfacial concentration points and induces subsequent Rayleigh convections. Nevertheless, by using the LBM-FDM method of computation, the Rayleigh convection firstly appears away from the wall as shown in Fig. 9.27. However, in spite of the location of the initial disturbance, the appearance of both convections is developing with time and spreading out to the whole fluid body so as to promote the interface renewal and enhance the mass transfer until the process reaches stable state.

References

1. Frisch U, Hasslacher B, Pomeau Y (1986) Lattice-gas automata for the Navier-Stokes equation. Phys Rev Lett 56(14):1505–1508
2. Wolfram S (1986) Cellular automaton fluids 1: basic theory. J Stat Phys 45:471–526
3. Chen SY, Chen HD, Martinez D, Matthaeus W (1991) Lattice Boltzmann model for simulation of magnetohydrodynamics. Phys Rev Lett 67(27):3776–3780
4. Qian YH, D'Humieres D, Lallemand P (1992) Lattice BGK model for the Navier-Stokes equation. Europhys Lett 17(6):479–484
5. Bhatnagar PL, Gross EP, Krook M (1954) A model for collision processes in gases. I. Small amplitude processes in charged and neutral one-component systems. Phys Rev 94(3):511–525
6. McNamara GR, Zanetti G (1988) Use of the Boltzmann equation to simulate lattice-gas automata. Phys Rev Lett 61(20):2332–2335

7. Chen HD, Chen SY, Matthaeus WH (1992) Recovery of the Navier-Stokes equation using a lattice-gas Boltzmann method. Phys Rev A 45(8):5339–5342

8. Wagner AJ (2008) A practice introduction to lattice Boltzmann method. North Dakota State University

9. Hou S, Zou Q, Chen SY, Doolen GD, Cogley AC (1995) Simulation of cavity flow by the lattice Boltzmann method. J Compt Phys 118(329):347

10. Chen SY, Martinez D, Mei RW (1996) On boundary conditions in lattice Boltzmann methods. Phys Fluid 8(9):2527–2536

11. Skordos PA (1993) Initial and boundary conditions for the lattice Boltzmann method. Phys Rev E 48(6):4823–4842

12. Maier RS, Bernard RS, Grunau DW (1996) Boundary condition for the lattice Boltzmann method. Phys Fluids 8(7):1788–1801

13. Inamuro T, Yoshino M, Ogino F (1995) A non-slip boundary condition for lattice Boltzmann simulations. Phys Fluids 7(12):2928–2930

14. He XY, Chen SY, Zhang RY (1999) A lattice Boltzmann scheme for incompressible multiphase flow and its application in simulation of Rayleigh–Taylor instability. J Compt Phys 152:633–642

15. Dixit HN, Babu V (2006) Simulation of high Rayleigh number natural convection in a square cavity using the lattice Boltzmann method. Int J Heat Mass Transfer 49:727–739

16. Guo ZL, Zhao TS (2005) Lattice Boltzmann simulation of natural convection with temperature-dependent viscosity in a porous cavity. Prog Comput Fluid Dyn 5:110–117

17. He XY, Chen SY, Doolen GD (1998) A novel thermal model for the lattice Boltzmann method in incompressible limit. J Comput Phys 146:282–300

18. Dawson SP, Chen S, Doolen GD (1993) Lattice Boltzmann computations for reaction-diffusion equation. J Chem Phys 98(2):1514–1523

19. Fu B, Yuan XG, Liu BT, Yu GC, Chen SY (2010) Simulation of Rayleigh convection in gas-liquid mass transfer using lattice Boltzmann method. The 13th Asia Pacific Confederation of Chemical Engineering Congress, 2010

20. Fu B, Yuan XG, Chen SY, Liu BT, Yu GC (2011) Lattice-Boltzmann method for Rayleigh convection and its influence on interfacial mass transfer. CIESC J (Huagong Xuebao) 62(11):2933–3000

21. Fu B (2012) Rayleigh convection and its effect on interfacial mass transfer based on lattice-Boltzmann method. Ph.D. dissertation, Tianjin University, Tianjin, China

22. Fu B, Liu BT, Yuan XG, Chen SY, Yu KT (2013) Modeling of Rayleigh convection in gas–liquid interfacial mass transfer using lattice Boltzmann method. Chem Eng Res Design 91:437–447

23. Chen W (2010) Experimental measurement of gas–liquid interfacial Rayleigh- Bénard-Marangoni convection and mass transfer. Ph.D. dissertation, Tianjin University, Tianjin, China

24. Fu B, Yuan XG, Liu BT, Chen SY, Zhang HS, Zeng AW, Yu GC (2011) Characterization of Rayleigh convection in interfacial mass transfer by lattice Boltzmann simulation and experimental verification. Chinese J Chem Eng 19:845–854

25. Chen SY, Fu B, Yuan XG, Zhang HS, Chen W, Yu KT (2012) Lattice Boltzmann method for simulation of solutal interfacial convection in gas-liquid system. Ind Eng Chem Res 51:10955–10967

26. Servan-Camas B, Tsai FTC (2008) Lattice Boltzmann method with two relaxation times for advection-diffusion equation: third order analysis and stability analysis. Adv Water Resour 31(8):1113–1126

27. Chen SY, Fu B, Yuan XG, Zhang HS, Chen W, Yu KT (2012) Lattice Boltzmann method for simulation of solutal interfacial convection in gas–liquid system. Ind Eng Chem Res 51:10955–10967